



The
University
Of
Sheffield.

Identifying the transcriptomic basis underlying individualised drug response: moving towards personalised medicine in ALS using patient-derived astrocytes

Chloe Allen

A thesis submitted in partial fulfilment of the requirements for the degree of
Doctor of Philosophy

The University of Sheffield
Faculty of Medicine, Dentistry and Health
Department of Neuroscience
Sheffield Institute for Translational Neuroscience (SITraN)

January 2021

Preface

This thesis contains no material which has been accepted for the award of another degree or qualification. To the best of my knowledge, this thesis contains no previously published material, except where reference is made in the text.

My primary supervisor Dr Laura Ferraiuolo and co-supervisor Professor Dame Pamela Shaw provided supervision, technical guidance, assistance with study design as well as the preparation of this thesis.

This thesis follows the monograph thesis format. Chapter 1 provides a general introduction to amyotrophic lateral sclerosis (ALS) and how the cell model present within this study, astrocytes, have been used in personalised medicine for neurodegenerative disorders. Successively, Chapter 2 describes in detail the materials and methods used in the experiments displayed in chapters 3-6. The first results chapter, Chapter 3, presents the phenotypic data generated from the patient-derived cell model demonstrating how reprogrammed astrocytes are a reliable model for the heterogenous disease features seen in ALS patients. In succession, Chapter 4 seeks to examine the effects of antioxidant compounds onto the pathogenic features assessed in Chapter 3 to investigate how these compounds provided cellular benefit and survival *in vitro*. For example, I have shown that the addition of S[+]-apomorphine reduced the expression of misfolded SOD1 protein aggregates in patient-derived astrocytes and that the compound andrographolide had a significant effect on the levels of p62 protein across all cell lines. The following results chapters, Chapters 5 and 6, present the results of the RNA sequencing data of the patient cell lines before and after drug treatment. While Chapter 5 focuses on the main Gene Ontology (GO) pathways that differ between the patient genetic subgroups at baseline as well as after drug treatment, Chapter 6 presents the differences in gene expression between patient responders and non-responders to a particular compound. In fact, I have identified a panel of genetic biomarkers within each patient response group that were distinguishable from the patient non-responders, therefore having the potential to identify patients that respond to this treatment. Finally, Chapter 7 provides an overall discussion of the results presented in the previous chapters and how these data can drive future research.

Abstract

Medicine is moving away from a 'one size fits all' approach and instead focusing on how individual genetic characteristics determine treatment response. Therapeutic approaches towards ALS have always proven difficult due to the impressive genetic and phenotypic heterogeneity of the disease, indicating the need for a precision medicine approach. A previous in house high-throughput drug screening using directly reprogrammed iAstrocytes from patient fibroblasts identified compounds with a patient-specific neuroprotective profile. The goal of this study was to decipher the transcriptional signatures that will discriminate between patient responders to specific drugs as well as investigating drug response at a cellular level. A combination of immunofluorescence approaches, functional studies to assess glutamate handling and mitochondrial function, as well as RNA-sequencing of poly-adenylated RNAs was used to identify patient-specific pathogenic characteristics and drug response in iAstrocytes from three unaffected individuals, 3 C9ORF72, 3 SOD1 and 3 sALS patients, in response to riluzole as well as two Nrf2 activator compounds.

Immunostaining and functional studies showed that, overall, astrocytes derived from SOD1 patients displayed significantly higher levels of misfolded SOD1 aggregates, while C9ORF72 iAstrocytes displayed significantly higher levels of p62 puncta, as expected from post-mortem tissue data. While some SOD1 iAstrocytes displayed mitochondrial fragmentation, the C9ORF72 lines presented a more fused mitochondrial network. In addition, C9ORF72 iAstrocytes presented a significant impairment in glutamate uptake. Interestingly, sALS iAstrocytes displayed a mix of features, including accumulation of p62, SOD1 misfolding and TDP-43 nuclear loss and cytoplasmic aggregation.

Pathway analysis of the RNA-sequencing data demonstrated that all ALS patient lines shared common disease mechanisms, such as dysregulated glutamatergic neurotransmission, axonal maintenance and guidance, and vesicular trafficking within the cytoplasm. Further functional and transcriptional analysis taking into account drug response, regardless of the patient genotype, identified specific functional and transcriptional features that correlated with drug responders vs non-responders for riluzole and the two Nrf2 activators. In addition, and of potential massive impact for patient stratification, I identified a preliminary panel of specific gene signatures of patient responders to a certain drug. These transcriptional changes were absent in the patient non-responders to the specific compound, indicating that the drug acts upon a group of transcripts that identifies specific mechanisms that are impaired in a group of patients, but not in others.

By using patient-derived cells, this study has identified pathological and transcriptional patient-specific features, some of which are genotype-driven, while others are idiosyncratic, that have a great potential for patient stratification and precision medicine approaches.

Acknowledgements

I would like to begin by thanking both of my supervisors, Dr Laura Ferraiuolo and Professor Dame Pamela Shaw, for all their support and guidance during my PhD. As my primary supervisor, Laura has helped me greatly with the development of my knowledge and training as a research scientist and Pam has provided me with great advice and thoughts for my future career. Additionally, a big thank you to Dr Mark Dunning for all his help with the preparation and analysis of my RNA-sequencing data. I would also like to thank the MRC DiMeN Doctoral Training Partnership for my research funding during my PhD. In particular, I would like to thank Dr Emily Goodall for organising some amazing events for all the students and for being the mother hen that many of us needed. Thank you also to my new team at IN-PART who have been so lovely, and no doubt will be keeping me calm during my viva preparations.

Furthermore, I would like to thank everyone in the Ferry lab, Matt, Cleide, Sophie, Nora, Monika, Noemi, Andre, Allan, Lai Mei, Simon, Jannigje and Marco for their continuous love and support. You are all amazing people and brilliant scientists, and I have no doubt that you will all go far in your endeavours. Thank you to all my wonderful colleagues in SITraN, I would particularly like to thank my fellow PhD students Katie, Ruby, Charlie, and Chris as well as Camilla and Aurélie for sharing this journey with me. A big thank you to Amy and Charlotte for always checking up on me and for forming the amazing PhD support group for those of us struggling with mental health. Also big thanks to the wonderful people I have met through the DiMeN program, especially Josh who has been a great friend of mine during these past few years!

Next, I would like to acknowledge my family, my parents Mark and Sue and my human siblings Claire, James, and Jonny as well as my fur siblings Mollie, Dexter, and Archie. Thank you for all your love and support during this difficult and challenging time. I would also like to thank my best friends Kerry, Georgia, Emma, and Sam for keeping me smiling although we are thousands of miles apart.

Lastly, I would like to thank my little family, my partner Harry, and our rescue greyhound Blue. Thank you so much to Harry, for being my rock and helping me through my darkest times. I do not think I could have done this without you. And thank you to Blue for giving me cuddles when I needed them most.

Thank you very much to everyone (sorry if I missed you!), honestly everyone I have met over this period of my life had made an impact on me in some way. I cannot quite believe this journey is over, but I am excited for what the future holds!

Don't cry because it is over, cry because it happened. Ethan Nestor, Unus Annus, 2020

Table of Contents

Chapter 1 - Introduction	1
1.1. Amyotrophic Lateral Sclerosis.....	1
1.1.1 Clinical features.....	1
1.1.2. Epidemiology and genetics	2
1.1.2.1. SOD1.....	4
1.1.2.2. TARDBP	5
1.1.2.3. FUS	6
1.1.2.4. C9ORF72.....	6
1.1.2.5. Other ALS-associated genes.....	7
1.1.2.6. Environmental factors.....	10
1.1.3. Pathogenesis	10
1.1.3.1. Oxidative stress.....	10
1.1.3.2. Protein misfolding and aggregation.....	11
1.1.3.3. Endoplasmic-reticulum stress.....	12
1.1.3.4. Dysregulated RNA metabolism	12
1.1.3.5. Axonal transport	13
1.1.3.6. Mitochondrial dysfunction.....	13
1.2. Non-cell autonomous toxicity.....	14
1.2.1. The role of astrocytes in ALS.....	14
1.2.1.1. Glutamate metabolism	15
1.2.1.2. Neuronal development and support	17
1.2.1.3. Inflammation and immune response.....	18
1.2.1.4. Protein aggregation	19
1.2.2. Astrocyte models of ALS	19
1.2.2.1. Primary astrocytes and neural progenitor cells.....	19
1.2.2.2. iPSC-derived astrocytes	20
1.2.2.3. Direct reprogramming	21
1.2.2.4. Astrocyte-MN co-culture	22
1.3. ALS therapeutics	22
1.3.1. Gene replacement therapy	22
1.3.2. Therapeutic compounds	23
1.3.2.1. Riluzole.....	23
1.3.2.2. Edaravone	24
1.3.2.3. Traditional antioxidants	24
1.3.2.4. Nrf2 activators	25

1.4. Personalised medicine	27
1.4.1. The uses of personalised medicine in disease	27
1.4.2. Personalised medicine in neurodegeneration	28
1.4.2.1. ALS.....	28
1.4.2.2. Alzheimer’s disease.....	29
1.4.2.3. Parkinson’s disease	30
1.4.3 Astrocytes driving therapeutics	32
1.4.3.1. Cellular transplantation therapy.....	32
1.4.3.2. Drug screening	33
1.4.3.3. Genomics and Transcriptomics.....	35
1.4.3.4. Biomarkers	36
1.5. Hypothesis & Aims	39
Chapter 2 - Materials & Methods	41
2.1. Materials	41
2.1.1. Cell culture media and reagents	41
2.1.2 Solutions.....	43
2.1.3. Cell culture	43
2.1.3.1. Induced neural progenitor cells (iNPCs)	43
2.1.3.2. Hb9-GFP mouse embryonic stem cells (mESC).....	44
2.1.4. Antibodies	45
2.1.4.1. Immunocytochemistry antibodies	45
2.1.4.2. Western blot antibodies	46
2.1.5. Primers.....	47
2.2 Methods.....	47
2.2.1 Derivation of the cell model.....	47
2.2.1.1. Preparation of iAstrocytes for cellular assay	47
2.2.1.2 Drug treatment	49
2.2.1.3. Differentiation and dissociation of mouse embryonic motor neurons for cellular assay	49
2.2.2. Survival assay – iAstrocyte-MN co-culture	51
2.2.3 Immunocytochemistry	52
2.2.3.1 Cell fixing.....	52
2.2.3.2 Immunofluorescent staining.....	52
2.2.3.3 Columbus analysis.....	52
2.2.4. Western blotting	55
2.2.4.1. Preparation of soluble, RIPA and insoluble protein fractions.....	55

2.2.4.2. SDS Page.....	55
2.2.4.3. Immunoblotting and densitometry	57
2.2.4.4. SYPRO Ruby Red staining	57
2.2.5. Mitochondrial membrane potential assay.....	58
2.2.5.1 MMP preparation	58
2.2.5.2 IN-CELL analysis.....	58
2.2.6. Genome-wide RNA Analysis of Stalled Protein Synthesis (GRASPS).....	60
2.2.6.1. Ribosomal purification	60
2.2.6.2. mRNA purification.....	61
2.2.6.3. RNA quality assessment.....	62
2.2.6.4. Ribosomal RNA depletion	62
2.2.7. Sample validation.....	64
2.2.7.1. Reverse transcription.....	64
2.2.7.2. Quantitative Polymerase Chain Reaction (QPCR).....	64
2.2.8. RNA-sequencing.....	65
2.2.8.1. Quality Control.....	65
2.2.8.2. Sequence Alignment and Differential Expression.....	66
2.2.8.3. Normalisation of read counts	66
2.2.8.4. Functional annotation and Pathway analysis	67
2.2.9. Glutamate analysis.....	67
2.2.9.1. Media collection.....	67
2.2.9.2. Colorimetric assay.....	67
2.3. Statistical analysis methods.....	69
Chapter 3 - Characterisation of the pathophysiological characteristics of iAstrocytes derived from ALS patient fibroblasts with C9ORF72 expansions, SOD1 mutations and sporadic cases.....	70
3.1. Introduction	70
3.2. Results.....	72
3.2.1. Expression of glial markers	72
3.2.2. Immunocytochemistry of pathological markers.....	74
3.2.2.1. TDP-43.....	74
3.2.2.2. Misfolded SOD1 (misSOD1)	76
3.2.2.3. Sequestosome-1 / p62.....	78
3.2.3 Mitochondrial dynamics	80
3.2.4. Glutamate buffering.....	85
3.2.4.1. Extracellular glutamate assay	85
3.2.4.2. Glutamate transporters and receptors.....	87

3.3 Discussion.....	89
3.3.1. TDP-43 mislocalisation and aggregation.....	90
3.3.2. SOD1 misfolding.....	91
3.3.3. Autophagy.....	92
3.3.4. Mitochondrial dynamics.....	94
3.3.5. Glutamate transport.....	95
3.3.6. Toxicity.....	97
3.3.7. Conclusions.....	99
Chapter 4 - Investigating the effect of Nrf2 activators on cellular function in ALS astrocytes.....	100
4.1. Introduction.....	100
4.2. Results.....	101
4.2.1. NRF2-ARE pathway.....	101
4.2.2. MN survival in iAstrocyte co-culture.....	103
4.2.3. TDP-43 proteinopathy.....	105
4.2.4. SOD1 misfolding.....	107
4.2.4.1. Misfolded SOD1 aggregates.....	107
4.2.4.2. Molecular protein chaperones.....	109
4.2.5. Autophagy regulator expression – p62 and LC3 proteins.....	113
4.2.6. Mitochondrial dynamics.....	118
4.2.7. Glutamate buffering.....	122
4.2.7.1. Extracellular glutamate assay.....	122
4.2.7.2. Glutamate transporters and receptors.....	124
4.3. Discussion.....	126
4.3.1. Protein aggregation.....	126
4.3.2. Autophagy and p62.....	128
4.3.3. Mitochondrial dynamics.....	129
4.3.4. Glutamate transport.....	130
4.3.5. Conclusion.....	132
Chapter 5 - RNA-sequencing data determines mechanism of action of antioxidant compounds across different genetic subgroups of ALS patients.....	134
5.1. Introduction.....	134
5.2. Results.....	136
5.2.1. RNA extraction and quality control.....	136
5.2.2. RNA-sequencing data quality assessment.....	138
5.2.3. Pathway analysis discriminating different patient subgroups.....	143
5.2.4. S[+]-Apomorphine treatment across patient subgroups.....	154

5.2.5. Andrographolide treatment across patient subgroups	160
5.2.6. Riluzole treatment across patient subgroups	166
5.3. Discussion.....	172
5.3.1. Baseline gene expression in patient subgroups vs controls	172
5.3.1.1. Glutamate excitotoxicity and neuroinflammation	173
5.3.1.2. Vesicle trafficking.....	177
5.3.1.3. Cholesterol and axonal guidance	178
5.3.2. Mechanism of action of Nrf2 compounds; S[+]-apomorphine and andrographolide	180
5.3.3. Riluzole treatment	185
5.3.4. Conclusion.....	186
Chapter 6 - Investigating the potential for a personalised medicine approach in ALS using patient-derived astrocytes.....	188
6.1. Introduction	188
6.2. Results.....	189
6.2.1. Patient response at baseline.....	189
6.2.2. S[+]-Apomorphine response	198
6.2.3. Andrographolide response	205
6.2.4. Riluzole response	211
6.3 Discussion.....	216
Chapter 7 - General Discussion	219
Chapter 8 - Bibliography	225
Chapter 9 - Output from my PhD work: awards, communications, and publications.....	265
9.1 Awards	265
9.2 Communications at national and international scientific meetings	265
9.3 Publications.....	266
Chapter 10 - Appendix	267

List of Tables

Table 1.1 Genetic variants associated with ALS.	8
Table 1.2 Protocols for astroglial differentiation from stem cells.....	21
Table 1.3 Current clinical trials using transplantation of glia progenitors for ALS	32
Table 2.1 Composition of solutions used in experiments	43
Table 2.2 Patient information of the iNPC lines	44
Table 2.3 Primary and secondary antibodies used to detect astrocyte and pathological markers	45
Table 2.4 Primary and secondary antibodies used to detect proteins on a nitrocellulose membrane.....	46
Table 2.5 List of genes used for RT-PCR validation and their corresponding primer sequences	47
Table 2.6 Composition of 5% Stacking gels, 10%, 12% and 15% Resolving gels.	56
Table 2.7 Composition of the RNA/probe Master Mix per sample	62
Table 2.8 PCR programme for Ribosomal RNA Depletion Protocol	62
Table 2.9 Composition of RNase H Digestion Master Mix.....	63
Table 2.10 Composition of DNase I Digestion Master Mix.....	63
Table 2.11 Composition of cDNA Reverse Transcription Master Mix	64
Table 2.12 PCR programme for cDNA Reverse Transcription Protocol.....	64
Table 2.13 Composition of qPCR Master Mix	65
Table 2.14 PCR programme for RT-PCR.....	65
Table 2.15 Composition of the glutamate standard according to protocol	68
Table 2.16 Dilution factor of iAstrocyte condition media with glutamate assay buffer for different samples	68
Table 2.17 Composition of Glutamate Reaction Mix and Background Reaction Mix	68
Table 5.1 List of bioinformatic comparisons for baseline RNA-sequencing and the gene output	143
Table 5.2 List of GO pathways shared between ALS patient subgroups	148
Table 5.3 Gene Ontology pathways unique to C9ORF72 patient iAstrocyte lines	151
Table 5.4 Gene Ontology pathways unique to SOD1 patient iAstrocyte lines	153
Table 5.5 Gene Ontology pathways unique to sALS patient iAstrocyte lines.....	153
Table 5.6 List of bioinformatic comparisons for S[+]-apomorphine treated iAstrocytes and gene count	156
Table 5.7 List of GO pathways shared between ALS patient subgroups treated with S[+]-apomorphine	158
Table 5.8 List of bioinformatic comparisons for andrographolide treated iAstrocytes and gene count	162
Table 5.9 List of GO pathways shared between ALS patient subgroups treated with andrographolide	164
Table 5.10 List of bioinformatic comparisons for riluzole treated iAstrocytes and gene count	167
Table 5.11 List of GO pathways shared between ALS patient subgroups treated with riluzole	169
Table 6.1 Patient responders to S[+]-apomorphine, andrographolide and riluzole	190
Table 6.2 List of bioinformatic comparisons for patient responders at baseline.....	190
Table 6.3 List of shared transcripts between patient response groups	191
Table 6.4 List of transcripts unique to S[+]-apomorphine patient line responders	194
Table 6.5 List of transcripts unique to andrographolide patient line responders.....	196
Table 6.6 List of transcripts unique to riluzole patient line responders.....	197
Table 6.7 List of bioinformatic comparisons for S[+]-apomorphine patient responders.....	199
Table 6.8 List of genes unique to S[+]-apomorphine responders untreated vs CTR untreated.....	201
Table 6.9 List of bioinformatic comparisons for andrographolide patient responders	205
Table 6.10 List of genes unique to andrographolide responders untreated vs CTR untreated	207

Table 6.11 List of bioinformatic comparisons for riluzole patient responders 211
Table 6.12 List of genes unique to riluzole responders untreated vs CTR untreated 213

List of Figures

Figure 1.1 Proportion of ALS explained by the four most common mutant genes across European and Asian populations.....	3
Figure 1.2 The non-cell autonomous mechanisms of disease in ALS astrocytes	16
Figure 1.3 The KEAP1/NRF2 pathway	26
Figure 1.4 Astrocytes as a target for personalised medicine in ALS.....	38
Figure 2.1 Direct conversion of ALS patient fibroblasts into iNPC	48
Figure 2.2 Differentiation of mESCs into murine Hb9-GFP+ MNs over a 7 day differentiation	50
Figure 2.3 Columbus image analysis of immunocytochemistry	54
Figure 2.4 IN-CELL Developer analysis of mitochondrial staining	59
Figure 3.1 Representative images showing the expression of glial membrane and cytoplasmic marker.....	73
Figure 3.2 TDP-43 localisation and protein expression in control and patient iAstrocytes.	75
Figure 3.3 Quantification of misSOD1 in control and patient iAstrocytes	77
Figure 3.4 Quantification of p62 expression in control and patient iAstrocytes.....	79
Figure 3.5 Optimisation of mitochondrial membrane potential (MMP) assay with one control and one sALS patient iAstrocyte line	81
Figure 3.6 Quantification of the morphological changes in control and patient iAstrocyte mitochondria.....	84
Figure 3.7 Quantification of extracellular glutamate in control and patient iAstrocytes	86
Figure 3.8 Quantification of glutamate transporters and receptors in control and C9ORF72 iAstrocytes	88
Figure 3.9 Summary of the pathological markers in patient iAstrocytes compared to the level of toxicity of iAstrocytes in co-culture	98
Figure 4.1 ARE protein NQO1 expression in control and patient iAstrocytes before and after drug treatment.....	102
Figure 4.2 High through-put drug screening analysis of antioxidant compounds andrographolide, S[+]-apomorphine and MMF, alongside riluzole in iAstrocyte-MN co-culture experiments	104
Figure 4.3 Quantification of soluble and insoluble TDP-43/TDP-35 protein in control and C9ORF72 iAstrocytes before and after andrographolide treatment.....	106
Figure 4.4 Quantification of misSOD1 aggregates in the perinuclear region of iAstrocytes before and after drug treatment.....	108
Figure 4.5 Quantification of total SOD1 protein in control, sALS and SOD1 iAstrocytes before and after drug treatment.....	110
Figure 4.6 Quantification of HSF1 and HSP70 baseline protein levels in control, sALS and SOD1 iAstrocytes	111
Figure 4.7 Quantification of HSP70 protein levels in control, sALS and SOD1 iAstrocytes before and after drug treatment.....	112
Figure 4.8 Representative images showing the expression of p62 and CD44 in control and patient cells before and after treatment with S[+]-apomorphine and andrographolide	114
Figure 4.9 Quantification of p62 expression in control and patient iAstrocytes before and after drug treatment.....	115
Figure 4.10 Quantification of autophagy markers p62 and LC3-I/LC3-II protein expression in control and C9ORF72 patient iAstrocytes before and after drug treatment.....	117
Figure 4.11 Visualisation of mitochondria in control and patient iAstrocytes before and after treatment with andrographolide.....	119

Figure 4.12 Quantification of mitochondrial dynamics in control and patient iAstrocytes before and after andrographolide treatment	120
Figure 4.13 Quantification of mitochondrial form factor in control and patient iAstrocytes before and after treatment	121
Figure 4.14 Quantification of extracellular glutamate in iAstrocyte-conditioned media before and after riluzole treatment	123
Figure 4.15 Quantification of EAAT2 and NMDAR2B protein levels in control and C9ORF72 iAstrocytes before and after drug treatment	125
Figure 4.16 Summary table of the effect of riluzole and the antioxidant compounds in each of the phenotypic assays	133
Figure 5.1 PicoChip analysis of RNA quality and integrity assessed using the Agilent 2100 Bioanalyser	137
Figure 5.2 Quality assessment of RNA sequencing reads for all 96 samples before and after the removal of the rRNA mapped reads	140
Figure 5.3 RNA-sequencing quality control analysis.....	142
Figure 5.4 PCA plot of the gene expression values of control and patient iAstrocyte lines at untreated baseline	144
Figure 5.5 Visual representation of the dysregulated transcripts shared between the different patient subgroups	146
Figure 5.6 PCA plot of the gene expression values of control and patient astrocyte lines before and after S[+]-apomorphine treatment.....	155
Figure 5.7 Visual representation of the DEGs shared between the control and different patient subgroups after S[+]-apomorphine treatment	157
Figure 5.8 PCA plot of the gene expression values of control and patient astrocyte lines before and after andrographolide treatment	161
Figure 5.9 Visual representation of the DEGs shared between the control and different patient subgroups after andrographolide treatment.....	163
Figure 5.10 PCA plot of the control and patient astrocyte lines before and after riluzole treatment..	168
Figure 5.11 Visual representation of the DEGs shared between the control and different patient subgroups after riluzole treatment.....	170
Figure 5.12 Heatmap of RNA-sequencing data from untreated control and patient iAstrocyte lines	187
Figure 6.1 Visual interpretation of the DEGs shared between the different patient response groups	192
Figure 6.2 Visual interpretation of the DEGs shared between S[+]-apomorphine response comparisons.....	200
Figure 6.3 The normalised gene counts for patient responders and non-responders to S[+]-apomorphine before and after drug treatment	203
Figure 6.4 The summary of the gene expression change in each biomarker identified within the S[+]-apomorphine treatment response group.....	204
Figure 6.5 Visual interpretation of the DEGs shared between andrographolide response comparisons	206
Figure 6.6 The normalised gene counts for patient responders and non-responders to andrographolide before and after drug treatment	209
Figure 6.7 The summary of the gene expression change in each biomarker identified within the andrographolide treatment response group.....	210
Figure 6.8 Visual interpretation of the DEGs shared between riluzole response comparisons.....	212

Figure 6.9 The normalised gene counts for patient responders and non-responders to riluzole before and after drug treatment..... 214

Figure 6.10 The summary of the gene expression change in each biomarker identified within the riluzole treatment response group 215

List of Abbreviations

A β	Amyloid beta
ABC	ATP-binding cassette transporter
ABCG1	ATP binding cassette subfamily G member 1
AD	Alzheimer's disease
AhR	Aryl hydrocarbon receptor
AHRR	Aryl-hydrocarbon receptor repressor
AKR1C1/2/3	Aldo-keto reductase family 1 member C1/2/3
AKT1	AKT serine/threonine kinase 1
ALDH3A1	Aldehyde dehydrogenase 3 family member A1
ALK	Anaplastic lymphoma kinase
ALOX15B	Arachidonate 15-lipoxygenase type B
ALS	Amyotrophic Lateral Sclerosis
ALS2	Alsin rho guanine nucleotide exchange factor
ALSFRS-R	Revised ALS Functional Rating scale
AMPA	α -amino-3-hydroxy-5-methyl-4-isoxazolepropionic acid
ANG	Angiogenin
APC	Astrocyte progenitor cell
ApoE/L	Apolipoprotein E/L
AQP4	Aquaporin 4
ARE	Antioxidant response element
ARNT	AhR nuclear transporter
ARTN	Artemin
ASO	Antisense oligonucleotide
ATG16L1	Autophagy related 16 like 1
ATM	Ataxia–telangiectasia mutated
ATP	Adenosine triphosphatase
ATXN1/2	Ataxin 1/2
BAX	BCL2 associated X, apoptosis regulator
BBB	Blood brain barrier
BCL-2	B-cell lymphoma 2
BDNF	Brain-derived growth factor
BID	BH3 interacting domain death agonist
BMAA	β -N-methylamino-L-alanine
BPI	Bactericidal/permeability-increasing protein
C9ORF72	Chromosome 9 opening reading frame 72
CCCP	Carbonyl cyanide 3-chlorophenylhydrazone
CCL2	Chemokine motif ligand 2
CCS	Copper chaperone for superoxide dismutase
CD44	CD44 molecule
CDC37	Cell division cycle 37, HSP90 cochaperone
CDH2	Cadherin 2
CDK5	Cyclin-dependent kinase 5
cDNA	Complementary DNA

CF	Cystic fibrosis
CHCHD10	Coiled-coil-helix-coiled-coil-helix domain containing 10
CHMP2B	Charged multivesicular body protein 2B
CLU	Clusterin
CNS	Central nervous system
CNTF	Ciliary neurotrophic factor
CNTN1	Contactin 1
COL5A3	Collagen type V alpha 3 chain
CREB	cAMP-response element binding protein
CRM1	Exportin 1
CSF	Cerebrospinal fluid
CSF2RB	Colony stimulating factor 2 receptor subunit beta
CXCL1/10/12	C-X-C motif chemokine ligand
CYP1A1/B1	Cytochrome P450 family 1 subfamily A/B member 1
DAT	Dopamine active transporter 1
DEGs	Differentially expressed genes
DGE	Differential gene expression
DMF	Dimethylfumarate
DMSO	Dimethyl sulphoxide
DNA	Deoxyribonucleic acid
DPRs	Dipeptide repeat proteins
DRD2	Dopamine receptor D2
DRP1	Dynamin-like protein
DUOX1	Dual oxidase 1
EAAT1/2	Excitatory amino acid transporter ½
EB	Embryoid body
ECAS	Edinburgh Cognitive and Behavioural ALS Screen
ECL	Enhanced chemiluminescence
EF	Embryonic fibroblast
EOAD	Early onset Alzheimer's disease
EPHA3/B1	Ephrin receptor A3/B1
ER	Endoplasmic reticulum
ERAD	ER-associated degradation
ERK	Extracellular signal regulated kinase
ESC	Embryonic stem cell
EWSR1	EWS RNA binding protein 1
FALS	Familial Amyotrophic Lateral Sclerosis
FBS	Fetal bovine serum
FC	Fold change
FDA	Food and drugs administration
FDR	False discovery rate
FPKM	Fragments per kilobase per million
FTD	Frontotemporal dementia
FUS	Fused In Sarcoma
GABA	Gamma aminobutyric acid

GDNF	Glial cell line-derived neurotrophic factor
GFAP	Glial fibrillary acidic protein
GFP	Green fluorescent protein
GMF	Glial maturation factor
GNTF	Glial cell-derived neurotrophic factor
GO-BP	Gene ontology-biological process
GRASPS	Genome-wide RNA analysis of stalled protein synthesis
GRIN3A/2B	Glutamate ionotropic receptor NMDA type subunit 3A/2B
GRM3/4	Glutamate metabotropic receptor 3/4
GSH	Reduced glutathione
GTP	Guanosine-5'-triphosphate
GWAS	Genome-wide association studies
HCA	High content analysis
HCI	Hyaline conglomerate inclusion
HCN1/3	Hyperpolarisation activated cyclic nucleotide gated potassium channel 1/3
HD	Huntington's disease
HLA-DOA	Major histocompatibility complex, class II, DO alpha
HLA-DQB1	Major histocompatibility complex, class II, DQ beta 1
HLA-DRA	Major histocompatibility complex, class II, DR alpha
HMGB1	High mobility group box 1
HO-1	Haem-oxygenase 1
HRE	Hypoxia-response element
HRP	Horseradish peroxidase
HSF1	Heat shock transcription factor 1
HSP70/90	Heat shock protein 70/90
HT-22	Mouse hippocampal neuronal cell line
iAstrocyte	Induced astrocytes
ICC	Immunocytochemistry
IFN	Interferon
IL-1/6	Interleukin 1/6
IMS	Industrial methylated spirit
INA	Internexin neuronal intermediate filament protein alpha
iNOS	Inducible nitric oxide synthase
iNPC	Induced neural progenitor cell
IP	Immunoprecipitation
IP3	Inositol trisphosphate
iPSC	Induced pluripotent stem cell
ISGs	Interferon stimulated genes
JAK1	Janus kinase 1
JNK	c-Jun N-terminal kinase
JUN	Transcription factor AP-1
kDa	Kilodaltons
KEAP1	Kelch-like ECH-associated protein-1
LBP	Lipopolysaccharide binding protein
LC3	Microtubule-associated protein 1A/1B-light chain 3

LCAT	Lecithin-cholesterol acyltransferase
LCM	Laser capture microdissection
LCN2	Lipocalin-2
LMN	Lower motor neuron
LOAD	Late onset Alzheimer's disease
LRRK2	Leucine Rich Repeat Kinase 2
MAF	Transcription factor Maf
MAPK	Mitogen-activated protein kinase
MC	Multiple comparisons
MC1R	Melanocortin 1 receptor
MERTK	MER proto-oncogene, tyrosine kinase
mESC	Mouse embryonic stem cell
mGluR	Metabotropic glutamate receptor
MIF	Migration inhibitory factor
miRNA	MicroRNA
misSOD1	Misfolded SOD1
MMF	Mono-methyl fumarate
MMP	Mitochondrial membrane potential
MN	Motor neuron
MND	Motor neurone disease
mRNA	Messenger RNA
MRPS9	Mitochondrial ribosomal protein S9
MS	Multiple sclerosis
mSOD1	Mutant SOD1
MTA	Material transfer agreement
mtDNA	Mitochondrial DNA
mTOR	Mechanistic target of rapamycin kinase
MW	Molecular weight
NADPH	Reduced nicotinamide adenine dinucleotide phosphate
NCAM	Neural cell adhesion molecule
NECTIN3	Nectin cell adhesion molecule 3
NES	Nuclear export signal
NF- κ B	Nuclear factor-kappa β
NGF	Nerve growth factor
NINCDS-ADRDA	National Institute of Neurological and Communicative Disorders and Stroke and the Alzheimer's Disease and Related Disorders Association
NLRP3	NLR family pyrin domain containing 3
NMDAR2B	N-methyl D-aspartate receptor subtype 2B
NMJ	Neuromuscular junction
NMOSD	Neuromyelitis optica spectrum disorders
NO	Nitric oxide
NOS	Nitric oxide synthase
NPC	Neural progenitor cell
NQO1	NAD(P)H quinone dehydrogenase 1
NR2E1	Nuclear receptor subfamily 2 group E member 1

NRF2	Nuclear factor erythroid 2-related factor 2
NSC	Neural stem cell
NSC34	Spinal cord & neuroblastoma hybrid cell line
NSG	NOD scid gamma mouse
NTSR1/2	Neurotensin receptor 1/2
OPA1	Mitochondrial Dynamin Like GTPase
OPTN	Optineurin
OSGIN1	Oxidative stress induced growth inhibitor 1
P53	Tumour suppressor protein 53
P62	Ubiquitin-binding protein p62
PBS	Phosphate buffered saline
PCA	Principle component analysis
PCDH10/18	Protocadherin 10/18
Pcdh- γ C4	Protocadherin gamma C4
PCR	Polymerase chain reaction
PD	Parkinson's disease
PET	Positron emission tomography
PI3K	Phosphatidyl inositol 3-kinase
PIB	Pittsburgh compound B
PIK3CA/D	Phosphatidylinositol-4,5-bisphosphate 3-kinase catalytic subunit alpha/delta
PINK1	PTEN induced kinase 1
PLXNA2	Plexin A2
PMI	KEAP1-NRF2 protein-protein interaction inhibitor HB229
PMT	Post-mitochondrial fraction
POSTN	Periostin
PPI	Protein-protein interaction
PRDX1	Peroxiredoxin 1
Ptau	Hyperphosphorylated tau
PTEN	Phosphatase and tensin homolog
PTGS1	Prostaglandin-endoperoxide synthase 1
PXDN	Peroxidasin
Q3BDG	Quercetin 3- β -D-glucoside
QPCR	Quantitative PCR
RAB1A/3B	Member RAS Oncogene Family
RAN	Repeat-associated non-ATG
RBX1	E3 ubiquitin-protein ligase
RIPA	Radio-immunoprecipitation assay
RNA	Ribonucleic acid
RNS	Reactive nitrogen species
ROS	Reactive oxygen species
RPFs	Ribosome-protected fragments
RPM	Reads per million
RPS6KB1	Ribosomal protein S6 kinase B1
RRB	Ribosome resuspension buffer
rRNA	Ribosomal ribonucleic acid

RT-PCR	Real-time PCR
RT-QuIC	Real-time quaking-induced conversion
sALS	Sporadic Amyotrophic Lateral Sclerosis
SCI	Spinal cord injury
SEMA3/6A	Semaphorin 3/6A
SH-SY5Y	Human neuroblastoma cell line
siRNA	Short interfering RNA
SNP	Single nucleotide polymorphism
SOD1	Superoxide dismutase 1
SQSTM1	Sequestosome 1
SRXN1	Sulfiredoxin 1
STAT1/2	Signal transducer and activator of transcription 1
TAF15	TATA-binding protein-associated factor 2N
TARDBP	Transactive response (TAR) DNA-binding protein
TBI	Traumatic brain injury
TBST	Tris buffered saline, with tween® 20
TC	Tissue culture
TDP-43	TAR DNA-binding protein 43
TGF-β1	Transforming growth factor beta 1
TMRM	Tetramethylrhodamine, methyl ester, perchlorate
TNF-α	Tumour necrosis factor alpha
TNFAIP3/6	Tumour necrosis factor alpha-induced protein 3/6
TNR	Tenascin R
TPM	Transcripts per million
TRIM16	Tripartite motif containing 16
TYK2	Tyrosine kinase 2
UBQLN2	Ubiquilin 2
ULK1	Unc-51 like autophagy activating kinase 1
UMN	Upper motor neuron
UNC13A	Unc-13 Homolog A
UPR	Unfolded protein response
UPS	Ubiquitin-proteasome system
UV	Ultraviolet
VAPB	VAMP (Vesicle-Associated Membrane Protein) Associated Protein B And C
VCP	Valosin Containing Protein
VDAC1	Voltage dependent anion channel 1
VEGF	Vascular endothelial growth factor
WGCNA	Weighted gene co-expression network analysis
WRCRP	Wide-range C-reactive protein
WT	Wild type
XCR1	X-C motif chemokine receptor 1
XRE	Xenobiotic response element

Chapter 1 - Introduction

1.1. Amyotrophic Lateral Sclerosis

Amyotrophic Lateral Sclerosis (ALS) is the most common form of motor neurone disease (MND). It is also commonly known as Lou Gehrig's disease in the United States after a famous baseball player was diagnosed in the 1930's. While the phenotypic nature of the disease varies greatly, it is characterised as a fatal neurodegenerative disease caused by the progressive loss of the upper and lower motor neurons (UMNs and LMNs). Currently, there is no cure for the disease and the current therapeutic treatments, riluzole and edaravone, provide only a modest disease modifying effect.

1.1.1 Clinical features

Depending on the site of MN degeneration, patients will experience a spinal onset, leading to limb muscle weakness, or a bulbar onset, leading to difficulty in speech and swallowing. Rarely, the disease onset may involve respiratory dysfunction. The limb-onset diagnosis is more common, accounting for ~60% of patient cases, while one third of patients are diagnosed with a bulbar-onset disease (Hardiman *et al.*, 2017). Up to 5% of ALS patients present respiratory dysfunction at onset, and in many of these cases, patients present unexplained weight loss suggesting that they are hypermetabolic (Dupuis *et al.*, 2011).

Although the primary symptom in ALS is the weakening of the muscle, 50% of patients develop cognitive or behavioural impairment; apathy is the most common behavioural change reported in patients (Witgert *et al.*, 2010). Approximately 13% of ALS patients develop features of Frontotemporal dementia (FTD) (Phukan *et al.*, 2012).

The scale used to assess disability in ALS, the revised ALS Functional Rating Scale (ALSFRS-R), assesses the extent of deterioration of the UMNs and LMNs as well as the site of onset (bulbar or limb), however this does not take into account the cognitive and behavioural symptoms seen in patients (Al-Chalabi *et al.*, 2016). The Edinburgh Cognitive and Behavioural ALS Screen (ECAS) is a diagnostic tool used to identify ALS patients with cognitive and behavioural changes in the clinic (Abrahams *et al.*, 2014).

1.1.2. Epidemiology and genetics

The incidence of ALS is unique among populations based on ancestral origin. European populations have an incidence of >3 cases per 100,000, while Asian populations have a lower incidence; ~0.8 cases per 100,000 in East Asia and ~0.7 cases per 100,000 in South Asia (Marin *et al.* 2014; 2016). The length of patient survival also differs between populations; the mean survival time from symptom onset in Europe is only 24 months as opposed to the mean survival length in Asia of 48 months (Marin *et al.* 2016). However, this may be because the age of diagnosis and first disease symptoms are higher in Europe than in Asia; the average age of onset in Europe is 65 years old (Logroscino *et al.*, 2010). There are also gender-specific differences in Europe; men are more commonly diagnosed with a spinal onset disorder while women are more likely to have a bulbar onset disease (Logroscino *et al.*, 2010). However, current data on global ALS epidemiology is limited to the fact that 80% of studies have been carried out in Europe and North America, which is not representative of patients worldwide (Hardiman *et al.*, 2017).

ALS is a complex genetic disorder. Most patient cases are diagnosed with sporadic ALS (sALS) where the cause of the disease is unknown. However, there are some familial cases (fALS) with mutations in genes across a wide variety of biological functions, meaning that the genotype cannot be predictive of phenotype in all patient cases. The multistep model based upon population data of ALS pathogenesis suggests that individuals carry 'at risk' genetic variants that interact with environmental factors and result in disease manifestation (Al-Chalabi *et al.* 2017). Genome-wide association studies (GWAS) on non-fALS cases suggest that the genetic pathogenesis of ALS is based upon rare variants, in contrast to other diseases such as schizophrenia which rely upon a large number of common variants (van Rheenen *et al.*, 2016). It is thought that these rare variants confer risk to specific individuals and families, making GWAS technology less reliable to study variants that are causative of disease. The Project MinE Consortium aims to produce data from whole-genome sequencing of >15,000 ALS patients alongside >7500 healthy individuals to provide clarity on the genetic basis of ALS (Al-Chalabi *et al.* 2017).

The characterisation of ALS inheritance into 'familial' and 'sporadic' is over-simplified. Alongside the >30 genes discovered for fALS (Mejzini *et al.*, 2019), there is also evidence of oligogenic inheritance, where a trait is determined by more than one gene, and genetic pleiotropy, where one gene can produce multiple traits (Al-Chalabi *et al.* 2017). In European populations, 20% of total patient cases are deemed as fALS in which there are four major genetic variants associated with disease; *SOD1*, *TARDBP*, *C9ORF72* and *FUS* (Figure 1.1), these are described in further detail below.

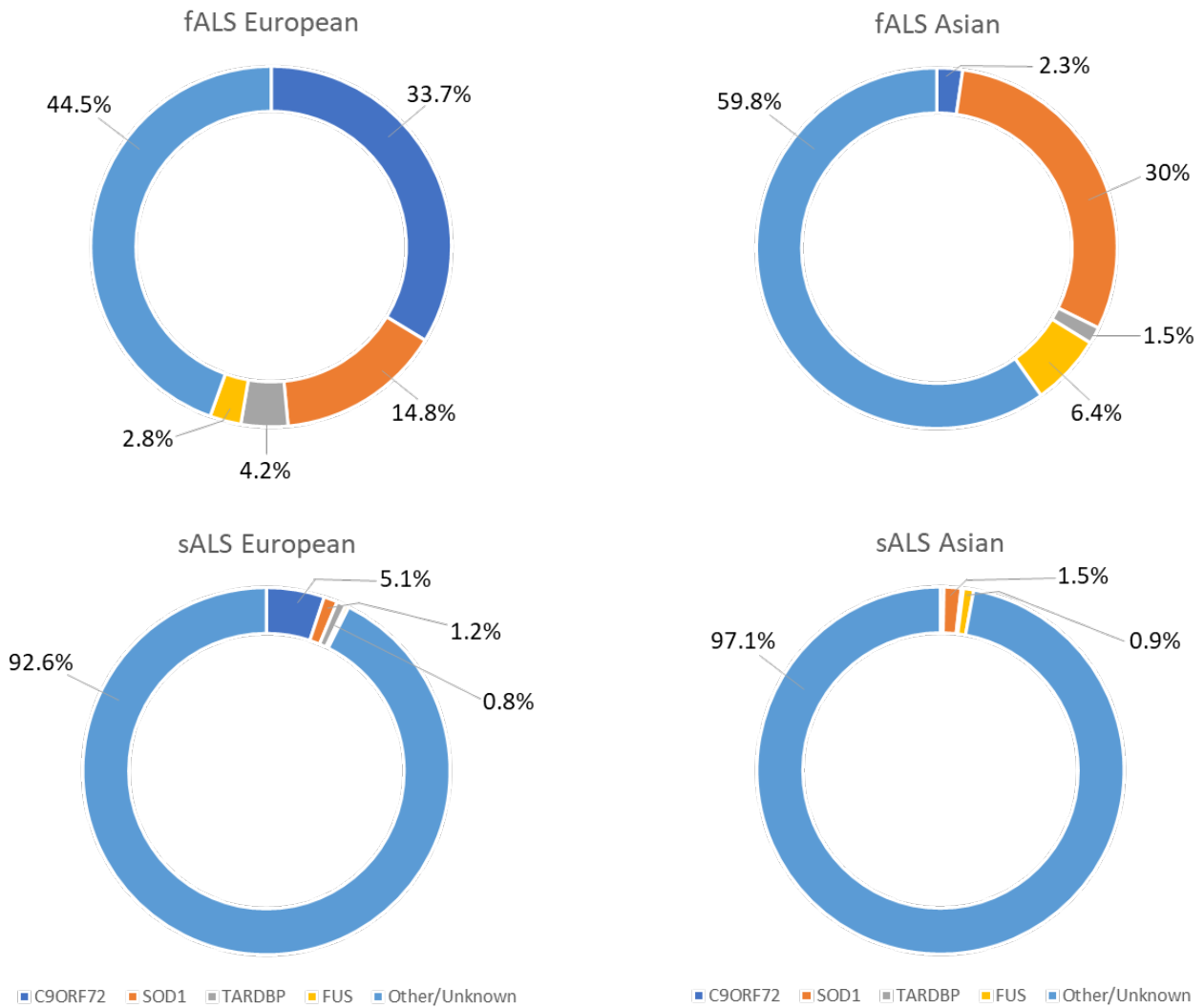


Figure 1.1 Proportion of ALS explained by the four most common mutant genes across European and Asian populations; groups with a percentage below 0.5% were omitted from the charts (figure modified from Mezzini et al. 2019).

1.1.2.1. SOD1

The *SOD1* gene was the first ALS-causing gene discovered in 1993 (Rosen *et al.*, 1993). The gene encodes a 153 amino acid metalloenzyme belonging to the superoxide dismutase enzyme family. The enzyme catalyses the production of oxygen and hydrogen peroxide from the superoxide ions formed during cellular respiration, protecting the cell from oxidative stress (Rosen *et al.*, 1993). Mutations in *SOD1* account for approximately 15-30% of fALS and less than 2% of sALS cases (Figure 1.1).

Over the years, more than 185 disease-causing variants have been identified in *SOD1*, the majority of which consist of missense mutations, with the *D90A* variant as the most prevalent worldwide (Mejzini *et al.*, 2019). The disease duration and severity in patients differs significantly based upon the mutation; patients with the *A4V*, *H43R*, *L84V*, *G85R*, *N86S* or *G93A* variant display a faster disease progression and shorter survival than patients with the *G93C*, *D90A* or *H46R* mutation (Cudkowicz *et al.* 1997; Régal *et al.* 2006; Aoki *et al.* 2008). Distinct clinical features will also manifest in patients with specific *SOD1* mutations, for example the *A4V* mutation is associated with an aggressive, limb-onset form of ALS (Juneja *et al.*, 1997). Variations also occur between patients with either one or two forms of the mutation; patients with a homozygous *D90A* mutation demonstrate a slow-progressing, limb-onset disorder while patients heterozygous for the *D90A* variant present bulbar, upper or lower limb-onset with a faster disease progression (Andersen *et al.*, 1996; Robberecht *et al.*, 1996; Parton *et al.*, 2002).

To begin with, variants in *SOD1* were believed to cause disease through a loss of enzymatic activity; early studies found a 50-80% decrease in enzyme activity (Deng *et al.* 1993; Rosen *et al.* 1993). However, a later study demonstrated that enzyme activity did not correlate with disease severity (Cleveland *et al.*, 1995) and the proposed 'toxic gain of function' was further supported when a *SOD1* knockout mouse model did not display an ALS phenotype (Reaume *et al.*, 1996). The mutant *SOD1* (mSOD1) protein promotes cellular toxicity through multiple disease mechanisms, including excitotoxicity, oxidative stress, endoplasmic reticulum (ER) stress, mitochondrial dysfunction, and prion-like propagation (Hayashi *et al.* 2016). Misfolded wild-type *SOD1* (misSOD1) protein inclusions have also been detected in patients without the *SOD1* mutation (Forsberg *et al.*, 2010, 2019), indicating that the misfolding of *SOD1* may represent a common downstream event in ALS disease progression.

1.1.2.2. TARDBP

The *TARDBP* gene encodes TDP-43, a DNA/RNA binding protein responsible for the regulation of gene expression and RNA processing, including pre-mRNA splicing, mRNA stability and transport, translation, and regulation of non-coding RNAs (Buratti and Baralle, 2010; Tollervey *et al.*, 2011; Ratti and Buratti, 2016). This protein comprises of 414 amino acids with both a nuclear localisation and export signal, allowing it to shuttle back and forth between the nucleus and the cytoplasm (Ayala *et al.*, 2008). Around 48 variants of *TARDBP* have been associated with ALS; the majority consist of missense mutations located in the glycine-rich region at the carboxy-terminal (Lattante *et al.* 2013). Mutations in the C-terminal region are pathogenic since this region is required for pre-mRNA splicing regulation as well as other interactions with ribonucleoproteins (Buratti *et al.*, 2005; Neumann *et al.*, 2006).

In ALS, the accumulation of cytoplasmic TDP-43 protein aggregates correlates with the loss of nuclear TDP-43, potentially underpinning both a loss of normal TDP-43 function in the nucleus alongside a toxic gain of function of the aggregated protein in the cytoplasm (Neumann *et al.*, 2006). TDP-43 expression is vital in embryonic development as homozygous *Tardbp* null mice are not embryonically viable (Sephton *et al.*, 2010), while an inducible *Tardbp* knockout in adult mice is also lethal (Chiang *et al.*, 2010). Overexpression of human wild type and mutant TDP-43 in mouse models has resulted in a neurodegenerative phenotype as well as the fragmentation of the TDP protein, similar to the production of the 35 and 25kDa fragments seen in ALS patients (Wils *et al.*, 2010; Xu *et al.*, 2011).

Stable TDP-43 expression is, therefore, vital for normal cellular function; excess TDP-43 contained within cytoplasmic aggregates leads to organelle and cellular pathology, while nuclear loss of TDP-43 induces widespread dysregulation of mRNA metabolism and altered expression of hundreds of target genes (Highley *et al.*, 2014). While the mechanism surrounding nuclear TDP-43 depletion is unknown, this depletion is proposed to result in the continuous overexpression and synthesis of TDP-43 (Koyama *et al.*, 2016). There are also several post-translational modifications associated with TDP-43 pathology, including ubiquitination, proteolytic cleavage, phosphorylation, acetylation, and disulphide bridge formation, as reviewed in Buratti (2018), however the role each of these play in disease onset is still unclear. Like the SOD1 protein, TDP-43 could also propagate inclusions to neighbouring cells through the protein's prion-like domain (Nonaka *et al.*, 2013).

1.1.2.3. FUS

In 2009, mutations in the gene *fused in sarcoma (FUS)* were identified in a subgroup of ALS patients by two research groups (Kwiatkowski *et al.*, 2009; Vance *et al.*, 2009). This gene encodes for a ubiquitously expressed, 526 amino acid protein belonging to a family of RNA binding proteins. Like TDP-43, FUS is also responsible for nucleocytoplasmic transport as well as transcription, pre-mRNA splicing, RNA transport and regulation of translation, however they are known to regulate different RNA targets (Lagier-Tourenne *et al.*, 2012). FUS is also involved in DNA repair mechanisms, including homologous recombination for DNA double-strand break repair and non-homologous end joining (Wang *et al.* 2013).

There are over 50 mutational variants of the *FUS* gene in ALS; while the majority are missense mutations, insertions, deletions, splicing and nonsense mutations have also been reported (Lattante *et al.* 2013). Many of these mutations are located within the nuclear localisation signal, while others increase the propensity of the FUS protein to form solid aggregates, both leading to the cytoplasmic aggregation of FUS (Vance *et al.*, 2013; Nomura *et al.*, 2014). Since TDP-43 aggregation is not commonly seen in FUS-ALS patients, this suggests the FUS disease pathway is independent of TDP-43 (Vance *et al.*, 2009).

1.1.2.4. C9ORF72

In 2011, two research groups simultaneously identified a hexanucleotide repeat expansion (GGGGCC) in the first intron of the *C9ORF72* gene (DeJesus-Hernandez *et al.*, 2011; Renton *et al.*, 2011). Healthy individuals have <30 copies of the expansion in *C9ORF72* while ALS patients have hundreds to thousands of repeats of the expansion (DeJesus-Hernandez *et al.*, 2011). This repeat expansion is found in approximately 34% of fALS and 5% of sALS cases in Europe but it is less prevalent in the Asian population (Figure 1.1).

Studies have reported a reduction of *C9ORF72* mRNA and protein levels in ALS patients, implying a loss of function disease mechanism (Waite *et al.*, 2014). The *C9orf72* protein is responsible for the regulation of endosomal trafficking and autophagy (Farg *et al.*, 2014), while *C9orf72* deficient mouse models demonstrated immune system dysregulation, implying an additional role in the immune response (Atanasio *et al.*, 2016). However, *C9orf72* knockout mice did not show evidence of MN degeneration or motor deficits (Koppers *et al.*, 2015), and the targeted reduction of *C9ORF72* RNA did not result in a pathological phenotype in both mice and patient induced pluripotent stem cell (iPSC) derived neurons (Donnelly *et al.*, 2013; Lagier-Tourenne *et al.*, 2013), indicating that loss of function alone is insufficient to cause disease.

There is evidence to support several toxic gain of function mechanisms of the *C9ORF72* repeat expansion. RNA misprocessing of the repeat transcript promotes the production of further transcripts containing the repeat expansion, establishing a positive feedback loop (Sareen *et al.*, 2013). The transcript is also susceptible to other RNA misprocessing events, including abortive transcription, decreased splicing of the repeat-containing intron and nuclear aggregation, as reviewed in Barker *et al.* (2017). Some of these transcripts are also subjected to repeat-associated non-ATG (RAN) translocation which produces dipeptide repeat proteins (DPRs) that establish neuronal inclusions within the central nervous system (CNS) (Ash *et al.*, 2013). Finally, these transcripts are also able to form RNA foci within the nucleus. These foci interact and sequester surrounding RNA-binding proteins, promoting dysregulation of RNA expression and downstream splicing events (DeJesus-Hernandez *et al.*, 2011).

1.1.2.5. Other ALS-associated genes

There are a great number of rare genetic variants for ALS which are included in Table 1.1. While rare, the discovery of these variants is important in identifying all possible disease mechanisms underpinning ALS. As well as disease progression, some genetic variants influence the ALS clinical phenotype and patient susceptibility. Variations of *UNC13A* have been associated with increased disease susceptibility and a shorter survival length in patients (Diekstra *et al.*, 2012). Repeat expansions within *ATXN1* and *ATXN2* increase disease risk, particularly in *C9ORF72*-ALS patients (Sproviero *et al.*, 2017; Lattante *et al.*, 2018), while on the other hand, deletions in *EPHA3* have been proposed as a protective factor in ALS (Uyan *et al.*, 2013).

Table 1.1 Genetic variants associated with ALS.

Disease mechanism	Gene	Protein	Protein function	References
RNA processing	ANG	Angiogenin	RNA processing, neurite outgrowth, vascularisation, stress granule formation	Greenway <i>et al.</i> 2006
	SETX	Senataxin	DNA/RNA metabolism, helicase activity	Chen <i>et al.</i> 2004
	MATR3	Matrin 3	RNA processing, chromatin organisation	Johnson <i>et al.</i> 2014
	ATXN2	Ataxin 2	RNA processing (TDP-43), endocytosis, modulates mTOR signalling	Sproviero <i>et al.</i> 2017
	TAF15	TATA-binding protein-associated factor 2N	Transcription initiation, RNA polymerase II	Ticozzi <i>et al.</i> 2011
	EWSR1	EWS RNA Binding Protein 1	RNA splicing, transcriptional repressor	Couthouis <i>et al.</i> 2012
	hnRNPa1	Heterogenous nuclear ribonucleoprotein A1	mRNA processing, splicing & transport	Kim <i>et al.</i> 2013
	hnRNPA2B1	Heterogenous nuclear ribonucleoproteins A2/B1	mRNA processing, splicing & transport	Kim <i>et al.</i> 2013
	ELP3	Elongator complex protein 3	Protein synthesis, maturation of projection neurons	Simpson <i>et al.</i> 2009
Protein trafficking and degradation	ALS2	Alsin	Endosomal trafficking, neurite outgrowth	Hadano <i>et al.</i> 2001
	VAPB	Vesicle-associated membrane protein-associated protein B/C	Vesicle trafficking	Nishimura <i>et al.</i> 2004
	CHMP2B	Charged multivesicular body protein 2b	Multivesicular body formation, protein trafficking to lysosomes	Parkinson <i>et al.</i> 2006
	FIG4	Polyphosphoinositide phosphatase	Endosomal trafficking to Golgi network, autophagy regulation	Chow <i>et al.</i> 2009
	UBQLN2	Ubiquilin-2	Protein degradation via UPS	Deng <i>et al.</i> 2011
	SQSTM1	Sequestosome-1 (p62)	Protein degradation via UPS and autophagy	Fecto <i>et al.</i> 2011; Rubino <i>et al.</i> 2012
	SIGMAR1	Sigma non-opioid intracellular receptor 1	Lipid transport from ER, mitochondrial axonal transport	Luty <i>et al.</i> 2010; Al-Saif <i>et al.</i> 2011
	OPTN	Optineurin	Golgi maintenance, exocytosis, autophagy	Maruyama <i>et al.</i> 2010
	VCP	Valosin Containing Protein	Protein degradation via UPS, autophagy, membrane fusion	Johnson <i>et al.</i> 2010
	TBK1	Tank Binding Kinase 1	Autophagy, innate immunity signalling	Cirulli <i>et al.</i> 2015
	KIF5A	Kinesin heavy chain isoform 5A	Intracellular transport of organelles	Nicolas <i>et al.</i> 2018
	ANXA11	Annexin A11	Vesicular trafficking between the Golgi and the ER	Smith <i>et al.</i> 2017

Table 1.1 Continued.

Disease mechanism	Gene	Protein	Protein function	References
Cytoskeletal and axonal dynamics	DCTN1	Dynactin subunit 1	Axonogenesis, microtubule anchoring, vesicle transport, cilia formation	Münch <i>et al.</i> 2004; 2005
	PFN1	Profilin 1	Cytoskeletal signalling, actin polymerisation	Wu <i>et al.</i> 2012
	SPG11	Spatacsin	Cytoskeletal stability, synaptic vesicle transport	Orlacchio <i>et al.</i> 2010
	TUBA4A	Tubulin α -4A chain	Component of microtubules	Smith <i>et al.</i> 2014
	NEFH	Neurofilament heavy polypeptide	Maintenance of neuronal calibre, intracellular transport	Figlewicz <i>et al.</i> 1994
	PRPH	Perpherin	Cytoskeletal protein, neurite elongation, axonal regeneration	Gros-Louis <i>et al.</i> 2004
	NEK1	NIMA (Never In Mitosis Gene A)-Related Kinase 1	DNA-damage response, microtubule stability, neuronal morphology, axonal polarity	Kenna <i>et al.</i> 2016
Mitochondria	CHCHD10	Coiled-Coil-Helix-Coiled-Coil-Helix Domain Containing 10	Mitochondrial protein, cristae morphology, oxidative phosphorylation	Bannwarth <i>et al.</i> 2014
Other	UNC13A	Unc-13 Homolog A	Neurotransmitter release, glutamate	Diekstra <i>et al.</i> 2012
	C19ORF12	Protein C19orf12	Mitochondrial protein	Deschauer <i>et al.</i> 2012
	ERBB4	Receptor tyrosine-protein kinase erbB-4	Neuronal cell mitogenesis and differentiation	Takahashi <i>et al.</i> 2013
	SS18L1	Calcium-responsive transactivator	Neuron specific chromatin remodelling	Teyssou <i>et al.</i> 2014
	PNPLA6	Neuropathy target esterase	Regulation of neuronal membrane composition	Rainier <i>et al.</i> 2008
	PON1-3	Paraoxonase 1-3	Enzymatic breakdown of nerve toxins	Saeed <i>et al.</i> 2006
	DAO	D-amino-acid oxidase	Regulates D-serine levels, N-methyl-D-aspartate receptor regulation	Mitchell <i>et al.</i> 2010
	CHRNA3, 4, B4	Neuronal acetylcholine receptor subunit α -3, α -4, β -4	Cholinergic neurotransmission	Sabatelli <i>et al.</i> 2009
	ALS3	ALS3	Disulphide redox protein	Hand <i>et al.</i> 2002
	GLT8D1	Glycosyltransferase 8 domain-containing protein 1	TBD	Cooper-Knock <i>et al.</i> 2019
	NIPA1	Magnesium transporter NIPA1	Magnesium ion transmembrane transporter activity, nervous system development and maintenance.	Tazelaar <i>et al.</i> 2019
	DNAJC7	DnaJ homolog subfamily C member 7	Protein co-chaperone, folding of steroid receptors	Farhan <i>et al.</i> 2019

Table modified from Mezzini *et al.* 2019.

1.1.2.6. Environmental factors

Epidemiological studies from Guam and the Kii peninsula of Japan have hinted a role for neurotoxins as a risk factor for ALS. Chronic exposure to the neurotoxic amino acid β -N-methylamino-L-alanine (BMAA) present in water containing cyanobacterial blooms has been considered a risk factor in susceptible individuals (Bradley *et al.*, 2013). Historically, ALS has been reported in a high number of athletes but whether physical activity is considered as an actual risk factor is still unclear. One study from the UK reported that individuals with ALS had higher rates of cardiovascular fitness (Turner *et al.*, 2012), while recent data suggest that exercise has no effect or is potentially protective from ALS (Tsitkanou *et al.*, 2019). Other studies on environment factors of ALS have made suggestions that smoking might increase disease risk, while high levels of circulating lipids and female contraceptive hormones may decrease risk (Wang *et al.* 2017; Rooney *et al.* 2017).

1.1.3. Pathogenesis

The main pathological features of ALS are the deterioration of the skeletal muscle and the motor cortex, alongside the thinning of the hypoglossal nerves, which control the tongue muscles, and the ventral roots of the spinal cord (Hardiman *et al.*, 2017). On average, at autopsy at least 50% of spinal MNs are lost, alongside the presence of astrocyte gliosis and microglial infiltration into the grey and white matter of the spinal cord (Coan and Mitchell, 2015). There is commonly axonal loss, gliosis, and myelin pallor in the corticospinal tracts, while astrocyte gliosis is also seen in the motor cortex, accompanied by the depletion of the UMNs. The skeletal muscle of ALS patients shows features of denervation and re-innervation of muscle fibres (Fischer *et al.*, 2004).

In reality, the occurrence of ALS is likely due to many different interacting mechanisms that result in the disruption of a larger network, and some researchers believe that focusing on a single mechanism in a disease model gives an artificial view of the disease pathology (Hardiman *et al.*, 2017). The extent to which each of the following mechanisms contribute towards disease is unknown and not all of these mechanisms will contribute to MN injury in all patient cases. However, individually they are being used to understand this complex disease and are driving current research into disease therapeutics (Hardiman *et al.*, 2017).

1.1.3.1. Oxidative stress

Reactive oxygen species (ROS) are produced as a by-product of cellular respiration in the mitochondria. When antioxidants are unable to neutralise ROS, they accumulate and cause serious damage to macromolecules, including DNA, proteins, and phospholipids. Shibata *et al.* (2001)

reported the presence of oxidative damage, such as lipid peroxidation and protein glycoxylation in the spinal cord MNs and glial cells of sALS patients.

Oxidative stress could be viewed as the primary initiating factor in ALS pathogenesis because it can exacerbate numerous pathological mechanisms, including those described below. Originally a cytosolic antioxidant enzyme, mSOD1 is thought to increase ROS production through interactions with the mitochondria and other proteins (Cozzolino *et al.*, 2009). Increases in ROS also result in the mislocalisation and aggregation of regulatory RNA-binding proteins TDP-43 and FUS, leading to impairment in RNA processing (Vance *et al.*, 2013; Cohen *et al.*, 2015). A lack of interaction between these RNA binding proteins and the mitochondria leads to further mitochondrial damage; FUS is thought to localise to the mitochondria through interaction with the heat shock protein 60 (HSP60), while TDP-43 may directly affect the mRNA coding for proteins involved in mitochondrial dynamics (Deng *et al.* 2015; Wang *et al.* 2013).

1.1.3.2. Protein misfolding and aggregation

The primary neuropathological hallmark in ALS is the aggregation and accumulation of ubiquitinated protein inclusions which disrupt the proteasomal or autophagic machinery, leading to impaired protein turnover (Blokhuys *et al.*, 2013). The autophagy pathway is important for maintaining cellular homeostasis through the recycling of damaged proteins and organelles (Webster *et al.*, 2016). While in the ubiquitin-proteasome system (UPS), proteins are tagged for degradation by ubiquitination and delivered to the proteasome (Blokhuys *et al.*, 2013).

Mutations in *SOD1* have been found to reduce the activity of the UPS (Urushitani *et al.*, 2002) and chaperone dysfunction has been reported in cases with *SOD1* and *UBQLN2* mutations (Bergemalm *et al.*, 2010; Chang and Monteiro, 2015). Webster *et al.* (2016) demonstrated that the C9orf72 protein plays a key role in the initiation of autophagy, so a loss of protein function in C9ORF72-ALS results in the accumulation of protein aggregates. Several other genes described in Table 1.1 are also involved in protein degradation, including *OPTN*, *SQSTM1*, and *VCP*. Many of the pathological protein aggregates in ALS are ubiquitin-tagged, implying the presence of an impaired or simply overwhelmed protein clearance machinery (Mejzini *et al.*, 2019).

The most common constituent of these protein inclusions is TDP-43, which is interesting seeing as *TARDBP* mutations are quite rare among ALS patients (Van Deerlin *et al.*, 2008). Across all types of ALS, 97% of patients will display features of TDP-43 proteinopathy (Prasad *et al.*, 2019). It was previously believed that only specific subgroups of patients will have other types of protein aggregates, for example the presence of misSOD1 is only witnessed in SOD1-associated ALS,

however more recent studies have identified the presence of misSOD1 in other ALS genetic subpopulations (Forsberg *et al.*, 2019).

The presence of hyaline conglomerate inclusions (HCIs) has also been reported in the MNs of ALS patients (Hays *et al.*, 2006). These neurofilamentous inclusions are thought to be specific to the autosomal dominant form of SOD1-ALS, including the *A4V*, *A4T*, *H48Q* and *I113T* mutations (Ince *et al.*, 1998; Hays *et al.*, 2006). In addition, these hyaline inclusions have been shown to be strongly immuno-positive for the SOD1 protein (Shibata *et al.*, 1996), while there was little association with TDP-43 and FUS proteins (Nakamura *et al.*, 2014).

1.1.3.3. Endoplasmic-reticulum stress

Protein degradation can also be impaired through ER stress. The ER is responsible for protein synthesis, post-translational processing, and protein folding. The accumulation of misfolded proteins promotes ER stress which is relieved through the activation of the unfolded protein response (UPR) to remove these aggregates from the ER (Matus *et al.*, 2013).

Nishitoh *et al.* (2008) reported that mSOD1 binds to the cytoplasmic surface of the ER by the membrane protein Derlin-1, inhibiting the ER-associated degradation (ERAD) pathway which removes misfolded proteins from the ER. As well as autophagic regulators, ALS-associated genes *OPTN* and *VCP* also have roles in ERAD and sorting endosomal proteins (Maruyama *et al.* 2010; Johnson *et al.* 2010). The VAPB protein functions in the UPR and the vesicular trafficking of the protein from the ER to the proteasome (Nishimura *et al.*, 2004). Saxena *et al.* (2009) demonstrated that reduction of ER stress attenuated disease onset and delayed disease progression in animal models of fALS.

1.1.3.4. Dysregulated RNA metabolism

Once messenger RNA (mRNA) has been transcribed, it needs to undergo complex processing such as 5' capping, splicing and polyadenylation while it transfers from the nucleus to the ribosomes where translation occurs (Butti and Patten, 2018). As mentioned previously, mutations in RNA binding proteins TARDBP and FUS have demonstrated that dysfunctional RNA processing is a key theme in ALS pathology. In TARDBP-ALS, one third of the transcriptome is altered (Amlie-Wolf *et al.*, 2015), and changes in transcription, alternative splicing, mRNA transport and microRNA biogenesis have all been witnessed in models with mutations with *C9ORF72*, *SOD1* and *FUS* (Butti and Patten, 2018).

Reddy *et al.* (2013) reported that transcripts containing the GGGGCC repeat expansion of *C9orf72* can form G-quadruplex structures which disrupt RNA processing factors; these complexes lead to the production of abnormal RNA foci which sequester RNA-binding proteins as mentioned previously. This mutation could also lead to DNA damage through the production of R-loops, DNA-RNA hybrid structures, alongside the formation of double-stranded breaks and defective serine-protein kinase ATM-mediated DNA repair (Walker *et al.*, 2017). There are many other genetic mutations that have functions in RNA metabolism, including *ANG* which is important for RNA processing (Greenway *et al.*, 2006) as well as *TAF15* and *EWSR1* which are responsible for transcription initiation and RNA splicing (Ticozzi *et al.*, 2011; Couthouis *et al.*, 2012).

1.1.3.5. Axonal transport

The transport of vesicles through the axon is vital for neuronal health. As well as RNA metabolism, TDP-43 also has a role in the regulation of endosomal trafficking; Schwenk *et al.* (2016) showed that the loss of TDP-43 function resulted in altered dendritic endosomes and reduced neuronal health. The *ALS2* gene encodes for the protein alsin, which is involved in endosome trafficking and fusion. Devon *et al.* (2006) reported altered trophic receptor trafficking in the MNs of a homozygous null *Als2* mouse model.

1.1.3.6. Mitochondrial dysfunction

The mitochondria are the powerhouse of the cell, generating the energy required for the essential processes maintaining cellular homeostasis. Abnormal mitochondrial morphology has been observed in the spinal cord of ALS patients (Sasaki and Iwata, 2007) as well as in transgenic mouse models of ALS; vacuoles containing protein aggregates including mSOD1 have been seen in the mitochondrial inter-membrane space in *SOD1* mice (Wong *et al.*, 1995). Oxidative damage of mitochondrial proteins by this protein aggregation and peroxisomes leads to impaired protein transport (Higgins *et al.* 2003), defects in the respiratory chain by oxidative phosphorylation (Mattiuzzi *et al.*, 2002) and axonal transport which contributes to axonopathy at the neuromuscular junction (NMJ) (De Vos *et al.*, 2007; Bilisland *et al.*, 2010).

Signalling between the ER and the mitochondria is disrupted by mutant *TARDBP* and *FUS* (Stoica *et al.*, 2014, 2016). Wang *et al.* (2016) found that both wild type and mutant TDP-43 binds to mRNAs encoding respiratory chain complex 1 subunits which causes complex disassembly and the accumulation of protein in the mitochondria. The DPR aggregates seen in C9ORF72-ALS also

compromise the mitochondria, elevating oxidative stress and DNA damage (Lopez-Gonzalez *et al.*, 2016). Mutations in *CHCHD10* disrupt mitochondrial DNA repair mechanisms, promoting the loss of mitochondrial cristae junctions, and preventing cytochrome c release which impairs the apoptotic machinery (Genin *et al.*, 2016).

1.2. Non-cell autonomous toxicity

Over the past 10 years, numerous studies have provided evidence that MN death in ALS occurs via a non-cell autonomous process in which the neighbouring glial cells, astrocytes, microglia and oligodendrocytes, have a crucial role (Ferraiuolo *et al.* 2011a). Clement *et al.* (2003) demonstrated that healthy MNs developed an ALS pathology when surrounded by mSOD1-expressing glial cells in a *SOD1* mouse model. Boillée *et al.* (2006) generated double transgenic mice expressing the Cre-Lox recombination system to remove the pathogenic mutation from either the MNs or the glial cells. When the *SOD1* mutation was removed from the MNs, there was a delayed disease onset in *SOD1* transgenic mice, but there was no difference in disease course. However, when the same mutation was removed from the surrounding microglia, there was no change in disease onset, but disease progression was reduced by 50% (Boillée *et al.*, 2006). Therefore, while MN pathology highlights the beginning of disease onset, the neighbouring glial cells control the speed of disease progression, making them an attractive therapeutic target for ALS.

1.2.1. The role of astrocytes in ALS

Astrocytes are the most abundant non-neural cell type residing within the CNS. Once believed to be 'passive support cells for electrically active neurons' (Chandrasekaran *et al.*, 2016), astrocytes are now recognised to play an active role in CNS homeostasis by establishing connections with the surrounding neurons, microglia and endothelial cells (Sofroniew and Vinters, 2010). The main roles of astrocytes are to provide metabolic support for neurons, neurotransmitter homeostasis and maintain the integrity of the blood brain barrier (BBB) (Chandrasekaran *et al.*, 2016). There is strong evidence to suggest that astrocytes contribute to neurodegeneration in the damaged CNS, either through a lack of support or active toxicity.

The most common genetic variants of ALS, described previously in 1.1.2, reflect mutations in basic biological processes such as RNA processing, and are ubiquitously expressed in the patient. Therefore, current research has proved difficult to identify genetic mutations that are specific to astrocytes alone, however, astrocytes are likely to be affected just like neurons by these mutations.

Previous studies have shown an impairment in astrocytic maintenance of the MNs in ALS (Liddelow *et al.*, 2017; Tyzack *et al.*, 2017), as well as demonstrated toxicity towards surrounding MNs (Nagai *et al.* 2007; Di Giorgio *et al.* 2007; Meyer *et al.* 2014; Tripathi *et al.* 2017). There is still controversy within the research community whether MN death occurs because of the former, the latter, or a combination of both. The disease mechanisms of action witnessed in ALS astrocytes are described in further detail below.

1.2.1.1. Glutamate metabolism

MNs are especially sensitive to influxes of calcium caused by high levels of extracellular glutamate. They have a limited capability for calcium buffering and increased permeability to calcium through the AMPA (α -amino-3-hydroxy-5-methyl-4-isoxazolepropionic acid) receptors at the cell surface (Laslo *et al.*, 2001). There is an increased chance of elevated synaptic glutamate levels in ALS because of reduced expression of the main synaptic glutamate reuptake transporter, excitatory amino acid transporter 2 (EAAT2) (Howland *et al.*, 2002). Neuronal excitotoxicity is a common disease mechanism seen across ALS cases and the commonly prescribed drug riluzole is thought to attenuate disease progression by inhibiting glutamate release from the MNs (Wang *et al.* 2004).

Astrocytes maintain homeostasis in the CNS through the strict regulation of cellular ions, osmotic balance and the buffering of glutamate, the main excitatory neurotransmitter (Coulter and Eid, 2012). Impaired glutamate uptake from the synaptic cleft leads to MN overactivation and excitotoxicity through the activation of calcium dependent enzymatic pathways, as demonstrated in Figure 1.2 (Van Damme *et al.*, 2005). EAAT1 and EAAT2 are responsible for glutamate transport into the astrocytes. After uptake, glutamate is converted into glutamine by glutamine synthase and the newly available glutamine is transported back to the pre-synaptic neurons; this process is known as glutamate-glutamine cycling (Pajarillo *et al.*, 2019). The process of glutamate uptake also stimulates glycolysis within astrocytes, generating and releasing lactate to the surrounding MNs, which is an important energy source (Ferraiuolo *et al.* 2011b).

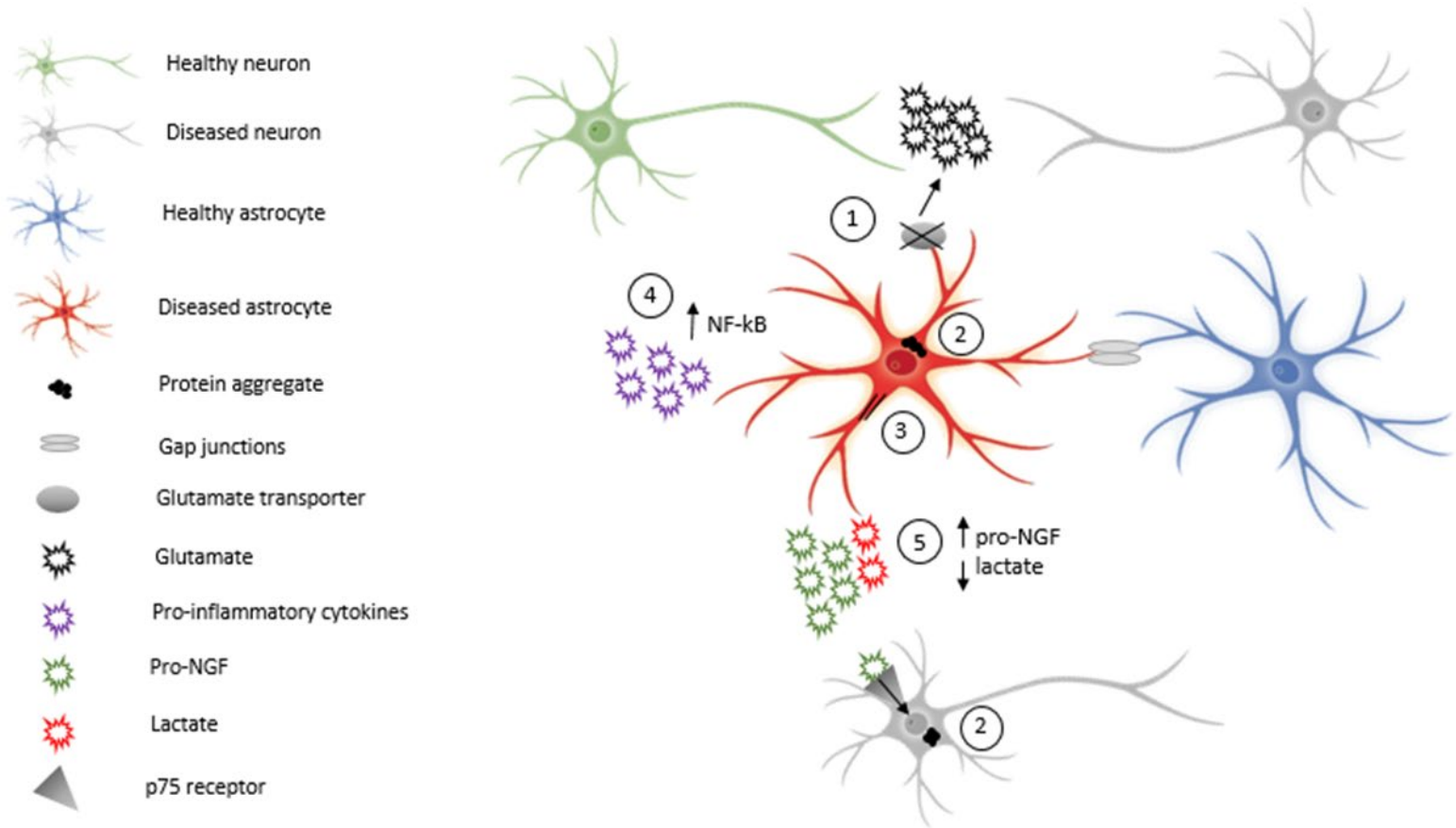


Figure 1.2 The non-cell autonomous mechanisms of disease in ALS astrocytes (Allen et al. 2017). 1) The dysregulation of glutamate transporters in astrocytes results in the accumulation of glutamate within the synaptic cleft, leading to MN excitotoxicity. 2) The accumulation of misSOD1 aggregates in astrocytes. 3) The increased expression of GFAP is a common feature of reactive astrocytes. 4) The increased NF-kB signalling promotes the expression of pro-inflammatory cytokines, resulting in neuroinflammation. 5) The suggested increase in pro-NGF which binds to p75 receptor on neurons, increasing death signalling. The consequential reduced lactate processing in astrocytes contributes to astrocyte toxicity towards MNs.

Historical studies performed by Rothstein *et al.* (1992) and Bruijn *et al.* (1997) documented that astrocytes from the motor cortex and spinal cord of patients with sALS or fALS, as well as mutant *SOD1* mouse models, had a reduced expression of EAAT2. Rothstein *et al.* (1996) also discovered that the complete knockdown of the transporter resulted in paralysis and MN degeneration. One mechanism in which EAAT2 function is lost could be through the action of the caspase-3 enzyme, a mediator of programmed cell death. Boston-Howes *et al.* (2006) demonstrated that caspase-3 cleaves EAAT2 at the cytosolic C-terminal domain of the transporter, selectively inhibiting the transporter and creating protein fragments that accumulate within the astrocytic nuclei of the spinal cord. These aggregates are known to further dysregulate astrocytic gene expression for mitochondrial function, cellular respiration and protein ubiquitination and processing (Foran *et al.*, 2011). Gallardo *et al.* (2014) demonstrated that astrocytes with the *SOD1*-G93A mutation also overexpressed the $\alpha 2$ subunit of the Na⁺/K⁺ ATPase, which has a direct effect on EAAT1 and EAAT2 through the maintenance of the electrochemical gradient (Rose *et al.*, 2009). However, how this change is affected by the reduced expression of EAAT2 is still undetermined (Filipi *et al.*, 2020).

1.2.1.2. Neuronal development and support

Astrocytes play a fundamental role in the maintenance of synaptic connectivity in the CNS. The 'tripartite synapse' formed between astroglial and neuronal synapses demonstrates the role of astrocytes in synaptic transmission mediated by the astrocytic release of neurotransmitters (Verkhratsky and Zorec, 2019). They are responsible for regulating neurite outgrowth through the secretion of growth promoting molecules, including laminin, N-cadherin, neural cell adhesion molecule (NCAM) and fibronectin, which all guide the direction of neurite growth during development as well as after injury (Wang and Bordey 2008). Astrocytes also secrete growth factors vital for brain development and homeostasis, such as brain-derived growth factor (BDNF), glial cell line-derived neurotrophic factor (GDNF), glial maturation factor (GMF), nerve growth factor (NGF) and vascular endothelial growth factor (VEGF) (Jurič *et al.* 2016).

When astrocytes detect lesions in the brain, they undergo 'reactive astrogliosis' and these activated astrocytes are thought to lack the ability to support the survival and recovery of MNs in neurodegenerative disease. The astrocytes become hypertrophic and rapidly proliferate, increasing glial fibrillary acidic protein (GFAP) expression which is the main marker for the astroglial response (Figure 1.2). Reactive astrocytes secrete cytokines and growth factors, including interleukin 6 (IL-6), C-X-C motif chemokine ligand 1, 10, 12 (CXCL1, CXCL10, CXCL12), tumour necrosis factor alpha (TNF- α) and transforming growth factor beta 1 (TGF- β 1), causing alterations in MN morphology, such as

smaller cell bodies, shorter axons, axonal swelling, and the accumulation of ubiquitin-tagged protein aggregates within the axons and somata of the MNs (Bruijn *et al.*, 1997; Tripathi *et al.*, 2017). Ferraiuolo *et al.* (2011b) demonstrated that astrocytes derived from mutant *SOD1* mouse models have altered lactate and NGF processing, leading to increased vulnerability and death of the surrounding MNs (Figure 1.2).

1.2.1.3. Inflammation and immune response

Inflammation is another common hallmark of ALS and can be easily detected in imaging studies of the cerebral cortex of ALS patients (Corcia *et al.*, 2012). Non-neuronal cells, including astrocytes and microglia, release a variety of hazardous and neuroprotective factors to the surrounding MNs. Microglia have two activated phenotypes, the neuroprotective phenotype is known as the M2 phenotype, while the toxic phenotype is classed as the M1 phenotype (Frakes *et al.*, 2014). Although widely used, this classification is quite simplistic and reductive, as microglia exist in many activation states which transition between M1 and M2. A study in a mutant *SOD1* transgenic mouse model showed that the microglia changed from the M2 phenotype to the M1 phenotype at the time of disease onset and this led to the release of pro-inflammatory cytokines at disease end-stage (Liao *et al.*, 2012).

Astrocytes are responsible for keeping inflammatory and immune responses under control to prevent neuronal damage within the brain. They can increase the permeability of the BBB by releasing neuroprotective factors towards endothelial cells, such as cytokines IL-1 and IL-6, macrophage inflammatory protein, endothelin-1 and TNF (Abbott, 2002). Astrocytes also modulate inflammatory signalling through the release of both pro-inflammatory cytokines (IL-1, IL-6, and TNF) or anti-inflammatory molecules (prostaglandin E2 and TGF- β) depending on the neurological insult (Font-Nieves *et al.*, 2012).

Neuroinflammation is a classic disease hallmark, previously presented in both mouse models and human patients with fALS and sALS cases. Mutant *SOD1*-positive astrocytes and microglia have been shown to express a multitude of pro-inflammatory genes (Philips and Rothstein, 2014). The nuclear factor-kappa β (NF- κ B) protein was identified as the master regulator of inflammation in ALS astrocytes derived from post-mortem tissue using microarray analysis (Haidet-Phillips *et al.*, 2011). The study by Frakes *et al.* (2014) demonstrated that NF- κ B signalling was activated within glia during disease progression in a mutant *SOD1* mouse model, presenting the hypothesis that NF- κ B signalling regulates microglial activation in ALS.

1.2.1.4. Protein aggregation

Like MNs, the accumulation of protein aggregates has also been demonstrated in ALS astrocytes (Figure 1.2). The transcripts produced by the *C9ORF72* hexanucleotide repeat in astrocytes leads to the formation of poly-proline-arginine peptide aggregates within the astrocytic nucleus, blocking protein transcription (Kanekura *et al.*, 2016; Hautbergue *et al.*, 2017). Astrocytes containing the mutant TDP-43 protein also presented intracellular cytoplasmic aggregates, more commonly known as stress granules, which accumulated over time and resulted in cell death (Haidet-Phillips *et al.*, 2013; Serio *et al.*, 2013). The mislocalisation of the TDP-43 protein was also present in mutant *SOD1* models as well as ALS patient post-mortem tissue (Jeon *et al.*, 2019).

1.2.2. Astrocyte models of ALS

Due to the complexity of the disease, there exist a wide variety of *in vitro* and *in vivo* models of ALS, ranging from cell lines and primary cell cultures to various small animal and rodent models, to investigate different aspects of the disease. While animal models are a crucial resource in the research of disease pathology and new treatments for ALS, they cannot truly replicate the heterogeneity witnessed in patients since transgenic animals only model the disease associated with their genetic mutation, as well as the unsuitability of animal models for large-scale high-throughput drug screening (Rinaldi *et al.*, 2017). The advancements in genetics and *in vitro* modelling over the past 10 years has greatly influenced new discoveries of ALS pathogenesis and therapeutics (Myszczynska and Ferraiuolo, 2016). In this section, I will describe and evaluate the technologies of patient-derived cellular models alongside primary cell culture.

1.2.2.1. Primary astrocytes and neural progenitor cells

Historically, studies investigating the role of astrocytes in health and disease relied upon primary cells isolated from transgenic animal models as well as cell lines. Neural progenitor cells (NPCs) isolated from post-mortem spinal cord of ALS patients have the capability to be differentiated into different cell types, including MNs, astrocytes and oligodendrocytes *in vitro*, without introducing large epigenetic alterations (Haidet-Phillips *et al.*, 2011). In 2014, Re *et al.* (2014) isolated primary astrocytes from the spinal cord and brain biopsies of ALS patients, providing another cellular model to study ALS pathology. The limitations of these models are that they only model the very late stages of disease and have limited growth and expansion for large-scale assays (Rinaldi *et al.*, 2017).

The transplantation of mutant *SOD1*-G93A expressing astrocyte precursor lines into the spinal cord of wild-type mice leads to local MN degeneration and motor system deterioration (Papadeas *et al.*,

2011). Studies have shown that transplanted wild-type astrocyte progenitor cells can survive and differentiate within the host brain; astrocyte precursor cells were transplanted into the cervical spinal cord and slowed disease progression in mutant *SOD1* rats (Lepore *et al.*, 2008). However, these protocols require the extraction of cells from the neonatal brain, for which there is a limited resource. These cells also have a different immunology profile to the host, resulting in possible rejection to transplantation, meaning that they have limited use as a cellular therapy (Bucchia *et al.*, 2015).

1.2.2.2. iPSC-derived astrocytes

In 2006, Takahashi and Yamanaka (2006) demonstrated how to reprogram adult somatic cells into iPSCs using four transcription factors: Klf4, Oct3/4, Sox2 and cMyc. This technology created excellent opportunities to study the pathological mechanism of cells directly from diseased patients. Subsequent studies reported the successful generation of MNs and glial cells from ALS patient iPSC lines carrying the mutation of interest to model both familial and sporadic disease (Dimos *et al.*, 2008; Bilican *et al.*, 2012; Burkhardt *et al.*, 2013).

Many studies have successfully reprogrammed astrocytes from human-derived iPSCs (Roybon *et al.*, 2013; Serio *et al.*, 2013). However, these protocols are time-consuming, complex and vary greatly in the maturation time of the astrocytes (Table 1.2). iPSC technology also has limitations in the fact that there is clonal selection from one donor cell as well as the loss of the epigenetic 'ageing signature' that is critical when studying diseases related to age such as ALS (Mertens *et al.*, 2015). Therefore, a promising alternative to iPSC resources is the direct reprogramming of fibroblasts into astrocytes from an immuno-matched host (Bucchia *et al.*, 2015).

Table 1.2 Protocols for astroglial differentiation from stem cells (Allen *et al.* 2017)

Cell Source	Method of Differentiation	Key transcription/growth factors	Astrocyte Outcome	Reference
Human ESCs	Neurospheres	Heparin: 2µg/ml FGF2: 20ng/ml BDNF/GDNF: 10ng/ml cAMP: 1µM Ascorbic acid: 200µM	Astrocytes appeared after 9 weeks	Johnson <i>et al.</i> 2007
Human ESCs and iPSC	Embryoid bodies	Retinoic acid: 0.5µm FGF8: 50ng/ml SHH: 500ng/ml EGF/FGF2: 10ng/ml CNTF/LIF: 10ng/ml	Populations of immature astrocytes	Krencik <i>et al.</i> 2011; Krencik and Zhang 2011
Human ESCs and iPSCs	Embryoid bodies	SB43152: 10µM Noggin: 500ng/ml	55-70% GFAP+ cells after 5 weeks	Emdad <i>et al.</i> 2012
Human IPSC	Neurospheres/ EZ spheres	EGF/FGF2: 20ng/ml CNTF: 10µl/ml	90% GFAP+ cells after 9 weeks	Serio <i>et al.</i> 2013
Mouse ESC, human ESC and IPSC	Monolayer	LDN193189: 0.2µM SB43152: 10µM Ascorbic acid: 0.4µg/ml Retinoic acid: 1µM BDNF/GDNF: 10ng/ml	100% S100β+ and 70% GFAP+ cells after 80 days	Roybon <i>et al.</i> 2013
Mouse EF, human fibroblast	Direct reprogramming	Lentiviral vectors: NFIA, NFIB, SOX9 TFs	Astrocytes derived from fibroblasts after 2-3 weeks	Caiazzo <i>et al.</i> 2015
Human fibroblast	Direct reprogramming	Retroviral vectors: Klf4, Oct3/4, Sox2 and c-Myc FGF2/EGF: 20ng/ml Heparin: 5µl/ml DMEM: 10% FBS & 0.3% N2	iAstrocytes generated from patients in less than 4 weeks	Meyer <i>et al.</i> 2014

Abbreviations: embryonic stem cell (ESC), embryonic fibroblast (EF)

1.2.2.3. Direct reprogramming

Direct reprogramming involves the use of cell-lineage transcription factors to convert adult somatic cells into a different type of cell (Meyer *et al.* 2014). Since this reprogramming method skips the pluripotent stage, cells are more likely to retain the ageing signature as well as the donor mosaicism, more accurately reflecting the pathology of the patient (Rinaldi *et al.*, 2017). This technology has been used to generate sub-specific neural lineages such as motor, dopaminergic and cholinergic neurons (Son *et al.* 2011; Pfisterer *et al.* 2011; Liu *et al.* 2013). Meyer *et al.* (2014) generated tripotent induced NPCs (iNPCs) from ALS patients as well as healthy individuals, using the protocol from Kim *et al.* (2011), within one month. When these cells were differentiated into astrocytes, they displayed similar toxicity towards MNs in co-culture as autopsy-derived astrocytes (Haidet-Phillips *et al.*, 2011), making them useful tools in the development of drug screens (Allen *et al.* 2017).

1.2.2.4. Astrocyte-MN co-culture

Previous studies have demonstrated that sALS and fALS astrocytes derived from patient post-mortem tissue can cause MN death *in vitro* (Haidet-Phillips *et al.*, 2011; Re *et al.*, 2014). However, as mentioned in the previous section, there are limitations with using primary astrocytes, including the limited availability and scalability. Due to the advancements in iPSC and direct reprogramming described previously, the research community no longer needs to rely on post-mortem tissue and animal models of disease which lack translational efficacy (Stopford *et al.* 2019).

In the protocol described by Stopford *et al.* (2019), iNPCs were derived from ALS patient fibroblasts and healthy, non-ALS control fibroblasts, and were differentiated into induced astrocytes (iAstrocytes) as described in a previous study (Meyer *et al.* 2014). These iAstrocytes were co-cultured with mouse MNs expressing the green fluorescent protein (GFP) under the Hb9 MN-specific promoter, derived using the protocol from Wichterle *et al.* (2002). Using this method, the iAstrocyte support of MNs can be measured in a high-throughput, cost-effective fashion under experimental conditions, including drug treatment, nutritional supplementation or iAstrocyte conditioned media (Hautbergue *et al.* 2017; Allen *et al.* 2019; Varcianna *et al.* 2019). This approach is more physiologically representative of the *in vivo* state of disease than astrocyte mono-culture screening methods, therefore it has a greater potential for translational research (Stopford *et al.* 2019).

1.3. ALS therapeutics

There is currently no cure for ALS, the treatment options available for patients only attempt to slow the progression of disease. Patient care also involves a multidisciplinary management of disease symptoms, including nutritional and respiratory support (Goyal and Mozaffar, 2014). The treatment options available to patients as well as upcoming advancements in ALS therapeutics are described below.

1.3.1. Gene replacement therapy

There are two main RNA targeted therapies under development for ALS, these include short interfering RNAs (siRNAs) and antisense oligonucleotide (ASO) molecules. siRNAs are double-stranded RNA molecules that downregulate the expression of complementary target genes through interaction with the RNA-induced silencing complex (Ding *et al.*, 2003). At the present time, siRNAs are still under preclinical investigation and have not yet reached clinical trials (Nishimura *et al.*, 2014; Mezzini *et al.*, 2019).

ASOs are short, single-stranded transcripts that bind to complementary RNA molecules to alter gene expression. These transcripts can be administered directly to the CNS through intrathecal injection and are readily taken up by neurons and glia once inside the body (Smith *et al.* 2006). The first AO drug in clinical trial for ALS targets both the mutant and wild type *SOD1* transcripts for RNase H-mediated degradation (Miller *et al.* 2013). This approach is now at Phase 3 clinical trials with promising results from Phases 1 and 2 recently published (Miller *et al.* 2020).

ASO technology has also been used to restore pathogenesis in *C9ORF72* patients by targeting only hypoxia-response element (HRE) containing transcripts or all *C9ORF72* transcripts for RNase H-mediated degradation. Studies using this technology have shown a reduction in the presence of RNA foci in patient-derived fibroblasts and iPSCs (Donnelly *et al.*, 2013; Lagier-Tourenne *et al.*, 2013; Sareen *et al.*, 2013) as well as the reduction of *C9ORF72* RNA in transgenic mice (Jiang *et al.*, 2016). With the continuing advancement of RNA-based technology and discovery of the genetic basis for ALS, ASOs are a promising area of research for future therapeutic developments in genetic subgroups of ALS patients (Miller *et al.* 2020).

1.3.2. Therapeutic compounds

There are only two approved drug treatments for ALS patients. Within the 20 years between the approval of these two drugs, over 60 molecules have been investigated and failed to demonstrate efficacy in ALS clinical trials (Petrov *et al.*, 2017). Some have suggested that the use of preclinical models that are not fully representative of the human disease process as well as the incredible heterogeneity within the patient population are factors contributing to the lack of translation from bench to bedside (Petrov *et al.*, 2017).

1.3.2.1. Riluzole

Riluzole is the most widely used therapeutic compound given to ALS patients. It was first approved by the FDA in 1995 and has proven to be only mildly effective, prolonging patient survival on average by 3-6 months (Bensimon *et al.* 1994). The main effect of riluzole treatment is the reduction of glutamate release from the pre-synaptic terminals via the inhibition of persistent sodium channels (Urbani and Belluzzi, 2000). The most effective treatment with riluzole requires an early diagnosis since the beneficial effects of the therapy are seen in the first 6 months of treatment (Cetin *et al.*, 2015). Originally thought to act via modulation of glutamatergic transmission (Bensimon *et al.* 1994), extensive research into the mechanism of action of riluzole has shown limited effect on glutamate

transporters, suggesting a more complex mechanism of action (Bellingham, 2011). Other anti-glutamatergic compounds, including Talampanel, Memantine and Ceftriaxone, have failed to show therapeutic benefit in ALS clinical trials (Pascuzzi *et al.* 2010; de Carvalho *et al.* 2010; Cudkovicz *et al.* 2014), further supporting the theory that riluzole acts via other mechanisms.

1.3.2.2. Edaravone

Two decades after the launch of riluzole, a new treatment for ALS was approved in Japan, South Korea, and the United States. Edaravone is an antioxidant compound thought to act via the reduction of oxidative stress, although like riluzole, the exact mechanism of action is unclear (Jaiswal, 2019). The efficacy of edaravone was assessed in two phase III clinical trials; the study reported a modest but significant improvement in the ALSFRS-R scores of a small subset of patients after edaravone treatment (Writing Group; Edaravone (MCI-186) ALS 19 Study Group, 2017).

1.3.2.3. Traditional antioxidants

Vitamin E is the most studied antioxidant compound to counteract ALS, providing protection against lipid peroxidation, reactive nitrogen species (RNS) and ROS (Barber and Shaw, 2010). In one clinical trial, vitamin E supplementation alone had no effect on survival or MN deficits in ALS patients. However, when it was combined with riluzole treatment, there was an increase in reduced glutathione (GSH), and a reduction of reactive species present in patient plasma (Desnuelle *et al.*, 2001). Regular vitamin E dietary supplementation has also been associated with a lower risk of patient mortality (Ascherio *et al.*, 2005). However, further trials on vitamin E have obtained varying results; other studies have reported that there is insufficient evidence to claim that high doses of vitamin E or dietary supplementation are able to slow disease progression (Graf *et al.*, 2005; Galbussera *et al.*, 2006).

Natural substances present in fruits and vegetables, such as carotenes and flavanoids, are also protective against ROS. In a study conducted across 5 cohorts in Korea, high dietary intake of β -carotene and lutein were associated with a reduced risk of sALS (Jin *et al.*, 2014). B-carotene has even been proposed as a potential therapeutic molecule for treating neuroinflammation and apoptosis in ALS (Krishnaraj *et al.* 2016). Quercetin is an abundant dietary flavanoid that has been shown to reduce mitochondrial damage in oxidative stress-related animal models (Carrera-Juliá *et al.*, 2020). The study by Ip *et al.* (2017) proposed that quercetin and its derivative quercetin 3- β -D-glucoside (Q3BDG) could act as chemical chaperones, preventing the misfolding and aggregation of the SOD1 protein.

1.3.2.4. Nrf2 activators

Nuclear factor erythroid 2-related factor 2 (NRF2) is known as the master regulator of cellular homeostasis, regulating more than 1% of genes within the human genome (McBean *et al.* 2017). It regulates the expression of antioxidant and cytoprotective genes through the antioxidant response element (ARE) region, as well as genes related to GSH synthesis, redox regulation, and drug metabolism (Ishii *et al.*, 2000; Thimmulappa *et al.*, 2002). More recently, genes contributing towards NADPH generation, lipid and glucose/glycogen metabolism, and hydrogen sulphide production have also been identified as Nrf2-regulated transcripts (Hayes and Dinkova-Kostova, 2014).

Under basal conditions, Nrf2 is kept at a low level through the continuous synthesis and degradation of the protein. Kelch-like ECH-associated protein-1 (KEAP1) binds to an E3 ubiquitin ligase complex (RBX1) by a cullin-3 protein adaptor (Kobayashi *et al.*, 2004); this complex provides a ubiquitin tag to Nrf2 for proteasomal degradation (Figure 1.3). However, under oxidative stress conditions, modifications of the cysteine residues of KEAP1 (Cys151, Cys273 and Cys288) prevent the poly-ubiquitination of Nrf2 by this complex. The transcription factor translocates to the nucleus, heterodimerises with small MAF or JUN proteins and binds to the ARE of target genes (Kobayashi *et al.*, 2004).

Previous studies have demonstrated a loss of Nrf2-related gene expression in the MNs of mutant *SOD1 in vitro* models and the spinal cord of ALS patients (Kirby *et al.*, 2005; Sarlette *et al.*, 2008), as well as the presence of Keap1-positive intracellular inclusions in neuronal and glial cells within patient spinal cord tissue (Tanji *et al.*, 2013). There was also a reduction of NRF2 mRNA and protein with a simultaneous increase of KEAP1 mRNA found in the motor cortex of ALS patients (Sarlette *et al.*, 2008). Vargas *et al.* (2008) demonstrated that the MN toxicity of astrocytes harbouring the *SOD1* mutation could be reversed by overexpressing Nrf2, significantly delaying disease onset, and extending survival of *SOD1* mice. Since Nrf2 has such a wide cast gene expression network, antioxidant compounds that stimulate Nrf2 production are emerging as a valuable therapeutic approach in neurodegenerative disorders in which oxidative stress plays a key role (McBean *et al.* 2017).

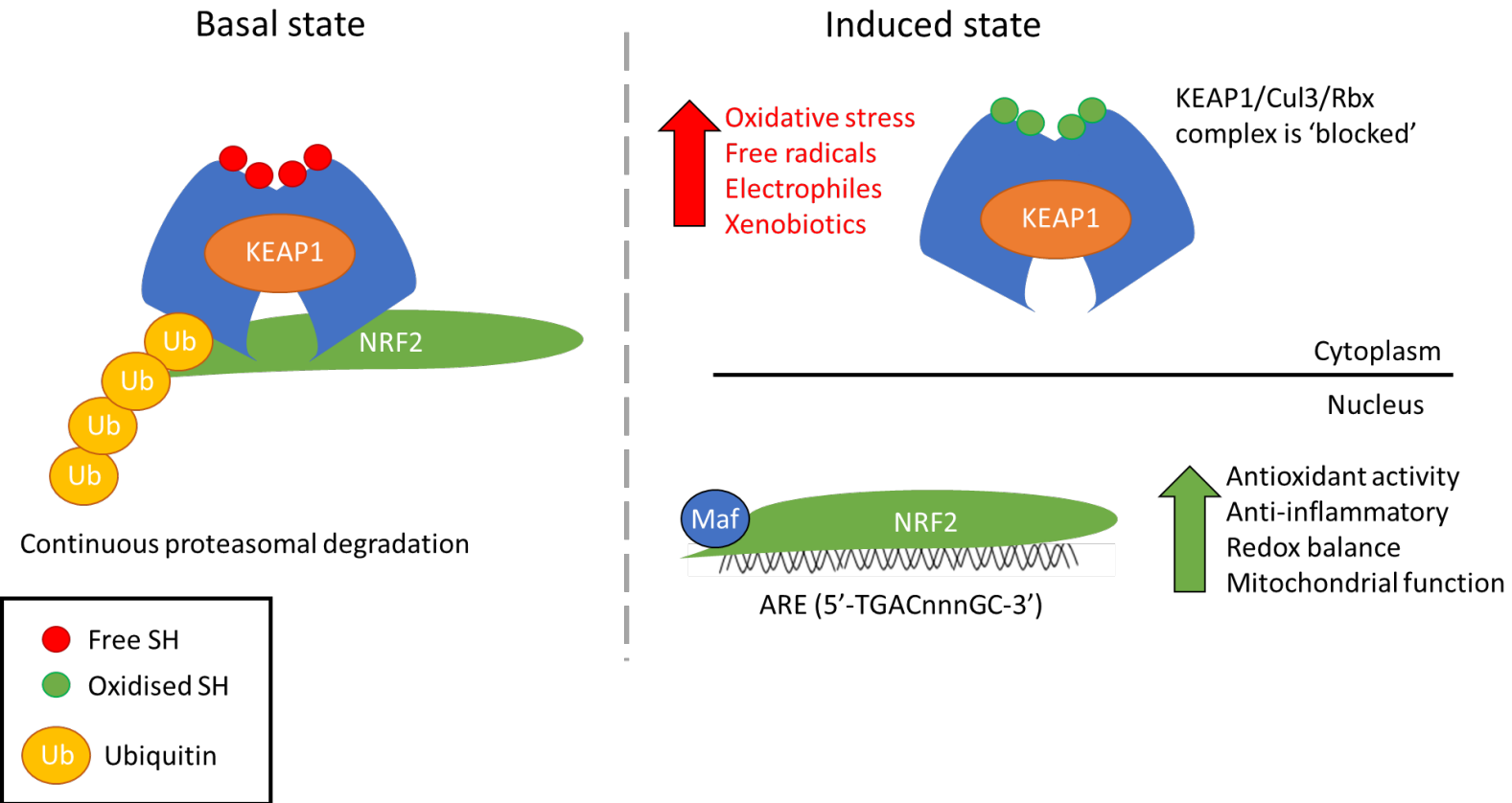


Figure 1.3 The KEAP1/NRF2 pathway (modified from Keapstone Therapeutics). Under normal conditions, the KEAP1 complex binds to the Nrf2 transcription factor and delivers it to the proteasome for degradation. Under oxidative stress conditions, the KEAP1 complex becomes 'blocked', allowing Nrf2 to translocate to the nucleus and activate the expression of ARE genes. SH = sulphhydryl group.

1.4. Personalised medicine

There are many different definitions of personalised medicine but in the broad term it is 'the use of combined knowledge (genetic or otherwise) about a person to predict disease susceptibility, disease prognosis, or treatment response and thereby improve that person's health' (Redekop and Mladi, 2013). The idea of treating patients based on their genomic blueprint has coincided with the completion of the Human Genome Project, as a greater knowledge of the human genome will allow for more effective treatments. The three main goals of personalised medicine focus on identifying disease susceptibility, diagnostic and prognostic testing, and finally, treatment of the condition.

1.4.1. The uses of personalised medicine in disease

Genomics can be used to identify patients with a specific mutation which increases their disease susceptibility. For example, genome screening can identify women who have a deleterious *BRCA1/BRCA2* mutation associated with a higher risk of developing breast or ovarian cancer. Depending on the percentage probability of disease occurrence, the patient can decide whether to undergo disease surveillance, lifestyle changes, chemoprevention or even mastectomy (Redekop and Mladi, 2013). Combining genetic information with other factors such as age, sex and lifestyle can improve estimates on disease susceptibility and prognosis.

Diagnostic tests aim to detect disease occurrence during the pre-symptomatic stage as catching the disease early will provide a better prognosis; examples of diagnostic tests include mammography screening for cancerous breast tissue and the Papanicolaou test for cervical cancer (Redekop and Mladi, 2013). Prognostic tests allow clinicians to decide the best therapy during the most optimal therapeutic window based on disease severity and patient benefit. For example, the Mamaprint prognostic test relies on gene expression profiling analysis of 70 known susceptibility genes to subgroup patients with low-risk, high-risk and intermediate prognoses (Li *et al.*, 2013).

Single nucleotide polymorphism (SNP) variability between individuals is the main cause of therapeutic failure and adverse drug reactions in patient subpopulations (Noetzli and Eap, 2013). Pharmacogenetic tests highlight if a patient is going to have an adverse reaction to a drug treatment by analysing the individual's genome and pharmacokinetics of the drug (Meckley and Neumann, 2010). For example, patients with HLA-B*1502 epilepsy are more likely to have an adverse skin reaction to the drug carbamazepine than other patients, therefore patients should be tested before commencing carbamazepine therapy (Redekop and Mladi, 2013).

These pharmacogenetic tests can also determine optimum drug dosage; for example, the anticoagulant drug warfarin needs to be administered at just the right dose because a too low dose increases the risk of thromboembolic events, while a high dose increases the risk of patient bleeding. Patients with polymorphisms in *CYP2C9* and *VKORC1* have a lower dose requirement due to a higher risk of bleeding, therefore the genotypes of the patient can be used to predict the optimum drug dose (van Schie *et al.*, 2011).

1.4.2. Personalised medicine in neurodegeneration

Since many neurodegenerative diseases share common pathological hallmarks, identifying the common pathological mechanisms between diseases will allow for the development of stratified therapeutics for more than one neurological disorder (Allen *et al.* 2017). For example, the cytoplasmic accumulation of TDP-43 has been demonstrated in multiple neurodegenerative disorders, thus creating a new spectrum of diseases called TDP-43 proteinopathies (Geser *et al.* 2010). Tan *et al.* (2015) assessed the severity of TDP-43 pathology in selected regions of the brain in patients with ALS, FTD as well as Alzheimer's disease (AD), and the authors proposed that the regional concentration of TDP-43 could potentially characterise these distinct clinical disorders.

Advances in genetics have allowed medical professionals to start tailoring the treatment to the individual for neurological disorders; however, these are still early days. To date, the main efforts towards personalised medicine have focused on improving the classification of the neurodegenerative condition using disease-specific biomarkers, as highlighted in the following sections.

1.4.2.1. ALS

The early diagnosis of ALS patients is difficult for clinicians due to the phenotypic overlap between the disease and other MN disorders (Morgan *et al.* 2018). Biomarkers, proteins, lipids, or mutant transcripts associated with disease, could provide a more accurate diagnosis as well as patient stratification of the population into groups of responders to a specific therapeutic compound. Multiple candidate protein markers for ALS have been discovered in the blood and cerebrospinal fluid (CSF). Out of these proteins, CSF neurofilaments have the best potential as neurochemical biomarkers in diagnosis and prognosis; the concentration of neurofilament-L and heavy neurofilament subunit H rise in the CSF during disease progression (Steinacker *et al.*, 2016). However, the collection of CSF samples is expensive as well as relatively invasive compared to the collection of patient blood samples (Morgan *et al.* 2018). Higher heavy neurofilament levels have

also been detected in the plasma and serum of ALS patients and were associated with a faster decline in the ALSFRS-R score and a faster disease progression (Boylan *et al.*, 2013). Increased levels of inflammatory proteins, including wide-range C-reactive protein (wrCRP), granzyme B and high mobility group box 1 (HMGB1) autoantibody, have also been correlated with a rapid decline in patient health (Keizman *et al.*, 2009; Iłżecka, 2011; Hwang *et al.*, 2013). While prognostic and diagnostic biomarkers have been identified in ALS patients, most of these biomarkers are non-specific markers of neuronal death, meaning their ability to direct patient stratification and drug development is currently minimal (Morgan *et al.* 2018).

MUNIX, a reliable electrophysiological biomarker, has also been used to track the progressive loss of LMN innervation of muscles in ALS patients and it is now a reliable prognostic indicator identifying the speed of disease progression (Neuwirth *et al.*, 2015).

As mentioned in previous sections, there are genetic mutations associated with ALS that are directly involved in mRNA processing, indicating that microRNAs (miRNAs) may play a role in the disease. Butovsky *et al.* (2015) demonstrated that the inhibition of pro-inflammatory miR-155 in mutant *SOD1* mice led to rescue from the disease phenotype by promoting the restoration of dysfunctional microglia. Interestingly, miR-125b was also expressed by microglia and activated NF- κ B signalling in the CNS through the expression of the tumour necrosis factor alpha-induced protein 3 (TNFAIP3) A20. This microRNA has also been shown to regulate NF- κ B-dependent inflammatory and oxidative stress pathways in models of AD as well as ALS (Zhao *et al.*, 2014; Parisi *et al.*, 2016). More recently, Varciana *et al.* (2019) identified the downregulation of miR-494-3p in astrocytes derived from C9ORF72-ALS patients. MiR-494-3p is a negative regulator of semaphorin 3A which is involved in axonal maintenance; the study found that restoration of miR-494-3p levels increased the survival of MNs *in vitro*. These studies highlight specific miRNAs as potential biomarkers and therapeutic targets in neurodegenerative disease.

1.4.2.2. Alzheimer's disease

Alzheimer's disease (AD) is the most common form of dementia among the elderly population (Barker *et al.* 2002). Patients are classified as having early onset AD (EOAD) if they present cognitive symptoms before the age of 65, and late onset AD (LOAD) if clinical symptoms are seen after 65 years of age (Freudenberg-Hua *et al.* 2018). The clinical features of EOAD present pathogenic hallmarks, including extracellular plaques consisting of the amyloid-beta ($A\beta$) protein and intracellular neurofibrillary tangles of abnormally hyperphosphorylated tau protein (Scheltens *et al.*, 2016), as well as a cognitive decline that affects language, reasoning and behavioural changes in the

patient (Freudenberg-Hua *et al.* 2018). The clinical classification system for AD, the NINCDS-ADRDA criteria, has a high sensitivity for diagnosing patients with AD from individuals without dementia, however it is less accurate at distinguishing between different types of dementia (Scheltens *et al.*, 2016). Therefore, in 2011, the diagnostic criteria were revised to include imaging and CSF biomarkers to discriminate between patients with pre-clinical stage, mild cognitive impairment, and dementia (Freudenberg-Hua *et al.* 2018).

The main fluid biomarkers in AD diagnosis monitor the levels of A β 42, tau and hyperphosphorylated tau (ptau) in the CSF as markers for amyloid plaques and neurofibrillary tangles (Freudenberg-Hua *et al.*, 2018; Reid *et al.*, 2020). Decreased levels of A β 42 and increased levels of tau and ptau are consistently found in the CSF of AD patients (Schindler and Fagan, 2015). The reduction in A β 42 has been associated with brain atrophy in the non-demented elderly population, indicating a pre-clinical stage of AD (Fagan *et al.*, 2009).

Alongside CSF biomarkers, there have been major advances in the identification of A β and tau deposits in brain imaging using a combination of 18-fluoro-deoxyglucose positron emission tomography (PET) and Pittsburgh compound B (PIB) PET imaging (Freudenberg-Hua *et al.* 2018). Radioactive PET ligand 1 ([¹⁸F]florbetapir) is used in the diagnosis of patients with cognitive defects to discriminate between a diagnosis of AD or other forms of dementia (Yang *et al.* 2012), while PET ligands 2 ([¹⁸F]flutemetamol) and 3 ([¹⁸F]florbetaben) are used to quantify the presence of amyloid plaques (Mason *et al.* 2013; Abou-Gharbia and Childers 2014). These ligands have the potential to improve patient treatment by monitoring patients undergoing therapy, identifying patient-risk analysis as well as patient selection for A β -targeting therapy (Allen *et al.* 2017).

1.4.2.3. Parkinson's disease

Parkinson's disease (PD) is the second most common neurodegenerative disease among the ageing population (Elbaz *et al.*, 2016). The localised death of the dopaminergic neurons within the substantia nigra pars compacta disrupts the motor control network within the basal ganglia, resulting in the motor symptoms characteristic of PD, including tremors, bradykinesia and changes in speech and gait (Stoddard-Bennett and Pera 2019). Lewy bodies and Lewy neurites containing misfolded α -synuclein are present in the neurons of PD patients and contribute to the pathogenesis of the disease (Kahle *et al.*, 2000). By the time of diagnosis, patients will have already lost on average 60-70% of their dopaminergic neurons (Khoo *et al.*, 2012), hence the need for biomarkers in the early stages of disease (Allen *et al.* 2017).

Since PD shares common clinical features with other neurodegenerative diseases, such as dementia with Lewy bodies, synucleinopathies multiple system atrophy and progressive supranuclear palsy, the rate of misdiagnosis is around 25% in early stage PD (Stoddard-Bennett and Pera 2019).

Therefore, reliable biomarkers are required for an accurate patient diagnosis. The levels of α -synuclein were reported as significantly lower in the CSF of PD patients compared to healthy individuals (Mollenhauer *et al.*, 2011). Real-time quaking-induced conversion (RT-QuIC) is a novel method to detect abnormal α -synuclein; aggregated α -synuclein is used to induce further aggregation of normal α -synuclein (Stoddard-Bennett and Pera 2019). This method can detect abnormal α -synuclein in the CSF of PD patients with 95% sensitivity and 100% specificity (Fairfoul *et al.*, 2016).

MiRNAs have also been proposed as reliable, non-invasive biomarkers for PD disease due to their tissue-specificity as well as their stability and easily quantifiable nature (Stoddard-Bennett and Pera 2019). Khoo *et al.* (2012) identified 9 pairs of miRNAs that are predictive of PD as well as 13 differentially expressed miRNAs that could be potential biomarkers. The number of predictive miRNAs was reduced to three candidate markers that showed the highest predictive biomarker performance: k-TSP1(miR-1826/miR-450b-3p), miR-626, and miR-505. More recently, Chen *et al.* (2017) identified 31 upregulated and 19 downregulated miRNAs within PD patients. MiR-4639-5p was significantly upregulated in PD patients, which was not affected by gender, age of disease onset or disease severity, indicating that this miRNA could be a stable biomarker for the diagnosis of pre-clinical PD (Chen *et al.* 2017).

Alongside the discovery of diagnostic biomarkers, the field of pharmacogenetics has identified genetic differences for the heterogeneous response to L-Dopa treatment in PD patients, especially related to dopamine transporters, receptors and enzymes responsible for dopamine processing (Stoddard-Bennett and Pera 2019). Patients harbouring a polymorphism of the dopamine active transporter 1 (DAT1) gene are more likely to develop dyskinesias after treatment with L-Dopa. Consequently, patients with a different point mutation in DAT1 were shown to have a higher risk of hallucinations when treated with L-Dopa (Stoddard-Bennett and Pera 2019). Gender-specific factors have also been investigated; polymorphisms in dopamine receptor D2 (DRD2) protect against L-Dopa induced dyskinesias in male but not female patients (Zappia *et al.*, 2005). These known genetic differences will aid the tailoring of the treatment to the individual in PD.

1.4.3 Astrocytes driving therapeutics

As summarised in the previous section, astrocytes contribute to a series of toxic and/or reduced support mechanisms affecting neuronal function and survival. Therefore, these cells are vital in the development of personalised medicine as described in the areas below (summarised in Figure 1.4).

1.4.3.1. Cellular transplantation therapy

Cellular replacement is an upcoming therapy for neurodegenerative disease as it is able to provide therapeutic benefit through replenishment of lost or dysfunctional cell types as well as reducing inflammation and protein aggregates (Bucchia *et al.*, 2015). As described previously, astrocytes play a large role in homeostasis within the CNS, therefore cellular transplantation of healthy astrocytes from an external source could provide benefit to neurological disorders in which endogenous astrocytic support has been lost.

Izrael *et al.*, (2018) generated astrocyte progenitor cells (APCs) from human embryonic stem cells (ESCs) that could be further expanded and differentiated into astrocytes. These cells demonstrated the functional properties of healthy astrocytes, including glutamate uptake, promotion of axonal growth, neuroprotective growth factor secretion and protection from oxidative stress. Intrathecal injection of these astrocytes into the CSF of human *SOD1-G93A* mice and rats significantly delayed disease onset and death in the animal models (Izrael *et al.*, 2018). These cells were also injected into NSG immune-deficient mice to assess key safety aspects, including toxicity, biodistribution, tumour formation and long-term engraftment, in preparation for moving towards human clinical trials. The safety and efficacy of these astrocytes are currently being investigated in human clinical trials (ClinicalTrials.gov identifier: NCT03482050). Other clinical trials using the transplantation of glial progenitors for ALS are listed in Table 1.3.

Table 1.3. Current clinical trials using transplantation of glia progenitors for ALS
(<https://clinicaltrials.gov/ct2/home>)

Study name	Condition	Intervention
Safety of the Injection of Human Glial Restricted Progenitor Cells Into Subjects With ALS	ALS	Transplantation of human glia progenitor cells
Dose Escalation and Safety Study of Human Spinal Cord Derived Neural Stem Cell Transplantation in ALS Patients	ALS	Transplantation of human spinal cord stem cells
Transplantation of Human Neural Progenitor Cells Secreting GDNF for the Treatment of ALS	ALS	Transplantation of human glia progenitor cells

Transplantation studies have shown that human NPCs engineered to secrete the neurotrophic factor GDNF (hNPC^{GDNF}) are able to survive, differentiate and release GDNF when transplanted into the *SOD1*-G93A rat lumbar spinal cord (Suzuki *et al.*, 2007). While GDNF secretion had a significant effect on MN survival, there was no effect on motor function in the animal studies, potentially due to the delayed differentiation of the progenitors into mature astrocytes. GMP-manufactured hNPC^{GDNF} cells (CNS1-hNPC-GDNF) were investigated in a Phase 1 ALS clinical trial (ClinicalTrials.gov identifier: NCT02943850). Thomsen *et al.* (2018) speculated that the lack of motor system benefit was due to the localised delivery to the spinal cord, while hNPC^{GDNF} cells transplanted into the cortex of *SOD1*-G93A rats were able to enhance survival of UMNs and LMNs as well as delaying paralysis and extending the lifespan of the animal. The authors state that the delivery method, tissue, as well as the targeting of specific cell types within the tissue are all critical for maximising the therapeutic benefit of GDNF release from transplanted progenitors (Thomsen *et al.*, 2018).

More recently, human neural stem cells (NSCs) were delivered via spinal subpial injection into immunodeficient rats, leading to near complete cellular occupation of the whole rat spinal cord after 6-8 months (Marsala *et al.*, 2020). Many of the subpial-injected cells differentiated into astrocytes and were incorporated into the glia limitans, a thin layer of GFAP positive astrocytes on the surface of the spinal cord. Marsala *et al.* (2020) found that the hNSC-derived astrocytes acquired morphological and functional characteristics of endogenous astrocytes within the glia limitans, for example, the expression of the *SOD1* protein as well as the expression of human-specific laminin. Since the pathophysiology of ALS is so widespread, patients would benefit from subpial hNSC homogenous delivery throughout the spinal cord. In addition, this delivery method resulted in the repopulation of the glia limitans with *SOD1* and GLAST-expressing astrocytes, restoring astrocytic function, especially in mutant *SOD1* associated ALS (Marsala *et al.*, 2020).

1.4.3.2. Drug screening

As described previously, almost all experimental drugs for ALS have failed clinical trials, potentially because of the unreliability of current animal models or the heterogeneity of the patient population (Petrov *et al.*, 2017). To investigate this issue, Isobe *et al.* (2015) used hESC-derived MNs with identical genetic backgrounds but differing mutations in the *SOD1* gene to investigate whether differentiation in the genetic mutation would lead to a differential drug response. The authors discovered mutant-specific morphological alterations within the MNs, and this led to observed differential drug responses. This indicates that heterogeneous patient populations will not benefit

from the same drug treatment, thus indicating that there is a great need for targeted personalised medicine, especially in diseases with variable phenotypes such as ALS (Allen *et al.* 2017).

Consistently, Shichinohe *et al.* (2004) found that edaravone only provided neuroprotective effects to MNs expressing the *SOD1*-G93A mutational variant. This suggests that some neuroprotective drugs may be effective at treating ALS phenotypes with specific genetic mutations. Currently, there are no reports that astrocytes also display these *SOD1* mutational-dependent drug responses, but this question should be addressed if we are to attempt to classify ALS into patient-responsive categories (Allen *et al.* 2017).

Most drugs have a targeted approach; they target only one gene/biological pathway which selectively promotes disease treatment while avoiding adverse effects. However, drugs with a selective target do not always deliver an effective treatment, as target engagement and phenotypic effect do not always match, especially in complex disease pathologies (Allen *et al.* 2017). For this reason, there is more interest in the development of phenotypic screening assays with a disease-relevant readout (Stopford *et al.* 2019).

High content analysis (HCA) combines microscopic imaging with automated analysis to investigate morphological features in tissue or *in vitro* models. It has previously been adopted by pharmaceutical companies to perform high-throughput image-based drug screening platforms to identify new compounds (Rinaldi *et al.*, 2017). The combination of the right *in vitro* model with a gene expression array, HCA could be a valuable application for functional genomic studies as well as phenotypic profiling in disease models (Rinaldi *et al.*, 2017). Using iPSC technology, Egawa *et al.* (2012) were the first to apply HCA to investigate the disease phenotypes of MNs derived from ALS patient fibroblasts. This study demonstrated that the model recapitulated several hallmarks of the disease as well as the application in a small drug screen to identify compounds that would promote MN survival (Egawa *et al.*, 2012). While this approach has been adopted for MNs, few studies have focused on astrocytes and the application of co-cultures investigating multiple cell types.

By adopting the methods described in Meyer *et al.* (2014), Rinaldi and colleagues obtained a homogenous base layer of iAstrocytes derived from ALS patient fibroblasts and cultured Hb9-GFP positive MNs on top of the iAstrocytes in 96 well plates; this protocol was later optimised to run in 384-well dishes for a greater scale (Rinaldi *et al.*, 2017). Phenotypic features of the MNs, such as the average number of branch points and neurite area, were monitored for 4 days as an indication of MN health and survival. The authors later described this robust assay to identify drugs that can dampen ALS astrocyte toxicity against MNs with a Z-score of 0.679, indicating the quality of the assay and the suitability of HCA applications, thus supporting the idea that astrocytes and co-culture

screenings can be used for high-throughput drug screening (Rinaldi *et al.*, 2017). More recently, studies have used the optimised protocol described in Stopford *et al.* (2019) to investigate different mechanisms of the toxic effect of patient-derived iAstrocytes on MN survival in co-culture (Hautbergue *et al.* 2017; Allen *et al.* 2019; Varcianna *et al.* 2019).

Screening a large number of patient-derived cells will allow us to investigate the different cellular features of sALS and fALS cases, potentially identifying biomarkers associated with specific genetic mutations (Rinaldi *et al.*, 2017). Grouping patients by these differences in disease pathology could improve the efficacy of current clinical trials as well as moving towards patient stratification of drug treatment in ALS.

1.4.3.3. Genomics and Transcriptomics

Gene expression profiling has contributed greatly to the understanding of the molecular mechanisms underlying neurodegenerative diseases by identifying specific biochemical pathways and cellular processes that are altered during disease (Allen *et al.* 2017). Clear gene expression profiles of the CNS are difficult to obtain due to the complex interplay of glial cells interspersed between different subtypes of neurons. This means that cell specific gene expression changes are difficult to identify in whole brain tissue (Srinivasan *et al.*, 2016).

To overcome this problem, laser capture microdissection (LCM) is used to isolate single cells from the brain or spinal cord, collecting a highly enriched cell population for transcriptomic analysis for the identification of pathways specifically altered in astrocytes during ALS disease progression (Ferraiuolo *et al.* 2011b; Baker *et al.* 2015; Waller *et al.* 2016). In a longitudinal study analysing astrocytes isolated from the spinal cord of mutant *SOD1* mice, Ferraiuolo *et al.* (2011b) identified the dysfunction within the lactate shuttle between astrocytes and neurons at the pre-symptomatic stage of ALS for the first time. Using similar methods, Baker *et al.* (2015) demonstrated the increase in inflammatory pathways and cytokine production, along with astrocytic lysosomal and phagocytic activity, correlated with disease progression.

More recently, *in vitro* models have been applied to investigate transcriptomic changes in disease. Birger *et al.* (2019) demonstrated the transcriptional and functional changes induced by the *C9ORF72* mutation using iPSC-derived astrocytes from *C9ORF72*-ALS patient donors. Whole transcriptome analysis revealed that a total of 899 genes were significantly differentially regulated in the *C9ORF72* astrocyte lines compared to control. Gene enrichment analysis of these significantly altered genes highlighted pathways associated with cell cycle inhibition and activation of cellular

senescence in patient astrocytes (Birger *et al.*, 2019). This study demonstrates how *in vitro* models, such as patient-derived cells, can be used alongside mouse models and post-mortem tissue studies to identify the underlying disease mechanisms within ALS pathology.

Looking at multiple cell types, Aronica *et al.* (2015) performed a whole-genome expression analysis of post-mortem cortex tissue from sALS patients and healthy individuals to investigate the entire spectrum of gene expression and molecular pathways associated with disease pathology in these patients. Gene expression analysis allowed for the discrimination between patient and control samples, and the patient samples were further subdivided into groups based upon similarities in expression profile changes. The molecular taxonomy of patients by gene expression analysis is commonly used in cancer to diagnose and tailor the personalised treatment of patients (Biswas *et al.* 2016); this gene expression data could be applied in similar way to uncover the unknown pathogenic mechanisms and develop personalised treatment in sALS (Aronica *et al.*, 2015). This gene expression data was applied in a later study to identify new drug target candidates for ALS by comparing the expression changes between the sALS patient tissue and a mutant *SOD1* mouse model; the authors found that the candidate target genes in mouse exhibited similar expression patterns as the human tissue as well as common pathway dysregulation within the gene targets, implying the existence of a conserved transcriptional signature underlying disease pathology (Morello *et al.*, 2017).

1.4.3.4. Biomarkers

Biomarkers are typically divided into three sub-categories: prognostic (determining the stage of disease), therapeutic (determining the right drug at the right dose) and predictive (determining the effectiveness of the treatment). A reliable biomarker is sensitive, specific, and has a positive predictive value (Dosay-Akbulut, 2016). Over the past few years, genomic, proteomic and bioinformatic technology have been used to develop more accurate biomarkers for disease. Establishing reliable biomarkers for ALS will increase treatment efficiency and safety as well as reducing the cost of diagnostic methods and treatments (Dosay-Akbulut, 2016).

As described previously, biomarkers for neurological disease are detected in patient CSF, blood or serum and previous studies have identified proteins that are indicative of glial health. The detection of GFAP in the CSF is a useful marker of astrocytic damage and activation (Benninger *et al.*, 2016). Papa *et al.* (2014) detected increased levels of GFAP in the blood serum after traumatic brain injury (TBI). Another astrocytic marker, S100 β , has also been detected in the blood of patients with neurological disorders. Increased levels of S100 β have been reported in the astrocytes and MNs of ALS patient spinal cord as well as in patient CSF, correlating with disease progression (Migheli *et al.*,

1999; Süßmuth *et al.*, 2010). A comparative study between GFAP and S100 β as clinical biomarkers for TBI found that S100 β rose and peaked within the serum at 2 hours post-injury while GFAP had a longer, more stable increase over 4 hours after injury (Papa *et al.*, 2014). Using GFAP as a clinical biomarker for neurodegenerative disease could be a cost-effective replacement to expensive imaging scans while still retaining diagnostic sensitivity (Sajja *et al.* 2016). Unfortunately, while GFAP levels were elevated in the CSF of ALS patients, due to the wide range of distribution within the patients tested, the authors could not define a cut-off level for an accurate diagnosis of ALS (Benninger *et al.*, 2016).

Shepherd *et al.* (2014) identified the extracellular domain of the neurotrophin receptor p75 (p75NTR^{ECD}) as a potential biomarker for ALS; increased levels of p75NTR^{ECD} were detected in the urine of human ALS patients and mutant *SOD1* mice. The increased activation of p75 signalling, alongside pro-nerve growth factor, was previously identified as an important component of astrocyte toxicity in ALS (Ferraiuolo *et al.* 2011b).

Recent studies investigating the role of astrocytes in ALS pathogenesis have led to the discovery of more potential astrocytic biomarkers in disease. YKL40 is a glycoprotein, mainly expressed in astrocytes, belonging to the family of chitinase-like proteins and the increased expression of this protein has been previously linked to inflammation in stroke, TBI and multiple sclerosis (MS) (Andrés-Benito *et al.*, 2018). The upregulation of YKL40 mRNA was previously detected in the motor cortex and increased proteins levels in the CSF were found to correlate with disease progression in sALS (Sanfilippo *et al.*, 2017; Illán-Gala *et al.*, 2018). Since the functional implications of elevated YKL40 levels in ALS and other neurodegenerative diseases are unknown, it was speculated that while the increased protein level may not be disease specific, YKL40 remains a good biomarker for disease progression in sporadic disease (Andrés-Benito *et al.*, 2018). Another protein secreted by reactive astrocytes, lipocalin-2 (LCN2) (Staurenghi *et al.*, 2020), was recently detected at elevated levels in the plasma of ALS patients; since LCN2 is resistant to degradation and detectable in CSF, plasma and urine, it is a good potential diagnostic biomarker for ALS (Ngo *et al.*, 2015; Petrozziello *et al.*, 2020).

As described previously, miRNAs have been identified as potential disease biomarkers for both PD as well as ALS. Changes in miRNA expression have been linked to astrocyte reactivity in disease as well as the secretion of miRNAs within astrocyte-derived extracellular vesicles to target MN degeneration (Gomes *et al.*, 2019; Varcianna *et al.*, 2019). Gomes *et al.* (2019) reported the downregulation of miR-146a as a pivotal player in the early stages of ALS pathology as it was responsible for mediating inflammation as well as promoting astrocytic proliferation, making it a pivotal new biomarker and therapeutic target in ALS.

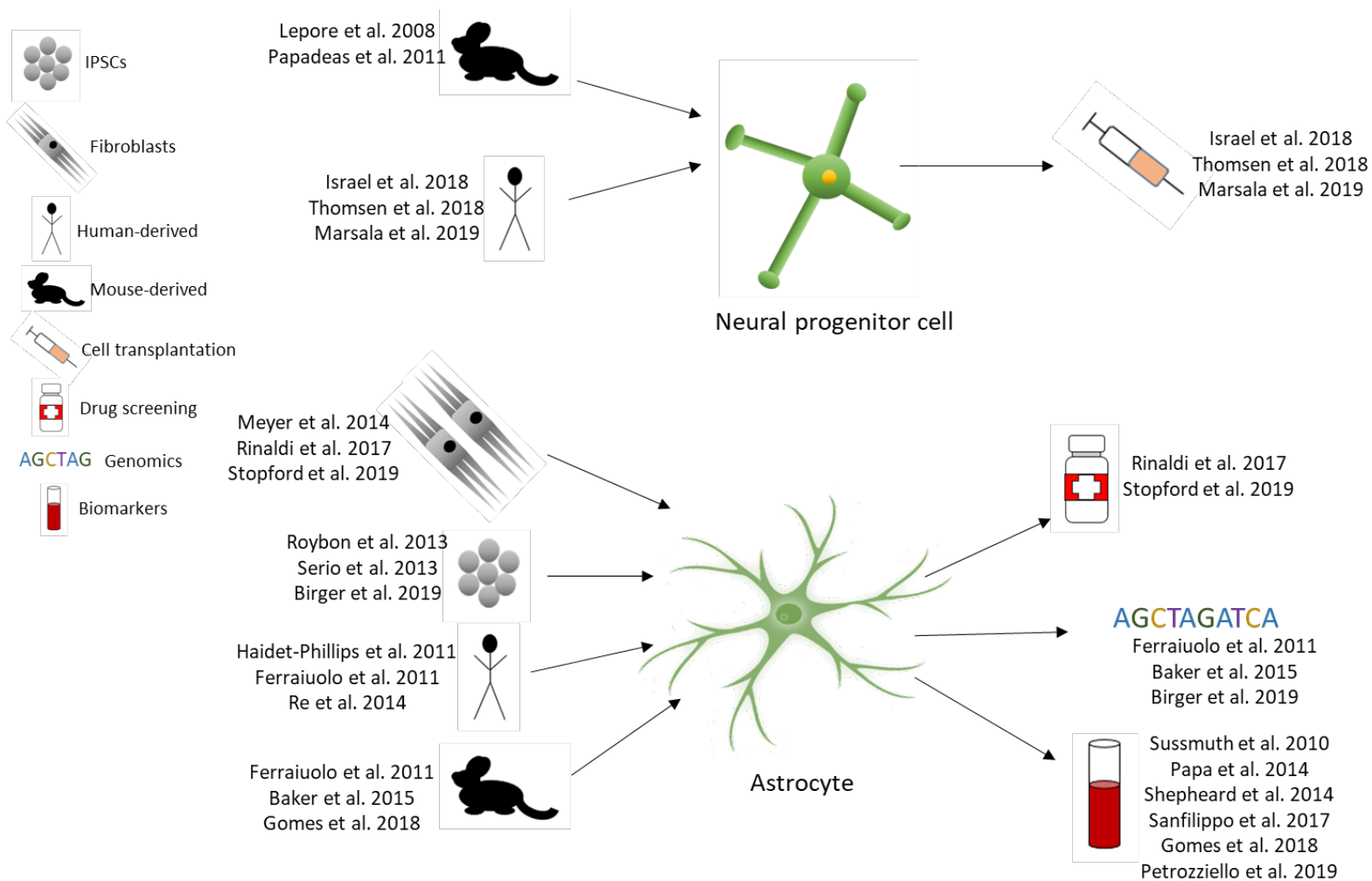


Figure 1.4 Astrocytes as a target for personalised medicine in ALS (modified from Allen et al 2017). Astrocytes and NPCs can be harvested from mice, human brain, or spinal cord, or derived from fibroblasts or stem cells using differentiation and reprogramming technology. They have a wide variety of uses in personalised medicine, including cellular transplantation therapy, drug screening, genomic expression, and biomarker studies.

1.5. Hypothesis & Aims

ALS is a widely heterogeneous disease with any of the large variety of genetic mutations and mostly unknown environmental factors contributing to the disease progression of any one patient. This variability no doubt contributes to the drug failure seen in clinical trials over the past 20 years due to the involvement of different disease mechanisms at different time points. The treatment method of diseases with such a high level of variability, such as cancer, are beginning to adopt a more personalised method with the aim to stratify drug development and give the patient the best possible chance of survival.

Oxidative stress has been a major focus in ALS research over the years as it is known to exacerbate multiple pathological mechanisms. In this study, we will use three antioxidant compounds that target the Nrf2 pathway that has reported downregulation in ALS cases over healthy controls. We believe that these Nrf2 activators will be able to overcome this patient variability as they activate a large cascade that affects several pathways.

In order to assess the potential to adopt a precision medicine approach, a rigorous model is required that also reflects this patient variability. Directly reprogrammed cells have the upper hand in this case as this technology can be used to capture each patient's unique condition in the laboratory within a few months. Not only do these cells resemble the pathological aberrations discovered in the patient, but they also retain the epigenetic profile after the reprogramming as opposed to iPSCs, which is vital when modelling age-related neurological disorders. These cells can then be subjected to a high-throughput drug screen to find hits for each individual patient.

The underlying hypothesis of the present study is that there is the potential to improve the treatment of ALS by adopting a personalised medicine approach to treatment. In the case of the antioxidant compounds used in this study, they are exerting their beneficial effects through the targeting of different pathways, hence why one drug is more beneficial to one subgroup over another. Therefore, the aims of this project are:

Aim 1: To identify the pathological aberrations that distinguish ALS patient subgroups.

Objective 1: To characterise the control and patient astrocytes, I will use phenotypic assays such as immunocytochemistry, western blot and mitochondrial membrane potential assays to assess classical pathologies associated with ALS, including TDP-43 proteinopathy, SOD1 protein misfolding, autophagic regulation, mitochondrial function and glutamate buffering.

Aim 2: To identify the modes of action of the antioxidant drugs and discover genetic signatures that can be used to discriminate between patients that respond to a certain treatment versus non-

responders.

Objective 2: This aim will be achieved through RNA sequencing analysis of the genes and pathways differentially regulated in response to the drug treatment and analysing how these pathways differ between specific subgroups. The use of the phenotypic readouts used previously alongside the RNA sequencing data, should help determine the mechanism of action of the compounds.

Aim 3: To evaluate the efficiency of the current prescribed treatment of ALS, riluzole.

Objective 3: To evaluate the efficacy of riluzole, I will also assess how riluzole impacts TDP-43 pathology, protein misfolding, autophagic regulation and mitochondrial function through the same phenotypic assays and RNA sequencing data as well as investigating the effects of riluzole on glutamate buffering in specific patient astrocytes.

Chapter 2 - Materials & Methods

2.1. Materials

All plastics for cell culture were purchased from Greiner Bio One, unless otherwise specified.

All cell culture reagents and chemicals were purchased as described as follows:

2.1.1. Cell culture media and reagents

- iAstrocyte medium
 - Dulbecco's Modified Eagle's Medium (DMEM) (Sigma)
 - Foetal Bovine Serum (FBS) (Life Science Products)
 - N2-Supplement (Gibco Life Technologies)
 - Pencillin/Streptomycin (Lonza BioWhittaker)
- Hu Plasma Fibronectin (Millipore)
- StemPro® Accutase® (Gibco Life Technologies)
- iNPC medium
 - B27-Supplement (Gibco Life Technologies)
 - DMEM/F-12 (1:1) (1X) + GlutaMAX (Gibco Life Technologies)
 - N2-Supplement (Gibco Life Technologies)
 - bFGF (Peprotech)
- Andrographolide (Flurochem; 078895)
- S[+]-Apomorphine (SIGMA; D043)
- Mono-methyl fumarate (MMF) (Aldrich; 651419-IG)
- Riluzole (Apollo Scientific Ltd; PC1100C)
- Dimethyl Sulphoxide Hybri-max® (DMSO) anhydrous 99.9% (SIGMA)
- Mouse Embryonic Stem Cell medium
 - KnockOut DMEM (Gibco Life Technologies)
 - Embryonic Stem Cell FBS (Gibco Life Technologies)
 - L-glutamine (Lonza BioWhittaker)
 - Minimum Essential Medium Non-Essential Amino Acids (MEM NEAA) (100x) (Gibco Life Technologies)
 - 2-mercaptoethanol (SIGMA)
- Embryoid bodies/motor neuron medium
 - KnockOut DMEM/F12 Nutrient Mix (Gibco Life Technologies)
 - KnockOut Serum (Gibco Life Technologies)
 - N2-Supplement (Gibco Life Technologies)
 - L-glutamine (Lonza BioWhittaker)
 - 30% filtered glucose (SIGMA)
 - 2-mercaptoethanol (SIGMA)
- Motor neuron factors
 - Retinoic acid (RA) and Smoothened agonist (SAG) (SIGMA)
 - Brain-Derived Neurotrophic Factor (BDNF), Ciliary Neurotrophic Factor (CNTF) and Glial Cell-Derived Neurotrophic Factor (GNTF) (Peprotech)
- Papain (SIGMA)
- DNase I (SIGMA)
- Formaldehyde (Fischer Scientific)

- Triton™ X-100 (AppliChem)
- Hoechst 33342, Trihydrochloride, Trihydrate (Life Technologies)
- Phosphostop (PS) (Roche)
- Proteinase Inhibitor Cocktail (PIC) (Roche)
- ProtoGel 30% (w/v) Acrylamide: 0.8% (w/v) Bis-Acrylamide Stock Solution (Gene Flow Limited)
- Ammonium persulphate (APS) (SIGMA)
- Tetramethylethylenediamine (Temed) (SIGMA)
- Bradford protein assay dye reagent (Bio-Rad Laboratories)
- Pre-stained protein ladder (Geneflow)
- Dried Skimmed Milk (Marvel)
- EZ-ECL (Biological Industries)
- SYPRO Ruby protein blot stain (Invitrogen)
- Galactose (SIGMA)
- Minimum Essential Medium (Gibco Life Technologies)
- Carbonyl cyanide 3-chlorophenylhydrazone (CCCP) (SIGMA)
- Tetramethylrhodamine, Methyl Ester, Perchlorate (TMRM) (Invitrogen)
- Phenylmethanesulfonyl fluoride (PMSF) (SIGMA)
- Ribosafe RNase inhibitor (0.16 U/μl; Bioline)
- NP-40 (IGEPAL®CA-630; SIGMA)
- Proteinase K (Melford, SIGMA)
- PureZOL RNA isolation reagent (Bio-Rad Laboratories).
- Direct Zol RNA Miniprep Plus kit (Zymo Research).
- NEB Next® Poly(A)+ mRNA Magnetic Isolation Module (New England BioLabs Inc.)
- NEB Next® rRNA depletion kit (New England BioLabs Inc.)
- High Capacity cDNA Reverse Transcription Kit (Applied Biosystems)
- 2 x SYBR Green/Rox PCR Master Mix (Bimike.com)
- Glutamate Assay Kit (Abcam)

2.1.2 Solutions

Table 2.1 Composition of solutions used in experiments

Solution	Components
PBS 1X	137mM NaCl, 2.68mM KCl, 10.14mM Na ₂ HPO ₄ (anhydrous), 1.76mM KH ₂ PO ₄ (anhydrous) made up to volume with deionised water
DEPC treated water	0.2% v/v of diethyl pyrocarbonate (DEPC) in H ₂ O solution was left to stand in the fume hood overnight and then autoclaved.
Enzyme buffer	116mM NaCl, 5.4 mM KCl, 26mM NaHCO ₃ , 1 mM NaH ₂ PO ₄ , 1.5 mM CaCl ₂ , 1 mM MgSO ₄ , 25mM glucose, 0.5 mM EDTA, 1 mM cysteine
Blocking Buffer Immunostaining	5% horse serum (Dako), 0.05% Triton in PBS
IP lysis buffer	150mM NaCl, 50mM HEPES, 1mM EDTA, 1mM DTT, 0.5% (v/v) Triton™ X-100, pH 8.0
RIPA buffer	150mM NaCl, 50mM Tris, 0.5% (w/v) SDS, 0.5% (w/v) deoxycholate, 1% (v/v) Triton™ X-100, pH 8.0
Urea buffer	7M Urea, 30mM Tris, 1mM EDTA, 2M Thiourea, pH 8.5
Resolving buffer	1.5 M Trizma®, 13.9 mM SDS, pH 8.8, filtered
Stacking buffer	0.5 M Trizma®, 13.9 mM SDS, pH 6.8, filtered
4x Laemmli buffer	228mM Tris-HCl, 38% (v/v) glycerol, 277mM SDS, 0.038% (w/v) bromophenol blue, 5% (v/v) β-mercaptoethanol pH 6.8
Running buffer	25mM Tris, 3.5mM SDS, 20mM glycine
Transfer buffer	47.9mM Tris, 38.6mM glycine, 1.38mM SDS, 20% methanol
Ponceau	0.1% (w/v) Ponceau S (Sigma), 5% 9v/v acetic acid in dH ₂ O
Tris Buffered Saline, with Tween® 20 (TBST)	20mM Tris, 137mM NaCl, 0.2% (v/v) Tween® 20, pH 7.6
GRASPs Buffer A	250mM sucrose, 5mM KCl, 50mM Tris-HCl
GRASPs Buffer B	250mM sucrose, 500mM KCl, 50mM Tris-HCl, 5mM MgCl ₂
Sucrose cushion	1M sucrose, 5mM MgCl ₂ , 50mM Tris-HCl
Ribosomal resuspension buffer	50mM HEPES, 150mM NaCl, 1mM DTT, 1mM EDTA

2.1.3. Cell culture

2.1.3.1. Induced neural progenitor cells (iNPCs)

The iNPCs used in this study were reprogrammed from fibroblasts donated by healthy individuals and ALS patients; further information is presented in Table 2.2. Professor Pamela Shaw provided the fibroblast samples from the University of Sheffield (UoS; Study number STH16573, Research

Committee reference 12/YH/0330), Professor Stephen Kolb provided the fibroblast samples from Ohio State University (OSU; ethics number 04304AR) and two fibroblast lines were purchased from the biorepository Coriell under the material transfer agreement (MTA). Informed consent was obtained from all donors before sample collection.

Table 2.2 Patient information of the iNPC lines

Sample	Type of ALS	Sex	Age at biopsy collection (years)	Ethnicity	Onset to death (months)	Biobank of origin
3050	Non-ALS control	M	68	Caucasian	-	UoS
155	Non-ALS control	M	40	Caucasian	-	UoS
AG08620	Non-ALS control	F	64	Caucasian	-	Coriell
209	Non-ALS control	F	69	Caucasian	-	UoS
009	sALS	F	61	Caucasian	21	OSU
12	sALS	M	29	Caucasian	90	OSU
17	sALS	M	47	Caucasian	72	OSU
78	C9ORF72	M	66	Caucasian	31.7	UoS
183	C9ORF72	M	50	Caucasian	27	UoS
201	C9ORF72	F	66	Caucasian	19.4	UoS
100	SOD1 (A4V)	F		Caucasian	100	OSU
102	SOD1 (A4V)	F		Caucasian	200	OSU
ND29505	SOD1 (D90A)	M	56	Caucasian	?	Coriell

2.1.3.2. Hb9-GFP mouse embryonic stem cells (mESC)

To visualise the MNs in the high throughput iAstrocyte-MN co-culture system, MNs were harvested from the differentiation of a transgenic mESC line in which GFP complementary DNA (cDNA) was expressed under the control of the homeobox gene Hb9 MN-specific promoter into embryoid bodies (EBs) (Wichterle *et al.*, 2002). The Hb9-GFP mESCs used in this study were a kind gift from Professor Thomas Jessell.

2.1.4. Antibodies

2.1.4.1. Immunocytochemistry antibodies

Table 2.3 Primary and secondary antibodies used to detect astrocyte and pathological markers

Astrocyte/Pathological marker	Primary antibody	Conc.	Supplier	Secondary antibody (all 1:1000)	Conc.	Supplier
Vimentin	1:1000 dilution (chicken)	N/A	Millipore; AB5733	Goat anti-chicken Alexa 488	2mg/ml	Invitrogen; A11039
CD44	1:200 dilution (rabbit)	1mg/ml	AbCam; ab157107	Goat anti-rabbit Alexa 488	2mg/ml	Invitrogen; A11008
TDP-43 (C-terminus)	1:100 dilution (rabbit)	1µg/150µl	Proteintech; 12892-1-AP	Goat anti-rabbit Alexa 568	2mg/ml	Invitrogen; A11011
SOD1	1:100 dilution (mouse)	N/A	MEDIMABS; MM-0070-P	Donkey anti-mouse Alexa 568	2mg/ml	Invitrogen; A10037
p62	1:200 dilution (mouse)	250µl/ml	BD Biosciences; 610833			

2.1.4.2. Western blot antibodies

Table 2.4 Primary and secondary antibodies used to detect proteins on a nitrocellulose membrane

Protein of interest	Primary antibody	Conc.	Supplier	Secondary antibody (all 1:1000)	Conc.	Supplier
TDP-43	1:1000 dilution (rabbit)	1µg/150µl	Proteintech; 12892-1-AP	Rabbit HRP	1mg/ml	Promega; W401B
NQO1	1:1000 dilution (rabbit)	1mg/ml	AbCam; ab34173			
HSF1	1:1000 dilution (rabbit)	N/A	Cell Signalling; 4356S			
HSP70	1:1000 dilution (rabbit)	N/A	AbCam; Ab69412			
SOD1	1:1000 dilution (rabbit)	N/A	Cell Signalling; 2770S			
LC3	1:1000 dilution (rabbit)	1mg/ml	Novus Biologicals; NBP2-46888			
EAAT2	1:1000 dilution (rabbit)	3µg/20µl	Proteintech; 22515-1-AP			
NMDAR2B	1:2000 dilution (rabbit)	7µl/20µl	Proteintech; 21920-1-AP			
p62	1:1000 dilution (mouse)	1mg/ml	BD Biosciences; 610833			
b-actin	1:10000 dilution (mouse)	2.2mg/ml	AbCam; ab6276			

2.1.5. Primers

Table 2.5 List of genes used for RT-PCR validation and their corresponding primer sequences

Gene name	Gene symbol	Primer sequences	Supplier
Nuclear factor (erythroid-derived) like 2	NRF2	F: TGCAAATCATAGCCAAACTAGTATAGA R: TGGTGTCTAAGAAATTGTTTACAGTTAA	MWG Biotech
NAD(P)H quinone dehydrogenase 1	NQO1	F: GTCATTCTCTGGCCAATTCAGAGT R: TGGAGTGTGCCCAATGCTATAT	MWG Biotech
Kelch-like ECH-associated protein 1	KEAP1	F: GTGTGGAGAGGTATGAGCCAG R: CCACGGCATAAAGGAGACGAT	SIGMA
Beta-actin	B-actin	F: TCCCCCAACTTGAGATGTATGAAG R: AACTGGTCTCAAGTCAGTGACAGG	SIGMA

2.2 Methods

2.2.1 Derivation of the cell model

Fibroblasts grown from skin biopsies were directly converted into tripotent iNPCs by Dr Ferraiuolo and Dr Meyer using the process described in Meyer *et al.* (2014) (Figure 2.1). INPCs were maintained by Misses M. Mysczynska, N. Gatto and L. Wan and were differentiated into iAstrocytes by culturing approximately 200,000 progenitor cells in iAstrocyte medium (DMEM, 10% FBS, 1% Penicillin-Streptomycin, 0.2% N2-supplement) into a 10cm dish coated with human fibronectin (2.5µg/ml) for a total of 7 days with a medium change at day 3.

2.2.1.1. Preparation of iAstrocytes for cellular assay

Induced NPCs were differentiated as described above in 10cm dishes. At day 5 of differentiation, a 96 well tissue culture treated plate with a lid was coated with fibronectin diluted 1:400 in PBS and allowed to set for cell adhesion. iAstrocytes were first washed with PBS to remove traces of FBS before incubating in 1ml of accutase for 5 minutes at 37°C. The accutase was neutralised in an equal volume of iAstrocyte medium and cells were collected in a 15ml falcon (Scientific Laboratory Supplies) and centrifuged at 200g for 4 minutes to form a pellet. The pellet was resuspended in medium and the cells were counted using a 0.100 mm Burker haemocytometer (Marienfield). The cells were seeded at the desired density (3000 cells per well for MMP, 6000 cells per well for immunocytochemistry (ICC) and 10,000 cells per well for glutamate assay collection) and were left for 24 hours to adhere.

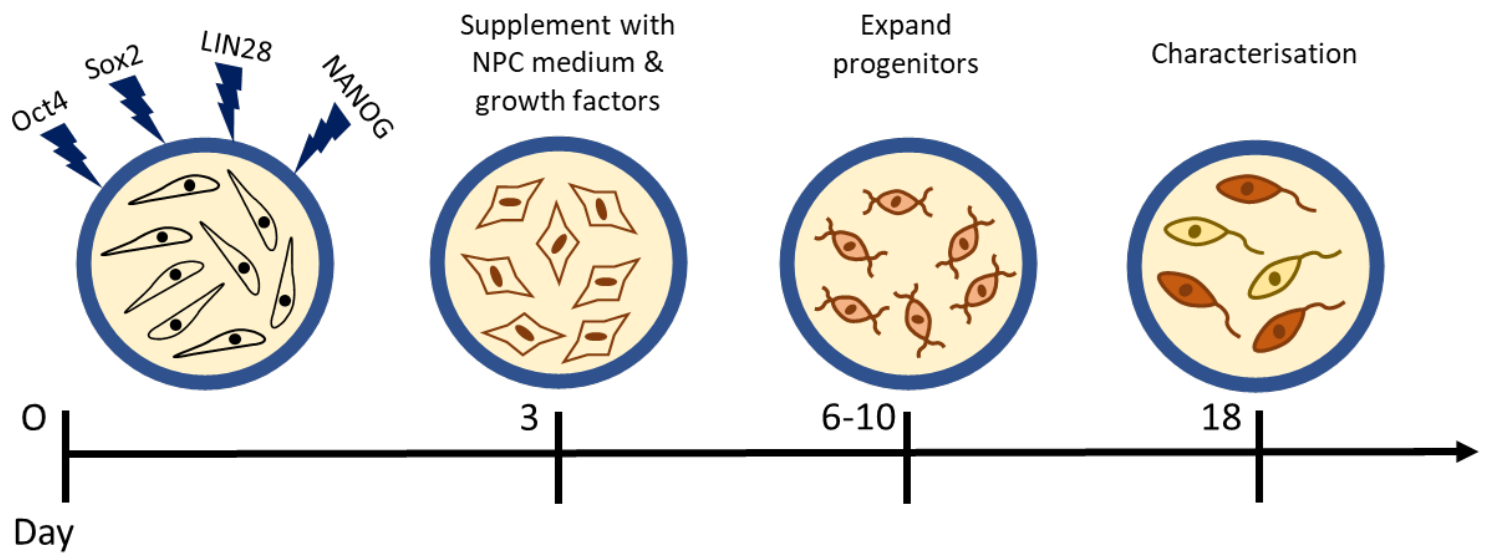


Figure 2.1 Direct conversion of ALS patient fibroblasts into iNPCs (Meyer et al 2014). Fibroblasts were transduced using retroviral vectors containing the reprogramming factors Oct4, Sox2, LIN28 and NANOG and supplemented with NPC medium and growth factors. Cells were grown until the 18-day mark where iNPCs were obtained.

2.2.1.2 Drug treatment

Antioxidant drugs, andrographolide, S[+]-apomorphine, MMF, and riluzole were made up to a 10mM stock concentration and diluted 1:1000 in iAstrocyte medium to have a 10 μ M working concentration. At day 6, the cells were treated with drugs 24 hours prior to cell assay.

2.2.1.3. Differentiation and dissociation of mouse embryonic motor neurons for cellular assay

Mouse embryonic stem cells were maintained in mESC medium (Knockout DMEM, 15% Embryonic Stem Cell FBS, 1% L-glutamine, 1% Minimum Essential Medium Non-Essential Amino Acids, 0.0007% 2-mercaptoethanol) on 10cm dishes with a layer of mouse embryonic fibroblasts (mEFs) and split twice a week on Tuesdays and Fridays. At each split, depending on the amount of MNs required for the weekly experiments, a proportion of mESCs were plated in EB media (KnockOut DMEM/F12 Nutrient Mix, 10% KO Serum, 1% N2-supplement, 0.5% L-glutamine, 0.5% filtered glucose, 0.0008% 2-mercaptoethanol) into non-TC treated 10cm dishes (Scientific Laboratory Supplies) to form EBs. The addition of 2 μ M retinoic acid (RA) and 1 μ M smoothed agonist (SAG) over 5 days starting from day 2 drove differentiation into MNs. On day 7 of differentiation, the brightness of the EB culture was assessed using a fluorescent microscope. The EBs should display clear borders and contain between 50-80% GFP+ MNs. Plates containing 'dim' EBs were discarded as this showed poor EB differentiation; MNs from these EBs would display poor survival. Figure 2.2 demonstrates the differentiation of mESCs into Hb9-GFP+ MNs over the course of 7 days.

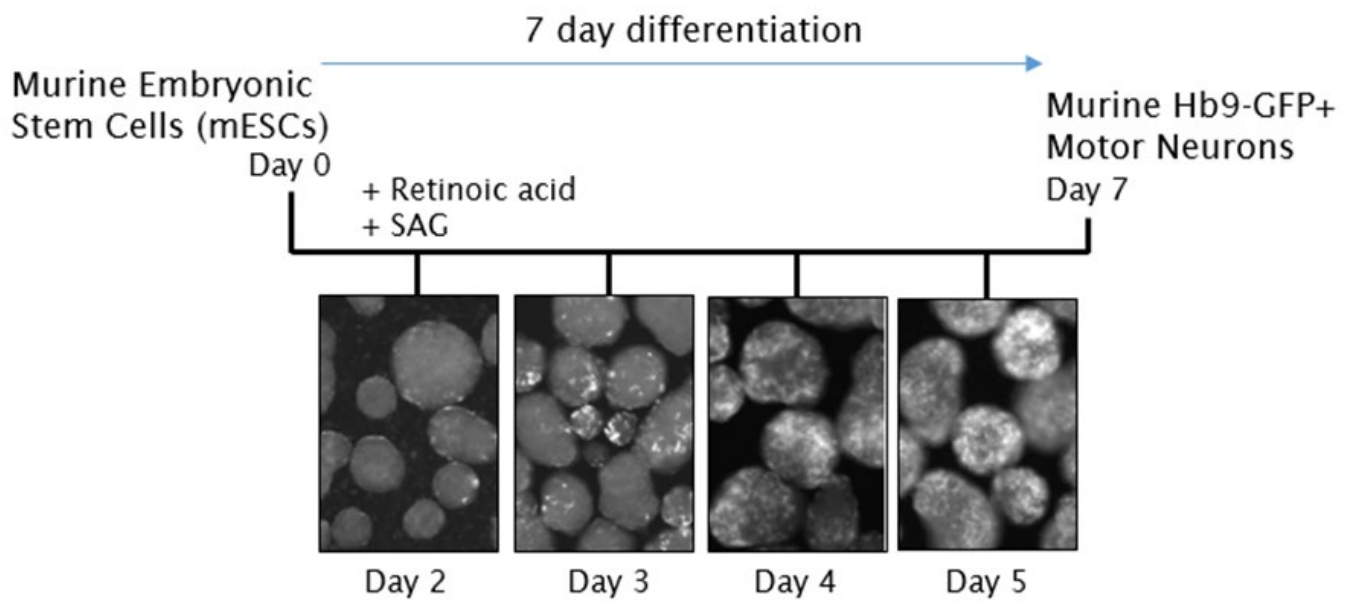


Figure 2.2 Differentiation of mESCs into murine Hb9-GFP+ MNs over a 7 day differentiation period (images provided by Dr M. Stopford). Media was supplemented with RA and SAG from Day 2 to drive the neuronal fate. MNs were visualised using the GFP expressed under the control of the Hb9 promoter region. This characteristic enabled us to evaluate the efficiency of the differentiation process and visualise the MNs live.

To dissociate the EBs and isolate the MNs, we used a combination of papain and DNase I. Briefly, the papain enzyme buffer was prepared according to the recipe in Table 2.1; it was then filtered using a 0.2µm pore filter (Falcon) and stored in the fridge. On the day of dissociation, both MN media (50ml EB media, 0.01% BDNF, CNTF, GDNF) and enzyme buffer were warmed to 37°C in the waterbath for 10 minutes prior to use while FBS, papain and DNase I were left to reach room temperature. The EBs were transferred to a pair of 50ml falcons (CELLSTAR) using a stripette and were centrifuged at 200g for 2 minutes to collect them at the bottom of the falcon. After centrifugation, the supernatant was removed, the cells were washed gently in 10ml PBS and centrifuged again at 200g for 2 minutes. The PBS was removed and 2.75ml of enzyme buffer plus 200 Unit of papain were added to the EBs. The solution was mixed gently against the side of the falcon using a P1000 pipette and then incubated at 37°C for 5 minutes with a gentle shake at 3 minutes. After 5 minutes, another 2ml enzyme buffer (and 200U of papain if the EBs were still large and intact) was added and mixed gently. The falcon was returned to the waterbath at 37°C for another 5 minutes. This step was repeated until the EBs had dissociated, but avoiding cell lysis, which would lead to DNA release. The solution was centrifuged at 300g for 5 minutes. The supernatant was removed from the cell pellet and a mix of 2.7ml enzyme buffer, 300µl FBS and 150µl of 1mg/ml DNase I was mixed with the cell pellet. 5ml FBS was added very slowly to the bottom of the falcon to form a cushion so the interface of the two solutions should be clearly visible. The tubes were centrifuged at 100g for 6 minutes for the FBS cushion to filter the heavy dissociated cells from the lighter debris to give a cleaner MN preparation. The supernatant was removed, and the cells were gently re-suspended in 5ml MN media. These cells were then passed through a 40µm filter (Falcon) to remove non-dissociated EBs before counting using a haemocytometer. The MNs can be distinguished as round, bright cells as opposed to contaminating non-neuronal cells with rough edges and a grey appearance. MNs were diluted to the desired concentration and plated immediately onto human iAstrocytes in a 96 well tissue culture treated plate with a lid.

2.2.2. Survival assay – iAstrocyte-MN co-culture

On day 1 (the day after the MNs were plated), 40µl of media was removed and discarded and replaced with 60µl of fresh MN media. The 96 well plate was scanned daily on the IN-CELL Analyser 2000 plate reader (GE Healthcare) across 3 days and then the plate was fixed with paraformaldehyde (described in 2.2.3.1.). The INCELL plate reader took images of 9 fields of view across each well and the cells were visualised under the 350nm Hoechst and 490nm GFP channel. The images were exported into Columbus (Perkin Elmer) analysis software. In each condition, the number of MNs with

axons was established. The MN survival was quantified as a percentage comparing the number of cells with axons on day 3 over the number of cells with axons on day 1.

2.2.3 Immunocytochemistry

2.2.3.1 Cell fixing

iAstrocytes were prepared and plated as described previously in 2.2.1.1. PBS containing 4% formaldehyde was prepared as a fixative for the cells. The cells were washed with 100 μ l of PBS before incubating in 100 μ l of 4% paraformaldehyde at room temperature for 10 minutes. After this incubation, the cells were washed twice with PBS and wrapped in parafilm (Alpha Laboratories) and stored at 4°C.

2.2.3.2 Immunofluorescent staining

The cells were washed with 100 μ l PBS before incubating in 70 μ l blocking buffer (Table 2.1) at room temperature for 30-60 minutes. Primary antibody preparations (Table 2.3) diluted in blocking buffer were then added to the cells and incubated overnight at 4°C. After overnight incubation, the wells were washed three times in PBS before incubating in 1:1000 dilution of secondary antibody in PBS (Table 2.3) at room temperature in the dark for 30 minutes. The wells were then incubated in Hoechst, diluted 1:4000 in PBS, at room temperature in the dark for 5 minutes. The cells were washed three times in PBS before imaging on the OPERA phoenix (Perkin Elmer).

2.2.3.3 Columbus analysis

Columbus analysis software was used to quantify ICC images (Figure 2.3). Typically, 1000-4000 cells were counted per well. In each condition, the number of nuclei was established by selecting all nuclei in a field with an area greater than 100 μ m². The cytoplasm surrounding each nucleus was selected by measuring the decrease in intensity with the distance from the nucleus. This method only used one parameter, the individual threshold which determined the intensity of each individual object; this parameter was set based on how accurately the software predicted the cytoplasm border. The perinuclear region was established in a similar way to the cytoplasm; by identifying the surrounding region of the nucleus and applying a common threshold parameter of 0.5 and an individual threshold of 0.85. The common threshold parameter determined the first guess borders of the surrounding region, while the individual threshold allowed for fine tuning of the border.

Spots were identified in the cells using the parameters relative spot intensity and splitting coefficient. The relative spot intensity was the ratio of the spot peak intensity to the mean intensity of the cell region where the spot was located. The splitting coefficient was responsible for split/merge decisions; the lowest value (0.0) detected regions if connected spots were considered as a single spot, while at the highest value (1.0), there was a maximum number of split lines. Threshold levels for relative spot intensity were set at the background level of each staining while the splitting coefficient was set depending on the size of the protein of interest e.g. larger protein aggregates required a lower splitting coefficient.

Figure 2.3 panel A-C demonstrates how mSOD1 protein aggregates were selected in iAstrocytes. In this staining, spots were first identified based on a relative spot intensity greater than 0.03 and a splitting coefficient of 0.4. mSOD1 aggregates were then selected based on a relative spot intensity higher than the average of the control iAstrocytes; this threshold number would vary between staining experiments. The number, intensity, and area of the selected mSOD1 aggregates within the nucleus and surrounding perinuclear area were calculated by the software.

Similar to the mSOD1 analysis protocol, the number, intensity and area of perinuclear p62 spots was quantified by identifying spots that had a relative spot intensity greater than 0.03 and a splitting coefficient of 0.4. Populations of perinuclear spots were then selected based on the relative spot intensity greater than that of the controls on the same plate. Figure 2.3 panel D-F demonstrates how p62 positive iAstrocytes were selected. The percentage of cells positive for p62 accumulation were determined by selecting cells based on the cytoplasmic Cy3 intensity mean and the number of spots. The average cytoplasmic Cy3 intensity mean and the number of spots in the control across two wells was set as the threshold level and the software detected cells that had a higher average cytoplasmic intensity and higher number of spots than the threshold.

In the iAstrocytes stained for TDP-43 protein aggregates, the number, intensity and area of TDP-43 aggregates within the nucleus and cytoplasm were quantified by identifying all spots that had a relative spot intensity greater than 0.03 and a splitting coefficient of 0.8. Aggregates were then selected based on a relative spot intensity greater than the control. The percentage of iAstrocytes with TDP-43 nuclear loss was determined by selecting cells based on the nuclear Cy3 intensity mean; the software would select cells with a lower nuclear intensity than the control average intensity.

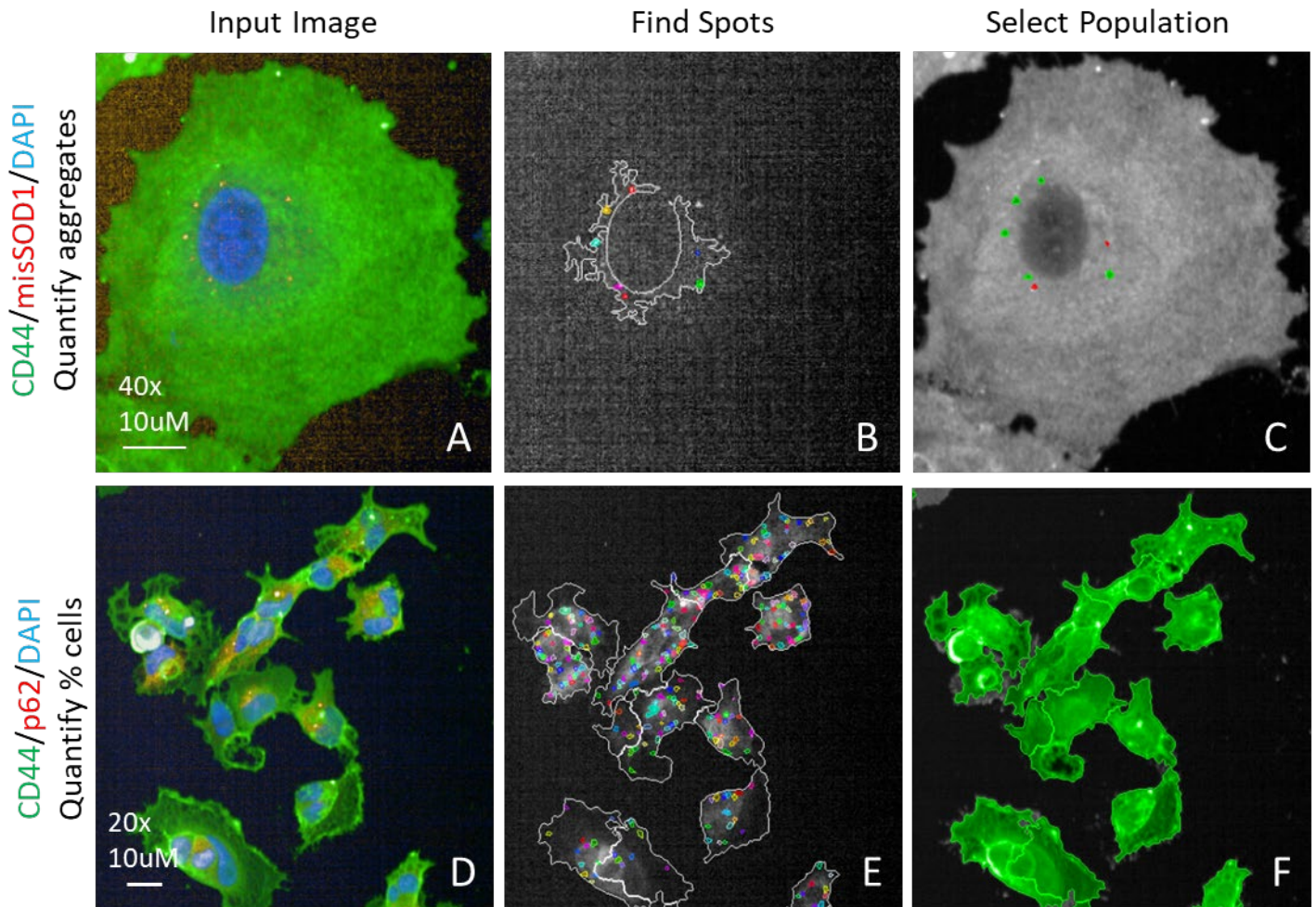


Figure 2.3 Columbus image analysis of immunocytochemistry. (A). Misfolded SOD1 aggregates were quantified by (B). the identification of spots in the Cy3 channel within the perinuclear region and (C). selected based upon relative spot intensity higher than the control threshold; spots labelled in green by the software passed the threshold parameters, while the spots labelled in red spots were discarded based on the threshold by the programme analysis. (D). Percentage of cells positive for p62 staining was quantified also through (E). the identification of spots in the Cy3 channel within the cytoplasm and (F). selected based on spot number and Cy3 cytoplasmic intensity higher than the control. Scale bar 10µM.

2.2.4. Western blotting

2.2.4.1. Preparation of soluble, RIPA and insoluble protein fractions

iAstrocytes were plated onto 6 well plates (3 wells per condition) and the media was changed on day 3 and day 5 of differentiation. On day 5, 10mM of drug in DMSO was added to the iAstrocyte medium at a final concentration of 10 μ M (0.001% DMSO). On day 7, the cells were washed and scraped in PBS and collected into 1.5ml Eppendorf tubes (SARSTEDT) and centrifuged at 16,000g for 1 minute to pellet the cells. The PBS was removed, and the cell pellets were stored at -80°C.

The IP, RIPA and urea buffer were prepared according to Table 2.1. 20-60 μ l of ice-cold IP lysis buffer (890 μ l IP Lysis Buffer, 10 μ l PIC (100%), 100 μ l PS (10%)) was added depending on the size of each pellet. The pellets were left on ice for 15 minutes. The lysates were centrifuged at 17,000g for 5 minutes at 4°C and the supernatant containing the soluble protein was transferred to a clean 1.5ml Eppendorf and stored at -80°C. 500 μ l of ice-cold RIPA buffer with 10% PIC was added to the cell pellet and the pellet was sonicated using the Soniprep 150 (MSE) for 10 seconds at 25% amp. The samples were centrifuged at 17,000g for 30 minutes at 4°C and the RIPA supernatant was placed into a clean 1.5ml Eppendorf and stored at -80°C. The samples were mixed with another 500 μ l of ice-cold RIPA buffer and centrifuged at 17,000g for 15 minutes at 4°C. The supernatant was removed and discarded, and this last step was repeated to wash the cell pellet, ensuring that all RIPA-soluble protein had been removed before the addition of urea. The supernatant was replaced with 10 μ l of urea buffer and the sample was pipetted a few times to solubilise RIPA-insoluble, urea-soluble proteins before it was stored at -80°C.

2.2.4.2. SDS Page

Spacer plates with 1.0mm integrated spacers and short plates were cleaned with industrial methylated spirit (IMS) and assembled on the Mini-PROTEAN® Tetra Cell Casting Stand (BioRad). Resolving gels of the required acrylamide % (w/v) were prepared by mixing reagents in the table below (Table 2.6).

Table 2.6 Composition of 5% Stacking gels, 10%, 12% and 15% Resolving gels.

Components	5% Stacking gel	10% Resolving gel	12% Resolving gel	15% Resolving gel
dH₂O	5.8 ml	4.2 ml	3.5 ml	2.5 ml
30 % (w/v) Acrylamide	1.7 ml	3.3 ml	4.0 ml	5.0 ml
Resolving buffer (1.5 M Trizma[®], 13.9 mM SDS, pH 8.8, filtered)	-	2.5 ml	2.5 ml	2.5 ml
Stacking buffer (0.5 M Trizma[®], 13.9 mM SDS, pH 6.8, filtered)	2.5 ml	-	-	-
10 % (w/v) APS	50 µl	50 µl	50 µl	50 µl
TEMED	20 µl	10 µl	20 µl	10 µl

The tube was inverted to mix the reagent and 5ml of gel was added on to the glass plate with a 1ml layer of isopropanol added on the top. The gel was left to set for 15 minutes, afterwards the isopropanol was poured off and dried with filter paper. 5% stacking gels were prepared by mixing reagents described in Table 2.6, and then poured onto the set resolving gels in the glass plates. 1.0mm 15-well Mini-PROTEAN[®] Combs (BioRad) were inserted into the stacking gels and left for at least 15 minutes to set. After 15 minutes, the gel was removed from the rack with the clips and the comb was removed. If the gel was not to be used straight away, it was wrapped in wet blue paper roll. The packaging was compressed, wrapped in cling film, and stored at 4°C.

Bradford protein assay dye reagent concentrate was diluted in dH₂O in a 1:4 ratio to make a working concentration of Bradford reagent (1ml Bradford reagent + 4ml milli Q water). To quantify total protein concentration, 1µl of cell lysate was added to 1ml Bradford reagent and mixed. The sample was loaded into a polystyrene cuvette (SARSTEDT) with 1cm path length, and the optical density shift at A595nm (OD595nm) of the sample relative to a blank control was measured using a WPA S1200 Diode Array Spectrophotometer (Biochrom). The concentration of the protein lysate was calculated and converted to µg/ml using the Beer-Lambert law equation ($OD_{595nm} = \epsilon cl$; where $\epsilon = 1/15$, and $l = 1cm$). Using this equation, the volume of sample required for gel electrophoresis was calculated and made up to 15µl with lysis buffer. Typically, between 20-30µg protein were loaded.

The cell lysates were mixed with 4X Laemmli buffer (Table 2.1) and boiled for 5 minutes at 95°C to denature the proteins. The SDS-Polyacrylamide gels were loaded into a Mini-PROTEAN[®] Tetra Vertical Electrophoresis Cell (BioRad), and the apparatus was filled with running buffer (Table 2.1). The calculated volume of 20-30µg of denatured protein was loaded per well onto the SDS-polyacrylamide gels. 2µl of pre-stained protein ladder was loaded as a molecular weight marker in one well per gel. The gel electrophoresis was run at 50V for 30 minutes, then 150V for

approximately 1.3 hours using a PowerPac™ Basic (BioRad) attached to the tank until the dye front reached the bottom of the gel.

The gels were removed from the electrophoresis cell and the stacking layer was cut off. Two large pieces of Whatman filter paper (GE Healthcare) wetted with transfer buffer were placed on to the Biometra Fastblot™ transfer (Analytik Jena). A piece of small dry filter paper was used to peel the gel off the glass plate. A piece of wet Amersham Protron nitrocellulose blotting membrane (GE Healthcare) was then placed on top of the gel. Another small piece of wet filter paper was placed on top of the nitrocellulose membrane. The stacked gel was placed on the semi-dry transfer apparatus and another two pieces of large wet filter paper were placed on the top. A small amount of transfer buffer was poured on top of the stack. Any bubbles were rolled out of the stack using a stripette and any excess transfer buffer was dried off. Electrophoretic transfer of the proteins from the gels to the membranes was performed at 0.15A/gel transferred for 1 hour. Membranes were stained with 4% Ponceau stain (Table 2.1) and cut to size.

2.2.4.3. Immunoblotting and densitometry

The membranes were blocked in 5% milk (w/v)/TBST (Table 2.1) for 1 hour at room temperature on a roller. The membranes were then incubated with primary antibody (Table 2.4) in 5% milk (w/v)/TBST over-night at 4°C on a roller. The next day, the primary antibody was removed and stored at -20°C for future blot incubations (typically each primary antibody mix was used three times). The membranes were washed 3 times in TBST for 15 minutes at room temperature on a roller. Afterwards, the membranes were incubated with secondary antibody conjugated to horseradish peroxidase (HRP) (Table 2.4) in 5% milk/TBST for 1 hour at room temperature on a roller. The secondary antibody was then discarded, and the membranes were again washed 3 times in TBST for 15 minutes at room temperature. To visualise the protein bands, the membranes were incubated with EZ-ECL for 1 minute and imaged in the G:BOX using GeneSnap software (Syngene). The quantification of proteins by densitometric analysis of bands obtained by immunoblotting was measured using GeneTools (Syngene) image analysis software.

2.2.4.4. SYPRO Ruby Red staining

Total protein levels for insoluble protein was quantified using SYPRO Ruby protein blot stain for normalisation of protein levels. After the semi-dry transfer of proteins onto the nitrocellulose membrane, the membrane was immersed in a 30ml solution of 7% acetic acid, 10% methanol and

deionised water and incubated on a plate shaker for 15 minutes. The membrane was then washed 4 times in deionised water for 5 minutes each. 10ml of SYPRO Ruby protein blot stain was poured onto the membrane and was incubated for 15 minutes. The membrane was washed 6 times in deionised water for 1 minute each to remove excess stain. The protein bands were imaged using UV epi-illumination in the G:BOX using GeneSnap software. Total protein levels in the whole lane were quantified using GeneTools image analysis software and this was used for normalisation of the insoluble protein.

2.2.5. Mitochondrial membrane potential assay

2.2.5.1 MMP preparation

iAstrocytes were prepared and plated as described previously in 2.2.1.1. On day 6 of differentiation, galactose was diluted 1:100 in iAstrocyte medium along with the drug treatments and applied to the cells 24 hours prior to the cell assay. On day 7, CCCP was diluted to 1:1000 in phenol red free media (MEM) and the cells were incubated for 1 hour at 37°C. A working buffer of MEM with 80nM TMRM and 10µM Hoechst (and 10µM CCCP for the CCCP-treated conditions) was added to the cells and incubated for 1 hour at 37°C. The cells were washed with 100µl MEM and placed inside the IN-CELL Analyser 2000 plate reader where images of 20 randomised fields of view across each well were collected, excluding a 1mm border around the well.

2.2.5.2 IN-CELL analysis

IN-CELL Developer Toolbox 1.9.2. software (GE Healthcare) was used to quantify mitochondrial morphological changes within iAstrocyte lines. Typically, 500-1500 cells were counted per well. The established parameters focused on identifying nuclei, correct segmentation of the cells and individual mitochondria to quantify the number of nuclei, the cell area, as well as the mitochondrial intensity, form factor, count, area and perinuclear count. For each run, object segmentation parameters such as kernel size, sensitivity of nuclei and mitochondria were set manually. Size exclusion parameters were applied to omit any abnormal nuclei or mitochondria, as demonstrated in Figure 2.4.

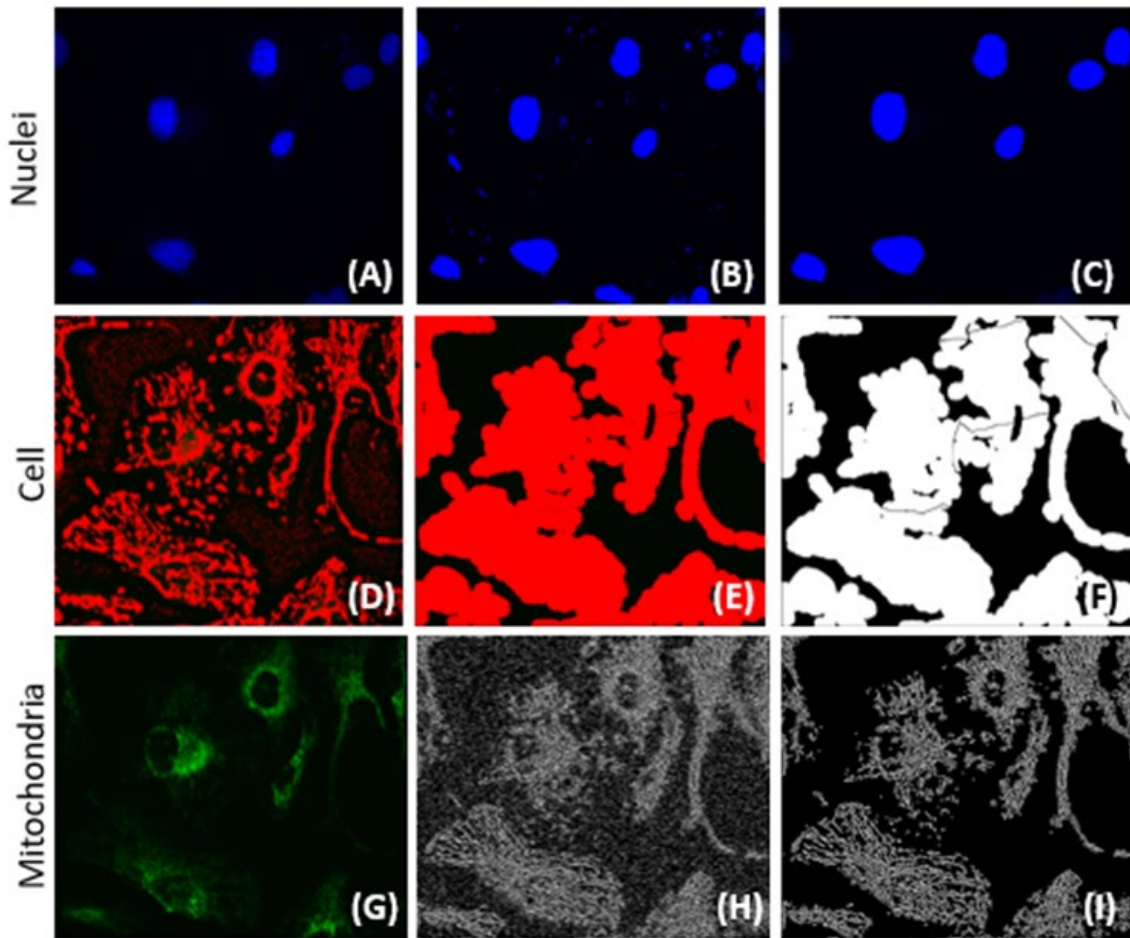


Figure 2.4 *IN-CELL Developer* analysis of mitochondrial staining. (A). Nuclei stained with Hoechst were quantified through (B). modification of nuclear segmentation and kernel size and (C). selected nuclei were sieved based upon size. (D). Cellular segmentation was identified through image sensitivity and kernel size. (E). Cells were selected based upon cell area and then (F). separated based upon nuclei position. (G). Mitochondria stained with TMRM were (H). segmented based upon sensitivity and kernel size parameters and (I). sieved by size.

2.2.6. Genome-wide RNA Analysis of Stalled Protein Synthesis (GRASPS)

The buffers required for the extraction of polyadenylated RNA from the cells were prepared as described in Table 2.1.

2.2.6.1. Ribosomal purification

Cells were grown on 10cm plates (3 plates per condition) and treated with drugs 48 hours prior to extraction. All GRASPS buffers were treated with 0.1% DEPC treatment. The iAstrocyte medium was removed and the cells were scraped from the plate and pooled within a 15ml falcon tube. The cells were centrifuged at 500g for 5 minutes at 4°C and the supernatant was removed.

The cell pellet was resuspended in 3x the volume of the pellet itself of cold Buffer A containing PIC, 2mM PMSF and 0.16U/μl RNase inhibitor. A final concentration of 0.7% v:v NP-40 from a 10% stock solution was gently mixed into the lysate. The lysate was incubated on ice for 5 minutes, mixed with a cut pipette tip and then incubated on ice for another 5-10 minutes. On a 6 well plate, the lysate was UV-irradiated on ice at 0.3 J/cm² and then centrifuged at 750g for 10 minutes at 4°C to pellet the nuclear fraction. This nuclear pellet was discarded, and the supernatant was centrifuged at 12500g for 10 minutes at 4°C to pellet the mitochondrial fraction. The supernatant, the post-mitochondrial (PMT) fraction was transferred to a new cold Eppendorf tube and 4M KCl was added to give a final concentration of 0.5M KCl.

1ml of sucrose cushion was added to the bottom of clean, cold TLA100 centrifuge tubes. The PMT fraction was made up to 1ml with Buffer B. 900μl of the 0.5 KCl-adjusted PMT fraction was slowly dispensed on top of the sucrose cushion and the tubes were balanced precisely within 0.01g of each other before centrifuging at 250,000 g/75,000 rpm for 2 hours at 4°C in the TL-100 benchtop ultracentrifuge (Beckman).

The ribosome pellet was quickly washed with cold DEPC water before the pellet was resuspended in 250μl of Ribosome Resuspension Buffer (RRB). 0.16U/μl Ribosafe RNase inhibitor and 100μg/ml proteinase K was added to the RRB and this was incubated for 30 minutes at 37°C with a pulse vortex every 5 minutes. After incubation, 10mM EDTA and 50mM NaAc was added and the RRB was vortexed.

750μl of PureZOL RNA isolation reagent was added and left for 10 minutes at room temperature before the RNA was extracted using the Direct Zol RNA Miniprep Plus kit.

2.2.6.2. mRNA purification

The mRNA extracted from the ribosome purification was then isolated using the NEB Next[®] Poly(A)+ mRNA Magnetic Isolation Module. 15µl of Oligo d(T)₂₅ beads were dispensed into 0.2ml tubes and the beads were washed twice with 100µl of 2 x RNA binding buffer to ensure removal of the supernatant. An equal volume (50µl) of 2 x RNA binding buffer and sample RNA were added to the beads. The samples were incubated at 65°C for 5 minutes and immediately placed on ice for 2 minutes. The samples were incubated at room temperature for 5 minutes before they were placed on a DynaMag[™]-2 magnet (Life Technologies) for 2 minutes. The supernatant was removed and kept on ice. Previous work investigating this technology had incorporated an additional binding step which increased the yield of ribosomal poly(A)+ RNA. The beads were washed twice with 200µl of wash buffer and placed on the magnetic rack for 2 minutes. The beads were then stored on ice while the initial saved supernatant was heated to 65°C for 5 minutes and directly on ice for 2 minutes. The supernatant was then re-added to the beads and the binding of the poly(A)+ RNA was repeated as above.

After the supernatant was removed and kept on ice, the beads were washed twice with 200µl wash buffer. After ensuring the total removal of the wash buffer, 50µl of Tris-buffer was added to the beads. The samples were incubated at 80°C for 2 minutes then immediately left at room temperature. 50µl of RNA binding buffer was then added to the beads and the samples were incubated at room temperature and inverted every few minutes before placing the tubes on the magnetic rack and removing the supernatant. The beads were washed twice again in 200µl of wash buffer. The poly(A)+ mRNA was eluted from the beads by adding 20µl of Tris-buffer, incubating samples at 80°C for 2 minutes and then placing on the magnetic rack to transfer the supernatant to a new nuclease-free PCR tube.

mRNA purification at this point did not result in a high enough yield of RNA for efficient sequencing. Therefore, the protocol was optimised with another binding of poly(A)+ to the magnetic beads to gain a higher yield. The 20µl elution was pooled with the previously kept supernatants and incubated at 65°C for 5 minutes and immediately on ice for 2 minutes. The sample was then added to the beads and the binding of the poly(A)+ was repeated as described above. After this incubation, the tubes were placed on the magnetic rack to remove the supernatant. The mRNA was again eluted from the beads through the addition of 20µl of Tris-buffer and the process described above.

The quantity of purified mRNA was assessed using the NanoDrop Spectrophotometer ND-1000 (Labtech International). The purity of the sample was measured based on the 260/280nm

absorbance ratio; a ratio of approximately 2 is considered as pure RNA. The 260/230nm absorbance ratio could be used as a secondary measure of purity with ratios of 2-2.2 determining pure RNA.

2.2.6.3. RNA quality assessment

2µl of sample was assessed using a Picochip and an Agilent 2100 Bioanalyser (Agilent Technologies) to check RNA quality and the presence of remaining rRNA. This assessed the size distributions of the 18S and 28S rRNA peaks on an electropherogram. If there was any rRNA detected in the sample, the samples underwent ribosomal RNA depletion as described below.

2.2.6.4. Ribosomal RNA depletion

If the quality assessment identified the presence of rRNA in the sample, any remaining rRNA was removed using the NEBNext® rRNA depletion kit.

An RNA/probe Master Mix was produced for the total number of samples using the table below (Table 2.7):

Table 2.7 Composition of the RNA/probe Master Mix per sample

Component	Volume
NEBNext® rRNA Depletion Solution	1µl
Probe Hybridisation Buffer	2µl
Total volume (per sample)	3µl

3µl of the above mix was added to 12µl of RNA sample as stated in the protocol and pipetted up and down 10 times. The samples were briefly spun in a tabletop centrifuge and immediately placed in the G-STORM thermocycler (LABCARE) with a heated lid of 80°C running the following program (Table 2.8):

Table 2.8 PCR programme for Ribosomal RNA Depletion Protocol

Temperature	Time
95°C	2 min
95-22°C	0.1°C/sec
22°C	5 min

The samples were spun down briefly and placed on ice while the RNase H Digestion Master Mix was prepared using the table below (Table 2.9):

Table 2.9 Composition of RNase H Digestion Master Mix

Component	Volume
NEBNext® RNase H	2µl
RNase H Reaction Buffer	2µl
Nuclease-free water	1µl
Total volume (per sample)	5µl

5µl of the above mix was added to each sample and was mixed thoroughly with a pipette. The samples were briefly spun and immediately placed in a thermocycler with a heated lid of 40°C and incubated at 37°C for 30 minutes. After incubation, the samples were spun down briefly again and placed on ice while the DNase I Digestion Master Mix was prepared using the table below (Table 2.10):

Table 2.10 Composition of DNase I Digestion Master Mix

Component	Volume
DNase I Reaction Buffer	5µl
DNase I (RNase-free)	2.5µl
Nuclease-free water	22.5µl
Total volume (per sample)	30µl

30µl of the above mix was added to each sample and thoroughly mixed with a pipette. The samples were briefly spun and immediately incubated at 37°C for 30 minutes in the thermocycler. After incubation, the samples were spun down again and placed on ice.

A 1ml aliquot of NEBNext® RNA Sample Purification Beads was vortexed into suspension and 110µl of this suspension was added to each sample. The samples were then thoroughly mixed with a pipette and incubated on ice for 15 minutes. The tubes were placed on a magnetic rack to separate the beads from the supernatant. After 5 minutes, the supernatant was removed and discarded, and the beads were washed twice with 200µl of freshly prepared 80% ethanol; beads were incubated in ethanol for 30 seconds between washes. The tubes were briefly spun to remove any excess ethanol. The beads were then air dried for 5 minutes while the tubes were left on the magnetic rack with the lids open. The samples were eluted while the beads were still dark brown and glossy looking; if the beads were over-dried this would impact the yield. 8µl of nuclease free water was added to the beads, thoroughly mixed, and incubated on ice for 2 minutes to elute the RNA sample from the beads. The tubes were placed on the magnetic rack for 5 minutes to sediment the beads and the RNA sample was transferred to a fresh 0.2µl Eppendorf.

2.2.7. Sample validation

2.2.7.1. Reverse transcription

A master mix from the High Capacity cDNA Reverse Transcription Kit was prepared for the total number of samples using the table below (Table 2.11):

Table 2.11 Composition of cDNA Reverse Transcription Master Mix

Component	Volume
10 x RT Buffer	2.0µl
25 x dNTP Mix (100mM)	0.8µl
10 x RT Random Primers	2.0µl
MultiScribe™ Reverse Transcriptase	1.0µl
RNase Inhibitor	-
Nuclease-free H₂O	3.2µl
Total per Reaction	10.0µl

This master mix was mixed gently on ice before adding 10µl to each reaction tube. 10µl of RNA sample was added to each tube and pipetted up and down to mix. The tubes were spun briefly in a tabletop centrifuge and immediately placed in the DNA Engine PTC-200 thermocycler (MJ Research) with a heated lid of 80°C running the following program (Table 2.12):

Table 2.12 PCR programme for cDNA Reverse Transcription Protocol

Temperature	Time
25°C	10 min
37°C	120 min
85°C	5 min
4°C	-

Samples were used immediately or stored at -20°C.

2.2.7.2. Quantitative Polymerase Chain Reaction (QPCR)

Each primer pair (Table 2.5) was diluted from a 100µM stock to a 5µM working concentration and vortexed. A master mix was prepared for each gene of interest for the total number of wells using the table below (Table 2.13):

Table 2.13 Composition of qPCR Master Mix

Component	Volume
SYBR green	10µl
Forward primer	1µl
Reverse primer	1µl
dH₂O	7µl
Total per Reaction	19µl

The cDNA samples were briefly vortexed and spun down using a tabletop centrifuge. 19µl of master mix and 1µl of 200ng/µl cDNA sample were added to each well of a 96 well low-profile PCR plate. The plate was sealed with 8-cap strips and centrifuged at 1760g for 1 minute. The plate was placed in the Mx3000p Real Time PCR machine (Stratagene) and ran on a thermal profile described in the table below (Table 2.14):

Table 2.14 PCR programme for RT-PCR

Segment	Temperature	Time	Cycles
1	95°C	10 min	1
2	95°C	30 secs	40
	60°C	60 secs	
3	95°C	60 secs	1
	55°C	30 secs	
	95°C	30 secs	

2.2.8. RNA-sequencing

RNA sequencing was outsourced at the Centre for Genomic Research at the University of Liverpool. RNA samples were prepared and quality controlled at SITraN before they were sent to the centre. The centre prepared a dual-indexed, strand-specific RNA-Seq library from the submitted poly(A)+ enriched RNA sample using the NEB Next Ultra Directional RNA library preparation kit. Samples were sequenced on lanes of the Illumina Nova Seq using S4 chemistry (paired-end, 2x150 base pair sequencing) which generated approximately 2500 M clusters per lane. RNA sequencing data was quality controlled at the centre by removal of any low-quality bases and sequencing adapters before transfer back to SITraN.

2.2.8.1. Quality Control

The processing of the RNA sequencing data was completed by Dr M. Dunning of the Sheffield Bioinformatics Core.

Bcbio is a python toolkit providing best-practice pipelines for fully automated high throughput sequencing analysis (<https://bcbio-nextgen.readthedocs.io/en/latest/>). The *bcbio* pipeline was used to merge all 5-6 FastQ files per sample together for quality control and further processing.

Inspecting the GC-content histograms from *FastQC*

(<https://www.bioinformatics.babraham.ac.uk/projects/fastqc/>) revealed a bimodal distribution for some samples; attributed to ribosomal contamination. Therefore, the *bbsplit* tool was used to remove any residual rRNA sequences prior to alignment.

2.2.8.2. Sequence Alignment and Differential Expression

Salmon (<https://salmon.readthedocs.io/en/latest/>) is a tool for quantifying the expression of transcripts using RNA sequencing data; performing an inference step to estimate the relative abundance of all the known transcripts without aligning the reads. The genecode set of transcripts (v28) was used for quantification, giving a matrix of transcript-level quantifications for each sample. The *tximport* Bioconductor package was used to aggregate the counts to the gene-level and these counts were imported into the *DESeq2* Bioconductor package for quality control and analysis. Visualisation of the raw count distributions and unsupervised analysis prompted to the removal of two patients from further analysis (control 155 and C9ORF72 patient 183).

2.2.8.3. Normalisation of read counts

RNA sequencing allows for detection of differential gene expression between sample groups and across treatments. The raw counts themselves are subject to many sources of variation and normalisation needs to be conducted to adjust the technical differences between samples such as library size and gene specific features.

The *DESeq2* differential expression methods incorporates gene-length and library size correction as part of the model. Prior to visualisation in other analysis tools, the RNA sequencing data were normalised by the FPKM (fragments per kilobase per million reads) method. The total number of reads in a sample was divided by 1,000,000. The read counts were then divided by this scaling factor, normalising for sequence depth and giving the 'reads per million' (RPM). The RPM were divided by the length of the gene in kilobases, giving the FPKM mapped reads.

2.2.8.4. Functional annotation and Pathway analysis

Lists of differentially expressed genes were obtained by comparing different groups of patients based on genotype, drug treatment and drug response as described in the result chapters.

Lists of genes that were statistically differentially expressed were identified by applying a p-value <0.05 and absolute log₂ fold-change >1.5. The gene lists were inputted into DAVID Functional Annotation Bioinformatics Microarray Analysis programme (<https://david.ncifcrf.gov/>). The list of Gene Ontology Term “Biological Process” (GO-BP) terms were exported from DAVID to categorise differentially expressed genes (DEG).

To visualise group segregation based on DEGs, Principal Component Analysis (PCA) plots and heatmaps were generated using Qlucore Omics Explorer software (Qlucore).

2.2.9. Glutamate analysis

2.2.9.1. Media collection

On day 5, the iAstrocytes were plated at a density of 10,000 cells per well in iAstrocyte medium in a clear 96 well cell culture plate. On day 6, the media was replaced with MN media with either 10 μ M of drug or 0.001% DMSO. On day 7, the media from the iAstrocyte monoculture was collected and immediately snap frozen in liquid nitrogen to prevent glutamate degradation. On the same day, MNs were plated on top of the iAstrocyte monolayer at a density of 8,000 cells per well in MN medium containing 10 μ M riluzole or 0.001% DMSO. On day 8, i.e. 24 hours after MN seeding, the media was once again collected and snap frozen, and replaced with fresh MN medium. On the final day, day 9, i.e. 48 hours after MN seeding, the media was collected and spun frozen and the plate was fixed as described before (2.2.3.1).

2.2.9.2. Colorimetric assay

Components of the Glutamate Assay kit (Abcam) were prepared according to the manufacturer’s instructions. The Glutamate Assay Buffer was equilibrated to room temperature while the Glutamate Standard was kept on ice. The Glutamate Enzyme Mix was reconstituted in 220 μ l Assay Buffer while the Glutamate Developer was reconstituted in 820 μ l ddH₂O; these were both kept on ice and protected from light.

A 1mM Glutamate standard was prepared by diluting 5 μ l of 0.1M Glutamate Standard in 495 μ l of Assay Buffer. Using the 1mM standard, a standard curve dilution as described in Table 2.15 was prepared in a 96 well EIA/RIA High Binding flat bottom plate (Corning Inc.):

Table 2.15 Composition of the glutamate standard according to protocol

Standard	Volume of Standard (µl)	Assay buffer (µl)	Final volume in well (µl)	End [glutamate] in well
1	0	150	50	0 nmol/well
2	6	144	50	2 nmol/well
3	12	138	50	4 nmol/well
4	18	132	50	6 nmol/well
5	24	126	50	8 nmol/well
6	30	120	50	10 nmol/well

After protocol optimisation, it was discovered that some of the patient samples were always far past the 10nmol glutamate level, therefore it required a dilution factor to fit within the standard range.

The samples were diluted in assay buffer as shown in the table below (Table 2.16):

Table 2.16 Dilution factor of iAstrocyte condition media with glutamate assay buffer for different samples

Cell line	Dilution	Assay Buffer	Sample
Controls	1:3	33µl	17µl
Patients	1:5	40µl	10µl
183 & 201	1:7	43µl	7µl

100µl of Reaction Mix was prepared for each reaction using the table below and the following calculation for the number of reactions: **X µl component x (no. of samples + standards + 1)**.

100µl of Background Reaction Mix was prepared using the table below (Table 2.17):

Table 2.17 Composition of Glutamate Reaction Mix and Background Reaction Mix

Component	Reaction Mix Samples	Background Reaction Mix
Glutamate Assay Buffer	90µl	92µl
Glutamate Developer	8µl	8µl
Glutamate Enzyme Mix	2µl	0µl

100µl of Reaction Mix was added to each standard and the sample wells, and 100µl of Background Reaction Mix was added into the background sample wells. The 96 well plate was placed onto a PMS-1000i plate shaker (Grant-Bio) and incubated at 37°C for 30 minutes protected from light. After incubation, the OD450nm of the samples was measured on the FLUOstar Omega microplate reader (BMG Labtech).

2.3. Statistical analysis methods

All statistical analysis and graphical configuration were completed in GraphPad Prism software.

For immunofluorescence, western blot and MMP analysis; a one-way ANOVA was used for analysing differences between untreated cell lines while a two-way ANOVA with multiple comparisons test was used to compare untreated vs drug treated conditions. For correction, a Dunnett's multiple comparisons test was run alongside the one-way ANOVA while a Tukey's multiple comparisons test was run with the two-way ANOVA.

For glutamate assay analysis, a one-way ANOVA was used for analysing the differences between the glutamate levels in iAstrocyte monoculture between all untreated cell lines, with a Dunnett's multiple comparisons test for correction. A two-way ANOVA with multiple comparisons test was used to compare the difference in glutamate levels over the time course between untreated and riluzole treated conditions for each individual cell line, with a Tukey's multiple comparisons test for correction. Individual paired t-tests were also used to compare the untreated vs treated iAstrocyte-MN co-cultures at the 48 hour time point.

Chapter 3 - Characterisation of the pathophysiological characteristics of iAstrocytes derived from ALS patient fibroblasts with C9ORF72 expansions, SOD1 mutations and sporadic cases.

3.1. Introduction

Over the past 10 years, numerous studies have provided evidence that MN death in ALS occurs via a non-cell autonomous process in which the neighbouring glial cells, astrocytes, microglia, and oligodendrocytes, have a crucial role (Ferraiuolo *et al.* 2011a). Possibly the most convincing evidence was provided by Boillée *et al.* (2006); there was a delayed disease onset in *SOD1* transgenic mice when the *SOD1* mutation was removed from the MNs, but there was no difference in disease course. However, when the mutation was removed from the surrounding astrocytes or microglia, while there was no change in disease onset, disease progression was slowed down by 50% (Boillée *et al.*, 2006; Yamanaka *et al.*, 2008). In summary, while MN pathology highlights the beginning of disease onset, neighbouring glial cells control the speed of disease progression, making them an attractive therapeutic target for ALS.

Astrocytes maintain brain homeostasis through strict regulation of ion distribution, osmotic balance, and recycling of glutamate (Chandrasekaran *et al.*, 2016). Glutamate uptake by astrocytes is an essential process as high extracellular concentrations of glutamate result in the over-stimulation of neurons which could lead to excitotoxicity or cell death. During disease progression, the expression of glutamate transporter EAAT2 is reduced in astrocytes within the spinal cord of m*SOD1* mouse models (Howland *et al.*, 2002), resulting in MN excitotoxicity and death.

Reactive astrocytes are commonly reported in human sALS and fALS cases as well as mouse models (Haidet-Phillips *et al.*, 2011; Qian *et al.*, 2017). These astrocytes secrete cytokines and growth factors causing alterations in MN morphology, such as smaller cell bodies, shorter axons, axonal swelling and accumulation of ubiquitin-tagged protein aggregates within the axons and somata of the MNs (Bruijn *et al.*, 1997; Frakes *et al.*, 2014; Tripathi *et al.*, 2017). The study by Ferraiuolo *et al.* (2011b) demonstrated that astrocytes derived from m*SOD1* mouse models have altered lactate and NGF processing which increases neuronal death signalling and vulnerability. The presence of m*SOD1* protein aggregates have also been found to contribute to MN death via impairment of mitochondrial functions (Shi *et al.*, 2010) and increased nitrosative stress (Rojas *et al.*, 2014); damaged mitochondria release 'pro-cell death factors' leading to MN necroptosis (Re *et al.*, 2014).

Like MNs, the accumulation of protein aggregates has also been demonstrated in ALS astrocytes. The transcripts produced by the *C9ORF72* hexanucleotide repeat in astrocytes leads to the formation

of poly-proline-arginine peptide aggregates within the astrocytic nucleus, blocking protein transcription (Kanekura *et al.*, 2016; Hautbergue *et al.*, 2017). Astrocytes containing the mutant TDP-43 protein also presented intracellular cytoplasmic aggregates, which accumulated over time and were associated with cell death (Haidet-Phillips *et al.*, 2013; Serio *et al.*, 2013). Misfolded SOD1 aggregates have been detected in the nuclei of astrocytes and other glial cells from the ventral horn of ALS patients with *SOD1* mutations as well as sporadic cases (Forsberg *et al.*, 2011).

Due to the complexity of the disease, there exist a wide variety of *in vitro* and *in vivo* models of ALS, ranging from cell lines and primary cell cultures to various small animal and rodent models, to investigate different aspects of the disease (Mejzini *et al.*, 2019). The advancements in genetics and *in vitro* modelling over the past 10 years have greatly influenced new technologies modelling astrocytic disease mechanisms in ALS (Myszczyńska and Ferraiuolo, 2016).

The discovery by Takahashi and Yamanaka (2006) that adult human fibroblasts could be reprogrammed into iPSCs, created the opportunity to model not only fALS, but also sporadic disease *in vitro* (Myszczyńska and Ferraiuolo, 2016). Many studies have been able to reprogram astrocytes from human-derived iPSCs (Roybon *et al.*, 2013; Serio *et al.*, 2013). However, the problem is that these protocols are time-consuming, complex and are highly variable in the maturation time of the astrocytes. Therefore, a promising alternative to iPSC resources is the direct reprogramming of fibroblasts into astrocytes from an immuno-matched host.

The study by Meyer *et al.* (2014) used direct reprogramming technology to derive astrocytes from ALS patient fibroblasts. Using the protocol from Kim *et al.* (2011), iNPC lines were generated from ALS patients and controls within one month. These cells displayed a similar toxicity towards MNs in co-cultures as autopsy-derived astrocytes when they were differentiated into iAstrocytes (Haidet-Phillips *et al.*, 2011), making them useful tools in the development of drug screens.

The direct conversion protocol used in this study gives the opportunity to capture the individual patient condition within an *in vitro* cell model through the generation of iAstrocytes from patient fibroblasts. Not only is this method of reprogramming faster and less time-consuming than iPSC derivation, these iAstrocytes also retain the ageing signatures of the patient which makes them a valuable tool for modelling neurodegenerative disease where the main factor is age (Gatto *et al.*, 2020). They can also recapitulate oxidative stress conditions without the need for external stimuli, e.g. hydrogen peroxide. Astrocytes derived from patient iPSC lines displayed oxidative stress at 70-90 days of differentiation (Birger *et al.*, 2019), while the iAstrocytes used in this study present disease related oxidative stress pathology after 7 days of differentiation from iNPC lines.

The one obvious downside of using cell models to study disease is that they can only tell us part of the story as they lack the complete interconnected multi-cellular system that is available with animal models, so *in vivo* models cannot be discarded completely to support investigation of disease mechanisms. However, these cells are a valuable tool when it comes to screening the patient's response to a drug which is ultimately what this project aims to accomplish.

In particular, in this first results chapter we aim to identify the pathological aberrations that distinguish ALS patient subgroups.

3.2. Results

3.2.1. Expression of glial markers

iNPCs derived from the fibroblasts of ALS patients and non-ALS controls were plated and differentiated into iAstrocytes over the course of one week. Since iNPCs can give rise to multiple cell types, iAstrocytes were visualised using immunocytochemistry; nuclear staining in Hoechst and cytoplasmic staining with either vimentin or CD44 (Figure 3.1A-B), to ensure astrocytic differentiation. Vimentin is a cytoplasmic intermediate filament protein that is found in cell types across the body, from mesenchymal cells to glial cells of the nervous system (Schnitzer *et al.* 1981). CD44 is a transmembrane glycoprotein involved in cellular communication, but is also considered as a marker for astrocyte differentiation (Liu *et al.* 2004). These cells have also been thoroughly characterised for glial markers, including S100 β and GFAP. In Allen *et al.* (2019b), >99% of cells were positive for both markers, indicating a pure astrocytic population.

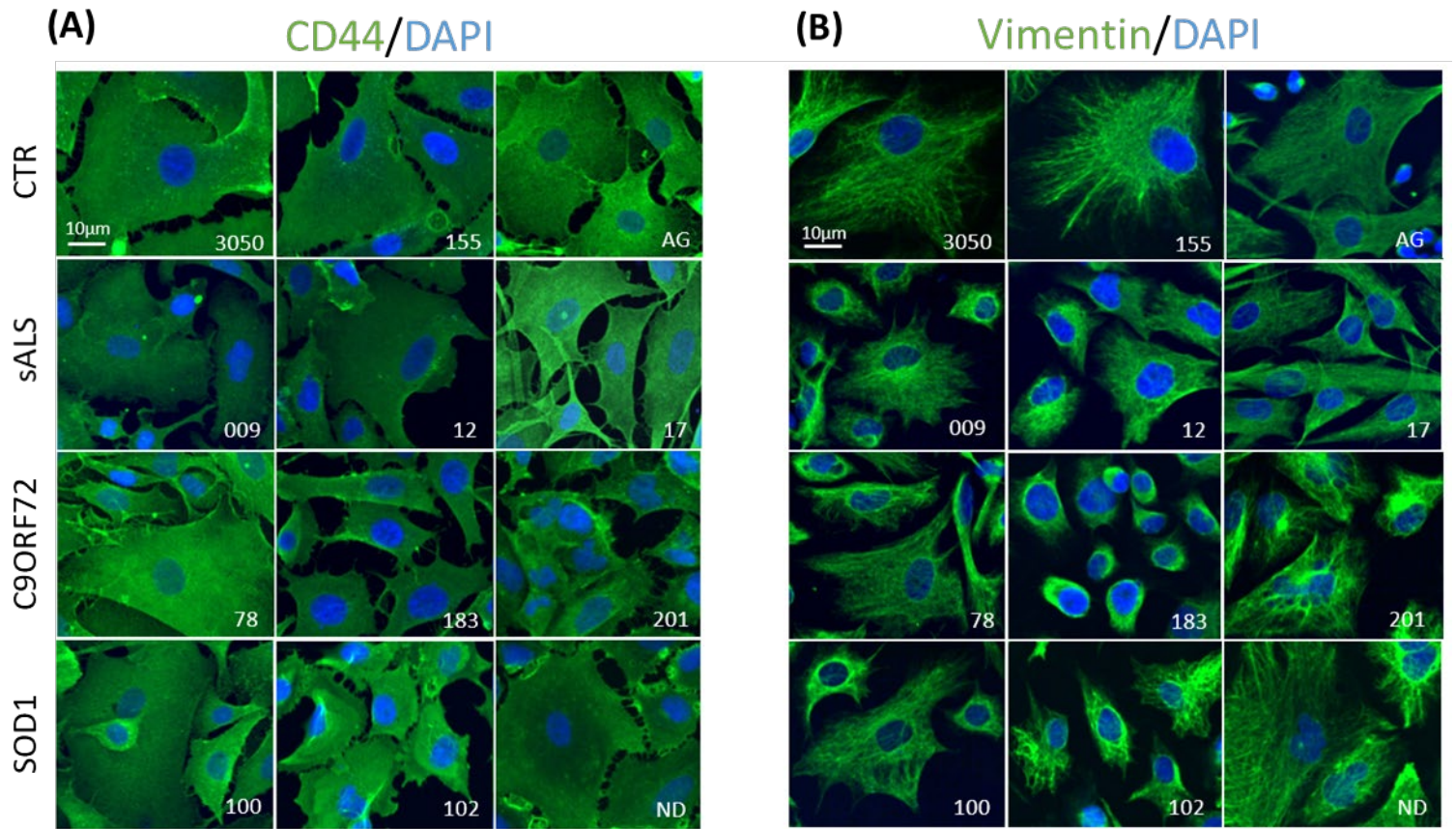


Figure 3.1 Representative images showing the expression of glial membrane and cytoplasmic markers (A). CD44 and (B). vimentin, nuclear staining in Hoechst, in all the human iAstrocyte lines used in this study. Scale bar 10 μ m.

3.2.2. Immunocytochemistry of pathological markers

In order to assess how representative these iAstrocytes are to the condition they model, the initial aim was to characterise the iAstrocytes through immunocytochemistry of pathological markers of ALS: TDP-43, misSOD1 protein aggregates and p62 expression. The presence of astrocytic TDP-43 and misSOD1 protein aggregates in ALS is well documented in several studies using mouse models (Forsberg *et al.*, 2011; Tong *et al.*, 2013; Rojas *et al.*, 2014). In addition, p62 is responsible for protein homeostasis through the generation of autophagosomes for disposal of ubiquitinated protein aggregates and this pathway has been reported as being dysregulated in all forms of ALS (Cheroni *et al.*, 2009; Al-Sarraj *et al.*, 2011; Sasaki 2011).

3.2.2.1. TDP-43

I first assessed TDP-43 proteinopathy, as nuclear loss and cytoplasmic aggregates of this protein are common to >97% of the ALS patient population (Prasad *et al.*, 2019).

Cells were stained for TDP-43 using an antibody that recognises the C-terminal domain of the TDP-43 protein. Control and SOD1 iAstrocyte lines displayed a large amount of nuclear staining, while there was less nuclear staining and more cytoplasmic staining observed in the sALS and C9ORF72 lines, with the formation of large aggregates in some lines (Figure 3.2A), in keeping with previous reports from SOD1 mouse models which lack TDP proteinopathy (Turner *et al.* 2008). The Columbus software analysis of these images mainly focused upon the number of TDP-43 aggregates and TDP-43 nuclear intensity to investigate how TDP-43 localisation changed in the patient iAstrocytes. C9ORF72 and sALS iAstrocytes showed the highest number of TDP-43 aggregates per cell and demonstrated a reduced TDP-43 nuclear intensity when compared to control lines (Supplementary 3.1). However, there was a large variability between the runs of TDP-43 staining as indicated by the large standard error bars, underlying that, although the trend of TDP-43 aggregation and nuclear loss is clear, the number of cells affected by TDP proteinopathy might vary between preparations and the quality of the staining might be quite variable between runs and antibody batches.

Because of the difficulties experienced in the analysis of TDP-43 immunocytochemistry images, soluble TDP-43 protein expression was investigated in control and patient iAstrocytes by Western blot (Figure 3.2B, courtesy of Miss Noemi Gatto). In ALS, the TDP-43 protein is cleaved to generate C-terminal fragments which are detected in the cytoplasm (Neumann *et al.*, 2006). While there was little change in overall TDP-43 protein expression, the soluble 35kDa TDP protein fragment was only detected in sALS and C9ORF72 iAstrocytes (Figure 3.2C-D), which is reflective of the presence of the aggregates in the TDP-43 immunocytochemistry images.

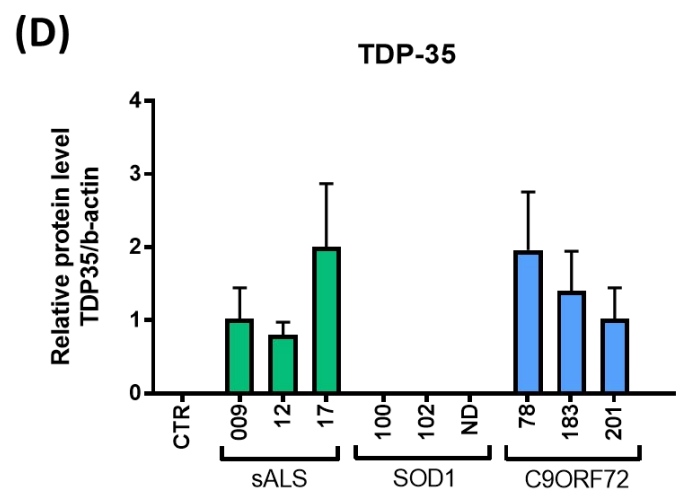
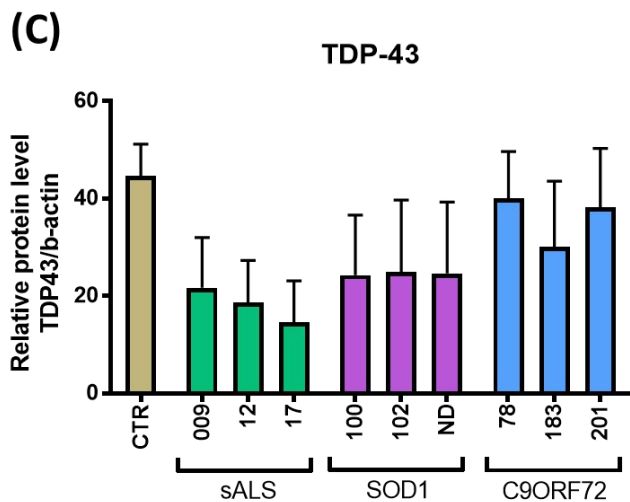
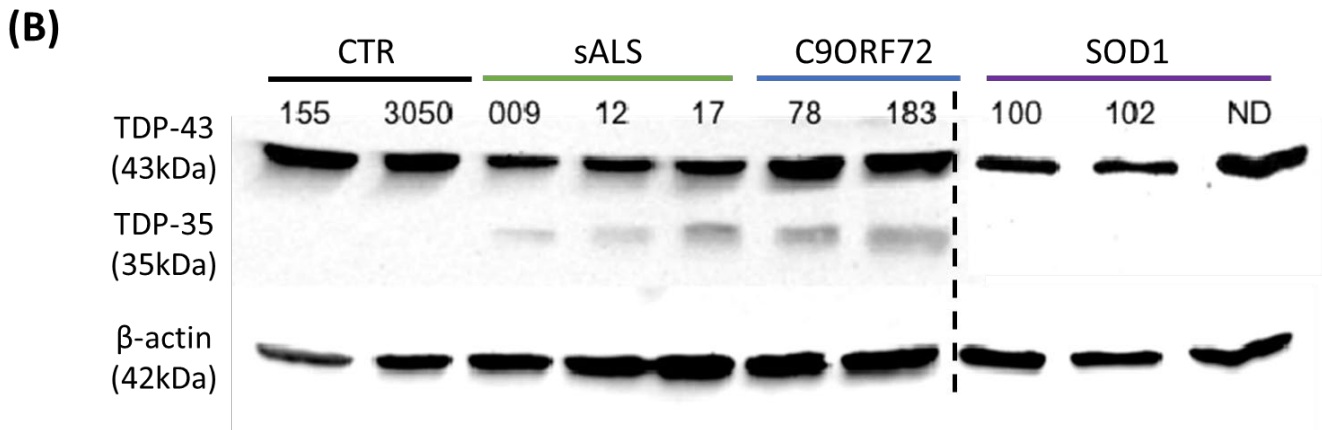
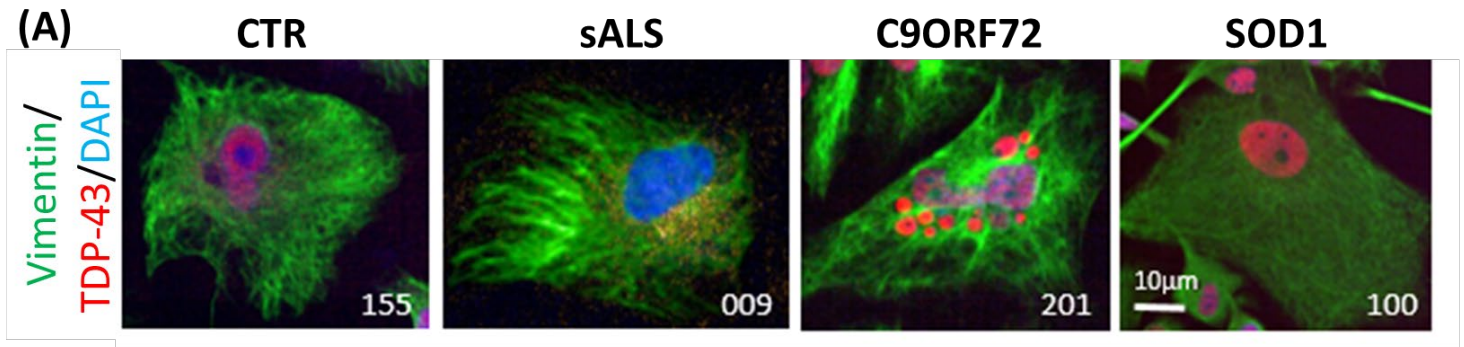


Figure 3.2 TDP-43 localisation and protein expression in control and patient iAstrocytes. (A). Immunocytochemistry of TDP-43 (568) and vimentin (488), nuclei in Hoechst, in cell lines. Scale bar 10µM. (B). Western blot of total (43kDa) and cleaved (35kDa) TDP protein in both controls and patients, and (C). Quantification of protein expression of TDP-43 (mean \pm SD, n=2-3) and (D). TDP-35 (mean \pm SD, n=2-3), courtesy of Miss Noemi Gatto. Control bar consists of control lines 3050, 155 & AG pooled together.

3.2.2.2. Misfolded SOD1 (misSOD1)

I next assessed misSOD1 presence in patient iAstrocytes, as several papers have reported that spinal cord tissue from a large percentage of familial and sALS cases, beyond mutant SOD1, display misSOD1 aggregates (Bosco *et al.*, 2010; Forsberg *et al.*, 2011, 2019).

Columbus analysis software was able to detect misSOD1 aggregates within the nucleus and the perinuclear area of the iAstrocytes, where aggregates were more likely to be identified (Figure 3.3A). Within the nucleus, two SOD1 iAstrocyte lines and one sALS patient cell line had a higher number of aggregates when compared to the control sample (Figure 3.3B). Aggregates in the perinuclear region were more common than in the nucleus for all patient lines while the control samples maintained an even ratio. The cell lines with the highest number of perinuclear aggregates were the two SOD1 cell lines 100 and ND29505, as well as sALS line 17 (Figure 3.3C). SOD1 line 102 had less misfolded SOD1 than the other SOD1s, possibly because the patient was pre-symptomatic at the time of collection. Similar to the TDP-43 staining, there was no significant difference identified between the patients and controls due to a high variability between different runs of staining.

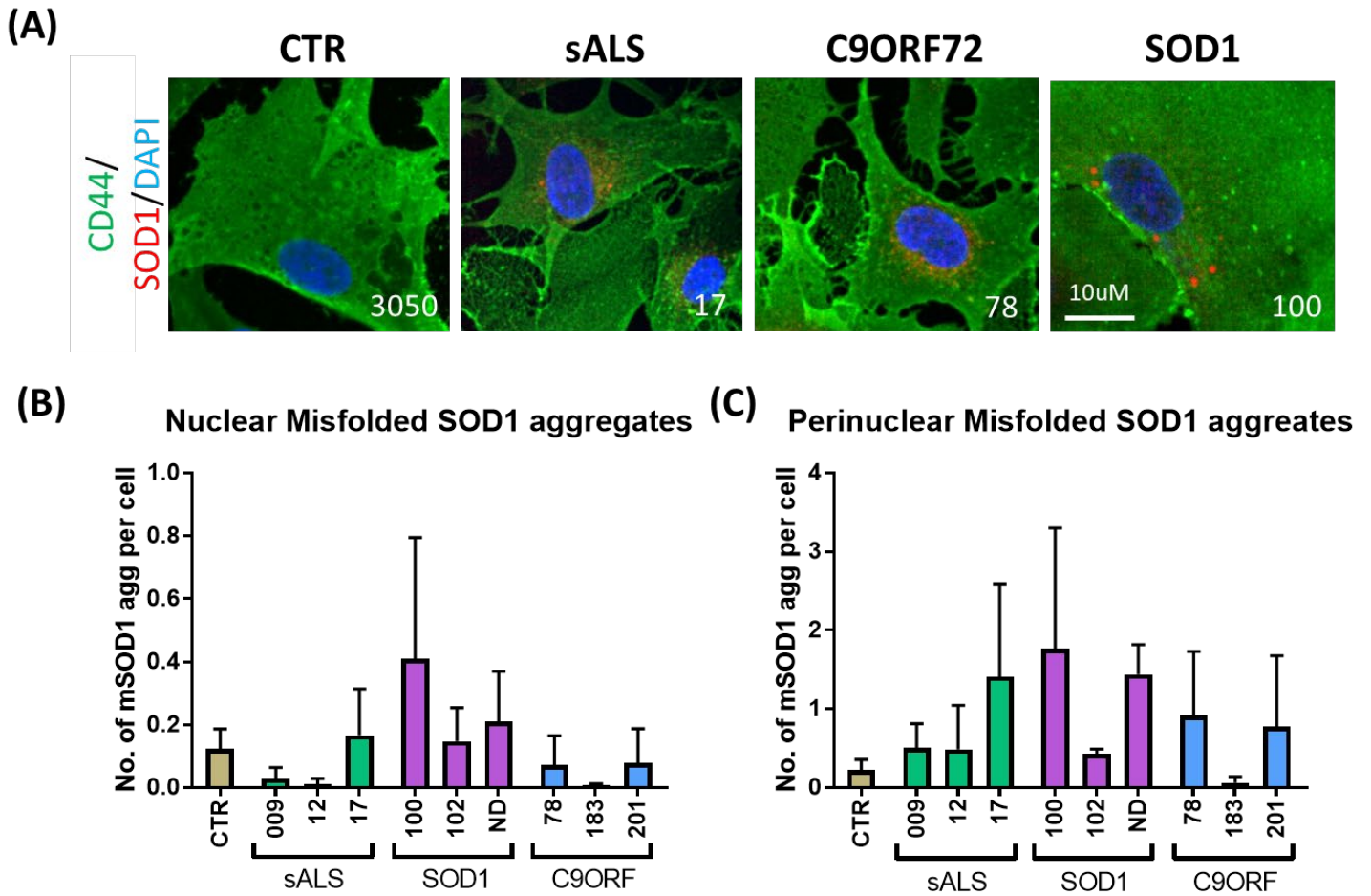


Figure 3.3 Quantification of misSOD1 in control and patient iAstrocytes. (A). Immunocytochemistry of misSOD1 aggregates (568) and CD44 (488), nuclei in Hoechst, in cell lines. Scale bar 10µM. (B). Columbus analysis relative to the number of nuclear misSOD1 aggregates per cell (mean ±SD, one-way ANOVA, n=3, technical repeats = 2, multiple comparisons (MC), p=0.1141) and (C). Number of perinuclear misSOD1 aggregates per cell (mean ±SD, one-way ANOVA, MC, n=3, technical repeats = 2, p=0.1589). Control bar consists of control lines 3050, 155 & AG pooled together.

3.2.2.3. Sequestosome-1 / p62

The p62 protein plays a role in the autophagy process through the generation of autophagosomes to deal with ubiquitinated damaged or misfolded proteins. P62 accumulation is a sign of impaired protein homeostasis and a hallmark of C9ORF72 pathology and other genetic forms of ALS (Cheroni *et al.*, 2009; Al-Sarraj *et al.*, 2011; Sasaki, 2011). For this reason, I set out to determine whether our patient iAstrocytes displayed this feature.

Control and patient iAstrocytes were immunostained for the p62 protein and the percentage of cells with cytoplasmic p62, along with perinuclear p62 spots, was quantified using the Columbus software (Figure 3.4A). All patient cells displayed a significantly higher percentage of p62 positive cells (Figure 3.4B; one-way ANOVA, multiple comparisons, $n=3$, $p<0.01$). Two C9ORF72 lines presented the highest percentage of p62 positive cells; this was in keeping with the expected pathophysiology as C9ORF72 patients are known to have dysregulated autophagy (Webster *et al.*, 2016), thus leading to p62 accumulation.

In most cell lines, p62 distribution was organised in puncta rather than diffusely in the cytoplasm, suggesting that the protein was recruited at the phagosome. Multiple patient cell lines displayed significantly more perinuclear p62 puncta than the control lines (Figure 3.4C; one-way ANOVA, multiple comparisons, $n=3$, $p<0.05$). However, C9ORF72 lines 78 and 183 presented a much more diffuse p62 staining as indicated by the lack of perinuclear p62 spots, indicating an impairment in the recruitment of p62 which has been documented in C9ORF72 pathology (Webster *et al.*, 2016).

The Western blot data reflect the quantification of the staining (Figure 3.4D, courtesy of Miss Noemi Gatto); the ALS patient iAstrocyte lines displayed significantly higher levels of the p62 protein compared to control iAstrocytes (Figure 3.4E; one-way ANOVA, multiple comparisons, $n=3$, $p<0.05$).

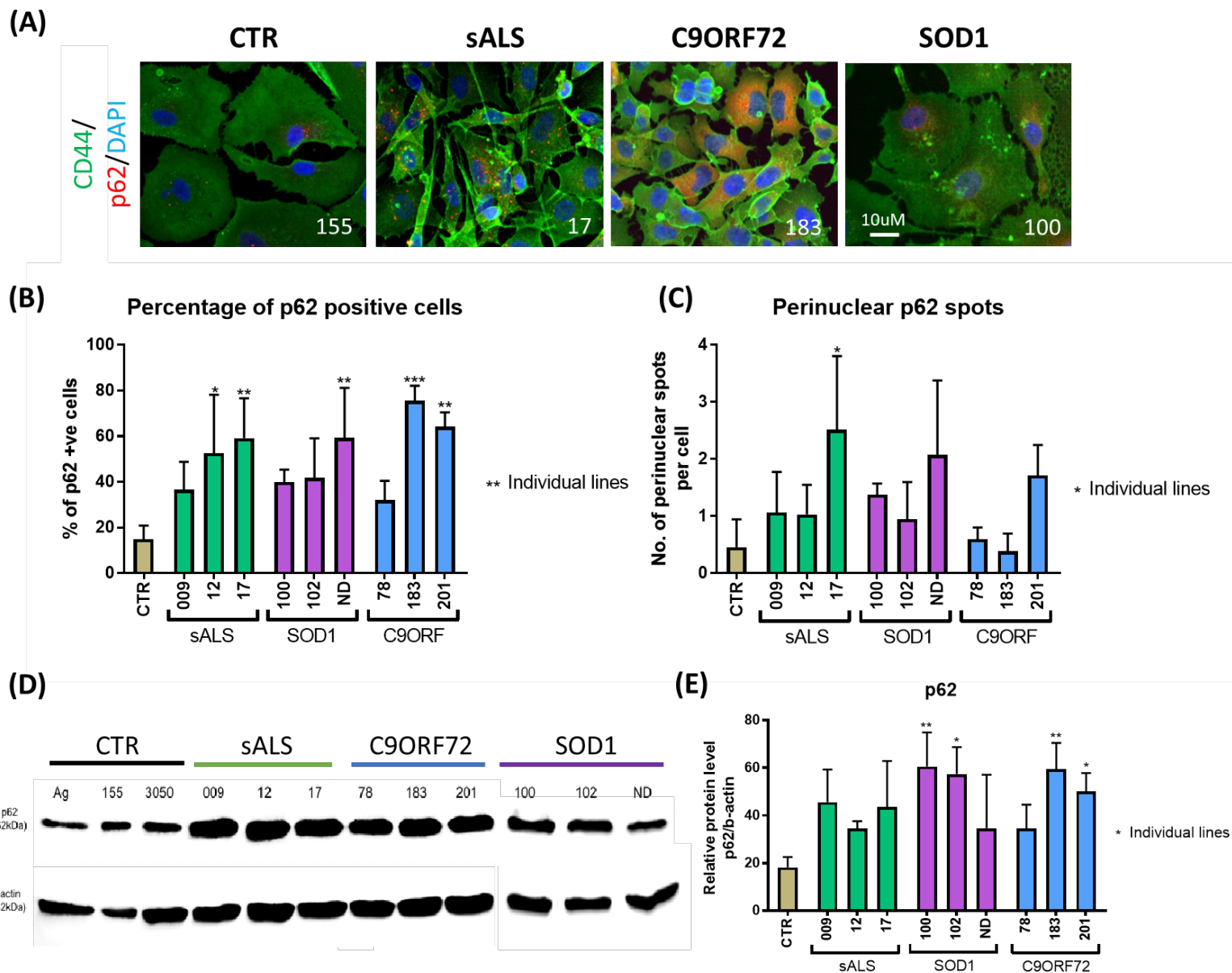


Figure 3.4 Quantification of p62 expression in control and patient iAstrocytes. (A). Immunocytochemistry of p62 expression (568) and CD44 (488), nuclei in Hoechst, in cell lines. Scale bar 10 μ M. (B). Columbus analysis relative to the percentage of cells with cytoplasmic p62 (mean \pm SD, one-way ANOVA, MC, n=3, technical repeats = 2, $p < 0.01$) and (C). Average perinuclear p62 puncta per cell (mean \pm SD, one-way ANOVA, MC, n=3, technical repeats = 2, $p < 0.05$). Individual significance is displayed on the graph (* $p < 0.05$, ** $p < 0.01$, *** $p < 0.001$, **** $p < 0.0001$). Control bar consists of control lines 3050, 155 & 161 pooled together. Data from control 161 courtesy of Mr Allan Shaw. (D). Western blot of the control and patient iAstrocyte lines for p62 protein and (E). Quantification of p62 protein expression (mean \pm SD, one-way ANOVA, MC, n=3, $P < 0.05$), courtesy of Miss Noemi Gatto. Control bar consists of control lines 3050, 155 & AG pooled together.

3.2.3 Mitochondrial dynamics

Mitochondrial dysfunction is common across many neurological disorders associated with ageing and has a massive impact upon cellular function. Therefore, I decided to characterise changes in mitochondrial morphology across patient iAstrocyte lines.

The mitochondria were labelled with TMRM, a cationic dye that is incorporated into the mitochondrial matrix in proportion to the MMP (Figure 3.5A). CCCP was added to the cells as a control; this compound depolarises the mitochondria by increasing mitochondrial permeability to protons, resulting in the quenched TMRM dye exiting the mitochondria and the collapse of the membrane potential (Perry *et al.*, 2011). This ensures that the directional change in the TMRM signal was interpreted appropriately. In order to optimise the protocol in iAstrocytes, two different concentrations of TMRM were tested, alongside media treated with either glucose or galactose.

There was a greater difference between control and patient untreated and CCCP condition in the 80nM concentration over the 40nM, so this concentration was used in further assays, as it is the dye concentration that saturates the mitochondrial membrane, thus showing the largest membrane potential collapse with CCCP (Figure 3.5B). There was also a greater difference in mitochondrial morphology distinguished between the control and patient iAstrocyte lines in the galactose treated conditions in the 80nM concentration. The sALS iAstrocyte line had a lower mitochondrial form factor as well as a lower number of total mitochondria within the network, implying the mitochondria were more fused as shown by the increase in mitochondrial area (Figure 3.5C-E). The addition of galactose prevents energy production through glycolysis, instead increasing cell reliance on oxidative phosphorylation which generates a larger membrane potential. Therefore, the addition of galactose was used in further assays. There was little change in the percentage of perinuclear mitochondria between the control and patient iAstrocyte lines (Figure 3.5F).

While the 40nM TMRM concentration displayed larger changes between the control and patient iAstrocyte lines in some parameters, ultimately, I decided to use 80nM TMRM for further assays because the concentration needed to be optimised in terms of the MMP, therefore I focused the decision more on the delta in intensity rather than the other parameters.

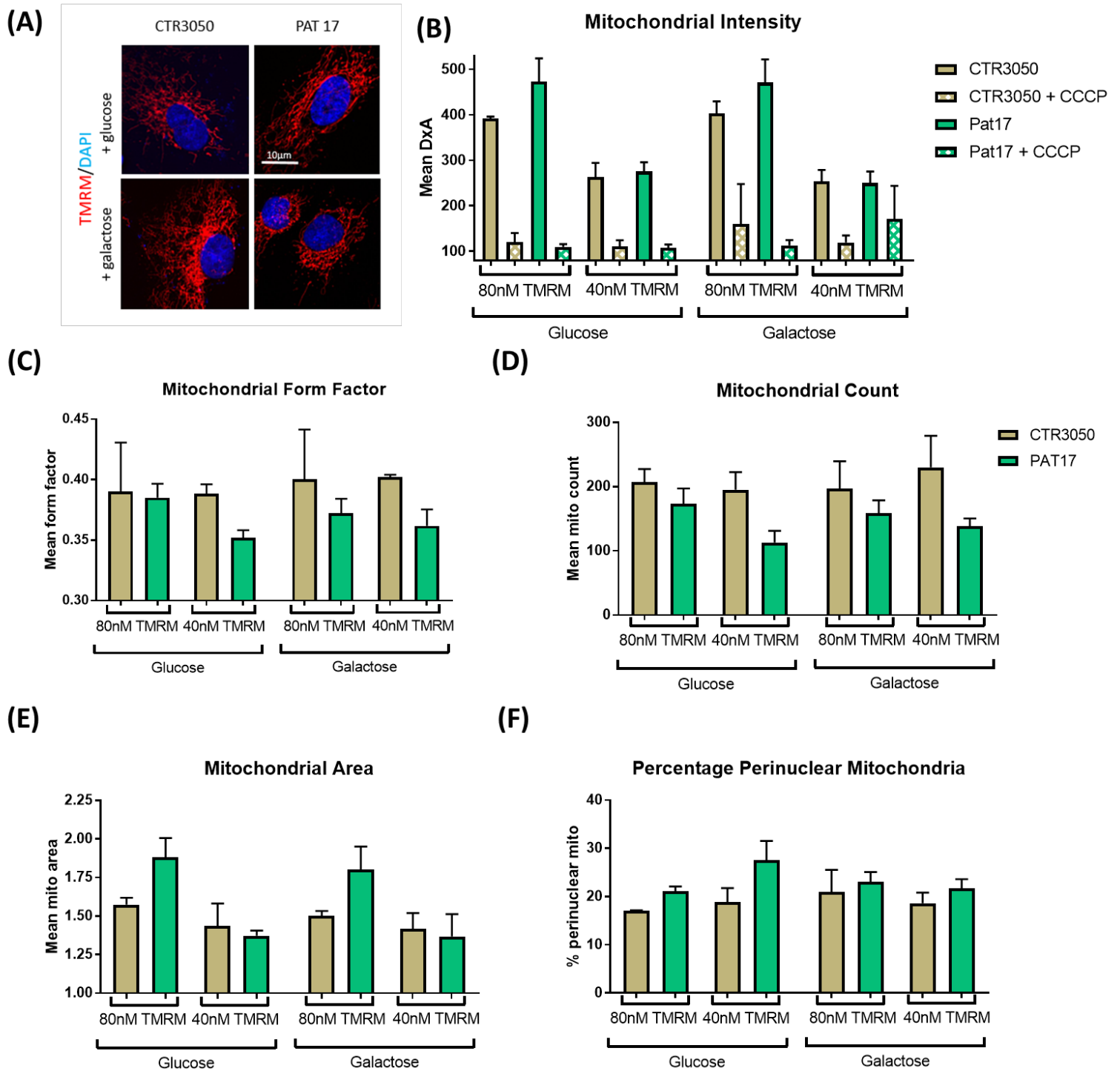


Figure 3.5 Optimisation of mitochondrial membrane potential (MMP) assay with one control and one *sALS* patient *iAstrocyte* line. (A). Visualisation of mitochondria (TMRM) and nuclei (Hoechst) allows for quantification of mitochondrial function and morphology. Scale bar 10 μ M. (B). INCELL Developer analysis relative to the mitochondrial membrane potential, (C). Mitochondrial form factor, (D). Total mitochondrial count, (E). Mitochondrial area and (F). Percentage of perinuclear mitochondria (mean \pm SD, n=3, technical replicates).

Once the assay had been optimised, the next step was to run MMP assays on all control and patient iAstrocyte lines to determine individual differences in mitochondrial network dynamics (Figure 3.6A).

The majority of cellular ATP is produced by the mitochondria through oxidative phosphorylation. The mitochondrial electron transport chain generates an electrochemical gradient through redox reactions. This gradient drives ATP synthesis as well as generating the MMP which can be used to evaluate mitochondrial function (Sakamuru *et al.* 2016). There were significant alterations in the MMP in most patient lines compared to control (Figure 3.6B; one-way ANOVA, multiple comparisons, $n=3$, $p<0.0001$). C9ORF72 lines 183 & 201 displayed a significantly increased membrane potential; this indicates that the cells were working harder to increase their proton gradient across the mitochondrial membrane either to produce more ATP than normal control cells, or to compensate for the potential uncoupling of the respiratory chain. A reduction in the membrane potential could imply an inability to mount a membrane potential able to produce sustainable levels of ATP such as shown in SOD1 line ND29505.

The mitochondrial form factor is a measure of the degree of mitochondrial branching; this was calculated based on the length of the mitochondrial outline and the area of the mitochondrion (Mortiboys *et al.*, 2008) A low form factor value indicates a fused mitochondrial network while a fragmented network will result in a high form factor value. There were small fluctuations in form factor in most patient lines compared to control lines (Figure 3.6C). SOD1 ND29505 presented the highest increase in form factor since the mitochondrial network was extensively fragmented in this cell line, from looking at images alone. However, due to the variation between runs, this change was not identified as significant.

INCELL Developer software mitochondrial segmentation analysis allowed for the isolation of a single mitochondrion within a network; this was used to investigate mitochondrial count and area. Most patient cell lines demonstrated a significant reduction in total mitochondrial count compared to controls (Figure 3.6D; one-way ANOVA, multiple comparisons, $n=3$, $p<0.05$). Observation of the iAstrocytes morphology showed that many of these patient lines were smaller in size than the control (Figure 3.1). To control for cell size, the total mitochondrial count was divided by the cell area. After this normalisation, there was no significant difference between patient and control lines, indicating that cell area was the main determinant of the alteration of mitochondrial number (Figure 3.6E).

The size of the mitochondrion can be indicative of mitochondrial health, for example smaller mitochondria may imply a more fragmented mitochondrial network. There were significant alterations in mitochondrial area in patient iAstrocytes (Figure 3.6F; one-way ANOVA, multiple

comparisons, $n=3$, $p<0.05$). sALS line 17 displayed a higher mitochondrial area while SOD1 patient ND29505 presented a lower mitochondrial area which matched the increased mitochondrial branching of these cell lines.

The percentage of perinuclear mitochondria is also indicative of the health of the mitochondrial network. The positioning of mitochondria within the cell is known to be dependent on the local energy requirement; perinuclear mitochondrial movement has been associated with reduced ATP synthesis and membrane potential as well as increased ROS (Armstrong *et al.*, 2018). Most patient lines displayed significantly more perinuclear mitochondria than the control (Figure 3.6F; one-way ANOVA, multiple comparisons, $n=3$, $p<0.0001$). C9ORF72 lines 183 & 201 presented significantly more mitochondrial clustering around the nucleus, almost double to that of the control, implying network dysfunction. This may be linked to the significantly increased intensity we also see in these two cell lines (Figure 3.6B).

In summary, different patient iAstrocyte lines varied in the mitochondrial network morphology, indicating that various factors beyond genotype may contribute to mitochondrial dysfunction. To identify potential common characteristics, I ranked the different iAstrocytes lines in terms of a mild or severe morphology based on the number of parameters deviated from the control. sALS line 12, C9ORF72 78 and SOD1 100 displayed a mild alteration in mitochondrial morphology (one altered parameter), while sALS 009 & 17 lines and SOD1 102 presented a moderate phenotype (two altered parameters). The cell lines with the most dysfunctional mitochondrial morphology were C9ORF72 lines 183 & 201 and SOD1 ND29505. Interestingly, this ranking mostly matched with their neurotoxicity in culture, as shown in Chapter 4.2.2.

In addition, the C9ORF72 lines shared an increased membrane potential, reduced form factor, reduced total mitochondrial count and an increased percentage of perinuclear mitochondria, implying network fusion or a shift in mitochondrial localisation towards the nucleus, indicating that C9ORF72 mutations might have a direct impact on mitochondrial dynamics which may contribute to the underlying pathogenic role of these mutations (Onesto *et al.*, 2016). On the other hand, the SOD1 ND29505 line demonstrated a reduced membrane potential, an increased form factor and total mitochondrial count, and a reduced area, signs of a fragmented mitochondrial network.

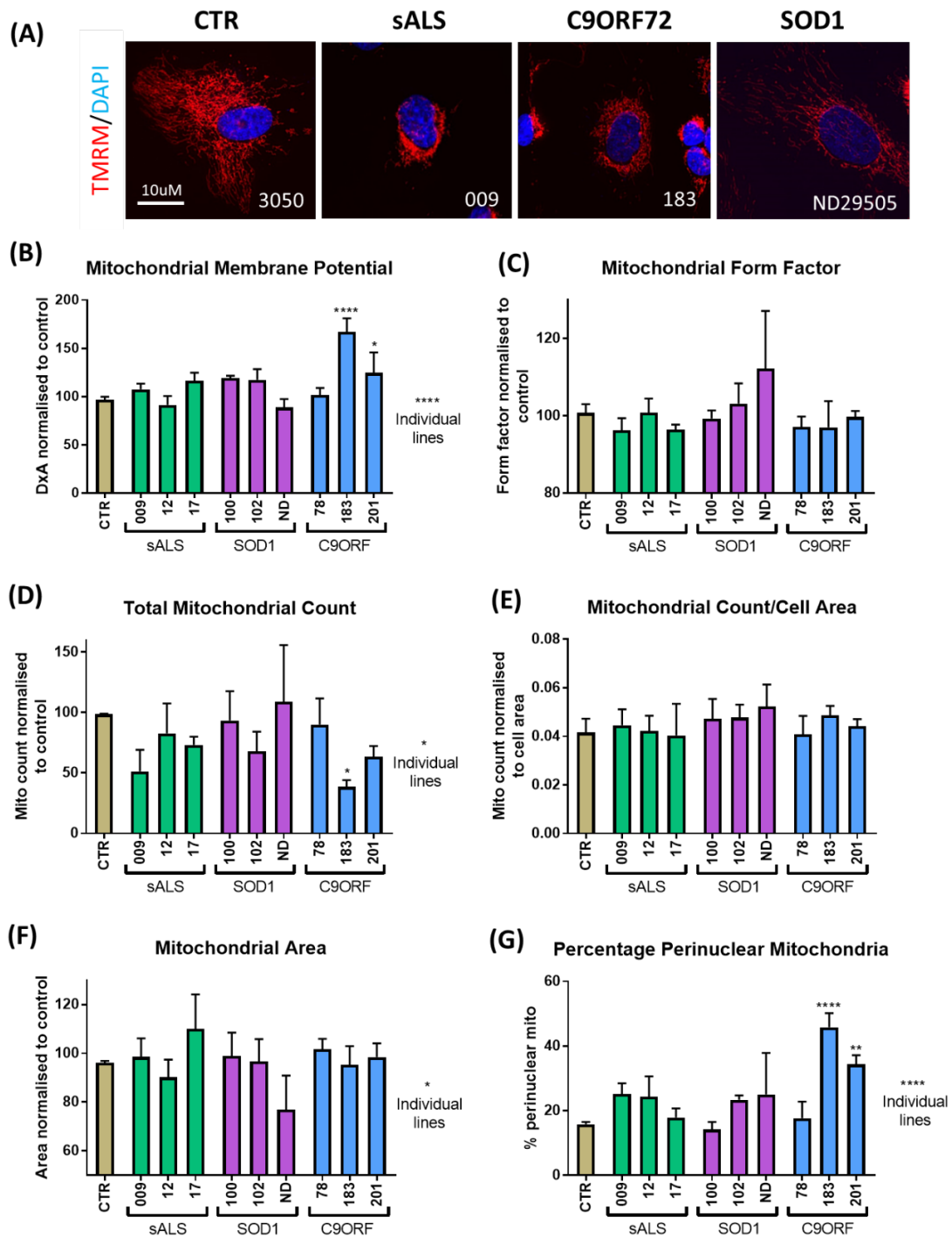


Figure 3.6 Quantification of the morphological changes in control and patient iAstrocyte mitochondria. (A). Visualisation of mitochondria (TMRM) and nuclei (Hoechst). Scale bar 10µM. (B). INCELL Developer analysis relative to the mitochondrial membrane potential (mean ±SD, one-way ANOVA, MC, n=3, technical repeats = 3, p<0.0001), (C). Mitochondria form factor (mean ±SD, one-way ANOVA, MC, n=3, technical repeats = 3, p=0.0893), (D). Total mitochondria count (mean ±SD, one-way ANOVA, MC, n=3, technical repeats = 3, p<0.05), (E). Mitochondrial count normalised to cell area (mean ±SD, one-way ANOVA, MC, n=3, technical repeats = 3, p=0.5796), (F). Mitochondrial area (mean ±SD, one-way ANOVA, MC, n=3, technical repeats = 3, p<0.05) and (G). Percentage perinuclear mitochondria (mean ±SD, one-way ANOVA, MC, n=3, technical repeats = 3, p<0.0001). Individual significance is displayed on the graph. Control bar consists of control lines 3050, 155 & 209 pooled together.

3.2.4. Glutamate buffering

3.2.4.1. Extracellular glutamate assay

A common pathological mechanism in ALS is neuronal death by excitotoxicity caused by high extracellular levels of the neurotransmitter glutamate. Healthy astrocytes protect neurons from glutamate excitotoxicity by taking up glutamate from the extracellular space. Therefore, I investigated the potential of the patient iAstrocytes to uptake glutamate either in monoculture or in co-culture with MNs by measuring glutamate levels within the media.

When control iAstrocytes were plated in monoculture, the glutamate concentration in the media remained around 10nmol 24 hours after medium change. Most of the patient iAstrocyte lines also presented a similar extracellular glutamate concentration when plated in monoculture, apart from C9ORF72 183 which displayed a significantly higher level of extracellular glutamate at monoculture (Figure 3.7; one-way ANOVA, multiple comparisons, $n=3$, $p<0.05$). When MNs were plated on top of the control iAstrocytes, the extracellular glutamate concentration in the media remained stable after 24 and 48 hours of co-culture. However, C9ORF72 patient lines showed a significant increase in extracellular glutamate after 24 and 48 hours of co-culture (two-way RM ANOVA, multiple comparisons, $n=3$, Time $p<0.0001$), implying an impaired ability of these iAstrocytes to maintain healthy glutamate levels over time.

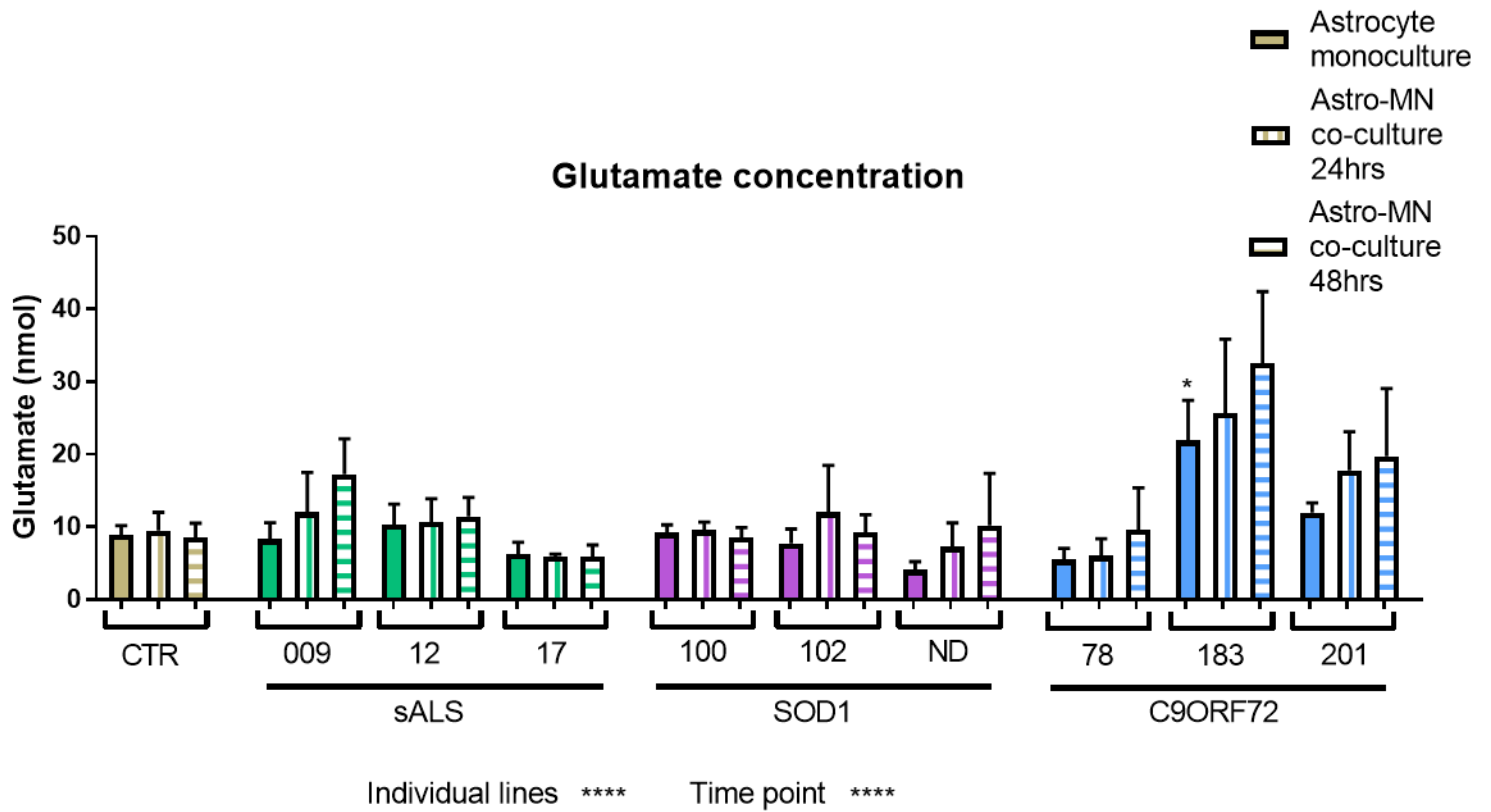


Figure 3.7 Quantification of extracellular glutamate in control and patient iAstrocytes. Extracellular glutamate levels present in media collected from iAstrocyte monoculture and MN-iAstrocyte co-culture (mean \pm SD, two-way RM ANOVA, MC, $n=3$, technical repeats = 2, Time $p<0.0001$, Column Factor $p<0.0001$) individual significance is displayed on the graph. Control bar consists of 3050 & 155 pooled together.

3.2.4.2. Glutamate transporters and receptors

To understand why extracellular glutamate accumulated in the media of C9ORF72 monocultures and co-cultures, I proceeded to investigate the expression of glutamate transporters and receptors on the C9ORF72 iAstrocytes.

EAAT2 is the major glutamate transporter in astrocytes and is reportedly downregulated in ALS, resulting in neuronal excitotoxicity from the accumulation of glutamate in the synaptic space (Howland *et al.*, 2002). The study by Swanson *et al.* (1997) found that EAAT2 had a molecular weight (MW) of ~70kDa in primary cortical rat astrocytes while mouse striatal and cortical astrocytes reported the presence of two bands; a monomeric receptor with a MW of ~67kDa and a multimer with a MW of ~90kDa (Carbone *et al.* 2012). There were three protein isoforms of EAAT2 expressed in the control and patient iAstrocytes (Figure 3.8A); the 62kDa active monomer and another two protein forms with MWs at ~70kDa and ~90kDa, which are described in the literature as glycosylated forms or multimeric complexes (Kalandadze *et al.*, 2004). The C9ORF72 line 183 demonstrated a significantly increased expression of the total EAAT2 protein overall (Figure 3.8B; one-way ANOVA, multiple comparisons, n=2, p<0.001), especially the 90kDa protein form compared to the control (Figure 3.8C; one-way ANOVA, multiple comparisons, n=2, p<0.01). This line also had a higher expression of the 62kDa protein; however, this was not significant due to variability in technical replicates.

Ionotropic glutamate receptors activate calcium and other ionic flux in response to the level of glutamate in the synaptic cleft. N-Methyl D-Aspartate Receptor Subtype 2B (NMDAR2B) is a prominent ionotropic receptor present on the astrocyte cell membrane (Lee *et al.*, 2010), therefore I proceeded to investigate if the C9ORF72 lines had altered protein expression of this glutamate receptor in response to the higher levels of extracellular glutamate in the media. The C9ORF72 iAstrocyte lines demonstrated an increased expression of NMDAR2B protein in comparison to the control (Figure 3.8D-E; one-way ANOVA, multiple comparisons, n=3, p<0.05).

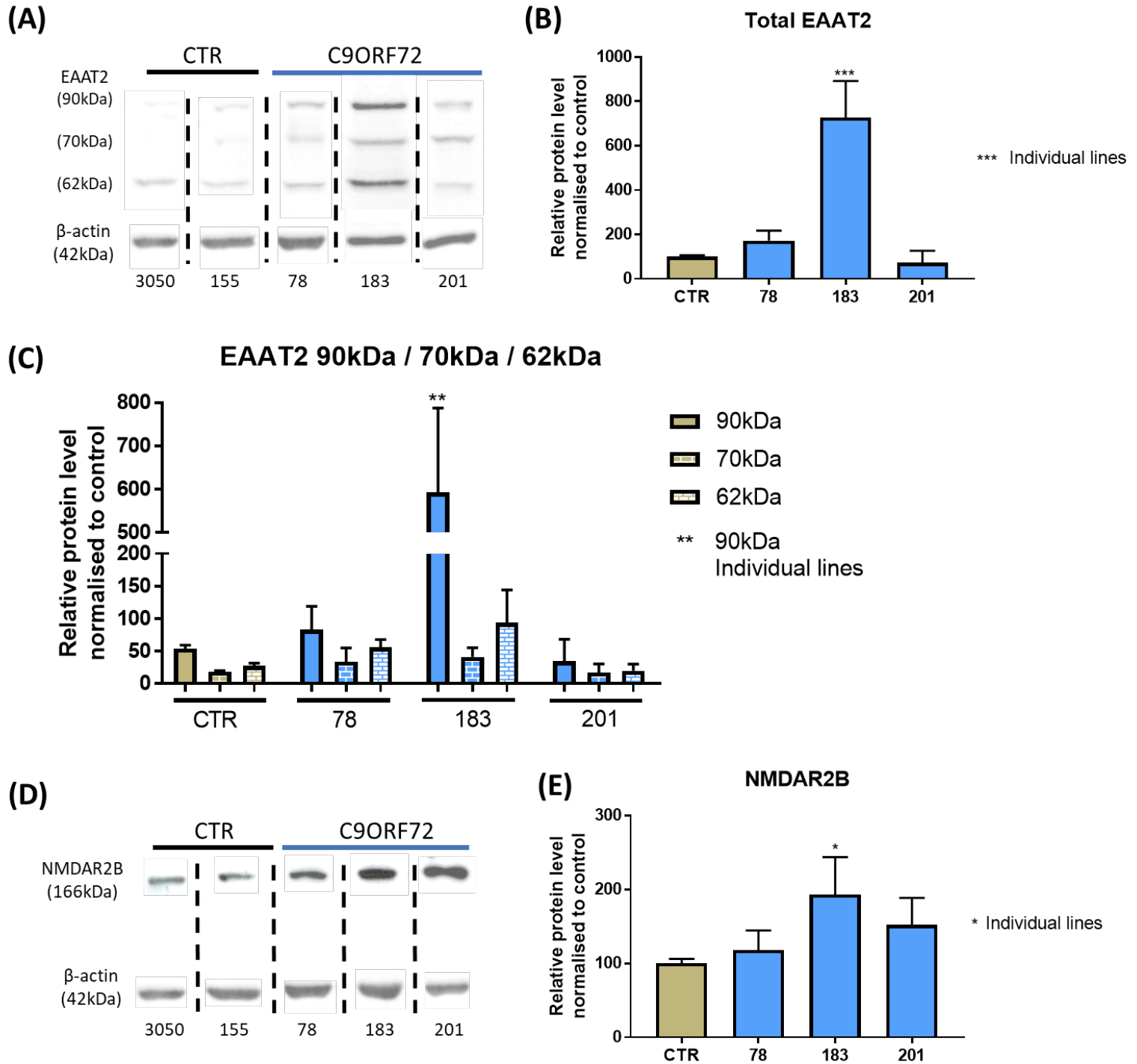


Figure 3.8 Quantification of glutamate transporters and receptors in control and C9ORF72 *i*Astrocytes (A). Western blot of EAAT2 in control and C9ORF72 patient lines and (B). Quantification of protein expression of total EAAT2 (mean \pm SD, one-way ANOVA, MC, $n=2$, $p<0.001$, individual significance is displayed on the graph) and (C). Distribution of the 62, 70 and 90kDa protein bands (mean \pm SD, one-way ANOVA, MC, $n=2$, 90kDa: $p<0.01$, 70kDa: $p=0.2588$, 62kDa: $p=0.0599$. Control bar consists of control lines 155 & AG pooled together. (D). Western blot of NMDAR2B in control and C9ORF72 patient lines and (E). Quantification of protein expression (mean \pm SD, one-way ANOVA, MC, $n=3$, $p<0.05$). Control bar consists of control lines 3050, 155 & AG pooled together.

3.3 Discussion

ALS is a genetically diverse disease promoted by a complex interplay of multiple cellular mechanisms. The discovery of non-neuronal cell involvement in the disease has presented a new therapeutic direction for ALS research, targeting the toxic mechanisms in astrocytes rather than the MNs themselves (Clement *et al.* 2003; Boill e *et al.* 2006). For this reason, the first aim of the project was to characterise the expression of pathological markers associated with ALS patient-derived iAstrocyte lines to assess whether these cells would be representative of the disease and display quantifiable disease biomarkers.

The immunocytochemistry staining of glial membrane and cytoplasmic markers vimentin and CD44 of control and patient iAstrocytes demonstrated that there were differences in cell size and morphology between cell lines as well as within specific cell lines, for example the differences in cell size in SOD1 100 shown in Figure 3.1 (3.2.1). Observations such as this alongside the variability seen across the immunocytochemistry results highlights the need to address whether technical/patient variability is a limitation of the cell model. The results show that generally within the same cell line, there is not too much variability; there was larger standard deviation seen in the immunocytochemistry results which occurred because of technical variability rather than the cell lines themselves. In other techniques, such as western blotting or glutamate assay, the standard deviation was smaller within the same patient cell line. I would argue that the technical variability did not influence the disease-relevant heterogeneity of the cell lines since the patients clearly separate from one another. On the other hand, data from the control lines was pooled together because there was less variability between the controls than there was between controls and patients, providing further evidence of the relevance of this cell model to the disease. The differences observed are, therefore, unlikely to be related to the variability of the model as a whole, as these would be, otherwise, visible in the controls as well. This evidence further indicates that the differences observed between patients underlie biological differences.

Recent research focused on single cell RNA-sequencing studies of the CNS are aiding in the identification of specific astrocytic subtypes. In depth examination of the mouse nervous system found that there are molecularly distinct types of astrocytes with a clear regionally specialised distribution in the CNS (Zeisel *et al.* 2018; Batiuk *et al.* 2020). Astrocyte subtypes could be identified by the enrichment of specific genes; telencephalon astrocytes were distinguished by the expression of *Mfge8* and *Lhx2* (Zeisel *et al.* 2018). It would be interesting to use the set of RNA-sequencing markers generated in this previous study (Batiuk *et al.* 2020) to identify the specific astrocytic subtype of the reprogrammed cell lines and to assess that the subtype is consistent across patients and controls.

3.3.1. TDP-43 mislocalisation and aggregation

As discussed previously (1.1.3.2), cytoplasmic inclusions containing TDP-43 are a common pathogenic hallmark of all ALS cases, with the exception of patients carrying SOD1 and FUS mutations (Mackenzie *et al.*, 2007; Rademakers *et al.*, 2010). Immunocytochemistry images of control and patient iAstrocytes stained for total TDP-43 show that there was reduced nuclear TDP-43 staining and the presence of TDP-43 positive aggregates in both C9ORF72 and sALS cell lines that were absent in control and SOD1 cases. This recapitulates what is known about TDP-43 mislocalisation in previous ALS studies; TDP-43 is reportedly removed from the nucleus, potentially causing a loss of TDP-43 nuclear function, and cleaved to generate C-terminal fragments which are detected in the cytoplasm (Neumann *et al.*, 2006). Quantification of the number of TDP-43 aggregates per cell as well as average TDP-43 nuclear staining intensity was attempted using Columbus analysis software of immunocytochemistry images. However, due to the motility of the TDP-43 protein, the varying cellular stress levels in different cultures, as well as the variability related to antibody batches, there was a large variability between multiple runs of staining, showing this to be an unreliable method of quantifying TDP aggregates. Laboratory members are currently trialling other TDP-43 antibodies that also tag the C-terminal fragments to improve staining for the protein. TDP-43 protein expression in Western blot, on the other hand, demonstrated the presence of the 35kDa protein band in sALS and C9ORF72 iAstrocytes only. This was interesting, since TDP-43 aggregates were only detected in the sALS and C9ORF72 patient lines in the immunocytochemistry images. The study by Che *et al.* (2011) identified that this 35kDa fragment could form cytoplasmic protein aggregates by recruiting the full length TDP-43 to the cytoplasm, removing it from the nucleus. Considering both data from the protein expression levels and the localisation of TDP within the sALS and C9ORF72 patient iAstrocytes, it appears that directly reprogrammed astrocytes recapitulate this disease mechanism.

TDP-43 ubiquitin positive, tau negative inclusions have been reported in both MNs and surrounding glial cells in the post-mortem spinal cord tissue of ALS and FTD patients (Arai *et al.*, 2006; Neumann *et al.*, 2006; Mackenzie *et al.*, 2007). Previous attempts to model TDP proteinopathy *in vitro* have had varying results. Astrocytes derived from genetically modified mice either overexpressing mutant TDP-43 or lacking TDP-43 had no effect on MN survival in co-culture (Haidet-Phillips *et al.*, 2013). When Serio *et al.* (2013) generated astrocytes from patient-derived iPSC lines with the M337V TDP-43 mutation, while these mutant TDP-43 astrocytes exhibited higher levels of cytoplasmic TDP than control, they reported these astrocytes did not display TDP nuclear loss, nor a non-cell autonomous

toxicity towards MNs in co-culture. A later study found similar results in iPSC-derived astrocytes harbouring the C9ORF72 mutation, suggesting that iPSC-derived astrocytes may not display all the manifestations of TDP proteinopathy (Zhao *et al.* 2020). In this case, the directly reprogrammed cells used in this study may be a better model as they retain the ageing phenotype (Gatto *et al.*, 2020) and recapitulate both the TDP-43 nuclear loss and cytoplasmic aggregation as well as the non-cell autonomous toxicity seen with ALS patient post-mortem astrocytes (Haidet-Phillips *et al.*, 2011).

3.3.2. SOD1 misfolding

MisSOD1 protein inclusions are another pathological hallmark of ALS. Several publications report the presence of misfolded wtSOD1 in sporadic ALS patients (Bosco *et al.*, 2010; Forsberg *et al.*, 2011), but consensus has not been reached yet (Da Cruz *et al.*, 2017). We set out to investigate the presence of misSOD1 in all patient and control iAstrocytes included in this study using an antibody specific for misSOD1 with no distinction between wtSOD1 and mSOD1, hence why aggregates were detected in the control and patient samples.

As expected, iAstrocytes derived from SOD1 patients demonstrated the highest number of nuclear and perinuclear misSOD1 aggregates, since these patient lines carry a mutation favouring the misfolding of the SOD1 protein. Perinuclear SOD1 aggregates were also detected in sALS and C9ORF72, albeit at lower levels than the SOD1 patient iAstrocytes, in keeping with studies from post-mortem tissue (Forsberg *et al.*, 2011, 2019), and implying that there are other mechanisms involved in the misfolding of SOD1 where there is no mutation in the *SOD1* gene. Studies investigating wtSOD1 in comparison to mtSOD1 aggregation have found that wtSOD1 misfolds and gains a toxic function similar to that of mtSOD1 when exposed to oxidative damage (Ezzi *et al.* 2007; Guareschi *et al.* 2012). The aberrant cytoplasmic accumulation of TDP-43 has also been reported as a trigger for misfolding of human wtSOD1 (Pokrishevsky *et al.*, 2012), which was detected within the sALS and C9ORF72 patient iAstrocytes in this study. Interestingly, SOD1 line 102 has very little perinuclear aggregates as opposed to the other SOD1 patient lines. Since this patient was asymptomatic at the time of sample collection, this might suggest that misfolded SOD1 aggregates correlate with the disease stage in SOD1-ALS patients. This is a single observation, however, the hypothesis that this reprogramming method, beside ageing, might retain epigenetic changes that reflect various disease stages should be further investigated.

The localisation of the SOD1 protein is different within the SOD1 patient iAstrocytes than the control or other genetic subgroups. From the staining images, the SOD1 protein seemed to be more diffused around the perinuclear area in the sALS and C9ORF72 iAstrocytes, while there was less diffuse

staining and more large aggregates presented in the perinuclear region and further on into the cytoplasm in SOD1 iAstrocytes. The quantification also demonstrated that SOD1 patient iAstrocytes displayed more nuclear misSOD1 aggregates than controls or other patient lines. Zhong *et al.* (2017) discovered that SOD1 protein misfolding uncovered a normally buried nuclear export signal (NES) consensus sequence, allowing export out of the nucleus by the CRM1-dependent nuclear export pathway. The accumulation of misfolded proteins within the nucleus results in nuclear proteotoxicity (Shibata and Morimoto 2014), therefore the removal of misSOD1 from the nucleus via CRM1 nuclear export should reduce this toxicity. Results from NSC34 MN-like cells and a *C.elegans* ALS model revealed that the accumulation of mSOD1 in both the nucleus and the cytoplasm was more toxic than accumulation only in the cytoplasm (Zhong *et al.*, 2017), highlighting a therapeutic intervention for SOD1-ALS.

Quantification of cytoplasmic misSOD1 aggregates was restricted towards the perinuclear area because this was where the most aggregates were located in the staining. One potential explanation for this is that misSOD1 has been reported to be directly associated with mitochondria derived from ALS patient spinal cord (Vande Velde *et al.*, 2008). One study reported that this is attributed to a lack of the chaperone macrophage migration inhibitory factor (MIF) (Israelson *et al.*, 2015). MisSOD1 aggregates accumulated within both the intermembrane space and the outer mitochondrial membrane and have both reported to exert toxicity through interaction with B-cell lymphoma 2 (Bcl-2) and voltage dependent anion channel 1 (VDAC1), an interaction that can be prevented by MIF (Tafari *et al.*, 2015). Perinuclear misSOD1 in the patient iAstrocytes may also be inhibiting ER-Golgi transport, resulting in ER stress and accumulation of misSOD1 in the ER, as reported in previous studies (Nishitoh *et al.*, 2008; Atkin *et al.*, 2014).

3.3.3. Autophagy

We also examined the expression of p62, an adaptor protein for autophagy, responsible for the formation of aggresome-like structures containing ubiquitinated proteins targeted for autophagy (Pankiv *et al.*, 2007). The autophagy process removes cytoplasmic proteins through sequestration by autophagosomes which are then degraded by lysosomal fusion; this pathway differs from that of the ubiquitin-proteasome system as it is less selective (Levine and Klionsky, 2004). The higher levels of p62 seen in the patient cells indicate that there is high level of ubiquitinated proteins as well as potentially an impairment in the autophagy pathway, which is commonly reported in C9ORF72-ALS (Al-Sarraj *et al.*, 2011; Sasaki, 2011).

Indeed, the immunocytochemistry showed that p62 expression was higher in patient iAstrocytes when compared to the control lines. However, there were variations in p62 expression within the same genetic patient subgroup, indicating that p62 expression may increase with disease severity or with the level of impairment in the autophagy or proteasome system, as both pathways are involved in the removal of misfolded or damaged proteins. One study reported that the activation of autophagy can play either a neuroprotective or deleterious role depending on disease stage in *SOD1* mice (Rudnick *et al.*, 2017), therefore the level of p62 could be indicative of early/late-stage disease of the patients from whom the lines were derived.

While both *SOD1* and *C9ORF72* iAstrocytes displayed p62 accumulation, reports from the literature indicate that it is unlikely that this accumulation occurs via the same disease pathway. There is abundant evidence in the literature that mutations in *SOD1* result in proteasome dysfunction and the accumulation of large *SOD1* aggregates (Puttapparthi *et al.*, 2003), as detected in our immunocytochemistry results. There have also been reports of reduced expression of proteasome subunits during disease progression in *SOD1* mice (Cheroni *et al.*, 2009). However, there have also been reports of increased autophagy in m*SOD1* mouse models (Morimoto *et al.*, 2007). In addition, m*SOD1* has also been documented to activate autophagy through activation of BECLIN-1 (Nassif *et al.*, 2014) as well as interacting with the p62 protein to sequester mis*SOD1* into protein inclusions (Gal *et al.*, 2007).

The role of *C9orf72* in autophagy is multifaceted, with the depletion of the protein known to inhibit autophagy through the ULK1-mediated pathway (Webster *et al.*, 2016), as well as influencing mTOR signalling and lysosomal function in later stages of autophagy (Ugolino *et al.* 2016; Amick *et al.* 2016). In most cell lines, p62 distribution was organised into small spots or 'puncta', while the staining in the *C9ORF72* iAstrocytes was more diffused within the perinuclear area and the cytoplasm. The initial step in autophagy involves the recruitment of the ULK1 complex to the phagophore, initiating the formation of the autophagosome which later recruits the p62-tagged protein aggregates for lysosomal digestion. Webster *et al.* (2016) demonstrated that the *C9orf72* protein acts as a mediator between Rab1a and the ULK1 complex in the formation of the autophagosome, meaning that in the *C9ORF72* iAstrocytes, the p62-tagged protein aggregate is not recruited inside of the phagophore due to the loss of this interaction. This might explain why there were less p62 spots but an increase in diffuse staining detected in *C9ORF72* patient iAstrocytes.

3.3.4. Mitochondrial dynamics

Mitochondria play a vital role in cellular metabolism and survival; they are responsible for ATP production as well as phospholipid biogenesis, calcium homeostasis, and apoptosis. Since neurons are non-dividing cells, they persist throughout the entire lifetime of an individual and therefore are susceptible to the accumulating damage from mitochondrial dysfunction. Because of this, mitochondrial dysfunction is regularly associated with neurodegenerative diseases, where many of the identified mutant genes have mitochondrial associated functions (Smith *et al.* 2019). Mitophagy is a well-characterised form of autophagy which functions in the selective degradation of damaged mitochondria. In PD, mutations in *PINK1* and Parkin destabilise the mitophagy pathway as well as influencing mitochondrial dynamics by inhibiting the fusion of damaged mitochondria (Gao *et al.*, 2017). Mutations in *LRRK2* are also reported to prevent mitochondrial motility in neurons, slowing the initiation of mitophagy (Hsieh *et al.*, 2016).

Because of the importance of these organelles and their reported dysfunction in neurodegenerative disease, we set out to characterise mitochondrial network morphology in patient iAstrocytes and determine differences between controls and patients, and patient subgroups. There were clear individual differences in mitochondrial dynamics between patient cell lines; each line could be characterised as having a mild or toxic mitochondrial phenotype based on the number of parameters that deviated from the control iAstrocytes. While many lines displayed mild changes in the mitochondrial network, the C9ORF72 lines shared changes in parameters that suggested a more fused mitochondrial network, such as an increased membrane potential, reduced form factor, reduced total mitochondrial count and an increased percentage of perinuclear mitochondria. On the other hand, the SOD1 line ND29505 demonstrated a fragmented network as seen by a reduced membrane potential, an increased form factor and total mitochondrial count.

Consistent with my data showing that the most severe SOD1 mutant patient displayed a reduced MMP, both *mSOD1* fibroblast and mouse models have been reported to show reduced oxidative phosphorylation (Mattiuzzi *et al.* 2002; Allen *et al.* 2014). Moreover, Ferri *et al.* (2010) reported a decrease in mitochondrial fusion protein Opa1 and an increase in mitochondrial fission protein Drp1 in *SOD1 G93A* expressing SH-SY5Y and NSC-34 cell models, leading to the formation of a fragmented mitochondrial network. This is in line with our findings, indicating that patients carrying *mSOD1* have a more fragmented mitochondrial network.

The p62 protein is recruited to the mitochondria by the PINK1/Parkin-mediated mitophagy pathway. The accumulation of p62 has been previously reported in MNs derived from PD patients with the *LRRK2* mutation which delays the onset of mitophagy (Hsieh *et al.*, 2016; Song *et al.*, 2016), implying

that the blocking of mitophagy could be another reason for the increased p62 levels in the ALS patient iAstrocytes. Most patient lines had a higher percentage of perinuclear mitochondria compared to the control, which correlates with the perinuclear localisation of the p62 protein in the staining images, implying that p62 could be bound to the abnormal mitochondria within the network.

Although in this study, we focused on mitochondrial morphology rather than function, Walczak *et al.* (2019) found that mitochondrial oxygen consumption rate and ATP production were altered in sALS and fALS patient fibroblasts in comparison to control cells. They observed a reduced mitochondrial membrane potential in both sALS and fALS patient fibroblasts, while there was increased oxygen consumption rate in fALS samples and reduced ATP levels in sALS cells. Principle component analysis of the investigated parameters allowed for the clear distinction between control, fALS and sALS fibroblasts (Walczak *et al.*, 2019). Two studies investigating the metabolic flexibility within the C9ORF72 patient iAstrocytes showed that these lines presented defects in mitochondrial energy substrate usage which resulted in a shift towards glycolytic ATP production in these cells (Allen *et al.* 2019a; 2019b), potentially explaining the increased MMP witnessed in C9ORF72 183 and 201.

3.3.5. Glutamate transport

There is strong evidence that excitatory neurotransmission has a key role in disease progression in ALS (King *et al.*, 2016). Regulated glutamatergic transmission is a complex process, following a constant cycle of extracellular glutamate uptake and resynthesis in the astrocytes, while finding a balance of the firing thresholds within individual neurons. A prolonged increase of synaptic glutamate will cause a neuron to fire more frequently, increasing intracellular calcium levels and potentiating excitotoxicity (King *et al.*, 2016). This excitotoxicity causes prolonged pathological changes, such as ER stress and mitochondrial overload, all establishing MN vulnerability to excitotoxicity (Van Damme *et al.*, 2005). Glutamate exposure also decreases cysteine uptake by inhibiting the glutamate/cysteine antiporter, depleting the glutathione levels within the cell, and reinforcing oxidative stress conditions (Murphy *et al.*, 1989).

When glutamate is released into the synaptic cleft, the extracellular glutamate is rapidly transported into the astrocytes, mainly by the glutamate transporter EAAT2. Our data showed that the C9ORF72 iAstrocytes 183 & 201 had a higher level of extracellular glutamate while in monoculture. Since MNs are the main cells that release glutamate into the extracellular space, these iAstrocytes must have an impairment that makes them release glutamate. All C9ORF72 lines, as well as sALS 009 and SOD1 ND29505, displayed rising extracellular glutamate levels when MNs were added to the culture,

implying that the astrocytes were unable to uptake the glutamate released by the MNs, while control iAstrocytes were able to maintain consistent extracellular glutamate levels.

Both control and patient iAstrocytes presented three isoforms of EAAT2 detected within the cell lysate; with MWs of 62kDa, 70kDa and 90kDa. While there was no significant difference in EAAT2 62kDa and 70kDa in the C9ORF72 iAstrocytes, there was a significant increase in the 90kDa band in C9ORF72 line 183, as well as a shift in the balance of the three protein bands. The study by Kalandadze *et al.* (2004) investigating the posttranslational processing of EAAT2 in the ER defined the ~75kDa band as the 'mature terminally glycosylated' and the ~60kDa band represented the 'immature partially glycosylated' forms of the transporter. Larger proteins present at ~100kDa were described as 'immature multimeric complexes'. Glycosylation is an important event in the export of the transporter from the ER to the Golgi, without it the protein is retained within the ER (Kalandadze *et al.*, 2004). This implies that the C9ORF72 line 183 may have an inhibition of glycosylation events that increased ER retention, causing the accumulation of the 90kDa band and the reduction of the lower bands. Less glycosylation of EAAT2 has been reported in patients with schizophrenia and is thought to decrease glutamate uptake due to the decreased plasma membrane expression and trafficking of the transporter (Bauer *et al.*, 2010).

One group of ionotropic glutamate receptors are the family of N-methyl D-aspartate receptors which are ligand-gated channels activated by neurotransmitters such as glutamate and NMDA (Paoletti and Neyton, 2007). Ten years ago, the expression of these receptors was thought to be limited to neurons, while the research into astrocytic NMDARs was still controversial and the functional expression was yet to be confirmed in human studies. The study by Lee *et al.* (2010) showed that adult and foetal human primary astrocytes expressed known NMDAR subunits including GluN1, GluN2A-D and GluN3A-B. They also demonstrated that astrocytic calcium concentrations were significantly increased when NMDARs were stimulated with glutamate.

Interestingly, C9ORF72 lines displayed higher levels of extracellular glutamate and they also expressed significantly higher levels of NMDAR2B, implying that the excess glutamate in the media is stimulating the expression of the receptor. However, it is unclear how the extracellular glutamate levels are so much higher in C9ORF72 iAstrocyte monoculture in the first place. In AD, soluble oligomeric amyloid beta has been reported to activate astrocytic NMDARs, which was calcium influx-dependent, to induce glutamate release from astrocytes (Talanta *et al.*, 2013). Although not investigated in this study, astrocytic intracellular calcium levels can also rise through cytosolic calcium release from internal stores by the IP3 pathway following activation of G-protein coupled

metabotropic glutamate receptors (mGluRs) which would result in glutamate release (Benarroch, 2005).

In conclusion, there may be a positive feedback loop in the C9ORF72 astrocytes; extracellular glutamate levels stimulate NMDARs which leads to increased calcium influx and the release of more glutamate into the media. To test this hypothesis, I would need to measure calcium levels and signalling within the C9ORF72 iAstrocytes and whether inhibition of the NMDAR2B receptor would reduce extracellular glutamate levels.

3.3.6. Toxicity

In this chapter, I have covered several pathological markers of ALS that play a distinct role in astrocyte dysfunction as well as toxicity towards MNs, therefore it is important to summarise and hypothesise how these different parameters influence the overall condition of the cell. In theory, which parameters make a cell toxic and do all parameters contribute equally towards the toxicity of the astrocyte?

Figure 3.9 demonstrates the results of this chapter in terms of a hierarchy with colours relating to cellular dysfunction or toxicity; green being mild, yellow being moderate and red being severe. The cell lines were assessed by 'severity' which has been taken from previous MN-iAstrocyte co-culture experiments with the read out of MN survival. The value of the pathological marker increased in severity the further away from the control value. Interestingly, the most neurotoxic iAstrocyte lines displayed severe impairment in 4 or more parameters, while the distinction between mild and moderately toxic lines was not as clear.

In terms of which parameters correlated best with the toxicity of the cell line, extracellular glutamate concentration, especially when co-cultured with MNs, appeared to match the best with the individual severity of the lines. This is understandable since the extracellular glutamate will have a direct effect on the surrounding MNs. Certain parameters such as p62 accumulation and mitochondrial dynamics seemed to correlate well only with the extreme end of the spectrum, suggesting that these parameters were highly toxic when they were most dysregulated, while the cell might be able to cope or compensate for milder levels of impairment through other mechanisms. Consistent with post-mortem data, protein aggregation of TDP-43 and SOD1 alone did not appear to correlate with neurotoxicity in ALS (Cykowski *et al.*, 2017). This finding allowed us to hypothesise that one parameter alone was not responsible for the toxicity of the cell, but it was the accumulation of multiple dysfunctional pathways overtime that led to MN death.

Pathological marker	CTR	12	17	100	102	009	78	ND29505	183	201
TDP-43 cyto. aggregates		1.5	2.5	0	0	7	1.5	0	2.5	7
SOD1 nuclear aggregates		0.01	0.17	0.41	0.15	0.03	0.07	0.21	0.008	0.08
SOD1 perinuclear agg.		0.49	1.41	1.77	0.43	0.51	0.91	1.44	0.07	0.78
p62 % positive cells		53	59	40	42	37	32	59	76	64
p62 perinuclear agg.		1.03	2.52	1.38	0.95	1.07	0.6	2.07	0.39	1.71
Mitochondrial MMP		91	116	119	117	108	102	89	167	125
Mitochondrial count		83	73	93	68	51	90	109	39	63
% perinuclear mito.		24	18	14	23	25	18	25	46	34
Glutamate co-culture		11.5	5.9	8.4	8.6	16.5	10	10.2	34.8	19.7
Score		3.5	5	3	2.5	3.5	2	5.5	6.5	8
Severity		1	1	1	2	2	2	3	3	3

Figure 3.9 Summary of the pathological markers in patient iAstrocytes investigated in this chapter compared to the level of toxicity of iAstrocytes in co-culture. Each patient cell line was given a final score depending on whether each parameter was considered 'mild' (green) = 0, 'moderate' (yellow) = 0.5, or 'severe' (red) = 1. The severity score was taken from previous data of MN-iAstrocyte co-culture experiments with the read out of MN survival.

Following on from this hypothesis, it was interesting to look at which parameters made a cell line toxic. The most neurotoxic cell lines were SOD1 ND29505 and C9ORF72 183 & 201; the toxicity of patient ND29505 seemed to draw from misSOD1 aggregation and p62 accumulation while C9ORF72 183 displayed glutamate excitotoxicity and mitochondrial dysfunction. C9ORF72 201 presented moderate to severe dysregulation in all investigated parameters. This is highly important when it comes to patient treatment as these patients essentially have different contributing disease pathways.

3.3.7. Conclusions

In conclusion, characterisation of patient-derived iAstrocyte lines through phenotypic assays demonstrated characteristics that have been documented in previous studies of *in vitro* and *in vivo* ALS models, providing evidence that they are a good *in vitro* model for drug screening and functional assays. SOD1 patient iAstrocytes demonstrated nuclear and perinuclear accumulation of misSOD1 while sALS and C9ORF72 iAstrocytes demonstrated cytoplasmic aggregation of TDP-43 protein. The high levels of p62 expression in patient iAstrocytes indicated dysfunction in autophagy, or potentially mitophagy when drawn together with the changes in mitochondrial dynamics, which also resulted in the accumulation of these protein aggregates. C9ORF72 iAstrocyte lines demonstrated a higher MMP due to the hyperfusion of the mitochondrial network while one SOD1 line suffered a fall in intensity from a more fragmented, perinuclear network. Evaluation of the high levels of extracellular glutamate in the C9ORF72 iAstrocytes identified differential expression of glutamate transporters and receptors which could lead to this impairment in glutamate buffering. Finally, it is important to take multiple pathological factors into consideration when evaluating iAstrocyte toxicity as well as patient treatment, as each patient cell line displayed a variable contribution of different pathophysiological mechanisms contributing to astrocyte pathology.

Chapter 4 - Investigating the effect of Nrf2 activators on cellular function in ALS astrocytes.

4.1. Introduction

The therapeutic targeting of oxidative stress in ALS has not made much progress into clinical benefit for patients; this may be due to the use of specific antioxidant molecules that were too downstream and, therefore, ineffective (Barber *et al.* 2006). Therefore, an alternative approach is to target the whole pathway by engaging the master regulator, the transcription factor Nrf2, and thus, involving the activation of several neuroprotective pathways (Nguyen *et al.* 2003). Under normal conditions, Nrf2 activation is maintained at low levels through negative regulation by the KEAP1 complex (Itoh *et al.*, 1999). When exposed to oxidative stress, the cysteine residues on KEAP1 are oxidised, dissociating the interaction between Nrf2 and KEAP1 (Wakabayashi *et al.*, 2004). This prevents ubiquitination of Nrf2, allowing its translocation to the nucleus and driving the expression of detoxification and antioxidant enzymes via its interaction with the ARE on multiple cytoprotective genes (Nguyen *et al.* 2003).

The expression of Nrf2 activates a 'programmed cell life' response, upregulating cytoprotective and antioxidant genes as well as genes related to GSH synthesis, NADPH generation and, lipid and glucose/glycogen metabolism, which are neuroprotective (Hayes and Dinkova-Kostova, 2014). Downregulation of Nrf2 has also been reported in both mouse models and human cases of sALS (Kirby *et al.*, 2005; Sarlette *et al.*, 2008). Previous studies have demonstrated the beneficial effects of Nrf2 activation on ALS models; in particular, the astrocytic-specific expression of Nrf2 delayed disease onset and extended survival in SOD1 transgenic mouse models (Vargas *et al.* 2008). In theory, Nrf2 activating compounds could protect against astrocytic toxicity towards MNs, delaying disease progression in ALS patients.

The screening of a commercial small molecule library in SITraN identified S[+]-apomorphine and andrographolide as two NRF2-ARE activators capable of penetrating the CNS (Mead *et al.*, 2013). Andrographolide, identified as the most potent ARE inducer in this screen, is a natural compound derived from the herb *Andrographis paniculate* and is widely used as an anti-inflammatory agent in herbal medicine across Asian countries (Tan *et al.* 2017). Since 1985, andrographolide and its analogs have been shown to be beneficial in a wide variety of inflammatory disease models as well as some cancers. S[+]-Apomorphine is a receptor inactive enantiomer of a clinically approved dopamine agonist, R[-]-apomorphine, which is used to treat PD (Pessoa *et al.*, 2018). Hit compounds did not activate the NRF2-ARE pathway, and therefore did not exert neuroprotective effects in the NSC34

MN cell line, that were seen in the C6 astrocytic line (Mead *et al.*, 2013), implying that astrocytes were a better target for these compounds. In addition, many *in vitro* MN models are stimulated with hydrogen peroxide, sodium arsenite or serum withdrawal to induce oxidative stress (Cookson *et al.* 1998; Egawa *et al.* 2012; Barber and Shaw 2010), while patient-derived iAstrocytes displayed increased ROS without prior stimulation (Gatto *et al.*, 2020), therefore we chose to investigate the effect of these compounds on patient iAstrocytes in this study.

The effect of S[+]-apomorphine and andrographolide treatment was tested alongside MMF, a derivative of dimethylfumarate (DMF), another Nrf2 activator currently used as a disease modifying therapy for MS (Bomprezzi, 2015), and riluzole, the current prescribed drug for ALS.

4.2. Results

4.2.1. NRF2-ARE pathway

First, we needed to address whether the patient iAstrocyte lines had an impairment in Nrf2 signalling. Figure 4.1A shows a Western blot measuring the protein expression levels of the downstream target of the Nrf2 pathway NQO1 in the control and patient iAstrocytes before and after drug treatment, data courtesy of Dr Sufana Al Mashhadi. In most patient lines, there was a significant reduction in NQO1 protein levels compared to the control (Figure 4.1B; one-way ANOVA, multiple comparisons, n=3, p<0.0001). The sALS 009 cell line had a significantly higher expression of NQO1 than the control iAstrocytes (one-way ANOVA, multiple comparisons, n=3, p<0.001).

The next objective was to validate that the compounds tested did activate the NRF2-ARE pathway. Andrographolide potently upregulated the expression of NQO1 in control as well as SOD1 and C9ORF72 cell lines (Figure 4.1C-E). S[+]-Apomorphine and MMF treatment also increased NQO1 protein levels across control and patient lines but to a lesser extent compared to andrographolide treatment. Riluzole treatment had no effect on NQO1 protein expression, indicating that it does not activate the Nrf2 pathway. Therefore, the three antioxidant compounds are indeed capable of activating the NRF2-ARE pathway in human-derived astrocytes.

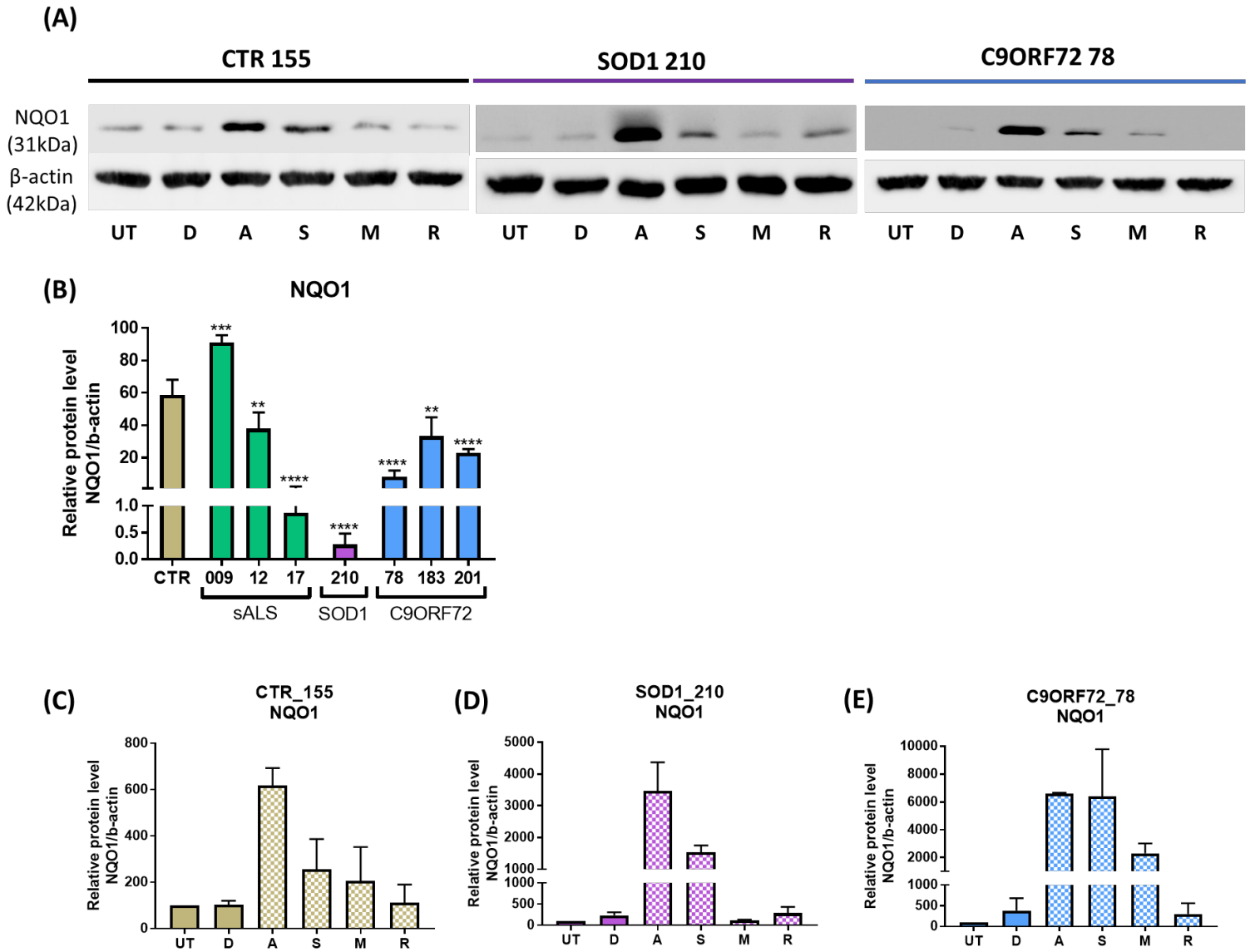


Figure 4.1 ARE protein NQO1 expression in control and patient *i*Astrocytes before and after drug treatment. (A). Western blot of NQO1 protein expression and quantification of (B). Baseline NQO1 protein levels (mean \pm SD one-way ANOVA, multiple comparisons (MC), $n=3$, $p<0.0001$), individual significance is displayed on the graph (* $p<0.05$, ** $p<0.01$, *** $p<0.001$, **** $p<0.0001$). Control bar consists of 3050, 155 & 209 pooled together. Quantification of NQO1 protein levels after drug treatment in (C). control 155, (D). SOD1 210, and (E). C9ORF72 78 (mean \pm SD, $n=2$). These data were a kind courtesy of Dr Sufana Al Mashhadi. Abbreviations: UT = untreated, D = DMSO, A = andrographolide, S = S[+]-apomorphine, M = MMF, and R = riluzole.

4.2.2. MN survival in iAstrocyte co-culture

To assess the neuroprotective effect of riluzole and the antioxidant drugs on the toxicity of patient iAstrocytes towards healthy MNs, MNs derived from mESCs were plated onto iAstrocyte monocultures and MN survival was assessed over three days using the IN-CELL Analyser 2000 plate reader. The mouse MNs were GFP tagged to the Hb9 promoter region so they could be visualised live at the 490nm wavelength. This robust, high-throughput assay could also be used to screen new therapeutic compounds to protect MNs from iAstrocyte toxicity with the percentage of MN survival at day 3 as the phenotypic readout (Figure 4.2A, Stopford *et al.* 2019). Control and patient iAstrocytes were plated on day 5 of differentiation, treated with compound diluted in 0.1% DMSO for 24 hours before MNs were cultured on the top and survival was recorded for three days.

After three days, roughly 70% of MNs survived when co-cultured with control iAstrocytes and drug treatment had no effect on MN survival (Figure 4.2B). However, when MNs were cultured with patient iAstrocytes, the survival significantly fell below 50% (two-way ANOVA, multiple comparisons, $n=3$, $p<0.0001$). Patient iAstrocytes demonstrated a range of toxicity within a subgroup, without any specific patient subgroup showing higher toxicity than the others. All sALS patient iAstrocytes showed a significant increase in MN survival after treatment with andrographolide (Figure 4.2C-E, two-way ANOVA, multiple comparisons, $n=3$, 009 $p<0.0001$, 12 $p<0.0001$, 17 $p<0.0001$) while sALS 009 showed significant improvement when treated with S[+]-apomorphine (two-way ANOVA, multiple comparisons, $n=3$, 009 $p<0.001$), and sALS 12 with MMF (two-way ANOVA, multiple comparisons, $n=3$, 009 $p<0.001$). When SOD1 patient iAstrocytes were treated with S[+]-apomorphine, there was a significant rise in MN survival (two-way ANOVA, multiple comparisons, $n=3$, 100 $p<0.0001$, 102 $p<0.05$) that was not seen with any other drug treatment (Figure 4.2F-H). Like sALS lines, MN survival was significantly increased when C9ORF72 patient iAstrocytes were treated with andrographolide (Figure 4.2I-K, two-way ANOVA, multiple comparisons, $n=3$, 78 $p<0.0001$, 183 $p<0.0001$, 201 $p<0.0001$) as well as a significant increase in survival when the lines were treated with S[+]-apomorphine (two-way ANOVA, multiple comparisons, $n=3$, 78 $p<0.01$, 183 $p<0.001$, 201 $p<0.05$) and MMF (two-way ANOVA, multiple comparisons, $n=3$, 78 $p<0.01$, 183 $p<0.0001$, 201 $p<0.001$). Treatment with riluzole showed a significant increase in MN survival in sALS and C9ORF72 lines (one-way ANOVA, multiple comparisons, $n=3$, sALS 009 $p<0.0001$, 12 $p<0.05$ & C9ORF72 78 $p<0.05$) assessed. These results highlighted that each drug treatment was neuroprotective in a certain group of patients, but not in others, beyond their genetic subtype.

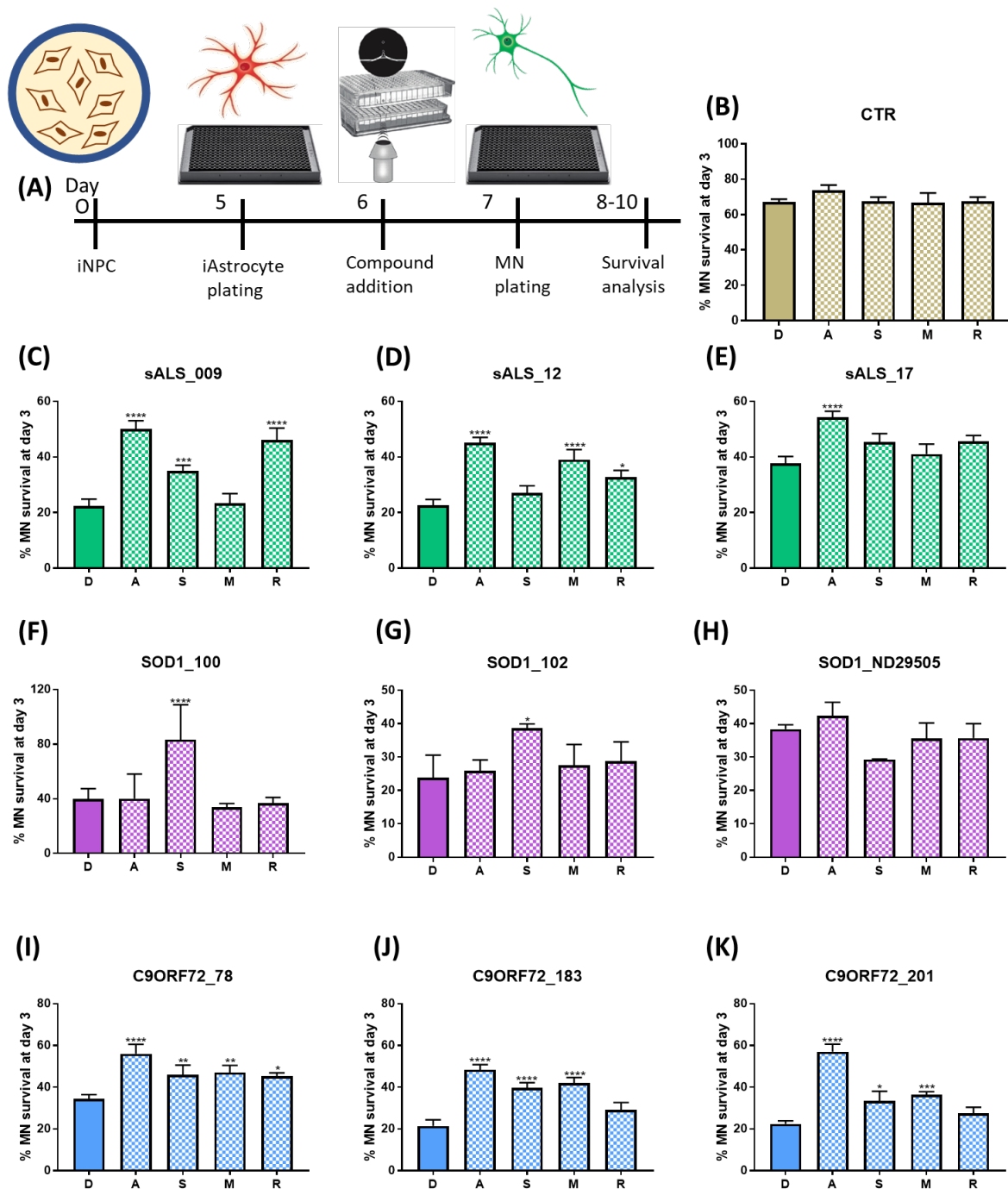


Figure 4.2 High through-put drug screening analysis of antioxidant compounds andrographolide, S[+]-apomorphine and MMF, alongside riluzole in iAstrocyte-MN co-culture experiments. (A). Time course of iAstrocyte-MN co-culture drug screen. The percentage survival of MNs at day3/day1 after drug treatment with andrographolide, S[+]-apomorphine, MMF and riluzole in (B). CTR, (C). sALS 009, (D). sALS 12, (E). sALS 17 (CTR & sALS mean \pm SD, two-way ANOVA, MC, $n=3$, technical repeats = 3, Row Factor $p<0.0001$, Column Factor $p<0.0001$), (F). SOD1 100, (G). SOD1 102, (H). SOD1 ND29505, (CTR & SOD1 mean \pm SD, two-way ANOVA, MC, $n=2-3$, technical repeats = 3, Row Factor $p<0.01$, Column Factor $p<0.0001$), (I). C9ORF72 78, (J). C9ORF72 183, and (K). C9ORF72 201 (CTR & C9ORF72 mean \pm SD, two-way ANOVA, MC, $n=3$, technical repeats = 3, Row Factor $p<0.0001$, Column Factor $p<0.0001$), individual significance is displayed on the graph. The data for CTR, sALS and C9ORF72 were a kind courtesy of Dr Sufana Al Mashadi. Abbreviations: UT = untreated, D = DMSO, A = andrographolide, S = S[+]-apomorphine, M = MMF, and R = riluzole.

4.2.3. TDP-43 proteinopathy

In Chapter 3.2.2.1, immunocytochemistry for the TDP-43 protein showed that C9ORF72 and sALS iAstrocytes presented TDP-43 nuclear loss as well as cytoplasmic protein aggregates. Western blot data showed very clearly that only sALS and C9ORF72 iAstrocytes displayed the 35kDa fragment of TDP-43 that is accumulated in the cytoplasm. Since the immunocytochemistry quantification had a large variation between runs (Supplementary 4.1A-B), I decided to investigate the effect of the compounds on protein levels of TDP-43 and TDP-35 rather than the localisation of the protein. Since the C9ORF72 patient iAstrocytes presented the most cytoplasmic protein aggregates, I decided to focus on these cell lines. MN survival was significantly increased when C9ORF72 iAstrocytes were treated with andrographolide in the previous co-culture data, therefore I chose to investigate the effect of andrographolide and S[+]-apomorphine on TDP-43 and TDP-35 protein levels, with DMSO as a negative control (Figure 4.3A).

Andrographolide treatment had no effect on the level of soluble TDP-43 in the C9ORF72 iAstrocytes (Figure 4.3B). As shown previously, C9ORF72 iAstrocyte lines have significantly higher levels of the TDP-35 band compared to the control, however there was no change after andrographolide treatment (Figure 4.3C).

TDP-43 is an aggregation prone protein that is known to form insoluble, detergent-resistant protein aggregates under cellular stress conditions (Neumann *et al.*, 2006; Mackenzie *et al.*, 2007). To investigate the effect of the compounds on TDP-43 protein aggregation, I had to prepare western blotting for insoluble as well as soluble TDP-43. C9ORF72 iAstrocytes presented increased levels of both insoluble TDP-43 and TDP-35, unfortunately due to the variability between experiments this was not considered significant. However, similar to the soluble TDP protein, andrographolide treatment had no effect on the levels of insoluble protein (Figure 4.3D-E). The insoluble protein was difficult to normalise since protein concentration cannot be detected by Bradford reagent, therefore the total insoluble protein level in the whole lane was quantified using SYPRO Ruby protein blot stain and this was used for normalisation of the insoluble TDP protein bands.

Drug treatment with S[+]-apomorphine also did not have a significant effect on soluble or insoluble TDP protein levels (Supplementary 4.2A-D).

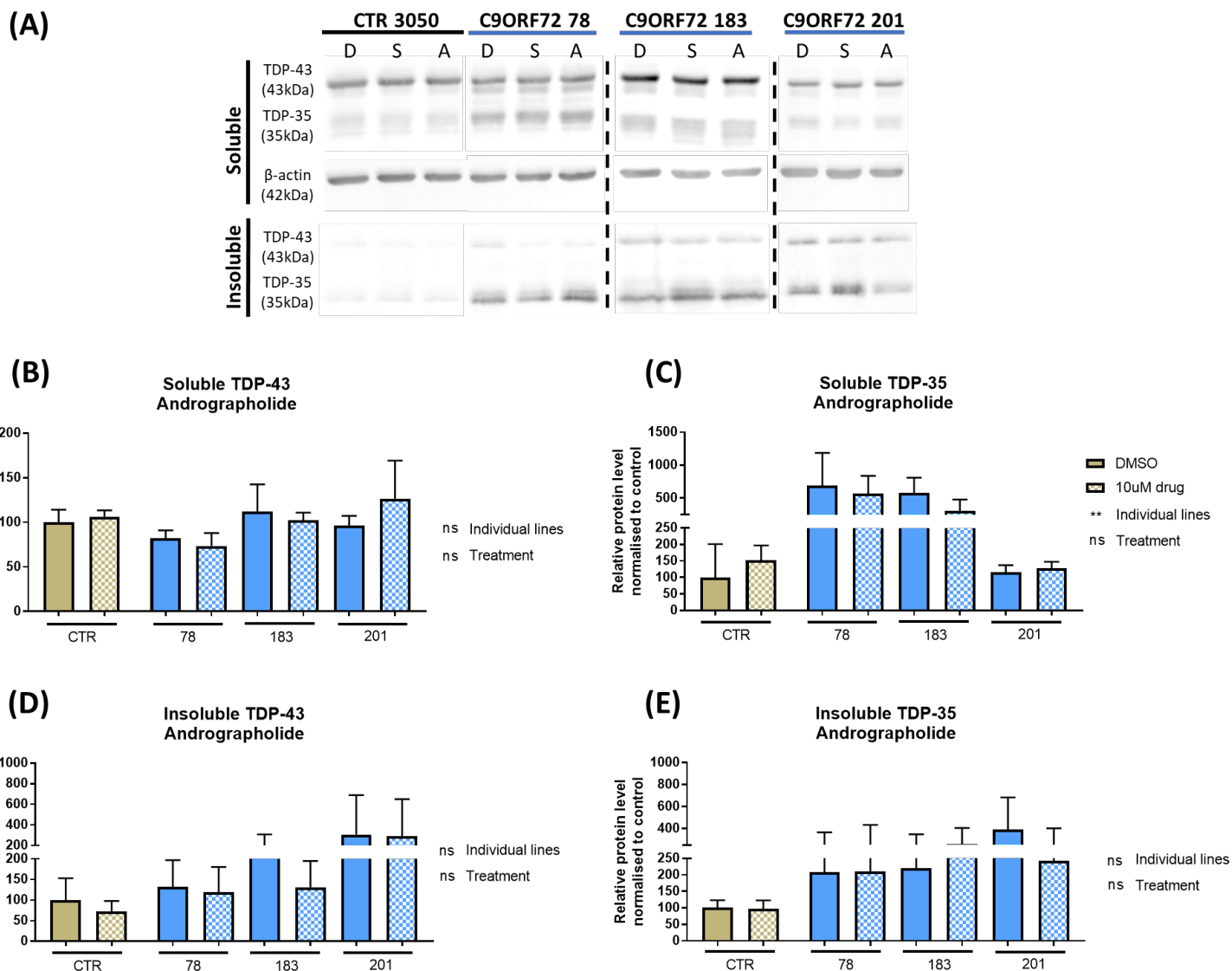


Figure 4.3 Quantification of soluble and insoluble TDP-43/TDP-35 protein in control and C9ORF72 *i*Astrocytes before and after andrographolide treatment. (A). Western blot of soluble and insoluble TDP-43/TDP-35 protein and quantification of (B). Soluble TDP-43 protein level (mean \pm SD, two-way ANOVA, MC, $n=3$, Row Factor $p=0.6025$, Column Factor $p=0.0532$), (C). Soluble TDP-35 protein level (mean \pm SD, two-way ANOVA MC, $n=3$, Row Factor $p=0.3975$, Column Factor $p<0.01$), (D). Insoluble TDP-43 protein level (mean \pm SD, two-way ANOVA, MC, $n=3$, Row Factor $p=0.6900$, Column Factor $p=0.2967$), and (E). Insoluble TDP-35 protein level (mean \pm SD, two-way ANOVA, MC, $n=3$, Row Factor $p=0.6815$, Column Factor $p=0.1948$). The control bar consists of 3050, 155 & AG pooled together. Abbreviations: D = DMSO, S = S[+]-apomorphine, A = andrographolide.

4.2.4. SOD1 misfolding

4.2.4.1. Misfolded SOD1 aggregates

In Chapter 3.2.2.2., using immunocytochemistry, I demonstrated that patient iAstrocytes displayed a higher number of misSOD1 aggregates within the perinuclear region compared to control iAstrocytes. I next investigated whether the addition of the antioxidant compounds or riluzole could reduce the presence of misfolded protein aggregates using the same protocol.

S[+]-Apomorphine treatment led to a significant decrease of misSOD1 aggregates in the perinuclear region in all patient iAstrocytes, in particular, sALS 009, 12 & 17, SOD1 100 & ND29505 and C9ORF72 201 displayed the largest reductions (Figure 4.4A; two-way ANOVA, multiple comparisons, $n=3$, $p<0.05$). Andrographolide and MMF treatment had no effect on perinuclear misSOD1 aggregation (Figure 4.4B-C).

There was a decrease in nuclear aggregates after S[+]-apomorphine treatment in most patient cell lines, however due to the variability in staining, this was not significant (Supplementary 4.3A). Similar to perinuclear aggregation, andrographolide and MMF treatment also had no effect on nuclear misSOD1 aggregates (Supplementary 4.3B-C). Treatment with riluzole had no effect on perinuclear or nuclear aggregation of the SOD1 protein in patient iAstrocytes (Supplementary 4.4A-B).

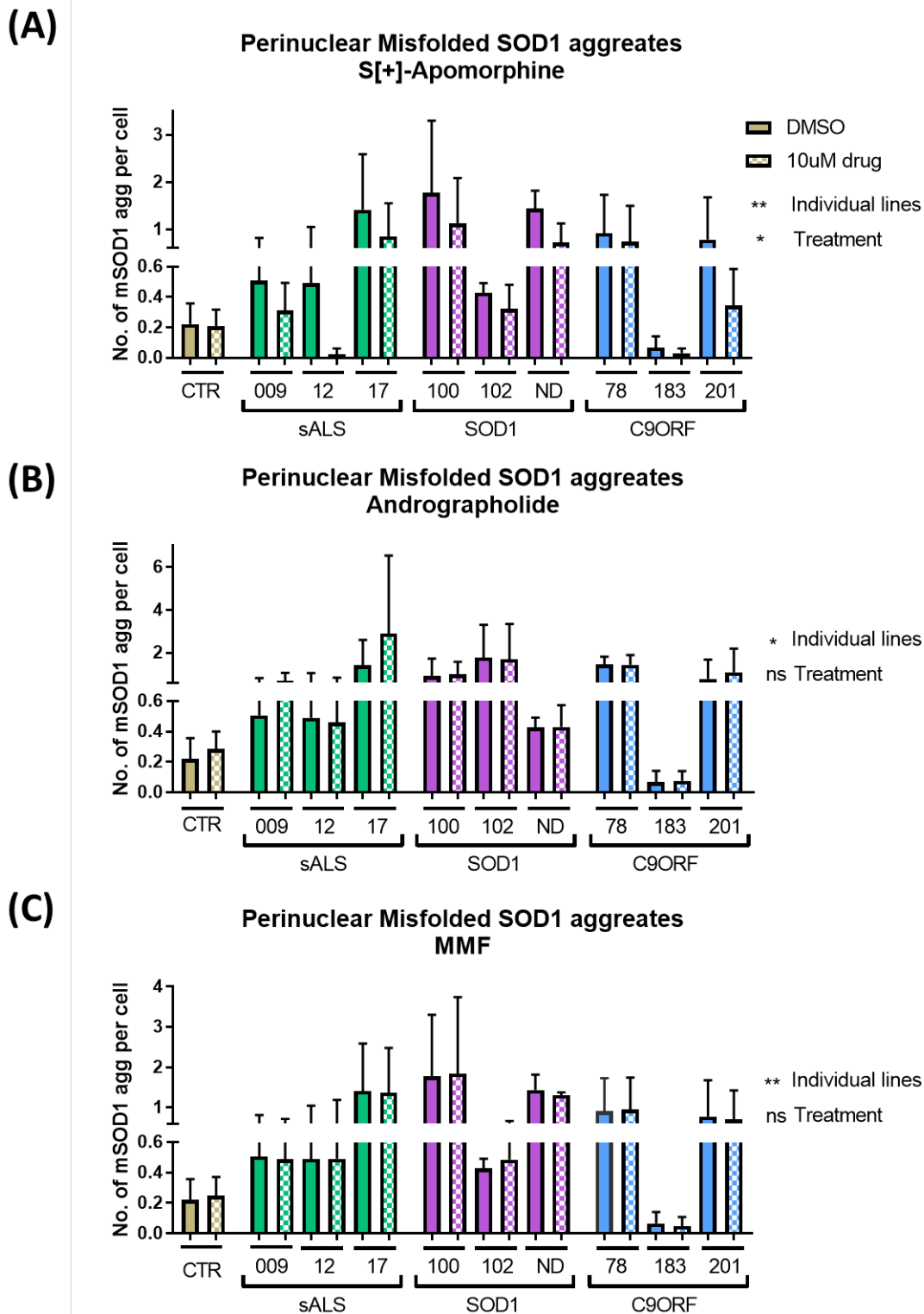


Figure 4.4 Quantification of misSOD1 aggregates in the perinuclear region of iAstrocytes before and after drug treatment. The number of perinuclear aggregates per cell after treatment with (A). S[+]-apomorphine (mean \pm SD, two-way ANOVA, MC, $n=3$, technical repeats = 2, Row Factor $p<0.05$, Column Factor $p<0.01$), (B). Andrographolide (mean \pm SD, two-way ANOVA, MC, $n=3$, technical repeats = 2, Row Factor $p=0.4790$, Column Factor $p<0.05$), and (C). MMF (mean \pm SD, two-way ANOVA, MC, $n=3$, technical repeats = 2, Row Factor $p=0.9705$, Column Factor $p<0.01$). The control bar consists of 3050, 155 & AG pooled together.

4.2.4.2. Molecular protein chaperones

Following on from the immunocytochemistry results relative to misSOD1 protein aggregates, I wanted to investigate if S[+]-apomorphine treatment reduced misSOD1 aggregation by lowering the expression of the total SOD1 protein. In the iAstrocyte-MN co-culture screen, S[+]-apomorphine provided the highest MN survival in co-cultures containing SOD1 and sALS patient iAstrocytes, therefore C9ORF72 iAstrocytes were not investigated further in regards to the effect of S[+]-apomorphine on SOD1 aggregation. Since andrographolide had no effect on perinuclear misSOD1 in the immunocytochemistry experiments, this drug, along with DMSO, was used as a negative control.

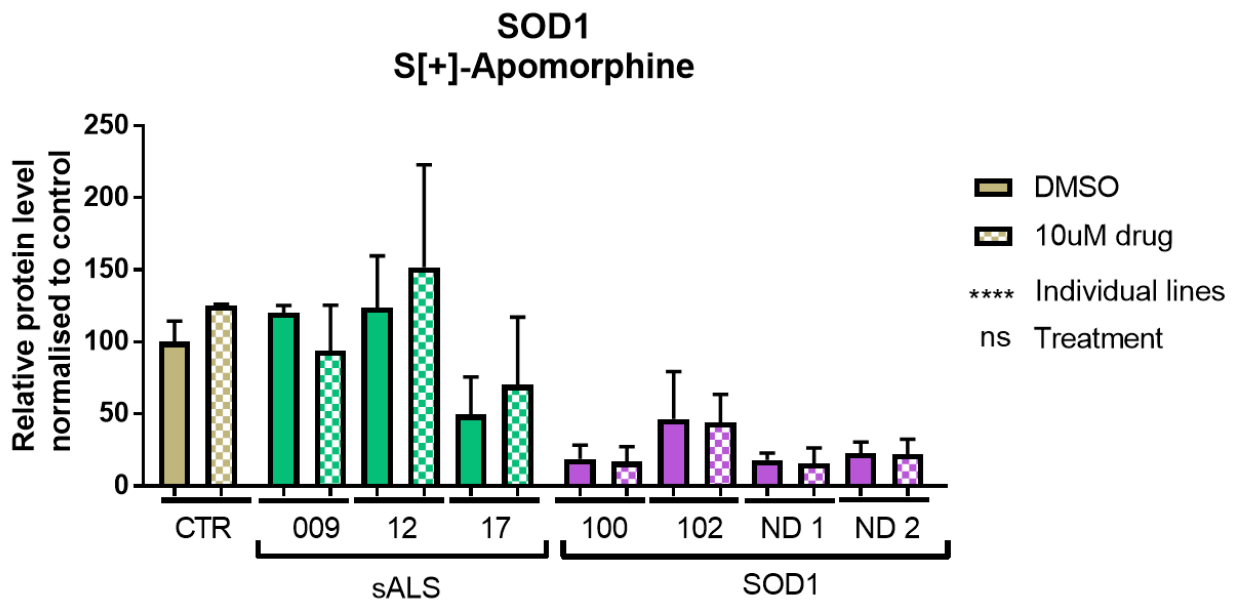
Western blot analysis revealed that S[+]-apomorphine treatment did not significantly reduce total SOD1 levels in control and patient iAstrocytes (Figure 4.5A). However, there was a significant increase in total SOD1 protein observed with andrographolide treatment, both in control and all patient iAstrocyte lines (Figure 4.5B; two-way ANOVA, multiple comparisons, $n=3$, $p<0.01$), probably as a result of its antioxidant action.

Since S[+]-apomorphine did not seem to reduce misSOD1 by reducing the expression of the SOD1 protein, I next investigated the possibility of molecular chaperone activity to unfold the SOD1 protein aggregates or prevent SOD1 misfolding. Heat shock factor 1 (HSF1) is a transcriptional activator of heat shock genes; upon cellular proteotoxic stress, HSF1 translocates to the nucleus, binding to the promoters of heat shock elements and inducing expression of heat shock proteins (HSP), including HSP70. The HSP70 family are ubiquitously expressed proteins that participate in protein trafficking, polypeptide folding and the refolding or degradation of misfolded protein aggregates (Lackie *et al.*, 2017).

The western blot data in Figure 4.6A showed that, although there was high variability between the levels of HSF1 in the various patient lines; overall, patient iAstrocyte lines do not significantly differ in the baseline expression of HSF1 from controls (Figure 4.6B). However, there was a significant difference in HSP70 protein expression (one-way ANOVA, multiple comparisons, $n=3$, $p<0.01$) with sALS 009 displaying a significantly higher expression of the HSP70 protein at baseline (Figure 4.6C).

Interestingly, S[+]-apomorphine treatment did not have a significant effect on HSP70 protein expression (Figure 4.7A), however there was a significant increase in HSP70 protein level with andrographolide treatment across control and patient iAstrocyte lines (two-way ANOVA, multiple comparisons, $n=3$, $p<0.001$); the highest increase was seen in SOD1 100 (Figure 4.7B). There was no significant difference in HSF1 expression after S[+]-apomorphine or andrographolide treatment (Supplementary 4.5A-B).

(A)



(B)

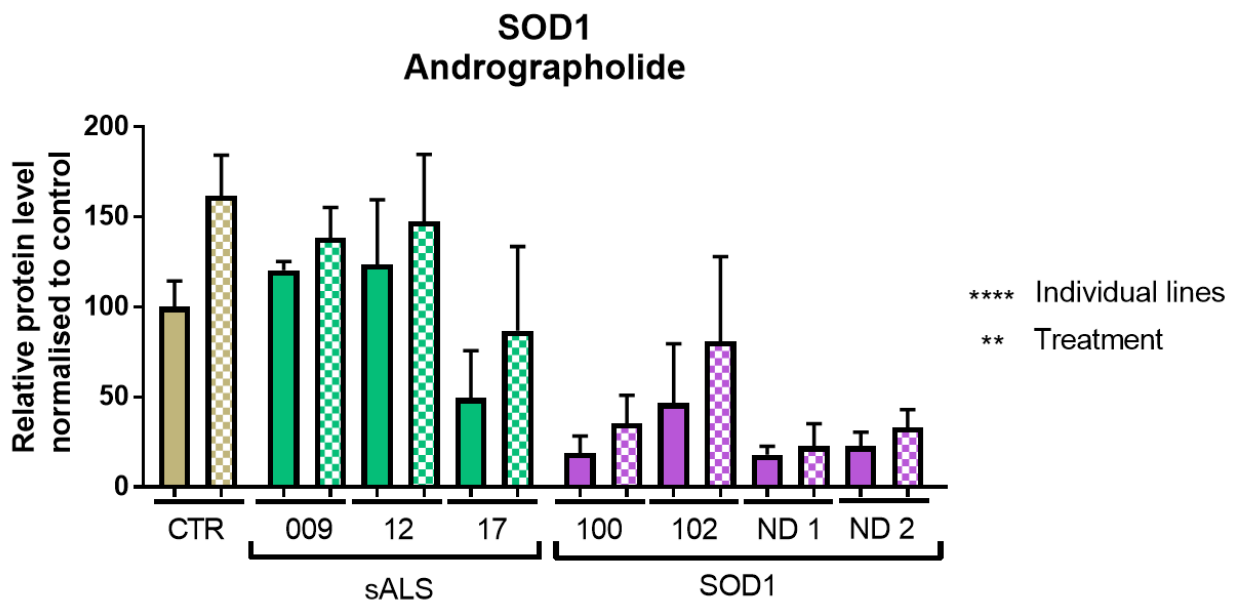


Figure 4.5 Quantification of total SOD1 protein in control, sALS and SOD1 iAstrocytes before and after drug treatment. Total SOD1 protein level after treatment with (A). S[+]-apomorphine (mean \pm SD, two-way ANOVA, MC, $n=3$, Row Factor $p=0.5374$, Column Factor $p<0.0001$), and (B). Andrographolide (mean \pm SD, two-way ANOVA, MC, $n=3$, Row Factor $p<0.01$, Column Factor $p<0.0001$). The control bar consists of 3050, 155 & AG pooled together.

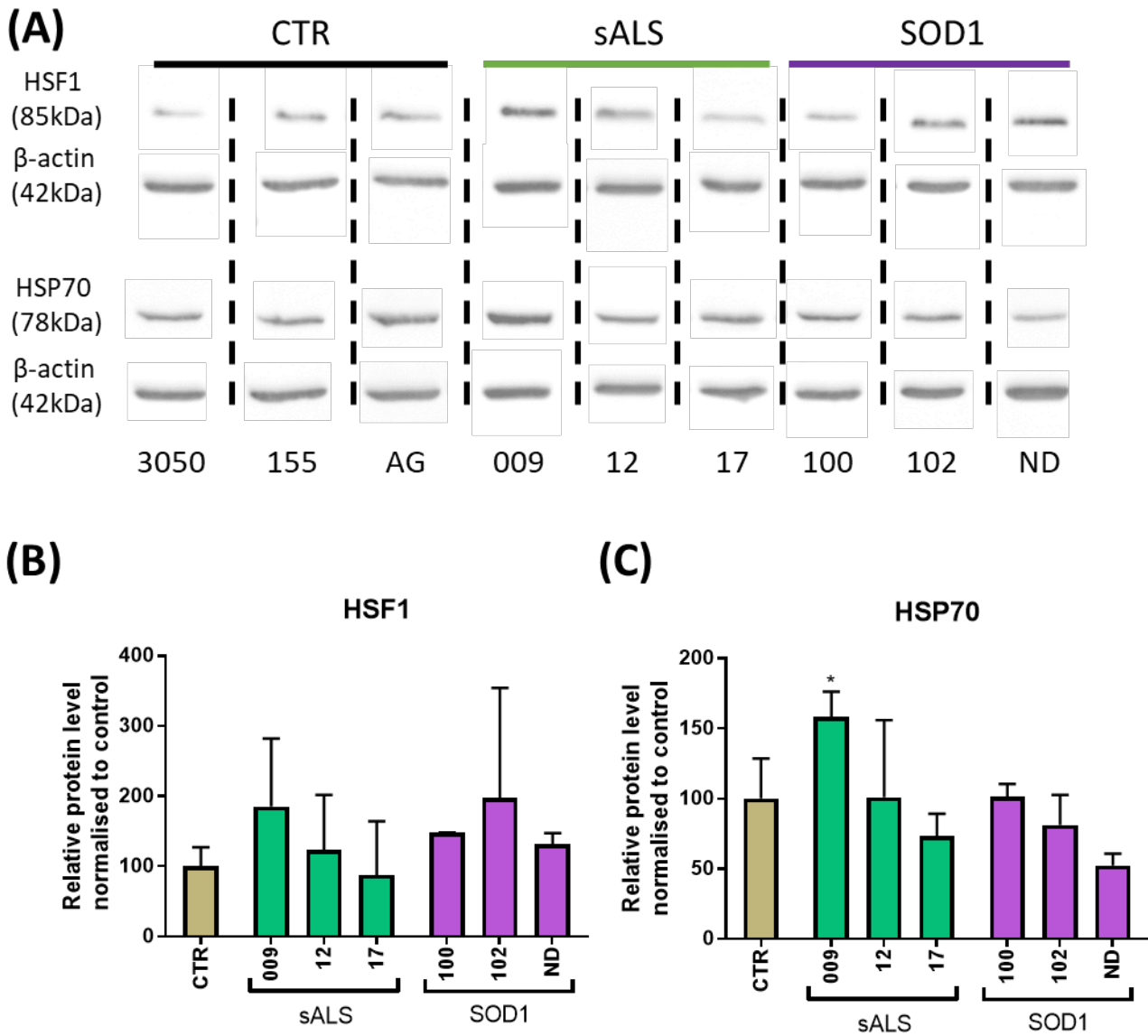


Figure 4.6 Quantification of HSF1 and HSP70 baseline protein levels in control, sALS and SOD1 *i*Astrocytes. (A). Western blot of HSF1 and HSP70 protein levels and quantification of (B). HSF1 (mean \pm SD, one-way ANOVA, MC, $n=3$, $p=0.6208$), and (C). HSP70 (mean \pm SD, one-way ANOVA, MC, $n=3$, $p<0.01$), individual significance is displayed on the graph. The control bar consists of 3050, 155 & AG pooled together.

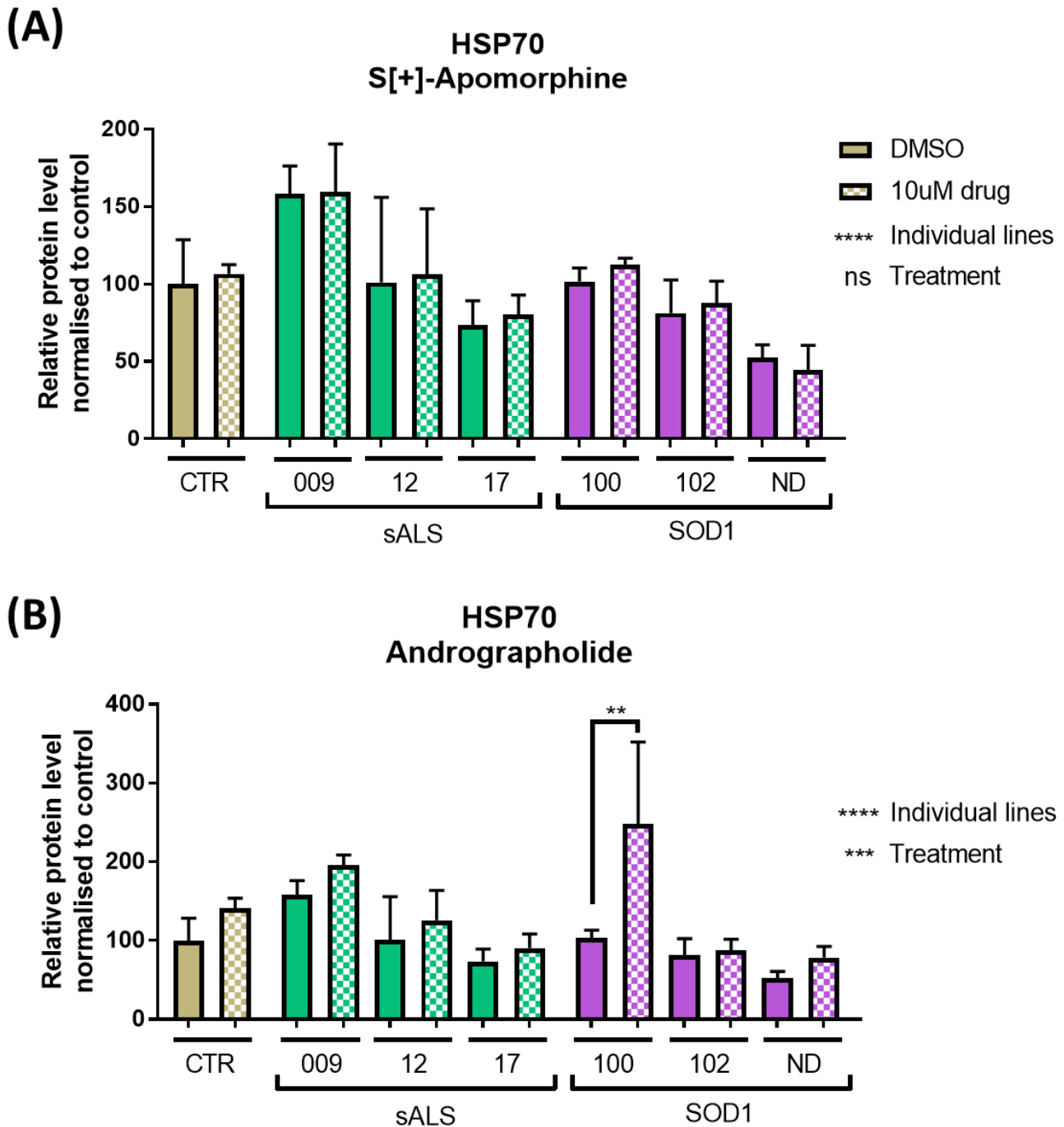


Figure 4.7 Quantification of HSP70 protein levels in control, sALS and SOD1 iAstrocytes before and after drug treatment. HSP70 protein level after treatment with (A). S[+]-apomorphine (mean \pm SD, two-way ANOVA, MC, $n=3$, Row Factor $p=0.5964$, Column Factor $p<0.0001$), and (B). Andrographolide (mean \pm SD, two-way ANOVA, MC, $n=3$, Row Factor $p<0.001$, Column Factor $p<0.0001$), individual significance is displayed on the graph. The control bar consists of 3050, 155 & AG pooled together.

4.2.5. Autophagy regulator expression – p62 and LC3 proteins

In Chapter 3.2.2.3., I used immunocytochemistry to detect the percentage of cells positive for cytoplasmic p62 and the number of perinuclear p62 spots within the cytoplasm. In this staining, all patient cells had a higher percentage of p62 positive cells as well as a higher number of perinuclear p62 spots than the control iAstrocytes. I next investigated whether treatment with the antioxidant compounds, S[+]-apomorphine, andrographolide and MMF, or riluzole would influence the presence of p62 using the same protocol.

Immunocytochemistry images showed that p62 expression was increased in control and all patient iAstrocyte lines with S[+]-apomorphine and andrographolide treatment, specifically in the perinuclear region of the cell (Figure 4.8). When these images were quantified in terms of the percentage of p62 positive cells, there was a significant increase in the number of cells expressing the p62 protein 24 hours after S[+]-apomorphine treatment across control and patient cell lines (Figure 4.9A; two-way ANOVA, multiple comparisons, $n=3$, $p<0.05$). This increase in p62 protein was more dramatic when control and patient iAstrocytes were treated with andrographolide (Figure 4.9B; two-way ANOVA, multiple comparisons, $n=3$, $p<0.0001$). The addition of MMF had no significant effect on p62 expression levels in control or patient iAstrocytes (Figure 4.9C).

Similar to the percentage of p62 positive cells, there was also a significant increase in the number of perinuclear p62 spots across control and patient iAstrocyte lines when treated with S[+]-apomorphine; the highest increase was seen in the sALS iAstrocytes (Supplementary 4.6A; two-way ANOVA, multiple comparisons, $n=3$, $p<0.05$). There was a more dramatic significant increase in the number of perinuclear spots when cells were treated with andrographolide (Supplementary 4.6B; two-way ANOVA, multiple comparisons, $n=3$, $p<0.001$). On the contrary, MMF treatment had little effect on perinuclear p62 spots (Supplementary 4.6C). When control and patient iAstrocytes were treated with riluzole, there was little change in both the percentage of p62 positive cells and the number of perinuclear p62 spots (Supplementary 4.7A-B).

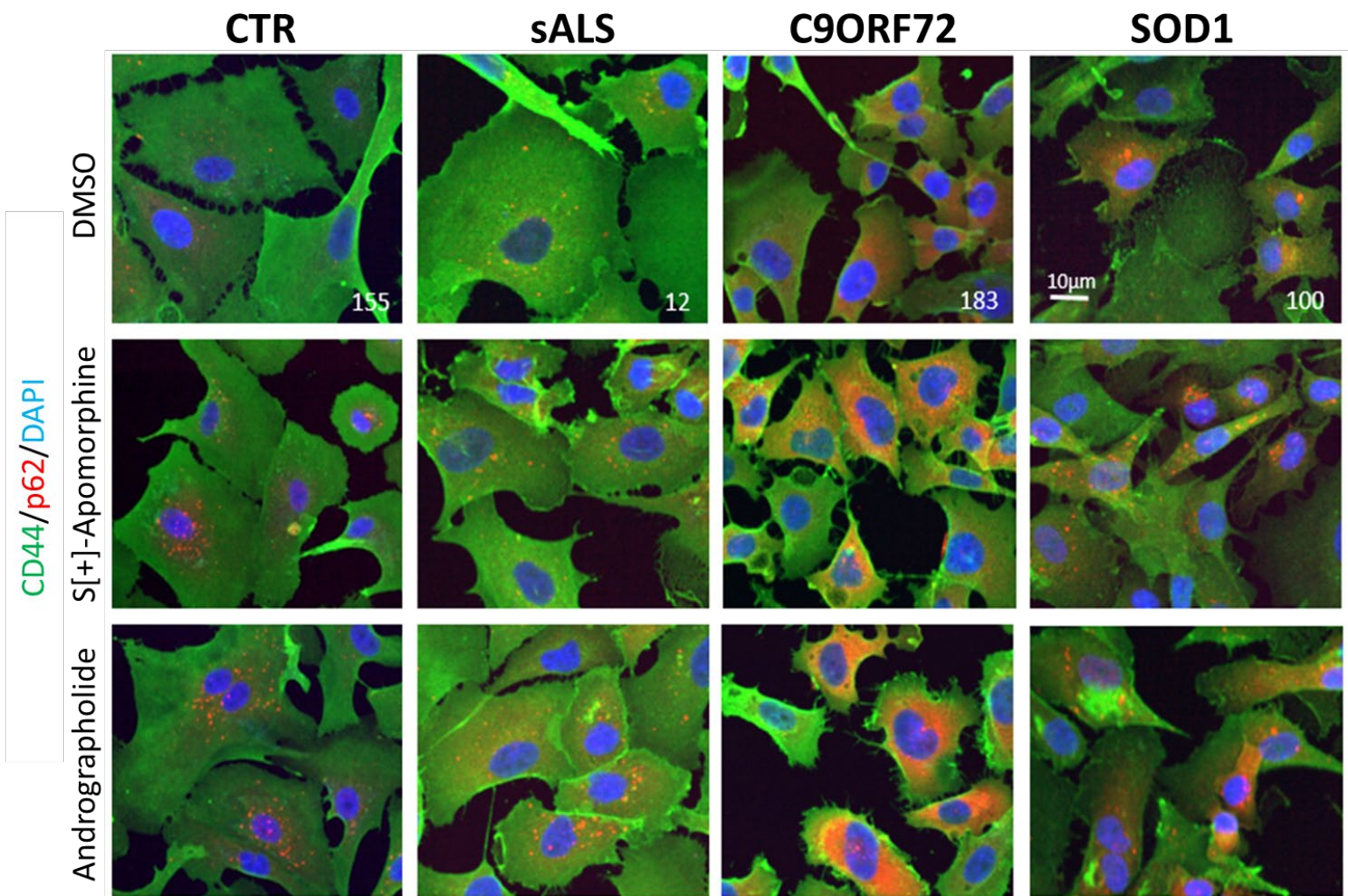


Figure 4.8 Representative images showing the expression of p62 (568) and cytoplasmic marker CD44 (488), nuclei in Hoechst, in control and patient cells before and after treatment with Nrf2 activator compounds S[+]-apomorphine and andrographolide. Scale bar 10µm.

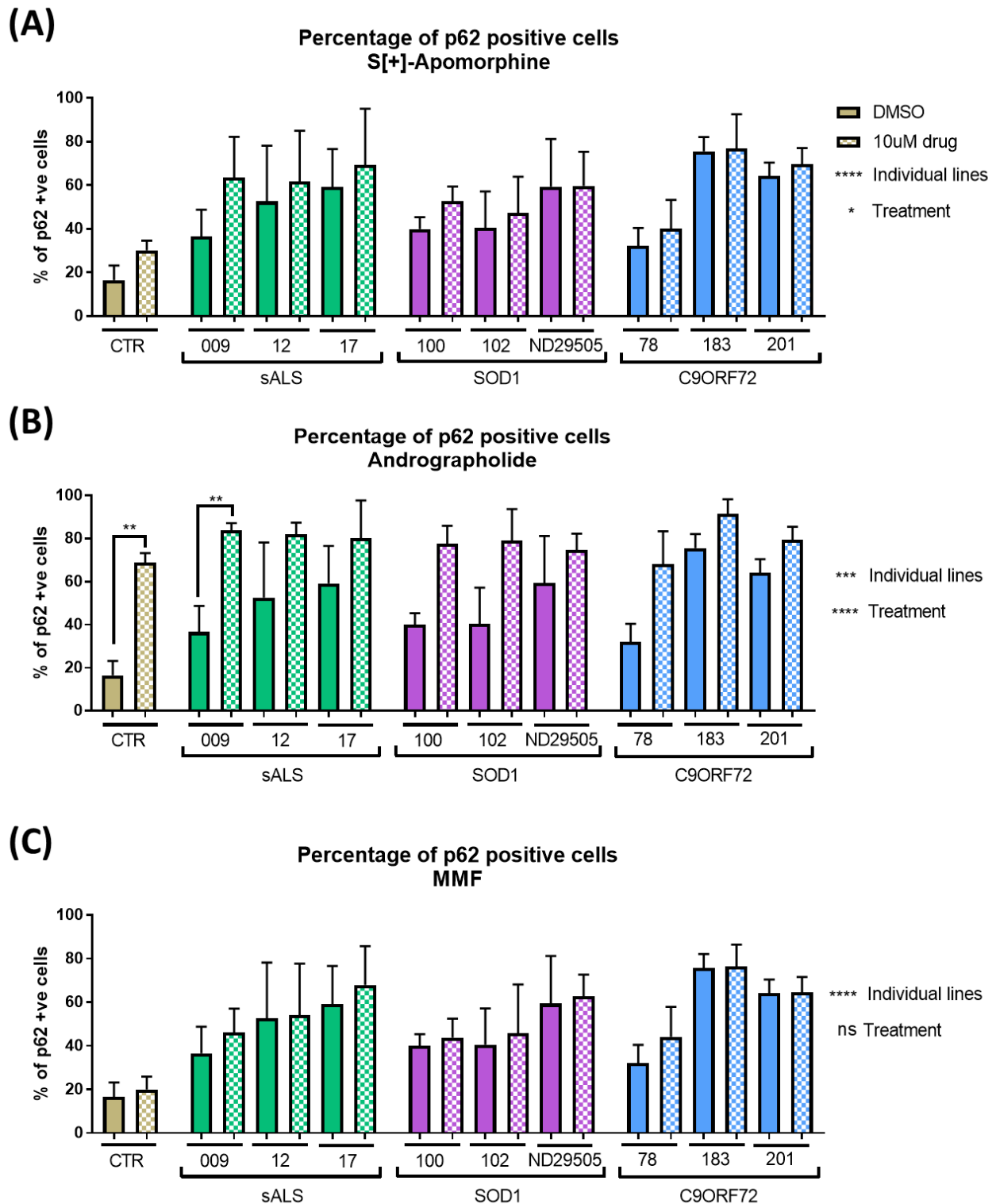


Figure 4.9 Quantification of p62 expression in control and patient iAstrocytes before and after drug treatment. The percentage of p62 positive cells after treatment with (A). S[+]-apomorphine (mean \pm SD, two-way ANOVA, MC, $n=3$, technical repeats = 2, Row Factor $p<0.05$, Column Factor $p<0.0001$), (B). Andrographolide (mean \pm SD, two-way ANOVA, MC, $n=3$, technical repeats = 2, Row Factor $p<0.0001$, Column Factor $p<0.001$), and (C). MMF (mean \pm SD, two-way ANOVA, MC, $n=3$, technical repeats = 2, Row Factor $p=0.1945$, Column Factor $p<0.0001$), individual significance is displayed on the graph. The control bar consists of 3050 & 155 pooled together.

This increase in p62 expression after treatment with S[+]-apomorphine and andrographolide could be explained by the activation of the autophagy pathway. Therefore, I decided to investigate the effect of these two compounds on the protein expression of autophagic markers LC3-I/LC3-II. Since autophagy deficits are commonly reported in C9ORF72-ALS, I decided to focus on this genetic subgroup of cell lines.

Similar to the p62 staining results, western blotting confirmed higher levels of p62 protein in C9ORF72 iAstrocyte lines compared to the control (Figure 4.10A) and this protein level was increased further after treatment with S[+]-apomorphine and andrographolide (Figure 4.10B-C). The LC3 protein is responsible for the formation of autophagosomes, vesicles that carry unwanted proteins sent for degradation. It exists in two forms, LC3-I which is located within the cytoplasm and LC3-II which is bound to the membrane of autophagosomes (Giménez-Xavier *et al.*, 2008). The conversion of LC3-I to LC3-II is indicative of the initiation of autophagosome formation and therefore is a useful biomarker to detect autophagy. As previously reported by Webster *et al.* (2016), C9ORF72 iAstrocytes presented increased levels of LC3-I protein compared to the control cell lines (Figure 4.10D); this is a known mechanism that has been linked to C9ORF72 haploinsufficiency, resulting in an initial activation of autophagy, which is then affected by the defective interaction of the protein encoded by C9ORF72 with Rab1 and the ULK1 complex (Webster *et al.*, 2016), thus preventing the formation of autophagosomes and allowing the accumulation of LC3-I in the cytoplasm. However, treatment with S[+]-apomorphine or andrographolide had no effect on the levels of LC3-I or LC3-II in control and C9ORF72 iAstrocytes (Figures 4.10E-F).

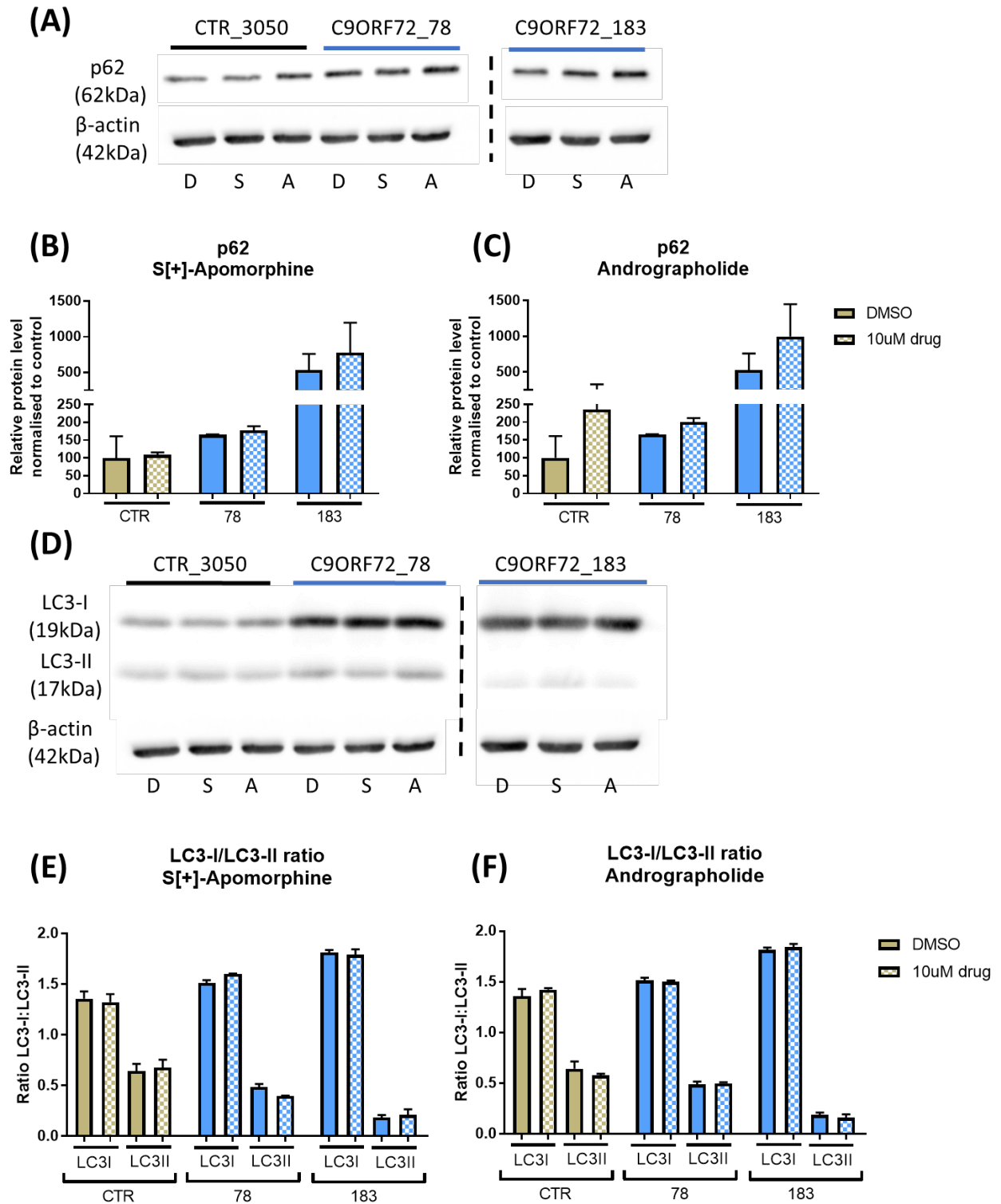


Figure 4.10 Quantification of autophagy markers p62 and LC3-I/LC3-II protein expression in control and C9ORF72 patient iAstrocytes before and after drug treatment. (A). Western blot of p62 expression in control and C9ORF72 iAstrocytes and quantification of p62 protein expression (mean \pm SD, $n=2$) after treatment with (B). S[+]-apomorphine, and (C). Andrographolide. (D). Western blot of LC3-I/LC3-II protein expression in control and C9ORF72 iAstrocytes and quantification of the ratio between LC3-I/LC3-II protein expression (mean \pm SD, $n=2$) after treatment with (E). S[+]-apomorphine, and (F). Andrographolide. The control bars consist of 3050 & 155 pooled together. Abbreviations: D = DMSO, S = S[+]-apomorphine, A = andrographolide.

4.2.6. Mitochondrial dynamics

In Chapter 3.2.3., mitochondria were labelled and visualised with a fluorescent TMRM dye to investigate mitochondrial morphology in the patient iAstrocytes. Patient iAstrocytes demonstrated differences in mitochondrial dynamics in comparison to control lines; there was extensive mitochondrial fragmentation observed in SOD1 ND29505 and all patients lines had a significantly higher percentage of perinuclear mitochondria compared to the control. Next, I investigated if the addition of antioxidant compounds or riluzole would influence changes in the mitochondrial dynamics of the cell.

Mitochondrial staining images showed that there was an intense fusion of the mitochondrial network after treatment with andrographolide; the mitochondrial network of sALS 17 after treatment with the compound appears to form thin, hairlike structures around the network (Figure 4.11). When the staining images were quantified, there was a significant decrease in the mitochondrial form factor with andrographolide treatment, implying that the mitochondrial network had become more fused together and there was less mitochondrial branching (Figure 4.12A; two-way ANOVA, multiple comparisons, $n=3$, $p<0.0001$). This network fusion was reflected by the significant increase in mitochondrial area after andrographolide treatment (Figure 4.12B; two-way ANOVA, multiple comparisons, $n=3$, $p<0.001$). However, there was no significant difference in the percentage of perinuclear mitochondria after treatment with andrographolide (Figure 4.12C), indicating that treatment does not have an effect on the localisation of the mitochondria within the network.

Mitochondrial branching was also influenced by the other antioxidant compounds as well as riluzole; there was a reduction in mitochondrial form factor of varying significance with all compounds tested (Figure 4.13, two-way ANOVA, multiple comparisons, $n=3$, A: S[+]-apomorphine $p<0.001$, B: MMF $p<0.05$ and C: riluzole $p<0.01$). However, there was no significant difference in mitochondrial area with S[+]-apomorphine, MMF or riluzole treatment (Supplementary 4.8A-C). Consistently, S[+]-apomorphine, MMF and riluzole treatment also had no effect on the percentage of perinuclear mitochondria (Supplementary 4.9A-C).

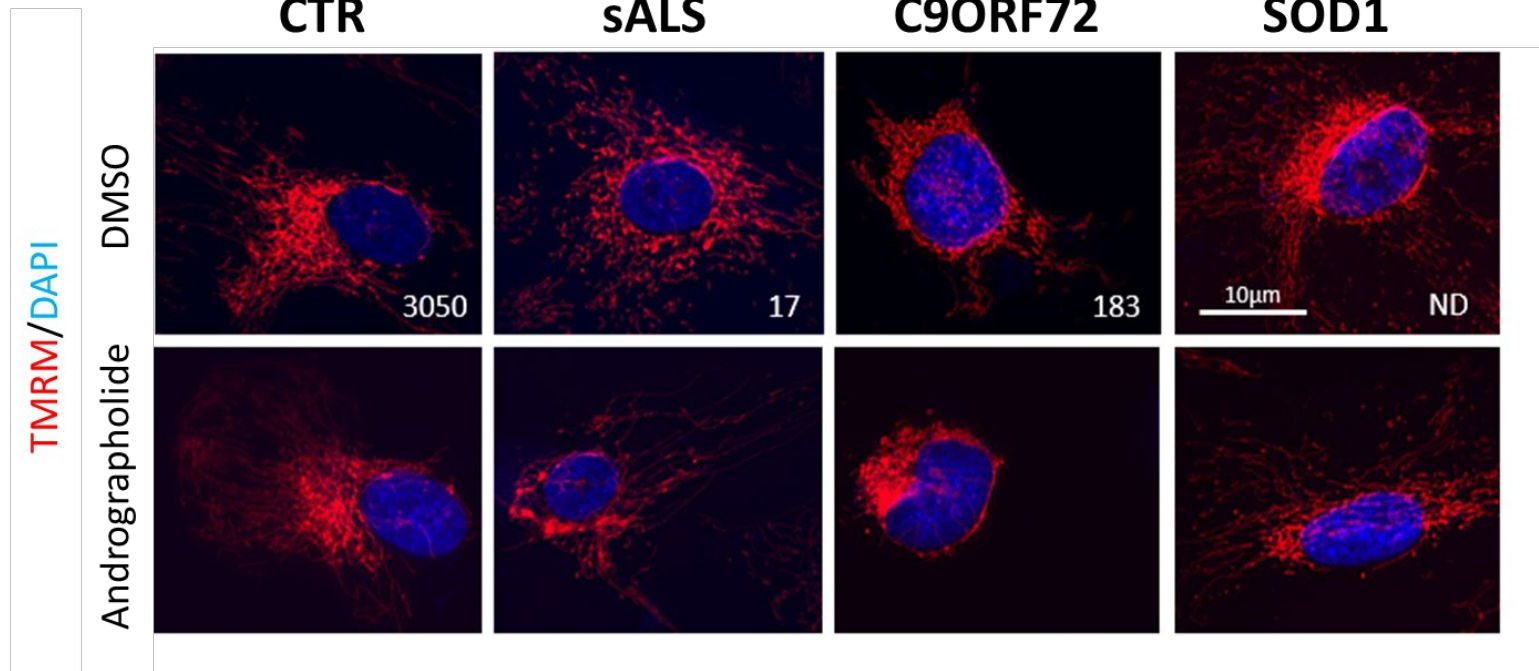


Figure 4.11 Visualisation of mitochondria (TMRM) and nuclei (Hoechst) in control and patient *i*Astrocytes before and after treatment with andrographolide. Scale bar 10µm.

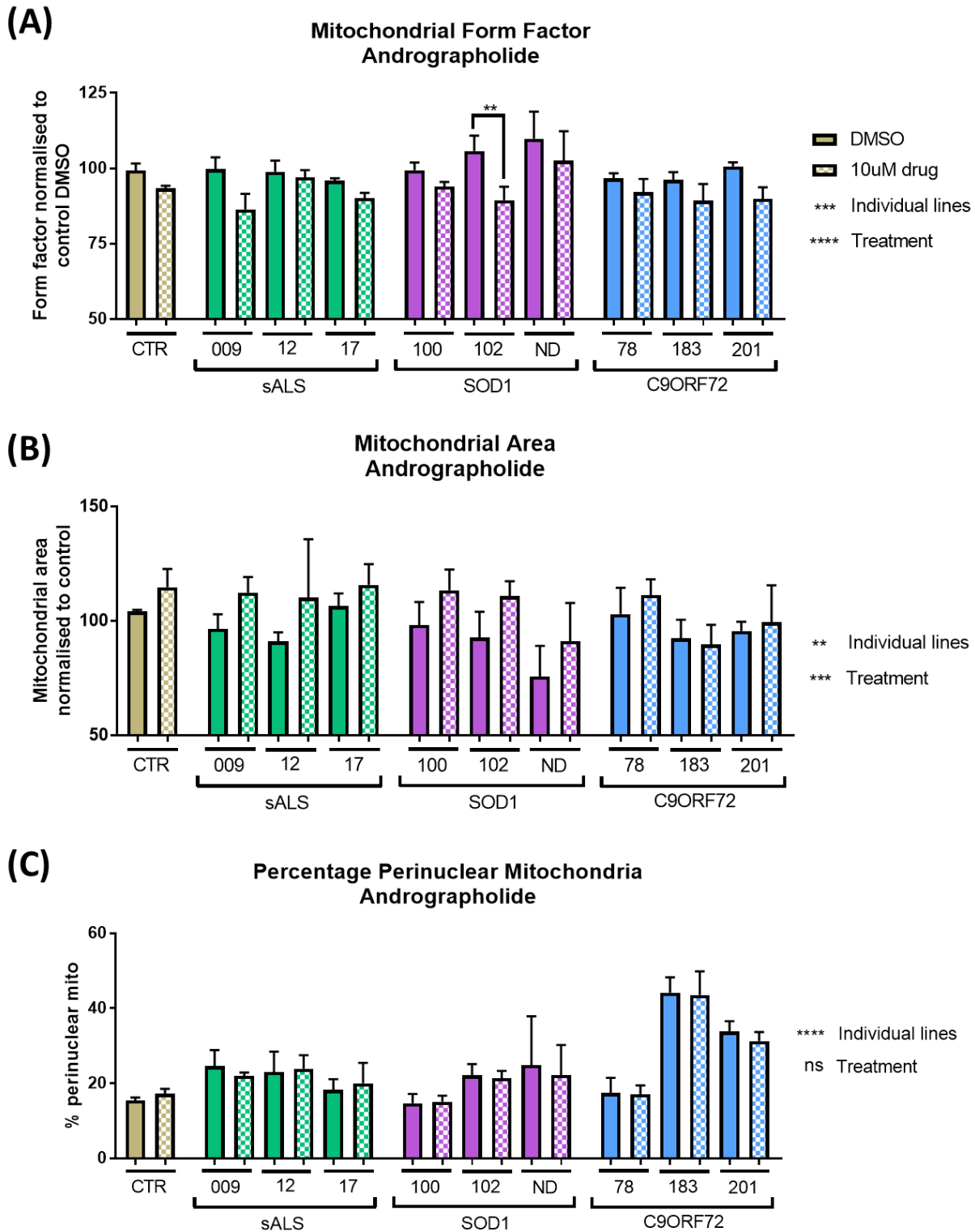


Figure 4.12 Quantification of mitochondrial dynamics in control and patient *iAstrocytes* before and after andrographolide treatment. (A). Mitochondrial form factor (mean \pm SD, two-way ANOVA, MC, $n=3$, technical repeats = 3, Row Factor $p<0.0001$, Column Factor $p<0.001$), individual significance is displayed on the graph. (B). Mitochondrial area (mean \pm SD, two-way ANOVA, MC, $n=3$, technical repeats = 3, Row Factor $p<0.001$, Column Factor $p<0.01$). (C). The percentage of perinuclear mitochondria (mean \pm SD, two-way ANOVA, MC, $n=3$, technical repeats = 3, Row Factor $p=0.7070$, Column Factor $p<0.0001$). The control bar consists of 3050, 155 & 209 pooled together.

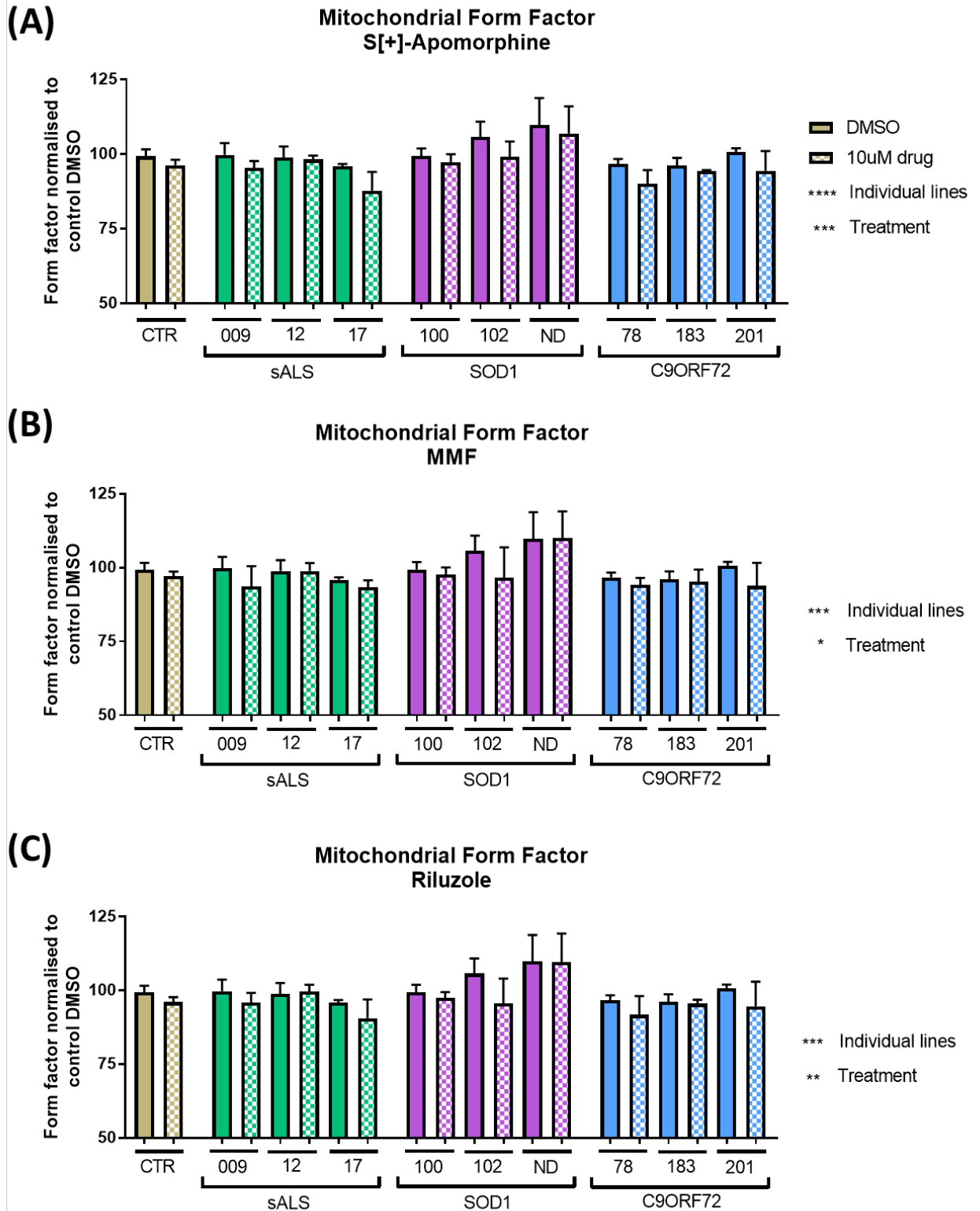


Figure 4.13 Quantification of mitochondrial form factor in control and patient iAstrocytes before and after treatment with. (A). S[+]-apomorphine (mean \pm SD, two-way ANOVA, MC, $n=3$, technical repeats = 3, Row Factor $p<0.001$, Column Factor $p<0.0001$), (B). MMF (mean \pm SD, two-way ANOVA, MC, $n=3$, technical repeats = 3, Row Factor $p<0.05$, Column Factor $p<0.001$), and (C). Riluzole (mean \pm SD, two-way ANOVA, MC, $n=3$, technical repeats = 3, Row Factor $p<0.01$, Column Factor $p<0.001$). The control bar consists of 3050, 155 & 209 pooled together.

4.2.7. Glutamate buffering

4.2.7.1. Extracellular glutamate assay

The current treatment for ALS, riluzole, provides MN benefit through the inhibition of neuronal glutamate release by inactivation of sodium-dependent channels on nerve terminals, preventing neuronal excitotoxicity (Doble, 1996). The next step was to investigate if riluzole treatment reduced the levels of extracellular glutamate in patient iAstrocyte monoculture as well as MN-iAstrocyte co-culture.

When control iAstrocytes were treated with riluzole, there was no change in extracellular glutamate concentration in either iAstrocyte monoculture or MN-iAstrocyte co-culture (Figure 4.14A). The C9ORF72 patient lines displayed the highest glutamate accumulation in the media at baseline but there was no significant change in extracellular glutamate levels in either iAstrocyte monoculture or MN-iAstrocyte co-culture after riluzole treatment (Figure 4.14B-D). There was also no significant change in extracellular glutamate in the media collected from sALS and SOD1 iAstrocytes in monoculture or in co-culture with MNs after riluzole treatment (Supplementary 4.10A-F).

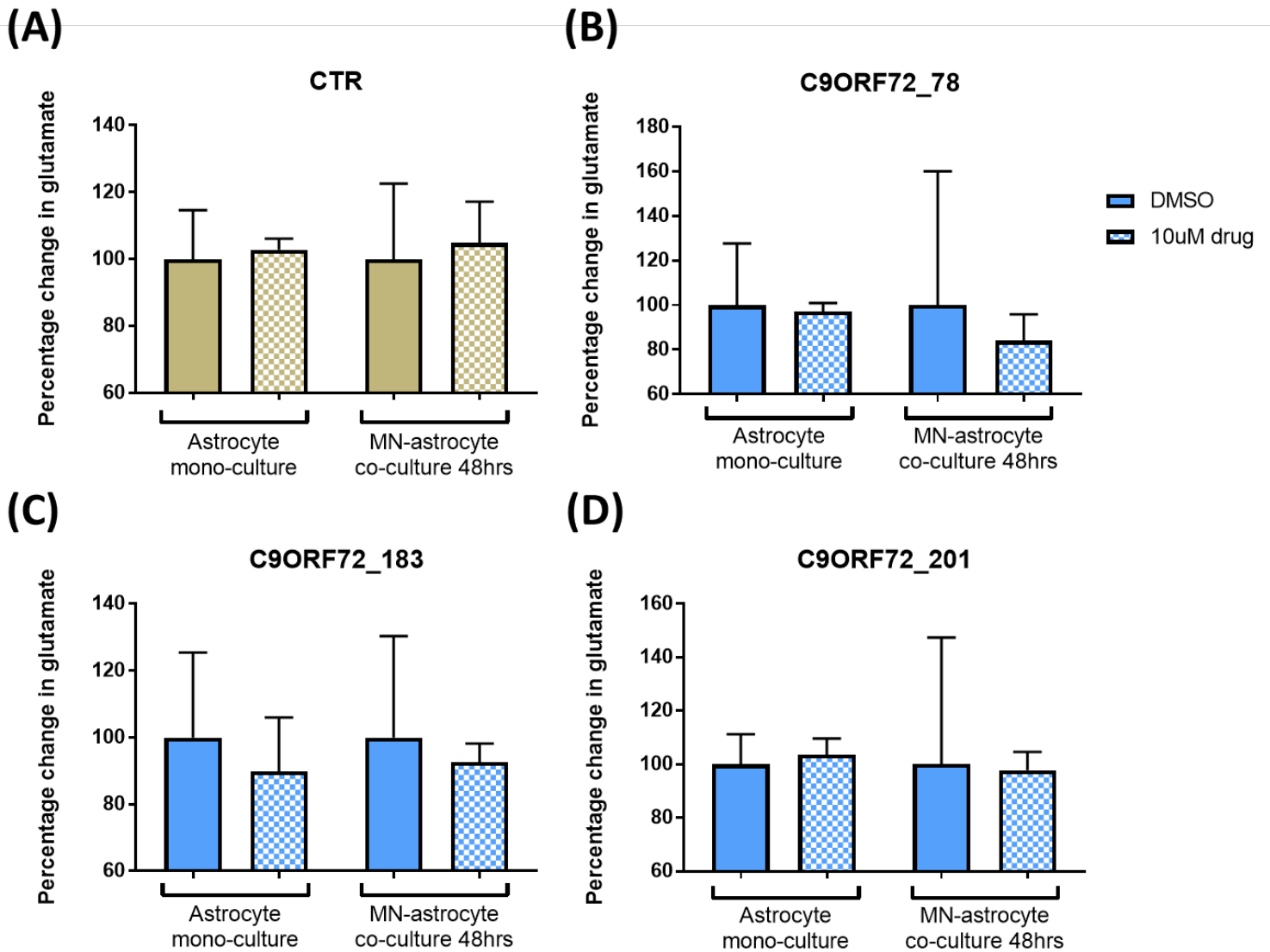


Figure 4.14 Quantification of extracellular glutamate in iAstrocyte-conditioned media before and after riluzole treatment. The percentage change in glutamate in (A). CTR (mean \pm SD, paired *t*-test, $n=3$, technical repeats = 2, mono-culture $p=0.7640$, co-culture $p=0.7630$), (B). C9ORF72 78 (mean \pm SD, paired *t*-test, $n=3$, technical repeats = 2, mono-culture $p=0.8769$, co-culture $p=0.7312$), (C). C9ORF72 183 (mean \pm SD, paired *t*-test, $n=3$, technical repeats = 2, mono-culture $p=0.3268$, co-culture $p=0.6540$), and (D). C9ORF72 201 (mean \pm SD, paired *t*-test, $n=3$, technical repeats = 2, mono-culture $p=0.7321$, co-culture $p=0.9413$). The control bar consists of 3050 & 155 pooled together.

4.2.7.2. Glutamate transporters and receptors

In the previous chapter (3.2.4.2), I identified a significant increase in the expression of the EAAT2 90kDa protein in C9ORF72 183, which also had a significant increase in extracellular glutamate levels at iAstrocyte monoculture. Therefore, I decided to investigate if the antioxidant compound andrographolide, which led to the highest improvement in MN survival when added in the C9ORF72 co-cultures, or riluzole treatment, would be able to reduce the expression of this protein.

There was a significant reduction of the 90kDa EAAT2 protein in C9ORF72 183 after treatment with andrographolide (Figure 4.15A; two-way ANOVA, multiple comparisons, $n=3$, $p<0.001$), while riluzole treatment had no significant effect on protein levels in the control and C9ORF72 iAstrocytes (Figure 4.15B). There was no significant change in the expression of EAAT2 70kDa or EAAT2 62kDa protein with either andrographolide or riluzole treatment (Supplementary 4.11A-D).

In the previous chapter (3.2.4.2), I showed that the C9ORF72 iAstrocytes displayed a significant increase in the ionotropic receptor NMDAR2B protein. Therefore, I wanted to investigate if andrographolide or riluzole treatment would reduce the protein expression in these cell lines.

All C9ORF72 iAstrocytes showed a significant decrease in NMDAR2B protein expression after andrographolide treatment (Figure 4.15C; two-way ANOVA, multiple comparisons, $n=3$, $p<0.05$), while this reduction was not seen in the control iAstrocytes. However, the opposite was seen when the C9ORF72 iAstrocytes were treated with riluzole; there was a significant increase in NMDAR2B protein expression in all C9ORF72 iAstrocytes as well as control cell lines after riluzole treatment (Figure 4.15D; two-way ANOVA, multiple comparisons, $n=3$, $p<0.01$).

However, even with the reduction of EAAT2 90kDa and NMDAR2B protein, andrographolide treatment had no significant effect on extracellular glutamate levels in C9ORF72 iAstrocyte monoculture or iAstrocyte-MN co-culture (Supplementary 4.12).

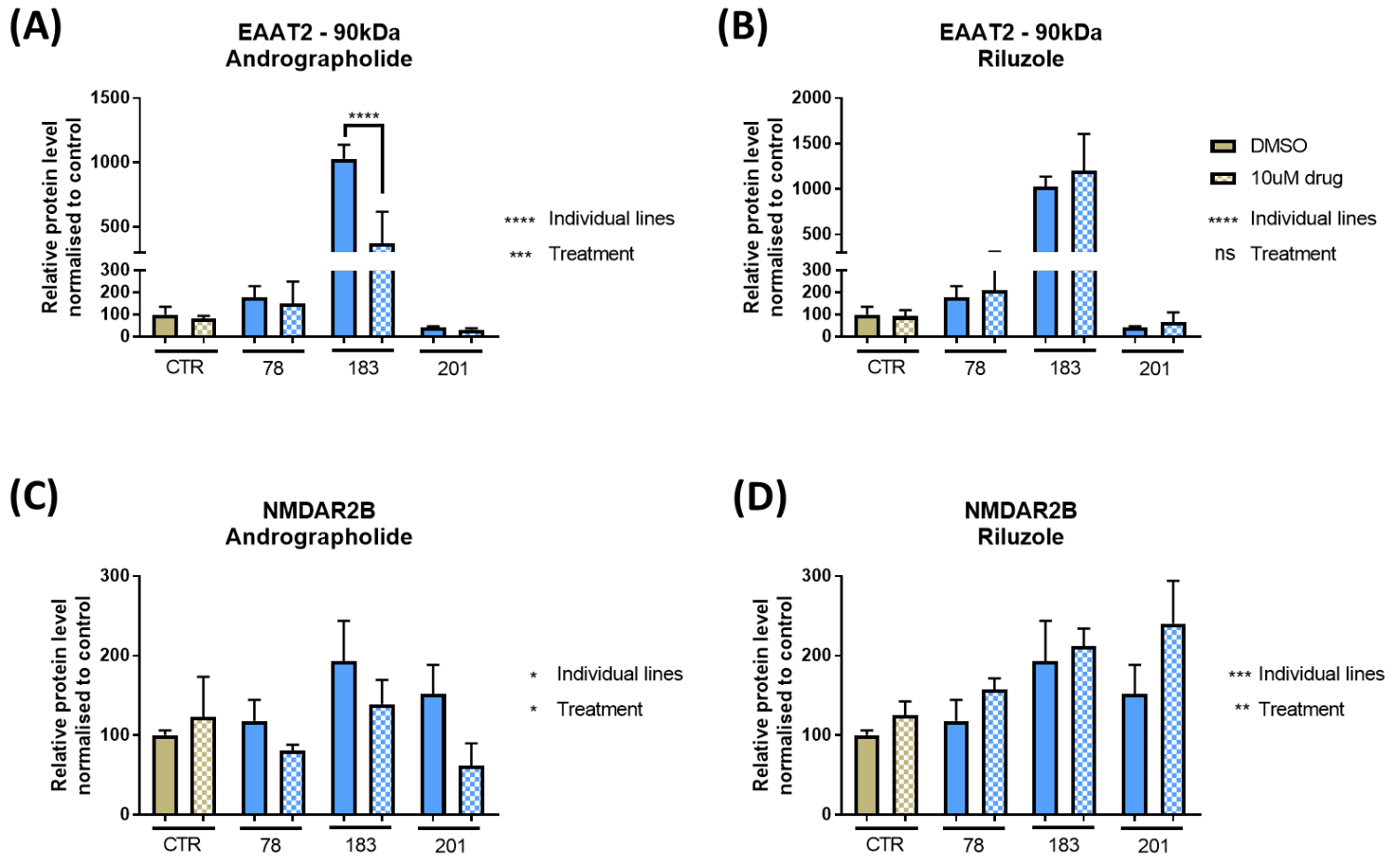


Figure 4.15 Quantification of EAAT2 and NMDAR2B protein levels in control and C9ORF72 iAstrocytes before and after drug treatment. 90kDa EAAT2 protein levels after treatment with (A). Andrographolide (mean \pm SD, two-way ANOVA, MC, $n=3$, Row Factor $p<0.001$, Column Factor $p<0.0001$), and (B). Riluzole (mean \pm SD, two-way ANOVA, MC, $n=3$, Row Factor $p=0.3856$, Column Factor $p<0.0001$), individual significance is displayed on the graph. NMDAR2B protein levels after treatment with (C). Andrographolide (mean \pm SD, two-way ANOVA, MC, $n=3$, Row Factor $p<0.05$, Column Factor $p<0.05$) and (D). Riluzole (mean \pm SD, two-way ANOVA, MC, $n=3$, Row Factor $p<0.01$, Column Factor $p<0.001$). The control bar consists of 3050, 155 & AG pooled together.

4.3. Discussion

The Nrf2 pathway is a master regulator of cellular survival, activating a multitude of downstream target genes involved in the defence against oxidative stress, making it an attractive therapeutic target for neurodegenerative disease. A previous study showed that Nrf2-overexpressing astrocytes delayed disease onset and extended survival in a *SOD1* mouse model through the secretion of glutathione which protected neurons against oxidative stress (Vargas *et al.* 2008). These data, in combination with the reported downregulation of Nrf2 in patient tissue (Sarlette *et al.*, 2008), imply that Nrf2 activators could protect against MN degeneration in ALS.

In the iAstrocyte-MN co-culture compound screen, andrographolide provided the highest MN survival in C9ORF72 iAstrocyte co-cultures, while S[+]-apomorphine provided the most beneficial effects in *SOD1* iAstrocytes, implying that these two Nrf2 activators have different mechanisms of action. After the characterisation of the patient iAstrocytes in the previous chapter, I decided to investigate the effect of these compounds using the same phenotypic assays to highlight the mechanism of action of each drug.

4.3.1. Protein aggregation

S[+]-Apomorphine promoted the highest MN rescue in astrocytes derived from *SOD1* patients so the next step was to investigate whether this drug influenced misSOD1 proteins. Indeed, S[+]-apomorphine was the only drug of the 4 tested that resulted in the reduction of misSOD1 in the *SOD1* patient iAstrocytes as well as some sporadic and C9ORF72 lines; these results match the iAstrocyte-MN co-culture data from the previous study. There was no difference in *SOD1* 102, which could be because this patient had the *SOD1* mutation but was asymptomatic at the time of sample collection and therefore, had the lowest amount of misSOD1 aggregates. There was also no reduction of misSOD1 in the control iAstrocytes implying that S[+]-apomorphine treatment has a disease-specific effect. This could be due to the low levels of misSOD1 detected in controls, but another explanation could be related to the fact that S[+]-apomorphine is known to be activated by the presence of oxidative stress. Published data (Birger *et al.*, 2019) indicated that astrocytes derived from patients display high levels of oxidative stress, which would activate S[+]-apomorphine.

Because of the effect on protein misfolding, we hypothesised that S[+]-apomorphine might have reduced misSOD1 through activation of molecular protein chaperones. At baseline, sALS 17 and *SOD1* ND29505 had lower levels of HSP70 than the controls and other patient lines, potentially explaining the larger number of misSOD1 protein aggregates within these cell lines (3.2.2.2). S[+]-Apomorphine treatment, however, had no significant effect on HSP70 or HSF1 protein expression in

sALS and SOD1 iAstrocytes, potentially suggesting that HSP70 was not involved in the misSOD1 decrease observed upon S[+]-apomorphine treatment. More experiments, testing different treatment time points, would be necessary to draw a firm conclusion. In contrast, andrographolide treatment led to a significant increase in HSP70 in sALS and SOD1 iAstrocytes, which could aid with protein misfolding; however, we did not detect a significant decrease in misSOD1 aggregates after andrographolide treatment. On the other hand, andrographolide significantly increased total SOD1 protein expression, probably due to its antioxidant properties. One could speculate that the upregulation of total SOD1 might feed into the accumulation of misSOD1, thus counteracting the positive upregulation of the chaperones.

The copper chaperone for SOD1 (CCS) recognises newly translated SOD1 protein and activates the enzyme by inserting the copper ion and catalysing the oxidation of the SOD1 intra-subunit disulphide bond (Brown *et al.*, 2004). A previous study found that mutant forms of SOD1 are not stabilised from this posttranslational modification by CCS, leading to protein misfolding and the formation of toxic aggregates (Winkler *et al.*, 2009). More recently, the SOD-like domain of the CCS has been reported to act as a molecular chaperone towards immature SOD1 protein and even helped to stabilise the folded state of SOD1 mutant proteins (Luchinat *et al.* 2017), so it is possible that S[+]-apomorphine could act via this molecular chaperone instead, given that the biggest reduction in misSOD1 was in the SOD1 mutant iAstrocytes.

The reduction of HSF1 and HSP70 expression has previously been reported in TDP-43 transgenic mice. This study also found reduced levels of HSP70 in sALS patient tissue but no difference in the level of HSF1 (Chen *et al.* 2016). Other studies have reported that HSF1 levels are not always correlated with the level of activity because post-translational modifications are required to activate the protein (Calderwood *et al.*, 2010), potentially explaining the mild HSF1 expression change noted after drug treatment.

While there is little in the literature about HSP70 and misSOD1, there are previous reports of the interaction between HSP70 and TDP-43. Lin *et al.* (2016) demonstrated that overexpression of HSF1 *in vitro* prevented the accumulation of TDP-43 protein aggregates, as well as preventing the phase transition of TDP-43 from a soluble to an insoluble state, through the increased production of HSP70 and HSP90. Interestingly, andrographolide treatment significantly increased HSP70 expression in control and patient iAstrocytes, however there was no significant reduction in insoluble TDP-43/TDP-35 with andrographolide treatment. Multiple HSPs have been reported to regulate TDP-43 homeostasis; HSP90 and the co-chaperone Cdc37 are important for TDP-43 turnover (Jinwal *et al.*, 2012), while HSP70 requires co-chaperone HSP40 to interact with the C-terminal domain, preventing

TDP-43 aggregation (Udan-Johns *et al.*, 2014). Therefore, in this model, the increase in HSP70 alone may not have been sufficient to reduce TDP-43 aggregation. Consistently, a recent study by Kitamura *et al.* (2018) similarly reported the inability to prevent the formation of TDP-25 inclusion bodies by HSP70 overexpression, also suggesting that other chaperones may be required to prevent TDP-25 aggregation.

4.3.2. Autophagy and p62

In the previous chapter, patient iAstrocyte lines had significantly higher levels of p62 than control cell lines. Treatment with andrographolide showed the largest upregulation of p62 in both patient and control iAstrocytes, while S[+]-apomorphine treatment also upregulated p62 expression across cell lines but to a lower extent than andrographolide. MMF and riluzole treatment showed no significant effect on any of the control and patient lines.

It has indeed also been shown that p62 can positively regulate Nrf2 accumulation within the nucleus through its interaction with KEAP1. A combination of protein crystallography and biochemistry analysis revealed that p62 competitively binds to the carboxyl-terminal domain in KEAP1 that is reserved for Nrf2 (Komatsu *et al.*, 2010), therefore it is possible that the protective antioxidant effect of andrographolide on the iAstrocytes is achieved through an increase in p62, causing Nrf2 to be released from KEAP1 and consequent Nrf2 activation. This, in contrast, can increase the expression of p62 by direct binding to the ARE upstream of p62, thus creating a positive feedback loop between Nrf2 and p62 (Jain *et al.*, 2010).

The study by Georgakopoulos *et al.* (2017) investigated the application of a novel chemical tool called PMI, an inhibitor of the protein-protein interaction between Nrf2 and KEAP1, which led to the upregulation of p62 and mitochondrial turnover. They investigated this compound alongside sulphoraphane and DMF, both covalent KEAP1 modifiers, which were unable to increase p62 or mitophagy. This is consistent with the lack of increase in p62 expression in the MMF treatment, and confirms that S[+]-apomorphine and andrographolide lead to Nrf2 activation through a different mechanism compared to MMF.

Andrographolide treatment was the most effective in improving MN survival in C9ORF72 iAstrocyte-MN co-cultures. There are strong associations between the C9ORF72 pathology and p62. The GGGGCC repeat RNA from C9ORF72-ALS is hypothesised to promote toxicity through the sequestration of proteins responsible for RNA processing, resulting in widespread RNA dysregulation and neuronal death (Conlon *et al.*, 2016). In a zebrafish model of C9ORF72-ALS, overexpression of p62 almost completely prevented repeat RNA toxicity, however it had no effect on the toxicity from

arginine-containing DPRs (Swinnen *et al.*, 2018). The authors suggested that this may relate to the activation of autophagy since it has been hypothesised that reduced autophagy by loss of C9orf72 function exacerbates RNA toxicity (Webster *et al.*, 2016). However, previous studies have reported that overexpression of p62 or autophagy activation in SOD1-ALS mouse models is detrimental to MN health by promoting the accumulation of SOD1 into insoluble aggregates as well as the excessive removal of mitochondria (Mitsui *et al.*, 2018; Perera *et al.*, 2018). This is in agreement with our data, since andrographolide treatment showed a nearly complete rescue in MN survival in C9ORF72 co-cultures, but little beneficial effect in SOD1 co-cultures. If andrographolide was confirmed to be an autophagy activator, this would explain the improvement in one genetic subgroup compared to another.

The increase in p62 protein could be indicative of the activation of the autophagy pathway. The study by Gu *et al.* (2018) showed that andrographolide treatment increased p62 and LC3A/B-II protein levels in a cell model of AD, suggesting that andrographolide promotes autophagy for the protection against A β cellular damage. However, while p62 expression was increased in the patient iAstrocytes with andrographolide treatment, the compound had no effect on the levels of LC3-I or LC3-II, therefore we cannot say with certainty that autophagy was activated. Since autophagy is a dynamic assay, further experiments using pathway activators and inhibitors would have to be performed to confirm the effect of andrographolide on this pathway.

Immunocytochemistry of patient iAstrocytes showed that this accumulation of p62 was predominantly seen in the perinuclear region of the cell and the number of perinuclear p62 spots was significantly increased with S[+]-apomorphine and andrographolide treatment. This localisation of p62 expression implies a connection with the mitochondrial network (Geisler *et al.*, 2010). Andrographolide has previously been described to trigger mitophagy in a chemically induced mouse model of colon carcinogenesis through the inhibition of the PIK3CA-AKT1-MTOR-RPS6KB1 pathway; this was beneficial to the mice since the selective clearance of the damaged mitochondria negatively regulated the activation of the NLRP3 inflammasome (Guo *et al.*, 2014). Further investigation into the co-localisation of p62 and the mitochondria is required to establish whether this increase in p62 protein is associated with the activation of mitophagy by andrographolide treatment.

4.3.3. Mitochondrial dynamics

As discussed in the previous chapter, dynamic changes in mitochondrial morphology have detrimental effects on mitochondrial function. Therefore, the next aim was to determine the effects of these antioxidant drugs on mitochondrial morphology.

The greatest change in mitochondrial dynamics was seen in the andrographolide treatment cohort; there were reductions in mitochondrial form factor witnessed across control and patient lines. There was also an increase in mitochondrial area in control, sALS and SOD1 lines in line with network fusion. As an indication that these drugs have different modes of action, S[+]-apomorphine, MMF and riluzole also displayed a significant reduction in mitochondrial form factor but had no effect on other mitochondrial parameters.

Indeed, the fusion of the mitochondrial network is protective against apoptotic signals, reduces production of ROS and promotes ATP production (Gao *et al.*, 2017), thus explaining the potential protective effect observed in patient iAstrocytes treated with andrographolide and, to some extent, S[+]-apomorphine. Sabouny *et al.* (2017) demonstrated that Nrf2 overexpression results in mitochondrial hyperfusion through loss of Drp1. Mitochondrial hyperfusion and loss of Drp1 was also observed in fibroblasts and rats treated with Nrf2 activators sulphoraphane and DMF (Sabouny *et al.*, 2017). It has been suggested that Nrf2 activation can lead to upregulation in proteasomal activity (Kwak *et al.* 2003; Pickering *et al.* 2012), which in turn, decreases the stability of the Drp1 protein through proteasomal degradation. A more recent study showed that andrographolide treatment in a chemically induced PD cell model inhibited Drp1 translocation to the mitochondria as well as the GTPase activity of Drp1 through direct binding with the protein, preventing Drp1-mediated mitochondrial fission (Geng *et al.*, 2019). This is in line with the mitochondrial fusion observed in patient iAstrocytes treated with andrographolide. To confirm this interesting hypothesis, it would be worth investigating the levels and phosphorylation of Drp1 in patient iAstrocytes after treatment with andrographolide.

4.3.4. Glutamate transport

In the previous chapter, we identified that the C9ORF72 iAstrocyte lines had an impairment in glutamate buffering both in monoculture and MN co-culture. Oxidative stress significantly affects the metabolism of glutamate by astrocytes. Oxidative stress conditions, in fact, have been shown to reduce the activity of glutamate transporters *in vitro* through the oxidation of reactive cysteine residues within the transporter structure (Miralles *et al.*, 2001). Our assay to determine the ability of iAstrocytes to uptake extracellular glutamate, however, did not show any improvement in glutamate levels upon antioxidant drug treatment, thus indicating that neither andrographolide nor S[+]-apomorphine had an effect on glutamate dynamics in iAstrocytes.

Andrographolide, however, significantly decreased the expression of the ionotropic receptor subunit NMDAR2B; this could lead to improved regulation of calcium influx into the cell, thus restoring

intracellular calcium homeostasis. In theory, this would reduce the release of glutamate from glutamate transporters such as EAAT2, but andrographolide treatment had no effect on extracellular glutamate levels. It would still be interesting to investigate the effect of andrographolide treatment on calcium influx in the C9ORF72 iAstrocytes since increased levels of intracellular calcium are detrimental to cellular health as well as a key process in neurological disease (Shigetomi *et al.*, 2019).

If andrographolide does not protect against neuronal excitotoxicity by preventing astrocytic release of glutamate, then we can hypothesise that it increases MN resilience to glutamate-induced excitotoxic attack. The study by Yang *et al.* (2014) demonstrated the neuroprotective effects of andrographolide against glutamate-induced apoptosis in HT22 neuronal cells by inhibition of calcium influx, intracellular ROS production and lipid peroxidation. Andrographolide treatment also suppressed mitochondrial damage by ROS through regulation of apoptotic factors Bcl-2, Bid and Bax, as well as reducing the phosphorylation of MAPK pathway effectors p38, ERK and JNK in the neuronal cell line (Yang *et al.* 2014). Other studies have reported the importance of haem-oxygenase 1 (HO-1), a downstream target of NRF2, and increased extracellular release of GSH from astrocytes in protecting neurons from glutamate excitotoxicity (Taguchi *et al.*, 2020). In our study, however, we have not assessed the effect that the compounds tested in co-culture have on MNs; these are, therefore, all interesting hypotheses that could be tested in future to discriminate what protective effects are achieved through restoring astrocyte function or protecting MNs from toxic stimuli.

Riluzole is a glutamate modulator approved for the treatment of ALS; it induces the clustering of dendritic spines by regulating synaptic glutamatergic activity and preventing glutamate accumulation in the extra-synaptic space. To do this, riluzole stabilises the inactivated state of the voltage-gated sodium channels and increases EAAT2 expression, stimulating glutamate uptake (Frizzo *et al.*, 2004; Fumagalli *et al.*, 2008). A previous study by Hunsberger *et al.* (2015) showed that riluzole reduced extra-synaptic glutamate levels and enhanced cognitive performance with increased glutamate uptake.

In this study, riluzole treatment had no significant effect on extracellular glutamate levels in both control and patient iAstrocytes with or without MNs present in culture. When investigating the cause of the high extracellular glutamate levels in the C9ORF72 iAstrocytes, there was also no significant change in EAAT2 expression after riluzole treatment. However, riluzole treatment significantly increased the expression of NMDAR2B in control and C9ORF72 iAstrocytes; this is also reflected in a study by Pereira *et al.* (2017) investigating hippocampal age-related gene expression

changes. Aged mice had reduced NMDAR2B gene expression that was reversed by riluzole treatment.

Persistent stimulation of NMDAR2B in astrocytes has been linked to neuronal survival through phospholipase C-mediated ER release of calcium, not extracellular calcium influx, and stabilisation of cyclin-dependent kinase-5 (Cdk5) cofactor. Cdk5 promotes Nrf2 activation, which increases glutathione metabolism in astrocytes, protecting neurons from oxidative damage (Jimenez-Blasco *et al.*, 2015). Riluzole has previously been described as having antioxidant properties, so we can hypothesise that increasing NMDAR2B might be a way in which riluzole treatment activates the ARE, providing MN benefit without reducing extracellular glutamate levels. However, since C9ORF72 iAstrocytes already have glutamate impairment, potentially through glutamate release due to influx of extracellular calcium, it is not surprising that riluzole treatment had no effect on MN survival in C9ORF72 iAstrocyte-MN co-cultures.

4.3.5. Conclusion

In conclusion, it appears that, although the three antioxidant compounds screened in this study all activate the master regulator Nrf2, they seem to elicit different responses downstream of this transcriptional activator, as summarised in Figure 4.16. In summary, S[+]-apomorphine treatment significantly reduced the presence of perinuclear misSOD1 aggregates across both control and patient iAstrocytes. This removal does not seem to be related to the increase of molecular protein chaperones since S[+]-apomorphine treatment had no significant effect on HSF1 or the downstream HSP70 protein. We cannot exclude, however, activation of other chaperones, including CCS, which has been associated with SOD1 folding (Luchinat *et al.* 2017). S[+]-Apomorphine treatment did significantly increase the levels of the p62 protein, highlighting the potential for the removal of misfolded protein aggregates by the autophagosome machinery.

Andrographolide treatment had a significant effect on mitochondrial dynamics, namely the fusion of the mitochondrial network, implying benefit to mitochondrial health. This antioxidant compound also significantly increased the expression of p62, particularly within this perinuclear area, indicating a potential effect on mitophagy. The final antioxidant compound MMF, as well as riluzole, did not influence significant changes in many of the pathological mechanisms examined in this chapter. Because of this, and the mild restoration of MN survival seen in the previous drug screening iAstrocyte-MN co-culture assay, I have decided not to take MMF further for RNA-sequencing where we hope to further define the mechanisms of action of these compounds (Chapter 5) and identify patient responders to a particular compound (Chapter 6).

Functional assay	Andrographolide	S[+]-Apomorphine	MMF	Riluzole
TDP-43 aggregation	0	0	N/T	N/T
SOD1 nuclear aggregates	1	1	0	0
SOD1 perinuclear agg.	1	2	0	0
p62 % positive cells	3	2	1	0
p62 perinuclear agg.	3	2	1	0
Mitochondrial form factor	3	3	2	2
Mitochondrial area	3	0	0	0
% perinuclear mito.	0	0	0	0
Glutamate co-culture	0	N/T	N/T	1
Score	14	10	4	3

Figure 4.16 Summary table of the effect of riluzole and the antioxidant compounds in each of the phenotypic assays described in this chapter. The drugs were scored on whether there was a strong effect (red = 3), moderate effect (yellow = 2), a mild effect (green = 1), or no change (white = 0) in the parameters investigated after drug treatment. Not all compounds were tested in each assay (N/T) and a total score was given for each drug at the bottom.

Chapter 5 - RNA-sequencing data determines mechanism of action of antioxidant compounds across different genetic subgroups of ALS patients.

5.1. Introduction

Genome-wide expression profiling is a widely used tool to investigate the transcriptome; changes in gene expression in ALS have previously been explored using microarray, a library to detect the expression of thousands of genes at the same time, or the sequencing of mRNA (Cooper-Knock *et al.* 2012; Heath *et al.* 2013). While transcriptome analysis gives a good indication of differential gene expression (DGE), the significance of the data is limited since mRNA levels do not necessarily correlate with the level of protein translated (King and Gerber 2016). This variation can be attributed to protein degradation, oxidative stress, or the control of protein synthesis (Schwanhäusser *et al.* 2011; Vogel *et al.* 2011). Therefore, the profiling of the translatome, which involves the sequencing of the mRNAs recruited to the ribosomes for protein synthesis, should be more reflective of protein expression changes and the directionality of disease processes in ALS iAstrocytes (King and Gerber 2016).

There are three main methodologies of translatome profiling: polysomal profiling, ribosomal profiling and most recently, ribosome affinity purification techniques. Early methods to study the global translatome were carried out by comparing the ribosome-bound mRNA to the total mRNA present within the sample (King and Gerber 2016). Polysomal profiling is a classical technique of mRNA extraction that involves the separation of mRNAs depending on the number of bound ribosomes (polysomes) using a sucrose gradient (Arava *et al.*, 2003). While polysome profiling was considered as the 'gold standard' for a number of years, the use of a sucrose gradient required specialised and expensive equipment as well as additional precipitation steps due to the heparin, a potent RNase inhibitor, present in the sucrose solution (King and Gerber 2016). Polysome fractions may also be contaminated with other high molecular weight complexes such as lipid rafts or pseudo-polysomes (Thermann and Hentze, 2007).

Ribosomal profiling is based on the sequencing of ribosome-protected fragments (RPFs) after RNase I treatment of the cell lysate. This methodology works on the basis that the average ribosome density per mRNA correlates with the level of protein synthesis (Ingolia *et al.*, 2012). For translatome analysis, mRNA extraction and sequencing are performed in parallel to normalise RPFs to the total mRNA (King and Gerber 2016). This method has its own challenges, including a sucrose gradient like polysome profiling, a labour intensive method and potential contamination with pseudoRPFs from

the structured double-stranded region of RNA, since RNase I only degrades single-stranded RNA, leading to misinterpretation of the data (King and Gerber 2016).

Ribosome affinity purification has become a popular tool to monitor gene expression in specific cell types such as neurons, due to the difficulty in the isolation of these cells without contamination from the surrounding cells or tissue (Heiman *et al.*, 2014). This method involves the construction of genetically modified cells/organisms which express affinity-tagged ribosomal subunits that can be controlled by a tissue-specific promoter (Sanz *et al.*, 2009). Tagged ribosomes are recovered by affinity selection, capturing ribosomes purely from the cells of interest. RNA is isolated from the captured ribosomes and measured through microarrays/RNA sequencing (King and Gerber 2016). While this method offers the best high-throughput prospects compared to polysome and ribosome profiling, this technology is still limited due to the lack of discrimination between actively translating and non-translating mRNA, which can be either mRNA indirectly bound to ribosomes or bound to other non-translating mRNA (Dodd *et al.*, unpublished).

A novel method of translome profiling has been developed in house by Dr G. Hautbergue known as GRASPS, which allows for the isolation of RNA molecules that co-precipitate with ribosomes and are, therefore, likely to be undergoing translation into protein. Unlike these methods described above, the GRASPS technique does not require the manipulation of sucrose gradients or the tagging of ribosomal subunits, thus removing the potential contamination by heparin within the sucrose solution and the need for the generation of transgenic cell lines. The protocol for GRASPs takes roughly 48 hours from cell lysis to completion and the purification of full-length RNA has been shown to improve mapping to the genome in a previous study (unpublished data, Dodd *et al.*). However, the RNA extracted at the time of lysis is purely a snapshot of what is occurring in the cell at that time, therefore we must take into consideration that some cellular mechanisms may be missed.

In this chapter, I have used the new technique GRASPS to identify the transcriptional changes triggered by each of the drugs I have tested on the *in vitro* culture system in Chapter 4. Considering that both andrographolide and S[+]-apomorphine have antioxidant characteristics, we hypothesised that additional different underlying mechanisms were responsible for the differential neuroprotection observed in co-culture. Indeed, the results shown in Chapter 4 support the hypothesis that andrographolide, S[+]-apomorphine and riluzole act through different mechanisms of action. Functional assays demonstrated that andrographolide and S[+]-apomorphine trigger common effects on cells, however, the mechanisms leading to those effects are still not clear.

My aim in the work described in this chapter is to use GRASPS transcriptomic analysis to identify the different mechanisms of action of andrographolide, S[+]-apomorphine and riluzole and assess

whether these drugs act through the same mechanisms in all ALS patient subgroups or if their action is influenced by the cellular environment.

5.2. Results

5.2.1. RNA extraction and quality control

Following on from the MN-iAstrocyte co-culture data, we hypothesised that the different mechanisms of action and specific targets of each drug would be responsible for the differential neuroprotective response observed in some patient iAstrocyte co-cultures over others. Hence, we wanted to investigate the mechanism of action of the drugs andrographolide and S[+]-apomorphine to define why each drug was beneficial at reducing the toxicity of a particular patient subgroup over another. To do this, control and patient iAstrocytes were plated into 10cm dishes as a monoculture and were treated with the compound diluted in 0.01% DMSO for 48 hours. This time frame was chosen to mirror the time frame of the MN-iAstrocyte co-culture experiments. The cells were lysed and the RNA was extracted using the GRASPs protocol.

The quality of the RNA samples, as well as the detection of any residual ribosomal RNA (rRNA), was assessed on a Picochip in an Agilent 2100 Bioanalyser, while sample quantity was assessed using the Nanodrop system (Supplementary 5.1). The electropherograms were used to assess whether samples could be taken forward for sequencing, required another collection because of RNA degradation or needed purification from contaminating rRNA. Figure 5.1A demonstrates a 'clean' RNA sample, which was devoid of any residual rRNA. The electropherograms of purified samples showed a ladder at the start followed by a smooth curve with no distinct peaks. The other sample present in Figure 5.1B did have ribosomal contamination; this electropherogram showed a ladder at the start followed by a steep, jagged curve with detection of the 18S and 28S ribosomal subunits. There was also a large difference in RNA concentration between the two samples; the sample with ribosomal contamination had almost 10x the amount of RNA.

The RNA samples with remaining rRNA contamination underwent rRNA depletion using the NEBNext® rRNA depletion kit and were re-assessed in the Bioanalyser before they were sent off for RNA sequencing (Figure 5.1C).

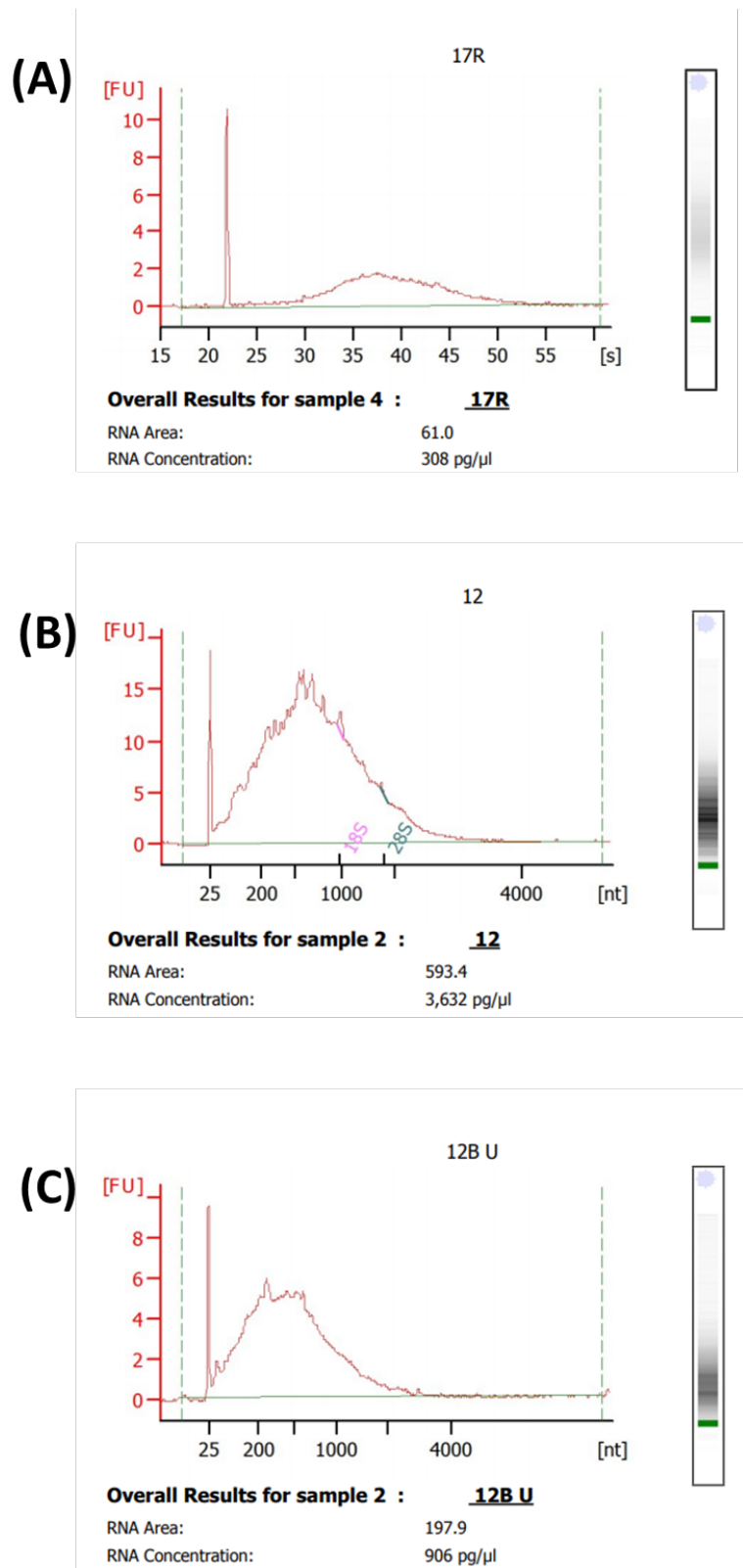


Figure 5.1 PicoChip analysis of RNA quality and integrity assessed using the Agilent 2100 Bioanalyser. (A). The electropherograms of an RNA sample devoid of any rRNA; there is a smooth curve with no distinct ribosomal peaks, (B). An RNA sample with rRNA contamination; there is a jagged curve with detection of the 18S and 28S ribosomal subunits, and (C). A clean RNA sample after rRNA depletion of the remaining rRNA still present after GRASPs.

5.2.2. RNA-sequencing data quality assessment

RNA isolated using the GRASPs method from control and patient iAstrocytes was sent to the Centre of Genomic Research at the University of Liverpool for sequencing (Supplementary 5.2), and the sequencing data was mapped and normalised by Dr M. Dunning of the Sheffield Bioinformatics Core.

FastQC is a quality control tool for high-throughput sequencing data, written by Simon Andrews at the Babraham Institute in Cambridge. The software identifies whether RNA sequencing samples have 'passed' or 'failed' quality control depending on meeting specific criteria. Dr M. Dunning generated *FastQC* reports for each sample

(<https://www.bioinformatics.babraham.ac.uk/projects/fastqc/>) and combined the individual reports together using the *multiqc* software (<https://multiqc.info/>). Despite checking for any residual rRNA within each sample sent for sequencing, roughly half of the reads still contained rRNA contamination. Therefore, Dr M. Dunning used the *bbmap* software (<https://sourceforge.net/projects/bbmap/>) to separate the reads that map to rRNA into separate *FastQ* files to give a more reliable measurement of the level of rRNA contamination. *FastQC* was generated on these new files to see if the rRNA had been removed successfully. The *FastQC* results before and after the removal of the rRNA reads are shown in Figure 5.2.

The sequence quality histograms showed the average quality value across all bases at each position in the *FastQ* file. The higher the score, the better the base call. The quality of the base calls on most platforms will degrade as the run progresses, therefore, it is common to see base calls falling towards the end of a read. All samples presented high quality base calls, and this did not change after the removal of rRNA (Figure 5.2A).

The per-sequence quality scores showed the number of reads with average quality scores; this allowed for the detection of sequences with low quality values. All samples presented a high number of reads with average quality scores and this was not affected after the removal of rRNA (Figure 5.2B). There was a second smaller peak present after the removal of the rRNA reads which corresponded to sequencing samples from CTR155 which were removed from the analysis.

The per sequence GC content measured the percentage of nitrogenous bases that were either guanine or cytosine across the whole length of each sequence and was compared against a modelled normal distribution of GC content. An unusual distribution could indicate contamination within the library. Before the removal of rRNA reads, 53 samples had 'passed', 37 samples were tagged with a 'warning', this was raised if the sum of deviations from the normal distribution represented more than 15% of the reads, while 6 samples had 'failed' because more than 30% of reads had an unusual distribution (Figure 5.2C). After removal of the rRNA, the number of 'passed' samples increased to

82, while 2 samples had 'warnings' and 12 samples had 'failed'. These failed samples corresponded to CTR155 and C9ORF72 183 samples which were removed from further analysis after quality control.

Existing methods for quantification of individual transcript abundances lack sample-specific bias models which detect important effects like the unusual GC content bias seen in some of our reads. When no correction is applied, this bias can lead to the loss of false discovery rate (FDR) control in differential expression studies (Love *et al.* 2016). Dr M. Dunning quantified the transcript-per-million abundance within all samples using *Salmon* (<https://github.com/COMBINE-lab/Salmon>); this software employs a dual-phase statistical inference procedure as well as a sample-specific bias model that accounts for the biases that are typical of RNA-sequencing data, including sequence-specific biases at the 5' and 3' ends of sequences, fragment GC-content and positional bias (Patro *et al.*, 2017). This software both aligns and quantifies transcripts in a single tool; in quasi-mapping mode, *Salmon* inputs the unaligned reads in the *FastQ* format alongside a reference transcriptome, and performs quantification directly, without generating intermediate alignment files (Patro *et al.*, 2017).

Before

After

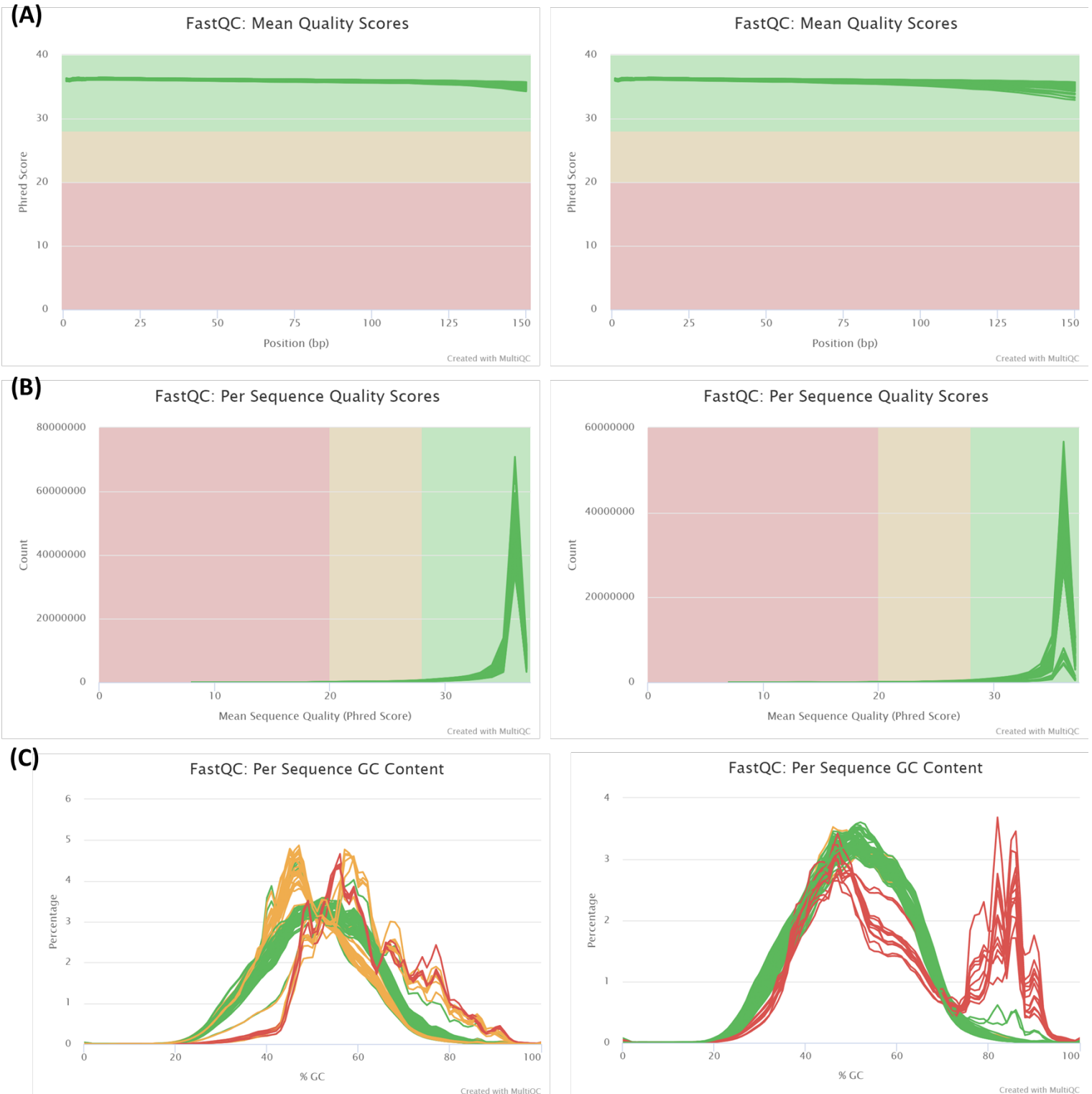


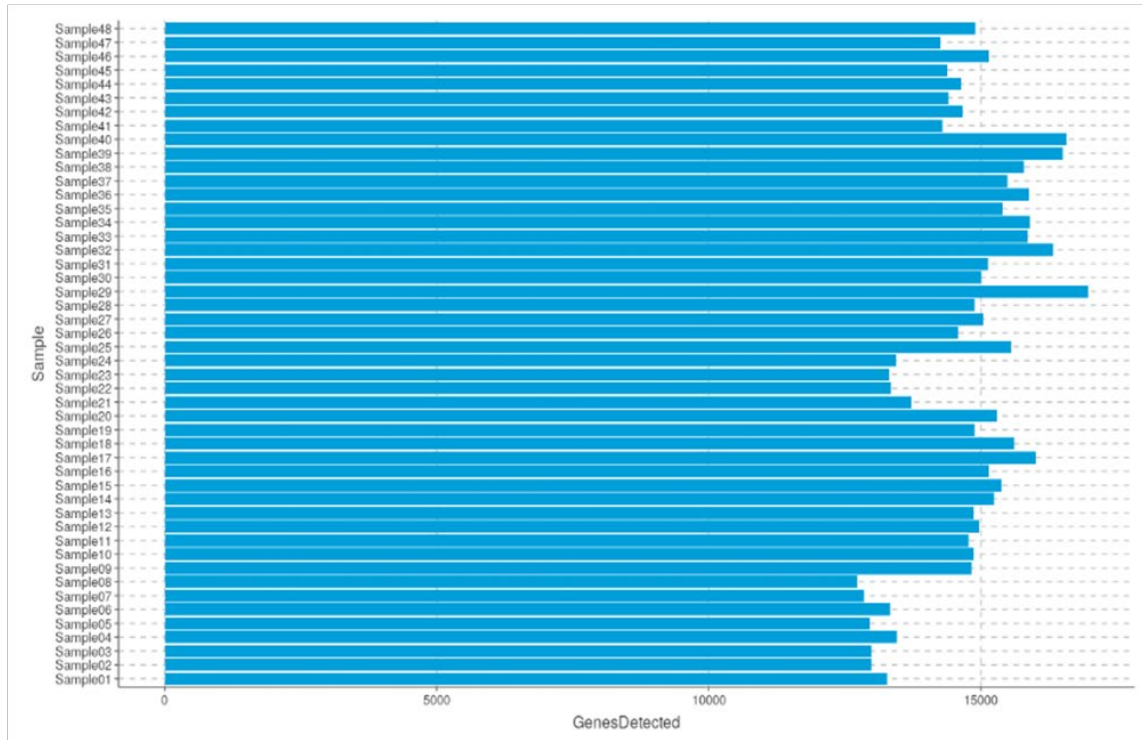
Figure 5.2 Quality assessment of RNA sequencing reads for all 96 samples before and after the removal of the rRNA mapped reads. (A). The mean per base sequence quality score. (B). The mean per sequence quality score. The background of the graph is divided into high quality base calls/sequences (green), calls/sequences of reasonable quality (orange) and poor-quality calls/sequences (red). (C). The average percentage GC content of the reads.

Gene-level abundance estimates offer advantages in accuracy, power and DGE interpretation over transcript-level analyses (Soneson *et al.* 2015). The R/Bioconductor package *tximport* (<http://bioconductor.org/packages/tximport>) was used to import the transcripts per million (TPM) estimates generated by *Salmon* and prepare estimated gene count matrices for the statistical engine *DESeq2*. This software corrects for technical biases and different transcript usage across samples, removing the need for an accompanying offset matrix (Love *et al.* 2018). The transcripts were given associated gene IDs using *tx2gene* from the *tximport* package and imported into R, collapsing the *Salmon* transcript quantifications to gene level using the information in *tx2gene*.

To convert the data for analysis with *DESeq2*, the metadata, including the patient number, the treatment group, the sample concentration and purification method, was imported into R. *DESeq2* has specially designed import functions for inputting estimated gene counts from *tximport* and generating differential gene expression (Love *et al.* 2018). The raw gene counts were imported into *DESeq2* (<http://www.bioconductor.org/packages/release/bioc/html/DESeq2.html>) for quality assessment. Figure 5.3A shows the number of genes that were detected in each sample; in most samples between 13,000 – 17,000 expressed genes were detected, which is a good estimate at the time of writing (Love *et al.* 2018).

A simple QC measure in *DESeq2* was investigating the number of reads obtained for each sample; if the RNA quality was high, there should not be substantial variation between samples or sample groups. In RNA-sequencing experiments, the number of DEGs with sequencing depth does not significantly increase after 10 million reads (Liu *et al.* 2014). To assess the differential expression of transcripts using GRASPs, therefore only transcripts that had an AUG start codon (excluding non-coding RNA), 10 million reads were enough to detect differential expression. Figure 5.3B shows that most of the samples had between 30-50 million reads, except for Samples 5-8 and Samples 30 & 31 which had less than 10 million reads. Samples 5-8 were CTR 155 untreated and with all the drug treatments and Samples 30 & 31 were C9ORF72 patient 183 treated with S[+]-apomorphine and andrographolide; these samples were all omitted from DGE analysis.

(A)



(B)

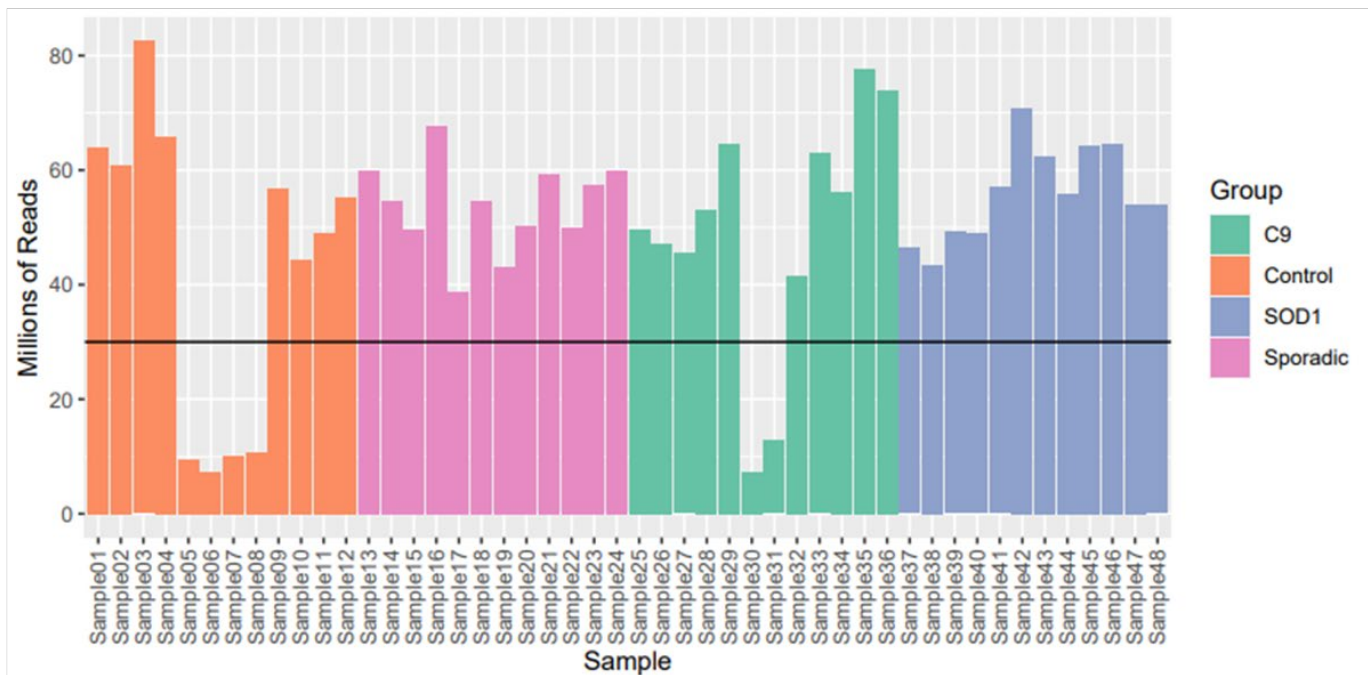


Figure 5.3 RNA-sequencing quality control analysis performed by Dr M. Dunning. (A). The number of genes detected in each RNA sample; all samples contained 13,000-17,000 genes. (B). The number of reads obtained for each RNA sample; 42/48 samples contained 30-50 million reads. Any samples containing less than 10 million reads were omitted from DGE analysis.

5.2.3. Pathway analysis discriminating different patient subgroups

Our first goal approaching the RNA-sequencing analysis was to understand how the different subgroups of patient iAstrocytes differed in gene expression profiling from the non-ALS control iAstrocytes, and what genes and pathways patient subgroups shared with one another. By identifying these similarities and differences at the baseline level, understanding the beneficial mechanism of the compounds on specific subgroups would become clearer.

The TPM values generated by *Salmon* were imported into a software programme called Qlucore, which allowed for the visualisation of the similarities and differences in gene expression between individual patient cell lines through a PCA plot (Figure 5.4). The plot showed that samples harbouring genetic mutations in the same gene cluster together on the PCA plot axes and were separate from samples carrying different genetic mutations or control samples.

The C9ORF72 patients separated further from the controls in the order of toxicity to MNs; C9ORF72 patient 78 was the least toxic to MNs and, although separate from controls, it was the closest C9ORF72 sample to healthy iAstrocytes, while C9ORF72 patient 201 was the most toxic cell line and it clustered further away from healthy iAstrocytes. The sALS patient cell lines fell between the SOD1 and C9ORF72 patient groups, indicating that these samples shared gene expression characteristics with genetic subgroups while retaining others that were unique to themselves. sALS patient 17, for example, shared more similarities with the SOD1 subgroup than sALS patients 009 and 12.

The raw counts were imported into *DESeq2* for differential expression analysis, generating a results table with log₂ fold changes, p-values and adjusted p-values. This software used shrinkage estimators for dispersion and fold change which improved the stability and reproducibility of the results, as well as outlier detection which recognised genes which the model assumed were unsuitable and avoided type-I errors (Love *et al.* 2015). Lists of differentially regulated transcripts between each patient iAstrocyte subgroup and the control iAstrocyte group (n=3 for SOD1, C9ORF72 and sALS groups, n=2 for CTR group) were generated by Dr M. Dunning using the R software platform by running the comparisons in the table below (Table 5.1):

Table 5.1 List of bioinformatic comparisons for baseline RNA-sequencing and the gene output

Bioinformatic comparison	Total genes	Upregulated genes	Downregulated genes
C9ORF72 U* vs CTR U	1760	1179	581
SOD1 U vs CTR U	1022	820	202
sALS U vs CTR U	1180	800	380

U* = untreated

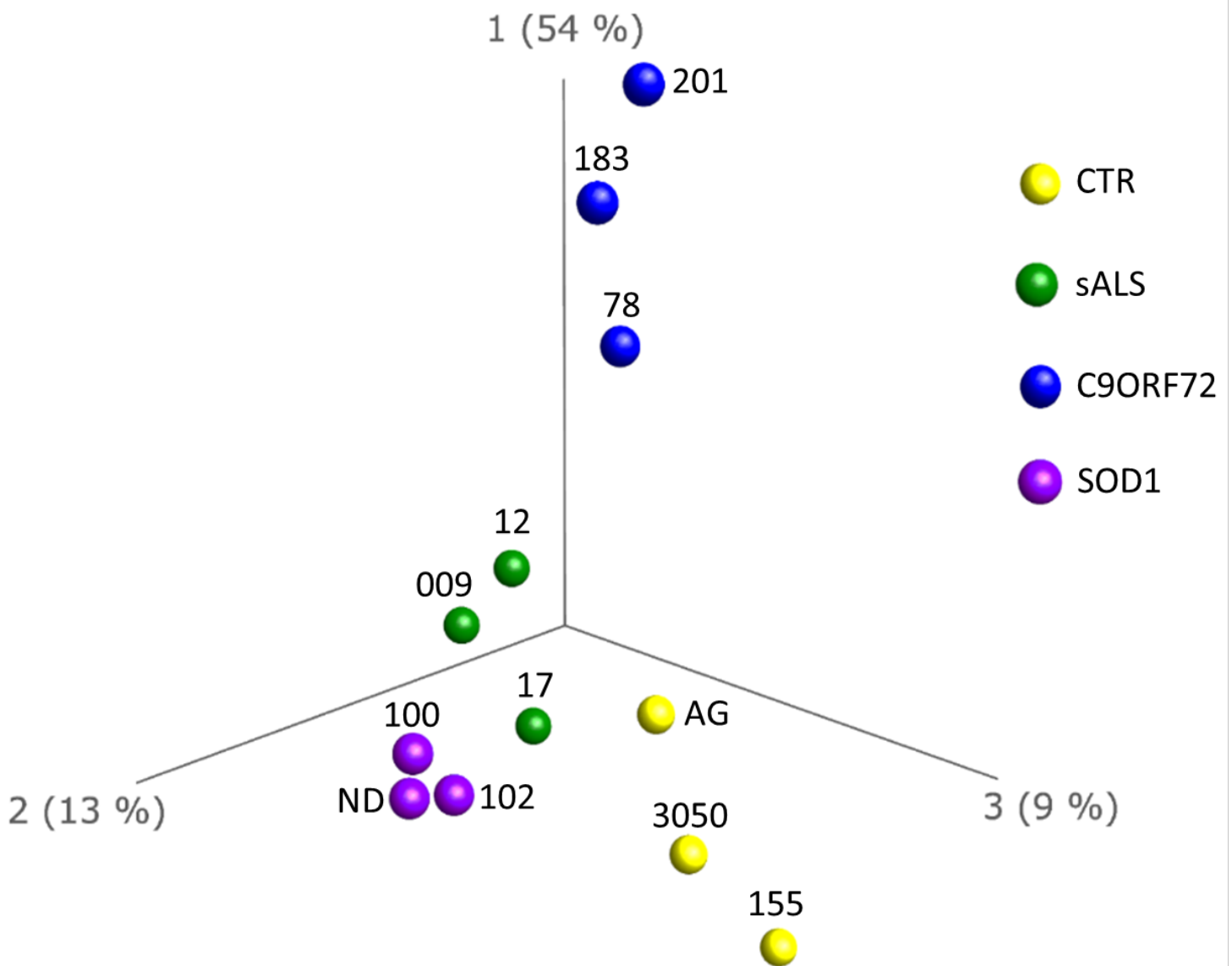


Figure 5.4 PCA plot of the gene expression values of control and patient iAstrocyte lines at untreated baseline (one-way ANOVA, multiple comparisons $p=0.05$ $\log_2FC < 1.5$). Subgroups are highlighted in colour: control = yellow, sALS = green, C9ORF72 = blue, & SOD1 = purple, and individual sample annotations (i.e. cell line number) are present on the plot.

Differentially regulated genes were then selected based on a p -value <0.05 and $\log_2\text{FoldChange}>1.5$. A p -value of 0.05 implies that 5% of significant DEGs are potentially false positive. The total number of significantly dysregulated genes from each bioinformatic comparison, as well as the number of upregulated and downregulated genes, is also presented in Table 5.1. C9ORF72 iAstrocytes presented the highest number of total significantly dysregulated genes and all patient subgroups displayed a higher percentage of genetic upregulation than downregulation.

To identify the genes that were shared between patient subgroups, I imported the lists of DEGs into the programme Venny (<https://bioinfogp.cnb.csic.es/tools/venny/>), which allowed me to generate a Venn diagram of shared genes between C9ORF72, SOD1 and sALS patient cell lines (Figure 5.5A). C9ORF72, SOD1 and sALS iAstrocytes shared a total of 278 genes. C9ORF72 & sALS lines shared a similar amount (306 genes), while SOD1 & sALS only shared 119 genes, and C9ORF72 & SOD1 shared 213 genes. C9ORF72 cell lines displayed the highest number of unique genes out of the patient subgroups.

The gene lists were separated into upregulated (shown in red) and downregulated (shown in blue) genes (Figure 5.5B). In total genes, SOD1 iAstrocytes displayed a much higher proportion of upregulated genes (285 up and 127 down) while C9ORF72 and sALS iAstrocytes presented similar proportions (575 up/388 down and 285 up/192 down respectively), still showing a skew towards upregulation. Out of the genes shared between all subgroups, 248 transcripts were upregulated while only 30 genes were downregulated, thus suggesting that ALS iAstrocytes mount a transcriptional response in disease compared to healthy iAstrocytes. The genes shared between C9ORF72 & SOD1 and SOD1 & sALS samples also presented a larger number of upregulated genes to downregulated genes while C9ORF72 & sALS samples shared 168 upregulated and 138 downregulated genes.

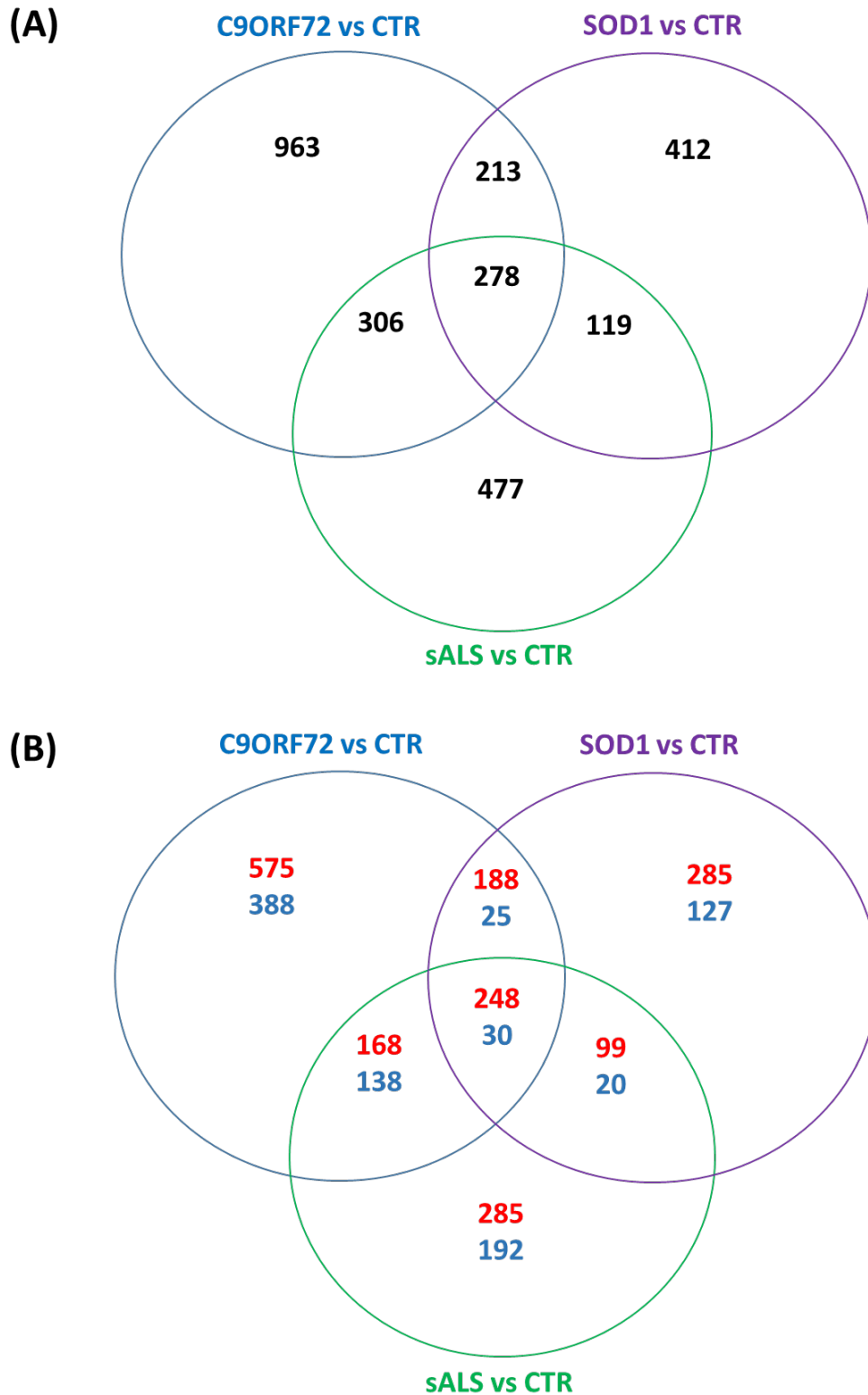


Figure 5.5 Visual representation of the dysregulated transcripts shared between the different patient subgroups generated from comparisons run in Table 5.1. (A). The total number of genes shared between C9ORF72, SOD1 and sALS patient iAstrocytes at baseline. (B). The number of upregulated (red) and downregulated (blue) transcripts shared between patient groups.

The DEGs from the lists generated in Table 5.1 were imported into the pathway analysis software programme DAVID (<https://david.ncifcrf.gov/summary.jsp>). To analyse gene expression changes in light of their biological impact on cell function, the Gene Ontology Term “Biological Process” (GO-BP) was used to categorise DEGs. The list of GO-BP terms for each subgroup were exported from DAVID and the p -value <0.05 cut was applied to discriminate against the 5% of pathways that may be a false positive. C9ORF72 iAstrocytes presented the highest number of significantly dysregulated pathways (180 pathways) while SOD1 and sALS iAstrocytes displayed 138 and 137 pathways respectively (Supplementary 5.3-5.5).

All the shared pathways between ALS patient subgroups are represented in Table 5.2. There were 14 pathways that were commonly dysregulated in C9ORF72, SOD1 and sALS lines (yellow highlight); these included pathways important for neuronal function, such as axonal guidance and glutamatergic synaptic transmission, as well as pathways involved in cellular maintenance, including cell adhesion molecules and calcium ion transmembrane transport. C9ORF72 and sALS cell lines shared 15 pathways (green highlight), which were related to inflammatory signalling and cholesterol metabolism. SOD1 and C9ORF72 lines displayed 6 common pathways (purple highlight) related to the transport of potassium and other ions as well as the commitment to the neuronal lineage, while sALS lines shared 5 pathways with SOD1 lines related to the processing of polysaccharides and regulation of exocytosis (blue highlight). Interestingly, the dysregulation of pathways relevant for neuronal development and function in iAstrocytes supports and highlights the importance of glial cells in neuronal maintenance and activity (Chandrasekaran *et al.*, 2016).

Since the RNA-sequencing analysis generated many different pathways, I decided to focus on those that were strongly associated with ALS pathogenesis as well as those that could explain the phenotypic assay data from previous chapters.

Within the axonal guidance category, there were a number of DEGs related to the semaphorin-plexin pathway. Semaphorins are axonal guidance proteins responsible for sculpting and maintaining the MN circuit. Secreted class III semaphorins act as axon repellents, inducing the collapse of spinal MN growth cones and repelling motor axons in ALS post-mortem tissue and *in vitro* (Varcianna *et al.*, 2019). All patient groups displayed differential expression in *SEMA3* genes (*SEMA3A*: C9ORF72 p -value = 0.02, \log_2FC = +2.44; *SEMA3B*: C9ORF72 p -value = 0.002, \log_2FC = -4.27, sALS p -value = 0.01, \log_2FC = -3.53; *SEMA3C*; SOD1 p -value = 0.04, \log_2FC = +1.79,) as well as a significant increase in *SEMA6A* expression in C9ORF72 and sALS (C9ORF72 p -value = 4.30E-04, \log_2FC = +5.36, sALS p -value = 0.03, \log_2FC = +3.26).

Table 5.2 List of GO pathways shared between ALS patient subgroups

Gene Ontology Term	C9ORF72 p-value	SOD1 p-value	sALS p-value
Nervous system development	4.10E-05	4.80E-02	5.30E-03
Axon guidance	8.30E-06	1.70E-06	1.40E-04
Positive regulation of synapse assembly	1.20E-02	6.80E-05	3.50E-02
Synaptic transmission, glutamatergic	5.90E-03	3.20E-02	1.90E-02
Calcium ion transmembrane transport	3.30E-06	3.60E-02	6.70E-03
Vesicle fusion	2.90E-03	1.40E-02	8.90E-03
Sensory perception of sound	2.40E-05	2.30E-04	2.80E-03
Cell adhesion	1.40E-09	1.00E-11	2.90E-13
Cell chemotaxis	2.10E-03	2.30E-02	1.60E-02
Positive regulation of cell migration	3.30E-03	6.90E-03	4.40E-02
Angiogenesis	3.80E-06	4.30E-03	8.30E-07
Cell fate commitment	1.30E-03	7.70E-04	1.30E-05
Canonical Wnt signalling pathway	1.50E-02	1.70E-02	3.90E-02
Collagen catabolic process	3.80E-02	1.80E-05	2.70E-06
Neuropeptide signalling pathway	2.80E-04	-	1.50E-04
Axon development	3.00E-02	-	1.00E-03
Inflammatory response	1.90E-07	9.90E-02	3.10E-06
Toll-like receptor 4 signalling pathway	7.40E-03	-	1.10E-02
Leukocyte migration	2.80E-02	-	3.70E-05
Positive regulation of cell proliferation	5.80E-04	-	2.90E-02
G-protein coupled receptor signalling pathway, coupled to cyclic nucleotide second messenger	1.60E-02	-	7.60E-03
Peptidyl-tyrosine phosphorylation	3.20E-02	-	2.10E-04
Positive regulation of protein kinase B signalling	3.80E-02	-	2.50E-02
Lipid transport	4.50E-02	-	3.60E-02
Response to glucocorticoid	4.20E-02	-	1.60E-02
Adherens junction organisation	4.60E-02	-	3.60E-02
Desmosome organisation	4.50E-02	-	2.30E-02
Matrix metalloproteinase activity	7.70E-03	-	3.60E-02
Keratinisation	7.40E-03	-	7.90E-05
Neurogenesis	9.10E-03	4.00E-04	-
Regulation of MAPK cascade	5.10E-04	8.30E-03	-
Cellular response to interleukin-6	1.50E-02	2.10E-02	-
Notch signalling pathway	3.60E-02	2.90E-02	-
BMP signalling pathway	7.70E-03	4.80E-02	-
Potassium ion transmembrane transport	3.80E-04	6.70E-03	-
Negative regulation of neuron apoptotic process	-	6.60E-04	3.40E-02
Positive regulation of dopamine secretion	-	2.50E-02	3.30E-02
Regulation of exocytosis	8.80E-02	4.80E-03	8.60E-03
Glycosaminoglycan metabolic process	-	7.80E-03	1.40E-02
O-glycan processing	-	1.50E-02	9.90E-03

Semaphorin proteins bind to plexins, either directly or through interaction with neuropilins. Class A plexins function as both Sema6 growth cone receptors, and Sema3 receptors through association with neuropilins (Zhou *et al.* 2008). All patient iAstrocyte groups displayed reduced expression of *PLXNA2* (C9ORF72 p-value = 0.002, log2FC = -2.70, SOD1 p-value = 0.04, log2FC = -1.80, sALS p-value = 0.03, log2FC = -1.96), implying a dysregulation in the semaphorin-plexin pathway. This pathway has been associated with a number of neurodegenerative diseases, including ALS, AD, PD and MS, as it plays a large role in cytoskeletal rearrangement and cellular migration (Quintremil *et al.*, 2018), therefore these DGE changes may account for the differences in the astrocyte morphology of patient lines compared to control identified in 3.2.1.

The identification of DEGs related to glutamatergic synaptic transmission was not surprising since the expression of receptors involved in glutamate signalling is central to astrocytic function and has been explored in previous chapters (3.2.4). Patient iAstrocytes shared a significant increase in transcripts related to metabotropic glutamate receptors, which mediate glutamate activity through the stimulation of intracellular signalling cascades (Spampinato *et al.*, 2018); *GRM3*: C9ORF72 p-value = 3.37E-04, log2FC = +8.89, sALS p-value = 2.63E-05, log2FC = +10.43; *GRM4*: C9ORF72 p-value = 2.08E-06, log2FC = +4.88, SOD1 p-value = 0.003, log2FC = +3.17, sALS p-value = 0.01, log2FC = +2.70.

All patient subgroups shared a significant increase in the ionotropic glutamate receptor *GRIN3A* (C9ORF72 p-value = 5.08E-04, log2FC = +2.70, SOD1 p-value = 0.01, log2FC = +1.99, sALS p-value = 0.004, log2FC = +2.24) while C9ORF72 and sALS iAstrocytes shared a significant downregulation of *GRIN2B* (C9ORF72 p-value = 3.24E-06, log2FC = -8.71, sALS p-value = 2.69E-05, log2FC = -8.12), which was shown to have increased protein expression in C9ORF72 iAstrocytes (3.2.4), implying a compensatory mechanism for the increase of the protein.

Another pathway of interest in the context of ALS was vesicle trafficking; indeed several ALS-linked genes are involved in this pathway, including *C9ORF72*, *VCP*, *ALS2* and *CHMP2B* (Burk and Pasterkamp, 2019). Within the vesicle fusion category, there were a number of DEGs related to Rab proteins. Rab GTPase proteins are key modulators of intracellular membrane trafficking in eukaryotic cells, particularly vesicle sorting and transport between membranes (Kiral *et al.*, 2018). Rab3 proteins regulate the priming and docking of synaptic vesicles for neurotransmitter release (Dulubova *et al.*, 2005). All patient subgroups displayed significantly increased expression of *RAB3B* (C9ORF72 p-value = 0.001, log2FC = +4.46, SOD1 p-value = 0.05, log2FC = +2.72, sALS p-value = 0.009, log2FC = +3.58) and *RAB3C* (C9ORF72 p-value = 0.006, log2FC = +5.36, SOD1 p-value = 0.05,

log₂FC = +3.88, sALS p-value = 0.01, log₂FC = +4.89), implying a dysregulation in the astrocytic secretion of vesicles.

Another well-documented pathway involved in ALS and transcriptionally dysregulated in iAstrocytes was neuroinflammation. This is a common characteristic in ALS and other neurodegenerative disorders; this inflammatory reaction is mainly regulated by glial cells, including microglia, astrocytes, and T cells (Philips and Robberecht 2011). All patient subgroups shared an upregulation in cellular chemotaxis molecules such as the Chemokine Motif Ligand 2 (*CCL2*: C9ORF72 p-value = 1.14E-05, log₂FC = +7.85, SOD1 p-value = 0.01, log₂FC = +4.58, sALS p-value = 2.23E-04, log₂FC = +6.60) which has been previously reported in ALS (Henkel *et al.*, 2004, 2006), as well as *CXCL12* (C9ORF72 p-value = 2.66E-04, log₂FC = +8.27, SOD1 p-value = 2.09E-05, log₂FC = +9.65, sALS p-value = 1.46E-04, log₂FC = +8.62) which attracts pro-inflammatory microglia (Rabinovich-Nikitin *et al.*, 2016).

The DAVID pathway analysis identified the inflammatory response GO-BP shared between C9ORF72 & sALS patient iAstrocytes. This included transcripts related to the regulation of the pro-inflammatory TNF pathway, which were significantly upregulated in C9ORF72 and sALS iAstrocytes only (*TNFAIP3*: C9ORF72 p-value = 0.02, log₂FC = +3.51; *TNFRSF11A*: C9ORF72 p-value = 0.05, log₂FC = +3.05, sALS p-value = 0.02, log₂FC = +3.61; *TNFAIP6*: sALS p-value = 0.03, log₂FC = +3.65), implying that there were other neuroinflammatory pathways at play in SOD1 iAstrocytes; SOD1 iAstrocytes uniquely expressed transcripts related to the Type I interferon (IFN) signalling pathway, which is described in more detail when investigating the pathway changes exclusive to SOD1 iAstrocytes.

There were a large variety of DEGs identified in the cell adhesion category, therefore I decided to focus on the transcripts that were also identified within the nervous system development category. Cadherins are a family of calcium-dependent cellular adhesion proteins that are widely expressed in the CNS, playing an essential role in nervous system development. All patient cells displayed a significant increase in cadherin 2 expression (*CDH2*: C9ORF72 p-value = 1.99E-06, log₂FC = +9.41, SOD1 p-value = 4.09E-04, log₂FC = +6.99, sALS p-value = 8.01E-04, log₂FC = +6.63). They also showed a significant increase in transcripts related to protocadherin 10 & 18 which are cadherin-related receptors responsible for the establishment of specific cell-cell connections in the brain (*PCDH10*: C9ORF72 p-value = 0.02, log₂FC = +4.35, sALS p-value = 0.04, log₂FC = +4.04; *PCDH18*: C9ORF72 p-value = 0.002, log₂FC = +2.45, SOD1 p-value = 0.03, log₂FC = +1.69, sALS p-value = 0.005, log₂FC = +2.21). This is interesting in light of the semaphorin-plexin dysregulation also identified in the patient iAstrocytes and this implies a dysregulation of cell-to-cell contact and signalling between the

cells. However, it is uncertain whether these transcripts are upregulated due to a dysregulation in protein levels or whether the upregulation is to counteract the invasive mechanism of the cells.

Following looking into shared pathways between patient iAstrocyte subgroups, I decided to investigate which pathways were unique to each genetic subgroup by importing the lists of DEGs only dysregulated in either C9ORF72, SOD1 and sALS iAstrocytes generated through Venny into the DAVID pathway analysis programme.

Since C9ORF72 iAstrocyte lines displayed the highest number of significant DEGs, it was unsurprising that they had the highest number of dysregulated pathways; 23 pathways shown in Table 5.3. While axonal guidance was a shared pathway between all genetic subgroups, C9ORF72 iAstrocytes displayed a significant increase in additional semaphorin transcripts which were unique to this subgroup identified within the semaphorin-plexin signalling pathway category (*SEMA4A*: p-value = 0.004, log₂FC = +3.08, *SEMA4D*: p-value = 0.02, log₂FC = +1.78).

Table 5.3 Gene Ontology pathways unique to C9ORF72 patient iAstrocyte lines

Gene Ontology Term	Gene Count	P-value
Semaphorin-plexin signalling pathway	5	3.30E-02
Negative regulation of neuron projection development	7	5.40E-03
Negative regulation of cell migration	9	2.50E-02
Regulation of postsynaptic membrane potential	5	8.10E-03
Chloride transmembrane transport	9	2.20E-02
Visual perception	15	1.80E-02
Wound healing	10	2.80E-03
Positive regulation of neutrophil extravasation	3	4.00E-03
Positive regulation of nitric oxide biosynthetic process	7	4.80E-03
Cellular response to lipopolysaccharide	15	7.50E-05
Long-chain fatty acid metabolic process	4	4.10E-02
Phospholipid metabolic process	6	4.90E-02
Positive regulation of pathway-restricted SMAD protein phosphorylation	8	1.80E-03
Negative regulation of protein autophosphorylation	4	5.00E-03
Transmembrane receptor protein tyrosine kinase signalling pathway	9	2.60E-02
Transport	21	3.50E-02
Proteolysis	28	3.30E-02
Positive regulation of protein processing	3	3.30E-02
Regulation of apoptotic process	17	6.00E-03
Cell differentiation	29	7.70E-03
Organisation of actin cytoskeleton	3	2.50E-02
Cytolysis	4	4.10E-02
Myosin binding	3	4.20E-02

Functional studies demonstrated that C9ORF72 iAstrocytes had an impairment in extracellular glutamate buffering, therefore it was interesting to note that only these cell lines showed an increased expression of hyperpolarisation activated cyclic nucleotide gated potassium channel transcripts (*HCN1*: p-value = 7.96E-04, log2FC = +5.39, *HCN3*: p-value = 0.04, log2FC = +1.53) which have been previously reported in reactive astrocytes (Honsa *et al.*, 2014). C9ORF72 iAstrocytes also displayed dysregulation of other ionotropic glutamate receptor transcripts that were not identified in other cell lines (*GRIN1*: p-value = 0.02, log2FC = +4.08, *GRIN2A*: p-value = 0.002, log2FC = -3.07). This is interesting in light of the dysregulation of the *GRIN2B* and *GRIN3B* transcripts reported previously which are shared with the other patient subgroups. The stoichiometry between the different subunits of the receptor is important for membrane docking, calcium permeability as well as sensitivity to glutamate (Balderas and Hernández 2018), therefore I can hypothesise that the imbalance between the subunits might change the properties of the receptor.

The DEGs that were unique to this genetic subgroup identified pathways involved in the metabolism and transport of fatty acids. The esterification of cholesterol is catalysed by lecithin-cholesterol acyltransferase which was significantly downregulated in C9ORF72 lines (*LCAT*: p-value = 0.01, log2FC = -2.74), while the cholesterol-efflux mediator ATP binding cassette subfamily G member 1 transcript was significantly increased (*ABCG1*: p-value = 0.048086994, log2FC = +2.45294689), both of which have previously been reported in AD (Demeester *et al.*, 2000; Marchi *et al.*, 2019).

There were DEGs related to 13 pathways in SOD1 patient iAstrocytes (Table 5.4). There was an upregulation in genes related to the regulation of neuron death, including ephrin type-B receptor (*EPHB1*: p-value = 0.031, log2FC = +3.54), clusterin (*CLU*: p-value = 0.04, log2FC = +3.19) and *LRRK2* (p-value = 0.016416405, log2FC = +5.360017012), which have previously been associated with ALS (Shtilbans *et al.*, 2011; Zinkie *et al.*, 2013; Tyzack *et al.*, 2017).

As described above, there is a long history of the role of neuroinflammation in ALS. The SOD1 iAstrocyte group uniquely expressed a downregulation of transcripts related to the Type I IFN signalling pathway (*IFI27*: p-value = 0.03, log2FC = -3.33; *IFITM1*: p-value = 0.02, log2FC = -2.47; *IRF7*: p-value = 0.02, log2FC = -2.16), while the activation of IFN signalling pathways have been previously reported in SOD1 ALS (Wang *et al.* 2011).

Table 5.4 Gene Ontology pathways unique to SOD1 patient iAstrocyte lines

Gene Ontology Term	Gene Count	P-value
Regulation of neuron differentiation	5	3.10E-04
Commitment of neuronal cell to specific neuron type in forebrain	3	5.60E-03
Negative regulation of neuron apoptotic process	8	6.90E-03
Regulation of neuron death	3	3.20E-02
Negative regulation of cerebellar granule cell precursor proliferation	2	3.30E-02
Epinephrine biosynthetic process	2	3.30E-02
Retinal ganglion cell axon guidance	3	4.00E-02
Type I interferon signalling pathway	10	1.10E-06
Positive regulation of interferon-gamma production	5	7.30E-03
Regulation of immune response	8	3.10E-02
Regulation of small GTPase mediated signal transduction	8	7.50E-03
Positive regulation of protein kinase C activity	2	3.30E-02
Regulation of somitogenesis	3	5.60E-03

The sALS patient iAstrocyte subgroup did not share a genetic mutation, however there were 18 pathways shared amongst the sALS patient lines that were not seen in other patient groups (Table 5.5).

Table 5.5 Gene Ontology pathways unique to sALS patient iAstrocyte lines

Gene Ontology Term	Gene Count	P-value
Regulation of synaptic transmission, cholinergic	3	3.50E-03
Memory	6	6.60E-03
Positive regulation of dendritic spine morphogenesis	3	3.20E-02
Sodium ion transmembrane transport	6	1.30E-02
Regulation of membrane potential	6	1.40E-02
Negative regulation of tumour necrosis factor production	5	5.80E-03
Positive regulation of neutrophil chemotaxis	4	8.10E-03
Positive regulation of reactive oxygen species metabolic process	4	1.90E-02
Melanosome transport	4	7.10E-03
Negative regulation of endopeptidase activity	10	5.30E-04
Positive regulation of phosphorylation	4	1.20E-02
Quinolate metabolic process	2	3.80E-02
Integrin-mediated signalling pathway	6	4.10E-02
Positive regulation of endothelial cell proliferation	5	4.30E-02
Retina layer formation	4	8.10E-03
Odontogenesis	4	1.40E-02
Bone morphogenesis	4	1.40E-02
Phosphate ion transmembrane transport	3	4.60E-02

Genes related to the pro-inflammatory TNF signalling pathway were increased in both C9ORF72 and sALS lines, while sALS iAstrocytes also significantly expressed genes related to the suppression of this pathway, including Melanocortin 1 Receptor (*MC1R*: p-value = 0.02, log₂FC = +1.73), Bactericidal/Permeability-Increasing Protein (*BPI*: p-value = 0.004, log₂FC = -5.68) and Lipopolysaccharide Binding Protein (*LBP*: p-value = 0.02, log₂FC = +4.15), implying an attempt to suppress neuroinflammation which was not seen in the C9ORF72 lines. sALS patient iAstrocytes also displayed DEGs in additional Rab proteins responsible for the formation of endosomes (*RAB17*; p-value = 0.04, log₂FC = -4.08; *RAB27A*; p-value = 0.01, log₂FC = +1.90), both of which have previously been reported in ALS (Iguchi *et al.*, 2016; Ono *et al.*, 2020).

In summary, the pathways that were shared between the patient iAstrocyte subgroups were related to neuronal survival and function, including axonal guidance, cell-cell signalling, glutamate transport as well as vesicle trafficking and astrocyte secretion. Neuroinflammation plays a key role in ALS pathogenesis and while transcripts related to inflammatory processes were discovered in all patient groups, C9ORF72 & sALS iAstrocytes shared an increase in TNF signalling, while SOD1 iAstrocytes demonstrated a dysregulation in the IFN pathway. While investigating the pathways that were unique to each patient subgroup, I discovered that C9ORF72 iAstrocytes displayed a dysregulation in cholesterol metabolism and transport, while SOD1 iAstrocytes presented an upregulation of transcripts that regulate neuronal death, and sALS cells displayed a suppression of neuroinflammation which may account for the reduced toxicity towards MNs observed in this group compared to C9ORF72 and SOD1 iAstrocytes.

5.2.4. S[+]-Apomorphine treatment across patient subgroups

After identifying the similarities and differences between the patient iAstrocyte subgroups, the next step was to interrogate the gene expression changes driven by drug treatment in each patient subgroup to determine the mechanism of action of each compound.

Interestingly, untreated and treated samples tend to cluster very closely on the PCA plot, with the exception of the C9ORF72 samples, which display a large shift on the main axis towards control samples after drug treatment (Figure 5.6). This suggests that S[+]-apomorphine treatment caused different expression changes in C9ORF72 patients compared to the other groups.

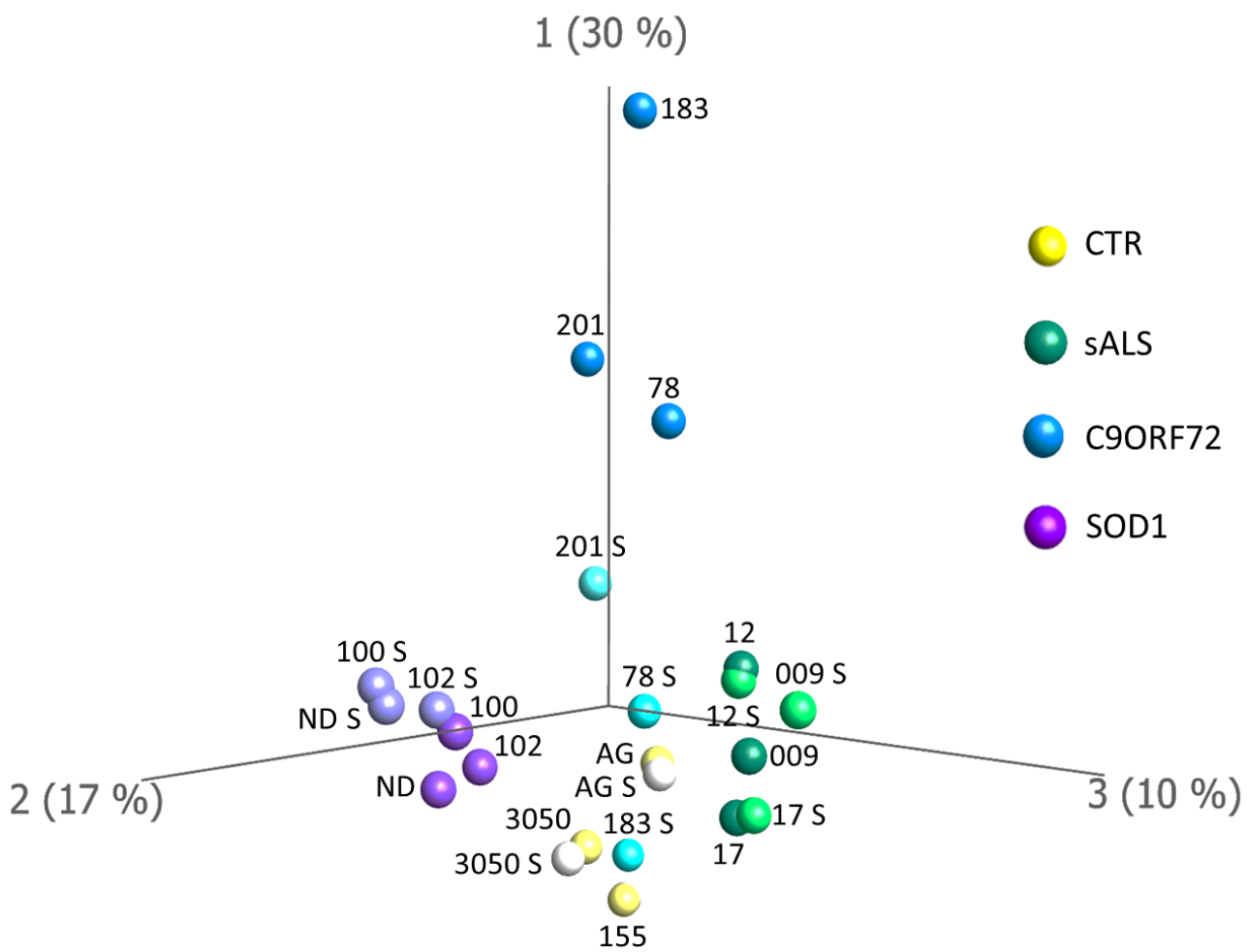


Figure 5.6 PCA plot of the gene expression values of control and patient astrocyte lines before and after S[+]apomorphine treatment (two-way ANOVA, multiple comparisons $p=0.05$ $\log_2FC < 1.5$). Subgroups are highlighted in colour; untreated samples: control = yellow, sALS = green, C9ORF72 = blue & SOD1 = purple, S[+]apomorphine treated samples: control = white, sALS = light green, C9ORF72 = light blue & SOD1 = light purple. Individual sample annotations are present on the plot. Abbreviations: S = S[+]apomorphine.

To investigate the mechanism of action of S[+]-apomorphine in the patient iAstrocytes, lists of differentially regulated transcripts between each patient iAstrocyte subgroup treated with the compound and each patient iAstrocyte subgroup untreated were generated by running the comparisons in the table below (Table 5.6):

Table 5.6 List of bioinformatic comparisons for S[+]-apomorphine treated iAstrocytes and gene count

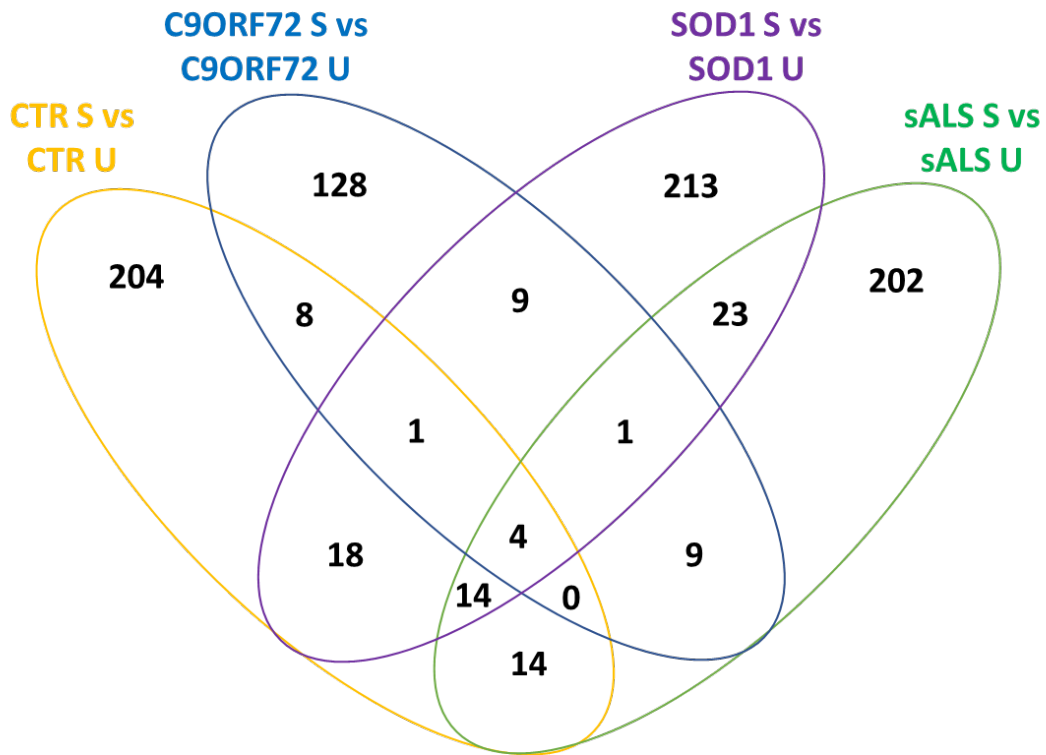
Bioinformatic comparison	Total genes	Upregulated genes	Downregulated genes
CTR S* vs CTR U#	263	169	94
C9ORF72 S vs C9ORF72 U	160	87	73
SOD1 S vs SOD1 U	283	212	71
sALS S vs sALS U	267	106	161

S* = S[+]-apomorphine, U# = untreated

A Venn diagram of shared genes between control and patient cell lines after S[+]-apomorphine treatment is shown in Figure 5.7. CTR, SOD1 and sALS iAstrocyte lines displayed a similar number of unique DEGs after S[+]-apomorphine treatment (CTR = 204 DEGs, 119 up and 85 down; SOD1 = 213 DEGs, 148 up and 65 down; and sALS = 202 DEGs, 47 up and 155 down). In C9ORF72 patient iAstrocytes, on the other hand, only 128 genes were significantly altered after S[+]-apomorphine treatment (64 up and 64 down). SOD1 & sALS lines shared the most genes (23 DEGs, 22 up and 1 down) while less genes were shared amongst the different subgroups (9 DEGs, 6 up and 3 down); treatment with S[+]-apomorphine resulted in transcriptional upregulation in the majority of genes shared between patient and control iAstrocytes.

When the original gene lists were imported into the DAVID pathway analysis software, SOD1 iAstrocytes displayed the highest number of significantly altered GO terms (44 pathways), followed by sALS (33 pathways), and CTR and C9ORF72 iAstrocytes (19 and 12 pathways respectively); all pathways are presented in Supplementary 5.6-5.9. To identify drug-induced transcriptional changes common to all patient groups, I only focused on the pathways shared between 2 or more iAstrocyte groups. All of the shared pathways between control and patient iAstrocyte subgroups after S[+]-apomorphine treatment are presented in Table 5.7.

(A)



(B)

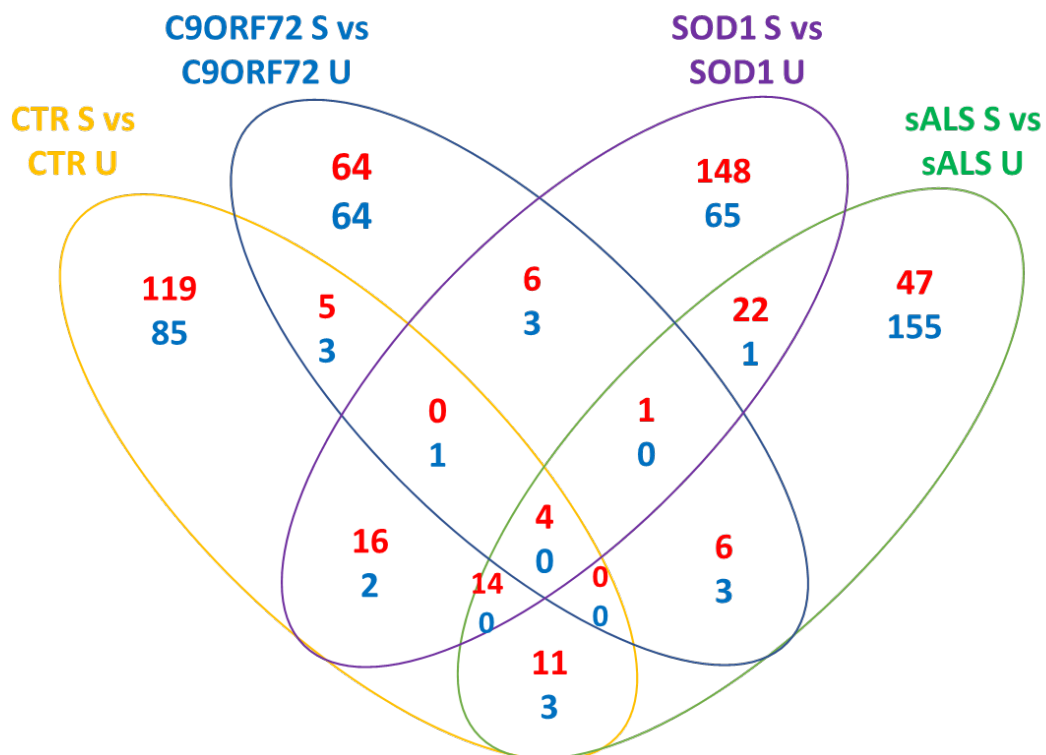


Figure 5.7 Visual representation of the DEGs shared between the control and different patient subgroups after S[+]-apomorphine treatment, generated from comparisons run in Table 5.6. (A). The total number of genes shared between groups. (B). The number of upregulated (red) and downregulated (blue) transcripts shared between subgroups. Abbreviations: U = untreated, S = S[+]-apomorphine.

Table 5.7 List of GO pathways shared between ALS patient subgroups treated with S[+]-apomorphine

Gene Ontology Term	CTR p-value	C9ORF72 p-value	SOD1 p-value	sALS p-value
Cellular response to organic cyclic compound	4.10E-03	-	2.20E-04	-
MAPK cascade	2.70E-02	-	3.60E-02	-
Morphogenesis of an epithelial fold	4.40E-02	-	-	4.00E-02
Cell adhesion	-	3.40E-05	2.80E-02	4.30E-02
Angiogenesis	-	3.20E-02	1.80E-02	2.50E-02
Inflammatory response	-	-	5.40E-05	3.80E-02
Immune response	-	-	1.90E-03	2.70E-02
Oxidation-reduction process	-	-	5.00E-02	3.70E-02
Xenobiotic metabolic process	5.60E-02	-	7.90E-04	4.40E-02
Synaptic transmission, cholinergic	-	-	3.70E-04	6.10E-03
Collagen fibril organisation	-	-	5.60E-03	6.20E-04

There were 2 pathways shared between CTR & SOD1 iAstrocytes; the cellular response to organic cyclic compound and the MAPK cascade. The first pathway refers to the change in activity of the cell in response to an organic cyclic compound, including movement, secretion, enzyme production or even further gene expression which is likely to reflect compound metabolism. This included a significant upregulation in the cytochrome P450 enzyme transcripts (*CYP1A1*: CTR p-value = 1.87E-74, log2FC = +6.99, SOD1 p-value = 2.18E-09, log2FC = +4.99; *CYP1B1*: CTR p-value = 5.81E-06, log2FC = +2.62, SOD1 p-value = 8.13E-27, log2FC = +2.59).

S[+]-apomorphine treatment also induced DGE changes in transcripts within the MAP kinase signalling pathway, in particular, artemin, a secreted ligand belonging to both the GDNF and TGF- β family of proteins (*ARTN*: CTR p-value = 0.03, log2FC = +2.06, SOD1 p-value = 0.004, log2FC = +2.93), and interleukin-1 beta, an important mediator of the inflammatory response (*IL1B*: CTR p-value = 4.36E-05, log2FC = +2.08, SOD1 p-value = 1.21E-04, log2FC = +2.05).

However, there were many pathways that were shared between the groups of patient iAstrocytes; 2 pathways between all the patient groups and 6 pathways between SOD1 & sALS iAstrocytes. This was interesting as S[+]-apomorphine treatment caused different pathways to change in control and patient iAstrocytes, with the control lines minimally affected, while the patients saw a large gene expression change. This reflected what was seen in the co-culture experiments, indicating a patient-specific drug response.

All patient groups presented DEGs related to cell adhesion, however different transcripts were targeted within each group, contactin and protocadherins in C9ORF72, integrins in SOD1 and cadherins in sALS iAstrocytes. There was a significant increase in protocadherin-related transcripts in all patient groups compared to control iAstrocytes, however, after S[+]-apomorphine treatment,

there was a reduction in protocadherin transcripts in C9ORF72 iAstrocytes only (*PCDHA4*: p-value = 7.90E-04, log2FC = -1.75; *PCDHB15*: p-value = 0.02, log2FC = -2.02; *PCDHGC4*: p-value = 0.003, log2FC = -3.06). There was also a significant increase in *CDH2* shared among all patient iAstrocytes, however, only sALS lines demonstrated a reduction in cadherin transcripts after S[+]-apomorphine treatment (*CDH2*: p-value = 0.003, log2FC = -1.92; *CDH6*: p-value = 7.51E-04, log2FC = -2.24). This suggests that S[+]-apomorphine treatment might have an effect on cellular migration and cell-cell contact but only in lines with a specific cellular environment.

SOD1 & sALS iAstrocytes displayed the highest number of shared transcripts after S[+]-apomorphine treatment, therefore it was unsurprising that they shared the most pathways. S[+]-Apomorphine appeared to target the inflammatory response within these cell types. SOD1 iAstrocytes displayed downregulation of the expression of X-C Motif Chemokine Receptor 1 (*XCR1*: p-value = 0.03, log2FC = -2.71), while there was an upregulation of the IFN-inducible T-cell alpha chemoattractant (*CXCL11*: p-value = 0.02, log2FC = +2.70). On the other hand, sALS iAstrocytes displayed downregulation of inflammatory chemoattractant molecules (*CXCL1*: p-value = 0.003, log2FC = -3.22; *CXCL6*: p-value = 0.02, log2FC = -3.87).

There were also DGE changes in the immune response after S[+]-apomorphine treatment; there was an increased expression of interleukin 1 alpha, alongside interleukin-1 beta, in SOD1 iAstrocytes (*IL1A*: p-value = 0.03, log2FC = +2.53), while there was a downregulation of interleukin 32 (*IL32*: p-value = 0.03, log2FC = -2.07) and DGE in transcripts expressing major histocompatibility complex, class II proteins in sALS iAstrocytes (*HLA-DOA*: p-value = 0.03, log2FC = +1.58; *HLA-DQB1*: p-value = 0.005, log2FC = -3.85).

SOD1 and sALS iAstrocytes also shared DGE changes in oxidation processes after treatment, as expected from the known antioxidant properties of this drug. Both groups displayed a significant upregulation in transcripts related to aldehyde dehydrogenase enzymes, that are responsible for the detoxification of long-chain aldehydes as well as the metabolism of neurotransmitters (*ALDH3A1*: SOD1 p-value = 1.58E-11, log2FC = +2.09, sALS p-value = 1.47E-11, log2FC = +1.85), which has been previously associated with Nrf2 (Duong *et al.*, 2017). Interestingly, sALS iAstrocytes displayed a significant downregulation in another aldehyde dehydrogenase transcript involved in the synthesis of retinoic acid from retinaldehyde (*ALDH1A2*: p-value = 0.04, log2FC = -1.94) which has been previously associated with MN death in ALS (Liang *et al.*, 2017). Cytochrome P450 enzymes involved in the metabolism of retinoic acid were also differentially regulated in SOD1 and sALS iAstrocytes after treatment (*CYP26B1*: SOD1 p-value = 1.83E-05, log2FC = +1.50, *CYP26A1*: sALS p-value = 0.009, log2FC = -5.16).

Treatment with S[+]-apomorphine significantly increased the expression of arachidonate 15-lipoxygenase, an essential factor for ferroptosis, in SOD1 iAstrocytes (*ALOX15B*: p-value = 3.19E-07, log2FC = +3.12), as well as an increased expression in Prostaglandin-Endoperoxide Synthase 1 that may be involved in iron binding (*PTGS1*: p-value 4.49E-06, log2FC = +1.57), implying that treatment might have an effect on iron levels in SOD1 iAstrocytes, as was witnessed in spinal cord injury (SCI) (Zhou *et al.* 2020). sALS iAstrocytes displayed a significant downregulation in expression of peroxidase, an enzyme that catalyses peroxidative reactions using hydrogen peroxide generated by NADPH oxidase enzymes (*PXDN*: p-value = 9.91E-05, log2FC = -3.57) which is a novel target of Nrf2 (Hanmer and Mavri-Damelin, 2018).

In summary, as hypothesised in the beginning, S[+]-apomorphine treatment resulted in specific DGE changes depending upon the mutational status of the patient group. There was a mild change in gene expression related to cytochrome P450 enzymes and MAPK signalling shared between CTR and SOD1 patient lines. While all patient groups shared DGE changes in cell adhesion, only C9ORF72 iAstrocytes presented changes in protocadherin transcripts and there was DGE in cadherin genes in sALS lines only. SOD1 and sALS lines displayed the most DGE changes after treatment with S[+]-apomorphine and these were related to pathways including inflammation, the immune response, oxidation, retinoic acid metabolism and iron binding.

5.2.5. Andrographolide treatment across patient subgroups

Like S[+]-apomorphine, andrographolide is also an Nrf2 activator therefore I hypothesised that there would be some changes in gene expression that were shared between both compounds. As with S[+]-apomorphine (5.2.4), there were little gene expression changes seen in the control after drug treatment (Figure 5.8). However, andrographolide treatment induced more gene expression changes in the C9ORF72 and sALS patient cell lines while there was little change in the SOD1 iAstrocytes; this was reflective of the results obtained from the iAstrocyte-MN co-cultures (4.2.2). The gene expression changes in all the C9ORF72 lines and sALS patient 12 moved towards the control while sALS line 009 moved in the opposite direction on the PCA plot. This is interesting because there was an increase in MN survival in the co-culture experiments with sALS 009 after both S[+]-apomorphine and andrographolide treatment and this same movement away from the control after drug treatment was also seen in the S[+]-apomorphine PCA plot (Figure 5.6). I can hypothesise that although there were no DGE changes towards the control after drug treatment in sALS 009, there were still changes in transcripts that dampened the astrocyte toxicity towards the MNs.

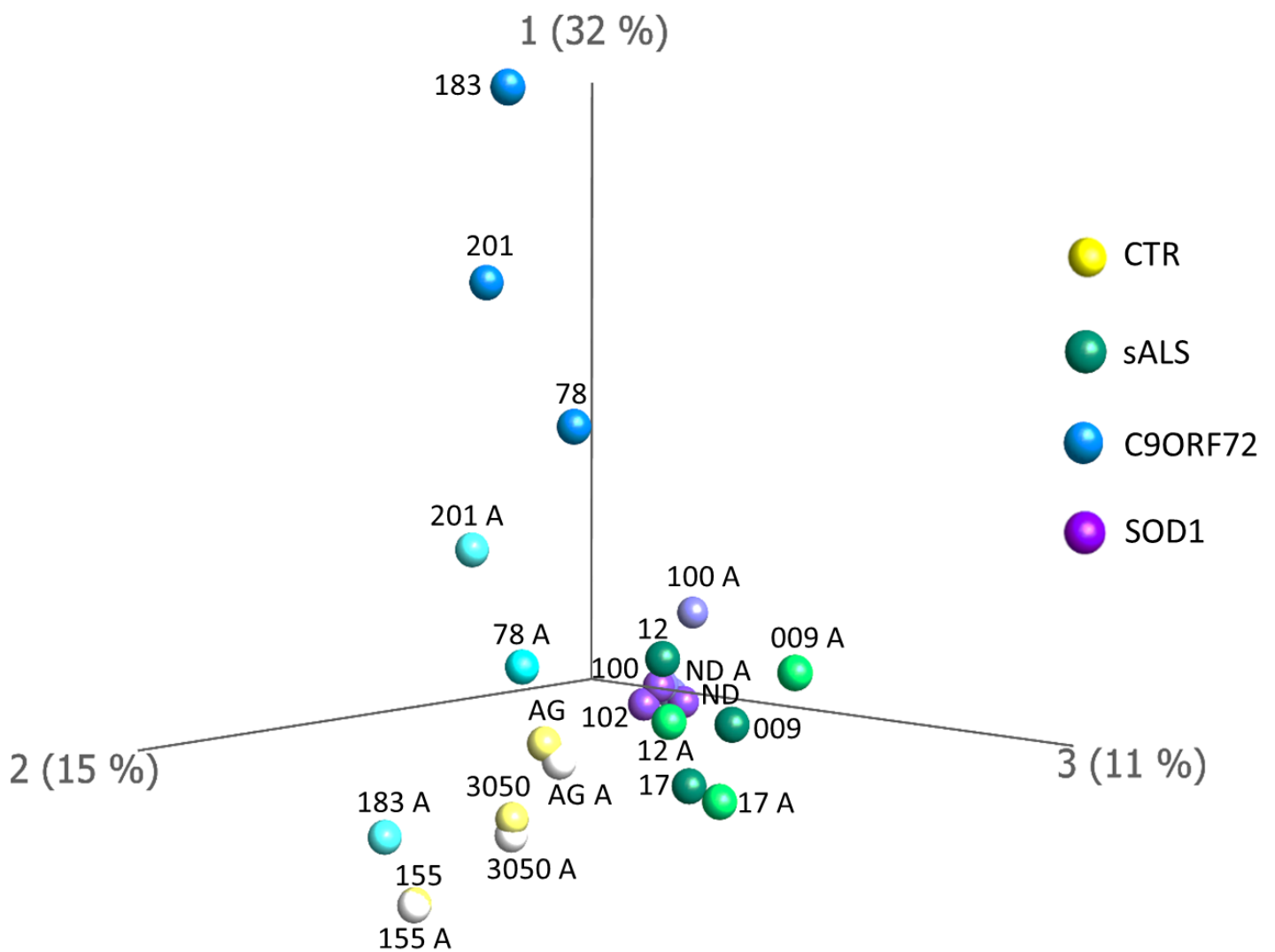


Figure 5.8 PCA plot of the gene expression values of control and patient astrocyte lines before and after andrographolide treatment (two-way ANOVA, multiple comparisons $p=0.05$ $\log_2FC < 1.5$). Subgroups are highlighted in colour; untreated samples: control = yellow, sALS = green, C9ORF72 = blue & SOD1 = purple, andrographolide treated samples: control = white, sALS = light green, C9ORF72 = light blue & SOD1 = light purple. Individual sample annotations are present on the plot. Abbreviations: A = andrographolide.

To investigate the mechanism of action of andrographolide in the patient iAstrocytes, lists of differentially regulated transcripts between each patient iAstrocyte subgroup treated with the compound and each patient iAstrocyte subgroup untreated were generated by running the comparisons in the table below (Table 5.8):

Table 5.8 List of bioinformatic comparisons for andrographolide treated iAstrocytes and gene count

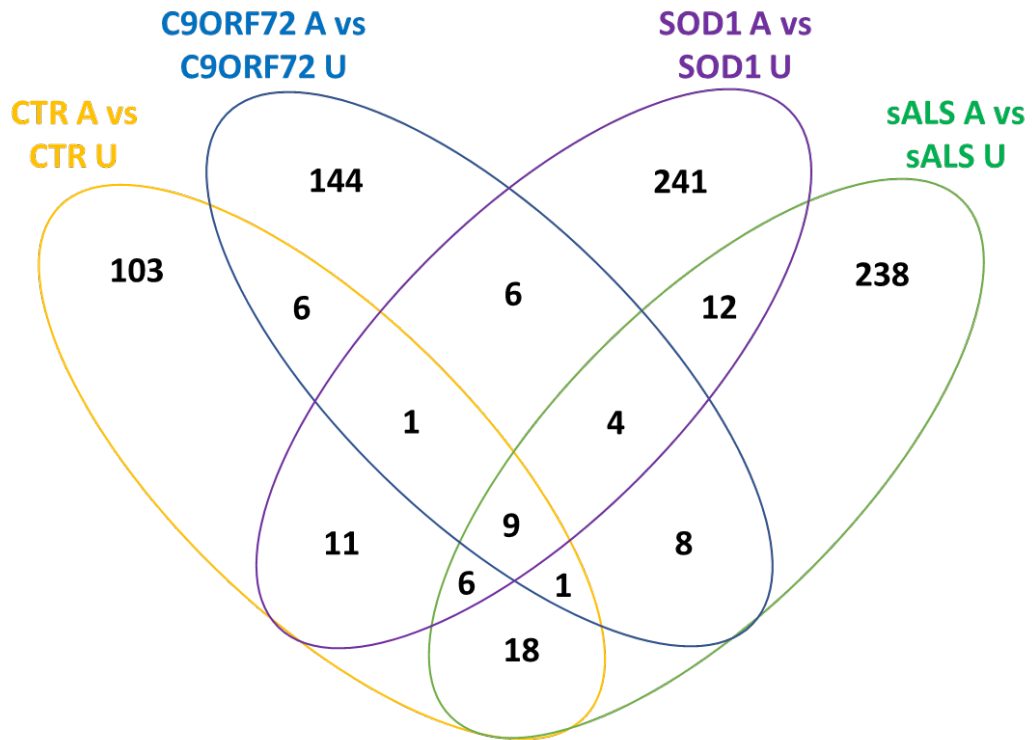
Bioinformatic comparison	Total genes	Upregulated genes	Downregulated genes
CTR A* vs CTR U#	155	88	67
C9ORF72 A vs C9ORF72 U	179	83	96
SOD1 A vs SOD1 U	290	193	97
sALS A vs sALS U	296	105	191

A* = andrographolide, U# = untreated

SOD1 & sALS iAstrocyte lines presented a similar number of unique DEGs after andrographolide treatment (Figure 5.9); SOD1 lines displayed the highest with 241 genes (155 up and 86 down) while sALS lines presented slightly less with 238 genes (62 up and 176 down). CTR and C9ORF72 patient iAstrocytes displayed roughly half of the amount of unique DEGs after andrographolide treatment (CTR = 103 DEGs, 49 up and 54 down, and C9ORF72 = 144 DEGs, 54 up and 90 down). CTR & sALS lines shared the most genes (18 DEGs, 12 up and 6 down) while less genes were shared amongst the different subgroups. Like S[+]-apomorphine, treatment with andrographolide resulted in transcriptional upregulation in the majority of genes shared between patient and control iAstrocytes.

When the original gene lists were imported into the DAVID pathway analysis software, sALS iAstrocytes displayed the highest number of significantly altered GO terms (65 pathways) with CTR, C9ORF72 and SOD1 iAstrocytes displaying half as many pathways (22, 19 and 26 pathways respectively); all pathways are presented in Supplementary 5.10-5.13. All the shared pathways between control and patient iAstrocyte subgroups after andrographolide treatment are presented in Table 5.9.

(A)



(B)

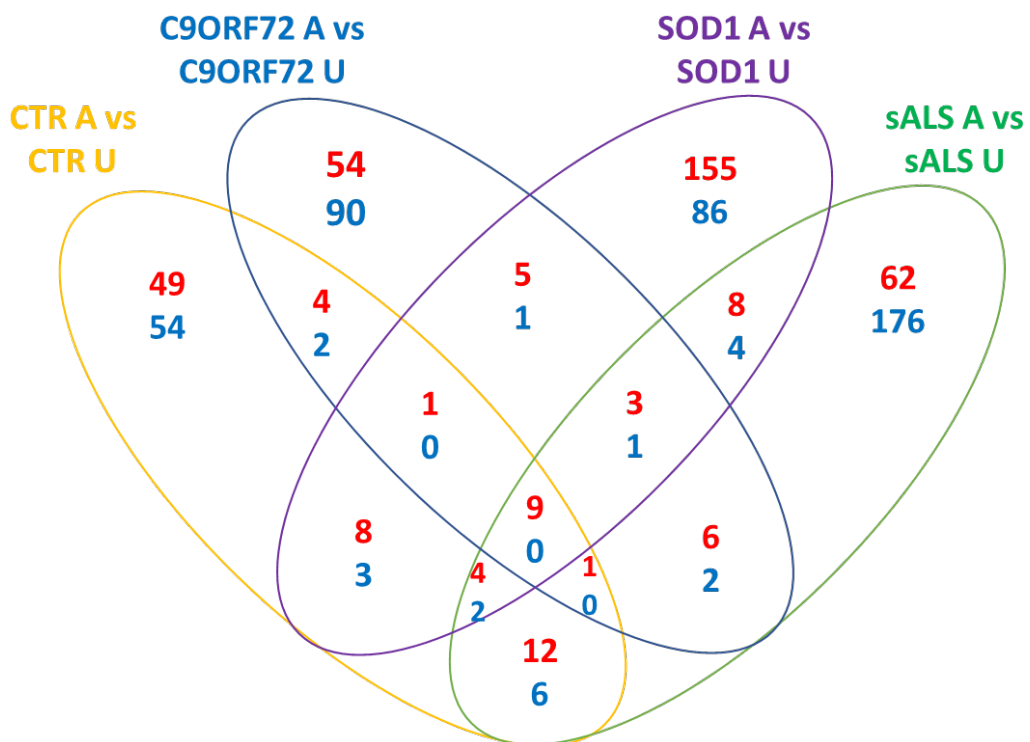


Figure 5.9 Visual representation of the DEGs shared between the control and different patient subgroups after andrographolide treatment, generated from comparisons run in Table 5.8. (A). The total number of genes shared between groups (B). The number of upregulated (red) and downregulated (blue) transcripts shared between subgroups. Abbreviations: U = untreated, A = andrographolide.

Table 5.9 List of GO pathways shared between ALS patient subgroups treated with andrographolide

Gene Ontology Term	CTR p-value	C9ORF72 p-value	SOD1 p-value	sALS p-value
Oxidation-reduction process	4.60E-04	2.40E-02	1.20E-03	4.40E-06
Aldo-keto reductase (NADP) activity	2.50E-04	2.80E-02	4.00E-04	7.70E-04
Xenobiotic metabolic process	1.70E-03	1.80E-02	3.90E-03	2.70E-04
Retinoid metabolic process	6.60E-04	-	1.40E-02	6.60E-04
Extracellular matrix organisation	3.90E-02	-	5.60E-03	7.50E-02
Metabolism of chemotherapy drugs	1.10E-03	5.50E-02	3.00E-05	7.90E-05
Ubiquitination through p62/KEAP1/NRF2 signalling	2.60E-02	-	-	4.50E-02
Positive regulation of cell proliferation	3.20E-02	-	-	9.60E-04
Response to oxidative stress	-	4.20E-02	-	3.80E-02
Inflammatory response	-	1.80E-02	-	1.20E-02
Cell adhesion	-	4.30E-02	8.50E-02	1.70E-02
Blood brain barrier and immune cell transmigration	-	1.50E-02	2.10E-02	-
Innate immune response	-	-	4.60E-02	4.00E-02

There were 3 pathways shared between the control and all patient iAstrocyte subgroups. Since andrographolide is a potent antioxidant compound, as demonstrated by the marked increase in NQO1 expression in control and patient iAstrocytes shown previously (4.2.1), it was unsurprising that andrographolide treatment resulted in DEGs related to the oxidation-reduction process across all iAstrocyte subgroups. This significant increase in *NQO1* was also detected at the RNA-seq level in all groups (CTR p-value = 1.25E-26, log2FC = +2.64, C9ORF72 p-value = 2.94E-46, log2FC = +2.84, SOD1 p-value = 3.22E-08, log2FC = +2.76, sALS p-value = 2.83E-76, log2FC = +2.82).

There was also a significant increase in antioxidant enzymes, including peroxiredoxin 1 and sulfiredoxin 1, in all iAstrocyte subgroups, however, this increase did not pass the 1.5 log2FC threshold in the CTR, C9ORF72 or SOD1 iAstrocytes (*PRDX1*: CTR p-value = 1.25E-11, log2FC = +1.15, C9ORF72 p-value = 5.93E-04, log2FC = +0.96, SOD1 p-value = 1.09E-05, log2FC = +1.01, sALS p-value = 2.79E-21, log2FC = +1.64; *SRXN1*: CTR p-value = 1.26E-11, log2FC = +1.05, C9ORF72 p-value = 9.15E-13, log2FC = +1.41, SOD1 p-value = 4.84E-05, log2FC = +0.79, sALS p-value = 1.19E-15, log2FC = +1.53); the upregulation of *SRXN1* in particular has been previously associated with MN protection while in co-culture with ALS astrocytes (Harlan *et al.*, 2019).

Interestingly, there was a significant increase in Oxidative Stress Induced Growth Inhibitor 1 across all groups (*OSGIN1*: CTR p-value = 2.71E-16, log2FC = +1.74, C9ORF72 p-value = 8.33E-23, log2FC = +2.31, SOD1 p-value = 1.10E-04, log2FC = +2.01, sALS p-value = 1.91E-16, log2FC = +2.59), which has been shown to induce cell-cycle inhibition and protection against oxidative stress in human

astrocytes (Brennan *et al.*, 2017). This could also explain the cell growth arrest I witnessed after andrographolide treatment when preparing the iAstrocytes for the functional assays, particularly in the C9ORF72 iAstrocytes.

There was a widespread increase in members of the aldo-keto reductase (AKR) gene family across all iAstrocyte groups after andrographolide treatment (*AKR1C1*: CTR p-value = 3.02E-07, log₂FC = +3.14, C9ORF72 p-value = 0.005, log₂FC = +2.27, SOD1 p-value = 2.27E-39, log₂FC = +3.14, sALS p-value = 2.04E-07, log₂FC = +3.22; *AKR1C2*: CTR p-value = 6.96E-04, log₂FC = +1.84, C9ORF72 p-value = 0.001, log₂FC = +1.55, SOD1 p-value = 2.95E-16, log₂FC = +2.49, sALS p-value = 1.55E-06, log₂FC = +2.85; *AKR1C3*: CTR p-value = 1.91E-07, log₂FC = +2.05, SOD1 p-value = 1.13E-09, log₂FC = +1.68, sALS p-value = 1.23E-17, log₂FC = +1.77). These enzymes catalyse the conversion of aldehydes and ketones into alcohols and have also been found to detoxify the toxic reactive molecules lipid peroxides, conferring resistance to cell death by ferroptosis (Gagliardi *et al.*, 2019). These transcripts have previously been identified as Nrf2-target marker genes in human cells (Jung *et al.*, 2013).

CTR and C9ORF72 iAstrocytes displayed a significant increase in expression of Dual Oxidase 1 (*DUOX1*: CTR p-value = 0.006, log₂FC = +2.48, C9ORF72 p-value = 0.007, log₂FC = +3.14), an NADPH oxidase enzyme that has previously been reported as activated by Nrf2 and promoted oxidative-stress resistance and longevity in *C. elegans* studies (Ewald *et al.*, 2017; Sasakura *et al.*, 2017).

There were an additional 3 pathways shared between CTR, SOD1 & sALS iAstrocytes. These subgroups shared DGE changes in transcripts related to the metabolism of retinoic acid (*RDH12*: CTR p-value = 0.04, log₂FC = + 2.06, SOD1 p-value = 0.001, log₂FC = +1.97; *RBP2*: CTR p-value = 0.02, log₂FC = -3.16; *RPE65*: sALS p-value = 0.02, log₂FC = -3.53); a recent study identified that retinoic acid signalling may be neuroprotective in ALS (Zhu *et al.*, 2020).

CTR and sALS iAstrocytes shared an upregulation of transcripts related to the ubiquitination of proteins through p62/KEAP1/Nrf2 signalling after andrographolide treatment; in particular E3 Ubiquitin-Protein Ligase *TRIM16* and its paralogue *TRIM16L* (*TRIM16*: CTR p-value = 6.32E-18, log₂FC = +1.68, sALS p-value = 1.36E-15, log₂FC = +1.59; *TRIM16L*: CTR p-value = 8.03E-14, log₂FC = +1.69, sALS p-value = 1.18E-14, log₂FC = +2.20). These transcripts were also significantly increased in C9ORF72 and SOD1 groups, but this increase did not pass the 1.5 log₂FC threshold (*TRIM16*: C9ORF72 p-value = 2.91E-04, log₂FC = +1.01, SOD1 p-value = 5.78E-06, log₂FC = +1.26; *TRIM16L*: C9ORF72 p-value = 5.25E-11, log₂FC = +1.35), apart from *TRIM16L* expression in SOD1 iAstrocytes (p-value = 7.53E-04, log₂FC = +1.66). The proteins encoded by these genes contribute to a variety of cellular processes including innate immunity, apoptosis and autophagy (Nisole *et al.* 2005;

Hatakeyama 2017), therefore, the significant increase in these transcripts might explain the significant increase in p62 protein after andrographolide treatment (4.2.5).

Like S[+]-apomorphine, treatment with andrographolide resulted in DGE changes in transcripts related to inflammation and the immune response in C9ORF72 and sALS lines. C9ORF72 iAstrocytes displayed a reduced expression of NLR Family Pyrin Domain Containing 3 (*NLRP3*; p-value = 0.04, log₂FC = -3.20), which is a sensory component of the NLRP3 inflammasome, while sALS iAstrocytes displayed further reduction in the expression of transcripts related to migratory cytokines (*CXCL1*: p-value = 7.51E-04, log₂FC = -3.73; *CXCL10*: p-value = 1.97E-05, log₂FC = -2.37; *CXCL5*: p-value = 0.03, log₂FC = -4.03; *CXCL6*: p-value = 0.02, log₂FC = -3.95) as well as a reduction in *TNF* in sALS iAstrocytes (p-value = 0.02, log₂FC = -1.51). Andrographolide treatment in SOD1 iAstrocytes reduced the expression of Colony Stimulating Factor 2 Receptor Subunit Beta (*CSF2RB*; p-value = 0.02, log₂FC = -2.01) and increased the expression of Interleukin 23 Receptor (*IL23R*; p-value = 0.02, log₂FC = +4.57). There was also a reduction in *LBP* which was described previously as a suppressor of the TNF pathway (p-value = 0.03, log₂FC = -2.74), implying an increase in inflammation which might explain why andrographolide treatment provided little benefit to MNs co-cultured with SOD1 iAstrocytes.

In summary, the widespread upregulation of transcripts related to the oxidation-reduction and antioxidant pathways have confirmed that andrographolide was the more potent antioxidant compound tested in this study. Similar to S[+]-apomorphine, there were also DEGs related to retinoic acid metabolism after andrographolide treatment, however, these were only shared between CTR, SOD1 and sALS lines, which also benefitted from S[+]-apomorphine, implying a potential shared mechanism of action between the two compounds. There were also DGE changes in transcripts related to neuroinflammation, however there appeared to be a more consistent reduction in pro-inflammatory transcripts in C9ORF72 and sALS lines after andrographolide treatment compared to SOD1 iAstrocytes. Interestingly, andrographolide treatment led to the increase in *TRIM16* across both control and patient iAstrocyte groups which could potentially be associated with the increase in p62 expression observed in the iAstrocytes after andrographolide treatment (4.2.5).

5.2.6. Riluzole treatment across patient subgroups

Riluzole is the current drug prescribed for ALS patients, so I decided to identify the mechanisms of action of the drug across the patient iAstrocyte groups as well as comparing the beneficial effects of riluzole with the two antioxidant compounds.

As with the other compounds used in this study, riluzole also had little effect on the gene expression in the control iAstrocytes (Figure 5.10). While riluzole treatment still induced DGE changes in the C9ORF72 cell lines, this was the mildest change seen out of the three compounds. It also had a mild effect in the sALS patient group, while it appeared to induce gene expression changes in SOD1 patient lines 100 & ND29505 away from the control iAstrocytes.

To investigate the mechanism of action of riluzole in the patient iAstrocytes, lists of differentially regulated transcripts between each patient iAstrocyte subgroup treated with the compound and each patient iAstrocyte subgroup untreated were generated by running the comparisons in the table below (Table 5.10):

Table 5.10 List of bioinformatic comparisons for riluzole treated iAstrocytes and gene count

Bioinformatic comparison	Total genes	Upregulated genes	Downregulated genes
CTR R* vs CTR U#	92	45	47
C9ORF72 R vs C9ORF72 U	85	38	47
SOD1 R vs SOD1 U	215	161	54
sALS R vs sALS U	192	55	137

R* = riluzole, U# = untreated

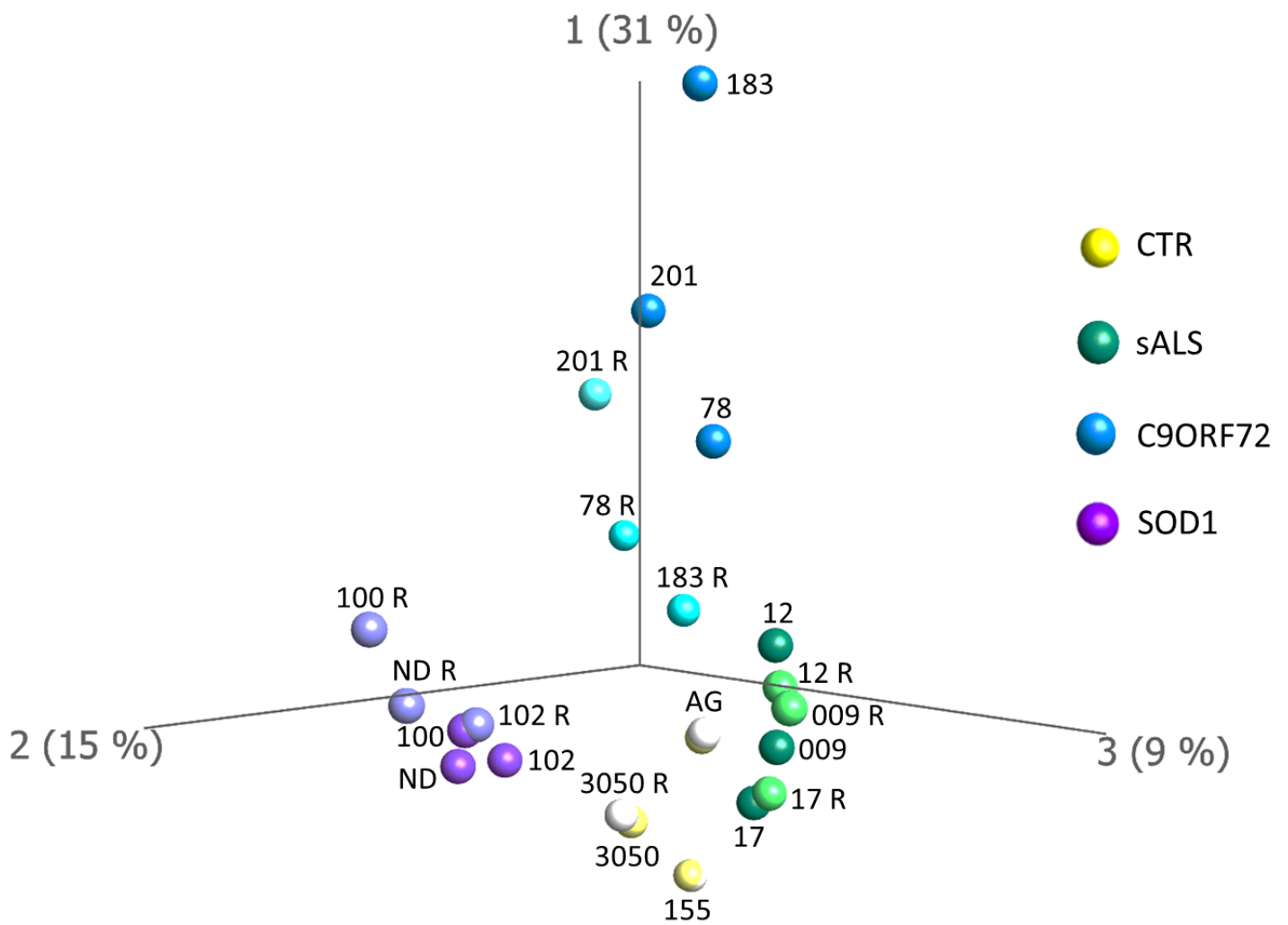


Figure 5.10 PCA plot of the control and patient astrocyte lines before and after riluzole treatment (two-way ANOVA, multiple comparisons $p=0.05$ $\log_2FC < 1.5$). Subgroups are highlighted in colour; untreated samples: control = yellow, sALS = green, C9ORF72 = blue & SOD1 = purple, riluzole treated samples: control = white, sALS = light green, C9ORF72 = light blue & SOD1 = light purple. Individual sample annotations are present on the plot. Abbreviations: R = riluzole.

SOD1 and sALS iAstrocyte lines presented a similar number of unique DEGs after riluzole treatment (Figure 5.11); SOD1 lines displayed the highest with 199 genes (150 up and 49 down) while sALS lines presented slightly less with 178 genes (44 up and 134 down). CTR and C9ORF72 patient iAstrocytes displayed roughly half of the amount of unique DEGs after riluzole treatment (CTR = 82 DEGs, 35 up and 47 down, C9ORF72 = 69 DEGs, 25 up and 44 down). Only a handful of transcripts were shared between subgroups; the most transcripts were shared between C9ORF & SOD1 (7 DEGs, 5 up and 2 down). While there were few DEGs after riluzole treatment, most shared genes displayed upregulation, as was common with the previous compounds.

When the original gene lists were imported into the DAVID pathway analysis software, sALS iAstrocytes displayed the highest number of significantly altered GO terms (24 pathways) while CTR and SOD1 iAstrocytes presented half as many pathways (15 and 12 pathways respectively); all pathways are presented in Supplementary 5.14-5.16. C9ORF72 iAstrocytes displayed no significantly altered pathways. The only shared pathways between subgroups were between SOD1 & sALS iAstrocytes treated with riluzole as shown in Table 5.11; these pathways were related to cellular adhesion and cell-cell signalling.

Table 5.11 List of GO pathways shared between ALS patient subgroups treated with riluzole

Gene Ontology Term	CTR p-value	C9ORF72 p-value	SOD1 p-value	sALS p-value
Homophilic cell adhesion via plasma membrane adhesion molecules	-	-	1.40E-02	2.50E-02
Cell adhesion	-	-	1.80E-02	1.40E-03

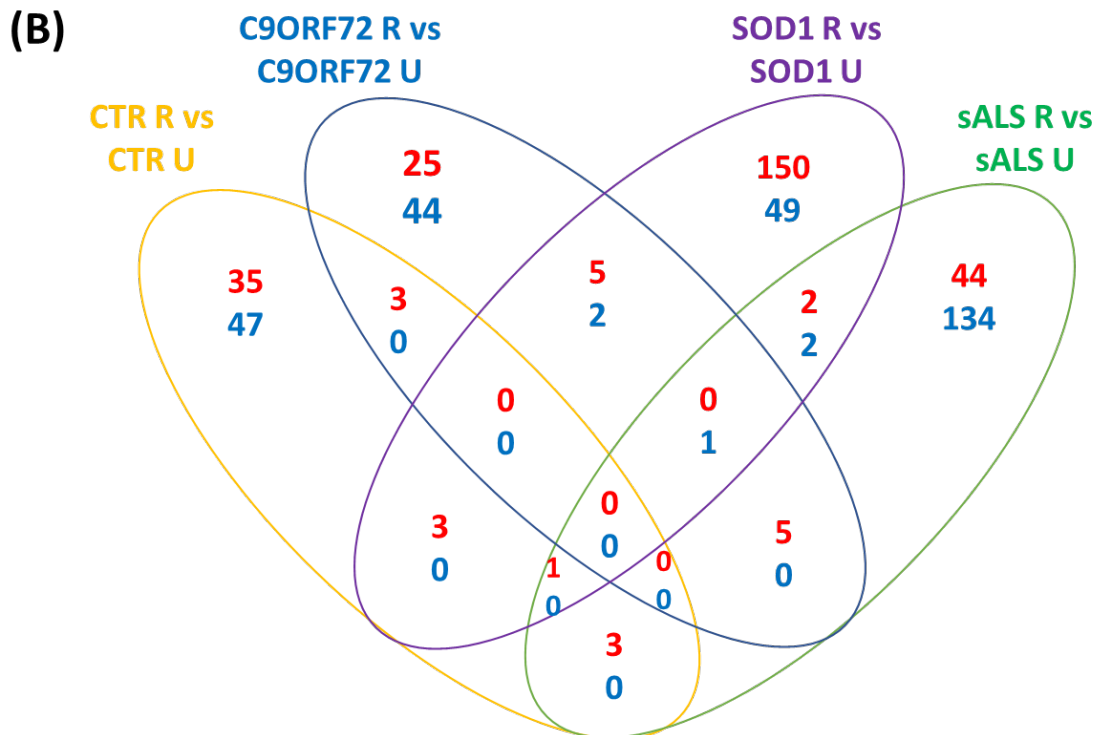
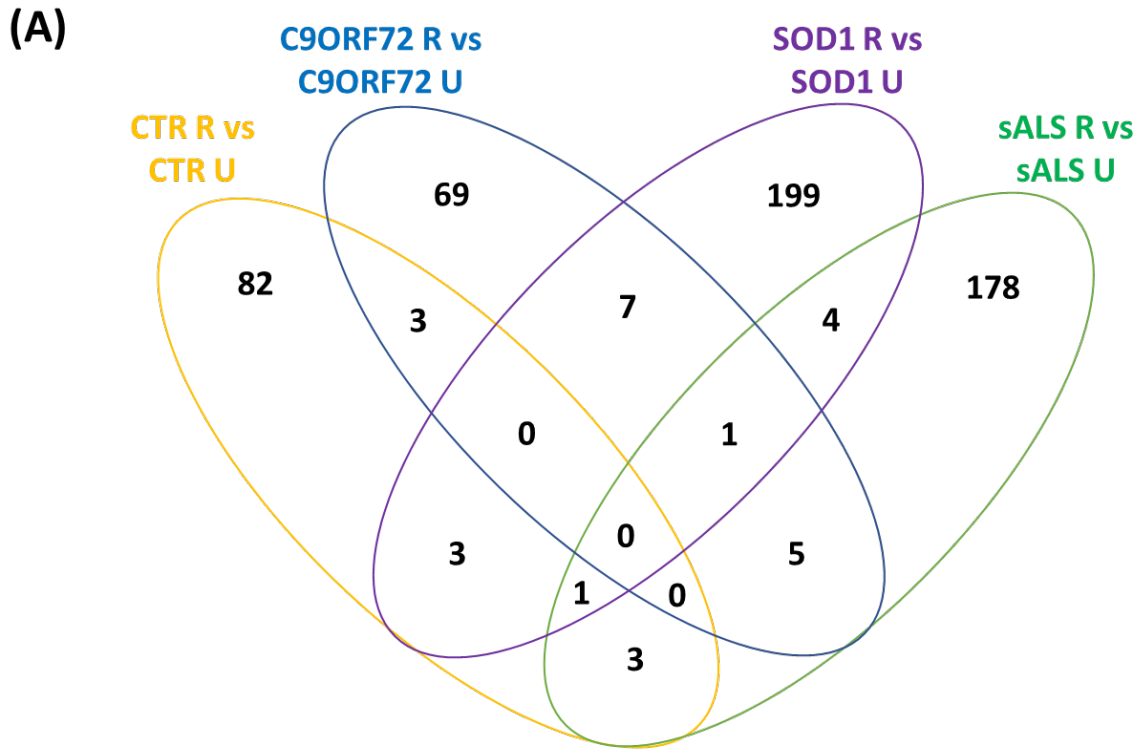


Figure 5.11 Visual representation of the DEGs shared between the control and different patient subgroups after riluzole treatment, generated from comparisons run in Table 5.10. (A). The total number of genes shared between groups. (B). The number of upregulated (red) and downregulated (blue) transcripts shared between subgroups. Abbreviations: R = riluzole.

In SOD1 iAstrocytes, there was widespread upregulation of genes related to protocadherin alpha (*PCDHA5*: p-value = 0.04, log₂FC = +2.99; *PCDHAC2*: p-value = 0.04, log₂FC = +3.65) and gamma subfamilies (*PCDHGA3*: p-value = 2.65E-04, log₂FC = +5.25; *PCDHGB1*: p-value = 0.02, log₂FC = +1.82; *PCDHGC4*: p-value = 0.02, log₂FC = +2.92). All of these genes are proposed to be involved in the establishment and maintenance of neuronal connections, in particular, protocadherin gamma C4 (*Pcdh-γC4*), which was upregulated at RNA level, is associated with contact points between neurons and astrocytes (Miralles *et al.* 2020). SOD1 iAstrocytes also displayed a significant upregulation in *NCAM2* (p-value = 0.02, log₂FC = +2.78). Upregulation of *NCAM1* has rescued MNs from models of ALS & SCI (Sokolov *et al.*, 2018).

On the other hand, sALS iAstrocytes displayed a downregulation in neuronal cell adhesion genes (*CDH2*: p-value = 0.01, log₂FC = -1.54; *CDH6*: p-value = 0.006, log₂FC = -1.83, *CADM1*: p-value = 7.45E-04, log₂FC = -2.44; *DSG2*: p-value = 0.01, log₂FC = -3.53), which have also been associated with inflammation in astrocytes (Hara *et al.*, 2017; Masvekar *et al.*, 2019). There was also a downregulation in CD molecules (*CD22*: p-value = 0.05, log₂FC = -2.40; *CD24*: p-value = 0.02, log₂FC = -2.32). Increased expression of CD24 has previously been identified in astrocytes in mice and patients with TBI (Li *et al.* 2014). There was an observed significant decrease in interleukin 32 (*IL32*: p-value = 0.02, log₂FC = -2.25); IL-32 expression in cultured astrocytes increased the production of ROS and nitric oxide (NO) as well as expression of inducible nitric oxide synthase (iNOS), implying riluzole may have anti-inflammatory properties in some lines (Cho *et al.*, 2010).

Perositin, a secreted protein, has been described as playing an essential role in axonal regeneration after SCI in a cell therapy model (Shih *et al.*, 2014); interestingly, riluzole treatment promoted a significant reduction in this transcript in sALS astrocytes (*POSTN*: p-value = 0.05, log₂FC = -2.39). Similarly, there was a reduced expression of tenascin R in sALS lines (*TNR*: p-value = 0.03, log₂FC = -2.70) which also appeared to be counter-intuitive since tenascin R regulates glutamate uptake in adult brain astrocytes (Okuda *et al.*, 2014). These mild DEG changes in patient iAstrocytes might explain why riluzole treatment only provides a modest benefit to patients.

In summary, there were the mildest DGE changes observed in the iAstrocytes after riluzole treatment which is reflective of the mild response to riluzole in both the co-culture data and the functional assays. Riluzole treatment appeared to induce different transcriptional changes in specific cell lines; while there was little change in either CTR or C9ORF72 iAstrocytes, there was a further increase in protocadherin-related transcripts presented in SOD1 iAstrocytes. There were DGE changes displayed in sALS cell lines after riluzole treatment that could potentially have a negative

effect on axonal regeneration and glutamate uptake, therefore possibly explaining why riluzole only provided a mild response in these lines.

5.3. Discussion

To fully characterise and investigate the differences between patient iAstrocytes, as well as the mechanism of action of the antioxidant compounds, RNA-sequencing of the transcriptome profile was adopted to identify the DGE changes occurring within the cells before and after drug treatment. This analysis revealed which cellular pathways were commonly affected by drug treatment in different genetic patient subgroups as well as which were uniquely altered in each group. By investigating pathway changes shared between different patient subgroups after treatment, the mechanisms of action of S[+]-apomorphine and andrographolide could be explored, assisting in the explanation as to why specific patients respond to one drug over another. This analysis will be the focus of Chapter 6.

A problem identified during the analysis of these data was the residual rRNA contamination in all the CTR 155 samples and the C9ORF72 183 samples that were treated with the antioxidant compounds, which led them to have a severely reduced number of reads. To prevent this rRNA contamination from skewing the data, these samples were removed from the DGE analysis presented in this chapter. This means that there were not homogenous numbers of samples between the patient vs the control comparisons, thus leaving some of the comparisons underpowered. In addition, the removal of C9ORF72 183 samples was a disadvantage because this patient line showed significantly improved MN survival when treated with both S[+]-apomorphine and andrographolide.

In this study, the use of GRASPs was particularly useful, as, by isolating only translating RNA molecules, it reduced the noise from other transcripts that would undergo decay (Houseley and Tollervey, 2009) or were stored in RNA pools in cellular stress conditions, including stress granule formation (Parton *et al.* 2014). This allowed us to obtain robust p-values and larger fold changes than the classic whole cell transcriptomics (unpublished data, Dodd *et al.*).

5.3.1. Baseline gene expression in patient subgroups vs controls

Since ALS is a heterogenous disease, it is important that the model we use is reflective of the patient variability. In the previous two chapters, I have discussed how the iAstrocyte lines differ in terms of disease pathology and toxicity, and in this chapter, I have focused on the gene expression changes underlying these differences. The PCA plot demonstrated how the patients and controls clustered

and formed subgroups based upon the genotype and disease status. The control lines showed the variability that was to be expected from non-ALS controls, as these individuals did not share any particular characteristic apart from not having ALS, while they were still different enough to be separated from the patient groups. The SOD1 genetic lines were the closest clustering groups; SOD1 100 and 102 lines were from genetically related individuals, and the C9ORF72 lines separated from the controls according to their toxicity. The sALS group also showed a degree of variability because they did not share a specific genetic mutation; sALS 17 appeared to cluster more closely to the SOD1 lines than the other sALS lines on the PCA plot, potentially indicating that this patient line shares common transcriptional alteration with SOD1 patients, especially since sALS 17 also presented a higher number of misfolded SOD1 protein aggregates compared to the other sALS lines (3.2.2.2).

Regardless of these differences, all three patient subgroups shared 14 GO-BP pathways that were significantly altered in comparison to iAstrocytes from non-ALS individuals. These included axonal guidance, glutamatergic synaptic transmission, calcium transport, vesicle transport and inflammation. This last pathway was just below significance as a GO-BP term in SOD1 iAstrocytes, which, however, displayed significant alteration specifically of the Type I IFN pathway. These pathways are recognised to be involved in the pathology of ALS (Schmidt *et al.* 2009; Armada-Moreira *et al.* 2020; Leal and Gomes 2015; Ferrara *et al.* 2018; McCauley and Baloh 2019), which represents a validation of our translome approach. These data, however, have not only confirmed other findings already present in the literature, but have also identified new findings and generated new hypotheses. In particular, there was strong evidence that altered excitatory neurotransmission has a key role in ALS disease progression (King *et al.* 2016) and that this pathway is tightly regulated by astrocytes (Armada-Moreira *et al.*, 2020). In the following sections, I will focus on pathways that have been identified as commonly dysregulated in various ALS genetic subgroups.

5.3.1.1. Glutamate excitotoxicity and neuroinflammation

In most neurodegenerative diseases, excitotoxicity has been linked to reduced glutamate uptake by astrocytes via glutamate transporters EAAT1 and EAAT2, with consequent glutamate accumulation in the synaptic cleft and neuronal hyperstimulation (Howland *et al.* 2002; Simpson *et al.* 2010). However, this reduction in the expression of glutamate transporters was not seen in the patient iAstrocytes *in vitro*, neither at the protein (3.2.4.2) or RNA level (5.2.3). Instead, there were significant DGE changes in metabotropic and ionotropic glutamate receptor transcripts, as well as an increased expression in NMDAR2B in C9ORF72 patient iAstrocytes (3.2.4.2).

Metabotropic glutamate receptors are G-protein coupled receptors that can be subdivided into three groups depending on the signalling transduction pathway, amino acid sequence homology and selectivity of agonists and antagonists (Planas-Fontánez *et al.* 2020). There was a shared increase in expression of the Group III subtype *mGluR4* in all patient lines, while C9ORF72 and sALS iAstrocytes also displayed an increased expression of Group II subtype *mGluR3*. Both groups of receptors are responsible for the negative regulation of adenylate cyclase as well as the activation of MAPK and phosphatidylinositol 3-kinase (PI3K) pathways (Spampinato *et al.*, 2018). *mGluR3* is the most abundant receptor in adult human cortical astrocytes as well as mouse cortical and hippocampal astrocytes and is suspected not to have a role in gliotransmitter release, since *mGluR3* agonists failed to trigger a calcium increase within astrocytes (Sun *et al.*, 2013). The increased expression of both *mGluR3* and *mGluR4* was observed in aged mouse astrocytes, potentially indicating that these DGE changes occur because of ageing rather than disease (Orre *et al.*, 2014). From this, I can hypothesise that ageing has an impact on the disease mechanisms; the baseline expression levels of these transcripts are increased with age and the disease exacerbates this increase further, leading to the observed pathology.

While the actions of Group II *mGluRs* in SOD1 astrocytes has not been investigated, injection of a Group II *mGluR* agonist into SOD1 mice reduced neuronal death and increased GDNF levels in the spinal cord; this GDNF release was enhanced by *mGluR3* in wild-type astrocytes (Battaglia *et al.*, 2015). Interestingly, this receptor was increased in both C9ORF72 and sALS lines but not in SOD1 iAstrocytes, implying that *mGluR3* upregulation may be beneficial within this genetic phenotype.

There was a strong expression of *mGluR4* observed within a population of reactive astrocytes localised to active lesions in tissue from patient with MS, suggesting a role for these receptor subtypes in the inflammatory response (Geurts *et al.*, 2005), which is increased in all patient groups. This implies that metabotropic receptors play a larger role in neuroinflammation in the patient iAstrocytes rather than glutamate buffering.

On the other hand, ionotropic glutamate receptors, in particular NMDARs, regulate calcium and other ionic fluxes in response to glutamate. While well characterised in neurons, research into NMDARs in astrocytes is more recent, but transcripts for all seven NMDAR subunits (*GluN1*, *GluN2A-D* & *GluN3A-B*) have all been identified in both human and rat astrocytes *in vitro* (Lee *et al.*, 2010; Montes de Oca Balderas and Aguilera, 2015), while *GluN2B* and *GluN3A* were also highly expressed *in vivo* (Rusnakova *et al.*, 2013).

There is strong evidence linking neuroinflammatory and excitotoxic processes in neurodegenerative disease. Elevated levels of TNF- α have been reported in AD, PD, MS as well as ALS (Mogi *et al.*, 1994;

Rieckmann *et al.*, 1995; Poloni *et al.*, 2000; Alvarez *et al.*, 2007). Interestingly, the upregulation of TNF transcripts was only witnessed in C9ORF72 and sALS patient iAstrocytes, both of which displayed higher levels of extracellular glutamate in monoculture or co-culture with MNs. TNF- α signalling can potentiate glutamate-mediated excitotoxicity through two mechanisms: either indirectly by inhibiting glutamate transporters or directly by altering the localisation of ionotropic receptors (Olmos and Lladó, 2014). The reduced expression of astrocytic EAAT2 is commonly reported in ALS; Wang *et al.* (2003) demonstrated an inhibition of glutamate uptake through downregulation of EAAT2 mRNA after exposure to TNF- α in primary human astrocytes. However, there was no reduction in EAAT2 observed in the patient iAstrocyte subgroups in this study. Similarly, Zou and Crews (2005) found that TNF- α exposure reduced glutamate transport without influencing EAAT2 expression in organotypic brain slice cultures, however, TNF- α potentiation of glutamate excitotoxicity was blocked by NMDA receptor antagonists, highlighting a role for ionotropic glutamate receptors.

Interestingly, there were significant DGE changes observed in transcripts associated with ionotropic glutamate receptors across all patient subgroups, in particular the C9ORF72 iAstrocyte lines. TNF- α signalling in astrocytes initiates an intracellular cascade, starting with the generation of prostaglandin E₂ which leads to the elevation of intracellular calcium, resulting in glutamate exocytosis (Bezzi *et al.*, 2001). The extracellular glutamate binds to the NMDA receptors, stimulating the expression of these receptors, hence the DGE changes in the transcripts as well as the increased protein expression of NMDAR2B.

The function and calcium permeability of astrocytic NMDARs has been debated for several years (Balderas and Hernández 2018), however, studies have provided evidence that different NMDAR subunits have different properties. All patient iAstrocytes shared an increase in the expression of *GRIN3A*, a subunit of NMDA receptors which is reportedly responsible for low calcium permeability and significantly reduced sensitivity to magnesium in astrocytes (Palygin *et al.*, 2010). Dzamba *et al.* (2015) also presented an upregulation of the *GRIN3A* gene in astrocytes after ischemic insult. Stimulation by NMDA evoked a largely reduced influx of calcium into the glial cells after ischaemia, implying that increased expression of *GRIN3A* may reduce calcium permeability of NMDA receptors.

On the other hand, the *GRIN2B* subunit was reported to mediate transient calcium signals in astrocytic NMDA receptors and this signalling was dependent on calcium release from intracellular stores (Gérard and Hansson, 2012). While the *GRIN2B* transcript was downregulated in both C9ORF72 and sALS lines, C9ORF72 lines displayed a significant increase in the protein level of the receptor (3.2.4.2), leading to speculation that sALS iAstrocytes may also present increased

NMDAR2B protein expression. This has led to the formulation of a new hypothesis that the extracellular glutamate stimulated the activity of the astrocytic NMDA receptors, hence the increased expression of NMDAR2B, leading to elevated intracellular calcium levels and excitotoxic glutamate release from the astrocytes, resulting in accumulation of extracellular glutamate in the media, as reported in 3.2.4.2.

Glutamate uptake by astrocytes relies on the normal functioning of sodium-dependent amino acid transporters which couple the transport of Na⁺ and K⁺ ions, establishing a concentration gradient that drives glutamate into the cell (Anderson and Swanson, 2000). During pathophysiological events, such as brain ischaemia, the dysregulation of this ionic gradient, specifically increased extracellular K⁺ levels, results in the reversal of the action of glutamate transporters (Malarkey and Parpura, 2008). C9ORF72 iAstrocytes displayed a significant increase in transcripts related to HCN channels, which has previously been reported in reactive astrocytes following ischaemia (Honsa *et al.*, 2014), implying a dysregulation of the Na⁺/K⁺ concentration gradient, potentially leading to transporter reversal and increased extracellular glutamate levels (3.2.4). The study by Molz *et al.* (2008) reported that NMDA receptor antagonists prevented glutamate/NMDA-induced cell damage while glutamate transport inhibitors blocked glutamate release in hippocampal slices, suggesting that both hypotheses could play a role in the accumulation of extracellular glutamate observed in cultures of C9ORF72 iAstrocytes.

There were no DGE changes in TNF related transcripts in SOD1 iAstrocytes and this is consistent with findings reported in the SOD1 mouse model (Gowing *et al.*, 2006). Instead, SOD1 iAstrocytes displayed a dysregulation in the Type 1 IFN signalling pathway. Type I interferons induce innate and adaptive immune responses by binding to heterodimeric receptors and triggering the phosphorylation of JAK1 and TYK2 kinases, which in turn phosphorylate STAT1/2 transcription factors, activating the transcription of interferon stimulated genes (ISGs) (Wang *et al.* 2011). The increase of ISGs were previously reported in the spinal cord of *SOD1 G93A* mice at the presymptomatic stage; microarray analysis identified significantly higher mRNA levels of ISGs in *SOD1* mice compared to wild type. In particular, *IFI27L2A*, *IFIT3* and *ISG15* (Wang *et al.* 2011), which were all found to be downregulated in SOD1 iAstrocytes in this study (*IFIT3*: p-value = 0.02, log₂FC = -2.02; *ISG15*: p-value = 0.01, log₂FC = -2.76). One explanation for these differences could be the absence of MNs; the authors found that the spatial expression of ISGs in *SOD1* mice suggested that activation of IFN signalling is triggered by pathological changes in MNs as well as the fact that cultured astrocytes showed the most robust ISG expression upon stimulation with IFN (Wang *et al.* 2011). Another hypothesis could be that the iAstrocytes are reacting to the toxic environment and attempting to protect the MNs by downregulating IFN signalling. Nevertheless, the SOD1 iAstrocytes

demonstrated an impairment in inflammation and the immune response which is commonly reported in SOD1-ALS as contributing to MN death (Aebischer *et al.*, 2011).

5.3.1.2. Vesicle trafficking

The trafficking of intracellular vesicles, especially the removal of misfolded proteins through the autophagic machinery, is a key element reported in ALS pathology (Burk and Pasterkamp, 2019). Rab3 proteins are essential for vesicle docking and exocytosis in cells; Hong *et al.* (2016) demonstrated that Rab3a was responsible for BDNF secretion from astrocytes. The overexpression of Rab3 proteins was shown to increase vesicle docking at the plasma membrane in PC12 cells (Martelli *et al.*, 2000). Therefore, I could speculate that there may be an increased secretion of exocytotic vesicles in patient lines since they all presented a significant upregulation of *RAB3B* and *RAB3C* transcripts. Anlauf and Derouiche (2005) found that glutamate-containing exocytosis vesicles displayed co-localisation with the Rab3 protein; Rab3 attachment to the glutamate-containing vesicles occurred shortly before it reached the cell membrane and was incorporated during vesicle fusion. In this case, the upregulation of *RAB3B/RAB3C* transcripts could also explain the increased extracellular glutamate levels in the C9ORF72 iAstrocytes since this implies a higher rate of glutamate exocytosis. However, sALS and SOD1 iAstrocytes also displayed an increased expression of these transcripts, therefore these lines could be secreting other molecules.

Rab6 also mediates vesicular transport, particularly, the retrograde trafficking from the Golgi to the ER (Scheper *et al.*, 2007). It is thought that Rab6 mediates the transport of misfolded proteins that have escaped ER quality control, back to the ER for refolding or ubiquitination (Arvan *et al.*, 2002). While there is little reported about Rab6 in astrocytes, the expression of Rab6 was increased in brain tissue from AD patients (Scheper *et al.*, 2007). The authors proposed that the increased retrograde trafficking to the ER mediated by Rab6 promotes the removal of protein from the Golgi, however, when the burden is too high, this can result in ER stress in neurons. ER stress is commonly reported in ALS (Matus *et al.*, 2013), and since Rab6 transcripts were downregulated in both C9ORF72 and sALS iAstrocytes (*RAB6D*: C9ORF72 p-value = 3.91E-07, log2FC = -22.96, sALS p-value = 0.02, log2FC = -10.76; *RAB6B*: sALS p-value = 0.03, log2FC = -1.73), it could be hypothesised that the lack of Rab6-mediated vesicle trafficking could add to the accumulation of misfolded proteins and ER stress seen in the iAstrocytes in the functional screening, particularly the accumulation of p62.

A number of Rab GTPases are responsible for different stages of the autophagy process. The autophagy process has been described in previous chapters (3.2.2.3, 4.2.4) because there was a significant increase in p62 expression across all patient iAstrocyte lines compared with the controls,

as well as a skewed ratio between LC3-I and LC3-II proteins in the C9ORF72 iAstrocytes, indicating an impairment in the autophagic machinery. Only the C9ORF72 iAstrocytes presented an upregulation of the transcript *RAB11FIP1* (p-value = 0.05, log₂FC = +2.15), which encodes a Rab11 effector protein. Rab11 is required at the 'completion' stage of the autophagosome; it is responsible for delivering multivesicular bodies to the autophagosome which are required for maturation (Webster *et al.*, 2016). This change in gene expression, as well as the skewed ratio for LC3-I/LC3-II, implies that the formation of autophagosomes cannot reach completion in the C9ORF72 iAstrocytes and the increased p62 expression, particularly the diffuse staining seen in 3.2.2.3, could be the result of a lack of correct recruitment of protein cargoes to the autophagosome.

5.3.1.3. Cholesterol and axonal guidance

The patient subgroups also displayed multiple dysregulated pathways that were unique to each group, demonstrating the heterogeneity seen in ALS patients and the different clinical phenotypes observed, for example, in SOD1 vs C9ORF72 patients (Millecamps *et al.*, 2012). In fact, the C9ORF72 iAstrocytes lines presented the highest number of DEGs and this was reflective in the diversity of the GO-BP pathways depicted in Table 5.3. Two pathways of particular interest in C9ORF72 iAstrocytes were cholesterol transport and the semaphorin-plexin pathway.

Cholesterol is an essential component of the brain tissue; ~20% of the whole body's cholesterol is found within the brain (Björkhem and Meaney, 2004). The majority is enclosed in myelin sheaths to insulate axons, while the rest is present in the plasma membranes of neurons and astrocytes to maintain morphology and synaptic transmission (Zhang and Liu, 2015). Cholesterol depletion within neurons disrupts synaptic vesicle exocytosis, neuronal activity and transmission, leading to axonal and synaptic degeneration, therefore defects in cholesterol metabolism have been associated with Huntington's disease (HD) and AD as well as cognitive deficits typical with ageing (Block *et al.*, 2010; Di Paolo and Kim, 2011).

Adult neurons rely on surrounding oligodendrocytes and astrocytes for the synthesis and transport of cholesterol. Apolipoprotein E (ApoE) is the main transport protein for cholesterol; ApoE-containing lipoproteins are secreted by astrocytes and bind to lipoprotein receptors to be taken up into neurons. ATP-binding cassette (ABC) transporters are responsible for the formation of ApoE-containing lipoproteins; it is thought that the ABCA1 transporter catalyses the initial transfer of lipids and ApoE to form particles which are then fully lipidated in a second phase of efflux mediated by ABCG1 (Karten *et al.*, 2006). The C9ORF72 iAstrocyte lines displayed a significant upregulation of the *ABCG1* transcript, implying an increased efflux of cholesterol and lipoproteins from the astrocytes.

Patients with AD have a higher level of cholesterol retention in the brain and this contributes to the production of A β (Xiong *et al.*, 2008). The C9ORF72 repeat expansion is commonly associated with FTD, the cognitive form of ALS, therefore there may be similarities in cholesterol metabolism deficits and their potential contribution to cognitive dysfunction between the two neurodegenerative disorders.

The C9ORF72 iAstrocytes also displayed a significant downregulation in the *LCAT* transcript. The reduction in *LCAT* activity has previously been reported in patients with AD and Down's syndrome and it is thought to be associated with an impairment in cholesterol esterification (Demeester *et al.*, 2000). Roughly 1% of cholesterol exists in an esterified form which is used to store excess cholesterol within the cell (Zhang and Liu, 2015). The combination of reduced cholesterol storage and increased cholesterol efflux from the astrocytes suggests that the C9ORF72 iAstrocytes are continuously exporting lipoproteins to the surrounding MNs.

All patient iAstrocytes demonstrated dysregulation in axonal guidance; there was a widespread downregulation of plexin A2 across all patient subgroups and there were DGE changes in *Sema3* related transcripts in each group. Class A plexins serve as receptors for *Sema3* proteins in both neurons and glial cells (Zhou *et al.* 2008). While not fully explored in astrocytes, *Sema3* signalling in neurons results in axonal repulsion as well as inhibition of PI3K-Akt signalling, cell cycle division and MAPK signalling, therefore the dysregulation of the semaphorin-plexin pathway within astrocytes could be detrimental to astrocyte health as well as interfering with neuronal-glial crosstalk.

C9ORF72 iAstrocytes presented a significant upregulation of *SEMA3A* which acts as a molecular inhibitor of axonal regeneration during SCI (Kaneko *et al.*, 2006). Increased expression of *Sema3A* has been previously reported in a SOD1 mouse model and ALS patients (De Winter *et al.*, 2006; Körner *et al.*, 2016). *Sema3A* has also been linked to extracellular calcium influx from MNs and downregulation of T-cell activation, both of which could contribute to MN death in ALS (Lepelletier *et al.*, 2006; Yamane *et al.*, 2012). In addition, analysis of extracellular vesicles secreted by the C9ORF72 iAstrocytes identified a reduced secretion of the microRNA miR-494-3p, which is a negative regulator of *SEMA3A*, compared to control iAstrocytes (Varcianna *et al.*, 2019). When healthy MNs were cultured in C9ORF72 iAstrocyte conditioned media, there was an increased *SEMA3A* expression in MNs, which affected neurite network maintenance and MN survival *in vitro*. Therefore, the increased expression of *SEMA3A* in C9ORF72 iAstrocytes could be detrimental to the surrounding MNs.

5.3.2. Mechanism of action of Nrf2 compounds; S[+]-apomorphine and andrographolide

In the previous chapter, I discussed the effect of the antioxidant drugs on pathological hallmarks common in ALS in the control and patient iAstrocyte subgroups. In this chapter, I aimed to use the RNA-seq data and DGE analysis to identify the mechanism of action of the two Nrf2 activators and to explain why one drug is beneficial to one specific subgroup over another.

Both S[+]-apomorphine and andrographolide are known activators of the NRF2/ARE pathway (Mead *et al.*, 2013), therefore there was an increased expression in transcripts related to the oxidation-reduction process across control and patient iAstrocyte lines after drug treatment. The ability of each compound to activate Nrf2 was demonstrated previously (4.2.1), S[+]-apomorphine was found to display a mild antioxidant response in patient cells which was reflective of the small number of Nrf2 targets identified in the RNA-seq data; S[+]-apomorphine treatment stimulated DGE changes in *ALDH3A1* in CTR, SOD1 and sALS lines and *PXDN* only in sALS iAstrocytes (Duong *et al.*, 2017; Hanmer and Mavri-Damelin, 2018). On the other hand, andrographolide treatment induced a strong upregulation of NQO1 protein expression across control and patient cell lines (4.2.1), and there were many antioxidant genes identified in the RNA-seq data; there was a widespread upregulation across control and patient iAstrocytes of *NQO1* and multiple transcripts belonging to the AKR family, which are all downstream targets of NRF2 (Hayes and Dinkova-Kostova, 2014).

The antioxidant properties of both compounds may also play a role in the regulation of retinoic acid signalling since there were DGE changes in transcripts related to different retinoic acid enzymes with both S[+]-apomorphine and andrographolide treatment. Interestingly, these changes were only observed in SOD1 and sALS iAstrocytes with both treatments, implying a patient-specific mechanism of action. Previous studies have found that retinoic acid signalling is impaired in the brain and spinal cord of *SOD1 G93A* mice and this can lead to neuronal death (Liang *et al.* 2017; Zhang *et al.* 2018). Stimulation of retinoic acid signalling through the all-trans retinoic acid ligand has proven to be neuroprotective in a wide variety of neurodegenerative diseases, including AD as well as ALS (Takamura *et al.*, 2017; Zhu *et al.*, 2020). Therefore, I could hypothesise that both compounds increased MN survival in co-culture by stimulating retinoic acid signalling.

The RNA-seq data confirmed that andrographolide is a stronger activator of the Nrf2 pathway compared to S[+]-apomorphine. Since both compounds are antioxidants, the selective response observed in the co-culture data had to be linked to their additional properties. These pathways are the most interesting as they can help identify the different mechanisms of action and help explain patient-specific response to treatment.

After S[+]-apomorphine treatment, there was a significant upregulation of transcripts related to cytochrome P450 enzymes CYP1A1 and CYP1B1 in control and patient iAstrocytes that was not seen after andrographolide treatment. Both enzymes are responsible for the metabolism of drugs and increased expression of *CYP1A1/CYP1B1* mRNA has previously been identified at blood-brain interfaces in the CNS (Nannelli *et al.*, 2009), proposing that these enzymes may aid the breakdown of S[+]-apomorphine within the iAstrocytes.

The expression of *CYP1A1* and *CYP1B1* genes is regulated by the expression of the aryl hydrocarbon receptor (AhR). While AhR is mainly known for mediating the detoxification of xenobiotics, it has also been associated with protein degradation via UPS, inflammation, and the immune response (Ramos-García *et al.*, 2020). While it has been shown that the upregulation of the CYP enzyme genes is associated with stimulated activity of AhR (Nannelli *et al.*, 2009), there was a significant upregulation of the Aryl-Hydrocarbon Receptor Repressor across control and patient lines (*AHRR*: CTR p-value = 2.60E-39, log2FC = +3.02, *SOD1* p-value = 1.88E-30, log2FC = +3.01, *C9ORF72* p-value = 1.66E-08, log2FC = +1.86, *sALS* p-value = 6.64E-12, log2FC = +2.06). Without a ligand, AhR is present in the cytoplasm in association with HSP90 (Mimura *et al.*, 1999). Upon ligand binding, AhR dissociates from the protein chaperone and translocates to the nucleus by forming a heterodimer with the AhR nuclear transporter (ARNT). This dimer binds upstream of the xenobiotic response element (XRE) genes, resulting in transcriptional activation of *CYP1A1* and *CYP1B1* (Hughes *et al.*, 2008). This also activates expression of *AHRR* which inhibits AhR function by competing with AhR for ARNT and XRE binding activity (Mimura *et al.* 1999). It is possible that the increased expression of *CYP1A1* and *CYP1B1* indicates the formation of the AhR-ARNT complex and therefore, HSP90 may be available for molecular chaperone activity. More evidence for the availability of HSP90 comes from a study which showed that HSP90 inhibitors suppressed the AhR-mediated activation of *CYP1A1* and *CYP1B1* transcription (Hughes *et al.*, 2008). Although the expression of HSP90 did not appear in the RNA-seq analysis, the interaction of HSP90 with AhR might help identify how S[+]-apomorphine aids in the removal of misfolded SOD1 from all patient iAstrocytes seen in 4.2.3. The mechanism of action is unique to S[+]-apomorphine since andrographolide treatment had no effect on misfolded SOD1 aggregation in the functional assays.

There has been a higher expression of AhR reported in the astrocytes from post-mortem brains of patients with AD and MS (Rothhammer *et al.*, 2016; Ramos-García *et al.*, 2020). Rothhammer *et al.* (2016) suggested that the CNS-produced IFN activated the AhR within astrocytes to suppress inflammation, while Ramos-García *et al.* (2020) speculated the opposite, that the IFN-AHR axis could be involved in the increase of AhR in AD. S[+]-apomorphine treatment provided the highest MN survival in the SOD1 iAstrocyte co-cultures, which presented the dysregulation in IFN signalling,

therefore, the treatment could also be providing benefit through the inhibition of AhR in the iAstrocytes.

Interestingly, S[+]-apomorphine treatment also upregulated the expression of artemin across control, SOD1 and sALS iAstrocytes, but not in C9ORF72 lines; this DGE change was also not observed after andrographolide treatment. Artemin is a part of the GDNF family of neurotrophic factors and acts via the PI3K pathway to improve the regeneration of injured neurons (Wong *et al.* 2015). Keller *et al.* (2020) found that the increased expression of artemin in astrocytes was neuroprotective towards dopaminergic neurons, thus indicating that S[+]-apomorphine might have a neurotrophic effect acting via astrocytes that is not seen with andrographolide.

As explained previously, neuroinflammation played a role in disease pathology across all patient cells and different genetic subgroups displayed DGE changes in separate pro-inflammatory signalling pathways. After S[+]-apomorphine treatment, there were DGE changes in transcripts related to pro-inflammatory signalling, including interleukins and circulating chemokines, in SOD1 and sALS iAstrocytes, but not in the C9ORF72 lines. In SOD1 iAstrocytes, there was a downregulation of *XCR1*; while there is little reported of *XCR1* in astrocytes, XCR1 receptor expression has previously been associated with microglial activation (Zychowska *et al.*, 2016). Therefore I could hypothesise that downregulation of the transcript implies a dampening of inflammation in SOD1 iAstrocytes after S[+]-apomorphine treatment. Similar to S[+]-apomorphine, there was a widespread decrease of inflammatory chemokines in sALS iAstrocytes after andrographolide treatment, as well as reduction of the *TNF* transcript. This is interesting because sALS iAstrocytes had increased TNF signalling at baseline therefore this could explain why andrographolide showed a greater increase in MN survival in co-culture with the sALS lines compared to S[+]-apomorphine. On the other hand, andrographolide treatment led to a reduction in *LBP* in SOD1 astrocytes, which is neuroprotective, therefore this could explain why there was little change in SOD1 iAstrocytes after andrographolide treatment. There was a decrease in the *NLRP3* transcript in C9ORF72 patient iAstrocytes after andrographolide treatment. The generation of ROS and the induction of oxidative stress are the most important factors that regulate the activation of the NLRP3 inflammasome (Tschopp and Schroder, 2010), therefore this downregulation may be associated with the strong antioxidant properties of andrographolide. A previous study also reported the reduced activity of the NLRP3 inflammasome through the upregulation of the Nrf2 pathway (Liu *et al.* 2020).

Based on our functional and transcriptomic data, I can conclude that andrographolide is a more potent activator of the NRF2-ARE response from both the increased expression of NQO1 (4.2.1) and the upregulation of transcripts related to other Nrf2 targets, the AKR family of genes, across control

and patient iAstrocytes; both of which were not observed after S[+]-apomorphine treatment. Both NQO1 and AKR enzymes catalyse NADPH-required reduction reactions that counteract the redox cycling of quinone molecules, preventing the production of ROS (Lin *et al.* 2016). In addition, the AKR enzymes are responsible for metabolising a wide range of substrates including steroids, lipids, sugars, and drugs (Shaw and Chattopadhyay, 2020). Andrographolide treatment stimulated the expression of *AKR1C1/AKR1C2/AKR1C3* genes across control and patient iAstrocytes; these transcripts encode hydroxysteroid dehydrogenases. *AKR1C2* encodes for a 3-ketosteroid reductase implicated in the metabolism of 5 β -dihydroprogesterone into allopreganolone, a neuroactive steroid that increases chloride conductance at the GABA receptor (Penning, 2015). Interestingly, treatment with allopreganolone provided neuroprotection in a mouse model of MN degeneration by reducing glial NOS/NADPH hyperactivity (Meyer *et al.* 2017), implying that andrographolide may provide protection to astrocytic health through up-regulation of AKR genes. At baseline, the C9ORF72 iAstrocytes demonstrated a dysregulation in cholesterol homeostasis. Since andrographolide treatment resulted in a significant increase in MN survival when co-cultured with C9ORF72 iAstrocytes, I could hypothesise that this increase in the AKR enzyme transcripts is potentially restoring cholesterol levels in these cell lines. The association of the AKR enzymes with NADPH could also potentially explain the effect of andrographolide on mitochondrial dynamics witnessed in 4.2.6, thus demonstrating a mechanism of action unique to andrographolide.

Interestingly, there was an increase in *OSGIN1* expression after andrographolide treatment across control and patient cell lines. While *OSGIN1* has previously been identified as an Nrf2 transcriptional target, the majority of studies state that the transcript is under the control of tumour suppressor protein 53 (p53) and mediates cell growth (Hu *et al.*, 2012), which is interesting because I commonly reported a reduced number of iAstrocytes after andrographolide treatment. Brennan *et al.* (2017) reported that *OSGIN1* is under the transcriptional control of Nrf2 in human astrocytes. They also reported that Nrf2 activated transcription of *OSGIN1* was responsible for the cytoprotective events following DMF treatment through the accumulation and nuclear translocation of p53, inhibiting cellular proliferation and combating oxidative stress (Brennan *et al.*, 2017). While this increase in *OSGIN1* was linked to the upregulation of Nrf2, it was a transcriptional change only observed after andrographolide treatment.

Andrographolide treatment increased the expression of p62 in control and patient iAstrocytes as demonstrated in 4.2.4. After treatment with andrographolide, CTR & sALS lines shared a significant increase in transcripts belonging to the pathway 'degradation of proteins through p62/Nrf2/KEAP1; these genes were *TRIM16* and its paralogue *TRIM16L*. Although these genes were also upregulated in C9ORF72 & SOD1 iAstrocytes after treatment, the log₂FC was less than +1.5. Tripartite motif

(TRIM) proteins are E3 ligases that contribute to a variety of cellular processes including innate immunity, apoptosis and autophagy (Jena *et al.*, 2018). It is interesting that, although S[+]-apomorphine also stimulated a mild increase in p62 expression across control and patient iAstrocytes, these transcripts were not identified after S[+]-apomorphine treatment, indicating a mechanism of action unique to andrographolide.

Previous studies have reported a strong association between p62 and Nrf2; p62 positively regulates Nrf2 expression through either interfering with the Nrf2-KEAP1 complex or facilitating the autophagic degradation of KEAP1 (Komatsu *et al.*, 2010). The p62 protein also stabilises Nrf2 expression, further amplifying the NRF2-ARE response (Jain *et al.*, 2010). Previous studies have shown that TRIM16 recognises damaged endomembranes and prepares the autophagic machinery for the selective sequestration of damaged lysosomes and phagosomes (Chauhan *et al.*, 2016), as well as interacting with SNARE proteins to recruit cargo to autophagosomes (Kimura *et al.* 2016), which could explain why there was a significant increase in the p62 protein after andrographolide treatment.

The study by Jena *et al.* (2018) showed that under oxidative stress, TRIM16 stimulates Nrf2 signalling via increasing the interaction between p62 and NRF1, as well as the sequestration and autophagic degradation of KEAP1. TRIM16 also promoted the removal of misfolded proteins through facilitating the recruitment of ubiquitin, p62 and LC3B as markers for protein aggregates. In addition, TRIM16 was found to associate with ULK1 and ATG16L1; ULK1 promotes autophagosome initiation while ATG16L1 mediates the elongation of the phagophore. The increased expression of p62 and LC3B-I at baseline in the patient iAstrocytes confirms that in our *in vitro* model, autophagy is stalled at the autophagosome formation stage (4.2.4), therefore inducing the expression of TRIM16 and potential activation of ULK1, which has been reported as defective in C9ORF72 patients (Webster *et al.*, 2016), may assist in autophagosome biogenesis and clearance of aggregates.

The TRIM family of proteins has also been implicated in multiple cancers as either an oncogene or tumour suppressor (Hatakeyama, 2017). TDP-43 was identified as a novel TRIM16 binding protein in neuroblastoma and breast cancer cell lines (Kim *et al.* 2016). The authors found that overexpression of the TRIM16 protein significantly increased endogenous TDP-43 protein levels. While andrographolide treatment showed little change in TDP-43/35 protein levels in C9ORF72 iAstrocytes, the increase in TRIM16 levels could have an effect on TDP-43 pathology, which is a potential hypothesis as to why andrographolide treatment promoted MN survival in C9ORF72 and sALS co-culture, but not SOD1 lines.

5.3.3. Riluzole treatment

As mentioned in the Introduction, Riluzole is the current therapeutic treatment for patients diagnosed with ALS, alongside edaravone which was introduced in 2017. As riluzole and edaravone only provide a modest patient benefit and survival extension, there is extensive research into more therapeutic compounds to treat ALS. From the co-culture survival data (4.2.2), riluzole treatment significantly increased MN survival in two ALS patient iAstrocytes out of 12 assessed, i.e. sALS 009 and C9ORF72 78, which is reflective of the patient population response to riluzole treatment (Miller *et al.* 2012).

The PCA plot of control and patient iAstrocytes before and after riluzole treatment showed that riluzole induced less significant gene expression changes in the patient iAstrocytes than the Nrf2 antioxidant compounds and this was also reflected in the reduced number of significantly altered transcripts present in each subgroup in Figure 5.11, especially in C9ORF72 patient iAstrocytes.

The inter-subject variability of riluzole is a major limitation of the compound; a previous study by Chow *et al.* (2012) showed that the pharmacokinetic profile of riluzole differed significantly across patients with different CNS disorders. This inter-subject variability was also seen between the patient iAstrocytes; there were few pathways shared between subgroups after riluzole treatment. Riluzole also has a very complex metabolism process and studies have found that genetic polymorphisms in the drug metabolising enzyme CYP1A2 could cause the high inter-subject variability of riluzole (Dash *et al.* 2018), and since we do not know the CYP1A2 genetic status of riluzole, this provides more evidence that patient treatment in ALS needs to be stratified to the individual.

Riluzole is known as an anti-glutamate agent and protects against neuronal excitability by blocking the excessive release of glutamate from pre-synaptic terminals in the vicinity of MNs (Jaiswal, 2016). The precise mechanism is unknown although there are a few theories; 1) inhibiting glutamate synaptic release or increasing glutamate uptake, 2) inactivating voltage-dependent sodium channels, 3) slowing potassium channel inactivation, 4) inhibiting protein kinase C, or 5) modulating intracellular events after transmitter binding at excitatory amino acid receptors (Jaiswal, 2019), although most of this work was assessed in MNs. Previous studies on astrocytes mainly focus on the effect of riluzole on glutamate transporters; riluzole was found to increase EAAT2 activity in striatal astrocytes (Carbone *et al.* 2012), however there was no difference in EAAT2 expression at either protein (4.2.6) at RNA level after riluzole treatment in this study.

Therefore, it is unclear whether riluzole treatment would reduce the toxic signalling in astrocytes or just provide benefit to the MNs. The latter may be true since riluzole had little effect in the disease

pathologies investigated in iAstrocytes in Chapter 4; there was only a mild decrease in extracellular glutamate in some cell lines, but little effect observed on glutamate transporter and NMDA receptor protein expression (4.2.6). Since riluzole had the least significantly changed transcripts in the C9ORF72 iAstrocytes, the patient group with the highest extracellular glutamate levels, it may be safe to conclude that riluzole had a mild effect on the astrocytic factors that contribute to glutamate excitotoxicity.

5.3.4. Conclusion

In conclusion, studying the transcriptome of iAstrocytes from different genetic subgroups of ALS patients has generated a wealth of information that can aid the understanding of the disease pathology of these patient groups. In all, ALS patients share common disease mechanisms such as dysregulated glutamatergic neurotransmission, axonal maintenance and guidance, and vesicular trafficking within the cytoplasm. However, it is the disease pathways that differ that might help us determine the patient response to drug treatment. An interesting aspect of the RNA-sequencing data is that when looking at the differential gene expression between controls and patients, the controls clearly separate from the patient iAstrocytes (Figure 5.12). Additionally, the patient iAstrocytes group according to their toxicity, shown in 3.3.7, for example the most toxic cell lines C9ORF72 183 & 201 and SOD1 ND29505 group together and separate from the milder patient lines. Nrf2 activators are able to provide neuroprotection far beyond the response to oxidative stress; S[+]-apomorphine regulates xenobiotic enzymes that are upstream of protein folding chaperones while andrographolide stimulates proteins that influence the autophagic machinery as well as calcium modulation within the cell. When the potential of these antioxidant compounds is compared to the currently used disease modifying drugs, it seems that riluzole causes mild functional and gene expression changes, thus confirming the need for novel, more effective, therapeutic agents and, in comparison, it shows that antioxidant compounds are likely to be good candidates for further drug development.

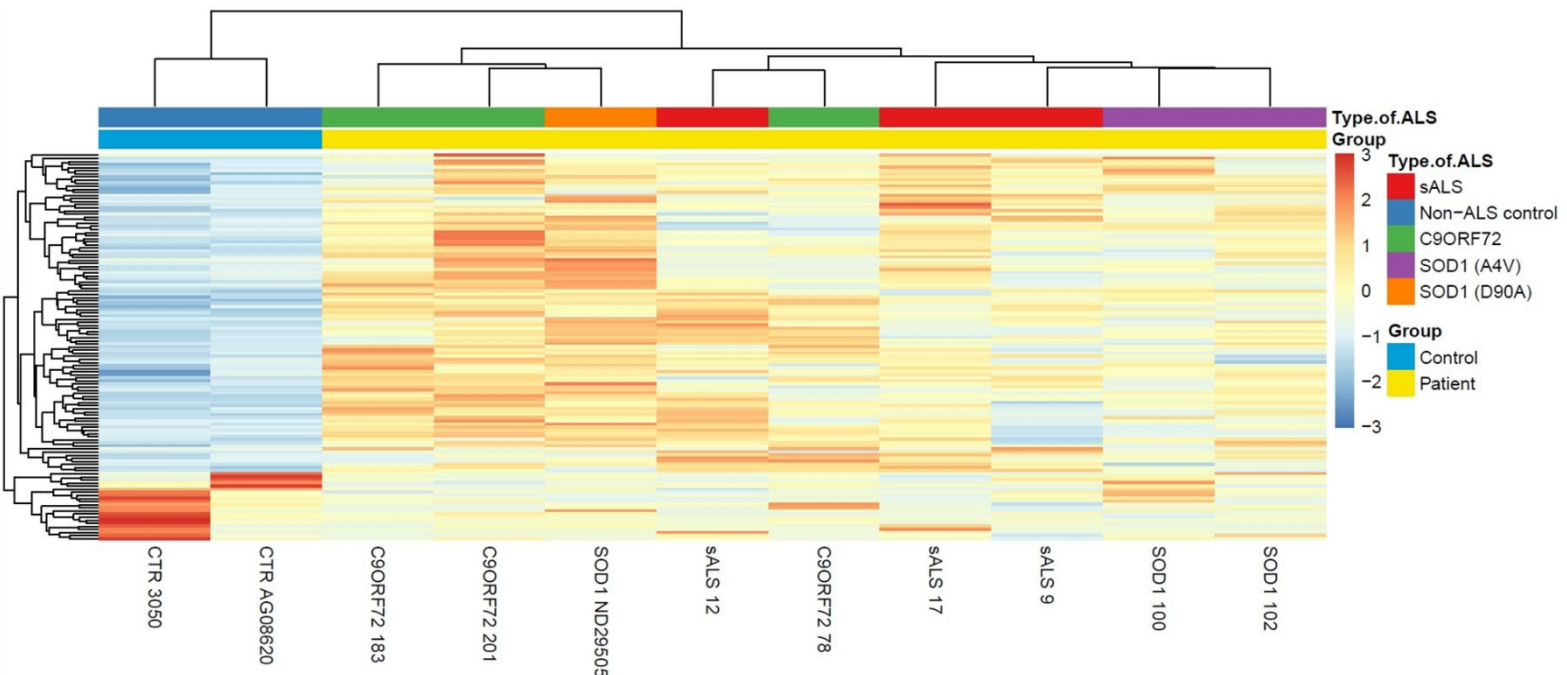


Figure 5.12 Heatmap of RNA-sequencing data from untreated control and patient iAstrocyte lines (p -adj<0.05; courtesy of Dr Mark Dunning).

Chapter 6 - Investigating the potential for a personalised medicine approach in ALS using patient-derived astrocytes

6.1. Introduction

While personalised medicine is new to the ALS field, it has been applied extensively to certain types of cancer and it is beginning to be applied to the treatment of AD and MS patients (Krzyszczuk *et al.* 2018; Hampel *et al.* 2016; Gafson *et al.* 2017). Over the past decade, there has been an accumulation of evidence that no two patient's cancers will be the same, leading to variable patient responses to the traditional cancer therapies such as radiation and chemotherapy. The application of the personalised medicine approach has led to the development of specialised treatments for each subtype of cancer based upon patient genetic data, including transcriptomics, metabolomics, and proteomics (Krzyszczuk *et al.*, 2018). One example of this is the discovery of a mutation in anaplastic lymphoma kinase (ALK) that drives tumour formation in roughly 5% of non-small-cell lung cancers (Soda *et al.*, 2007). After the identification of this mutation, ALK blockers were developed, such as crizotinib and certinib, and given specifically to patients who test positive for the ALK mutation (Krzyszczuk *et al.*, 2018).

In MS, clinical presentation alongside laboratory tests, imaging and CSF examinations are being used collectively to define the syndrome of each patient by rejecting possible alternative disorders and recognising the distinct sub-syndrome of primary progressive MS (Gafson *et al.* 2017). Neuromyelitis optica spectrum disorders (NMOSD) can be identified by serum antibodies against aquaporin 4 (AQP4-IgG) (Kitley *et al.*, 2012). It is important to be able to distinguish this disorder from MS as patients with NMOSD do not respond, or may worsen, with IFN treatment (Uzawa *et al.*, 2010). Similar to this application in MS, we are investigating potential RNA biomarkers in ALS patient-derived cells which define treatment response in this present study.

Like ALS, MS is a 'syndrome' with a large variation in the clinical phenotype, disease manifestation, as well as treatment response (Gafson *et al.* 2017). With an increasing number of available treatments for MS patients, all with different mechanisms of action, range of efficacy and relative risk, a personal tailored approach needs to be adapted to make the best decision for each individual patient. Understanding the heterogeneity of ALS involves the deconstruction of the biologically significant pathways that lead to disease and how patient-specific factors influence these pathways (Gafson *et al.* 2017). In this process, we hope to identify specific pathways of disease or transcriptional signatures that can aid in choosing the correct drug to give to a patient as well as identifying new compounds that target disease in specific patients.

In the concept of personalised medicine, a sub-group of 'responders' are selected based on specific criteria (Sadée and Dai, 2005). For example, in the present study, a patient responder to a drug was identified as a cell line achieving a ~50% increase in MN survival in the co-culture study after treatment with the compound (4.2.2). This stringent cut-off was chosen to avoid noise from mild responders. 'Non-responders', therefore, are a group that do not fulfil the specific criteria and will be compared against the 'responders' group. Biomarkers are used to identify the 'responders' from the 'non-responders' group, and the respective drug gains a more favourable risk-benefit ratio, allowing clinicians to make better treatment choices for their patients (Sadée and Dai, 2005).

In this chapter, I have identified a panel of biomarkers for each drug response group, S[+]-apomorphine, andrographolide and riluzole, by investigating how the significance of the DEGs in patient iAstrocytes compared to control changed after drug treatment, i.e. significantly dysregulated transcripts at baseline were no longer significantly dysregulated after treatment. Previously to determine significance, I have been using a p-value where there was a 5% chance of a false positive to investigate biological pathways attributed to the diseased cells as well as the mechanism of action of the drug. However, now that I am investigating changes in individual genes, I needed to apply a more stringent statistical analysis to decrease even further the probability of accepting false positive results. To do this, I applied a FDR to produce an adjusted p-value (p-adj); a p-adj<0.05 means that we were accepting the chance that 5% of the already selected DEGs (p<0.05) were false positives.

6.2. Results

6.2.1. Patient response at baseline

In the previous chapter, the RNA-sequencing data was investigated to uncover the similarities and differences between the patient subgroups, SOD1, C9ORF72 and sALS, as well as the mechanism of action of each drug across the patient subgroups. In this chapter, rather than grouping the patient samples on the basis of genetics, the RNA-sequencing samples have been collated based upon the response to drug, taken from the co-culture data in 4.2.2., as identified in Table 6.1 below:

Table 6.1 Patient responders to S[+]-apomorphine, andrographolide and riluzole

Drug	Patient responders
S[+]-Apomorphine	sALS 009
	SOD1 100
	SOD1 102
	C9ORF72 78
Andrographolide	sALS 009
	sALS 12
	sALS 17
	C9ORF72 78
	C9ORF72 201
Riluzole	sALS 009
	C9ORF72 78

The table shows that, within a patient response group, there were a variety of genetic subgroups and so the first aim was to investigate whether the response groups presented unique transcriptional features in comparison to controls, as this would help us identify what was unique about these patients. Lists of DEGs between each patient iAstrocyte response group and the control iAstrocyte group were generated by Dr M. Dunning by running the comparisons in the table below (Table 6.2):

Table 6.2 List of bioinformatic comparisons for patient responders at baseline

Bioinformatic comparisons	Total genes	Upregulated genes	Downregulated genes
Resp. S[+]-apomorphine U* vs CTR U	44	41	3
Resp. andrographolide U vs CTR U	187	152	35
Resp. riluzole U vs CTR U	37	27	10

U* = untreated

Since this analysis was looking into specific transcripts and not pathways, DEGs were selected based on a $p\text{-adj} < 0.05$, meaning that we expected less than 5% of the significant transcripts to be false positives. Patient responders to andrographolide displayed the highest number of significantly dysregulated transcripts, while the S[+]-apomorphine and riluzole response group presented fewer genes. All transcripts are presented in the supplementary, S[+]-apomorphine: Supplementary 6.1, andrographolide: Supplementary 6.2, and riluzole: Supplementary 6.3.

To identify the genes that were shared between patient response groups, I imported the gene lists into Venny to generate the Venn diagram shown in Figure 6.1. As expected, the andrographolide responders displayed the highest number of unique dysregulated transcripts (142 genes, 110 up, 32 down), with S[+]-apomorphine and riluzole responders presenting only 11 (8 up, 3 down) and 16

genes (9 up, 7 down) respectively. S[+]-Apomorphine & andrographolide response groups shared the most genes (25 transcripts, all up), while there were 7 genes (all up) shared between all of the patient response groups.

The 7 significant DEGs shared between all patient response groups are shown in Table 6.3. Like the pathways shared between different genetic patient subgroups (5.2.1), these shared transcripts were involved in neuronal connections, neurotransmitter release and protein metabolism.

Table 6.3 List of shared transcripts between patient response groups

Gene Name	S Resp.	A Resp.	R Resp.
Internexin Neuronal Intermediate Filament Protein Alpha (INA)	0.001239989 +4.869168925	1.88E-05 +5.373074674	0.04952992 +4.974606317
Contactin 1 (CNTN1)	0.008138741 +7.03596454	0.018427397 +7.031894468	0.018830004 +7.299183979
Adrenoceptor Alpha 2A (ADRA2A)	0.005152966 +5.645351809	0.01066841 +6.26059011	0.004277329 +6.3874973
Dynamin 1 (DMN1)	0.005731808 +4.689751948	0.049350963 +4.380718935	0.023990851 +5.304723501
ADAM Metallopeptidase With Thrombospondin Type 1 Motif 5 (ADAMTS5)	0.002621102 +7.757440947	0.004084036 +7.457464103	0.002914446 +8.701666328
Coiled-Coil Domain Containing 3 (CCDC3)	1.32E-04 +5.968514399	1.75E-04 +6.008352854	1.54E-04 +6.541867636
Four And A Half LIM Domains 1 (FHL1)	0.001239989 +3.625659572	6.49E-04 +4.207846013	1.54E-04 +3.645152433

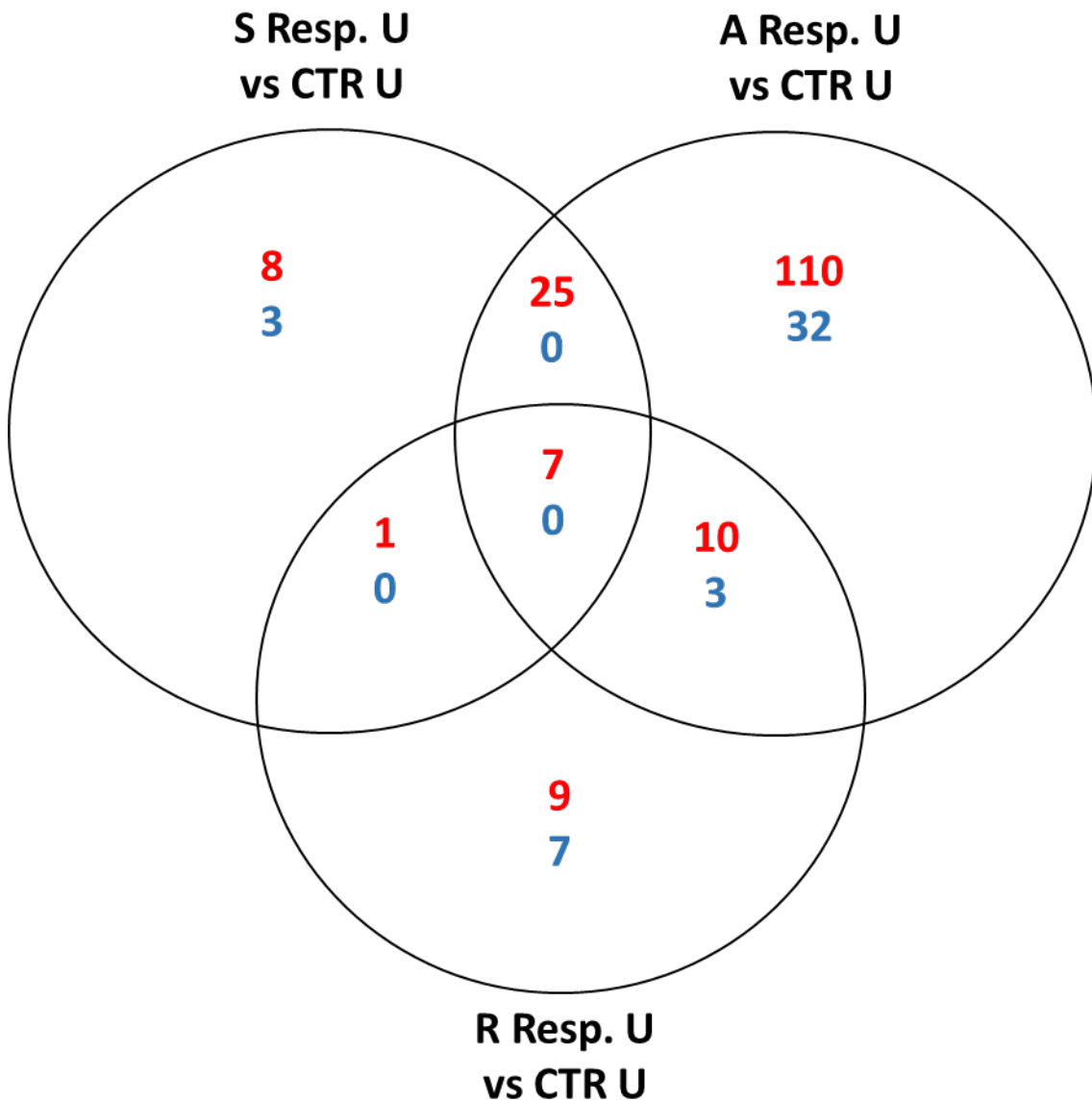


Figure 6.1 Visual interpretation of the DEGs shared between the different patient response groups generated from comparisons run in Table 6.2. The number of upregulated genes are shown in red and downregulated transcripts in blue. Abbreviations: U = untreated, S = S[+]-apomorphine, A = andrographolide, R = riluzole.

While the dysregulation of *INA* mRNA has previously been reported in ALS (Hawley *et al.* 2019), the expression of this transcript appears to be restricted to neuronal cells. Similarly, contactin is not usually expressed by astrocytes, however it was overexpressed in a glioblastoma cell line and acted as a repulsive agent to nearby glioma cells (Eckerich *et al.*, 2006). Since *CNTN1* is expressed at the junctions between neurons and glia (Chatterjee *et al.* 2019), it may play an important role in axonal growth. The increased expression of *CNTN1* in the patient cell lines may occur as the result of a feedback mechanism to counteract downregulation of the protein within the cell.

Stimulation of α -adrenergic receptors can increase intracellular calcium concentration, glutamate oxidation and oxidative metabolism in astrocytes (Peng *et al.*, 2010), as well as the secretion of GDNF which is mediated by cAMP-response element binding protein (CREB) and protein kinase C/MAPK signalling cascades (Yan *et al.*, 2011). While this increase may be beneficial in some patient iAstrocytes, the increased calcium and glutamate oxidation would be detrimental to the C9ORF72 iAstrocytes that already have a glutamate impairment as well as impaired energy metabolism (Allen *et al.* 2019b).

Dynamin proteins are critical components of the mitochondrial division machinery; dynamin 1 promotes spontaneous mitochondrial membrane fission upon the hydrolysis of GTP, while dynamin 2 works with Drp1 to constrict the membrane, separating the mitochondria (Feng *et al.*, 2020). It was interesting that this transcript was upregulated in all patient groups, since only SOD1 iAstrocyte ND29505 displayed mitochondrial fission (3.2.3); it could be that the increase in *DMN1* is causing membrane damage without the presence of Drp1 to split the mitochondrial network. The increase in *ADAMTS5* has previously been reported in astrocytes after SCI injury; the activation of ADAMTS proteins may reduce the deposition of chondroitin sulphate proteoglycans in the prevention of glial scar formation (Demircan *et al.*, 2013), thus demonstrating a way in which the patient cells are potentially attempting to combat the effects of reactive astrogliosis.

Looking at the DEGs that were unique to each patient response group (Figure 6.1), there were 11 DEGs unique to patient lines that responded to S[+]-apomorphine treatment (Table 6.4). These transcripts were involved in mitochondrial protein synthesis, cellular adhesion, and receptor tyrosine kinase signalling.

Table 6.4 List of transcripts unique to S[+]-apomorphine patient line responders

Gene Name	S Resp.	A Resp.	R Resp.
Islet Cell Autoantigen 1 (ICA1)	0.002763029 -3.182989003	0.300492471 -2.110586669	0.332609798 -2.798483526
Mitochondrial Ribosomal Protein S9 (MRPS9)	0.007926962 -1.790471204	0.208056451 -1.460571533	0.533036012 -1.771041124
Nuclear Receptor Interacting Protein 3 (NRIP3)	0.008085849 +3.541391126	0.098022507 +3.071419654	0.1303892 +2.802471282
Nectin Cell Adhesion Molecule 3 (NECTIN3)	0.011578209 +1.80096269	0.351072239 +1.632662288	0.175440036 +2.064348558
Glutamine Amidotransferase Like Class 1 Domain Containing 3A (GATD3A)	0.011865584 +3.957125386	0.488978026 +2.915583083	0.396247567 +3.620472183
Glutamine Amidotransferase Like Class 1 Domain Containing 3B (GATD3B)	0.011865584 +3.957125386	0.488978026 +2.915583083	0.396247567 +3.620472183
Collagen Type V Alpha 3 Chain (COL5A3)	0.016575879 +8.299829125	0.054840405 +6.572088436	- -
EPH Receptor A3 (EPHA3)	0.018808847 +7.463762783	N/A +7.334194404	- -
MFF Divergent Transcript (MFF-DT)	0.020551437 +2.10089669	0.210216812 +2.024841828	0.476386332 +2.246810156
Insulin Like Growth Factor Binding Protein 5 (IGFBP5)	0.023841488 +3.305056927	0.087516647 +4.09398254	0.421234519 +2.863177305
Rho Associated Coiled-Coil Containing Protein Kinase 1 Pseudogene 1 (ROCK1P1)	0.04726124 -4.663338277	0.069521216 -4.090183544	0.532431717 -4.104195585

While there is little known about the *MRPS9* gene in regards to ALS, the influence of mSOD1 on the mitochondria is widely reported; deviations from normal SOD1 levels increased the mtDNA copy number as well as the impaired mitochondrial protein synthesis associated with mSOD1 (Kawamata *et al.*, 2008; Masser *et al.*, 2016). The dipeptide repeats associated with C9ORF72-ALS were also found to preferentially bind to mitochondrial ribosomal proteins, compromising mitochondrial function (Lopez-Gonzalez *et al.*, 2016); this was interesting since both SOD1 and C9ORF72 iAstrocytes displayed differential mitochondrial dynamics in 3.2.3, as well as the significant reduction in mitochondrial form factor after S[+]-apomorphine treatment (4.2.6).

S[+]-apomorphine treatment was shown to have an effect on transcripts associated with cell adhesion in the previous chapter (5.2.4). *NECTIN3* encodes a cellular adhesion molecule responsible for cell-cell contact at adherens junctions, the expression of which can be altered by stress. In neurons, these proteins are present at synaptic junctions, forming inter-neuronal connections and maintaining synapse formation and transmission (Wang *et al.* 2020). The expression of Nectin-3 was reportedly reduced in models of AD in relation to tauopathy (Maurin *et al.*, 2013), however the increased expression witnessed in the patient iAstrocytes could be in relation to the stressed cellular environment. Differential regulation of *COL5A3* was also reported in AD as a target of miR-29a,

which was decreased in AD brains (Satoh, 2010). Interestingly, the expression of miR-29a was increased in a *SOD1* mouse model (Nolan *et al.*, 2014), therefore I can hypothesise that this miRNA is potentially regulating *COL5A3* expression in the *SOD1* patient iAstrocytes. This was interesting as ‘collagen fibril organisation’ was also a pathway associated with S[+]-apomorphine treatment (5.2.4).

Ephrin receptors are the largest protein family of receptor tyrosine kinases and are responsible for cell-cell interactions as well as the development of the nervous system, in particular neuronal cell migration and axon guidance (Uyan *et al.*, 2013). Loss of ephrin receptor signalling has been previously reported as protective in ALS; deletion of *EPHA3* was identified as a protective factor in a sALS patient population while inhibition of *Epha4* signalling increased survival in a *SOD1* mouse model (Van Hoecke *et al.*, 2012; Uyan *et al.*, 2013). This would imply that the significant upregulation of *EPHA3* within these patient iAstrocytes was detrimental to the surrounding MNs, as previously reported in reactive astrocytes after SCI (Irizarry-Ramírez *et al.*, 2005). While ephrin signalling was not identified as a specific target of S[+]-apomorphine treatment (5.2.4), the ‘epinephrine biosynthetic process’ was identified as a dysregulated pathway in the *SOD1* cell lines at baseline, which show the highest benefit from S[+]-apomorphine treatment (5.2.3).

On the contrary to the S[+]-apomorphine response group, there were a total of 142 DEGs unique to andrographolide responder cell lines (Figure 6.1). To shorten this list of transcripts, the list was imported into the DAVID pathway analysis programme and transcripts within the top GO-BP lists were selected as shown in Table 6.5. These transcripts were involved in the development and chemical function of the nervous system as well as the inflammatory response.

There were DGE changes identified in *GRIN2B* and *GRM3* transcripts shared between sALS and C9ORF72 at baseline reported in the previous chapter (5.2.3), therefore it was unsurprising that these two genes were identified as unique transcripts for responders of andrographolide, which consist of both sALS and C9ORF72 patient iAstrocytes. The activation of neurotensin receptors NTSR1 and NTSR2 have previously been associated with the intracellular release of calcium from both neurons and astrocytes (Tabarean, 2020), therefore the downregulation of *NTSR1* may be associated with the dysregulation of the ionotropic receptors and calcium signalling previously discussed in relation to the C9ORF72 iAstrocytes. This is interesting in relation to the effect of andrographolide treatment on the protein level of the ionotropic receptor *GRIN2B* (4.2.7.2), further indicating that andrographolide treatment regulates calcium levels in the patient iAstrocytes.

Table 6.5 List of transcripts unique to andrographolide patient line responders

GO Term	Gene Name	S Resp.	A Resp.	R Resp.
Nervous system development	Brain Derived Neurotrophic Factor (BDNF)	0.070469427 +4.655875861	0.018674402 +4.84687531	0.9999128 +3.258938076
	Dihydropyrimidinase Like 4 (DPY5L4)	0.163812962 +5.05799301	0.009264463 +4.0953912	0.20144225 +4.194670826
	Fasciculation And Elongation Protein Zeta 1 (FEZ1)	0.108715854 +4.006184455	0.048456655 +3.921821658	0.514395094 +2.953890596
	Frizzled Class Receptor 9 (FZD9)	0.452443055 +2.511160735	0.036777514 +3.314199656	0.564091922 +2.788203132
	Integral Membrane Protein 2A (ITM2A)	0.663423834 +3.92094298	0.019183759 +4.723138339	0.816451675 +3.486364977
	Nuclear Receptor Subfamily 2 Group E Member 1 (NR2E1)	0.127070044 -4.718475448	0.029286056 -5.732073114	0.560139255 -4.550994427
	Protocadherin 18 (PCDH18)	0.341412474 +1.827177435	0.036130505 +2.331750695	0.175440036 +2.407652983
Positive regulation of MAPK cascade	Cadherin 2 (CDH2)	N/A +7.193508944	5.12E-05 +8.599840562	0.206871305 +4.994405047
	Pellino E3 Ubiquitin Protein Ligase Family Member 2 (PELI2)	0.232798394 +2.343583118	0.018234678 +2.942811782	0.9999128 +1.728975327
Chemical synaptic transmission	5-Hydroxytryptamine Receptor 7 (HTR7)	N/A +6.981079305	0.003559166 +7.376318973	0.9999128 +3.178102601
	Glutamate Ionotropic Receptor NMDA Type Subunit 2B (GRIN2B)	0.999466702 -0.206541707	8.52E-04 -8.522048538	- -
	Glutamate Metabotropic Receptor 3 (GRM3)	N/A +8.171121614	0.013925811 +9.846500839	- -
	Hypocretin Neuropeptide Precursor (HCRT)	- -	5.43E-05 +22.09890679	- -
	Neurotensin Receptor 1 (NTSR1)	N/A -3.702324605	0.019183759 -6.248658287	0.099560923 -6.649850703
	Tachykinin Receptor 1 (TACR1)	0.109117428 +6.650118244	0.035860605 +6.607741735	- -
Axon guidance	Dorsal Inhibitory Axon Guidance Protein (DRAXIN)	0.525445039 +2.367518287	0.020025012 +2.557992208	0.657026732 +2.721955812
Negative regulation of leukocyte apoptotic process	C-X-C Motif Chemokine Ligand 12 (CXCL12)	0.070469427 +6.779124866	0.002456406 +8.524367718	0.101579632 +6.722686371
	MER Proto-Oncogene, Tyrosine Kinase (MERTK)	0.781445976 +2.357032823	0.013925811 +4.341384898	0.53164577 +2.919606046
Vitamin A metabolic process	Retinoid Isomerohydrolase (RPE65)	- -	0.011212684 +8.556956276	- -
	Aldehyde Dehydrogenase 1 Family Member A2 (ALDH1A2)	0.291780417 +6.558876077	0.004084036 +11.6522931	- -

Andrographolide treatment was shown to influence transcripts associated with inflammation and the immune response in the previous chapter (5.2.5). The orphan nuclear receptor NR2E1 is responsible for the regulation of Phosphatase and Tensin Homolog (PTEN) expression which is a negative regulator of PI3K signalling (Wang and Xiong 2016). The significant increase in *PIK3CD* in the

andrographolide response group (p-value = 7.40E-04, log2FC = 3.47) implied that PTEN expression was suppressed, which has been shown to be neuroprotective in SOD1 and C9ORF72 ALS (Kirby *et al.*, 2011; Stopford *et al.*, 2017). On the other hand, the increase in *MERTK* expression has been previously reported in ALS, albeit in macrophages (Saul *et al.*, 2020), although the expression of Mertk is thought to be essential in orchestrating the roles of astrocytes and microglia in the removal of dying neurons, particularly the astrocytic recruitment of lysosomes (Damisah *et al.*, 2020).

There were 16 unique DEGs in the patient lines that responded to riluzole treatment (Table 6.6).

These transcripts were found to be involved in the transport of lipids and ions as well as inflammatory signalling.

Table 6.6 List of transcripts unique to riluzole patient line responders

Gene Name	S Resp.	A Resp.	R Resp.
Gap Junction Protein Gamma 1 (GJC1)	0.999466702 -0.712944999	0.99882591 -0.632644909	1.54E-04 -3.305787665
Apolipoprotein L4 (APOL4)	0.409154734 +2.267211333	0.277091519 +2.672864372	0.002574136 +2.910621365
SFT2 Domain Containing 3 (SFT2D3)	N/A +22.49187978	0.228749252 +10.44055301	0.004487797 +10.36994819
PAX8 Antisense RNA 1 (PAX8-AS1)	N/A -2.441204925	0.966414595 -1.563360163	0.006916153 -4.552510636
Coagulation Factor VIII Associated 2 (F8A2)	0.761866077 +9.053412385	0.462186328 +8.787215476	0.007493098 +9.487077344
Major Histocompatibility Complex, Class II, DR Alpha (HLA-DRA)	N/A +8.051342037	N/A +7.785238693	0.008079026 +9.38598501
Amphiregulin (AREG)	N/A -3.683046734	N/A -5.275276227	0.008666302 -9.477991014
Iroquois Homeobox 1 (IRX1)	0.999466702 -1.281385284	N/A -3.535799184	0.017974946 -5.531647015
Ras Interacting Protein 1 (RASIP1)	N/A +5.862790673	N/A +5.678010098	0.024429744 +7.166083638
Claudin 10 (CLDN10)	0.759219652 -2.619299896	N/A +1.771675944	0.024429744 -4.885149921
TNF Alpha Induced Protein 6 (TNFAIP6)	0.967448428 +2.372015773	0.374214372 +3.158905795	0.029297762 +3.415148058
Collagen Type I Alpha 1 Chain (COL1A1)	0.761866077 +2.063227718	0.561823617 +2.572070562	0.029297762 +2.310305576
STEAP Family Member 1B (STEAP1B)	0.69863072 +2.633311799	0.094745037 +3.264458342	0.033048746 +3.475586331
Paired Box 8 (PAX8)	N/A -1.547957611	0.698527208 -2.187310657	0.037222303 -3.922783344
Collagen Type XVII Alpha 1 Chain (COL17A1)	N/A -0.673559214	0.927182189 -1.712673946	0.04952992 -5.431186952

Apolipoproteins play an essential role in brain homeostasis by facilitating the delivery of lipids and substrates to specific cells in the brain as well as regulating signal transduction pathways (Elliott *et al.* 2010). They also play a large role in neurodegenerative disease, particularly *APOE4* which is associated with an increased risk of AD and PD and adverse outcomes in SCI, TBI and stroke (Elliott *et al.* 2010). Different polymorphisms of *APOL* genes (*APOL1*, 2 & 4) have been associated with schizophrenia, however little is known about the function of these proteins in disease (Takahashi *et al.* 2008; Vanhollebeke and Pays 2006).

The presence of neuroinflammation in ALS was described in detail in the previous chapter (5.2.3). It was interesting that the *HLA-DRA* transcript was identified as unique to responders of riluzole treatment since this gene is an associated risk factor for sporadic ALS as well as FTD (Yang *et al.* 2017; Ferrari *et al.* 2014). *HLA-DRA* expression is activated by TNF α activity (Panek *et al.*, 1992), which is further supported by the increased expression of *TNFAIP6*. Amphiregulin is thought to suppress astrogliosis by inhibiting the production of the pro-inflammatory cytokine IL-6 from microglia and astrocytes, protecting the surrounding neurons (Ito *et al.*, 2019), therefore the downregulation of this transcript supports the idea of a proinflammatory environment. While inflammation was not identified as a target of riluzole treatment in the previous chapter (5.2.6), there was a decrease in *IL32* expression in sALS patient cell lines, implying that riluzole may possess some anti-inflammatory properties.

In summary, there were DEGs associated with different biological functions identified between the patient responder groups. It was interesting that some transcripts dysregulated at baseline in a response group were associated with a biological pathway that was also identified as a target of the specific drug in the previous chapter. This makes sense as we would speculate that this transcript predisposes the patient to have a beneficial response to a specific drug treatment due to the certain characteristics of that drug. However, this was not the case for every transcript, especially in the patient response group towards riluzole, in keeping with the mild benefit of the drug.

6.2.2. S[+]-Apomorphine response

To identify the transcripts that determine a 'patient responder'-specific response to S[+]-apomorphine treatment, I compared how the gene expression changed after drug treatment within the patient responder cell lines. Lists of differentially regulated transcripts between the S[+]-apomorphine iAstrocyte response group before and after treatment compared to the control iAstrocyte group were generated by running the comparisons in the table below (Table 6.7):

Table 6.7 List of bioinformatic comparisons for S[+]-apomorphine patient responders

Bioinformatic comparisons
Resp. S[+]-apomorphine U* vs CTR U = transcripts altered in the responder's group at baseline against healthy individuals
Resp. S[+]-apomorphine T# vs CTR U = transcripts altered in the responder's group after treatment against healthy individuals
Resp. S[+]-apomorphine T vs Resp. S[+]-apomorphine U = transcripts altered in the responder's group after treatment against the baseline value

U* = untreated, T# = treated

The highest number of significant DEGs was observed in the *S Resp. T vs S Resp. U* comparison (161 genes), while the other comparisons displayed fewer transcripts; the *S Resp. U vs CTR U* comparison presented 44 DEGs, while *S Resp. T vs CTR U* displayed 73 genes. A full list of transcripts generated from the *S Resp. T vs S CTR U* comparison are presented in Supplementary 6.4.

The gene lists were imported into Venny to identify transcripts that were uniquely or commonly dysregulated in the 3 comparisons (Figure 6.2). There were 153 genes (111 up, 42 down) unique to the *S Resp. T vs S Resp. U* comparison; this comparison identified genes where there was a large significant change in expression after treatment, potentially due to the mechanism of action of the drug discussed in the previous chapter (5.2.4), but this list did not share any transcripts with the *S Resp. U vs CTR U* comparison, implying that none of these transcripts were dysregulated at baseline. The 38 DEGs unique to the *S Resp. T vs CTR U* comparison (28 up, 10 down) highlighted transcripts that were significantly changed after treatment but did not combat the original dysfunction in the patient cell lines, as these transcripts were not altered in the baseline comparison. The DEGs shared between *S Resp. U vs CTR U* and *S Resp. T vs CTR U* comparisons (27 transcripts, 27 up, 0 down) identified transcripts that were dysregulated at baseline and remained dysregulated without changing regulation, increase or decrease, after drug treatment. Therefore, I chose to investigate further the 14 genes that were unique to the *S Resp. U vs CTR U* comparison (11 up, 3 down) because these transcripts were significantly different to control lines prior to treatment with S[+]-apomorphine, however this significance was lost after treatment, thus indicating that S[+]-apomorphine treatment has corrected their dysregulation. Hence, these transcripts would be good candidates to identify a response gene signature.

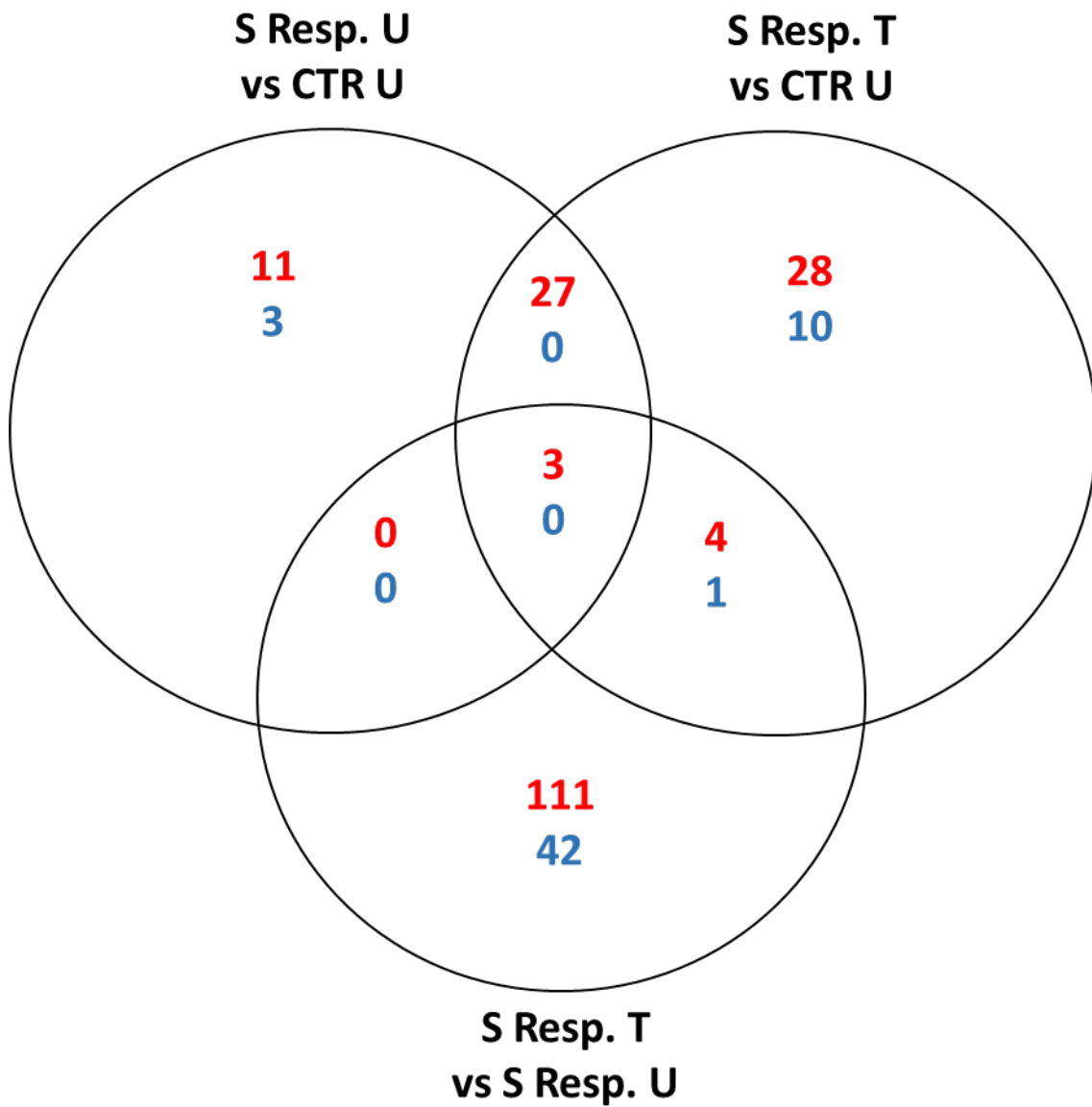


Figure 6.2 Visual interpretation of the DEGs shared between S[+]-apomorphine response comparisons demonstrated in Table 6.7. The number of upregulated genes are shown in red and downregulated transcripts in blue. Abbreviations: U = untreated, T = treated, S = S[+]-apomorphine.

Since I was looking for biomarkers that discriminated between patient responders, I expected the gene biomarker to be corrected after treatment. The baseline *S Resp. U vs CTR U* comparison in 6.2.1 was a starting point and these transcripts either 1) changed direction and were still significantly dysregulated compared to controls or 2) went back to baseline and were no longer significantly dysregulated anymore after treatment with S[+]-apomorphine.

There were 14 transcripts that were unique to the *S Resp. U vs CTR U* comparison, meaning that after treatment, these transcripts were no longer significantly dysregulated in the patient responder lines. Interestingly, *ICA1*, *MRPS9*, *NECTIN3*, *EPHA3*, *MFF-DT* & *ROCK1P1* were all previously investigated as significantly dysregulated transcripts unique to S[+]-apomorphine responders at baseline (Table 6.4) compared to other responder groups. Additional transcripts identified in the *S Resp. U vs CTR U* comparison would have been significantly dysregulated in other response groups at baseline. The transcripts with the biggest change in significance after S[+]-apomorphine treatment were *MRPS9*, *MFF-DT*, *ROCK1P1* & *GRM4* (Table 6.8).

Table 6.8 List of genes unique to S[+]-apomorphine responders untreated vs CTR untreated

Gene Name	S Resp. U	S Resp. T	S Resp. T vs U
Islet Cell Autoantigen 1 (ICA1)	0.002763029 -3.182989003	0.073098622 -2.689173435	0.993185008 +0.371115273
Mitochondrial Ribosomal Protein S9 (MRPS9)	0.007926962 -1.790471204	0.820777184 -1.469288698	0.999987173 +0.08749759
Nectin Cell Adhesion Molecule 3 (NECTIN3)	0.011578209 +1.80096269	0.537057077 +1.445576666	0.554922237 -0.355286774
EPH Receptor A3 (EPHA3)	0.018808847 +7.463762783	0.109400847 +4.614894797	0.999987173 +0.07997578
MFF Divergent Transcript (MFF-DT)	0.020551437 +2.10089669	0.414826404 +1.617945402	0.999987173 -0.41335037
Rho Associated Coiled-Coil Containing Protein Kinase 1 Pseudogene 1 (ROCK1P1)	0.04726124 -4.663338277	0.50619564 -3.725745171	N/A +0.624548088
LY6/PLAUR Domain Containing 6 (LYPD6)	0.017197276 +4.051552445	0.074418356 +4.408970448	0.999987173 -0.263408797
Dickkopf WNT Signalling Pathway Inhibitor 2 (DKK2)	0.02365336 +3.582472635	0.081359118 +3.660998321	0.999987173 +0.064916087
Cyclase Associated Actin Cytoskeleton Regulatory Protein 2 (CAP2)	0.038128159 +3.414751831	0.054969409 +3.458329823	0.999987173 -0.132158573
Glutamate Metabotropic Receptor 4 (GRM4)	0.04861494 +3.705822056	0.99969343 +1.999453342	N/A -2.120900612

To identify whether this change in significance after S[+]-apomorphine treatment was due to a response in just one or multiple patient responder lines, I plotted the normalised gene counts (TPM values) for each transcript before and after S[+]-apomorphine treatment in both patient responder and non-responder iAstrocytes (Figure 6.3). As the graphs indicate, not all of the biomarkers changed in all of the responder cell lines after treatment, therefore we hypothesised that none of these transcripts individually was a perfect biomarker of drug response, but maybe they could be used as a panel.

The patient cell lines were then given a score depending on the change in each biomarker after treatment with S[+]-apomorphine (Figure 6.4). If there was a change towards the control after treatment, there was given a score of +1, a score of 0 for no change and a score of -1 if the gene expression change was against the control after treatment; the total scores were presented at the bottom of the table. The figure shows that patient responders typically scored between 2 and 6 when they were assessed against the whole gene panel, while the patient non-responder lines scored between 0 and -2. This confirmed my previous hypothesis that not every biomarker changed in every patient line, but selected gene biomarkers can be used as a panel to discriminate between patient responders and non-responders.

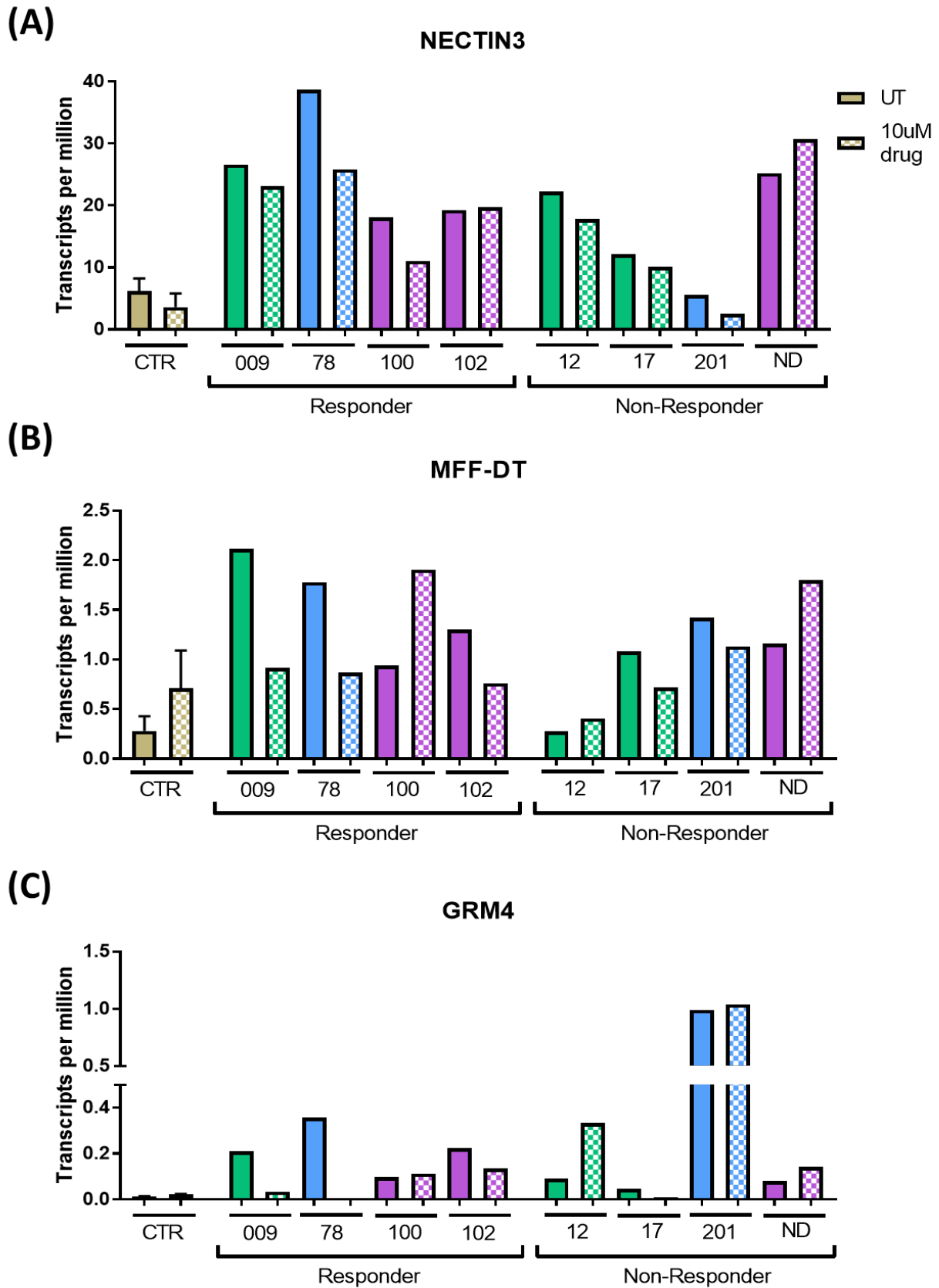


Figure 6.3 The normalised gene counts (TPM values) for patient responders and non-responders to *S[+]-apomorphine* before and after drug treatment. (A). Normalised gene counts for *NECTIN3* ($n=1$), (B). *MFF-DT* ($n=1$), (C). *GRM4* ($n=1$). Control bar consists of 3050 & AG.

Genetic Biomarker	Responder				Non-Responder			
	009	78	100	102	12	17	201	ND29505
ICA1	1	0	0	1	0	0	-1	0
MRPS9	0	1	0	0	0	0	0	0
NECTIN3	1	1	1	0	1	0	1	-1
EPHA3	0	1	0	0	0	0	0	-1
MFF-DT	1	1	-1	1	0	1	1	-1
ROCK1P1	1	0	1	0	0	-1	-1	1
LYPD6	0	0	1	1	0	0	0	0
DKK2	-1	1	0	0	0	0	0	0
CAP2	0	0	0	0	0	0	0	0
GRM4	1	1	0	1	-1	0	0	0
Score	4	6	2	4	0	0	0	-2

Figure 6.4 The summary of the gene expression change in each biomarker identified within the S[+]-apomorphine treatment response group. The normalised gene counts were plotted to determine how the transcript expression changed in each cell line after treatment with S[+]-apomorphine. Each one was given a score based on the response after treatment; a change in the direction of the control (+1, green), no change (0, yellow) or a change in the opposite direction of the control (-1, red), and the total value for each cell line was presented at the bottom.

6.2.3. Andrographolide response

Similarly to S[+]-apomorphine, I set out to identify gene biomarkers that would discriminate between responders and non-responders to andrographolide. Lists of differentially regulated transcripts between the andrographolide iAstrocyte response group before and after treatment compared to the control iAstrocyte group were generated by running the comparisons in the table below (Table 6.9):

Table 6.9 List of bioinformatic comparisons for andrographolide patient responders

Bioinformatic comparisons
Resp. andrographolide U* vs CTR U = transcripts altered in the responder's group at baseline against healthy individuals
Resp. andrographolide T# vs CTR U = transcripts altered in the responder's groups after treatment against healthy individuals
Resp. andrographolide T vs Resp. andrographolide U = transcripts altered in the responder's group after treatment against the baseline value

U* = untreated, T# = treated

The highest number of significant DEGs was observed in the *A Resp. U vs CTR U* comparison (187 genes) while the other comparisons presented fewer transcripts; *A Resp. T vs A Resp. U* displayed 151 DEGs and *A Resp. T vs CTR U* presented 106 DEGs. A full list of transcripts generated from the *A Resp. T vs CTR U* comparison are presented in Supplementary 6.5. When the lists were separated into Venny, the *A Resp. T vs A Resp. U* comparison displayed the most unique genes (146 DEGs, 133 up, 13 down), while there were 25 DEGs (17 up, 8 down) unique to the *A Resp. T vs CTR U* comparison, and 76 genes (63 up, 13 down) shared between *A Resp. U vs CTR U* & *A Resp. T vs CTR U* comparisons (Figure 6.5). The 108 DEGs (86 up, 22 down) that were unique to the *A Resp. U vs CTR U* comparison were investigated further to identify patient response transcripts to andrographolide.

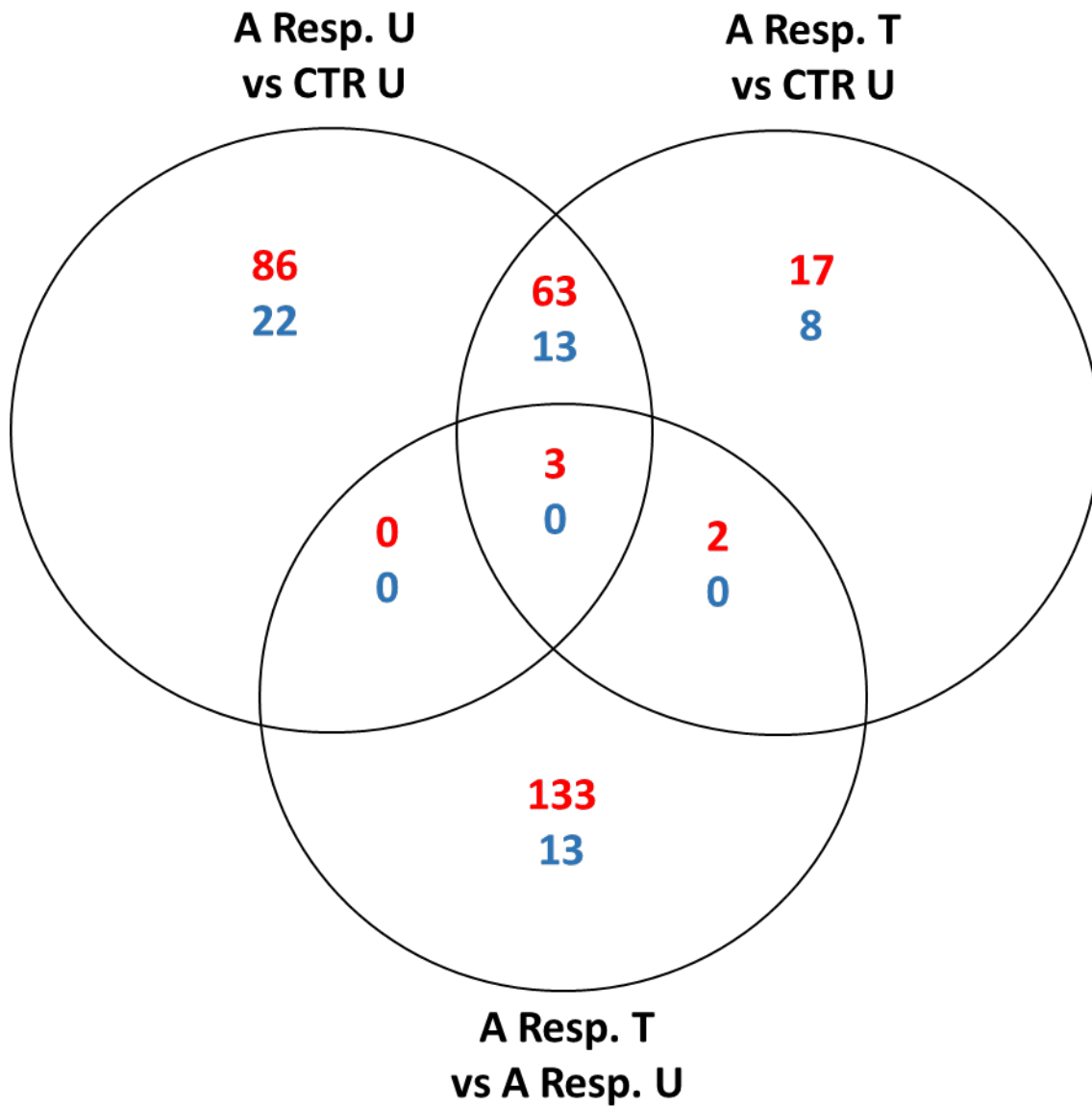


Figure 6.5 Visual interpretation of the DEGs shared between andrographolide response comparisons demonstrated in Table 6.9. The number of upregulated genes are shown in red and downregulated transcripts in blue. Abbreviations: U = untreated, T = treated, A = andrographolide.

Since there were a large number of DEGs unique to the *A Resp. U vs CTR U* comparison, the list was imported into DAVID and the transcripts within the top GO-BP lists were selected as shown in Table 6.10. The transcripts involved in chemical synaptic transmission, nervous system development and axon guidance were all previously identified as significantly dysregulated transcripts unique to andrographolide responders at baseline (Table 6.5). The transcripts with the biggest change in significance after andrographolide treatment were *GRIN2B*, *SORBS2* and *CYP26A1*.

Table 6.10 List of genes unique to andrographolide responders untreated vs CTR untreated

GO Term	Gene Name	A Resp. U	A Resp. T	A Resp. T vs U
Chemical synaptic transmission	Glutamate Ionotropic Receptor NMDA Type Subunit 2B (<i>GRIN2B</i>)	8.52E-04 -8.522048538	0.999638173 -2.649988821	0.999591513 -0.03491602
	Glutamate Metabotropic Receptor 4 (<i>GRM4</i>)	0.049350963 +4.127677713	N/A +3.758228779	0.234445258 -1.984300049
	Neurotensin Receptor 1 (<i>NTSR1</i>)	0.019183759 -6.248658287	0.121781859 -5.520051866	0.999591513 +0.607114631
	Tachykinin Receptor 1 (<i>TACR1</i>)	0.035860605 +6.607741735	0.058618505 +6.973639375	0.999591513 +0.060864436
Nervous system development	Brain Derived Neurotrophic Factor (<i>BDNF</i>)	0.018674402 +4.84687531	0.065815591 +4.226690131	0.999591513 -0.08802963
	Fasciculation And Elongation Protein Zeta 1 (<i>FEZ1</i>)	0.048456655 +3.921821658	0.048456655 +3.921821658	0.999591513 +0.054648027
	Frizzled Class Receptor 9 (<i>FZD9</i>)	0.036777514 +3.314199656	0.076863946 +3.523309106	0.999591513 +0.210385791
	Integral Membrane Protein 2A (<i>ITM2A</i>)	0.019183759 +4.723138339	0.101871516 +4.35519521	0.999591513 -0.148482373
	Nuclear Receptor Subfamily 2 Group E Member 1 (<i>NR2E1</i>)	0.029286056 -5.732073114	0.167838332 -4.612646122	N/A +1.204332416
Cell adhesion	Ameloblastin (<i>AMBN</i>)	0.019043065 +10.00369565	0.162178719 +7.45353075	0.81536258 -0.888083868
	Microfibril Associated Protein 4 (<i>MFAP4</i>)	0.030568839 +6.129343647	0.084378689 +5.782388131	0.094290998 -0.681986522
	Signal Regulatory Protein Alpha (<i>SIRPA</i>)	0.004084036 -5.708294018	0.05815284 -5.162754318	0.999591513 +0.101771016
	Sorbin And SH3 Domain Containing 2 (<i>SORBS2</i>)	0.024347765 -3.030962817	0.311591212 -2.753858107	0.999591513 +0.117095885
Axon guidance	Dorsal Inhibitory Axon Guidance Protein (<i>DRAXIN</i>)	0.020025012 +2.557992208	0.136046137 +2.491592515	0.999591513 0.014077558
Retinoic acid metabolic process	Cytochrome P450 Family 26 Subfamily A Member 1 (<i>CYP26A1</i>)	0.018406774 +7.267502932	0.25531216 +5.952020194	0.999591513 -1.312203373

As before, the normalised gene counts for each transcript before and after andrographolide treatment in both patient responder and non-responder iAstrocytes were plotted, as shown in Figure 6.6. The summary of the expression changes of each genetic biomarker in the patient responders and non-responders to andrographolide displayed a similar finding to the S[+]-apomorphine responders; that patient responder iAstrocytes typically presented a positive change or no change after treatment while patient non-responder lines displayed more no change or negative change (Figure 6.7). The responder lines to andrographolide ranged in the total score from 2 to 14, while the patient non-responder lines ranged from 0 to -3, allowing us to clearly discriminate patient responders from non-responder lines to andrographolide treatment.

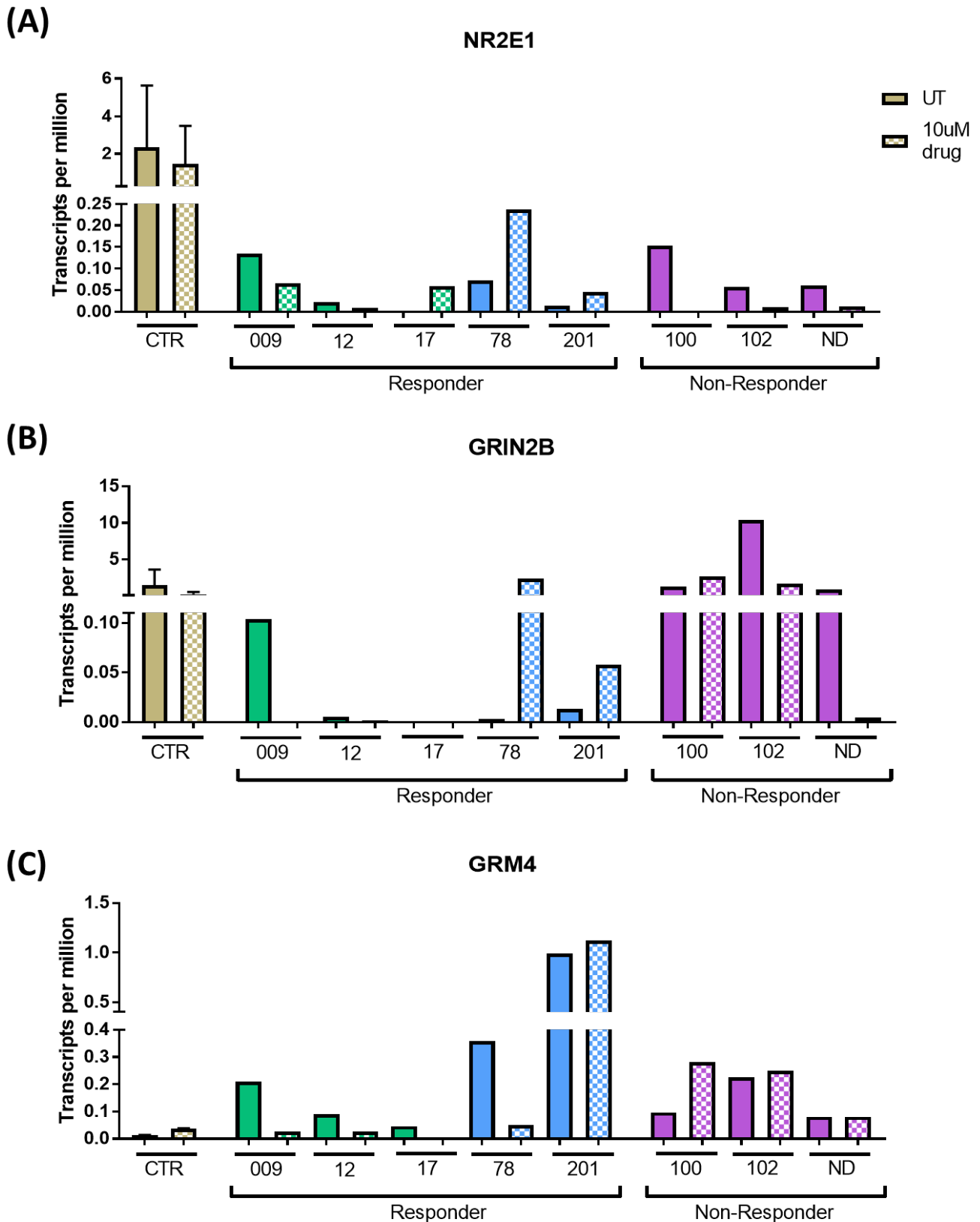


Figure 6.6 The normalised gene counts (TPM values) for patient responders and non-responders to andrographolide before and after drug treatment. (A). Normalised gene counts for NR2E1 (n=1), (B). GRIN2B (n=1), (C). GRM4 (n=1). Control bar consists of 3050 & AG.

Genetic Biomarker	Responder					Non-Responder		
	009	12	17	78	201	100	102	ND29505
BDNF	0	0	1	0	1	0	0	1
FEZ1	-1	-1	1	1	1	-1	0	1
FZD9	0	1	0	0	0	1	0	-1
ITM2A	0	1	1	0	1	0	0	1
NR2E1	-1	-1	1	1	1	-1	-1	-1
GRIN2B	-1	0	0	1	1	0	1	-1
NTSR1	1	0	1	0	0	0	-1	0
TACR1	0	-1	1	1	0	0	1	0
DRAXIN	0	1	1	1	-1	-1	0	0
RPE65	1	1	1	1	-1	0	-1	-1
GRM4	1	1	1	1	0	-1	0	0
AMBN	1	0	1	0	1	0	0	0
MFAP4	1	0	1	1	1	0	0	0
SIRPA	1	0	0	0	0	0	0	1
SORBS2	1	-1	1	0	1	-1	0	0
CYP26A1	1	1	1	-1	1	0	0	0
Score	6	2	14	7	8	-3	0	0

Figure 6.7 The summary of the gene expression change in each biomarker identified within the andrographolide treatment response group. The normalised gene counts were plotted to determine how the transcript expression changed in each cell line after treatment with andrographolide. Each one was given a score based on the response after treatment; a change in the direction of the control (+1, green), no change (0, yellow) or a change in the opposite direction of the control (-1, red), and the total value for each cell line was presented at the bottom.

6.2.4. Riluzole response

To identify the patient responder biomarkers for riluzole treatment, lists of differentially regulated transcripts between the riluzole iAstrocyte response group before and after treatment compared to the control iAstrocyte group were generated by running the comparisons in the table below (Table 6.11):

Table 6.11 List of bioinformatic comparisons for riluzole patient responders

Bioinformatic comparisons
Resp. riluzole U* vs CTR U = transcripts altered in the responder's group at baseline against healthy individuals
Resp. riluzole T# vs CTR U = transcripts altered in the responder's groups after treatment against healthy individuals
Resp. riluzole T vs Resp. riluzole U = transcripts altered in the responder's group after treatment against the baseline value

U* = untreated, T# = treated

The highest number of DEGs was observed in the *R Resp. T vs CTR U* comparison (84 genes) while the other comparisons presented fewer genes; *R Resp. U vs CTR U* displayed 37 genes while *R Resp. T vs R Resp. U* presented 18 DEGs. A full list of transcripts generated from the *R Resp. T vs CTR U* comparison are presented in Supplementary 6.6. When the lists were imported into Venny, I observed 16 genes (16 up, 0 down) unique to the *R Resp. T vs R Resp. U* comparison (Figure 6.8). There were 52 DEGs (29 up, 23 down) unique to the *R Resp. T vs CTR U* comparison and 30 transcripts (23 up, 7 down) shared between the *R Resp. U vs CTR U* & *R Resp. T vs CTR U* comparisons. The 7 DEGs (4 up, 3 down) that were unique to *R Resp. U vs CTR U* comparison were investigated further to identify patient response transcripts.

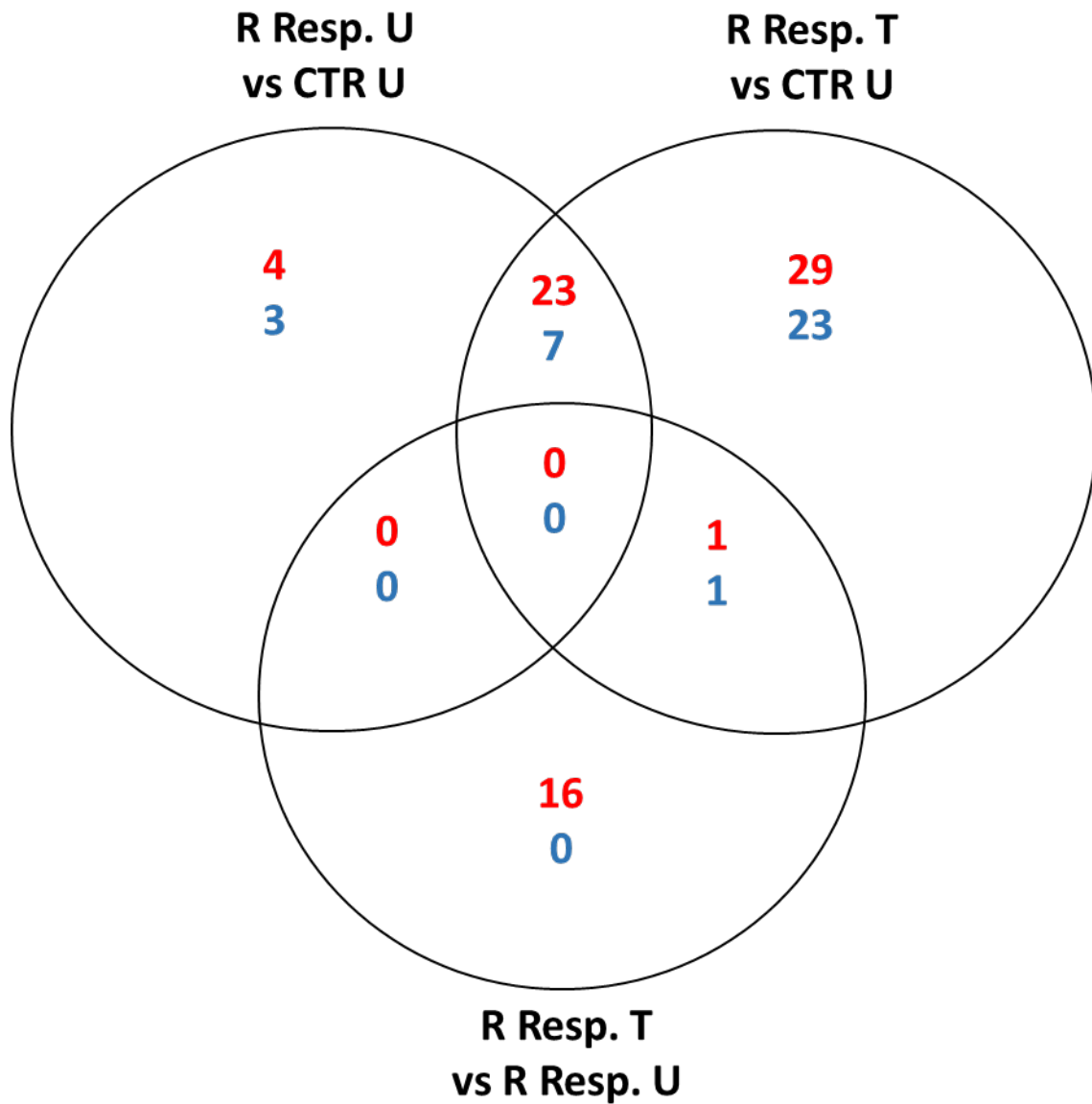


Figure 6.8 Visual interpretation of the DEGs shared between riluzole response comparisons demonstrated in Table 6.11. The number of upregulated genes are shown in red and downregulated transcripts in blue. Abbreviations: U = untreated, T = treated, R = riluzole.

The transcripts unique to the *R Resp. U vs CTR U* comparison implied that after riluzole treatment, these transcripts were no longer significantly different from the control iAstrocytes. *GJC1*, *CLD10*, *COL1A1* and *COL17A1* were all previously investigated as significantly dysregulated transcripts unique to riluzole responders at baseline (Table 6.6). Unlike previous analyses, no transcripts showed a high change in significance after riluzole treatment, implying that riluzole does not exert a strong beneficial response in the patient responders.

Table 6.12 List of genes unique to riluzole responders untreated vs CTR untreated

Gene Name	R Resp. U	R Resp. T	R Resp. T vs U
Gap Junction Protein Gamma 1 (GJC1)	1.54E-04 -3.305787665	0.082952226 -2.521448213	0.999782995 +0.787848845
Claudin 10 (CLD10)	0.024429744 -4.885149921	0.17772894 -4.720214903	N/A -1.453292895
Collagen Type I Alpha 1 Chain (COL1A1)	0.029297762 +2.310305576	0.133840211 +2.303047559	0.999782995 -0.007468018
Collagen Type XVII Alpha 1 Chain (COL17A1)	0.04952992 -5.431186952	0.090921901 -4.850080039	N/A +0.466784465
NFAT Activating Protein With ITAM Motif 1 (NFAM1)	0.024429744 +4.407210903	0.227628305 +3.607318772	0.999782995 -0.976229474
Intercellular Adhesion Molecule 1 (ICAM1)	0.041567054 +3.419195705	0.103844984 +3.573814109	0.999782995 -0.113588996
Olfactomedin 2 (OLFM2)	0.04952992 +3.154189243	0.06759179 +3.418939198	0.999782995 +0.140665212

As before, the normalised gene counts for each transcript before and after riluzole treatment in both patient responder and non-responder iAstrocytes were plotted, as shown in Figure 6.9. The distinction between patient responders and non-responders to riluzole treatment was not as clear as the previous two groups; this may be due to the mild response exerted by riluzole treatment. Figure 6.10 shows that the total score for patient responders ranged from 2 to 5 while the score for the non-responder lines ranged from 1 to -5. In the previous treatment groups, the non-responder lines did not score higher than 0, but after riluzole treatment, non-responder lines sALS patient 12 and C9ORF72 201 scored a total of 1. In the iAstrocyte-MN co-culture experiments, riluzole treatment did significantly improve the MN survival in co-culture with these two cell lines, however this response was not high enough for these lines to be considered as responders to riluzole treatment. Nevertheless, there was still a clear discrimination between the lines that responded to riluzole treatment from the lines that showed no improvement in MN survival with the drug.

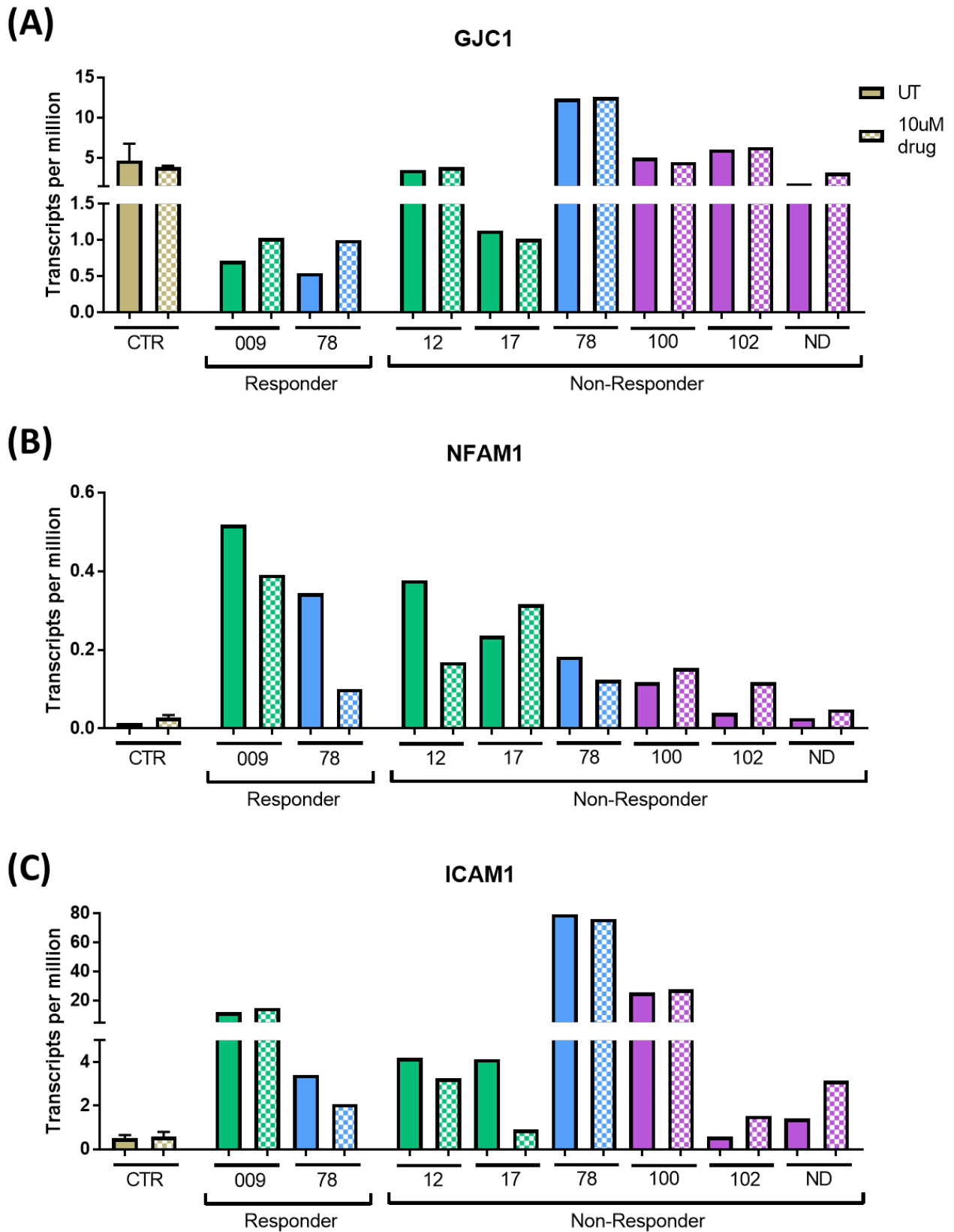


Figure 6.9 The normalised gene counts (TPM values) for patient responders and non-responders to riluzole before and after drug treatment. (A). Normalised gene counts for GJC1 (n=1), (B). NFAM1 (n=1), (C). ICAM1 (n=1). Control bar consists of 3050 & AG.

Genetic Biomarker	Responder		Non-Responder					
	009	78	12	17	201	100	102	ND29505
GJC1	1	1	0	0	0	0	0	1
CLDN10	1	-1	0	-1	0	0	-1	1
COL1A1	0	1	0	-1	0	1	-1	-1
COL17A1	0	1	1	-1	1	0	0	-1
NFAM1	1	1	1	-1	1	-1	-1	-1
ICAM1	0	1	0	1	0	0	-1	-1
OLFM2	-1	1	-1	-1	-1	0	-1	1
Score	2	5	1	-4	1	0	-5	-1

Figure 6.10 The summary of the gene expression change in each biomarker identified within the riluzole treatment response group. The normalised gene counts were plotted to determine how the transcript expression changed in each cell line after treatment with riluzole. Each one was given a score based on the response after treatment; a change in the direction of the control (+1, green), no change (0, yellow) or a change in the opposite direction of the control (-1, red), and the total value for each cell line was presented at the bottom.

6.3 Discussion

The personalised medicine approach of tailoring the treatment of a patient on their specific disease pathology has been used to treat cancer for many years and is beginning to make way in neurodegenerative diseases such as AD and MS (Krzyszczuk *et al.* 2018; Hampel *et al.* 2016; Gafson *et al.* 2017). Diseases like ALS, where there is widespread heterogeneity across the patient population, would benefit from the application of such an approach, especially since the current drug treatments provide only a modest benefit across different patients.

In this chapter, I have uncovered the genetic biomarkers that were associated with disease rescue with specific drug treatments as identified from the previous iAstrocyte-MN co-culture data. Each transcriptional signature was significantly dysregulated from the control prior to drug treatment and this significance was then lost after treatment, indicating that the gene expression had been reverted towards control levels. However, due to patient variability, not every biomarker was reverted to control levels after drug treatment within each patient, therefore I came to the conclusion that a panel of biomarkers were required to identify patient responders to a specific drug and these patients displayed gene expression changes in a number of the biomarkers that was not seen in the patient non-responders after treatment with the same compound.

Within this pilot study, we had groups of patient responders to a particular compound that varied in the number of cell lines, for example, there were 4 lines in the S[+]-apomorphine response group, 5 lines in the andrographolide response group and only 2 lines in the riluzole response group. While this may be reflective of the variation within the patient population, the varying number can lead to difficulties in translating the statistical analysis in the RNA-sequencing comparison tests. For example, there may be little difference in the log₂FC of a RNA biomarker, indicating only a small change in gene expression, from the control iAstrocytes between different response groups, however, there was a large difference in the padj value, potentially because of the different group sizes. This makes us uncertain whether these biomarkers were unique to the response group at baseline since there was little change in gene expression, or maybe they are shared with another group. However, since we have identified biomarkers that were shared between different response groups, for example *GRM4* was identified as a genetic biomarker for both S[+]-apomorphine and andrographolide, I am still confident that these were efficacy biomarkers, so long as this significance was lost after treatment with the compound.

I am also aware that some comparisons in the study may be lacking statistical power since unfortunately I could not include CTR 155 into the RNA-sequencing analysis due to the presence of contaminating rRNA identified in the previous chapter (5.2.2). So, while I am confident that the

efficacy biomarkers identified in this chapter were able to discriminate between patient responders and non-responders of a particular compound, this is a purely proof-of-concept study and extensive research, including a much larger patient cohort, is required before personalised medicine can be applied within the clinic.

The panel of biomarkers identified could be further refined by only including the transcripts that showed a large overall difference in the patient responders that was not seen in the non-responder group. An example of this would be *GRM4* in the andrographolide response group; 4 out of 5 patient responders to andrographolide scored a +1 in this RNA biomarker, while the majority of patient non-responders scored a 0. On the other hand, biomarkers that did not show a great difference between patient responders and non-responders after treatment could be excluded to refine the panel, for example both patient responders and non-responders for S[+]-apomorphine treatment scored a majority of a 0 in the *MRPS9* transcript biomarker.

It was particularly interesting that the panel of biomarkers for response to riluzole treatment managed to identify two patients that had a mild response to riluzole. The cell lines sALS 12 and C9ORF72 201 did present a significant increase in MN survival after riluzole treatment in the iAstrocyte-MN co-culture experiments, however these lines were discarded from the RNA-sequencing experiments since they did not meet the MN survival threshold of ~50% that was set to reduce the noise from incorporating mild responder lines. However, these cell lines still scored higher than the other patient non-responders in the biomarker panel for riluzole treatment, indicating that our RNA biomarker panels were able to identify both patients that give a strong response or a mild response to drug treatment, confirming the validity of our approach.

Since there were differences in the final scores of the biomarker panels for each patient responder line within a response group, I wanted to investigate whether this had a correlation with the level of toxicity of the patient iAstrocyte line towards MNs (3.3.6). While there did appear to be some level of correlation in specific response groups, overall, there was no correlation in the RNA biomarker score after drug treatment with the baseline toxicity of the patient iAstrocytes.

In Chapter 3 (3.2.4), the glutamate uptake study showed that C9ORF72 iAstrocytes fail to buffer extracellular glutamate, thus causing high levels of extracellular glutamate to accumulate in the media, even in monoculture. I also observed a dysregulation in genes involved in glutamate signalling and transport in the untreated baseline (5.2.3). Andrographolide treatment appeared to reduce the protein expression of the ionotropic glutamate receptor GluN2B, specifically in C9ORF72 patients which displayed elevated levels of these proteins, while it did not alter its expression in control iAstrocytes or patient iAstrocytes that displayed similar protein levels with the controls, as

demonstrated in Chapter 4 (4.2.7). Therefore, it was interesting that *GRIN2B* was identified as a genetic biomarker for the andrographolide response group; from the RNA-sequencing data we observed a gene expression change back towards the control levels and this was also reflected in the western blot as protein levels were reduced back towards control level after treatment with the compound. In terms of the biological significance of this protein reduction, we hypothesised that andrographolide reduced the expression of *GRIN2B* to modulate the intracellular cascade of calcium signalling, thus preserving cellular function. This mechanism should also prevent the excessive secretion of glutamate; however we did not observe such an effect on extracellular glutamate when C9ORF72 iAstrocytes were treated with andrographolide for 24 hours (4.2.7). To validate this hypothesis, extracellular glutamate levels, as well as intracellular calcium dynamics should be assessed after a longer period of drug treatment.

Another glutamate receptor, *GRM4*, was identified as a genetic biomarker for both S[+]-apomorphine and andrographolide response groups. While sALS 009 and C9ORF72 78 responded to both drug treatments, it was interesting to observe how the responders to S[+]-apomorphine treatment displayed no beneficial gene expression change after andrographolide treatment and this was the same with the andrographolide responders to S[+]-apomorphine. Whether these compounds have different effects on the metabotropic receptor function within the different patient lines would be interesting to investigate further.

In conclusion, we have successfully identified transcriptional signatures that discriminate between patient responders and non-responder lines to a specific drug treatment. Rather than focusing on just one biomarker for a whole group, observing the gene expression changes within a panel of known biomarkers will be more effective at finding the right treatment for an individual within a heterogenous population. While we are confident that moving towards a personalised approach to treatment in ALS would be beneficial to patient outcome, the lack of statistical power within some of the comparisons in this pilot study means that much more samples are required before I can say with certainty that these are the optimal transcriptional signatures for S[+]-apomorphine, andrographolide or riluzole treatment in the ALS patient population.

Chapter 7 - General Discussion

ALS is a complex disorder influenced by a variety of dysregulated transcripts and pathological mechanisms which can be altered at different stages of disease, painting the description of a multigenic, systemic disease (Morgan *et al.* 2018). Therefore, applying a personalised approach to molecular data could be beneficial to ALS patients if a specific disease mechanism can be identified as well as therapies that target this mechanism. For example, clinical trials involving edaravone treatment were unable to identify a significant benefit between treatment and placebo groups (Abe *et al.*, 2014), until later analysis identified a subpopulation of patients with early stage ALS that responded to treatment (Takei *et al.*, 2017; Writing Group; Edaravone (MCI-186) ALS 19 Study Group, 2017) implying that adopting personalised medicine approaches to tailor patient treatment may be necessary.

Personalised medicine is moving away from the 'one size fits all' approach to medicine and instead tailoring treatment to the individual patient. A good example of using personalised medicine to improve patient treatment is in cystic fibrosis (CF). In CF, patients are given specific drugs based on their genomic profile; ivacaftor benefits patients with at least one allele of the *G551D CFTR* gating mutation (Accurso *et al.*, 2010) while lumacaftor/ivacaftor and tezacaftor/ivacaftor combination treatments are provided for patients with the common *CFTR* mutation Phe508del (Wainwright *et al.*, 2015; Donaldson *et al.*, 2018). Since ALS is a multi-genetic disorder, it is unfeasible to believe that one therapeutic target could possibly treat the whole patient population (Morgan *et al.* 2018).

I hypothesised that a personalised medicine approach could be adopted to the treatment of ALS patients using a combination of RNA-sequencing analysis and *in vitro* phenotypic, functional assays in a patient-derived iAstrocyte model. The aims to be achieved were the identification of the pathological aberrations that distinguish ALS patient subgroups, identification of the modes of action of the two antioxidant drugs as well as the genetic signatures that would discriminate between patient responders versus non-responders to treatment.

Transcriptomic studies have shown differing genetic profiles between ALS patients, other neurodegenerative diseases with similar phenotypic features and healthy controls as well as enabling comparisons of transcriptomic profiles within ALS subgroups (Morgan *et al.* 2018). For example, the study comparing the transcriptomic profiles of C9ORF72-ALS FTD and sporadic ALS/FTD patients found similarities, suggesting a common disease mechanism (Conlon *et al.*, 2018). Gene expression data can also be represented as co-expression networks; identifying modules of genes that are co-expressed can help identify genetic interactions at the functional level (Stuart *et al.*, 2003; Langfelder and Horvath, 2008). Multiple studies have identified gene co-expression in several

disease pathways in ALS including cell adhesion, calcium ion binding, inflammatory processes, and TNF signalling (Saris *et al.* 2009; Holtman *et al.* 2015; Prudencio *et al.* 2015; Cooper-Knock *et al.* 2015; Kotni *et al.* 2016), all of which have been reported in this study. Brohawn *et al.* (2016) took gene expression data from the spinal cords of ALS patients and healthy controls and used a weighted gene co-expression network analysis (WGCNA) to predict genetic modules of highly associated genes that can be mapped to phenotypic traits. From this network, the authors identified the *TNFAIP2* gene which induced MN death when overexpressed in functional assays (Brohawn *et al.* 2016). Transcriptomic data can also be applied to protein-protein interaction networks to identify potential biomarkers; differently expressed genes identified between C9ORF72 and control samples were imported into a protein-protein interaction (PPI) network construction programme to define pathways involved in the DEGs; these included cell adhesion and cell-cell signalling (Kotni *et al.* 2016). RNA-sequencing of patient iAstrocytes at baseline identified numerous dysregulated pathways shared between FALS and SALS groups as well as pathways that were unique. Miller *et al.* (2017) performed a transcriptomic array on a pure astrocytic population from the spinal cord of *SOD1 G93A* mice at two different time points: early- and mid-symptomatic. They identified over 1000 markers that were differentially regulated between control and ALS astrocytes, including a strong dysregulation in energy metabolism, signalling, cell cycle, immune responses, MAPK signalling and apoptosis which were backed up by previous findings (Ferraiuolo *et al.* 2011b; Phatnani *et al.* 2013). Many of these pathways were found to be shared by the iAstrocytes across patient subgroups, therefore it is important to clarify which disease pathologies were unique to the individual group if we are hoping to adopt a personalised medicine approach.

Boisvert *et al.* (2018) profiled astrocyte mRNA taken from multiple regions of the adult (4 months) and ageing (2 years) mouse brain to identify astrocytic gene expression changes with age. They found that ageing astrocytes had an upregulation of inflammatory factors, including the complement pathway and MHC class I molecules, which damaged and eliminated synapses, as well as the loss of support through decreased cholesterol synthesis; similar to pathway alterations reported at baseline in patient iAstrocytes in this study. Genes responsible for thrombospondin and glypican family members as well as potassium channels and neurotransmitter up-take transporters, were unchanged and remain expressed throughout life. It is important that we can distinguish between degenerative mechanisms as a result of disease apart from those that are a result of the ageing process, especially as astrocytes in the ageing brain exhibit gene expression changes similar to reactive astrocytes (Boisvert *et al.*, 2018). Because of this, it has been proposed that these ageing changes predispose the brain to neurodegenerative disease by providing them with the optimum conditions for disease progression (Boisvert *et al.*, 2018).

Exploratory studies will use *in vitro* models to identify a disease phenotype at the cellular level and then go on to validate those phenotypes using human post-mortem tissue or genetics (Hawrot *et al.* 2020). Cellular models are also commonly used in screen-based studies to identify therapeutic compounds capable of restoring the disease phenotype back to control levels. Ultimately, these approaches are looking to translate the *in vitro* phenotype to the fundamental *in vivo* disease process in patients, therefore how well the phenotypes observed *in vitro* capture the disease pathogenesis is of great importance (Hawrot *et al.* 2020).

Since it is rarely possible to obtain diseased cells within the CNS directly from patients with neurodegenerative diseases, another approach is to reprogram patient fibroblasts into neuronal and non-neuronal cell types using either iPSC or direct reprogramming technology. Unfortunately iPSC technology has many disadvantages in modelling disease including the removal of epigenetic changes during the reprogramming process (Takahashi and Yamanaka 2006), accumulation of genetic mutations during reprogramming and iPSC processing (Gore *et al.*, 2011) and the instability of the C9ORF72 expansion during the differentiation process (Almeida *et al.*, 2013). Directly reprogrammed cells retain the age-associated features commonly seen in neurodegenerative disorders in both MNs and astrocytes (Tang *et al.*, 2017; Gatto *et al.*, 2020), therefore provide a more suitable model for late-onset ALS.

Directly reprogrammed astrocytes also provide a good model for sporadic disease since yeast, invertebrate and mouse models of SALS do not exist. Since SALS represents ~90% of patient cases, it is highly likely that subgroups of SALS will respond to different treatments (Hawrot *et al.* 2020). The study by Fujimori *et al.* (2018) showed that while FALS iPSC-derived MNs shared similar features including reduced neurite outgrowth and granule formation, SALS-derived cells showed a wider variety in both pathological phenotypes and response to drug treatment. In this study, we clearly showed individual heterogeneity in SALS patient lines in the baseline gene expression as well as in treatment response.

While many of the studies described in this thesis have investigated the astrocyte transcriptome, one strength of this study is that a novel RNA extraction method was undertaken to extract and sequence only the translated mRNA. The GRASPs protocol was less expensive and less time-consuming than previous methods to study the transcriptome and there was improved mapping of full-length mRNA to the genome. The use of RNA-sequencing technologies alongside functional assays to give a phenotypic read-out have allowed us to establish connections between gene expression and functionality within the cell, delivering a clearer understanding of the pathological

dysfunction taking place in patient iAstrocytes as well as the mechanisms of action of antioxidant compounds.

Immunocytochemistry of patient iAstrocyte lines demonstrated an increase in perinuclear misSOD1 compared to control. After S[+]-apomorphine treatment, there was a significant reduction in perinuclear misSOD1 aggregates across patient cell lines which was not seen after treatment with other antioxidant compounds. This reduction was not due to reduced expression of the SOD1 protein and did not appear to be influenced by the expression of HSF1 and HSP70 molecular protein chaperones. Since HSF1 is a transcription factor of heat shock genes, expression changes in HSF1 itself would potentially not be detected at the protein level. RNA-sequencing analysis of patient iAstrocytes after S[+]-apomorphine treatment showed an increase in CYP enzymes *CYP1A1* and *CYP1B1*, both of which interact with genes related to heat shock proteins. The increased expression of *AHRR* after S[+]-apomorphine treatment also led to the hypothesis that the increased availability of HSP90 from the formation of the AhR-ARNT complex may have played a role in this reduction of misSOD1 aggregation. Delving deeper into the molecular interaction network of these CYP genes might help identify how S[+]-apomorphine treatment leads to the reduction of misSOD1 aggregates.

C9ORF72 iAstrocyte lines were found to have higher levels of extracellular glutamate in the media at monoculture and this extracellular glutamate increased after iAstrocyte-MN co-culture at 24 and 48 hours. Western blot analysis identified that C9ORF72 lines had a significantly increased level of the NMDAR2B receptor. RNA-sequencing analysis of patient samples identified a downregulation of the NMDAR2B gene across all patient groups compared to controls; this could be in response to higher protein levels detected or possibly the aggregation of receptors. Andrographolide treatment significantly reduced NMDAR2B protein expression across all C9ORF72 iAstrocyte cell lines. Upon treatment with andrographolide, gene expression of NMDAR2B is flipped compared to baseline, implying restoration of normal protein levels of the glutamate receptor. Unfortunately, this change did not seem to influence extracellular glutamate levels. To fully understand how the C9ORF72 iAstrocytes handle glutamate buffering, electrophysiology experiments will be conducted in the future to investigate the cellular physiology and whether normal function can be restored through transporter/receptor inhibition. Currently, we are working with Dr Matthew Livesey to conduct the electrophysiology experiments by recording the cellular response to glutamate stimulation in the patient iAstrocytes and how this effects the intracellular calcium levels.

The early diagnosis of ALS patients is difficult due to the insidious onset of symptoms and the phenotypic overlap with other neurological disorders. Biomarkers have the potential to provide a more accurate diagnosis as well as stratifying the patient population into responder groups to

certain therapeutic agents and research new drug targets (Morgan *et al.* 2018). For example, previous studies have generated CSF diagnostic assays that are able to distinguish ALS patients from healthy controls with ~87% sensitivity and ~92% specificity (Mitchell *et al.* 2009; Ganesalingam *et al.* 2011). These diagnostic assays measure the levels of cytoskeletal protein such as neurofilament heavy chain and inflammatory markers in the CSF, however the collection of CSF samples is invasive and expensive compared to blood donation (Morgan *et al.* 2018). Many of these markers can also be used as prognostic biomarkers to predict disease severity; higher phosphorylated neurofilament levels in plasma, serum and CSF have been associated with a faster disease progression (Boylan *et al.*, 2013). While these diagnostic and prognostic biomarkers have been identified, their ability to direct drug development has not been thoroughly investigated (Morgan *et al.* 2018).

An alternative to CSF is peripheral blood which is routinely accessed from patients in a relatively non-invasive manner (Sharp *et al.*, 2006). The study by Bayatti *et al.* (2014) performed gene expression profiling of patient peripheral blood samples to identify potential diagnostic and therapeutic targets of ALS. This study found pathway enrichment for specific intracellular signalling pathways such as MAPK and PI3K (Cyclin Dependent Kinase 1, E2F Transcription Factor 2 & EPH Receptor B1) involved in cellular survival (Kim and Choi 2010; Kirby *et al.* 2011) as well as the JAK/STAT pathway (Early Growth Response 1 & Interleukin 23 Receptor) which is a regulator of neuronal apoptosis (Loucks *et al.*, 2006).

The transcriptional signatures associated with disease rescue in patient responders were identified as a signature that was significantly dysregulated from the control prior to drug treatment, and this significance was lost after treatment, indicating a directional change in gene expression towards the control. Since not every biomarker signature was changed after drug treatment within each patient responder, I identified a panel of genetic transcripts that displayed gene expression changes in the patient responder lines that was not seen in the patient non-responders after treatment with the same compound. The number of biomarkers varied between patient response group and this variability might have been associated with sample size, therefore it may be possible that additional genetic signatures are discovered as more patient samples are tested.

Obviously due to the small sample number in this study, the results described in this chapter represent preliminary data. The next step of the study would be to validate these patient responder transcripts by assessing gene expression level in new samples of the same patient lines. Many gene targets could be validated very quickly using the NanoString molecular diagnostic machine. Once these treatment response biomarkers had been validated, new FALS and SALS patient-derived iAstrocytes could be sequenced to assess the presence of these biomarkers as an indication to which

compound would be most beneficial. Afterwards, this hypothesis would be tested in the high-throughput drug screening model to assess if we can accurately determine patient response to treatment using the biomarkers identified in this preliminary study.

The future of bringing a precision medicine approach to the treatment of ALS patients would involve making the leap from *in vitro* models to patients. Since neither S[+]-apomorphine or andrographolide are approved for clinical testing, we would first need to focus on the current FDA-approved drugs given to patients, riluzole and edaravone. Biomarkers identified for patient samples that benefitted from riluzole treatment could be investigated in the peripheral blood of patients currently taking riluzole and comparisons could be made between the presence of these biomarkers and ALSFRS-R patient data to see if riluzole is beneficial in these patients.

In summary, we have been successful in applying a personalised medicine approach to a small subset of patient samples and have identified transcriptional signatures that associate with patient response to treatment. The baseline gene expression findings of this study are in agreement with the transcriptional dysregulation seen in both mouse and human studies within different ALS genetic subgroups. We have also been able to link differential gene expression to some functional, phenotypic assays to assess the different mechanisms of action between two antioxidant drugs. Similar to patient data, riluzole treatment had mild effects on the disease pathology in patient iAstrocytes and this is seen from the minimal gene expression changes induced by riluzole treatment as well as lack of phenotypic change in functional assays. Observing the gene expression changes between patient responders and non-responders after drug treatment has allowed us to compile a panel of genetic biomarkers that will be more effective at identifying the right treatment for the individual patient.

Chapter 8 - Bibliography

- Abbott, N. J. (2002) 'Astrocyte-endothelial interactions and blood-brain barrier permeability.', *Journal of Anatomy*, 200(6), pp. 629–638. doi: 10.1046/j.1469-7580.2002.00064.
- Abe, K. *et al.* (2014) 'Confirmatory double-blind, parallel-group, placebo-controlled study of efficacy and safety of edaravone (MCI-186) in amyotrophic lateral sclerosis patients.', *Amyotrophic Lateral Sclerosis & Frontotemporal Degeneration*, 15(7–8), pp. 610–617. doi: 10.3109/21678421.2014.959024.
- Abou-Gharbia, M. and Childers, W. E. (2014) 'Discovery of innovative therapeutics: Today's realities and tomorrow's vision. 2. Pharma's challenges and their commitment to innovation', *Journal of Medicinal Chemistry*, 57(13), pp. 5525–5553. doi: 10.1021/jm401564r.
- Abrahams, S. *et al.* (2014) 'Screening for cognition and behaviour changes in ALS.', *Amyotrophic Lateral Sclerosis & Frontotemporal Degeneration*. England, 15(1–2), pp. 9–14. doi: 10.3109/21678421.2013.805784.
- Accurso, F. J. *et al.* (2010) 'Effect of VX-770 in persons with cystic fibrosis and the G551D-CFTR mutation.', *The New England Journal of Medicine*, 363(21), pp. 1991–2003. doi: 10.1056/NEJMoa0909825.
- Aebischer, J. *et al.* (2011) 'IFN γ triggers a LIGHT-dependent selective death of motoneurons contributing to the non-cell-autonomous effects of mutant SOD1.', *Cell Death and Differentiation*, 18(5), pp. 754–768. doi: 10.1038/cdd.2010.143.
- Al-Chalabi, A. *et al.* (2016) 'Amyotrophic lateral sclerosis: moving towards a new classification system.', *The Lancet. Neurology*. England, 15(11), pp. 1182–1194. doi: 10.1016/S1474-4422(16)30199-5.
- Al-Chalabi, A., van den Berg, L. H. and Veldink, J. (2017) 'Gene discovery in amyotrophic lateral sclerosis: implications for clinical management.', *Nature Reviews. Neurology*. England, 13(2), pp. 96–104. doi: 10.1038/nrneurol.2016.182.
- Al-Saif, A., Al-Mohanna, F. and Bohlega, S. (2011) 'A mutation in sigma-1 receptor causes juvenile amyotrophic lateral sclerosis.', *Annals of Neurology*. United States, 70(6), pp. 913–919. doi: 10.1002/ana.22534.
- Al-Sarraj, S. *et al.* (2011) 'p62 positive, TDP-43 negative, neuronal cytoplasmic and intranuclear inclusions in the cerebellum and hippocampus define the pathology of C9orf72-linked FTL and MND/ALS.', *Acta Neuropathologica*. Germany, 122(6), pp. 691–702. doi: 10.1007/s00401-011-0911-2.
- Allen, C. F., Shaw, P. J. and Ferraiuolo, L. (2017) 'Can Astrocytes Be a Target for Precision Medicine?', *Advances in Experimental Medicine and Biology*. United States, 1007, pp. 111–128. doi: 10.1007/978-3-319-60733-7_7.
- Allen, S. P. *et al.* (2014) 'Superoxide dismutase 1 mutation in a cellular model of amyotrophic lateral sclerosis shifts energy generation from oxidative phosphorylation to glycolysis', *Neurobiology of Aging*. Elsevier Ltd, 35(6), pp. 1499–1509. doi: 10.1016/j.neurobiolaging.2013.11.025.
- Allen, S. P., Hall, B., Castelli, L. M., *et al.* (2019a) 'Astrocyte adenosine deaminase loss increases motor neuron toxicity in amyotrophic lateral sclerosis.', *Brain : A Journal of Neurology*, 142(3), pp. 586–605. doi: 10.1093/brain/awy353.

- Allen, S. P., Hall, B., Woof, R., *et al.* (2019b) 'C9orf72 expansion within astrocytes reduces metabolic flexibility in amyotrophic lateral sclerosis.', *Brain : A Journal of Neurology*, 142(12), pp. 3771–3790. doi: 10.1093/brain/awz302.
- Almeida, S. *et al.* (2013) 'Modeling key pathological features of frontotemporal dementia with C9ORF72 repeat expansion in iPSC-derived human neurons.', *Acta Neuropathologica*, 126(3), pp. 385–399. doi: 10.1007/s00401-013-1149-y.
- Alvarez, A. *et al.* (2007) 'Serum TNF-alpha levels are increased and correlate negatively with free IGF-I in Alzheimer disease.', *Neurobiology of Aging*. United States, 28(4), pp. 533–536. doi: 10.1016/j.neurobiolaging.2006.02.012.
- Amick, J., Rocznik-Ferguson, A. and Ferguson, S. M. (2016) 'C9orf72 binds SMCR8, localizes to lysosomes, and regulates mTORC1 signaling.', *Molecular Biology of the Cell*, 27(20), pp. 3040–3051. doi: 10.1091/mbc.E16-01-0003.
- Amlic-Wolf, A. *et al.* (2015) 'Transcriptomic changes due to cytoplasmic TDP-43 expression reveal dysregulation of histone transcripts and nuclear chromatin', *PLoS ONE*, 10(10), pp. 1–20. doi: 10.1371/journal.pone.0141836.
- Andersen, P. M. *et al.* (1996) 'Autosomal recessive adult-onset amyotrophic lateral sclerosis associated with homozygosity for Asp90Ala CuZn-superoxide dismutase mutation. A clinical and genealogical study of 36 patients.', *Brain : A Journal of Neurology*. England, 119 (Pt 4, pp. 1153–1172. doi: 10.1093/brain/119.4.1153.
- Anderson, C. M. and Swanson, R. A. (2000) 'Astrocyte glutamate transport: review of properties, regulation, and physiological functions.', *Glia*. United States, 32(1), pp. 1–14.
- Andrés-Benito, P. *et al.* (2018) 'YKL40 in sporadic amyotrophic lateral sclerosis: cerebrospinal fluid levels as a prognosis marker of disease progression.', *Aging*, 10(9), pp. 2367–2382. doi: 10.18632/aging.101551.
- Anlauf, E. and Derouiche, A. (2005) 'Astrocytic exocytosis vesicles and glutamate: a high-resolution immunofluorescence study.', *Glia*. United States, 49(1), pp. 96–106. doi: 10.1002/glia.20094.
- Aoki, M., Warita, H. and Itoyama, Y. (2008) 'Amyotrophic lateral sclerosis with the SOD1 mutations.', *Rinsho Shinkeigaku = Clinical Neurology*. Japan, 48(11), pp. 966–969. doi: 10.5692/clinicalneuro.48.966.
- Arai, T. *et al.* (2006) 'TDP-43 is a component of ubiquitin-positive tau-negative inclusions in frontotemporal lobar degeneration and amyotrophic lateral sclerosis.', *Biochemical and Biophysical Research Communications*. United States, 351(3), pp. 602–611. doi: 10.1016/j.bbrc.2006.10.093.
- Arava, Y. *et al.* (2003) 'Genome-wide analysis of mRNA translation profiles in *Saccharomyces cerevisiae*.', *Proceedings of the National Academy of Sciences of the United States of America*, 100(7), pp. 3889–3894. doi: 10.1073/pnas.0635171100.
- Armada-Moreira, A. *et al.* (2020) 'Going the Extra (Synaptic) Mile: Excitotoxicity as the Road Toward Neurodegenerative Diseases.', *Frontiers in Cellular Neuroscience*, 14, p. 90. doi: 10.3389/fncel.2020.00090.
- Armstrong, J. A. *et al.* (2018) 'Oxidative stress alters mitochondrial bioenergetics and modifies pancreatic cell death independently of cyclophilin D, resulting in an apoptosis-to-necrosis shift.', *The Journal of Biological Chemistry*, 293(21), pp. 8032–8047. doi: 10.1074/jbc.RA118.003200.
- Aronica, E. *et al.* (2015) 'Molecular classification of amyotrophic lateral sclerosis by unsupervised clustering of gene expression in motor cortex.', *Neurobiology of Disease*. United States, 74, pp. 359–

376. doi: 10.1016/j.nbd.2014.12.002.

Arvan, P. *et al.* (2002) 'Secretory pathway quality control operating in Golgi, plasmalemmal, and endosomal systems.', *Traffic (Copenhagen, Denmark)*. England, 3(11), pp. 771–780. doi: 10.1034/j.1600-0854.2002.31102.

Ascherio, A. *et al.* (2005) 'Vitamin E intake and risk of amyotrophic lateral sclerosis.', *Annals of Neurology*. United States, 57(1), pp. 104–110. doi: 10.1002/ana.20316.

Ash, P. E. A. *et al.* (2013) 'Unconventional translation of C9ORF72 GGGGCC expansion generates insoluble polypeptides specific to c9FTD/ALS.', *Neuron*, 77(4), pp. 639–646. doi: 10.1016/j.neuron.2013.02.004.

Atanasio, A. *et al.* (2016) 'C9orf72 ablation causes immune dysregulation characterized by leukocyte expansion, autoantibody production, and glomerulonephropathy in mice.', *Scientific Reports*, 6, p. 23204. doi: 10.1038/srep23204.

Atkin, J. D. *et al.* (2014) 'Mutant SOD1 inhibits ER-Golgi transport in amyotrophic lateral sclerosis.', *Journal of Neurochemistry*. England, 129(1), pp. 190–204. doi: 10.1111/jnc.12493.

Ayala, Y. M. *et al.* (2008) 'Structural determinants of the cellular localization and shuttling of TDP-43.', *Journal of Cell Science*. England, 121(Pt 22), pp. 3778–3785. doi: 10.1242/jcs.038950.

Baker, D. J. *et al.* (2015) 'Lysosomal and phagocytic activity is increased in astrocytes during disease progression in the SOD1 (G93A) mouse model of amyotrophic lateral sclerosis.', *Frontiers in Cellular Neuroscience*, 9, p. 410. doi: 10.3389/fncel.2015.00410.

Bannwarth, S. *et al.* (2014) 'A mitochondrial origin for frontotemporal dementia and amyotrophic lateral sclerosis through CHCHD10 involvement', *Brain*, 137(8), pp. 2329–2345. doi: 10.1093/brain/awu138.

Barber, S. C., Mead, R. J. and Shaw, P. J. (2006) 'Oxidative stress in ALS: A mechanism of neurodegeneration and a therapeutic target', *Biochimica et Biophysica Acta - Molecular Basis of Disease*, 1762(11–12), pp. 1051–1067. doi: 10.1016/j.bbadis.2006.03.008.

Barber, S. C. and Shaw, P. J. (2010) 'Oxidative stress in ALS: key role in motor neuron injury and therapeutic target.', *Free Radical Biology & Medicine*. United States, 48(5), pp. 629–641. doi: 10.1016/j.freeradbiomed.2009.11.018.

Barker, H. V *et al.* (2017) 'RNA Misprocessing in C9orf72-Linked Neurodegeneration.', *Frontiers in Cellular Neuroscience*, 11, p. 195. doi: 10.3389/fncel.2017.00195.

Barker, W. W. *et al.* (2002) 'Relative frequencies of Alzheimer disease, Lewy body, vascular and frontotemporal dementia, and hippocampal sclerosis in the State of Florida Brain Bank.', *Alzheimer Disease and Associated Disorders*. United States, 16(4), pp. 203–212. doi: 10.1097/00002093-200210000-00001.

Battaglia, G. *et al.* (2015) 'Activation of mGlu3 metabotropic glutamate receptors enhances GDNF and GLT-1 formation in the spinal cord and rescues motor neurons in the SOD-1 mouse model of amyotrophic lateral sclerosis.', *Neurobiology of Disease*. United States, 74, pp. 126–136. doi: 10.1016/j.nbd.2014.11.012.

Bauer, D. *et al.* (2010) 'Abnormal glycosylation of EAAT1 and EAAT2 in prefrontal cortex of elderly patients with schizophrenia.', *Schizophrenia Research*, 117(1), pp. 92–98. doi: 10.1016/j.schres.2009.07.025.

Bayatti, N. *et al.* (2014) 'Comparison of blood RNA extraction methods used for gene expression profiling in amyotrophic lateral sclerosis.', *PLoS One*, 9(1), p. e87508. doi:

10.1371/journal.pone.0087508.

Bellingham, M. C. (2011) 'A review of the neural mechanisms of action and clinical efficiency of riluzole in treating amyotrophic lateral sclerosis: what have we learned in the last decade?', *CNS Neuroscience & Therapeutics*, 17(1), pp. 4–31. doi: 10.1111/j.1755-5949.2009.00116.

Benarroch, E. E. (2005) 'Neuron-astrocyte interactions: partnership for normal function and disease in the central nervous system.', *Mayo Clinic Proceedings*. England, 80(10), pp. 1326–1338. doi: 10.4065/80.10.1326.

Benninger, F. *et al.* (2016) 'Glial fibrillary acidic protein as a marker of astrocytic activation in the cerebrospinal fluid of patients with amyotrophic lateral sclerosis.', *Journal of Clinical Neuroscience : Official Journal of the Neurosurgical Society of Australasia*. Scotland, 26, pp. 75–78. doi: 10.1016/j.jocn.2015.10.008.

Bensimon, G., Lacomblez, L. and Meininger, V. (1994) 'A controlled trial of riluzole in amyotrophic lateral sclerosis. ALS/Riluzole Study Group.', *The New England Journal of Medicine*. United States, 330(9), pp. 585–591. doi: 10.1056/NEJM199403033300901.

Bergemalm, D. *et al.* (2010) 'Superoxide dismutase-1 and other proteins in inclusions from transgenic amyotrophic lateral sclerosis model mice.', *Journal of Neurochemistry*. England, 114(2), pp. 408–418. doi: 10.1111/j.1471-4159.2010.06753.

Bezzi, P. *et al.* (2001) 'CXCR4-activated astrocyte glutamate release via TNFalpha: amplification by microglia triggers neurotoxicity.', *Nature Neuroscience*. United States, 4(7), pp. 702–710. doi: 10.1038/89490.

Bilican, B. *et al.* (2012) 'Mutant induced pluripotent stem cell lines recapitulate aspects of TDP-43 proteinopathies and reveal cell-specific vulnerability.', *Proceedings of the National Academy of Sciences of the United States of America*, 109(15), pp. 5803–5808. doi: 10.1073/pnas.1202922109.

Bilsland, L. G. *et al.* (2010) 'Deficits in axonal transport precede ALS symptoms in vivo.', *Proceedings of the National Academy of Sciences of the United States of America*, 107(47), pp. 20523–20528. doi: 10.1073/pnas.1006869107.

Birger, A. *et al.* (2019) 'Human iPSC-derived astrocytes from ALS patients with mutated C9ORF72 show increased oxidative stress and neurotoxicity.', *EBioMedicine*, 50, pp. 274–289. doi: 10.1016/j.ebiom.2019.11.026.

Biswas, S., Holyoake, D. and Maughan, T. S. (2016) 'Molecular Taxonomy and Tumourigenesis of Colorectal Cancer.', *Clinical Oncology (Royal College of Radiologists (Great Britain))*. England, 28(2), pp. 73–82. doi: 10.1016/j.clon.2015.11.001.

Björkhem, I. and Meaney, S. (2004) 'Brain cholesterol: long secret life behind a barrier.', *Arteriosclerosis, Thrombosis, and Vascular Biology*. United States, 24(5), pp. 806–815. doi: 10.1161/01.ATV.0000120374.59826.1b.

Block, R. C. *et al.* (2010) 'Altered cholesterol and fatty acid metabolism in Huntington disease.', *Journal of Clinical Lipidology*, 4(1), pp. 17–23. doi: 10.1016/j.jacl.2009.11.003.

Blokhuis, A. M. *et al.* (2013) 'Protein aggregation in amyotrophic lateral sclerosis', *Acta Neuropathologica*, 125(6), pp. 777–794. doi: 10.1007/s00401-013-1125-6.

Boillée, S. *et al.* (2006) 'Onset and progression in inherited ALS determined by motor neurons and microglia.', *Science (New York, N.Y.)*, 312(5778), pp. 1389–1392. doi: 10.1126/science.1123511.

Boisvert, M. M. *et al.* (2018) 'The Aging Astrocyte Transcriptome from Multiple Regions of the Mouse Brain.', *Cell Reports*, 22(1), pp. 269–285. doi: 10.1016/j.celrep.2017.12.039.

- Bomprezzi, R. (2015) 'Dimethyl fumarate in the treatment of relapsing-remitting multiple sclerosis: an overview.', *Therapeutic Advances in Neurological Disorders*, 8(1), pp. 20–30. doi: 10.1177/1756285614564152.
- Bosco, D. *et al.* (2010) 'Wild-type and mutant SOD1 share an aberrant conformation and a common pathogenic pathway in ALS', *Nature Neuroscience*, 13(11), pp. 1396–1403. doi: 10.1038/nn.2660.
- Boston-Howes, W. *et al.* (2006) 'Caspase-3 cleaves and inactivates the glutamate transporter EAAT2.', *The Journal of Biological Chemistry*. United States, 281(20), pp. 14076–14084. doi: 10.1074/jbc.M600653200.
- Boylan, K. B. *et al.* (2013) 'Phosphorylated neurofilament heavy subunit (pNF-H) in peripheral blood and CSF as a potential prognostic biomarker in amyotrophic lateral sclerosis.', *Journal of Neurology, Neurosurgery, and Psychiatry*. England, 84(4), pp. 467–472. doi: 10.1136/jnnp-2012-303768.
- Bradley, W. G. *et al.* (2013) 'Is exposure to cyanobacteria an environmental risk factor for amyotrophic lateral sclerosis and other neurodegenerative diseases?', *Amyotrophic Lateral Sclerosis & Frontotemporal Degeneration*. England, 14(5–6), pp. 325–333. doi: 10.3109/21678421.2012.750364.
- Brennan, M. S. *et al.* (2017) 'The NRF2 transcriptional target, OSGIN1, contributes to monomethyl fumarate-mediated cytoprotection in human astrocytes.', *Scientific Reports*, 7, p. 42054. doi: 10.1038/srep42054.
- Brohawn, D. G., O'Brien, L. C. and Bennett, J. P. J. (2016) 'RNAseq Analyses Identify Tumor Necrosis Factor-Mediated Inflammation as a Major Abnormality in ALS Spinal Cord.', *PloS One*, 11(8), p. e0160520. doi: 10.1371/journal.pone.0160520.
- Brown, N. M. *et al.* (2004) 'Oxygen and the copper chaperone CCS regulate posttranslational activation of Cu,Zn superoxide dismutase.', *Proceedings of the National Academy of Sciences of the United States of America*, 101(15), pp. 5518–5523. doi: 10.1073/pnas.0401175101.
- Brujn, L. I. *et al.* (1997) 'ALS-linked SOD1 mutant G85R mediates damage to astrocytes and promotes rapidly progressive disease with SOD1-containing inclusions.', *Neuron*. United States, 18(2), pp. 327–338. doi: 10.1016/s0896-6273(00)80272-x.
- Bucchia, M. *et al.* (2015) 'Therapeutic development in amyotrophic lateral sclerosis.', *Clinical Therapeutics*. United States, 37(3), pp. 668–680. doi: 10.1016/j.clinthera.2014.12.020.
- Buratti, E. *et al.* (2005) 'TDP-43 binds heterogeneous nuclear ribonucleoprotein A/B through its C-terminal tail: an important region for the inhibition of cystic fibrosis transmembrane conductance regulator exon 9 splicing.', *The Journal of Biological Chemistry*. United States, 280(45), pp. 37572–37584. doi: 10.1074/jbc.M505557200.
- Buratti, E. (2018) 'TDP-43 post-translational modifications in health and disease.', *Expert Opinion on Therapeutic Targets*. England, 22(3), pp. 279–293. doi: 10.1080/14728222.2018.1439923.
- Buratti, E. and Baralle, F. E. (2010) 'The multiple roles of TDP-43 in pre-mRNA processing and gene expression regulation.', *RNA Biology*. United States, 7(4), pp. 420–429. doi: 10.4161/rna.7.4.12205.
- Burk, K. and Pasterkamp, R. J. (2019) 'Disrupted neuronal trafficking in amyotrophic lateral sclerosis.', *Acta Neuropathologica*, 137(6), pp. 859–877. doi: 10.1007/s00401-019-01964-7.
- Burkhardt, M. F. *et al.* (2013) 'A cellular model for sporadic ALS using patient-derived induced pluripotent stem cells.', *Molecular and Cellular Neurosciences*, 56, pp. 355–364. doi: 10.1016/j.mcn.2013.07.007.
- Butovsky, O. *et al.* (2015) 'Targeting miR-155 restores abnormal microglia and attenuates disease in

- SOD1 mice.', *Annals of Neurology*, 77(1), pp. 75–99. doi: 10.1002/ana.24304.
- Butti, Z. and Patten, S. A. (2018) 'RNA Dysregulation in Amyotrophic Lateral Sclerosis.', *Frontiers in Genetics*, 9, p. 712. doi: 10.3389/fgene.2018.00712.
- Caiazzo, M. *et al.* (2015) 'Direct conversion of fibroblasts into functional astrocytes by defined transcription factors.', *Stem Cell Reports*, 4(1), pp. 25–36. doi: 10.1016/j.stemcr.2014.12.002.
- Calderwood, S. K. *et al.* (2010) 'Signal Transduction Pathways Leading to Heat Shock Transcription.', *Signal Transduction Insights*, 2, pp. 13–24. doi: 10.4137/STI.S3994.
- Carbone, M., Duty, S. and Rattray, M. (2012) 'Riluzole elevates GLT-1 activity and levels in striatal astrocytes.', *Neurochemistry International*, 60(1), pp. 31–38. doi: 10.1016/j.neuint.2011.10.017.
- Carrera-Juliá, S. *et al.* (2020) 'Antioxidant Alternatives in the Treatment of Amyotrophic Lateral Sclerosis: A Comprehensive Review.', *Frontiers in Physiology*, 11, p. 63. doi: 10.3389/fphys.2020.00063.
- de Carvalho, M. *et al.* (2010) 'A randomized, placebo-controlled trial of memantine for functional disability in amyotrophic lateral sclerosis.', *Amyotrophic Lateral Sclerosis : Official Publication of the World Federation of Neurology Research Group on Motor Neuron Diseases*. England, 11(5), pp. 456–460. doi: 10.3109/17482968.2010.498521.
- Cetin, H. *et al.* (2015) 'Epidemiology of amyotrophic lateral sclerosis and effect of riluzole on disease course.', *Neuroepidemiology*. Switzerland, 44(1), pp. 6–15. doi: 10.1159/000369813.
- Chandrasekaran, A. *et al.* (2016) 'Astrocyte Differentiation of Human Pluripotent Stem Cells: New Tools for Neurological Disorder Research', *Frontiers in Cellular Neuroscience*, 10(September), p. 215. doi: 10.3389/fncel.2016.00215.
- Chang, L. and Monteiro, M. J. (2015) 'Defective Proteasome Delivery of Polyubiquitinated Proteins by Ubiquilin-2 Proteins Containing ALS Mutations.', *PLoS One*, 10(6), p. e0130162. doi: 10.1371/journal.pone.0130162.
- Chatterjee, M., Schild, D. and Teunissen, C. E. (2019) 'Contactins in the central nervous system: role in health and disease.', *Neural Regeneration Research*, 14(2), pp. 206–216. doi: 10.4103/1673-5374.244776.
- Chauhan, S. *et al.* (2016) 'TRIMs and Galectins Globally Cooperate and TRIM16 and Galectin-3 Co-direct Autophagy in Endomembrane Damage Homeostasis.', *Developmental Cell*, 39(1), pp. 13–27. doi: 10.1016/j.devcel.2016.08.003.
- Che, M.-X. *et al.* (2011) 'Aggregation of the 35-kDa fragment of TDP-43 causes formation of cytoplasmic inclusions and alteration of RNA processing.', *FASEB Journal : Official Publication of the Federation of American Societies for Experimental Biology*. United States, 25(7), pp. 2344–2353. doi: 10.1096/fj.10-174482.
- Chen, H.-J. *et al.* (2016) 'The heat shock response plays an important role in TDP-43 clearance: evidence for dysfunction in amyotrophic lateral sclerosis.', *Brain : A Journal of Neurology*, 139(Pt 5), pp. 1417–1432. doi: 10.1093/brain/aww028.
- Chen, Y.-Z. *et al.* (2004) 'DNA/RNA helicase gene mutations in a form of juvenile amyotrophic lateral sclerosis (ALS4).', *American Journal of Human Genetics*, 74(6), pp. 1128–1135. doi: 10.1086/421054.
- Chen, Y. *et al.* (2017) 'MicroRNA-4639 Is a Regulator of DJ-1 Expression and a Potential Early Diagnostic Marker for Parkinson's Disease.', *Frontiers in Aging Neuroscience*, 9, p. 232. doi: 10.3389/fnagi.2017.00232.

- Cheroni, C. *et al.* (2009) 'Functional alterations of the ubiquitin-proteasome system in motor neurons of a mouse model of familial amyotrophic lateral sclerosis', *Human Molecular Genetics*, 18(1), pp. 82–96. doi: 10.1093/hmg/ddn319.
- Chiang, P.-M. *et al.* (2010) 'Deletion of TDP-43 down-regulates Tbc1d1, a gene linked to obesity, and alters body fat metabolism.', *Proceedings of the National Academy of Sciences of the United States of America*, 107(37), pp. 16320–16324. doi: 10.1073/pnas.1002176107.
- Cho, K. S. *et al.* (2010) 'The effects of IL-32 on the inflammatory activation of cultured rat primary astrocytes.', *Biochemical and Biophysical Research Communications*. United States, 402(1), pp. 48–53. doi: 10.1016/j.bbrc.2010.09.099.
- Chow, C. Y. *et al.* (2009) 'Deleterious Variants of FIG4, a Phosphoinositide Phosphatase, in Patients with ALS', *American Journal of Human Genetics*. The American Society of Human Genetics, 84(1), pp. 85–88. doi: 10.1016/j.ajhg.2008.12.010.
- Chow, D. S. L. *et al.* (2012) 'Pharmacology of riluzole in acute spinal cord injury.', *Journal of Neurosurgery. Spine*. United States, 17(1 Suppl), pp. 129–140. doi: 10.3171/2012.5.AOSPINE12112.
- Cirulli, E. T. *et al.* (2015) 'Exome sequencing in amyotrophic lateral sclerosis identifies risk genes and pathways', *Science*, 347(6229), pp. 1436–1441. doi: doi:10.1097/AOG.0000000000000696.
- Clement, A. M. *et al.* (2003) 'Wild-type nonneuronal cells extend survival of SOD1 mutant motor neurons in ALS mice.', *Science (New York, N.Y.)*. United States, 302(5642), pp. 113–117. doi: 10.1126/science.1086071.
- Cleveland, D. W. *et al.* (1995) 'Toxic mutants in Charcot's sclerosis.', *Nature*. England, pp. 342–343. doi: 10.1038/378342a0.
- Coan, G. and Mitchell, C. S. (2015) 'An Assessment of Possible Neuropathology and Clinical Relationships in 46 Sporadic Amyotrophic Lateral Sclerosis Patient Autopsies.', *Neuro-degenerative Diseases*, 15(5), pp. 301–312. doi: 10.1159/000433581.
- Cohen, T. J. *et al.* (2015) 'An acetylation switch controls TDP-43 function and aggregation propensity.', *Nature Communications*, 6, p. 5845. doi: 10.1038/ncomms6845.
- Conlon, E. G. *et al.* (2016) 'The C9ORF72 GGGGCC expansion forms RNA G-quadruplex inclusions and sequesters hnRNP H to disrupt splicing in ALS brains.', *eLife*, 5. doi: 10.7554/eLife.17820.
- Conlon, E. G. *et al.* (2018) 'Unexpected similarities between C9ORF72 and sporadic forms of ALS/FTD suggest a common disease mechanism.', *eLife*, 7. doi: 10.7554/eLife.37754.
- Cookson, M. R., Ince, P. G. and Shaw, P. J. (1998) 'Peroxyntirite and hydrogen peroxide induced cell death in the NSC34 neuroblastoma x spinal cord cell line: role of poly (ADP-ribose) polymerase.', *Journal of Neurochemistry*. England, 70(2), pp. 501–508. doi: 10.1046/j.1471-4159.1998.70020501.
- Cooper-Knock, J. *et al.* (2012) 'Gene expression profiling in human neurodegenerative disease.', *Nature Reviews. Neurology*. England, 8(9), pp. 518–530. doi: 10.1038/nrneuro.2012.156.
- Cooper-Knock, J. *et al.* (2015) 'C9ORF72 GGGGCC Expanded Repeats Produce Splicing Dysregulation which Correlates with Disease Severity in Amyotrophic Lateral Sclerosis.', *PloS One*, 10(5), p. e0127376. doi: 10.1371/journal.pone.0127376.
- Cooper-Knock, J. *et al.* (2019) 'Mutations in the Glycosyltransferase Domain of GLT8D1 Are Associated with Familial Amyotrophic Lateral Sclerosis.', *Cell Reports*, 26(9), pp. 2298–2306.e5. doi: 10.1016/j.celrep.2019.02.006.
- Corcia, P. *et al.* (2012) 'Molecular imaging of microglial activation in amyotrophic lateral sclerosis.',

- PloS One*, 7(12), p. e52941. doi: 10.1371/journal.pone.0052941.
- Coulter, D. A. and Eid, T. (2012) 'Astrocytic regulation of glutamate homeostasis in epilepsy.', *Glia*, 60(8), pp. 1215–1226. doi: 10.1002/glia.22341.
- Couthouis, J. *et al.* (2012) 'Evaluating the role of the FUS/TLS-related gene EWSR1 in amyotrophic lateral sclerosis.', *Human Molecular Genetics*, 21(13), pp. 2899–2911. doi: 10.1093/hmg/dds116.
- Cozzolino, M. *et al.* (2009) 'Oligomerization of mutant SOD1 in mitochondria of motoneuronal cells drives mitochondrial damage and cell toxicity.', *Antioxidants & Redox Signaling*. United States, 11(7), pp. 1547–1558. doi: 10.1089/ars.2009.2545.
- Da Cruz, S. *et al.* (2017) 'Misfolded SOD1 is not a primary component of sporadic ALS', *Acta Neuropathologica*. Springer Berlin Heidelberg, 134(1), pp. 97–111. doi: 10.1007/s00401-017-1688-8.
- Cudkovicz, M. E. *et al.* (1997) 'Epidemiology of mutations in superoxide dismutase in amyotrophic lateral sclerosis.', *Annals of Neurology*. United States, 41(2), pp. 210–221. doi: 10.1002/ana.410410212.
- Cudkovicz, M. E. *et al.* (2014) 'Safety and efficacy of ceftriaxone for amyotrophic lateral sclerosis: a multi-stage, randomised, double-blind, placebo-controlled trial.', *The Lancet. Neurology*, 13(11), pp. 1083–1091. doi: 10.1016/S1474-4422(14)70222-4.
- Cykowski, M. D. *et al.* (2017) 'Clinical Significance of TDP-43 Neuropathology in Amyotrophic Lateral Sclerosis.', *Journal of Neuropathology and Experimental Neurology*, 76(5), pp. 402–413. doi: 10.1093/jnen/nlx025.
- Damisah, E. C. *et al.* (2020) 'Astrocytes and microglia play orchestrated roles and respect phagocytic territories during neuronal corpse removal in vivo.', *Science Advances*, 6(26), p. eaba3239. doi: 10.1126/sciadv.aba3239.
- Van Damme, P. *et al.* (2005) 'GluR2 deficiency accelerates motor neuron degeneration in a mouse model of amyotrophic lateral sclerosis.', *Journal of Neuropathology and Experimental Neurology*. England, 64(7), pp. 605–612. doi: 10.1097/01.jnen.0000171647.09589.07.
- Dash, R. P., Babu, R. J. and Srinivas, N. R. (2018) 'Two Decades-Long Journey from Riluzole to Edaravone: Revisiting the Clinical Pharmacokinetics of the Only Two Amyotrophic Lateral Sclerosis Therapeutics.', *Clinical Pharmacokinetics*. Switzerland, 57(11), pp. 1385–1398. doi: 10.1007/s40262-018-0655-4.
- Van Deerlin, V. M. *et al.* (2008) 'TARDBP mutations in amyotrophic lateral sclerosis with TDP-43 neuropathology: a genetic and histopathological analysis.', *The Lancet. Neurology*, 7(5), pp. 409–416. doi: 10.1016/S1474-4422(08)70071-1.
- DeJesus-Hernandez, M. *et al.* (2011) 'Expanded GGGGCC hexanucleotide repeat in noncoding region of C9ORF72 causes chromosome 9p-linked FTD and ALS.', *Neuron*, 72(2), pp. 245–256. doi: 10.1016/j.neuron.2011.09.011.
- Demeester, N. *et al.* (2000) 'Characterization and functional studies of lipoproteins, lipid transfer proteins, and lecithin:cholesterol acyltransferase in CSF of normal individuals and patients with Alzheimer's disease.', *Journal of Lipid Research*. United States, 41(6), pp. 963–974.
- Demircan, K. *et al.* (2013) 'ADAMTS1, ADAMTS5, ADAMTS9 and aggrecanase-generated proteoglycan fragments are induced following spinal cord injury in mouse.', *Neuroscience Letters*. Ireland, 544, pp. 25–30. doi: 10.1016/j.neulet.2013.02.064.
- Deng, H.-X. *et al.* (2011) 'Mutations in UBQLN2 cause dominant X-linked juvenile and adult-onset ALS and ALS/dementia', *Nature*. Nature Publishing Group, 477(7363), pp. 211–5. doi:

10.1038/nature10353.

Deng, H. X. *et al.* (1993) 'Amyotrophic lateral sclerosis and structural defects in Cu,Zn superoxide dismutase.', *Science (New York, N.Y.)*. United States, 261(5124), pp. 1047–1051. doi: 10.1126/science.8351519.

Deng, J. *et al.* (2015) 'FUS Interacts with HSP60 to Promote Mitochondrial Damage.', *PLoS Genetics*, 11(9), p. e1005357. doi: 10.1371/journal.pgen.1005357.

Deschauer, M. *et al.* (2012) 'C19orf12 mutations in neurodegeneration with brain iron accumulation mimicking juvenile amyotrophic lateral sclerosis.', *Journal of Neurology*. Germany, 259(11), pp. 2434–2439. doi: 10.1007/s00415-012-6521-7.

Desnuelle, C. *et al.* (2001) 'A double-blind, placebo-controlled randomized clinical trial of alpha-tocopherol (vitamin E) in the treatment of amyotrophic lateral sclerosis. ALS riluzole-tocopherol Study Group.', *Amyotrophic Lateral Sclerosis and Other Motor Neuron Disorders : Official Publication of the World Federation of Neurology, Research Group on Motor Neuron Diseases*. England, 2(1), pp. 9–18. doi: 10.1080/146608201300079364.

Devon, R. S. *et al.* (2006) 'Als2-deficient mice exhibit disturbances in endosome trafficking associated with motor behavioral abnormalities.', *Proceedings of the National Academy of Sciences of the United States of America*, 103(25), pp. 9595–9600. doi: 10.1073/pnas.0510197103.

Diekstra, F. P. *et al.* (2012) 'UNC13A is a modifier of survival in amyotrophic lateral sclerosis.', *Neurobiology of Aging*. United States, 33(3), pp. 630.e3–8. doi: 10.1016/j.neurobiolaging.2011.10.029.

Dimos, J. T. *et al.* (2008) 'Induced pluripotent stem cells generated from patients with ALS can be differentiated into motor neurons', 321(5893), pp. 1218–1221. doi: 10.1126/science.1158799.

Ding, H. *et al.* (2003) 'Selective silencing by RNAi of a dominant allele that causes amyotrophic lateral sclerosis.', *Aging Cell*. England, 2(4), pp. 209–217. doi: 10.1046/j.1474-9728.2003.00054.

Doble, A. (1996) 'The pharmacology and mechanism of action of riluzole.', *Neurology*. United States, 47(6 Suppl 4), pp. S233-41. doi: 10.1212/wnl.47.6_suppl_4.233s.

Donaldson, S. H. *et al.* (2018) 'Tezacaftor/Ivacaftor in Subjects with Cystic Fibrosis and F508del/F508del-CFTR or F508del/G551D-CFTR.', *American Journal of Respiratory and Critical Care Medicine*, 197(2), pp. 214–224. doi: 10.1164/rccm.201704-0717OC.

Donnelly, C. J. *et al.* (2013) 'RNA toxicity from the ALS/FTD C9ORF72 expansion is mitigated by antisense intervention.', *Neuron*, 80(2), pp. 415–428. doi: 10.1016/j.neuron.2013.10.015.

Dosay-Akbulut, M. (2016) 'A Review on Determination and Future of the Predictive and Personalized Medicine', *International Journal of Biology*, 8(1), pp. 32–41. doi: 10.5539/ijb.v8n1p32.

Dulubova, I. *et al.* (2005) 'A Munc13/RIM/Rab3 tripartite complex: from priming to plasticity?', *The EMBO Journal*, 24(16), pp. 2839–2850. doi: 10.1038/sj.emboj.7600753.

Duong, H.-Q. *et al.* (2017) 'Silencing of NRF2 Reduces the Expression of ALDH1A1 and ALDH3A1 and Sensitizes to 5-FU in Pancreatic Cancer Cells.', *Antioxidants (Basel, Switzerland)*, 6(3). doi: 10.3390/antiox6030052.

Dupuis, L. *et al.* (2011) 'Energy metabolism in amyotrophic lateral sclerosis.', *The Lancet. Neurology*. England, 10(1), pp. 75–82. doi: 10.1016/S1474-4422(10)70224-6.

Dzamba, D. *et al.* (2015) 'Quantitative Analysis of Glutamate Receptors in Glial Cells from the Cortex of GFAP/EGFP Mice Following Ischemic Injury: Focus on NMDA Receptors.', *Cellular and Molecular*

- Neurobiology*. United States, 35(8), pp. 1187–1202. doi: 10.1007/s10571-015-0212-8.
- Eckerich, C. *et al.* (2006) 'Contactin is expressed in human astrocytic gliomas and mediates repulsive effects.', *Glia*. United States, 53(1), pp. 1–12. doi: 10.1002/glia.20254.
- Egawa, N. *et al.* (2012) 'Drug screening for ALS using patient-specific induced pluripotent stem cells.', *Science Translational Medicine*. United States, 4(145), p. 145ra104. doi: 10.1126/scitranslmed.3004052.
- Elbaz, A. *et al.* (2016) 'Epidemiology of Parkinson's disease.', *Revue Neurologique*. France, 172(1), pp. 14–26. doi: 10.1016/j.neurol.2015.09.012.
- Elliott, D. A., Weickert, C. S. and Garner, B. (2010) 'Apolipoproteins in the brain: implications for neurological and psychiatric disorders.', *Clinical Lipidology*, 51(4), pp. 555–573. doi: 10.2217/CLP.10.37.
- Emdad, L. *et al.* (2012) 'Efficient differentiation of human embryonic and induced pluripotent stem cells into functional astrocytes', *Stem Cells and Development*, 21(3), pp. 404–10.
- Ewald, C. Y. *et al.* (2017) 'NADPH oxidase-mediated redox signaling promotes oxidative stress resistance and longevity through memo-1 in *C. elegans*.', *eLife*, 6. doi: 10.7554/eLife.19493.
- Ezzi, S. A., Urushitani, M. and Julien, J.-P. (2007) 'Wild-type superoxide dismutase acquires binding and toxic properties of ALS-linked mutant forms through oxidation.', *Journal of Neurochemistry*. England, 102(1), pp. 170–178. doi: 10.1111/j.1471-4159.2007.04531.
- Fagan, A. M. *et al.* (2009) 'Decreased cerebrospinal fluid Abeta(42) correlates with brain atrophy in cognitively normal elderly.', *Annals of Neurology*, 65(2), pp. 176–183. doi: 10.1002/ana.21559.
- Fairfoul, G. *et al.* (2016) 'Alpha-synuclein RT-QuIC in the CSF of patients with alpha-synucleinopathies.', *Annals of Clinical and Translational Neurology*, 3(10), pp. 812–818. doi: 10.1002/acn3.338.
- Farg, M. A. *et al.* (2014) 'C9ORF72, implicated in amyotrophic lateral sclerosis and frontotemporal dementia, regulates endosomal trafficking', *Human Molecular Genetics*, 23(13), pp. 3579–3595. doi: 10.1093/hmg/ddu068.
- Farhan, S. M. K. *et al.* (2019) 'Exome sequencing in amyotrophic lateral sclerosis implicates a novel gene, DNAJC7, encoding a heat-shock protein.', *Nature Neuroscience*, 22(12), pp. 1966–1974. doi: 10.1038/s41593-019-0530-0.
- Fecto, F. *et al.* (2011) 'SQSTM1 mutations in familial and sporadic amyotrophic lateral sclerosis.', *Archives of Neurology*. United States, 68(11), pp. 1440–1446. doi: 10.1001/archneurol.2011.250.
- Feng, S.-T. *et al.* (2020) 'Dynamin-related protein 1: A protein critical for mitochondrial fission, mitophagy, and neuronal death in Parkinson's disease.', *Pharmacological Research*. Netherlands, 151, p. 104553. doi: 10.1016/j.phrs.2019.104553.
- Ferraiuolo, L., Higginbottom, A., *et al.* (2011b) 'Dysregulation of astrocyte-motoneuron cross-talk in mutant superoxide dismutase 1-related amyotrophic lateral sclerosis', *Brain*, 134(9), pp. 2627–2641. doi: 10.1093/brain/awr193.
- Ferraiuolo, L., Kirby, J., *et al.* (2011a) 'Molecular pathways of motor neuron injury in amyotrophic lateral sclerosis.', *Nature Reviews. Neurology*. England, 7(11), pp. 616–630. doi: 10.1038/nrneurol.2011.152.
- Ferrara, D. *et al.* (2018) 'Role of Extracellular Vesicles in Amyotrophic Lateral Sclerosis.', *Frontiers in Neuroscience*, 12, p. 574. doi: 10.3389/fnins.2018.00574.

- Ferrari, R. *et al.* (2014) 'Frontotemporal dementia and its subtypes: a genome-wide association study.', *The Lancet. Neurology*, 13(7), pp. 686–699. doi: 10.1016/S1474-4422(14)70065-1.
- Ferri, A. *et al.* (2010) 'Glutaredoxin 2 prevents aggregation of mutant SOD1 in mitochondria and abolishes its toxicity', *Human Molecular Genetics*, 19(22), pp. 4529–4542. doi: 10.1093/hmg/ddq383.
- Figlewicz, D. A. *et al.* (1994) 'Variants of the heavy neurofilament subunit are associated with the development of amyotrophic lateral sclerosis.', *Human Molecular Genetics*. England, 3(10), pp. 1757–1761. doi: 10.1093/hmg/3.10.1757.
- Filipi, T. *et al.* (2020) 'Glial Cells-The Strategic Targets in Amyotrophic Lateral Sclerosis Treatment.', *Journal of Clinical Medicine*, 9(1). doi: 10.3390/jcm9010261.
- Fischer, L. R. *et al.* (2004) 'Amyotrophic lateral sclerosis is a distal axonopathy: evidence in mice and man.', *Experimental Neurology*. United States, 185(2), pp. 232–240. doi: 10.1016/j.expneurol.2003.10.004.
- Font-Nieves, M. *et al.* (2012) 'Induction of COX-2 enzyme and down-regulation of COX-1 expression by lipopolysaccharide (LPS) control prostaglandin E2 production in astrocytes.', *The Journal of Biological Chemistry*, 287(9), pp. 6454–6468. doi: 10.1074/jbc.M111.327874.
- Foran, E. *et al.* (2011) 'Motor neuron impairment mediated by a sumoylated fragment of the glial glutamate transporter EAAT2', *Glia*, 59(11), pp. 1719–1731. doi: 10.1007/s11103-011-9767-z.
- Forsberg, K. *et al.* (2010) 'Novel antibodies reveal inclusions containing non-native SOD1 in sporadic ALS patients', *PLoS ONE*, 5(7), pp. 1–9. doi: 10.1371/journal.pone.0011552.
- Forsberg, K. *et al.* (2011) 'Glial nuclear aggregates of superoxide dismutase-1 are regularly present in patients with amyotrophic lateral sclerosis', *Acta Neuropathologica*, 121(5), pp. 623–634. doi: 10.1007/s00401-011-0805-3.
- Forsberg, K. *et al.* (2019) 'Misfolded SOD1 inclusions in patients with mutations in C9orf72 and other ALS/FTD-associated genes.', *Journal of Neurology, neurosurgery, and psychiatry*, 90(8), pp. 861–869. doi: 10.1136/jnnp-2018-319386.
- Frakes, A. E. *et al.* (2014) 'Microglia induce motor neuron death via the classical NF- κ B pathway in amyotrophic lateral sclerosis.', *Neuron*, 81(5), pp. 1009–1023. doi: 10.1016/j.neuron.2014.01.013.
- Freudenberg-Hua, Y., Li, W. and Davies, P. (2018) 'The Role of Genetics in Advancing Precision Medicine for Alzheimer's Disease-A Narrative Review.', *Frontiers in Medicine*, 5, p. 108. doi: 10.3389/fmed.2018.00108.
- Frizzo, M. E. dos S. *et al.* (2004) 'Riluzole enhances glutamate uptake in rat astrocyte cultures.', *Cellular and Molecular Neurobiology*. United States, 24(1), pp. 123–128. doi: 10.1023/b:cemn.0000012717.37839.07.
- Fujimori, K. *et al.* (2018) 'Modeling sporadic ALS in iPSC-derived motor neurons identifies a potential therapeutic agent.', *Nature Medicine*. United States, 24(10), pp. 1579–1589. doi: 10.1038/s41591-018-0140-5.
- Fumagalli, E. *et al.* (2008) 'Riluzole enhances the activity of glutamate transporters GLAST, GLT1 and EAAC1.', *European Journal of Pharmacology*. Netherlands, 578(2–3), pp. 171–176. doi: 10.1016/j.ejphar.2007.10.023.
- Gafson, A., Craner, M. J. and Matthews, P. M. (2017) 'Personalised medicine for multiple sclerosis care.', *Multiple Sclerosis (Houndmills, Basingstoke, England)*. England, 23(3), pp. 362–369. doi: 10.1177/1352458516672017.

- Gagliardi, M. *et al.* (2019) 'Aldo-keto reductases protect metastatic melanoma from ER stress-independent ferroptosis.', *Cell Death & Disease*, 10(12), p. 902. doi: 10.1038/s41419-019-2143-7.
- Gal, J. *et al.* (2007) 'p62 accumulates and enhances aggregate formation in model systems of familial amyotrophic lateral sclerosis.', *The Journal of Biological Chemistry*. United States, 282(15), pp. 11068–11077. doi: 10.1074/jbc.M608787200.
- Galbussera, A. *et al.* (2006) 'Vitamin E intake and quality of life in amyotrophic lateral sclerosis patients: a follow-up case series study.', *Neurological Sciences : Official Journal of the Italian Neurological Society and of the Italian Society of Clinical Neurophysiology*. Italy, 27(3), pp. 190–193. doi: 10.1007/s10072-006-0668-x.
- Gallardo, G. *et al.* (2014) 'An α 2-Na/K ATPase/ α -adducin complex in astrocytes triggers non-cell autonomous neurodegeneration.', *Nature Neuroscience*, 17(12), pp. 1710–1719. doi: 10.1038/nn.3853.
- Ganesalingam, J. *et al.* (2011) 'Combination of neurofilament heavy chain and complement C3 as CSF biomarkers for ALS.', *Journal of Neurochemistry*, 117(3), pp. 528–537. doi: 10.1111/j.1471-4159.2011.07224.
- Gao, F. *et al.* (2017) 'Mitophagy in Parkinson's Disease: Pathogenic and Therapeutic Implications.', *Frontiers in Neurology*, 8, p. 527. doi: 10.3389/fneur.2017.00527.
- Gatto, N. *et al.* (2020) 'Directly converted astrocytes retain the ageing features of the donor fibroblasts and elucidate the astrocytic contribution to human CNS health and disease.', *Aging Cell*. England, p. e13281. doi: 10.1111/accel.13281.
- Geisler, S. *et al.* (2010) 'PINK1/Parkin-mediated mitophagy is dependent on VDAC1 and p62/SQSTM1.', *Nature Cell Biology*. England, 12(2), pp. 119–131. doi: 10.1038/ncb2012.
- Geng, J. *et al.* (2019) 'Andrographolide alleviates Parkinsonism in MPTP-PD mice via targeting mitochondrial fission mediated by dynamin-related protein 1.', *British Journal of Pharmacology*, 176(23), pp. 4574–4591. doi: 10.1111/bph.14823.
- Genin, E. C. *et al.* (2016) 'CHCHD10 mutations promote loss of mitochondrial cristae junctions with impaired mitochondrial genome maintenance and inhibition of apoptosis.', *EMBO Molecular Medicine*, 8(1), pp. 58–72. doi: 10.15252/emmm.201505496.
- Georgakopoulos, N. D. *et al.* (2017) 'Reversible Keap1 inhibitors are preferential pharmacological tools to modulate cellular mitophagy.', *Scientific Reports*, 7(1), p. 10303. doi: 10.1038/s41598-017-07679-7.
- Gérard, F. and Hansson, E. (2012) 'Inflammatory activation enhances NMDA-triggered Ca²⁺ signalling and IL-1 β secretion in primary cultures of rat astrocytes.', *Brain Research*. Netherlands, 1473, pp. 1–8. doi: 10.1016/j.brainres.2012.07.032.
- Geser, F., Lee, V. M.-Y. and Trojanowski, J. Q. (2010) 'Amyotrophic lateral sclerosis and frontotemporal lobar degeneration: a spectrum of TDP-43 proteinopathies.', *Neuropathology : Official Journal of the Japanese Society of Neuropathology*, 30(2), pp. 103–112. doi: 10.1111/j.1440-1789.2009.01091.
- Geurts, J. J. G. *et al.* (2005) 'Expression patterns of Group III metabotropic glutamate receptors mGluR4 and mGluR8 in multiple sclerosis lesions.', *Journal of Neuroimmunology*. Netherlands, 158(1–2), pp. 182–190. doi: 10.1016/j.jneuroim.2004.08.012.
- Giménez-Xavier, P. *et al.* (2008) 'LC3-I conversion to LC3-II does not necessarily result in complete autophagy.', *International Journal of Molecular Medicine*. Greece, 22(6), pp. 781–785.

- Di Giorgio, F. P. *et al.* (2007) 'Non-cell autonomous effect of glia on motor neurons in an embryonic stem cell-based ALS model.', *Nature Neuroscience*, 10(5), pp. 608–614. doi: 10.1038/nn1885.
- Gomes, C. *et al.* (2019) 'Cortical Neurotoxic Astrocytes with Early ALS Pathology and miR-146a Deficit Replicate Gliosis Markers of Symptomatic SOD1G93A Mouse Model.', *Molecular Neurobiology*. United States, 56(3), pp. 2137–2158. doi: 10.1007/s12035-018-1220-8.
- Gore, A. *et al.* (2011) 'Somatic coding mutations in human induced pluripotent stem cells.', *Nature*, 471(7336), pp. 63–67. doi: 10.1038/nature09805.
- Gowing, G. *et al.* (2006) 'Absence of tumor necrosis factor-alpha does not affect motor neuron disease caused by superoxide dismutase 1 mutations.', *The Journal of Neuroscience : The Official Journal of the Society for Neuroscience*, 26(44), pp. 11397–11402. doi: 10.1523/JNEUROSCI.0602-06.2006.
- Goyal, N. A. and Mozaffar, T. (2014) 'Respiratory and nutritional support in amyotrophic lateral sclerosis.', *Current Treatment Options in Neurology*. United States, 16(2), p. 270. doi: 10.1007/s11940-013-0270-5.
- Graf, M. *et al.* (2005) 'High dose vitamin E therapy in amyotrophic lateral sclerosis as add-on therapy to riluzole: results of a placebo-controlled double-blind study.', *Journal of Neural Transmission (Vienna, Austria : 1996)*. Austria, 112(5), pp. 649–660. doi: 10.1007/s00702-004-0220-1.
- Greenway, M. J. *et al.* (2006) 'ANG mutations segregate with familial and "sporadic" amyotrophic lateral sclerosis', *Nature Genetics*, 38(4), pp. 411–413. doi: 10.1038/ng1742.
- Gros-Louis, F. *et al.* (2004) 'A frameshift deletion in peripherin gene associated with amyotrophic lateral sclerosis.', *The Journal of Biological Chemistry*. United States, 279(44), pp. 45951–45956. doi: 10.1074/jbc.M408139200.
- Gu, L. *et al.* (2018) 'Andrographolide Protects PC12 Cells Against β -Amyloid-Induced Autophagy-Associated Cell Death Through Activation of the Nrf2-Mediated p62 Signaling Pathway.', *International Journal of Molecular Sciences*, 19(9). doi: 10.3390/ijms19092844.
- Guareschi, S. *et al.* (2012) 'An over-oxidized form of superoxide dismutase found in sporadic amyotrophic lateral sclerosis with bulbar onset shares a toxic mechanism with mutant SOD1', *Proceedings of the National Academy of Sciences*, 109(13), pp. 5074–5079. doi: 10.1073/pnas.1115402109.
- Guo, W. *et al.* (2014) 'Small molecule-driven mitophagy-mediated NLRP3 inflammasome inhibition is responsible for the prevention of colitis-associated cancer.', *Autophagy*, 10(6), pp. 972–985. doi: 10.4161/auto.28374.
- Hadano, S. *et al.* (2001) 'A gene encoding a putative GTPase regulator is mutated in familial amyotrophic lateral sclerosis 2.', *Nature Genetics*. United States, 29(2), pp. 166–173. doi: 10.1038/ng1001-166.
- Haidet-Phillips, A. M. *et al.* (2011) 'Astrocytes from familial and sporadic ALS patients are toxic to motor neurons.', *Nature Biotechnology*, 29(9), pp. 824–828. doi: 10.1038/nbt.1957.
- Haidet-Phillips, A. M. *et al.* (2013) 'Altered astrocytic expression of TDP-43 does not influence motor neuron survival.', *Experimental Neurology*. United States, 250, pp. 250–259. doi: 10.1016/j.expneurol.2013.10.004.
- Hampel, H. *et al.* (2016) 'PRECISION MEDICINE - The Golden Gate for Detection, Treatment and Prevention of Alzheimer's Disease.', *The Journal of Prevention of Alzheimer's Disease*, 3(4), pp. 243–259. doi: 10.14283/jpad.2016.112.

- Hand, C. K. *et al.* (2002) 'A novel locus for familial amyotrophic lateral sclerosis, on chromosome 18q.', *American Journal of Human Genetics*, 70(1), pp. 251–256. doi: 10.1086/337945.
- Hanmer, K. L. and Mavri-Damelin, D. (2018) 'Peroxisin is a novel target of the redox-sensitive transcription factor Nrf2.', *Gene*. Netherlands, 674, pp. 104–114. doi: 10.1016/j.gene.2018.06.076.
- Hara, M. *et al.* (2017) 'Interaction of reactive astrocytes with type I collagen induces astrocytic scar formation through the integrin-N-cadherin pathway after spinal cord injury.', *Nature Medicine*. United States, 23(7), pp. 818–828. doi: 10.1038/nm.4354.
- Hardiman, O. *et al.* (2017) 'Amyotrophic lateral sclerosis.', *Nature Reviews. Disease primers*. England, 3, p. 17071. doi: 10.1038/nrdp.2017.71.
- Harlan, B. A. *et al.* (2019) 'Enhanced SIRT6 activity abrogates the neurotoxic phenotype of astrocytes expressing ALS-linked mutant SOD1.', *FASEB Journal : Official Publication of the Federation of American Societies for Experimental Biology*, 33(6), pp. 7084–7091. doi: 10.1096/fj.201802752R.
- Hatakeyama, S. (2017) 'TRIM Family Proteins: Roles in Autophagy, Immunity, and Carcinogenesis.', *Trends in Biochemical Sciences*. England, 42(4), pp. 297–311. doi: 10.1016/j.tibs.2017.01.002.
- Hautbergue, G. M. *et al.* (2017) 'SRSF1-dependent nuclear export inhibition of C9ORF72 repeat transcripts prevents neurodegeneration and associated motor deficits.', *Nature Communications*, 8, p. 16063. doi: 10.1038/ncomms16063.
- Hawley, Z. C. E., Campos-Melo, D. and Strong, M. J. (2019) 'MiR-105 and miR-9 regulate the mRNA stability of neuronal intermediate filaments. Implications for the pathogenesis of amyotrophic lateral sclerosis (ALS).', *Brain Research*. Netherlands, 1706, pp. 93–100. doi: 10.1016/j.brainres.2018.10.032.
- Hawrot, J., Imhof, S. and Wainger, B. J. (2020) 'Modeling cell-autonomous motor neuron phenotypes in ALS using iPSCs.', *Neurobiology of Disease*, 134, p. 104680. doi: 10.1016/j.nbd.2019.104680.
- Hayashi, Y., Homma, K. and Ichijo, H. (2016) 'SOD1 in neurotoxicity and its controversial roles in SOD1 mutation-negative ALS', *Advances in Biological Regulation*. Elsevier Ltd, 60, pp. 95–104. doi: 10.1016/j.jbior.2015.10.006.
- Hayes, J. D. and Dinkova-Kostova, A. T. (2014) 'The Nrf2 regulatory network provides an interface between redox and intermediary metabolism.', *Trends in Biochemical Sciences*. England, 39(4), pp. 199–218. doi: 10.1016/j.tibs.2014.02.002.
- Hays, A. P. *et al.* (2006) 'Sporadic amyotrophic lateral sclerosis and breast cancer: Hyaline conglomerate inclusions lead to identification of SOD1 mutation.', *Journal of the Neurological Sciences*. Netherlands, 242(1–2), pp. 67–69. doi: 10.1016/j.jns.2005.11.016.
- Heath, P. R., Kirby, J. and Shaw, P. J. (2013) 'Investigating cell death mechanisms in amyotrophic lateral sclerosis using transcriptomics.', *Frontiers in Cellular Neuroscience*, 7, p. 259. doi: 10.3389/fncel.2013.00259.
- Heiman, M. *et al.* (2014) 'Cell type-specific mRNA purification by translating ribosome affinity purification (TRAP).', *Nature Protocols*, 9(6), pp. 1282–1291. doi: 10.1038/nprot.2014.085.
- Henkel, J. S. *et al.* (2004) 'Presence of dendritic cells, MCP-1, and activated microglia/macrophages in amyotrophic lateral sclerosis spinal cord tissue.', *Annals of Neurology*. United States, 55(2), pp. 221–235. doi: 10.1002/ana.10805.
- Henkel, J. S. *et al.* (2006) 'The chemokine MCP-1 and the dendritic and myeloid cells it attracts are increased in the mSOD1 mouse model of ALS.', *Molecular and Cellular Neurosciences*. United States, 31(3), pp. 427–437. doi: 10.1016/j.mcn.2005.10.016.

- Higgins, C. M. J., Jung, C. and Xu, Z. (2003) 'ALS-associated mutant SOD1G93A causes mitochondrial vacuolation by expansion of the intermembrane space and by involvement of SOD1 aggregation and peroxisomes.', *BMC Neuroscience*, 4, p. 16. doi: 10.1186/1471-2202-4-16.
- Highley, J. R. *et al.* (2014) 'Loss of nuclear TDP-43 in amyotrophic lateral sclerosis (ALS) causes altered expression of splicing machinery and widespread dysregulation of RNA splicing in motor neurones', *Neuropathology and Applied Neurobiology*, 40(6), pp. 670–685. doi: 10.1111/nan.12148.
- Van Hoecke, A. *et al.* (2012) 'EPHA4 is a disease modifier of amyotrophic lateral sclerosis in animal models and in humans.', *Nature Medicine*. United States, 18(9), pp. 1418–1422. doi: 10.1038/nm.2901.
- Holtman, I. R. *et al.* (2015) 'Induction of a common microglia gene expression signature by aging and neurodegenerative conditions: a co-expression meta-analysis.', *Acta Neuropathologica Communications*, 3, p. 31. doi: 10.1186/s40478-015-0203-5.
- Hong, Y. *et al.* (2016) 'Mutant Huntingtin Impairs BDNF Release from Astrocytes by Disrupting Conversion of Rab3a-GTP into Rab3a-GDP.', *The Journal of Neuroscience : The Official Journal of the Society for Neuroscience*, 36(34), pp. 8790–8801. doi: 10.1523/JNEUROSCI.0168-16.2016.
- Honsa, P. *et al.* (2014) 'Increased expression of hyperpolarization-activated cyclic nucleotide-gated (HCN) channels in reactive astrocytes following ischemia.', *Glia*. United States, 62(12), pp. 2004–2021. doi: 10.1002/glia.22721.
- Houseley, J. and Tollervey, D. (2009) 'The many pathways of RNA degradation.', *Cell*. United States, 136(4), pp. 763–776. doi: 10.1016/j.cell.2009.01.019.
- Howland, D. S. *et al.* (2002) 'Focal loss of the glutamate transporter EAAT2 in a transgenic rat model of SOD1 mutant-mediated amyotrophic lateral sclerosis (ALS).', *Proceedings of the National Academy of Sciences of the United States of America*, 99(3), pp. 1604–1609. doi: 10.1073/pnas.032539299.
- Hsieh, C.-H. *et al.* (2016) 'Functional Impairment in Miro Degradation and Mitophagy Is a Shared Feature in Familial and Sporadic Parkinson's Disease.', *Cell Stem Cell*, 19(6), pp. 709–724. doi: 10.1016/j.stem.2016.08.002.
- Hu, J. *et al.* (2012) 'Interaction of OKL38 and p53 in regulating mitochondrial structure and function.', *PloS One*, 7(8), p. e43362. doi: 10.1371/journal.pone.0043362.
- Hughes, D. *et al.* (2008) 'Heat shock protein 90 inhibitors suppress aryl hydrocarbon receptor-mediated activation of CYP1A1 and CYP1B1 transcription and DNA adduct formation.', *Cancer Prevention Research (Philadelphia, Pa.)*, 1(6), pp. 485–493. doi: 10.1158/1940-6207.CAPR-08-0149.
- Hunsberger, H. C. *et al.* (2015) 'Riluzole rescues glutamate alterations, cognitive deficits, and tau pathology associated with P301L tau expression.', *Journal of Neurochemistry*, 135(2), pp. 381–394. doi: 10.1111/jnc.13230.
- Hwang, C.-S. *et al.* (2013) 'Elevated serum autoantibody against high mobility group box 1 as a potent surrogate biomarker for amyotrophic lateral sclerosis.', *Neurobiology of Disease*. United States, 58, pp. 13–18. doi: 10.1016/j.nbd.2013.04.013.
- Iguchi, Y. *et al.* (2016) 'Exosome secretion is a key pathway for clearance of pathological TDP-43.', *Brain : A Journal of Neurology*, 139(Pt 12), pp. 3187–3201. doi: 10.1093/brain/aww237.
- Illán-Gala, I. *et al.* (2018) 'CSF sAPP β , YKL-40, and NfL along the ALS-FTD spectrum.', *Neurology*. United States, 91(17), pp. e1619–e1628. doi: 10.1212/WNL.0000000000006383.
- Iłżecka, J. (2011) 'Granzymes A and B levels in serum of patients with amyotrophic lateral sclerosis.',

Clinical Biochemistry. United States, 44(8–9), pp. 650–653. doi: 10.1016/j.clinbiochem.2011.02.006.

Ince, P. G. *et al.* (1998) 'Amyotrophic lateral sclerosis associated with genetic abnormalities in the gene encoding Cu/Zn superoxide dismutase: molecular pathology of five new cases, and comparison with previous reports and 73 sporadic cases of ALS.', *Journal of Neuropathology and Experimental Neurology*. England, 57(10), pp. 895–904. doi: 10.1097/00005072-199810000-00002.

Ingolia, N. T. *et al.* (2012) 'The ribosome profiling strategy for monitoring translation in vivo by deep sequencing of ribosome-protected mRNA fragments.', *Nature Protocols*, 7(8), pp. 1534–1550. doi: 10.1038/nprot.2012.086.

Ip, P. *et al.* (2017) 'Quercitrin and quercetin 3- β -d-glucoside as chemical chaperones for the A4V SOD1 ALS-causing mutant.', *Protein Engineering, Design & Selection : PEDS*, 30(6), pp. 431–440. doi: 10.1093/protein/gzx025.

Irizarry-Ramírez, M. *et al.* (2005) 'Upregulation of EphA3 receptor after spinal cord injury.', *Journal of Neurotrauma*. United States, 22(8), pp. 929–935. doi: 10.1089/neu.2005.22.929.

Ishii, T. *et al.* (2000) 'Transcription factor Nrf2 coordinately regulates a group of oxidative stress-inducible genes in macrophages.', *The Journal of Biological Chemistry*. United States, 275(21), pp. 16023–16029. doi: 10.1074/jbc.275.21.16023.

Isobe, T. *et al.* (2015) 'Amyotrophic lateral sclerosis models derived from human embryonic stem cells with different superoxide dismutase 1 mutations exhibit differential drug responses', *Stem Cell Research*. Elsevier B.V., 15(3), pp. 459–468. doi: 10.1016/j.scr.2015.09.006.

Israelson, A. *et al.* (2015) 'Macrophage migration inhibitory factor as a chaperone inhibiting accumulation of misfolded SOD1.', *Neuron*, 86(1), pp. 218–232. doi: 10.1016/j.neuron.2015.02.034.

Ito, M. *et al.* (2019) 'Tissue regulatory T cells and neural repair.', *International Immunology*. England, 31(6), pp. 361–369. doi: 10.1093/intimm/dxz031.

Itoh, K. *et al.* (1999) 'Keap1 represses nuclear activation of antioxidant responsive elements by Nrf2 through binding to the amino-terminal Neh2 domain', *Genes and Development*, 13(1), pp. 76–86. doi: 10.1101/gad.13.1.76.

Izrael, M. *et al.* (2018) 'Safety and efficacy of human embryonic stem cell-derived astrocytes following intrathecal transplantation in SOD1(G93A) and NSG animal models.', *Stem Cell Research & Therapy*, 9(1), p. 152. doi: 10.1186/s13287-018-0890-5.

Jain, A. *et al.* (2010) 'p62/SQSTM1 is a target gene for transcription factor NRF2 and creates a positive feedback loop by inducing antioxidant response element-driven gene transcription.', *The Journal of Biological Chemistry*, 285(29), pp. 22576–22591. doi: 10.1074/jbc.M110.118976.

Jaiswal, M. K. (2016) 'Riluzole But Not Melatonin Ameliorates Acute Motor Neuron Degeneration and Moderately Inhibits SOD1-Mediated Excitotoxicity Induced Disrupted Mitochondrial Ca(2+) Signaling in Amyotrophic Lateral Sclerosis.', *Frontiers in Cellular Neuroscience*, 10, p. 295. doi: 10.3389/fncel.2016.00295.

Jaiswal, M. K. (2019) 'Riluzole and edaravone: A tale of two amyotrophic lateral sclerosis drugs.', *Medicinal Research Reviews*. United States, 39(2), pp. 733–748. doi: 10.1002/med.21528.

Jena, K. K. *et al.* (2018) 'TRIM16 controls assembly and degradation of protein aggregates by modulating the p62-NRF2 axis and autophagy.', *The EMBO Journal*, 37(18). doi: 10.15252/embj.201798358.

Jeon, G. S. *et al.* (2019) 'Pathological Modification of TDP-43 in Amyotrophic Lateral Sclerosis with SOD1 Mutations.', *Molecular Neurobiology*, 56(3), pp. 2007–2021. doi: 10.1007/s12035-018-1218-2.

- Jiang, J. *et al.* (2016) 'Gain of Toxicity from ALS/FTD-Linked Repeat Expansions in C9ORF72 Is Alleviated by Antisense Oligonucleotides Targeting GGGGCC-Containing RNAs.', *Neuron*, 90(3), pp. 535–550. doi: 10.1016/j.neuron.2016.04.006.
- Jimenez-Blasco, D. *et al.* (2015) 'Astrocyte NMDA receptors' activity sustains neuronal survival through a Cdk5-Nrf2 pathway.', *Cell Death and Differentiation*, 22(11), pp. 1877–1889. doi: 10.1038/cdd.2015.49.
- Jin, Y. *et al.* (2014) 'Dietary intake of fruits and beta-carotene is negatively associated with amyotrophic lateral sclerosis risk in Koreans: a case-control study.', *Nutritional Neuroscience*. England, 17(3), pp. 104–108. doi: 10.1179/1476830513Y.0000000071.
- Jinwal, U. K. *et al.* (2012) 'Cdc37/Hsp90 protein complex disruption triggers an autophagic clearance cascade for TDP-43 protein.', *The Journal of Biological Chemistry*, 287(29), pp. 24814–24820. doi: 10.1074/jbc.M112.367268.
- Johnson, J. O. *et al.* (2010) 'Exome sequencing reveals VCP mutations as a cause of familial ALS.', *Neuron*, 68(5), pp. 857–864. doi: 10.1016/j.neuron.2010.11.036.
- Johnson, J. O. *et al.* (2014) 'Mutations in the Matrin 3 gene cause familial amyotrophic lateral sclerosis', *Nature Neuroscience*, 17(5), pp. 664–666. doi: 10.1038/nn.3688.Mutations.
- Johnson, M. A. *et al.* (2007) 'Functional neural development from human embryonic stem cells: accelerated synaptic activity via astrocyte coculture.', *The Journal of Neuroscience : The Official Journal of the Society for Neuroscience*, 27(12), pp. 3069–3077. doi: 10.1523/JNEUROSCI.4562-06.2007.
- Juneja, T. *et al.* (1997) 'Prognosis in familial amyotrophic lateral sclerosis: progression and survival in patients with glu100gly and ala4val mutations in Cu,Zn superoxide dismutase.', *Neurology*. United States, 48(1), pp. 55–57. doi: 10.1212/wnl.48.1.55.
- Jung, K.-A. *et al.* (2013) 'Identification of aldo-keto reductases as NRF2-target marker genes in human cells.', *Toxicology Letters*. Netherlands, 218(1), pp. 39–49. doi: 10.1016/j.toxlet.2012.12.026.
- Jurič, D. M., Kržan, M. and Lipnik-Stangelj, M. (2016) 'Histamine and astrocyte function.', *Pharmacological Research*. Netherlands, 111, pp. 774–783. doi: 10.1016/j.phrs.2016.07.035.
- Kahle, P. J. *et al.* (2000) 'Subcellular localization of wild-type and Parkinson's disease-associated mutant alpha -synuclein in human and transgenic mouse brain.', *The Journal of Neuroscience : The Official Journal of the Society for Neuroscience*, 20(17), pp. 6365–6373. doi: 10.1523/JNEUROSCI.20-17-06365.2000.
- Kalandadze, A. *et al.* (2004) 'Identification of motifs involved in endoplasmic reticulum retention-forward trafficking of the GLT-1 subtype of glutamate transporter.', *The Journal of Neuroscience : The Official Journal of the Society for Neuroscience*, 24(22), pp. 5183–5192. doi: 10.1523/JNEUROSCI.0839-04.2004.
- Kaneko, S. *et al.* (2006) 'A selective Sema3A inhibitor enhances regenerative responses and functional recovery of the injured spinal cord.', *Nature Medicine*. United States, 12(12), pp. 1380–1389. doi: 10.1038/nm1505.
- Kanekura, K. *et al.* (2016) 'Poly-dipeptides encoded by the C9ORF72 repeats block global protein translation.', *Human Molecular Genetics*, 25(9), pp. 1803–1813. doi: 10.1093/hmg/ddw052.
- Karten, B. *et al.* (2006) 'Expression of ABCG1, but not ABCA1, correlates with cholesterol release by cerebellar astroglia.', *The Journal of Biological Chemistry*. United States, 281(7), pp. 4049–4057. doi: 10.1074/jbc.M508915200.

- Kawamata, H. *et al.* (2008) 'Lysyl-tRNA synthetase is a target for mutant SOD1 toxicity in mitochondria.', *The Journal of Biological Chemistry*, 283(42), pp. 28321–28328. doi: 10.1074/jbc.M805599200.
- Keizman, D. *et al.* (2009) 'Low-grade systemic inflammation in patients with amyotrophic lateral sclerosis.', *Acta Neurologica Scandinavica*. Denmark, 119(6), pp. 383–389. doi: 10.1111/j.1600-0404.2008.01112.
- Keller, S. *et al.* (2020) '9-Methyl- β -carboline inhibits monoamine oxidase activity and stimulates the expression of neurotrophic factors by astrocytes.', *Journal of Neural Transmission (Vienna, Austria : 1996)*. Austria, 127(7), pp. 999–1012. doi: 10.1007/s00702-020-02189-9.
- Kenna, K. P. *et al.* (2016) 'NEK1 variants confer susceptibility to amyotrophic lateral sclerosis.', *Nature Genetics*, 48(9), pp. 1037–1042. doi: 10.1038/ng.3626.
- Khoo, S. K. *et al.* (2012) 'Plasma-based circulating MicroRNA biomarkers for Parkinson's disease.', *Journal of Parkinson's Disease*. Netherlands, 2(4), pp. 321–331. doi: 10.3233/JPD-012144.
- Kim, E. K. and Choi, E.-J. (2010) 'Pathological roles of MAPK signaling pathways in human diseases.', *Biochimica et Biophysica Acta*. Netherlands, 1802(4), pp. 396–405. doi: 10.1016/j.bbadis.2009.12.009.
- Kim, H. J. *et al.* (2013) 'Mutations in prion-like domains in hnRNPA2B1 and hnRNPA1 cause multisystem proteinopathy and ALS.', *Nature*, 495(7442), pp. 467–473. doi: 10.1038/nature11922.
- Kim, J. *et al.* (2011) 'Direct reprogramming of mouse fibroblasts to neural progenitors.', *Proceedings of the National Academy of Sciences of the United States of America*, 108(19), pp. 7838–7843. doi: 10.1073/pnas.1103113108.
- Kim, P. Y. *et al.* (2016) 'High TDP43 expression is required for TRIM16-induced inhibition of cancer cell growth and correlated with good prognosis of neuroblastoma and breast cancer patients.', *Cancer Letters*. Ireland, 374(2), pp. 315–323. doi: 10.1016/j.canlet.2016.02.021.
- Kimura, T., Mandell, M. and Deretic, V. (2016) 'Precision autophagy directed by receptor regulators - emerging examples within the TRIM family.', *Journal of Cell Science*, 129(5), pp. 881–891. doi: 10.1242/jcs.163758.
- King, A. E. *et al.* (2016) 'Excitotoxicity in ALS: Overstimulation, or overreaction?', *Experimental Neurology*. United States, 275 Pt 1, pp. 162–171. doi: 10.1016/j.expneurol.2015.09.019.
- King, H. A. and Gerber, A. P. (2016) 'Translatome profiling: methods for genome-scale analysis of mRNA translation.', *Briefings in Functional Genomics*. England, 15(1), pp. 22–31. doi: 10.1093/bfpg/elu045.
- Kiral, F. R. *et al.* (2018) 'Rab GTPases and Membrane Trafficking in Neurodegeneration.', *Current Biology : CB*, 28(8), pp. R471–R486. doi: 10.1016/j.cub.2018.02.010.
- Kirby, J. *et al.* (2005) 'Mutant SOD1 alters the motor neuronal transcriptome: Implications for familial ALS', *Brain*, 128(7), pp. 1686–1706. doi: 10.1093/brain/awh503.
- Kirby, J. *et al.* (2011) 'Phosphatase and tensin homologue/protein kinase B pathway linked to motor neuron survival in human superoxide dismutase 1-related amyotrophic lateral sclerosis.', *Brain : A Journal of Neurology*, 134(Pt 2), pp. 506–517. doi: 10.1093/brain/awq345.
- Kitamura, A., Iwasaki, N. and Kinjo, M. (2018) 'Molecular chaperone HSP70 prevents formation of inclusion bodies of the 25-kDa C-terminal fragment of TDP-43 by preventing aggregate accumulation.', *Cell Stress & Chaperones*, 23(6), pp. 1177–1183. doi: 10.1007/s12192-018-0930-1.

- Kitley, J. *et al.* (2012) 'Prognostic factors and disease course in aquaporin-4 antibody-positive patients with neuromyelitis optica spectrum disorder from the United Kingdom and Japan.', *Brain : A Journal of Neurology*. England, 135(Pt 6), pp. 1834–1849. doi: 10.1093/brain/aws109.
- Kobayashi, A. *et al.* (2004) 'Oxidative Stress Sensor Keap1 Functions as an Adaptor for Cul3-Based E3 Ligase To Regulate Proteasomal Degradation of Nrf2', *Molecular and Cellular Biology*, 24(16), pp. 7130–7139. doi: 10.1128/MCB.24.16.7130.
- Komatsu, M. *et al.* (2010) 'The selective autophagy substrate p62 activates the stress responsive transcription factor Nrf2 through inactivation of Keap1.', *Nature Cell Biology*. Nature Publishing Group, 12(3), pp. 213–223. doi: 10.1038/ncb2021.
- Koppers, M. *et al.* (2015) 'C9orf72 ablation in mice does not cause motor neuron degeneration or motor deficits.', *Annals of Neurology*, 78(3), pp. 426–438. doi: 10.1002/ana.24453.
- Körner, S. *et al.* (2016) 'The Axon Guidance Protein Semaphorin 3A Is Increased in the Motor Cortex of Patients With Amyotrophic Lateral Sclerosis.', *Journal of Neuropathology and Experimental Neurology*. England, 75(4), pp. 326–333. doi: 10.1093/jnen/nlw003.
- Kotni, M. K., Zhao, M. and Wei, D.-Q. (2016) 'Gene expression profiles and protein-protein interaction networks in amyotrophic lateral sclerosis patients with C9orf72 mutation.', *Orphanet Journal of Rare Diseases*, 11(1), p. 148. doi: 10.1186/s13023-016-0531-y.
- Koyama, A. *et al.* (2016) 'Increased cytoplasmic TARDBP mRNA in affected spinal motor neurons in ALS caused by abnormal autoregulation of TDP-43.', *Nucleic Acids Research*, 44(12), pp. 5820–5836. doi: 10.1093/nar/gkw499.
- Krencik, R. *et al.* (2011) 'Specification of transplantable astroglial subtypes from human pluripotent stem cells.', *Nature Biotechnology*, 29(6), pp. 528–534. doi: 10.1038/nbt.1877.
- Krencik, R. and Zhang, S.-C. (2011) 'Directed differentiation of functional astroglial subtypes from human pluripotent stem cells.', *Nature Protocols*, 6(11), pp. 1710–1717. doi: 10.1038/nprot.2011.405.
- Krishnaraj, R. N., Kumari, S. S. S. and Mukhopadhyay, S. S. (2016) 'Antagonistic molecular interactions of photosynthetic pigments with molecular disease targets: a new approach to treat AD and ALS.', *Journal of Receptor and Signal Transduction Research*. England, 36(1), pp. 67–71. doi: 10.3109/10799893.2015.1024851.
- Krzyszczuk, P. *et al.* (2018) 'The growing role of precision and personalized medicine for cancer treatment.', *Technology*, 6(3–4), pp. 79–100. doi: 10.1142/S2339547818300020.
- Kwak, M.-K. *et al.* (2003) 'Antioxidants Enhance Mammalian Proteasome Expression through the Keap1-Nrf2 Signaling Pathway', *Molecular and Cellular Biology*, 23(23), pp. 8786–8794. doi: 10.1128/MCB.23.23.8786-8794.2003.
- Kwiatkowski, T. J. J. *et al.* (2009) 'Mutations in the FUS/TLS gene on chromosome 16 cause familial amyotrophic lateral sclerosis.', *Science (New York, N.Y.)*. United States, 323(5918), pp. 1205–1208. doi: 10.1126/science.1166066.
- Lackie, R. E. *et al.* (2017) 'The Hsp70/Hsp90 Chaperone Machinery in Neurodegenerative Diseases.', *Frontiers in Neuroscience*, 11, p. 254. doi: 10.3389/fnins.2017.00254.
- Lagier-Tourenne, C. *et al.* (2012) 'Divergent roles of ALS-linked proteins FUS/TLS and TDP-43 intersect in processing long pre-mRNAs.', *Nature Neuroscience*, 15(11), pp. 1488–1497. doi: 10.1038/nn.3230.

- Lagier-Tourenne, C. *et al.* (2013) 'Targeted degradation of sense and antisense C9orf72 RNA foci as therapy for ALS and frontotemporal degeneration.', *Proceedings of the National Academy of Sciences of the United States of America*, 110(47), pp. E4530-9. doi: 10.1073/pnas.1318835110.
- Langfelder, P. and Horvath, S. (2008) 'WGCNA: an R package for weighted correlation network analysis.', *BMC Bioinformatics*, 9, p. 559. doi: 10.1186/1471-2105-9-559.
- Laslo, P. *et al.* (2001) 'GluR2 AMPA receptor subunit expression in motoneurons at low and high risk for degeneration in amyotrophic lateral sclerosis.', *Experimental Neurology*. United States, 169(2), pp. 461–471. doi: 10.1006/exnr.2001.7653.
- Lattante, S. *et al.* (2018) 'ATXN1 intermediate-length polyglutamine expansions are associated with amyotrophic lateral sclerosis.', *Neurobiology of Aging*. United States, 64, pp. 157.e1-157.e5. doi: 10.1016/j.neurobiolaging.2017.11.011.
- Lattante, S., Rouleau, G. A. and Kabashi, E. (2013) 'TARDBP and FUS mutations associated with amyotrophic lateral sclerosis: summary and update.', *Human Mutation*. United States, 34(6), pp. 812–826. doi: 10.1002/humu.22319.
- Leal, S. S. and Gomes, C. M. (2015) 'Calcium dysregulation links ALS defective proteins and motor neuron selective vulnerability.', *Frontiers in Cellular Neuroscience*, 9, p. 225. doi: 10.3389/fncel.2015.00225.
- Lee, M.-C. *et al.* (2010) 'Characterisation of the expression of NMDA receptors in human astrocytes.', *PLoS One*, 5(11), p. e14123. doi: 10.1371/journal.pone.0014123.
- Lepelletier, Y. *et al.* (2006) 'Immunosuppressive role of semaphorin-3A on T cell proliferation is mediated by inhibition of actin cytoskeleton reorganization.', *European Journal of Immunology*. Germany, 36(7), pp. 1782–1793. doi: 10.1002/eji.200535601.
- Lepore, A. C. *et al.* (2008) 'Focal Transplantation-based Astrocyte Replacement is Neuroprotective in a Model of Motor Neuron Disease', *Nature Neuroscience*, 11(11), pp. 1294–1301. doi: 10.1038/nn.2210.Focal.
- Levine, B. and Klionsky, D. J. (2004) 'Development by self-digestion: molecular mechanisms and biological functions of autophagy.', *Developmental Cell*. United States, 6(4), pp. 463–477. doi: 10.1016/s1534-5807(04)00099-1.
- Li, W. *et al.* (2014) 'Elevated cerebral cortical CD24 levels in patients and mice with traumatic brain injury: a potential negative role in nuclear factor kb/inflammatory factor pathway.', *Molecular Neurobiology*. United States, 49(1), pp. 187–198. doi: 10.1007/s12035-013-8509-4.
- Li, Z. *et al.* (2013) 'Identification of a 24-gene prognostic signature that improves the European LeukemiaNet risk classification of acute myeloid leukemia: an international collaborative study.', *Journal of Clinical Oncology : Official Journal of the American Society of Clinical Oncology*, 31(9), pp. 1172–1181. doi: 10.1200/JCO.2012.44.3184.
- Liang, H. *et al.* (2017) 'Aldehyde Dehydrogenases 1A2 Expression and Distribution are Potentially Associated with Neuron Death in Spinal Cord of Tg(SOD1*G93A)1Gur Mice.', *International Journal of Biological Sciences*, 13(5), pp. 574–587. doi: 10.7150/ijbs.19150.
- Liao, B. *et al.* (2012) 'Transformation from a neuroprotective to a neurotoxic microglial phenotype in a mouse model of ALS.', *Experimental Neurology*, 237(1), pp. 147–152. doi: 10.1016/j.expneurol.2012.06.011.
- Liddel, S. A. *et al.* (2017) 'Neurotoxic reactive astrocytes are induced by activated microglia.', *Nature*, 541(7638), pp. 481–487. doi: 10.1038/nature21029.

- Lin, T.-Y., Cantley, L.C., DeNicola, G. . (2016) 'NRF2 Rewires Cellular Metabolism to Support the Antioxidant Response, in: A Master Regulator of Oxidative Stress - The Transcription Factor Nrf2', *InTech*, p. doi:10.5772/65141.
- Lin, P.-Y. *et al.* (2016) 'Overexpression of heat shock factor 1 maintains TAR DNA binding protein 43 solubility via induction of inducible heat shock protein 70 in cultured cells.', *Journal of Neuroscience Research*. United States, 94(7), pp. 671–682. doi: 10.1002/jnr.23725.
- Liu, H. *et al.* (2020) 'Adiponectin peptide alleviates oxidative stress and NLRP3 inflammasome activation after cerebral ischemia-reperfusion injury by regulating AMPK/GSK-3 β .', *Experimental Neurology*. United States, 329, p. 113302. doi: 10.1016/j.expneurol.2020.113302.
- Liu, M.-L. *et al.* (2013) 'Small molecules enable neurogenin 2 to efficiently convert human fibroblasts into cholinergic neurons.', *Nature Communications*, 4, p. 2183. doi: 10.1038/ncomms3183.
- Liu, Y. *et al.* (2004) 'CD44 expression identifies astrocyte-restricted precursor cells', *Developmental Biology*, 276(1), pp. 31–46. doi: 10.1016/j.ydbio.2004.08.018.
- Liu, Y., Zhou, J. and White, K. P. (2014) 'RNA-seq differential expression studies: more sequence or more replication?', *Bioinformatics (Oxford, England)*, 30(3), pp. 301–304. doi: 10.1093/bioinformatics/btt688.
- Logroscino, G. *et al.* (2010) 'Incidence of amyotrophic lateral sclerosis in Europe.', *Journal of Neurology, Neurosurgery, and Psychiatry*, 81(4), pp. 385–390. doi: 10.1136/jnnp.2009.183525.
- Lopez-Gonzalez, R. *et al.* (2016) 'Poly(GR) in C9ORF72-Related ALS/FTD Compromises Mitochondrial Function and Increases Oxidative Stress and DNA Damage in iPSC-Derived Motor Neurons.', *Neuron*, 92(2), pp. 383–391. doi: 10.1016/j.neuron.2016.09.015.
- Loucks, F. A. *et al.* (2006) 'Rho family GTPase inhibition reveals opposing effects of mitogen-activated protein kinase kinase/extracellular signal-regulated kinase and Janus kinase/signal transducer and activator of transcription signaling cascades on neuronal survival.', *Journal of Neurochemistry*. England, 97(4), pp. 957–967. doi: 10.1111/j.1471-4159.2006.03802.
- Love, M. I., Hogenesch, J. B. and Irizarry, R. A. (2016) 'Modeling of RNA-seq fragment sequence bias reduces systematic errors in transcript abundance estimation.', *Nature Biotechnology*, 34(12), pp. 1287–1291. doi: 10.1038/nbt.3682.
- Love, M. I., Soneson, C. and Patro, R. (2018) 'Swimming downstream: statistical analysis of differential transcript usage following Salmon quantification.', *F1000Research*, 7, p. 952. doi: 10.12688/f1000research.15398.3.
- Luchinat, E., Barbieri, L. and Banci, L. (2017) 'A molecular chaperone activity of CCS restores the maturation of SOD1 fALS mutants.', *Scientific Reports*, 7(1), p. 17433. doi: 10.1038/s41598-017-17815-y.
- Luty, A. A. *et al.* (2010) 'Sigma nonopioid intracellular receptor 1 mutations cause frontotemporal lobar degeneration-motor neuron disease.', *Annals of Neurology*. United States, 68(5), pp. 639–649. doi: 10.1002/ana.22274.
- Mackenzie, I. R. A. *et al.* (2007) 'Pathological TDP-43 distinguishes sporadic amyotrophic lateral sclerosis from amyotrophic lateral sclerosis with SOD1 mutations.', *Annals of Neurology*. United States, 61(5), pp. 427–434. doi: 10.1002/ana.21147.
- Malarkey, E. B. and Parpura, V. (2008) 'Mechanisms of glutamate release from astrocytes.', *Neurochemistry International*, 52(1–2), pp. 142–154. doi: 10.1016/j.neuint.2007.06.005.
- Marchi, C. *et al.* (2019) 'ABCA1- and ABCG1-mediated cholesterol efflux capacity of cerebrospinal

fluid is impaired in Alzheimer's disease.', *Journal of Lipid Research*, 60(8), pp. 1449–1456. doi: 10.1194/jlr.P091033.

Marin, B. *et al.* (2014) 'Population-based epidemiology of amyotrophic lateral sclerosis (ALS) in an ageing Europe--the French register of ALS in Limousin (FRALim register).', *European Journal of Neurology*. England, 21(10), pp. 1292–300, e78-9. doi: 10.1111/ene.12474.

Marin, B. *et al.* (2016) 'Clinical and demographic factors and outcome of amyotrophic lateral sclerosis in relation to population ancestral origin.', *European Journal of Epidemiology*. Netherlands, 31(3), pp. 229–245. doi: 10.1007/s10654-015-0090-x.

Marsala, M. *et al.* (2020) 'Spinal parenchymal occupation by neural stem cells after subpial delivery in adult immunodeficient rats.', *Stem Cells Translational Medicine*, 9(2), pp. 177–188. doi: 10.1002/sctm.19-0156.

Martelli, A. M. *et al.* (2000) 'Rab3A and Rab3D control the total granule number and the fraction of granules docked at the plasma membrane in PC12 cells.', *Traffic (Copenhagen, Denmark)*. England, 1(12), pp. 976–986.

Maruyama, H. *et al.* (2010) 'Mutations of optineurin in amyotrophic lateral sclerosis.', *Nature*. Nature Publishing Group, 465(7295), pp. 223–226. doi: 10.1038/nature08971.

Mason, N. S., Mathis, C. A. and Klunk, W. E. (2013) 'Positron emission tomography radioligands for in vivo imaging of A β plaques', *Journal of Labelled Compounds and Radiopharmaceuticals.*, 56, pp. 89–95. doi: 10.1038/jid.2014.371.

Masser, D. R. *et al.* (2016) 'Loss of the antioxidant enzyme CuZnSOD (Sod1) mimics an age-related increase in absolute mitochondrial DNA copy number in the skeletal muscle.', *Age (Dordrecht, Netherlands)*, 38(4), pp. 323–333. doi: 10.1007/s11357-016-9930-1.

Masvekar, R. *et al.* (2019) 'Cerebrospinal fluid biomarkers link toxic astrogliosis and microglial activation to multiple sclerosis severity.', *Multiple Sclerosis and Related Disorders*, 28, pp. 34–43. doi: 10.1016/j.msard.2018.11.032.

Mattiazzi, M. *et al.* (2002) 'Mutated human SOD1 causes dysfunction of oxidative phosphorylation in mitochondria of transgenic mice', *Journal of Biological Chemistry*, 277(33), pp. 29626–29633. doi: 10.1074/jbc.M203065200.

Matus, S. *et al.* (2013) 'ER Dysfunction and Protein Folding Stress in ALS.', *International Journal of Cell Biology*, 2013, p. 674751. doi: 10.1155/2013/674751.

Maurin, H. *et al.* (2013) 'Tauopathy differentially affects cell adhesion molecules in mouse brain: early down-regulation of nectin-3 in stratum lacunosum moleculare.', *PLoS One*, 8(5), p. e63589. doi: 10.1371/journal.pone.0063589.

McBean, G. J., López, M. G. and Wallner, F. K. (2017) 'Redox-based therapeutics in neurodegenerative disease.', *British Journal of Pharmacology*, 174(12), pp. 1750–1770. doi: 10.1111/bph.13551.

McCauley, M. E. and Baloh, R. H. (2019) 'Inflammation in ALS/FTD pathogenesis.', *Acta Neuropathologica*, 137(5), pp. 715–730. doi: 10.1007/s00401-018-1933-9.

Mead, R. J. *et al.* (2013) 'S[+] Apomorphine is a CNS penetrating activator of the Nrf2-ARE pathway with activity in mouse and patient fibroblast models of amyotrophic lateral sclerosis', *Free Radical Biology and Medicine*. Elsevier, 61, pp. 438–452. doi: 10.1016/j.freeradbiomed.2013.04.018.

Meckley, L. M. and Neumann, P. J. (2010) 'Personalized medicine: factors influencing reimbursement.', *Health Policy (Amsterdam, Netherlands)*. Ireland, 94(2), pp. 91–100. doi:

10.1016/j.healthpol.2009.09.006.

Mejzini, R. *et al.* (2019) 'ALS Genetics, Mechanisms, and Therapeutics: Where Are We Now?', *Frontiers in Neuroscience*, 13, p. 1310. doi: 10.3389/fnins.2019.01310.

Mertens, J. *et al.* (2015) 'Directly Reprogrammed Human Neurons Retain Aging-Associated Transcriptomic Signatures and Reveal Age-Related Nucleocytoplasmic Defects.', *Cell Stem Cell*, 17(6), pp. 705–718. doi: 10.1016/j.stem.2015.09.001.

Meyer, K. *et al.* (2014) 'Direct conversion of patient fibroblasts demonstrates non-cell autonomous toxicity of astrocytes to motor neurons in familial and sporadic ALS.', *Proceedings of the National Academy of Sciences of the United States of America*, 111(2), pp. 829–832. doi: 10.1073/pnas.1314085111.

Meyer, M. *et al.* (2017) 'Protective effects of the neurosteroid allopregnanolone in a mouse model of spontaneous motoneuron degeneration.', *The Journal of Steroid Biochemistry and Molecular Biology*. England, 174, pp. 201–216. doi: 10.1016/j.jsbmb.2017.09.015.

Migheli, A. *et al.* (1999) 'S-100beta protein is upregulated in astrocytes and motor neurons in the spinal cord of patients with amyotrophic lateral sclerosis.', *Neuroscience Letters*. Ireland, 261(1–2), pp. 25–28. doi: 10.1016/s0304-3940(98)01001-5.

Millecamps, S. *et al.* (2012) 'Phenotype difference between ALS patients with expanded repeats in C9ORF72 and patients with mutations in other ALS-related genes.', *Journal of Medical Genetics*. England, 49(4), pp. 258–263. doi: 10.1136/jmedgenet-2011-100699.

Miller, R. G., Mitchell, J. D. and Moore, D. H. (2012) 'Riluzole for amyotrophic lateral sclerosis (ALS)/motor neuron disease (MND).', *The Cochrane Database of Systematic Reviews*, 2012(3), p. CD001447. doi: 10.1002/14651858.CD001447.pub3.

Miller, S. J. *et al.* (2017) 'Astroglial transcriptome dysregulation in early disease of an ALS mutant SOD1 mouse model.', *Journal of Neurogenetics*. England, 31(1–2), pp. 37–48. doi: 10.1080/01677063.2016.1260128.

Miller, T. *et al.* (2020) 'Phase 1-2 Trial of Antisense Oligonucleotide Tofersen for SOD1 ALS.', *The New England Journal of Medicine*. United States, 383(2), pp. 109–119. doi: 10.1056/NEJMoa2003715.

Miller, T. M. *et al.* (2013) 'An antisense oligonucleotide against SOD1 delivered intrathecally for patients with SOD1 familial amyotrophic lateral sclerosis: a phase 1, randomised, first-in-man study.', *The Lancet. Neurology*, 12(5), pp. 435–442. doi: 10.1016/S1474-4422(13)70061-9.

Mimura, J. *et al.* (1999) 'Identification of a novel mechanism of regulation of Ah (dioxin) receptor function.', *Genes & Development*, 13(1), pp. 20–25. doi: 10.1101/gad.13.1.20.

Miralles, C. P. *et al.* (2020) 'Expression of protocadherin-γC4 protein in the rat brain.', *The Journal of Comparative Neurology*, 528(5), pp. 840–864. doi: 10.1002/cne.24783.

Miralles, V. J. *et al.* (2001) 'Na⁺ dependent glutamate transporters (EAAT1, EAAT2, and EAAT3) in primary astrocyte cultures: effect of oxidative stress.', *Brain Research*. Netherlands, 922(1), pp. 21–29. doi: 10.1016/s0006-8993(01)03124-9.

Mitchell, J. *et al.* (2010) 'Familial amyotrophic lateral sclerosis is associated with a mutation in D-amino acid oxidase.', *Proceedings of the National Academy of Sciences of the United States of America*, 107(16), pp. 7556–7561. doi: 10.1073/pnas.0914128107.

Mitchell, R. M. *et al.* (2009) 'A CSF biomarker panel for identification of patients with amyotrophic lateral sclerosis.', *Neurology*. United States, 72(1), pp. 14–19. doi: 10.1212/01.wnl.0000333251.36681.a5.

- Mitsui, S. *et al.* (2018) 'Systemic overexpression of SQSTM1/p62 accelerates disease onset in a SOD1(H46R)-expressing ALS mouse model.', *Molecular Brain*, 11(1), p. 30. doi: 10.1186/s13041-018-0373-8.
- Mogi, M. *et al.* (1994) 'Tumor necrosis factor-alpha (TNF-alpha) increases both in the brain and in the cerebrospinal fluid from parkinsonian patients.', *Neuroscience Letters*. Ireland, 165(1–2), pp. 208–210. doi: 10.1016/0304-3940(94)90746-3.
- Mollenhauer, B. *et al.* (2011) 'α-Synuclein and tau concentrations in cerebrospinal fluid of patients presenting with parkinsonism: a cohort study.', *The Lancet. Neurology*. England, 10(3), pp. 230–240. doi: 10.1016/S1474-4422(11)70014-X.
- Molz, S. *et al.* (2008) 'GMP prevents excitotoxicity mediated by NMDA receptor activation but not by reversal activity of glutamate transporters in rat hippocampal slices.', *Brain Research*. Netherlands, 1231, pp. 113–120. doi: 10.1016/j.brainres.2008.07.009.
- Montes de Oca Balderas, P. and Aguilera, P. (2015) 'A Metabotropic-Like Flux-Independent NMDA Receptor Regulates Ca²⁺ Exit from Endoplasmic Reticulum and Mitochondrial Membrane Potential in Cultured Astrocytes.', *PLoS One*, 10(5), p. e0126314. doi: 10.1371/journal.pone.0126314.
- Morello, G. *et al.* (2017) 'Selection and Prioritization of Candidate Drug Targets for Amyotrophic Lateral Sclerosis Through a Meta-Analysis Approach.', *Journal of Molecular Neuroscience : MN*, 61(4), pp. 563–580. doi: 10.1007/s12031-017-0898-9.
- Morgan, S., Duguez, S. and Duddy, W. (2018) 'Personalized Medicine and Molecular Interaction Networks in Amyotrophic Lateral Sclerosis (ALS): Current Knowledge.', *Journal of Personalized Medicine*, 8(4). doi: 10.3390/jpm8040044.
- Morimoto, N. *et al.* (2007) 'Increased autophagy in transgenic mice with a G93A mutant SOD1 gene', *Brain Research*, 1167(1), pp. 112–117. doi: 10.1016/j.brainres.2007.06.045.
- Mortiboys, H. *et al.* (2008) 'Mitochondrial function and morphology are impaired in parkin-mutant fibroblasts.', *Annals of Neurology*, 64(5), pp. 555–565. doi: 10.1002/ana.21492.
- Münch, C. *et al.* (2004) 'Point mutations of the p150 subunit of dynactin (DCTN1) gene in ALS.', *Neurology*. United States, 63(4), pp. 724–726. doi: 10.1212/01.wnl.0000134608.83927.b1.
- Münch, C. *et al.* (2005) 'Heterozygous R1101K mutation of the DCTN1 gene in a family with ALS and FTD.', *Annals of Neurology*. United States, 58(5), pp. 777–780. doi: 10.1002/ana.20631.
- Murphy, T. H. *et al.* (1989) 'Glutamate toxicity in a neuronal cell line involves inhibition of cystine transport leading to oxidative stress.', *Neuron*. United States, 2(6), pp. 1547–1558. doi: 10.1016/0896-6273(89)90043-3.
- Myszczyńska, M. and Ferraiuolo, L. (2016) 'New In Vitro Models to Study Amyotrophic Lateral Sclerosis.', *Brain Pathology (Zurich, Switzerland)*. Switzerland, 26(2), pp. 258–265. doi: 10.1111/bpa.12353.
- Nagai, M. *et al.* (2007) 'Astrocytes expressing ALS-linked mutated SOD1 release factors selectively toxic to motor neurons.', *Nature Neuroscience*, 10(5), pp. 615–22. doi: 10.1038/nn1876.
- Nakamura, S. *et al.* (2014) 'An autopsy case of sporadic amyotrophic lateral sclerosis associated with the I113T SOD1 mutation.', *Neuropathology : Official Journal of the Japanese Society of Neuropathology*. Australia, 34(1), pp. 58–63. doi: 10.1111/neup.12049.
- Nannelli, A. *et al.* (2009) 'Effect of beta-naphthoflavone on AhR-regulated genes (CYP1A1, 1A2, 1B1, 2S1, Nrf2, and GST) and antioxidant enzymes in various brain regions of pig.', *Toxicology*. Ireland, 265(3), pp. 69–79. doi: 10.1016/j.tox.2009.09.010.

- Nassif, M. *et al.* (2014) 'Pathogenic role of BECN1/Beclin 1 in the development of amyotrophic lateral sclerosis.', *Autophagy*, 10(7), pp. 1256–1271. doi: 10.4161/auto.28784.
- Neumann, M. *et al.* (2006) 'Ubiquitinated TDP-43 in frontotemporal lobar degeneration and amyotrophic lateral sclerosis', *Science*, 314(5796), pp. 130–133. doi: 10.1126/science.1134108.
- Neuwirth, C. *et al.* (2015) 'Tracking motor neuron loss in a set of six muscles in amyotrophic lateral sclerosis using the Motor Unit Number Index (MUNIX): a 15-month longitudinal multicentre trial.', *Journal of Neurology, Neurosurgery, and Psychiatry*. England, 86(11), pp. 1172–1179. doi: 10.1136/jnnp-2015-310509.
- Ngo, S. T. *et al.* (2015) 'Altered expression of metabolic proteins and adipokines in patients with amyotrophic lateral sclerosis.', *Journal of the Neurological Sciences*. Netherlands, 357(1–2), pp. 22–27. doi: 10.1016/j.jns.2015.06.053.
- Nguyen, T., Sherratt, P. J. and Pickett, C. B. (2003) 'Regulatory mechanisms controlling gene expression mediated by the antioxidant response element.', *Annual Review of Pharmacology and Toxicology*. United States, 43, pp. 233–260. doi: 10.1146/annurev.pharmtox.43.100901.140229.
- Nicolas, A. *et al.* (2018) 'Genome-wide Analyses Identify KIF5A as a Novel ALS Gene.', *Neuron*, 97(6), pp. 1268–1283.e6. doi: 10.1016/j.neuron.2018.02.027.
- Nishimura, A. L. *et al.* (2004) 'A mutation in the vesicle-trafficking protein VAPB causes late-onset spinal muscular atrophy and amyotrophic lateral sclerosis.', *American Journal of Human Genetics*, 75(5), pp. 822–831. doi: 10.1086/425287.
- Nishimura, A. L. *et al.* (2014) 'Allele-specific knockdown of ALS-associated mutant TDP-43 in neural stem cells derived from induced pluripotent stem cells.', *PLoS One*, 9(3), p. e91269. doi: 10.1371/journal.pone.0091269.
- Nishitoh, H. *et al.* (2008) 'ALS-linked mutant SOD1 induces ER stress- and ASK1-dependent motor neuron death by targeting Derlin-1.', *Genes & Development*, 22(11), pp. 1451–1464. doi: 10.1101/gad.1640108.
- Nisole, S., Stoye, J. P. and Saïb, A. (2005) 'TRIM family proteins: retroviral restriction and antiviral defence.', *Nature Reviews. Microbiology*. England, 3(10), pp. 799–808. doi: 10.1038/nrmicro1248.
- Noetzli, M. and Eap, C. B. (2013) 'Pharmacodynamic, pharmacokinetic and pharmacogenetic aspects of drugs used in the treatment of alzheimer's disease', *Clinical Pharmacokinetics*, 52(4), pp. 225–241. doi: 10.1007/s40262-013-0038-9.
- Nolan, K. *et al.* (2014) 'Increased expression of microRNA-29a in ALS mice: functional analysis of its inhibition.', *Journal of Molecular Neuroscience : MN*. United States, 53(2), pp. 231–241. doi: 10.1007/s12031-014-0290-y.
- Nomura, T. *et al.* (2014) 'Intranuclear aggregation of mutant FUS/TLS as a molecular pathomechanism of amyotrophic lateral sclerosis.', *The Journal of Biological Chemistry*, 289(2), pp. 1192–1202. doi: 10.1074/jbc.M113.516492.
- Nonaka, T. *et al.* (2013) 'Prion-like properties of pathological TDP-43 aggregates from diseased brains.', *Cell Reports*. United States, 4(1), pp. 124–134. doi: 10.1016/j.celrep.2013.06.007.
- Okuda, H. *et al.* (2014) 'Chondroitin sulfate proteoglycan tenascin-R regulates glutamate uptake by adult brain astrocytes.', *The Journal of Biological Chemistry*, 289(5), pp. 2620–2631. doi: 10.1074/jbc.M113.504787.
- Olmos, G. and Lladó, J. (2014) 'Tumor necrosis factor alpha: a link between neuroinflammation and excitotoxicity.', *Mediators of Inflammation*, 2014, p. 861231. doi: 10.1155/2014/861231.

- Onesto, E. *et al.* (2016) 'Gene-specific mitochondria dysfunctions in human TARDBP and C9ORF72 fibroblasts.', *Acta Neuropathologica Communications*, 4(1), p. 47. doi: 10.1186/s40478-016-0316-5.
- Ono, S. *et al.* (2020) 'ALS2, the small GTPase Rab17-interacting protein, regulates maturation and sorting of Rab17-associated endosomes.', *Biochemical and Biophysical Research Communications*. United States, 523(4), pp. 908–915. doi: 10.1016/j.bbrc.2019.12.122.
- Orlacchio, A. *et al.* (2010) 'SPATACSIN mutations cause autosomal recessive juvenile amyotrophic lateral sclerosis.', *Brain : A Journal of Neurology*, 133(Pt 2), pp. 591–598. doi: 10.1093/brain/awp325.
- Orre, M. *et al.* (2014) 'Acute isolation and transcriptome characterization of cortical astrocytes and microglia from young and aged mice.', *Neurobiology of Aging*. United States, 35(1), pp. 1–14. doi: 10.1016/j.neurobiolaging.2013.07.008.
- P.M. de O.Balderas, J. R. G. H. (2018) 'NMDA Receptors in Astroglia: Chronology, Controversies, and Contradictions from a Complex Molecule.', *Astrocyte - Physiology & Pathology, InTech*, p. 10.5772/intechopen.72975.
- Pajarillo, E. *et al.* (2019) 'The role of astrocytic glutamate transporters GLT-1 and GLAST in neurological disorders: Potential targets for neurotherapeutics.', *Neuropharmacology*, 161, p. 107559. doi: 10.1016/j.neuropharm.2019.03.002.
- Palygin, O. *et al.* (2010) 'Ionotropic NMDA and P2X1/5 receptors mediate synaptically induced Ca²⁺ signalling in cortical astrocytes.', *Cell Calcium*. Netherlands, 48(4), pp. 225–231. doi: 10.1016/j.ceca.2010.09.004.
- Panek, R. B. *et al.* (1992) 'Tumor necrosis factor alpha response elements in the HLA-DRA promoter: identification of a tumor necrosis factor alpha-induced DNA-protein complex in astrocytes.', *Proceedings of the National Academy of Sciences of the United States of America*, 89(23), pp. 11518–11522. doi: 10.1073/pnas.89.23.11518.
- Pankiv, S. *et al.* (2007) 'p62/SQSTM1 binds directly to Atg8/LC3 to facilitate degradation of ubiquitinated protein aggregates by autophagy.', *The Journal of Biological Chemistry*. United States, 282(33), pp. 24131–24145. doi: 10.1074/jbc.M702824200.
- Paoletti, P. and Neyton, J. (2007) 'NMDA receptor subunits: function and pharmacology.', *Current Opinion in Pharmacology*. England, 7(1), pp. 39–47. doi: 10.1016/j.coph.2006.08.011.
- Di Paolo, G. and Kim, T.-W. (2011) 'Linking lipids to Alzheimer's disease: cholesterol and beyond.', *Nature Reviews. Neuroscience*, 12(5), pp. 284–296. doi: 10.1038/nrn3012.
- Papa, L. *et al.* (2014) 'GFAP out-performs S100β in detecting traumatic intracranial lesions on computed tomography in trauma patients with mild traumatic brain injury and those with extracranial lesions.', *Journal of Neurotrauma*, 31(22), pp. 1815–1822. doi: 10.1089/neu.2013.3245.
- Papadeas, S. T. *et al.* (2011) 'Astrocytes carrying the superoxide dismutase 1 (SOD1G93A) mutation induce wild-type motor neuron degeneration in vivo.', *Proceedings of the National Academy of Sciences of the United States of America*, 108(43), pp. 17803–17808. doi: 10.1073/pnas.1103141108.
- Parisi, C. *et al.* (2016) 'MicroRNA-125b regulates microglia activation and motor neuron death in ALS', *Cell Death and Differentiation*, 23(3), pp. 531–541. doi: 10.1038/cdd.2015.153.
- Parkinson, N. *et al.* (2006) 'ALS phenotypes with mutations in CHMP2B (charged multivesicular body protein 2B).', *Neurology*. United States, 67(6), pp. 1074–1077. doi: 10.1212/01.wnl.0000231510.89311.8b.
- Parton, M. J. *et al.* (2002) 'D90A-SOD1 mediated amyotrophic lateral sclerosis: a single founder for all cases with evidence for a Cis-acting disease modifier in the recessive haplotype.', *Human*

- Mutation*. United States, 20(6), p. 473. doi: 10.1002/humu.9081.
- Parton, R. M. *et al.* (2014) 'Subcellular mRNA localisation at a glance.', *Journal of Cell Science*, 127(Pt 10), pp. 2127–2133. doi: 10.1242/jcs.114272.
- Pascuzzi, R. M. *et al.* (2010) 'A phase II trial of talampanel in subjects with amyotrophic lateral sclerosis.', *Amyotrophic Lateral Sclerosis : Official Publication of the World Federation of Neurology Research Group on Motor Neuron Diseases*. England, 11(3), pp. 266–271. doi: 10.3109/17482960903307805.
- Patro, R. *et al.* (2017) 'Salmon provides fast and bias-aware quantification of transcript expression.', *Nature Methods*, 14(4), pp. 417–419. doi: 10.1038/nmeth.4197.
- Peng, L. *et al.* (2010) 'Astrocytic transactivation by alpha2A-adrenergic and 5-HT2B serotonergic signaling.', *Neurochemistry International*. England, 57(4), pp. 421–431. doi: 10.1016/j.neuint.2010.04.018.
- Penning, T. M. (2015) 'The aldo-keto reductases (AKRs): Overview.', *Chemico-biological Interactions*, 234, pp. 236–246. doi: 10.1016/j.cbi.2014.09.024.
- Pereira, A. C. *et al.* (2017) 'Age and Alzheimer's disease gene expression profiles reversed by the glutamate modulator riluzole.', *Molecular Psychiatry*, 22(2), pp. 296–305. doi: 10.1038/mp.2016.33.
- Perera, N. D. *et al.* (2018) 'Rilmenidine promotes MTOR-independent autophagy in the mutant SOD1 mouse model of amyotrophic lateral sclerosis without slowing disease progression.', *Autophagy*, 14(3), pp. 534–551. doi: 10.1080/15548627.2017.1385674.
- Perry, S. W. *et al.* (2011) 'Mitochondrial membrane potential probes and the proton gradient: a practical usage guide.', *BioTechniques*, 50(2), pp. 98–115. doi: 10.2144/000113610.
- Pessoa, R. R. *et al.* (2018) 'Apomorphine in the treatment of Parkinson's disease: a review.', *Arquivos de Neuro-psiquiatria*. Brazil, 76(12), pp. 840–848. doi: 10.1590/0004-282X20180140.
- Petrov, D. *et al.* (2017) 'ALS Clinical Trials Review: 20 Years of Failure. Are We Any Closer to Registering a New Treatment?', *Frontiers in Aging Neuroscience*, 9, p. 68. doi: 10.3389/fnagi.2017.00068.
- Petrozziello, T. *et al.* (2020) 'Lipocalin-2 is increased in amyotrophic lateral sclerosis.', *Muscle & Nerve*. United States, 62(2), pp. 272–283. doi: 10.1002/mus.26911.
- Pfisterer, U. *et al.* (2011) 'Direct conversion of human fibroblasts to dopaminergic neurons.', *Proceedings of the National Academy of Sciences of the United States of America*, 108(25), pp. 10343–10348. doi: 10.1073/pnas.1105135108.
- Phatnani, H. P. *et al.* (2013) 'Intricate interplay between astrocytes and motor neurons in ALS.', *Proceedings of the National Academy of Sciences of the United States of America*, 110(8), pp. E756–65. doi: 10.1073/pnas.1222361110.
- Philips, T. and Robberecht, W. (2011) 'Neuroinflammation in amyotrophic lateral sclerosis: role of glial activation in motor neuron disease.', *The Lancet. Neurology*. England, 10(3), pp. 253–263. doi: 10.1016/S1474-4422(11)70015-1.
- Philips, T. and Rothstein, J. D. (2014) 'Glial cells in amyotrophic lateral sclerosis.', *Experimental Neurology*, 262 Pt B, pp. 111–120. doi: 10.1016/j.expneurol.2014.05.015.
- Phukan, J. *et al.* (2012) 'The syndrome of cognitive impairment in amyotrophic lateral sclerosis: a population-based study.', *Journal of Neurology, Neurosurgery, and Psychiatry*. England, 83(1), pp. 102–108. doi: 10.1136/jnnp-2011-300188.

- Pickering, A. M. *et al.* (2012) 'Nrf2-dependent induction of proteasome and Pa28 $\alpha\beta$ regulator are required for adaptation to oxidative stress.', *The Journal of Biological Chemistry*, 287(13), pp. 10021–10031. doi: 10.1074/jbc.M111.277145.
- Planas-Fontánez, T. M., Dreyfus, C. F. and Saitta, K. S. (2020) 'Reactive Astrocytes as Therapeutic Targets for Brain Degenerative Diseases: Roles Played by Metabotropic Glutamate Receptors.', *Neurochemical Research*, 45(3), pp. 541–550. doi: 10.1007/s11064-020-02968-6.
- Pokrishevsky, E. *et al.* (2012) 'Aberrant localization of FUS and TDP43 is associated with misfolding of SOD1 in amyotrophic lateral sclerosis.', *PloS One*, 7(4), p. e35050. doi: 10.1371/journal.pone.0035050.
- Poloni, M. *et al.* (2000) 'Circulating levels of tumour necrosis factor-alpha and its soluble receptors are increased in the blood of patients with amyotrophic lateral sclerosis.', *Neuroscience Letters*, Ireland, 287(3), pp. 211–214. doi: 10.1016/s0304-3940(00)01177-0.
- Prasad, A. *et al.* (2019) 'Molecular Mechanisms of TDP-43 Misfolding and Pathology in Amyotrophic Lateral Sclerosis.', *Frontiers in Molecular Neuroscience*, 12, p. 25. doi: 10.3389/fnmol.2019.00025.
- Prudencio, M. *et al.* (2015) 'Distinct brain transcriptome profiles in C9orf72-associated and sporadic ALS.', *Nature Neuroscience*, 18(8), pp. 1175–1182. doi: 10.1038/nn.4065.
- Puttaparthi, K. *et al.* (2003) 'Aggregate formation in the spinal cord of mutant SOD1 transgenic mice is reversible and mediated by proteasomes', *Journal of Neurochemistry*, 87(4), pp. 851–860. doi: 10.1046/j.1471-4159.2003.02028.
- Qian, K. *et al.* (2017) 'Sporadic ALS Astrocytes Induce Neuronal Degeneration In Vivo.', *Stem Cell Reports*, 8(4), pp. 843–855. doi: 10.1016/j.stemcr.2017.03.003.
- Quintremil, S. *et al.* (2018) 'Roles of Semaphorins in Neurodegenerative Diseases', *Neurons - Dendrites and Axons*. IntechOpen: London, UK. doi: 10.5772/intechopen.82046.
- Rabinovich-Nikitin, I. *et al.* (2016) 'Chronic administration of AMD3100 increases survival and alleviates pathology in SOD1(G93A) mice model of ALS.', *Journal of Neuroinflammation*, 13(1), p. 123. doi: 10.1186/s12974-016-0587-6.
- Rademakers, R. *et al.* (2010) 'Fus gene mutations in familial and sporadic amyotrophic lateral sclerosis.', *Muscle & Nerve*, 42(2), pp. 170–176. doi: 10.1002/mus.21665.
- Rainier, S. *et al.* (2008) 'Neuropathy target esterase gene mutations cause motor neuron disease.', *American Journal of Human Genetics*, 82(3), pp. 780–785. doi: 10.1016/j.ajhg.2007.12.018.
- Ramos-García, N. A. *et al.* (2020) 'Aryl Hydrocarbon Receptor in Post-Mortem Hippocampus and in Serum from Young, Elder, and Alzheimer's Patients.', *International Journal of Molecular Sciences*, 21(6). doi: 10.3390/ijms21061983.
- Ratti, A. and Buratti, E. (2016) 'Physiological functions and pathobiology of TDP-43 and FUS/TLS proteins.', *Journal of Neurochemistry*. England, 138 Suppl, pp. 95–111. doi: 10.1111/jnc.13625.
- Re, D. B. *et al.* (2014) 'Necroptosis drives motor neuron death in models of both sporadic and familial ALS', *Neuron*, 81(5), pp. 1001–1008. doi: 10.1016/j.neuron.2014.01.011.Necroptosis.
- Reaume, A. G. *et al.* (1996) 'Motor neurons in Cu/Zn superoxide dismutase-deficient mice develop normally but exhibit enhanced cell death after axonal injury.', *Nature Genetics*. United States, 13(1), pp. 43–47. doi: 10.1038/ng0596-43.
- Reddy, K. *et al.* (2013) 'The disease-associated r(GGGGCC) n repeat from the C9orf72 gene forms tract length-dependent uni- and multimolecular RNA G-quadruplex structures.', *The Journal of*

- Biological Chemistry*, 288(14), pp. 9860–9866. doi: 10.1074/jbc.C113.452532.
- Redekop, W. K. and Mladsi, D. (2013) 'The Faces of Personalized Medicine: A Framework for Understanding Its Meaning and Scope', *Value in Health*. Elsevier, 16(6 SUPPL.), pp. S4–S9. doi: 10.1016/j.jval.2013.06.005.
- Régal, L. *et al.* (2006) 'The G93C mutation in superoxide dismutase 1: clinicopathologic phenotype and prognosis.', *Archives of Neurology*. United States, 63(2), pp. 262–267. doi: 10.1001/archneur.63.2.262.
- Reid, M. J. *et al.* (2020) 'Astrocytes in Tauopathies.', *Frontiers in Neurology*, 11, p. 572850. doi: 10.3389/fneur.2020.572850.
- Renton, A. E. *et al.* (2011) 'A hexanucleotide repeat expansion in C9ORF72 is the cause of chromosome 9p21-linked ALS-FTD.', *Neuron*, 72(2), pp. 257–268. doi: 10.1016/j.neuron.2011.09.010.
- van Rheenen, W. *et al.* (2016) 'Genome-wide association analyses identify new risk variants and the genetic architecture of amyotrophic lateral sclerosis.', *Nature Genetics*, 48(9), pp. 1043–1048. doi: 10.1038/ng.3622.
- Rieckmann, P. *et al.* (1995) 'Tumor necrosis factor-alpha messenger RNA expression in patients with relapsing-remitting multiple sclerosis is associated with disease activity.', *Annals of Neurology*. United States, 37(1), pp. 82–88. doi: 10.1002/ana.410370115.
- Rinaldi, F. *et al.* (2017) 'High content analysis in amyotrophic lateral sclerosis.', *Molecular and Cellular Neurosciences*, 80, pp. 180–191. doi: 10.1016/j.mcn.2016.12.001.
- Robberecht, W. *et al.* (1996) 'D90A heterozygosity in the SOD1 gene is associated with familial and apparently sporadic amyotrophic lateral sclerosis.', *Neurology*. United States, 47(5), pp. 1336–1339. doi: 10.1212/wnl.47.5.1336.
- Rojas, F. *et al.* (2014) 'Astrocytes expressing mutant SOD1 and TDP43 trigger motoneuron death that is mediated via sodium channels and nitroxidative stress.', *Frontiers in Cellular Neuroscience*, 8(February), p. 24. doi: 10.3389/fncel.2014.00024.
- Rooney, J. P. K. *et al.* (2017) 'A case-control study of hormonal exposures as etiologic factors for ALS in women: Euro-MOTOR.', *Neurology*. United States, 89(12), pp. 1283–1290. doi: 10.1212/WNL.0000000000004390.
- Rose, E. M. *et al.* (2009) 'Glutamate transporter coupling to Na,K-ATPase.', *The Journal of Neuroscience : The Official Journal of the Society for Neuroscience*, 29(25), pp. 8143–8155. doi: 10.1523/JNEUROSCI.1081-09.2009.
- Rosen, D. *et al.* (1993) 'Mutations in Cu/Zn superoxide dismutase gene are associated with familial amyotrophic lateral sclerosis', *Nature*, 362(6415), pp. 59–62.
- Rothhammer, V. *et al.* (2016) 'Type I interferons and microbial metabolites of tryptophan modulate astrocyte activity and central nervous system inflammation via the aryl hydrocarbon receptor.', *Nature Medicine*, 22(6), pp. 586–597. doi: 10.1038/nm.4106.
- Rothstein, J. D. *et al.* (1996) 'Knockout of glutamate transporters reveals a major role for astroglial transport in excitotoxicity and clearance of glutamate.', *Neuron*. United States, 16(3), pp. 675–686. doi: 10.1016/s0896-6273(00)80086-0.
- Rothstein, J. D., Martin, L. J. and Kuncl, R. W. (1992) 'Decreased glutamate transport by the brain and spinal cord in amyotrophic lateral sclerosis.', *The New England Journal of Medicine*. United States, 326(22), pp. 1464–1468. doi: 10.1056/NEJM199205283262204.

- Roybon, L. *et al.* (2013) 'Human stem cell-derived spinal cord astrocytes with defined mature or reactive phenotypes', *Cell Reports*, 4(5), pp. 1035–1048. doi: 10.1038/nature09421.Oxidative.
- Rubino, E. *et al.* (2012) 'SQSTM1 mutations in frontotemporal lobar degeneration and amyotrophic lateral sclerosis.', *Neurology*, 79(15), pp. 1556–1562. doi: 10.1212/WNL.0b013e31826e25df.
- Rudnick, N. D. *et al.* (2017) 'Distinct roles for motor neuron autophagy early and late in the SOD1(G93A) mouse model of ALS.', *Proceedings of the National Academy of Sciences of the United States of America*, 114(39), pp. E8294–E8303. doi: 10.1073/pnas.1704294114.
- Rusnakova, V. *et al.* (2013) 'Heterogeneity of astrocytes: from development to injury - single cell gene expression.', *PLoS One*, 8(8), p. e69734. doi: 10.1371/journal.pone.0069734.
- Sabatelli, M. *et al.* (2009) 'Rare missense variants of neuronal nicotinic acetylcholine receptor altering receptor function are associated with sporadic amyotrophic lateral sclerosis.', *Human Molecular Genetics*. England, 18(20), pp. 3997–4006. doi: 10.1093/hmg/ddp339.
- Sabouny, R. *et al.* (2017) 'The Keap1-Nrf2 Stress Response Pathway Promotes Mitochondrial Hyperfusion Through Degradation of the Mitochondrial Fission Protein Drp1', *Antioxidants & Redox Signaling*, p. 1089/ars.2016.6855.
- Sadée, W. and Dai, Z. (2005) 'Pharmacogenetics/genomics and personalized medicine.', *Human Molecular Genetics*. England, 14 Spec No, pp. R207-14. doi: 10.1093/hmg/ddi261.
- Saeed, M. *et al.* (2006) 'Paraoxonase cluster polymorphisms are associated with sporadic ALS.', *Neurology*. United States, 67(5), pp. 771–776. doi: 10.1212/01.wnl.0000227187.52002.88.
- Sajja, V. S. S. S., Hlavac, N. and VandeVord, P. J. (2016) 'Role of Glia in Memory Deficits Following Traumatic Brain Injury: Biomarkers of Glia Dysfunction.', *Frontiers in Integrative Neuroscience*, 10, p. 7. doi: 10.3389/fnint.2016.00007.
- Sakamuru, S., Attene-Ramos, M. S. and Xia, M. (2016) 'Mitochondrial Membrane Potential Assay.', *Methods in Molecular Biology (Clifton, N.J.)*, 1473, pp. 17–22. doi: 10.1007/978-1-4939-6346-1_2.
- Sanfilippo, C. *et al.* (2017) 'CHI3L1 and CHI3L2 overexpression in motor cortex and spinal cord of sALS patients.', *Molecular and Cellular Neurosciences*. United States, 85, pp. 162–169. doi: 10.1016/j.mcn.2017.10.001.
- Sanz, E. *et al.* (2009) 'Cell-type-specific isolation of ribosome-associated mRNA from complex tissues.', *Proceedings of the National Academy of Sciences of the United States of America*, 106(33), pp. 13939–13944. doi: 10.1073/pnas.0907143106.
- Sareen, D. *et al.* (2013) 'Targeting RNA foci in iPSC-derived motor neurons from ALS patients with a C9ORF72 repeat expansion.', *Science Translational Medicine*, 5(208), p. 208ra149. doi: 10.1126/scitranslmed.3007529.
- Saris, C. G. J. *et al.* (2009) 'Weighted gene co-expression network analysis of the peripheral blood from Amyotrophic Lateral Sclerosis patients.', *BMC Genomics*, 10, p. 405. doi: 10.1186/1471-2164-10-405.
- Sarlette, A. *et al.* (2008) 'Nuclear erythroid 2-related factor 2-antioxidative response element signaling pathway in motor cortex and spinal cord in amyotrophic lateral sclerosis.', *Journal of Neuropathology and Experimental Neurology*, 67(11), pp. 1055–62. doi: 10.1097/NEN.0b013e31818b4906.
- Sasaki, S. (2011) 'Autophagy in spinal cord motor neurons in sporadic amyotrophic lateral sclerosis.', *Journal of Neuropathology and Experimental Neurology*. England, 70(5), pp. 349–359. doi: 10.1097/NEN.0b013e3182160690.

- Sasaki, S. and Iwata, M. (2007) 'Mitochondrial alterations in the spinal cord of patients with sporadic amyotrophic lateral sclerosis.', *Journal of Neuropathology and Experimental Neurology*. England, 66(1), pp. 10–16. doi: 10.1097/nen.0b013e31802c396b.
- Sasakura, H. *et al.* (2017) 'Lifespan extension by peroxidase and dual oxidase-mediated ROS signaling through pyrroloquinoline quinone in *C. elegans*.' , *Journal of Cell Science*. England, 130(15), pp. 2631–2643. doi: 10.1242/jcs.202119.
- Satoh, J. (2010) 'MicroRNAs and their therapeutic potential for human diseases: aberrant microRNA expression in Alzheimer's disease brains.' , *Journal of Pharmacological Sciences*. Japan, 114(3), pp. 269–275. doi: 10.1254/jphs.10r11fm.
- Saul, J. *et al.* (2020) 'Global alterations to the choroid plexus blood-CSF barrier in amyotrophic lateral sclerosis.' , *Acta Neuropathologica Communications*, 8(1), p. 92. doi: 10.1186/s40478-020-00968-9.
- Saxena, S., Cabuy, E. and Caroni, P. (2009) 'A role for motoneuron subtype-selective ER stress in disease manifestations of FALS mice.' , *Nature Neuroscience*. United States, 12(5), pp. 627–636. doi: 10.1038/nn.2297.
- Scheltens, P. *et al.* (2016) 'Alzheimer's disease.' , *Lancet (London, England)*. England, 388(10043), pp. 505–517. doi: 10.1016/S0140-6736(15)01124-1.
- Scheper, W. *et al.* (2007) 'Rab6 is increased in Alzheimer's disease brain and correlates with endoplasmic reticulum stress.' , *Neuropathology and Applied Neurobiology*. England, 33(5), pp. 523–532. doi: 10.1111/j.1365-2990.2007.00846.
- van Schie, R. M. F. *et al.* (2011) 'Loading and maintenance dose algorithms for phenprocoumon and acenocoumarol using patient characteristics and pharmacogenetic data.' , *European Heart Journal*. England, 32(15), pp. 1909–1917. doi: 10.1093/eurheartj/ehr116.
- Schindler, S. E. and Fagan, A. M. (2015) 'Autosomal Dominant Alzheimer Disease: A Unique Resource to Study CSF Biomarker Changes in Preclinical AD.' , *Frontiers in Neurology*, 6, p. 142. doi: 10.3389/fneur.2015.00142.
- Schmidt, E. R. E., Pasterkamp, R. J. and van den Berg, L. H. (2009) 'Axon guidance proteins: novel therapeutic targets for ALS?' , *Progress in Neurobiology*. England, 88(4), pp. 286–301. doi: 10.1016/j.pneurobio.2009.05.004.
- Schnitzer, J., Franke, W. W. and Schachner, M. (1981) 'Immunocytochemical demonstration of vimentin in astrocytes and ependymal cells of developing and adult mouse nervous system.' , *The Journal of Cell Biology*, 90(2), pp. 435–447. doi: 10.1083/jcb.90.2.435.
- Schwanhäusser, B. *et al.* (2011) 'Global quantification of mammalian gene expression control.' , *Nature*. England, 473(7347), pp. 337–342. doi: 10.1038/nature10098.
- Schwenk, B. M. *et al.* (2016) 'TDP-43 loss of function inhibits endosomal trafficking and alters trophic signaling in neurons.' , *The EMBO Journal*, 35(21), pp. 2350–2370. doi: 10.15252/embj.201694221.
- Sephton, C. F. *et al.* (2010) 'TDP-43 is a developmentally regulated protein essential for early embryonic development.' , *The Journal of Biological Chemistry*, 285(9), pp. 6826–6834. doi: 10.1074/jbc.M109.061846.
- Serio, A. *et al.* (2013) 'Astrocyte pathology and the absence of non-cell autonomy in an induced pluripotent stem cell model of TDP-43 proteinopathy.' , *Proceedings of the National Academy of Sciences of the United States of America*, 110(12), pp. 4697–4702. doi: 10.1073/pnas.1300398110.
- Sharp, F. R. *et al.* (2006) 'The future of genomic profiling of neurological diseases using blood.' , *Archives of Neurology*. United States, 63(11), pp. 1529–1536. doi: 10.1001/archneur.63.11.1529.

- Shaw, P. and Chattopadhyay, A. (2020) 'Nrf2-ARE signaling in cellular protection: Mechanism of action and the regulatory mechanisms.', *Journal of Cellular Physiology*. United States, 235(4), pp. 3119–3130. doi: 10.1002/jcp.29219.
- Shepherd, S. R. *et al.* (2014) 'The extracellular domain of neurotrophin receptor p75 as a candidate biomarker for amyotrophic lateral sclerosis.', *PLoS One*, 9(1), p. e87398. doi: 10.1371/journal.pone.0087398.
- Shi, P. *et al.* (2010) 'Mitochondrial dysfunction in amyotrophic lateral sclerosis.', *Biochimica et Biophysica Acta*, 1802(1), pp. 45–51. doi: 10.1016/j.bbadis.2009.08.012.
- Shibata, N. *et al.* (1996) 'Intense superoxide dismutase-1 immunoreactivity in intracytoplasmic hyaline inclusions of familial amyotrophic lateral sclerosis with posterior column involvement.', *Journal of Neuropathology and Experimental Neurology*. England, 55(4), pp. 481–490. doi: 10.1097/00005072-199604000-00011.
- Shibata, N. *et al.* (2001) 'Morphological evidence for lipid peroxidation and protein glycoxylation in spinal cords from sporadic amyotrophic lateral sclerosis patients.', *Brain Research*. Netherlands, 917(1), pp. 97–104. doi: 10.1016/s0006-8993(01)02926-2.
- Shibata, Y. and Morimoto, R. I. (2014) 'How the nucleus copes with proteotoxic stress', *Current Biology*. Elsevier Ltd, 24(10), pp. R463–R474. doi: 10.1016/j.cub.2014.03.033.
- Shichinohe, H. *et al.* (2004) 'Neuroprotective effects of the free radical scavenger Edaravone (MCI-186) in mice permanent focal brain ischemia', *Brain Research*, 1029(2), pp. 200–206. doi: 10.1016/j.brainres.2004.09.055.
- Shigetomi, E. *et al.* (2019) 'Aberrant Calcium Signals in Reactive Astrocytes: A Key Process in Neurological Disorders.', *International Journal of Molecular Sciences*, 20(4). doi: 10.3390/ijms20040996.
- Shih, C.-H. *et al.* (2014) 'Astroglial-derived periostin promotes axonal regeneration after spinal cord injury.', *The Journal of Neuroscience : The Official Journal of the Society for Neuroscience*, 34(7), pp. 2438–2443. doi: 10.1523/JNEUROSCI.2947-13.2014.
- Shtilbans, A. *et al.* (2011) 'Differential gene expression in patients with amyotrophic lateral sclerosis.', *Amyotrophic Lateral Sclerosis : Official Publication of the World Federation of Neurology Research Group on Motor Neuron Diseases*. England, 12(4), pp. 250–256. doi: 10.3109/17482968.2011.560946.
- Simpson, C. L. *et al.* (2009) 'Variants of the elongator protein 3 (ELP3) gene are associated with motor neuron degeneration.', *Human Molecular Genetics*, 18(3), pp. 472–481. doi: 10.1093/hmg/ddn375.
- Simpson, J. E. *et al.* (2010) 'Astrocyte phenotype in relation to Alzheimer-type pathology in the ageing brain.', *Neurobiology of Aging*. United States, 31(4), pp. 578–590. doi: 10.1016/j.neurobiolaging.2008.05.015.
- Smith, B. N. *et al.* (2014) 'Exome-wide Rare Variant Analysis Identifies TUBA4A Mutations Associated with Familial ALS', *Neuron*, 84(2), pp. 324–331. doi: 10.1177/1948550614552729.Behavior.
- Smith, B. N. *et al.* (2017) 'Mutations in the vesicular trafficking protein annexin A11 are associated with amyotrophic lateral sclerosis.', *Science Translational Medicine*, 9(388). doi: 10.1126/scitranslmed.aad9157.
- Smith, E. F., Shaw, P. J. and De Vos, K. J. (2019) 'The role of mitochondria in amyotrophic lateral sclerosis.', *Neuroscience Letters*. Ireland, 710, p. 132933. doi: 10.1016/j.neulet.2017.06.052.

- Smith, R. A. *et al.* (2006) 'Antisense oligonucleotide therapy for neurodegenerative disease.', *The Journal of Clinical Investigation*, 116(8), pp. 2290–2296. doi: 10.1172/JCI25424.
- Soda, M. *et al.* (2007) 'Identification of the transforming EML4-ALK fusion gene in non-small-cell lung cancer.', *Nature*. England, 448(7153), pp. 561–566. doi: 10.1038/nature05945.
- Sofroniew, M. V and Vinters, H. V (2010) 'Astrocytes: biology and pathology.', *Acta Neuropathologica*, 119(1), pp. 7–35. doi: 10.1007/s00401-009-0619-8.
- Sokolov, M. E. *et al.* (2018) 'Triple-Gene Therapy for Stroke: A Proof-of-Concept in Vivo Study in Rats.', *Frontiers in Pharmacology*, 9, p. 111. doi: 10.3389/fphar.2018.00111.
- Son, E. Y. *et al.* (2011) 'Conversion of mouse and human fibroblasts into functional spinal motor neurons.', *Cell Stem Cell*, 9(3), pp. 205–218. doi: 10.1016/j.stem.2011.07.014.
- Soneson, C., Love, M. I. and Robinson, M. D. (2015) 'Differential analyses for RNA-seq: transcript-level estimates improve gene-level inferences.', *F1000Research*, 4, p. 1521. doi: 10.12688/f1000research.7563.2.
- Song, P. *et al.* (2016) 'Parkin promotes proteasomal degradation of p62: implication of selective vulnerability of neuronal cells in the pathogenesis of Parkinson's disease.', *Protein & Cell*, 7(2), pp. 114–129. doi: 10.1007/s13238-015-0230-9.
- Spampinato, S. F. *et al.* (2018) 'Metabotropic Glutamate Receptors in Glial Cells: A New Potential Target for Neuroprotection?', *Frontiers in Molecular Neuroscience*, 11, p. 414. doi: 10.3389/fnmol.2018.00414.
- Sproviero, W. *et al.* (2017) 'ATXN2 trinucleotide repeat length correlates with risk of ALS.', *Neurobiology of Aging*, 51, pp. 178.e1-178.e9. doi: 10.1016/j.neurobiolaging.2016.11.010.
- Srinivasan, K. *et al.* (2016) 'Untangling the brain's neuroinflammatory and neurodegenerative transcriptional responses.', *Nature Communications*, 7, p. 11295. doi: 10.1038/ncomms11295.
- Staurengi, E. *et al.* (2020) 'Oxysterols present in Alzheimer's disease brain induce synaptotoxicity by activating astrocytes: A major role for lipocalin-2.', *Redox Biology*, 39, p. 101837. doi: 10.1016/j.redox.2020.101837.
- Steinacker, P. *et al.* (2016) 'Neurofilaments in the diagnosis of motoneuron diseases: a prospective study on 455 patients.', *Journal of Neurology, Neurosurgery, and Psychiatry*. England, 87(1), pp. 12–20. doi: 10.1136/jnnp-2015-311387.
- Stoddard-Bennett, T. and Reijo Pera, R. (2019) 'Treatment of Parkinson's Disease through Personalized Medicine and Induced Pluripotent Stem Cells.', *Cells*, 8(1). doi: 10.3390/cells8010026.
- Stoica, R. *et al.* (2014) 'ER-mitochondria associations are regulated by the VAPB-PTPIP51 interaction and are disrupted by ALS/FTD-associated TDP-43.', *Nature Communications*, 5, p. 3996. doi: 10.1038/ncomms4996.
- Stoica, R. *et al.* (2016) 'ALS/FTD-associated FUS activates GSK-3 β to disrupt the VAPB-PTPIP51 interaction and ER-mitochondria associations.', *EMBO Reports*, 17(9), pp. 1326–1342. doi: 10.15252/embr.201541726.
- Stopford, M. J. *et al.* (2017) 'C9ORF72 hexanucleotide repeat exerts toxicity in a stable, inducible motor neuronal cell model, which is rescued by partial depletion of Pten.', *Human Molecular Genetics*, 26(6), pp. 1133–1145. doi: 10.1093/hmg/ddx022.
- Stopford, M. J., Allen, S. P. and Ferraiuolo, L. (2019) 'A High-throughput and Pathophysiologically Relevant Astrocyte-motor Neuron Co-culture Assay for Amyotrophic Lateral Sclerosis Therapeutic

Discovery.', *Bio-protocol*, 9(17). doi: 10.21769/BioProtoc.3353.

Stuart, J. M. *et al.* (2003) 'A gene-coexpression network for global discovery of conserved genetic modules.', *Science (New York, N.Y.)*. United States, 302(5643), pp. 249–255. doi: 10.1126/science.1087447.

Sun, W. *et al.* (2013) 'Glutamate-dependent neuroglial calcium signaling differs between young and adult brain.', *Science (New York, N.Y.)*, 339(6116), pp. 197–200. doi: 10.1126/science.1226740.

Süssmuth, S. D. *et al.* (2010) 'CSF glial markers correlate with survival in amyotrophic lateral sclerosis.', *Neurology*. United States, 74(12), pp. 982–987. doi: 10.1212/WNL.0b013e3181d5dc3b.

Suzuki, M. *et al.* (2007) 'GDNF secreting human neural progenitor cells protect dying motor neurons, but not their projection to muscle, in a rat model of familial ALS.', *PLoS One*, 2(8), p. e689. doi: 10.1371/journal.pone.0000689.

Swanson, R. A. *et al.* (1997) 'Neuronal regulation of glutamate transporter subtype expression in astrocytes.', *The Journal of Neuroscience : The Official Journal of the Society for Neuroscience*, 17(3), pp. 932–940. doi: 10.1523/JNEUROSCI.17-03-00932.1997.

Swinnen, B. *et al.* (2018) 'A zebrafish model for C9orf72 ALS reveals RNA toxicity as a pathogenic mechanism.', *Acta Neuropathologica*. Germany, 135(3), pp. 427–443. doi: 10.1007/s00401-017-1796-5.

Tabarean, I. V (2020) 'Neurotensin induces hypothermia by activating both neuronal neurotensin receptor 1 and astrocytic neurotensin receptor 2 in the median preoptic nucleus.', *Neuropharmacology*, 171, p. 108069. doi: 10.1016/j.neuropharm.2020.108069.

Tafari, F. *et al.* (2015) 'SOD1 misplacing and mitochondrial dysfunction in amyotrophic lateral sclerosis pathogenesis.', *Frontiers in Cellular Neuroscience*, 9, p. 336. doi: 10.3389/fncel.2015.00336.

Taguchi, K. *et al.* (2020) 'Protective Effect of 2',3'-Dihydroxy-4',6'-dimethoxychalcone on Glutamate-Induced Neurotoxicity in Primary Cortical Cultures.', *Biological & Pharmaceutical Bulletin*. Japan, 43(1), pp. 184–187. doi: 10.1248/bpb.b19-00718.

Takahashi, K. and Yamanaka, S. (2006) 'Induction of pluripotent stem cells from mouse embryonic and adult fibroblast cultures by defined factors.', *Cell*. United States, 126(4), pp. 663–676. doi: 10.1016/j.cell.2006.07.024.

Takahashi, S. *et al.* (2008) 'Association of SNPs and haplotypes in APOL1, 2 and 4 with schizophrenia.', *Schizophrenia Research*, 104(1–3), pp. 153–164. doi: 10.1016/j.schres.2008.05.028.

Takahashi, Y. *et al.* (2013) 'ERBB4 mutations that disrupt the neuregulin-ErbB4 pathway cause amyotrophic lateral sclerosis type 19.', *American Journal of Human Genetics*, 93(5), pp. 900–905. doi: 10.1016/j.ajhg.2013.09.008.

Takamura, R. *et al.* (2017) 'All-trans retinoic acid improved impaired proliferation of neural stem cells and suppressed microglial activation in the hippocampus in an Alzheimer's mouse model.', *Journal of Neuroscience Research*. United States, 95(3), pp. 897–906. doi: 10.1002/jnr.23843.

Takei, K. *et al.* (2017) 'Edaravone and its clinical development for amyotrophic lateral sclerosis.', *Amyotrophic Lateral Sclerosis & Frontotemporal Degeneration*. England, 18(sup1), pp. 5–10. doi: 10.1080/21678421.2017.1353101.

Talantova, M. *et al.* (2013) 'A β induces astrocytic glutamate release, extrasynaptic NMDA receptor activation, and synaptic loss.', *Proceedings of the National Academy of Sciences of the United States of America*, 110(27), pp. E2518–27. doi: 10.1073/pnas.1306832110.

- Tan, R. H. *et al.* (2015) 'TDP-43 proteinopathies: Pathological identification of brain regions differentiating clinical phenotypes', *Brain*, 138(10), pp. 3110–3122. doi: 10.1093/brain/awv220.
- Tan, W. S. D. *et al.* (2017) 'Is there a future for andrographolide to be an anti-inflammatory drug? Deciphering its major mechanisms of action.', *Biochemical Pharmacology*. England, 139, pp. 71–81. doi: 10.1016/j.bcp.2017.03.024.
- Tang, Y. *et al.* (2017) 'Direct Reprogramming Rather than iPSC-Based Reprogramming Maintains Aging Hallmarks in Human Motor Neurons.', *Frontiers in Molecular Neuroscience*, 10, p. 359. doi: 10.3389/fnmol.2017.00359.
- Tanji, K. *et al.* (2013) 'Keap1 is localized in neuronal and glial cytoplasmic inclusions in various neurodegenerative diseases.', *Journal of Neuropathology and Experimental Neurology*. England, 72(1), pp. 18–28. doi: 10.1097/NEN.0b013e31827b5713.
- Tazelaar, G. H. P. *et al.* (2019) 'Association of NIPA1 repeat expansions with amyotrophic lateral sclerosis in a large international cohort.', *Neurobiology of Aging*. United States, 74, pp. 234.e9-234.e15. doi: 10.1016/j.neurobiolaging.2018.09.012.
- Teyssou, E. *et al.* (2014) 'Genetic analysis of SS18L1 in French amyotrophic lateral sclerosis.', *Neurobiology of Aging*. United States, 35(5), pp. 1213.e9-1213.e12. doi: 10.1016/j.neurobiolaging.2013.11.023.
- Thermann, R. and Hentze, M. W. (2007) 'Drosophila miR2 induces pseudo-polysomes and inhibits translation initiation.', *Nature*. England, 447(7146), pp. 875–878. doi: 10.1038/nature05878.
- Thimmulappa, R. K. *et al.* (2002) 'Identification of Nrf2-regulated genes induced by the chemopreventive agent sulforaphane by oligonucleotide microarray.', *Cancer Research*. United States, 62(18), pp. 5196–5203.
- Thomsen, G. M. *et al.* (2018) 'Transplantation of Neural Progenitor Cells Expressing Glial Cell Line-Derived Neurotrophic Factor into the Motor Cortex as a Strategy to Treat Amyotrophic Lateral Sclerosis.', *Stem Cells (Dayton, Ohio)*. United States, 36(7), pp. 1122–1131. doi: 10.1002/stem.2825.
- Ticozzi, N. *et al.* (2011) 'Mutational analysis reveals the FUS homolog TAF15 as a candidate gene for familial amyotrophic lateral sclerosis.', *American Journal of Medical Genetics. Part B, Neuropsychiatric Genetics: The Official Publication of the International Society of Psychiatric Genetics*. United States, 156B(3), pp. 285–290. doi: 10.1002/ajmg.b.31158.
- Tollervey, J. R. *et al.* (2011) 'Characterizing the RNA targets and position-dependent splicing regulation by TDP-43.', *Nature Neuroscience*, 14(4), pp. 452–458. doi: 10.1038/nn.2778.
- Tong, J. *et al.* (2013) 'Expression of ALS-linked TDP-43 mutant in astrocytes causes non-cell-autonomous motor neuron death in rats.', *The EMBO Journal*, 32(13), pp. 1917–1926. doi: 10.1038/emboj.2013.122.
- Tripathi, P. *et al.* (2017) 'Reactive Astrocytes Promote ALS-like Degeneration and Intracellular Protein Aggregation in Human Motor Neurons by Disrupting Autophagy through TGF- β 1.', *Stem Cell Reports*, 9(2), pp. 667–680. doi: 10.1016/j.stemcr.2017.06.008.
- Tschopp, J. and Schroder, K. (2010) 'NLRP3 inflammasome activation: The convergence of multiple signalling pathways on ROS production?', *Nature Reviews. Immunology*. England, pp. 210–215. doi: 10.1038/nri2725.
- Tsitkanou, S. *et al.* (2019) 'The Role of Exercise as a Non-pharmacological Therapeutic Approach for Amyotrophic Lateral Sclerosis: Beneficial or Detrimental?', *Frontiers in Neurology*, 10, p. 783. doi: 10.3389/fneur.2019.00783.

- Turner, B. J. *et al.* (2008) 'TDP-43 expression in mouse models of amyotrophic lateral sclerosis and spinal muscular atrophy.', *BMC Neuroscience*, 9, p. 104. doi: 10.1186/1471-2202-9-104.
- Turner, M. R. *et al.* (2012) 'Cardiovascular fitness as a risk factor for amyotrophic lateral sclerosis: indirect evidence from record linkage study.', *Journal of Neurology, Neurosurgery, and Psychiatry*. England, 83(4), pp. 395–398. doi: 10.1136/jnnp-2011-301161.
- Tyzack, G. E. *et al.* (2017) 'A neuroprotective astrocyte state is induced by neuronal signal EphB1 but fails in ALS models.', *Nature Communications*, 8(1), p. 1164. doi: 10.1038/s41467-017-01283-z.
- Udan-Johns, M. *et al.* (2014) 'Prion-like nuclear aggregation of TDP-43 during heat shock is regulated by HSP40/70 chaperones.', *Human Molecular Genetics*, 23(1), pp. 157–170. doi: 10.1093/hmg/ddt408.
- Ugolino, J. *et al.* (2016) 'Loss of C9orf72 Enhances Autophagic Activity via Deregulated mTOR and TFEB Signaling.', *PLoS Genetics*, 12(11), p. e1006443. doi: 10.1371/journal.pgen.1006443.
- Urbani, A. and Belluzzi, O. (2000) 'Riluzole inhibits the persistent sodium current in mammalian CNS neurons.', *The European Journal of Neuroscience*. France, 12(10), pp. 3567–3574. doi: 10.1046/j.1460-9568.2000.00242.
- Urushitani, M. *et al.* (2002) 'Proteasomal inhibition by misfolded mutant superoxide dismutase 1 induces selective motor neuron death in familial amyotrophic lateral sclerosis.', *Journal of Neurochemistry*. England, 83(5), pp. 1030–1042. doi: 10.1046/j.1471-4159.2002.01211.
- Uyan, Ö. *et al.* (2013) 'Genome-wide copy number variation in sporadic amyotrophic lateral sclerosis in the Turkish population: deletion of EPHA3 is a possible protective factor.', *PloS One*, 8(8), p. e72381. doi: 10.1371/journal.pone.0072381.
- Uzawa, A. *et al.* (2010) 'Different responses to interferon beta-1b treatment in patients with neuromyelitis optica and multiple sclerosis.', *European Journal of Neurology*. England, 17(5), pp. 672–676. doi: 10.1111/j.1468-1331.2009.02897.
- Vance, C. *et al.* (2009) 'Mutations in FUS, an RNA Processing Protein, Cause Familial Amyotrophic Lateral Sclerosis Type 6', *Science*, 323(5918), pp. 1208–1211. doi: 10.1126/science.1165942.
- Vance, C. *et al.* (2013) 'ALS mutant FUS disrupts nuclear localization and sequesters wild-type FUS within cytoplasmic stress granules.', *Human Molecular Genetics*, 22(13), pp. 2676–2688. doi: 10.1093/hmg/ddt117.
- Vanhollebeke, B. and Pays, E. (2006) 'The function of apolipoproteins L.', *Cellular and Molecular Life Sciences : CMLS*. Switzerland, 63(17), pp. 1937–1944. doi: 10.1007/s00018-006-6091-x.
- Varcianna, A. *et al.* (2019) 'Micro-RNAs secreted through astrocyte-derived extracellular vesicles cause neuronal network degeneration in C9orf72 ALS.', *EBioMedicine*, 40, pp. 626–635. doi: 10.1016/j.ebiom.2018.11.067.
- Vargas, M. R., Johnson, D. A., *et al.* (2008) 'Nrf2 activation in astrocytes protects against neurodegeneration in mouse models of familial amyotrophic lateral sclerosis.', *The Journal of Neuroscience: The Official Journal of the Society for Neuroscience*, 28(50), pp. 13574–13581. doi: 10.1523/JNEUROSCI.4099-08.2008.
- Vande Velde, C. *et al.* (2008) 'Selective association of misfolded ALS-linked mutant SOD1 with the cytoplasmic face of mitochondria.', *Proceedings of the National Academy of Sciences of the United States of America*, 105(10), pp. 4022–4027. doi: 10.1073/pnas.0712209105.
- Verkhatsky, A. and Zorec, R. (2019) 'Astroglial signalling in health and disease.', *Neuroscience Letters*. Ireland, pp. 1–4. doi: 10.1016/j.neulet.2018.07.026.

- Vogel, C., Silva, G. M. and Marcotte, E. M. (2011) 'Protein expression regulation under oxidative stress.', *Molecular & Cellular Proteomics : MCP*, 10(12), p. M111.009217. doi: 10.1074/mcp.M111.009217.
- De Vos, K. J. *et al.* (2007) 'Familial amyotrophic lateral sclerosis-linked SOD1 mutants perturb fast axonal transport to reduce axonal mitochondria content.', *Human Molecular Genetics*, 16(22), pp. 2720–2728. doi: 10.1093/hmg/ddm226.
- Wainwright, C. E. *et al.* (2015) 'Lumacaftor-Ivacaftor in Patients with Cystic Fibrosis Homozygous for Phe508del CFTR.', *The New England Journal of Medicine*, 373(3), pp. 220–231. doi: 10.1056/NEJMoa1409547.
- Waite, A. J. *et al.* (2014) 'Reduced C9orf72 protein levels in frontal cortex of amyotrophic lateral sclerosis and frontotemporal degeneration brain with the C9ORF72 hexanucleotide repeat expansion.', *Neurobiology of Aging*, 35(7), pp. 1779.e5-1779.e13. doi: 10.1016/j.neurobiolaging.2014.01.016.
- Wakabayashi, N. *et al.* (2004) 'Protection against electrophile and oxidant stress by induction of the phase 2 response: fate of cysteines of the Keap1 sensor modified by inducers.', *Proceedings of the National Academy of Sciences of the United States of America*, 101(7), pp. 2040–5. doi: 10.1073/pnas.0307301101.
- Walczak, J. *et al.* (2019) 'Distinction of sporadic and familial forms of ALS based on mitochondrial characteristics.', *FASEB Journal : Official Publication of the Federation of American Societies for Experimental Biology*. United States, 33(3), pp. 4388–4403. doi: 10.1096/fj.201801843R.
- Walker, C. *et al.* (2017) 'C9orf72 expansion disrupts ATM-mediated chromosomal break repair.', *Nature Neuroscience*, 20(9), pp. 1225–1235. doi: 10.1038/nn.4604.
- Waller, R. *et al.* (2016) 'Gene expression profiling of the astrocyte transcriptome in multiple sclerosis normal appearing white matter reveals a neuroprotective role.', *Journal of Neuroimmunology*. Netherlands, 299, pp. 139–146. doi: 10.1016/j.jneuroim.2016.09.010.
- Wang, D. D. and Bordey, A. (2008) 'The astrocyte odyssey.', *Progress in Neurobiology*, 86(4), pp. 342–367. doi: 10.1016/j.pneurobio.2008.09.015.
- Wang, H.-L. *et al.* (2020) 'Prefrontal Nectin3 Reduction Mediates Adolescent Stress-Induced Deficits of Social Memory, Spatial Working Memory, and Dendritic Structure in Mice.', *Neuroscience Bulletin*, 36(8), pp. 860–874. doi: 10.1007/s12264-020-00499-2.
- Wang, M.-D. *et al.* (2017) 'Identification of risk factors associated with onset and progression of amyotrophic lateral sclerosis using systematic review and meta-analysis.', *Neurotoxicology*. Netherlands, 61, pp. 101–130. doi: 10.1016/j.neuro.2016.06.015.
- Wang, R., Yang, B. and Zhang, D. (2011) 'Activation of interferon signaling pathways in spinal cord astrocytes from an ALS mouse model.', *Glia*, 59(6), pp. 946–958. doi: 10.1002/glia.21167.
- Wang, S.-J., Wang, K.-Y. and Wang, W.-C. (2004) 'Mechanisms underlying the riluzole inhibition of glutamate release from rat cerebral cortex nerve terminals (synaptosomes).', *Neuroscience*. United States, 125(1), pp. 191–201. doi: 10.1016/j.neuroscience.2004.01.019.
- Wang, T. and Xiong, J.-Q. (2016) 'The Orphan Nuclear Receptor TLX/NR2E1 in Neural Stem Cells and Diseases.', *Neuroscience Bulletin*, 32(1), pp. 108–114. doi: 10.1007/s12264-015-0004-7.
- Wang, W.-Y. *et al.* (2013) 'Interaction of FUS and HDAC1 regulates DNA damage response and repair in neurons.', *Nature Neuroscience*, 16(10), pp. 1383–1391. doi: 10.1038/nn.3514.
- Wang, W. *et al.* (2013) 'The ALS disease-associated mutant TDP-43 impairs mitochondrial dynamics

- and function in motor neurons.', *Human Molecular Genetics*, 22(23), pp. 4706–4719. doi: 10.1093/hmg/ddt319.
- Wang, W. *et al.* (2016) 'The inhibition of TDP-43 mitochondrial localization blocks its neuronal toxicity.', *Nature Medicine*, 22(8), pp. 869–878. doi: 10.1038/nm.4130.
- Wang, Z. *et al.* (2003) 'Reduced expression of glutamate transporter EAAT2 and impaired glutamate transport in human primary astrocytes exposed to HIV-1 or gp120.', *Virology*. United States, 312(1), pp. 60–73. doi: 10.1016/s0042-6822(03)00181-8.
- Webster, C. P. *et al.* (2016) 'The C9orf72 protein interacts with Rab1a and the ULK1 complex to regulate initiation of autophagy.', *The EMBO Journal*, 35(15), pp. 1656–76. doi: 10.15252/embj.201694401.
- Wichterle, H. *et al.* (2002) 'Directed differentiation of embryonic stem cells into motor neurons.', *Cell*. United States, 110(3), pp. 385–397. doi: 10.1016/s0092-8674(02)00835-8.
- Wils, H. *et al.* (2010) 'TDP-43 transgenic mice develop spastic paralysis and neuronal inclusions characteristic of ALS and frontotemporal lobar degeneration.', *Proceedings of the National Academy of Sciences of the United States of America*, 107(8), pp. 3858–3863. doi: 10.1073/pnas.0912417107.
- Winkler, D. D. *et al.* (2009) 'Structural and biophysical properties of the pathogenic SOD1 variant H46R/H48Q.', *Biochemistry*, 48(15), pp. 3436–3447. doi: 10.1021/bi8021735.
- De Winter, F. *et al.* (2006) 'The expression of the chemorepellent Semaphorin 3A is selectively induced in terminal Schwann cells of a subset of neuromuscular synapses that display limited anatomical plasticity and enhanced vulnerability in motor neuron disease.', *Molecular and Cellular Neurosciences*. United States, 32(1–2), pp. 102–117. doi: 10.1016/j.mcn.2006.03.002.
- Witgert, M. *et al.* (2010) 'Frontal-lobe mediated behavioral dysfunction in amyotrophic lateral sclerosis.', *European Journal of Neurology*. England, 17(1), pp. 103–110. doi: 10.1111/j.1468-1331.2009.02801.
- Wong, A. W. *et al.* (2015) 'Neurite outgrowth in normal and injured primary sensory neurons reveals different regulation by nerve growth factor (NGF) and artemin.', *Molecular and Cellular Neurosciences*. United States, 65, pp. 125–134. doi: 10.1016/j.mcn.2015.03.004.
- Wong, P. C. *et al.* (1995) 'An adverse property of a familial ALS-linked SOD1 mutation causes motor neuron disease characterized by vacuolar degeneration of mitochondria', *Neuron*, 14(6), pp. 1105–1116. doi: 10.1016/0896-6273(95)90259-7.
- Writing Group; Edaravone (MCI-186) ALS 19 Study Group (2017) 'Safety and efficacy of edaravone in well defined patients with amyotrophic lateral sclerosis: a randomised, double-blind, placebo-controlled trial.', *The Lancet. Neurology*. England, 16(7), pp. 505–512. doi: 10.1016/S1474-4422(17)30115-1.
- Wu, C.-H. *et al.* (2012) 'Mutations in the profilin 1 gene cause familial amyotrophic lateral sclerosis.', *Nature*, 488(7412), pp. 499–503. doi: 10.1038/nature11280.
- Xiong, H. *et al.* (2008) 'Cholesterol retention in Alzheimer's brain is responsible for high beta- and gamma-secretase activities and Aβ production.', *Neurobiology of Disease*, 29(3), pp. 422–437. doi: 10.1016/j.nbd.2007.10.005.
- Xu, Y.-F. *et al.* (2011) 'Expression of mutant TDP-43 induces neuronal dysfunction in transgenic mice.', *Molecular Neurodegeneration*, 6, p. 73. doi: 10.1186/1750-1326-6-73.
- Yamanaka, K. *et al.* (2008) 'Astrocytes as determinants of disease progression in inherited amyotrophic lateral sclerosis.', *Nature Neuroscience*, 11(3), pp. 251–253. doi: 10.1038/nn2047.

- Yamane, M. *et al.* (2012) 'Semaphorin3A facilitates axonal transport through a local calcium signaling and tetrodotoxin-sensitive voltage-gated sodium channels.', *Biochemical and Biophysical Research Communications*. United States, 422(2), pp. 333–338. doi: 10.1016/j.bbrc.2012.05.003.
- Yan, M. *et al.* (2011) 'Effects of dexmedetomidine on the release of glial cell line-derived neurotrophic factor from rat astrocyte cells.', *Neurochemistry International*. England, 58(5), pp. 549–557. doi: 10.1016/j.neuint.2011.01.013.
- Yang, E.-J. *et al.* (2014) 'Kaempferol attenuates the glutamate-induced oxidative stress in mouse-derived hippocampal neuronal HT22 cells.', *Food & Function*. England, 5(7), pp. 1395–1402. doi: 10.1039/c4fo00068d.
- Yang, L., Rieves, D. and Ganley, C. (2012) 'Brain amyloid imaging--FDA approval of florbetapir F18 injection.', *The New England Journal of Medicine*. United States, 367(10), pp. 885–887. doi: 10.1056/NEJMp1208061.
- Yang, X. *et al.* (2017) 'HLA-DRA/HLA-DRB5 polymorphism affects risk of sporadic ALS and survival in a southwest Chinese cohort.', *Journal of the Neurological Sciences*. Netherlands, 373, pp. 124–128. doi: 10.1016/j.jns.2016.12.055.
- Zappia, M. *et al.* (2005) 'Sex differences in clinical and genetic determinants of levodopa peak-dose dyskinesias in Parkinson disease: an exploratory study.', *Archives of Neurology*. United States, 62(4), pp. 601–605. doi: 10.1001/archneur.62.4.601.
- Zhang, J. *et al.* (2018) 'Preliminary Observation about Alteration of Proteins and Their Potential Functions in Spinal Cord of SOD1 G93A Transgenic Mice.', *International Journal of Biological Sciences*, 14(10), pp. 1306–1320. doi: 10.7150/ijbs.26829.
- Zhang, J. and Liu, Q. (2015) 'Cholesterol metabolism and homeostasis in the brain.', *Protein & Cell*, 6(4), pp. 254–264. doi: 10.1007/s13238-014-0131-3.
- Zhao, C. *et al.* (2020) 'Mutant C9orf72 human iPSC-derived astrocytes cause non-cell autonomous motor neuron pathophysiology.', *Glia*, 68(5), pp. 1046–1064. doi: 10.1002/glia.23761.
- Zhao, Y. *et al.* (2014) 'Regulation of neurotropic signaling by the inducible, NF-kB-sensitive miRNA-125b in Alzheimer's disease (AD) and in primary human neuronal-glial (HNG) cells', *Molecular Neurobiology*, 50(1), pp. 97–106. doi: 10.1016/j.immuni.2010.12.017.Two-stage.
- Zhong, Y. *et al.* (2017) 'Nuclear export of misfolded SOD1 mediated by a normally buried NES-like sequence reduces proteotoxicity in the nucleus', *eLife*, 6, pp. 1–23. doi: 10.7554/eLife.23759.
- Zhou, H. *et al.* (2020) 'Proanthocyanidin promotes functional recovery of spinal cord injury via inhibiting ferroptosis.', *Journal of Chemical Neuroanatomy*. Netherlands, 107, p. 101807. doi: 10.1016/j.jchemneu.2020.101807.
- Zhou, Y., Gunput, R.-A. F. and Pasterkamp, R. J. (2008) 'Semaphorin signaling: progress made and promises ahead.', *Trends in Biochemical Sciences*. England, 33(4), pp. 161–170. doi: 10.1016/j.tibs.2008.01.006.
- Zhu, Y. *et al.* (2020) 'All-Trans Retinoic Acid Exerts Neuroprotective Effects in Amyotrophic Lateral Sclerosis-Like Tg (SOD1*G93A)1Gur Mice.', *Molecular Neurobiology*. United States, 57(8), pp. 3603–3615. doi: 10.1007/s12035-020-01973-8.
- Zinkie, S. *et al.* (2013) 'Expression of the protein chaperone, clusterin, in spinal cord cells constitutively and following cellular stress, and upregulation by treatment with Hsp90 inhibitor.', *Cell Stress & Chaperones*, 18(6), pp. 745–758. doi: 10.1007/s12192-013-0427-x.
- Zou, J. Y. and Crews, F. T. (2005) 'TNF alpha potentiates glutamate neurotoxicity by inhibiting

glutamate uptake in organotypic brain slice cultures: neuroprotection by NF kappa B inhibition.', *Brain Research*. Netherlands, 1034(1–2), pp. 11–24. doi: 10.1016/j.brainres.2004.11.014.

Zychowska, M. *et al.* (2016) 'Microglial Inhibition Influences XCL1/XCR1 Expression and Causes Analgesic Effects in a Mouse Model of Diabetic Neuropathy.', *Anesthesiology*. United States, 125(3), pp. 573–589. doi: 10.1097/ALN.0000000000001219.

Chapter 9 - Output from my PhD work: awards, communications, and publications

9.1 Awards

DiMeN Scholarship Award Flexible Funding, February 2020

Poster Prize at ENCALS, May 2019

DiMeN Scholarship Award Flexible Funding, April 2018

9.2 Communications at national and international scientific meetings

Platform presentation International Symposium on MND/ALS 2019: *“Antioxidant drugs reveal the potential for patient stratification in Motor Neurone Disease”* Perth, Australia, December 2019

Poster presentation: *“Antioxidant drugs reveal the potential for patient stratification in Motor Neurone Disease”* University of Sheffield Medical School Research Meeting, June 2019

Poster presentation: *“Antioxidant drugs reveal the potential for patient stratification in Motor Neurone Disease”* DiMeN Knowledge Exchange Forum, June 2019

Poster presentation ENCALS 2019: *“Antioxidant drugs reveal the potential for patient stratification in Motor Neurone Disease”* Tours, France, May 2019

Poster presentation International Symposium on MND/ALS 2018: *“Antioxidant drugs reveal the potential for patient stratification in Motor Neurone Disease”* Glasgow, UK, December 2018

Platform presentation: *“Moving towards personalised medicine in ALS using patient-derived astrocytes”* University of Sheffield Medical School Research Meeting, June 2018

Platform presentation: *“Moving towards personalised medicine in ALS using patient-derived astrocytes”* DiMeN Media and Impact Event/MRC Student Conference, May 2018

Selected for Research Snapshot: *“Moving towards personalised medicine in ALS using patient-derived astrocytes”* Sheffield Glia Symposium, November 2017

Platform presentation: *“Moving towards personalised medicine in ALS using patient-derived astrocytes”* North East Postgraduate Conference, Newcastle, October 2017

Poster presentation: *“Astrocytes driving the future of personalised medicine in ALS”* Sheffield Neuroscience Conference, July 2017

Poster presentation: “*Individual characterisation of the pathological features of ALS patient derived astrocytes*” University of Sheffield Medical School Research Meeting, June 2017

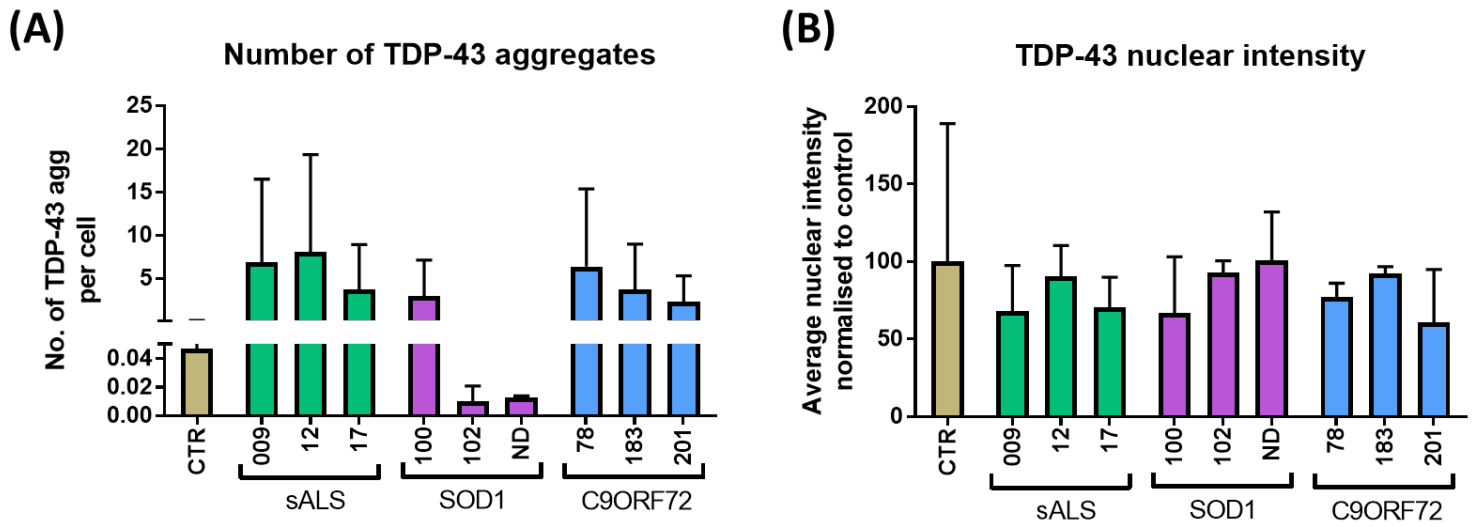
9.3 Publications

Adipose derived stem cells protect motor neurons and reduce glial activation in both in vitro and in vivo models of ALS. Yuri Ciervo, Noemi Gatto, **Chloe F Allen**, Andrew Grierson, Laura Ferraiuolo, Richard J Mead, Pamela J Shaw. *Molecular Neurodegeneration*, March 2021.

Astrocyte adenosine deaminase loss increases motor neuron toxicity in amyotrophic lateral sclerosis. Scott P Allen, Benjamin Hall, Lydia M Castelli, Laura Francis, Ryan Woof, Alexandros P Siskos, Eirini Kouloura, Elizabeth Gray, Alexander G Thompson, Kevin Talbot, Adrian Higginbottom, Monika Myszczyńska, **Chloe F Allen**, Matthew J Stopford, Jordan Hemingway, Claudia S Bauer, Christopher P Webster, Kurt J De Vos, Martin R Turner, Hector C Keun, Guillaume M Hautbergue, Laura Ferraiuolo, Pamela J Shaw. *Brain*, March 2019.

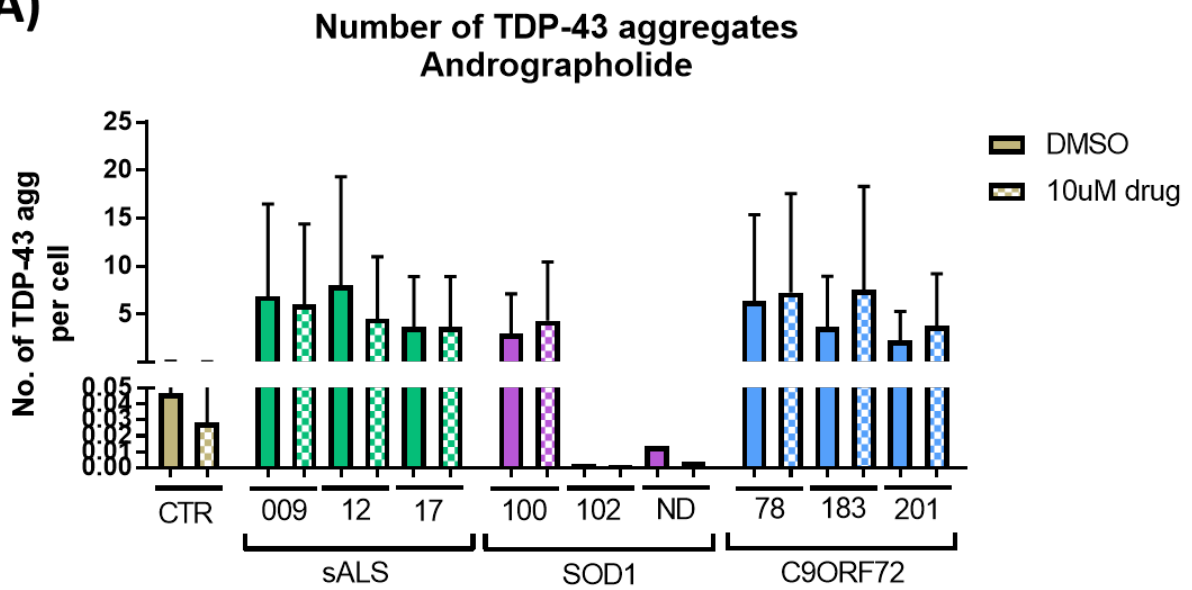
Can Astrocytes Be a Target for Precision Medicine? **Chloe F Allen**, Pamela J Shaw, Laura Ferraiuolo. *Advances in Experimental Medicine and Biology*, August 2017.

Chapter 10 - Appendix

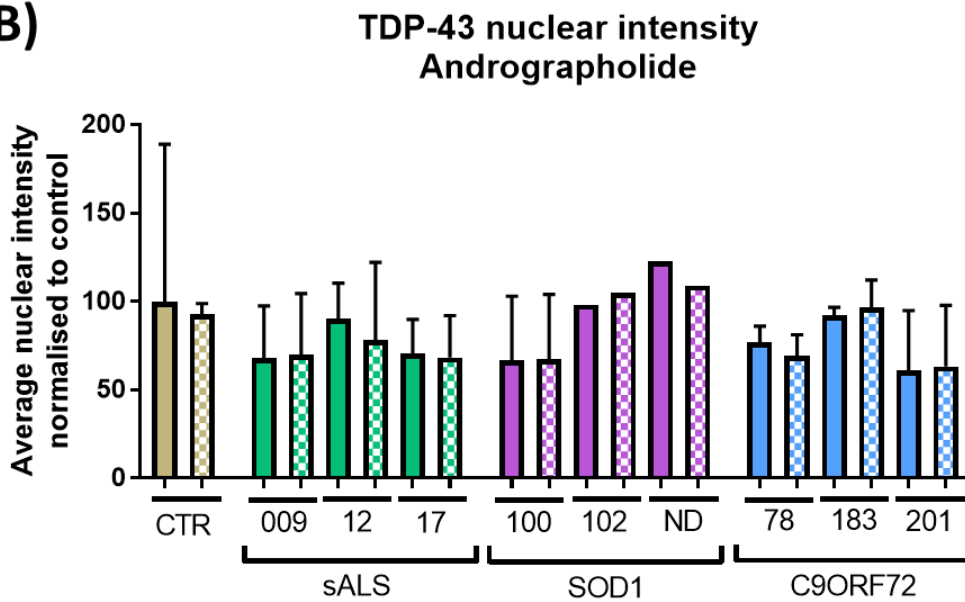


Supplementary 3.1 TDP-43 localisation and protein expression in control and patient *iAstrocytes*. (A). Columbus analysis relative to the number of TDP-43 aggregates per cell and (B). The average TDP-43 nuclear intensity (mean \pm SD, $n=2$, technical repeats = 2).

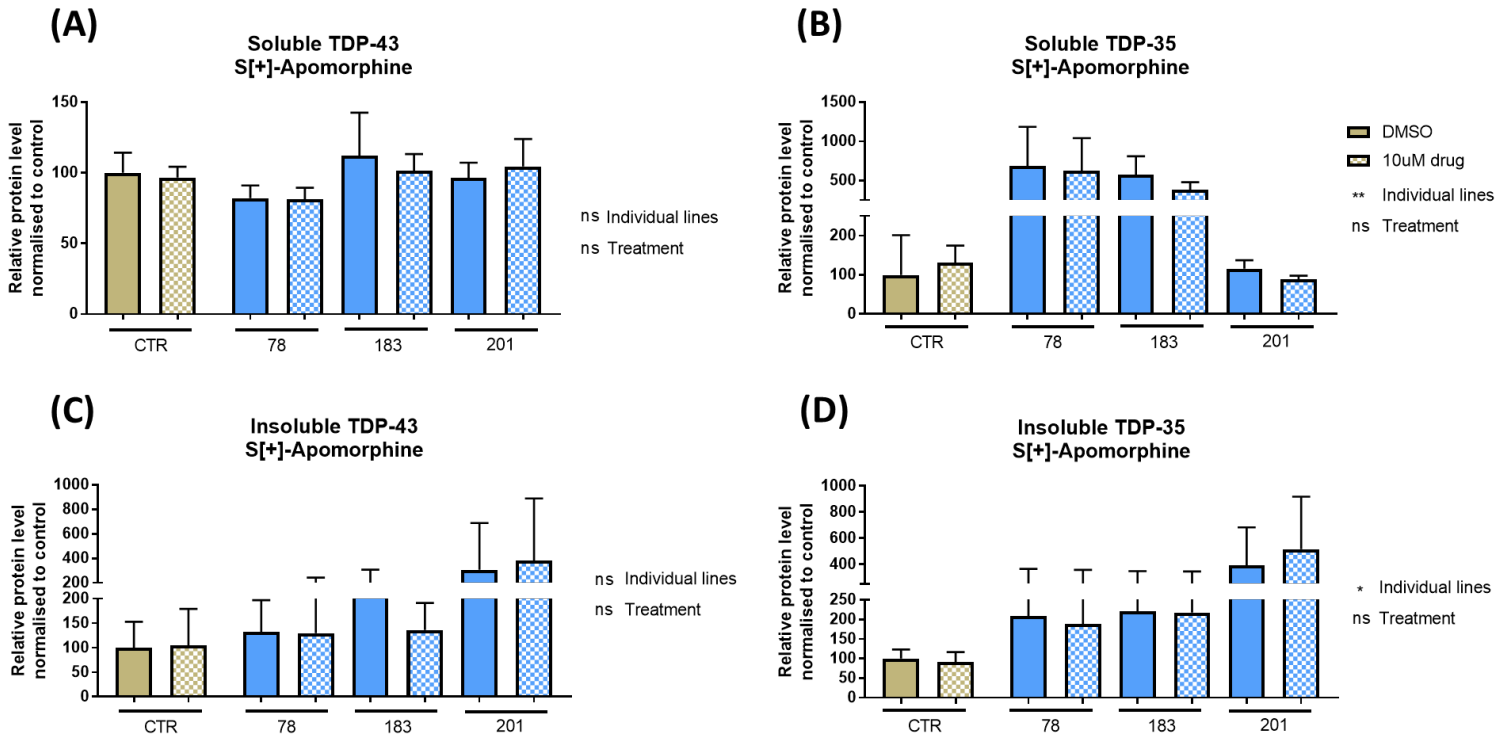
(A)



(B)

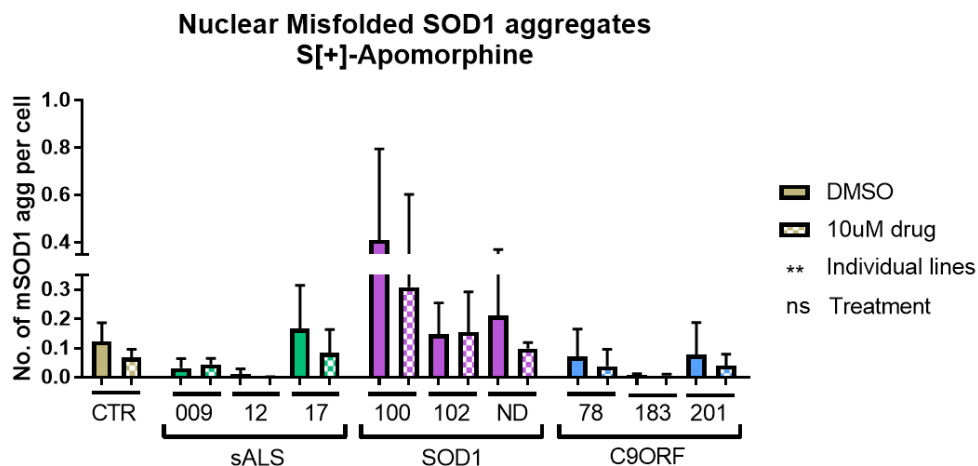


Supplementary 4.1 TDP-43 localisation in control and patient iAstrocytes before and after andrographolide treatment. Columbus analysis of TDP-43 immunocytochemistry (mean \pm SD, $n=1-2$, technical repeats = 2) of (A). The number of TDP-43 aggregates per cell and (B). The average TDP-43 nuclear intensity.

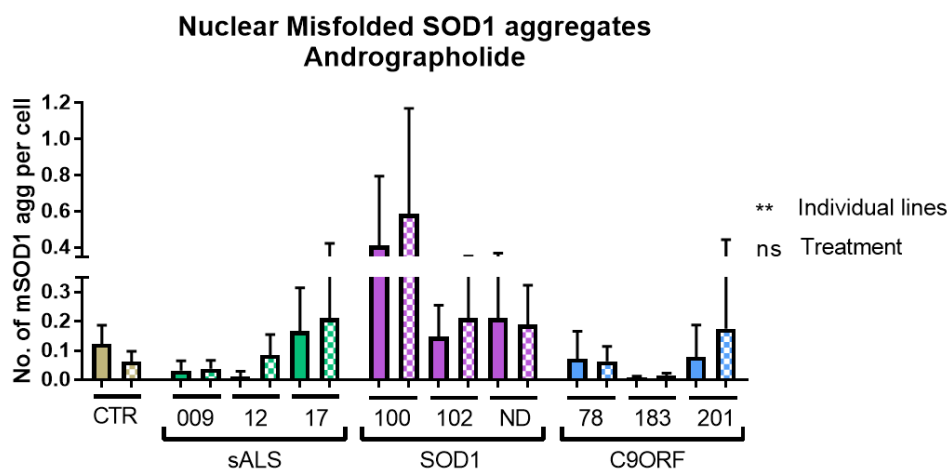


Supplementary 4.2 Quantification of soluble and insoluble TDP-43/TDP-35 protein in control and C9ORF72 iAstrocytes before and after S[+]-apomorphine treatment. (A). Soluble TDP-43 protein level (mean \pm SD, two-way ANOVA, MC, $n=3$, Row Factor $p=0.7923$, Column Factor $p=0.0709$). (B). Soluble TDP-35 protein level (mean \pm SD, two-way ANOVA, MC, $n=3$, Row Factor $p=0.5407$, Column Factor $p<0.01$). (C). Insoluble TDP-43 protein level (mean \pm SD, two-way ANOVA, MC, $n=3$, Row Factor $p=0.9793$, Column Factor $p=0.3192$). (D). Insoluble TDP-35 protein level (mean \pm SD, two-way ANOVA, MC, $n=3$, Row Factor $p=0.7795$, Column Factor $p<0.05$). The control bar consists of 3050, 155 & AG pooled together.

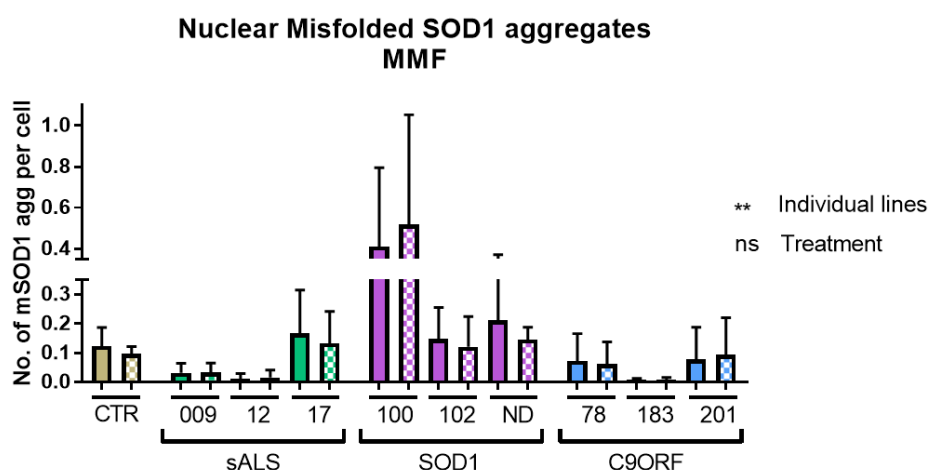
(A)



(B)



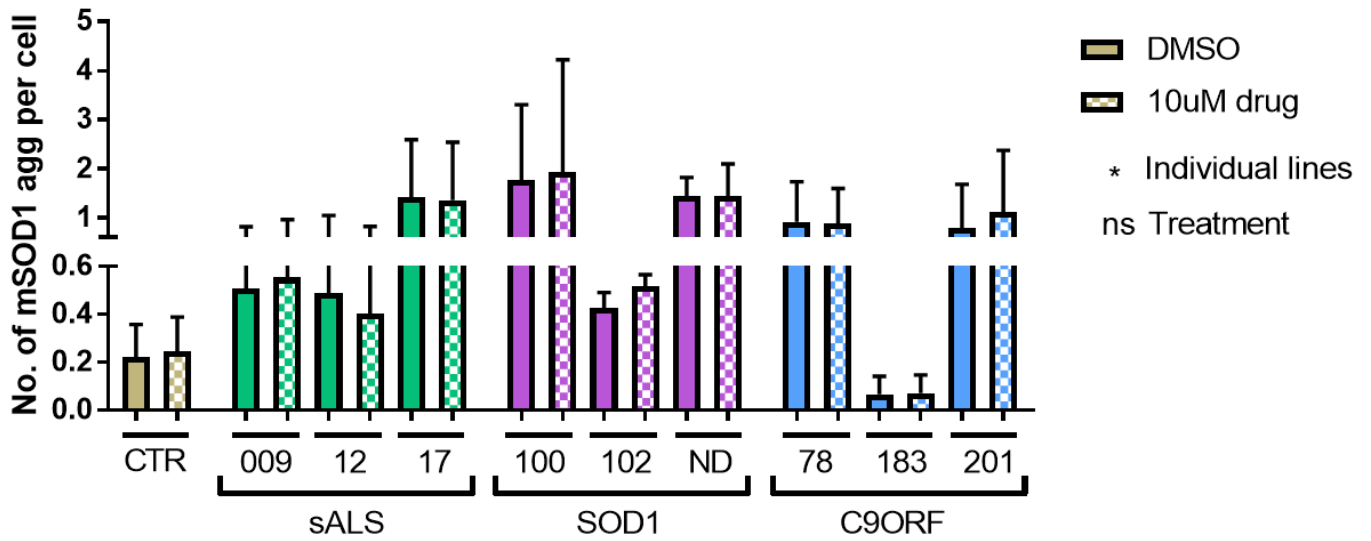
(C)



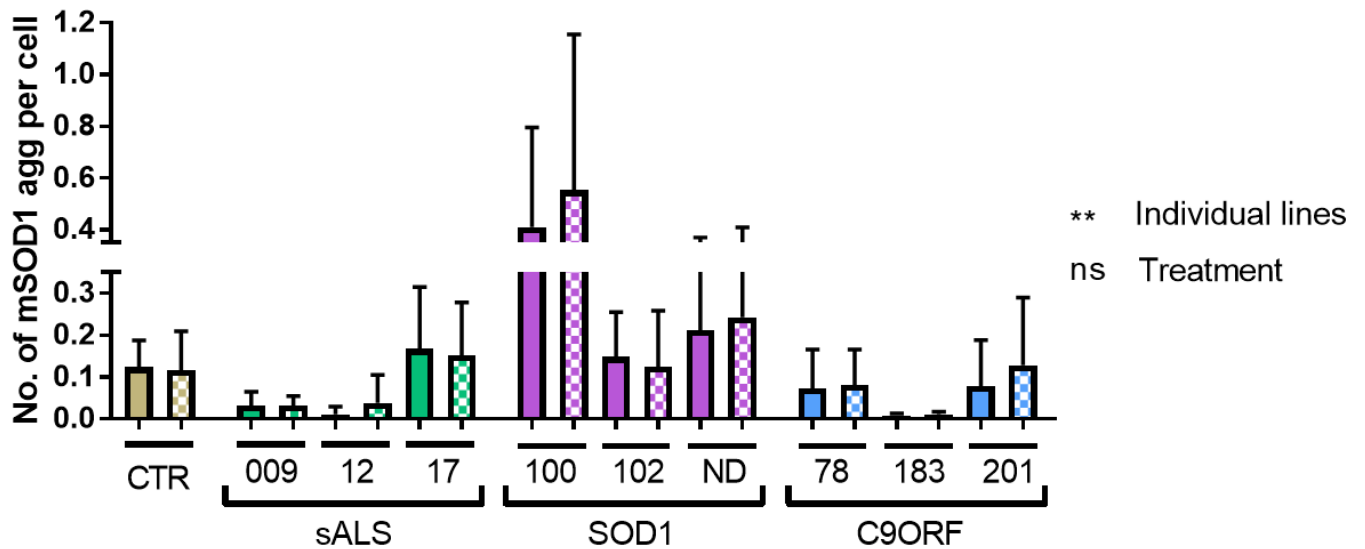
Supplementary 4.3 Quantification of misSOD1 aggregates in the nuclear region of iAstrocytes before and after drug treatment. The number of nuclear aggregates per cell after treatment with (A). S[+]-apomorphine (mean \pm SD, two-way ANOVA, MC, $n=3$, technical repeats = 2, Row Factor $p=0.2345$, Column Factor $p<0.01$), (B). Andrographolide (mean \pm SD, two-way ANOVA, MC, $n=3$, technical repeats = 2, Row Factor $p=0.4552$, Column Factor $p<0.01$) and (C). MMF (mean \pm SD, two-way ANOVA, MC, $n=3$, technical repeats = 2, Row Factor $p=0.9414$, Column Factor $p<0.01$). The control bar consists of 3050, 155 & AG pooled together.

(A)

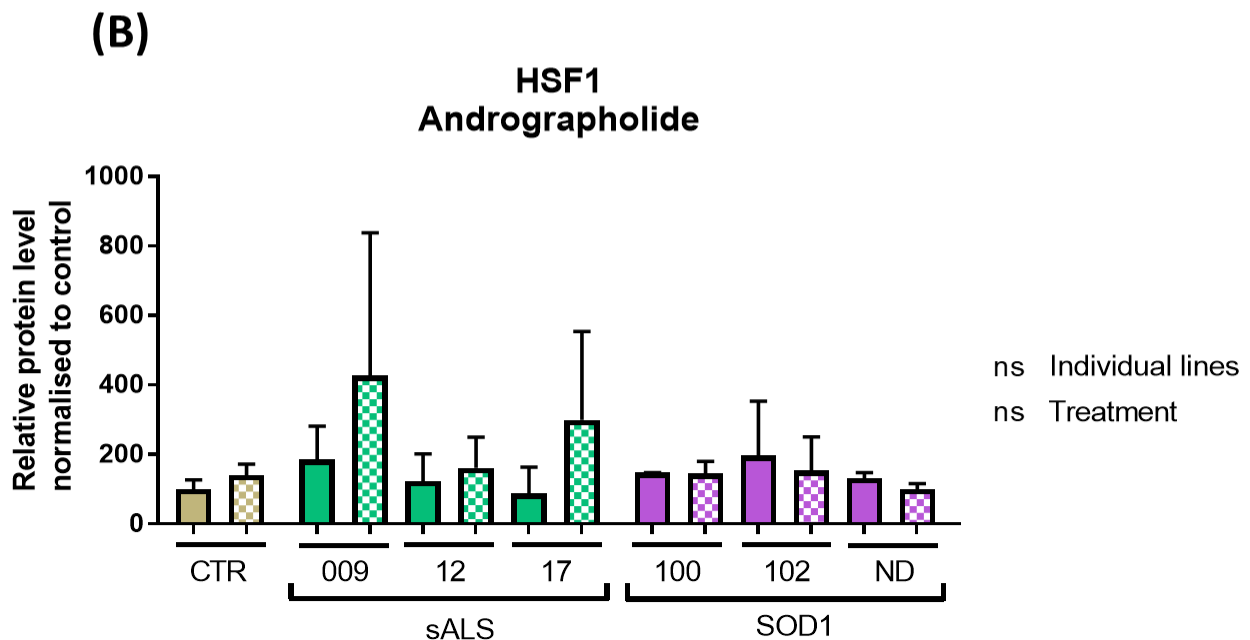
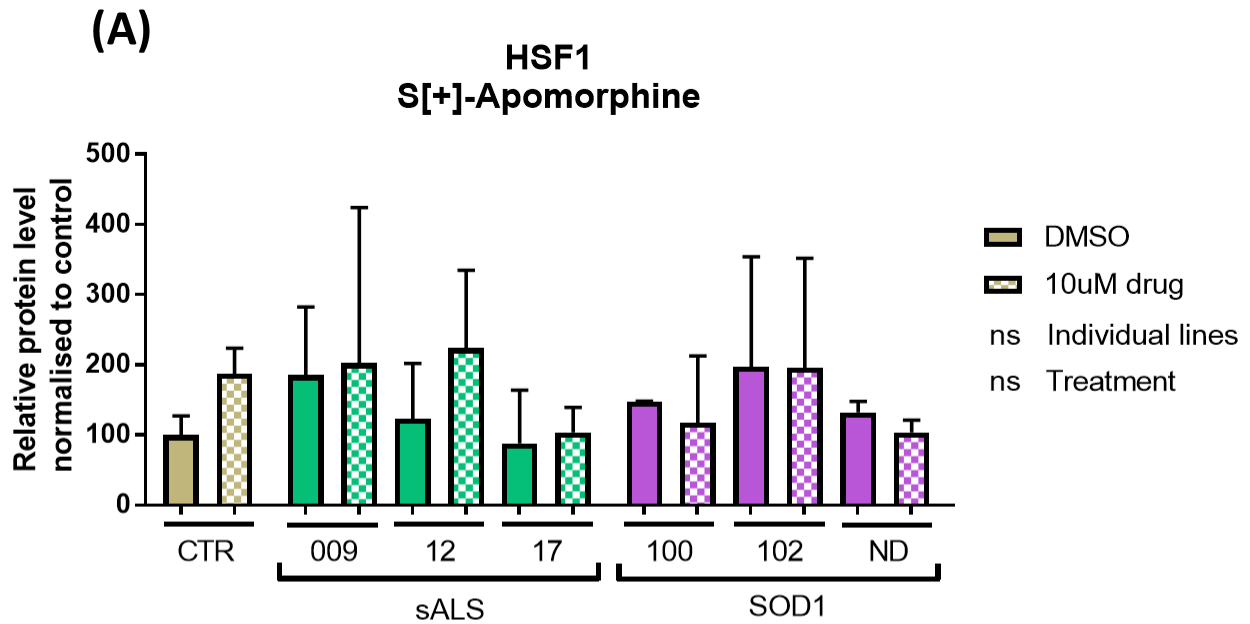
**Perinuclear Misfolded SOD1 aggregates
Riluzole**

**(B)**

**Nuclear Misfolded SOD1 aggregates
Riluzole**

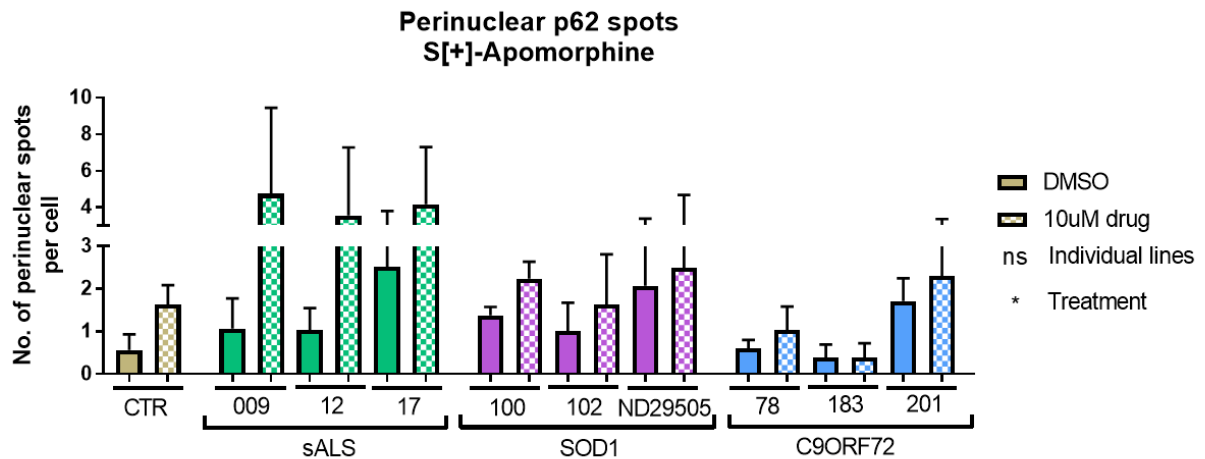


Supplementary 4.4 Quantification of misSOD1 aggregates in the nuclear and perinuclear region of *iAstrocytes* before and after riluzole treatment. (A). The number of perinuclear aggregates per cell (mean \pm SD, two-way ANOVA, MC, $n=3$, technical repeats = 2, Row Factor $p=0.8298$, Column Factor $p<0.05$). (B). The number of nuclear aggregates per cell (mean \pm SD, two-way ANOVA, MC, $n=3$, technical repeats = 2, Row Factor $p=0.6590$, Column Factor $p<0.01$). The control bar consists of 3050, 155 & AG pooled together.

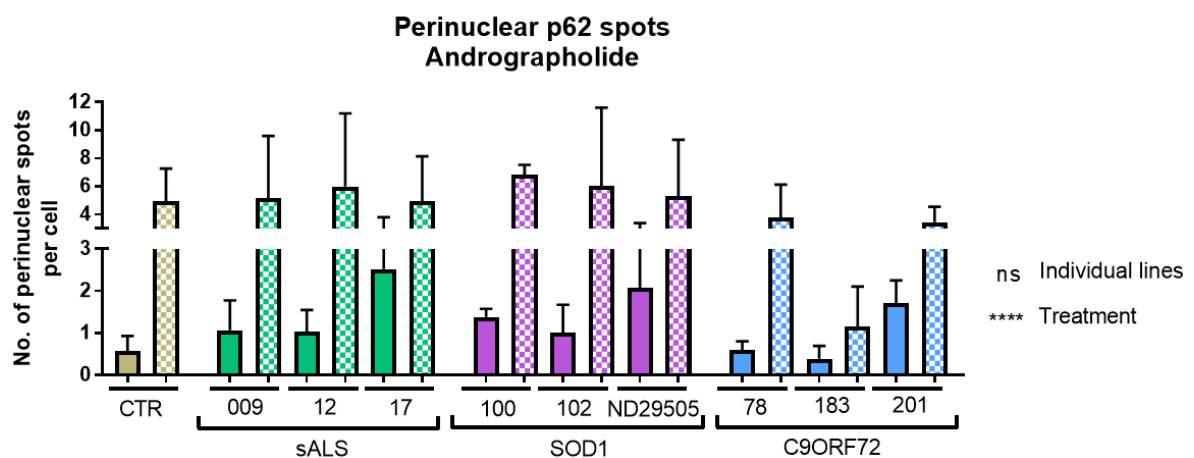


Supplementary 4.5 Quantification of HSF1 in control, sALS and SOD1 iAstrocytes before and after drug treatment. HSF1 protein level after treatment with (A). S[+]-apomorphine (mean \pm SD, two-way ANOVA, MC, $n=3$, Row Factor $p=0.4768$, Column Factor $p=0.5345$), and (B). Andrographolide (mean \pm SD, two-way ANOVA, MC, $n=3$, Row Factor $p=0.1614$, Column Factor $p=0.3377$). The control bar consists of 3050, 155 & AG pooled together.

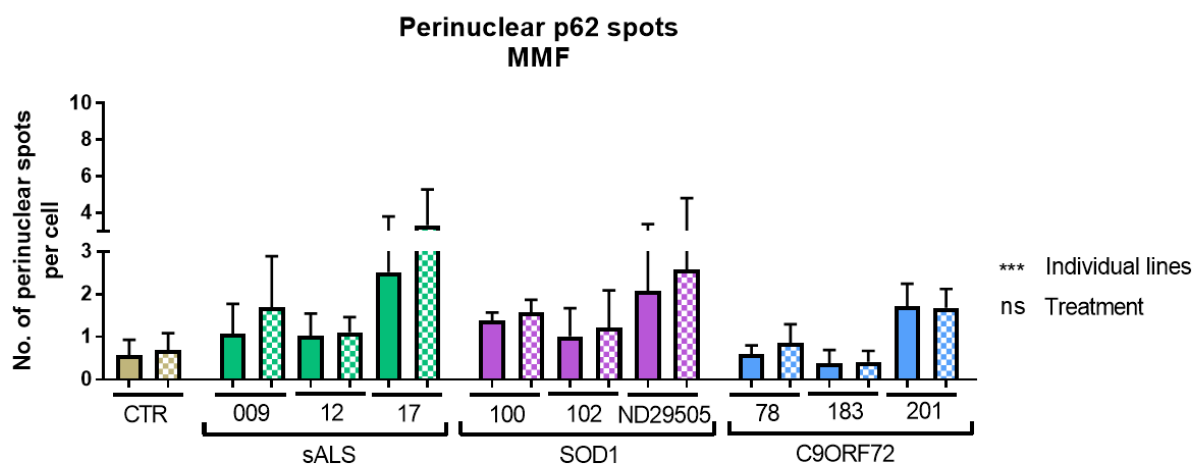
(A)



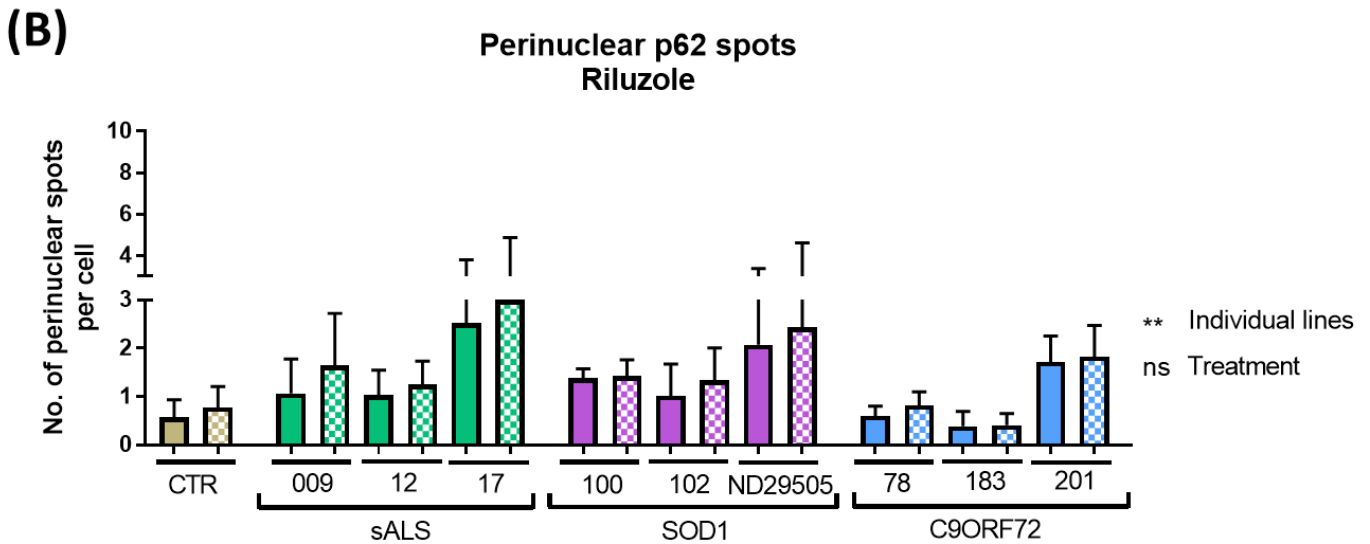
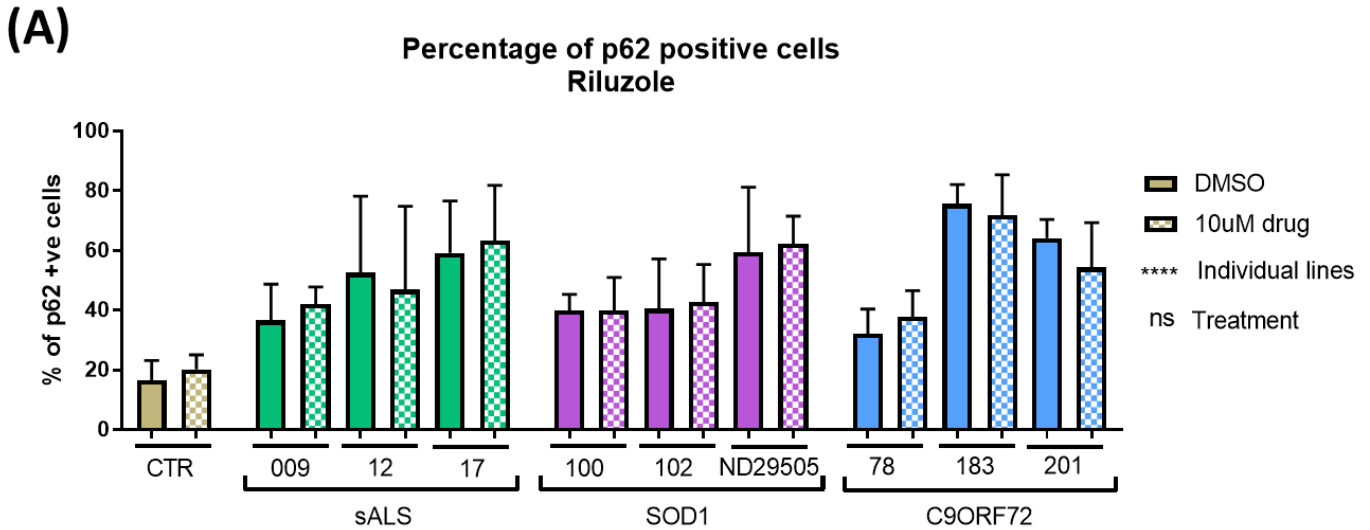
(B)



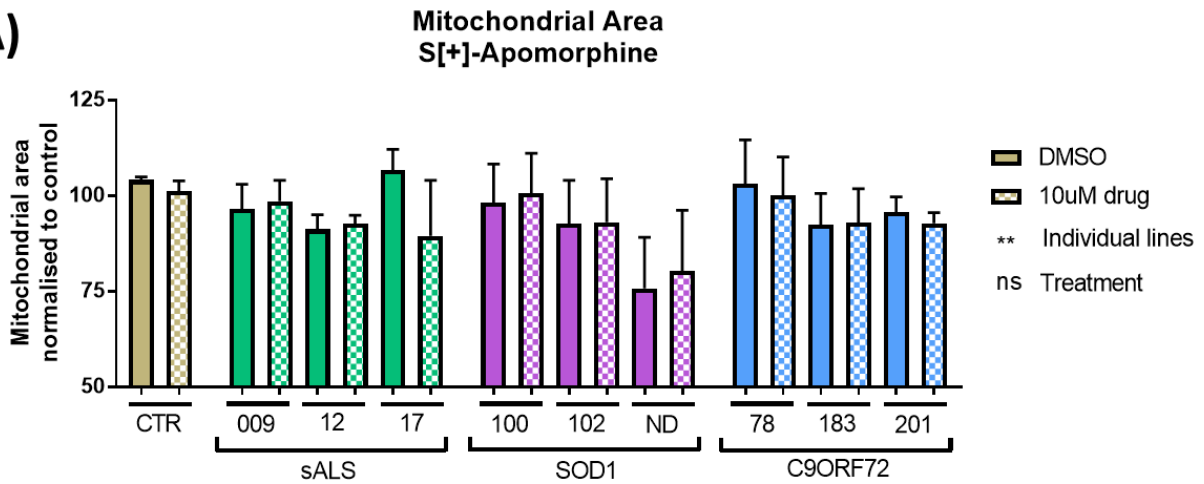
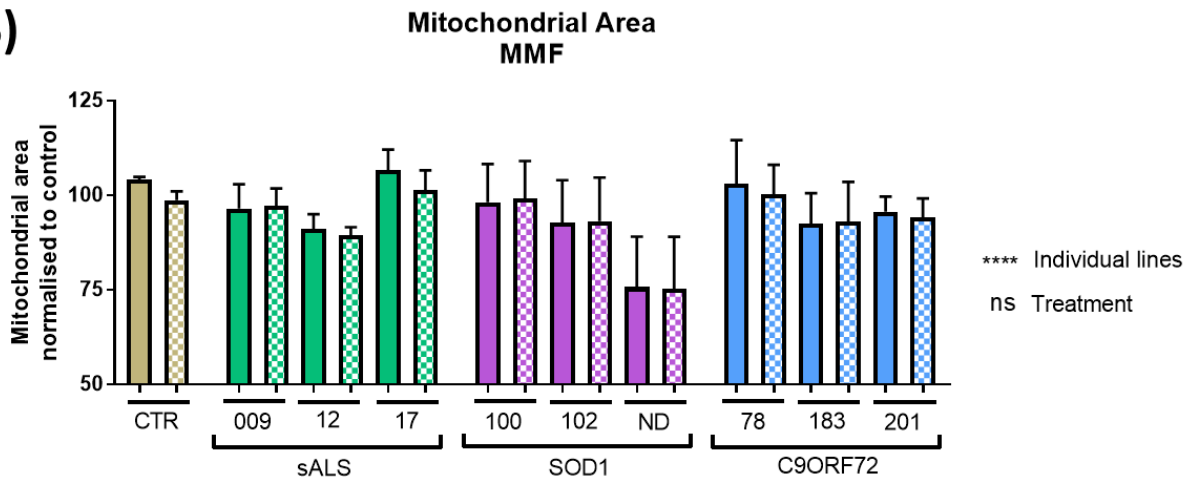
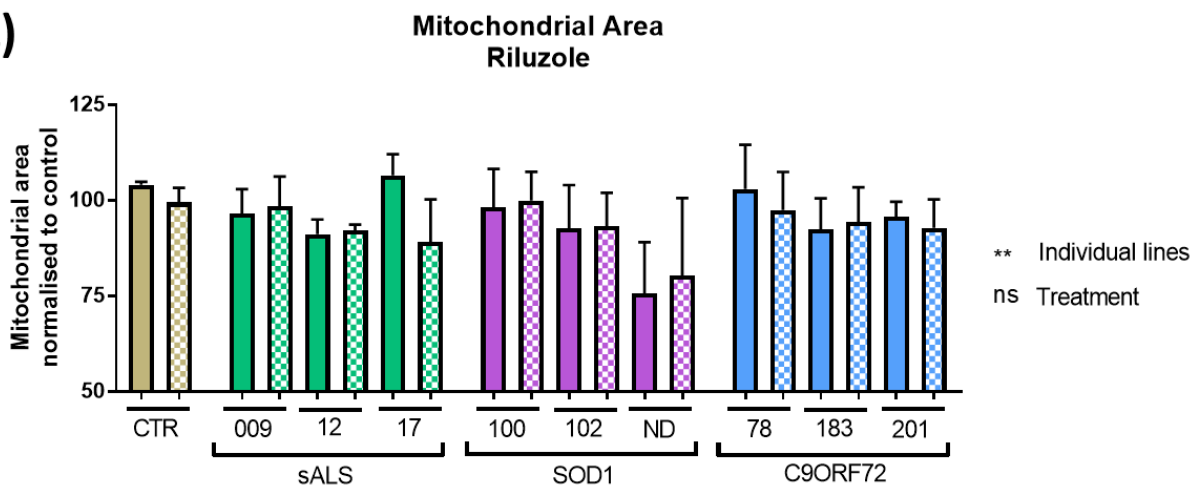
(C)



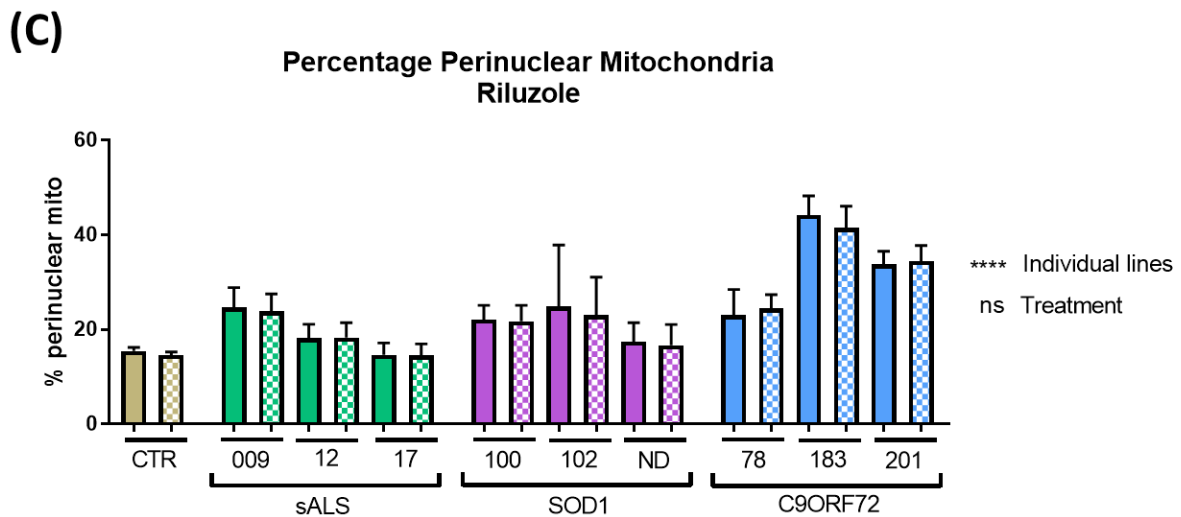
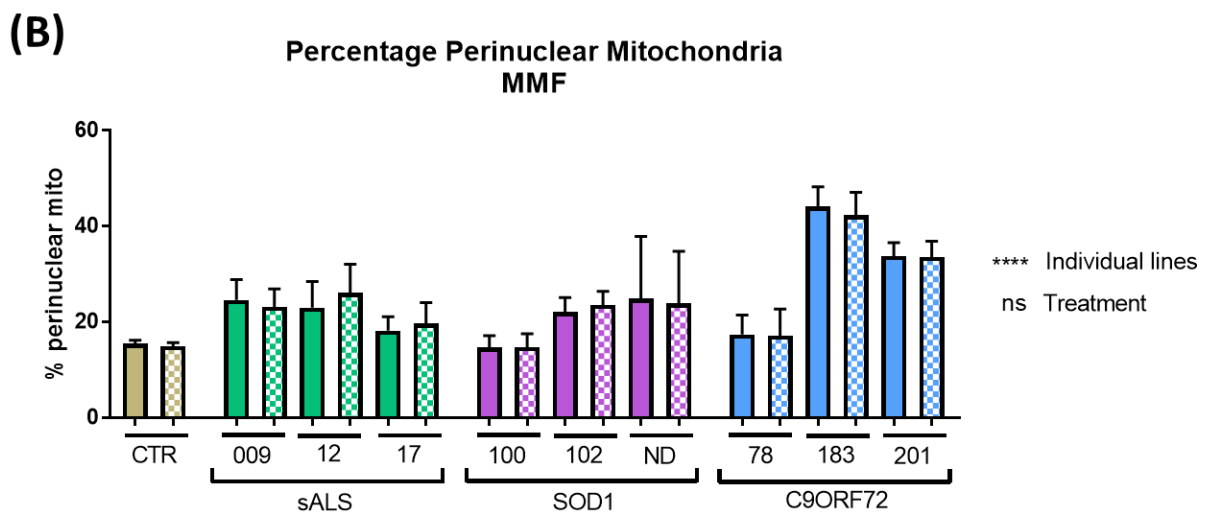
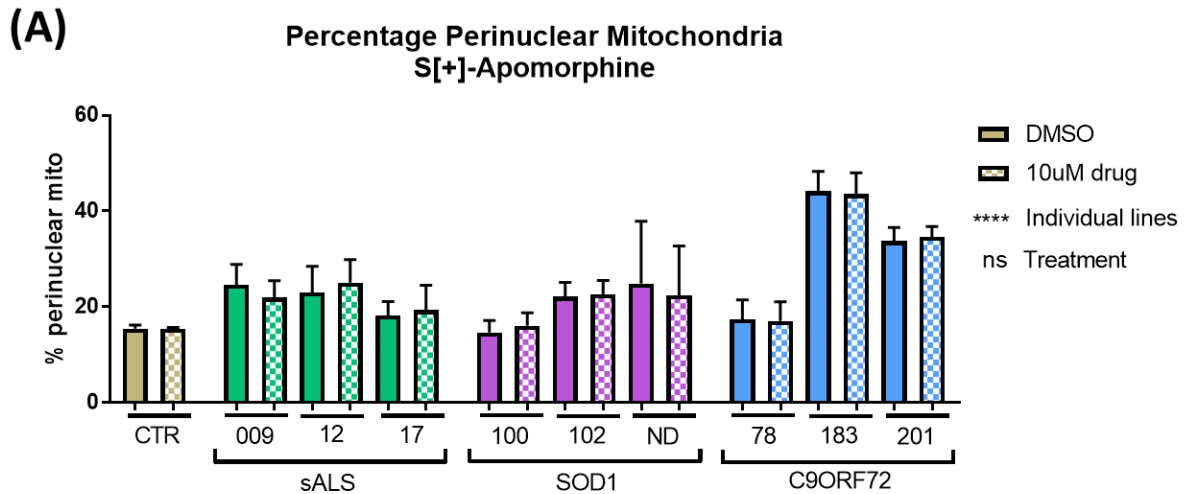
Supplementary 4.6 Quantification of p62 expression in the perinuclear region of control and patient *i*Astrocytes before and after drug treatment. The number of perinuclear spots after treatment with (A). S[+]-apomorphine (mean \pm SD, two-way ANOVA, MC, $n=3$, technical repeats = 2, Row Factor $p<0.05$, Column Factor $p=0.1104$), (B). Andrographolide (mean \pm SD, two-way ANOVA, MC, $n=3$, technical repeats = 2, Row Factor $p<0.0001$, Column Factor $p=0.5064$), and (C). MMF (mean \pm SD, two-way ANOVA, MC, $n=3$, technical repeats = 2, Row Factor $p=0.2456$, Column Factor $p<0.001$). The control bar consists of 3050 & 155 pooled together.



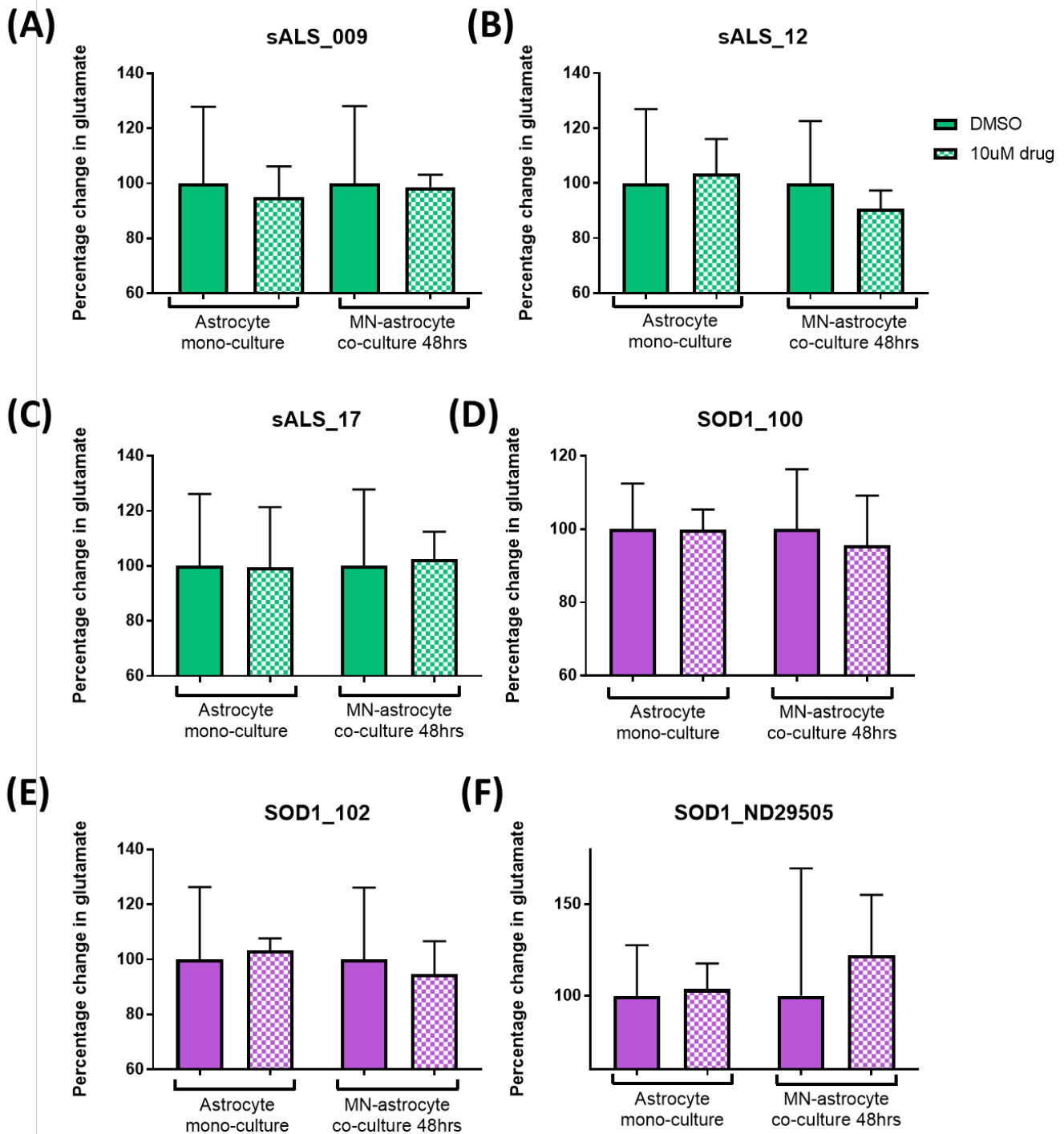
Supplementary 4.7 Quantification of p62 expression in the cytoplasm of control and patient *iAstrocytes* before and after Riluzole treatment. (A). The percentage of p62-positive cells (mean \pm SD, two-way ANOVA, MC, $n=3$, technical repeats = 2, Row Factor $p=0.8922$, Column Factor $p<0.001$). (B). The number of perinuclear spots (mean \pm SD, two-way ANOVA, MC, $n=3$, technical repeats = 2, Row Factor $p=0.2791$, Column Factor $p<0.01$). The control bar consists of 3050 & 155 pooled together.

(A)**(B)****(C)**

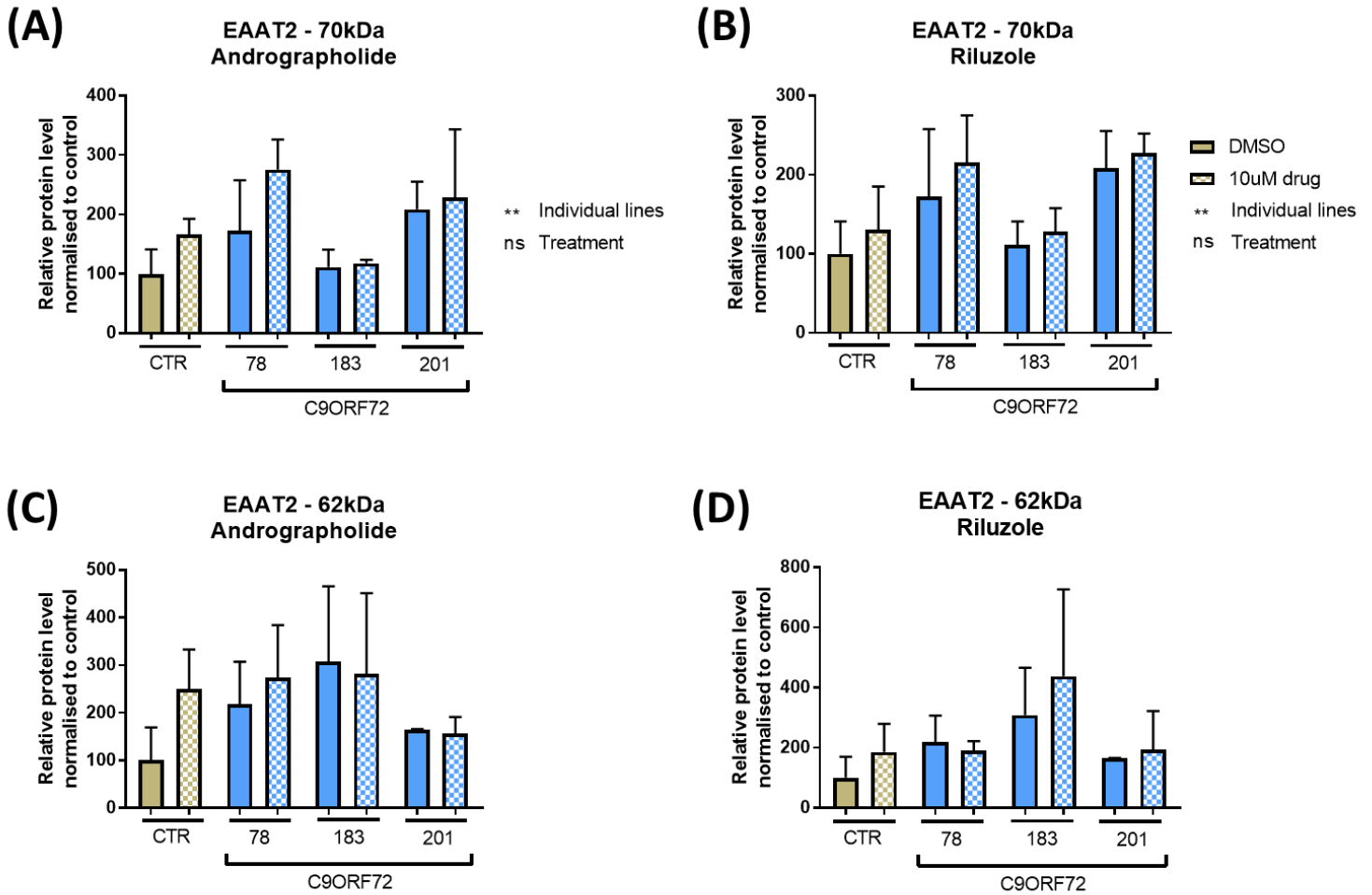
Supplementary 4.8 Quantification of mitochondrial area in control and patient iAstrocytes before and after treatment with (A). S[+]-apomorphine (mean \pm SD, two-way ANOVA, MC, $n=3$, technical repeats = 3, Row Factor $p=0.5343$, Column Factor $p<0.01$), (B). MMF (mean \pm SD, two-way ANOVA, MC, $n=3$, technical repeats = 3, Row Factor $p=0.5117$, Column Factor $p<0.0001$), and (C). Riluzole (mean \pm SD, two-way ANOVA, MC, $n=3$, technical repeats = 3, Row Factor $p=0.4373$, Column Factor $p<0.01$). The control bar consists of 3050, 155 & 209 pooled together.



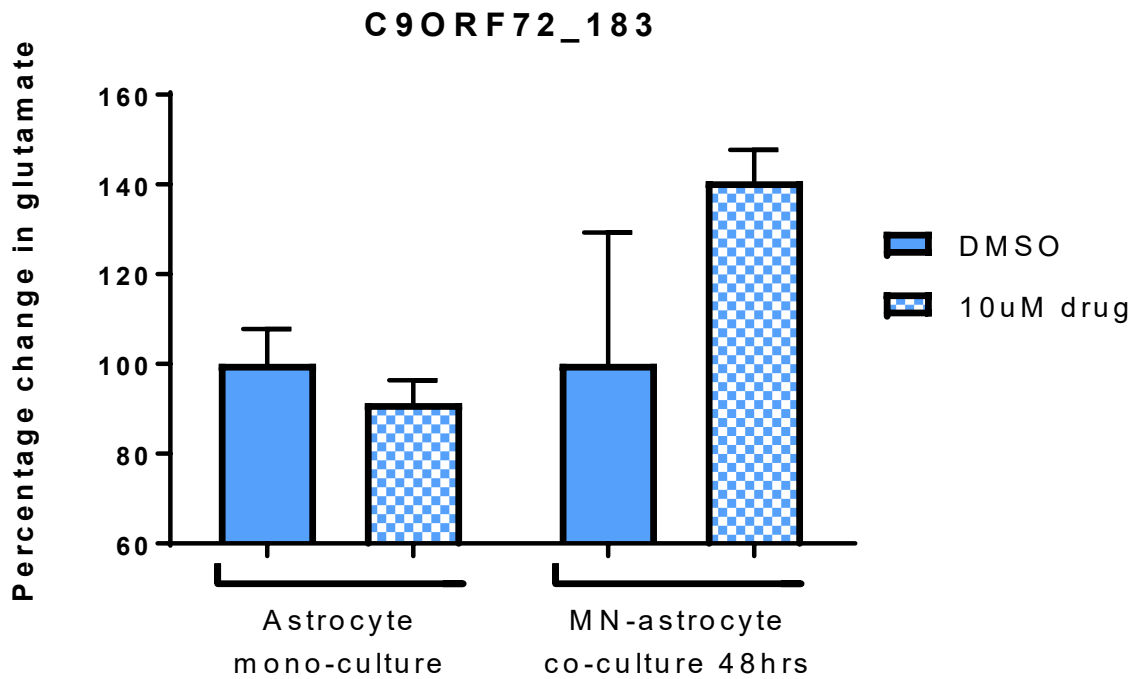
Supplementary 4.9 Quantification of the percentage of perinuclear mitochondria in control and patient *iAstrocytes* before and treatment with (A). S[+]-apomorphine (mean \pm SD, two-way ANOVA, MC, $n=3$, technical repeats = 3, Row Factor $p=0.9886$, Column Factor $p<0.0001$), (B). MMF (mean \pm SD, two-way ANOVA, MC, $n=3$, technical repeats = 3, Row Factor $p=0.9486$, Column Factor $p<0.0001$), and (C). Riluzole (mean \pm SD, two-way ANOVA, MC, $n=3$, technical repeats = 3, Row Factor $p=0.6795$, Column Factor $p<0.0001$). The control bar consists of 3050, 155 & 209 pooled together.



Supplementary 4.10 Quantification of extracellular glutamate in *i*Astrocyte-conditioned media before and after riluzole treatment. The percentage change in glutamate in (A). SALS 009 (mean \pm SD, paired *t*-test, *n*=3, technical repeats = 2, mono-culture *p*=0.7018, co-culture *p*=0.9370), (B). SALS 12 (mean \pm SD, paired *t*-test, *n*=3, technical repeats = 2, mono-culture *p*=0.8189, co-culture *p*=0.4279), (C). SALS 17 (mean \pm SD, paired *t*-test, *n*=3, technical repeats = 2, mono-culture *p*=0.9875, co-culture *p*=0.8923), (D). SOD1 100 (mean \pm SD, paired *t*-test, *n*=3, technical repeats = 2, mono-culture *p*=0.9884, co-culture *p*=0.5744), (E). SOD1 102 (mean \pm SD, paired *t*-test, *n*=3, technical repeats = 2, mono-culture *p*=0.8646, co-culture *p*=0.7306), and (F). SOD1 ND29505 (mean \pm SD, paired *t*-test, *n*=3, technical repeats = 2, mono-culture *p*=0.7489, co-culture *p*=0.7426). The control bar consists of 3050 & 155 pooled together.



Supplementary 4.11 Quantification of EAAT2 protein levels in control and C9ORF72 iAstrocytes before and after drug treatment. EAAT2 70kDa protein levels after treatment with (A). Andrographolide (mean \pm SD, two-way ANOVA, MC, $n=3$, Row Factor $p=0.0612$, Column Factor $p<0.01$), and (B). Riluzole (mean \pm SD, two-way ANOVA, MC, $n=3$, Row Factor $p=0.1997$, Column Factor $p<0.01$). Control bar consists of 3050, 155 & AG pooled together. EAAT2 62kDa protein levels after treatment with (C). Andrographolide and (D). Riluzole (mean \pm SD, $n=2$). The control bar consists of 155 & AG pooled together.



Supplementary 4.12 Quantification of extracellular glutamate in *i*Astrocyte-conditioned media before and after andrographolide treatment. The percentage change in glutamate (mean \pm SD, paired *t*-test, $n=3$, technical repeats = 2, mono-culture $p=0.3450$, co-culture $p=0.3582$).

Supplementary Table 5.1 Nanodrop quantifications of RNA samples before GRASPS purification

Sample Name	Concentration (ng/ μ l)	260/280 ratio	260/230 ratio
3050 U	725.53	2.05	2.17
3050 S	692.19	2.06	2.20
3050 A	589.59	2.05	2.15
3050 R	803.76	2.03	1.97
155 U	693.35	2.09	2.23
155 S	685.15	2.09	2.20
155 A	694.17	2.05	2.16
155 R	793.67	2.05	2.13
AG08620 U	2207.22	1.99	2.02
AG08620 S	1148.57	2.04	2.21
AG08620 A	1165.89	2.06	2.23
AG08620 R	874.46	2.02	2.21
009 U	659.31	2.05	2.24
009 S	693.10	2.07	2.23
009 A	554.53	2.10	2.17
009 R	597.31	2.07	2.22
12 U	2888.48	1.95	2.10
12 S	3438.67	1.79	1.92
12 A	3674.81	1.63	1.77
12 R	3516.16	1.61	1.82
17 U	406.47	1.99	1.96
17 S	480.95	1.99	2.02
17 A	454.70	2.00	1.92
17 R	357.04	2.02	2.04
78 U	1093.51	2.06	2.25
78 S	1769.26	2.01	2.20
78 A	2467.06	2.00	2.14
78 R	2180.47	1.99	2.07
183 U	1111.15	2.08	2.26
183 S	681.09	2.09	2.26
183 A	332.14	2.08	2.15
183 R	524.71	2.12	2.27
201 U	1163.35	2.05	2.20
201 S	1391.71	2.06	2.04
201 A	624.70	2.06	2.21
201 R	688.15	2.03	2.17
100 U	1212.50	2.07	2.20
100 S	661.07	2.03	1.82
100 A	466.45	2.05	2.17
100 R	500.52	2.08	2.14
102 U	1041.56	2.04	2.20
102 S	905.36	2.07	2.15
102 A	1039.09	2.07	2.18
102 R	672.18	2.06	2.15
ND29505 U	476.44	2.06	2.14
ND29505 S	374.08	2.04	2.08
ND29505 A	315.33	2.02	2.08
ND29505 R	365.04	2.03	2.09

Supplementary Table 5.2 Nanodrop quantifications of RNA samples sent for sequencing

Sample Name	Concentration (ng/ μ l)	260/280 ratio	260/230 ratio
3050 U	8.21	1.58	0.50
3050 S	8.92	2.54	0.86
3050 A	8.57	1.97	0.38
3050 R	9.16	2.35	0.65
155 U	25.30	1.88	1.01
155 S	39.04	1.76	0.90
155 A	32.86	1.69	0.98
155 R	31.37	1.64	0.93
AG08620 U	7.17	2.84	1.79
AG08620 S	13.47	1.92	1.18
AG08620 A	6.66	2.01	0.88
AG08620 R	11.34	2.85	0.94
009 U	10.26	1.35	0.69
009 S	17.34	1.11	0.76
009 A	8.04	1.17	0.56
009 R	9.93	1.28	1.24
12 U	13.20	1.30	-2.52
12 S	13.26	1.18	-2.81
12 A	14.19	1.77	-17.32
12 R	12.81	1.57	-1.32
17 U	6.33	1.01	1.87
17 S	7.35	1.31	0.67
17 A	5.58	3.01	1.45
17 R	7.41	0.98	0.29
78 U	9.78	6.89	1.00
78 S	21.27	5.74	1.54
78 A	19.17	3.41	1.17
78 R	18.90	2.26	0.49
183 S	39.71	1.74	0.83
183 A	15.95	1.32	0.62
183 R	5.49	2.55	0.92
201 U	6.60	3.27	0.83
201 S	10.17	1.86	0.29
201 A	4.40	2.27	0.80
201 R	5.40	1.93	1.00
100 U	19.26	4.18	0.60
100 S	6.63	1.32	0.97
100 A	12.09	1.56	0.66
100 R	7.32	0.95	0.76
102 U	11.31	1.11	1.25
102 S	17.34	0.94	0.62
102 A	9.00	1.51	1.24
102 R	11.49	0.97	1.58
ND29505 U	5.81	8.66	1.03
ND29505 S	4.68	3.32	0.47
ND29505 A	2.38	0.62	0.18
ND29505 R	2.85	4.35	0.22

Supplementary Table 5.3 List of GO pathways for C9ORF72 iAstrocytes at baseline

GO Pathway	Gene Count	p-value	Benjamini
Cell adhesion	71	1.40E-09	5.50E-06
Extracellular matrix organisation	39	1.60E-08	3.10E-05
Inflammatory response	57	1.90E-07	2.40E-04
Heterophilic cell-cell adhesion via plasma membrane cell adhesion molecules	16	1.30E-06	1.30E-03
Calcium ion transmembrane transport	25	3.30E-06	2.60E-03
Angiogenesis	37	3.80E-06	2.50E-03
Cell surface receptor signalling pathway	42	5.80E-06	3.30E-03
Axon guidance	29	8.30E-06	4.10E-03
Homophilic cell adhesion via plasma membrane adhesion molecules	28	2.10E-05	9.20E-03
Sensory perception of sound	25	2.40E-05	9.40E-03
Nervous system development	41	4.10E-05	1.50E-02
Signal transduction	119	6.30E-05	2.10E-02
Cell-cell signalling	37	6.80E-05	2.10E-02
Single organismal cell-cell adhesion	20	9.20E-05	2.60E-02
Regulation of ion transmembrane transport	21	1.10E-04	2.90E-02
Regulation of calcium ion-dependent exocytosis	11	1.20E-04	3.00E-02
Cellular response to lipopolysaccharide	21	1.50E-04	3.30E-02
Neuropeptide signalling pathway	19	2.80E-04	-
Calcium ion-regulated exocytosis of neurotransmitter	11	3.30E-04	-
Potassium ion transmembrane transport	21	3.80E-04	-
Positive regulation of pathway-restricted SMAD protein phosphorylation	12	4.80E-04	-
Regulation of MAPK cascade	11	5.10E-04	-
Chemical synaptic transmission	33	5.10E-04	-
Positive regulation of cell proliferation	54	5.80E-04	-
Cell recognition	8	6.30E-04	-
Skeletal system development	22	7.60E-04	-
Protein domain specific binding	5	7.80E-04	-
Neural crest cell migration	11	1.10E-03	-
Cell fate commitment	11	1.30E-03	-
Negative regulation of angiogenesis	13	1.30E-03	-
T cell chemotaxis	5	1.50E-03	-
Mesenchymal to epithelial transition	5	1.50E-03	-
Prepulse inhibition	6	1.50E-03	-
Wound healing	15	1.50E-03	-
Cell chemotaxis	13	2.10E-03	-
Cellular response to tumour necrosis factor	18	2.10E-03	-
Decidualisation	7	2.20E-03	-
Skin development	9	2.30E-03	-
Negative chemotaxis	9	2.30E-03	-
Sensory perception of light stimulus	5	2.50E-03	-
Vesicle fusion	12	2.90E-03	-
Positive regulation of nitric oxide biosynthetic process	10	3.00E-03	-
Positive regulation of vascular smooth muscle cell proliferation	6	3.10E-03	-
Positive regulation of cell migration	25	3.30E-03	-

Otic vesicle development	4	3.30E-03	-
DNA-binding transcription factor activity	11	3.50E-03	-
Negative regulation of smooth muscle cell proliferation	8	3.70E-03	-
Ventricular trabecula myocardium morphogenesis	6	4.20E-03	-
Antigen processing and presentation	11	5.30E-03	-
Potassium ion transport	14	5.40E-03	-
Behavioural response to pain	5	5.80E-03	-
Anatomical structure morphogenesis	15	5.80E-03	-
Synaptic transmission, glutamatergic	7	5.90E-03	-
Regulation of cardiac conduction	11	6.00E-03	-
Somatic stem cell population maintenance	12	6.20E-03	-
Cell differentiation	49	6.20E-03	-
Regulation of cytosolic calcium ion concentration	8	6.60E-03	-
Cell development	9	6.70E-03	-
Male gonad development	15	7.00E-03	-
Pharyngeal system development	6	7.40E-03	-
Toll-like receptor 4 signalling pathway	6	7.40E-03	-
Keratinisation	14	7.40E-03	-
Cellular response to transforming growth factor beta stimulus	10	7.40E-03	-
Matrix metalloproteinase activity	13	7.70E-03	-
BMP signalling pathway	13	7.70E-03	-
Regulation of heart rate	8	7.90E-03	-
Semaphorin-plexin signalling pathway	8	7.90E-03	-
Positive regulation of angiogenesis	17	8.00E-03	-
Kidney development	14	8.10E-03	-
Positive regulation of renal sodium excretion	5	8.20E-03	-
Cellular response to thyroid hormone stimulus	5	8.20E-03	-
Negative regulation of axon extension involved in axon guidance	7	9.00E-03	-
Neurogenesis	9	9.10E-03	-
Photoreceptor cell maintenance	8	9.40E-03	-
Parathyroid gland development	4	1.00E-02	-
Cellular response to alkaloid	4	1.00E-02	-
Positive regulation of urine volume	5	1.10E-02	-
ERK signalling	13	1.10E-02	-
Regulation of cell shape	19	1.10E-02	-
Central nervous system development	17	1.20E-02	-
Positive regulation of synapse assembly	11	1.20E-02	-
SMAD protein signal transduction	11	1.20E-02	-
Positive regulation of MAPK cascade	13	1.30E-02	-
Membrane depolarisation during action potential	7	1.30E-02	-
Positive regulation of gene expression	30	1.30E-02	-
Blood circulation	9	1.40E-02	-
Chemotaxis	17	1.40E-02	-
Positive regulation of inflammatory response	12	1.50E-02	-
Mast cell differentiation	3	1.50E-02	-
T cell activation via T cell receptor contact with antigen bound to MHC molecule on antigen presenting cell	3	1.50E-02	-
Positive regulation of neutrophil extravasation	3	1.50E-02	-
Cellular response to interleukin-6	5	1.50E-02	-
Canonical Wnt signalling pathway	13	1.50E-02	-
Endothelial cell migration	7	1.50E-02	-

G-protein coupled receptor signalling pathway, coupled to cyclic nucleotide second messenger	9	1.60E-02	-
T cell mediated cytotoxicity	4	1.60E-02	-
Dorsal aorta morphogenesis	4	1.60E-02	-
Feeding behaviour	6	1.70E-02	-
Transport	37	1.80E-02	-
Regulation of postsynaptic membrane potential	6	1.80E-02	-
Visual perception	24	1.80E-02	-
Eye development	7	1.80E-02	-
Regulation of apoptotic process	25	1.90E-02	-
Lung development	12	1.90E-02	-
Activation of MAPK activity	15	2.10E-02	-
Positive regulation of vascular associated smooth muscle cell migration	4	2.20E-02	-
Somatic stem cell division	4	2.20E-02	-
Cardiac ventricle morphogenesis	4	2.20E-02	-
Regulation of macrophage activation	4	2.20E-02	-
Righting reflex	4	2.20E-02	-
Embryonic limb morphogenesis	8	2.20E-02	-
Regulation of smooth muscle contraction	5	2.40E-02	-
Positive regulation of monocyte chemotaxis	5	2.40E-02	-
Sulphur compound metabolic process	5	2.40E-02	-
Acrosome reaction	5	2.40E-02	-
Positive regulation of MAP kinase activity	10	2.40E-02	-
Blood vessel remodelling	7	2.40E-02	-
Heart morphogenesis	7	2.40E-02	-
Cytokine-mediated signalling pathway	17	2.60E-02	-
Ageing	20	2.80E-02	-
Retinoic acid catabolic process	3	2.80E-02	-
Iron ion transmembrane transport	3	2.80E-02	-
Negative regulation of smooth muscle contraction	3	2.80E-02	-
Lens development in camera-type eye	7	2.80E-02	-
Leukocyte migration	16	2.80E-02	-
Branching involved in ureteric bud morphogenesis	8	2.90E-02	-
Lymph node development	5	3.00E-02	-
Cellular response to organic substance	5	3.00E-02	-
Chemokine-mediated signalling pathway	11	3.00E-02	-
Sprouting angiogenesis	6	3.00E-02	-
Leukocyte cell-cell adhesion	6	3.00E-02	-
Thyroid gland development	6	3.00E-02	-
Negative regulation of protein autophosphorylation	4	3.00E-02	-
Negative regulation of cytosolic calcium ion concentration	4	3.00E-02	-
Axon development	4	3.00E-02	-
Glial cell migration	4	3.00E-02	-
Negative regulation of retinoic acid receptor signalling pathway	4	3.00E-02	-
Cardiac septum morphogenesis	4	3.00E-02	-
Adult locomotory behaviour	9	3.10E-02	-
Multicellular organism development	50	3.10E-02	-
Peptidyl-tyrosine phosphorylation	12	3.20E-02	-
Platelet degranulation	14	3.30E-02	-
Chloride transmembrane transport	13	3.40E-02	-

Response to wounding	10	3.50E-02	-
Negative regulation of neuron projection development	8	3.60E-02	-
Positive regulation of leukocyte chemotaxis	5	3.60E-02	-
Response to vitamin D	5	3.60E-02	-
Notch signalling pathway	15	3.60E-02	-
Positive regulation of bone mineralisation	7	3.70E-02	-
Digestive tract development	7	3.70E-02	-
Positive regulation of protein kinase B signalling	12	3.80E-02	-
Response to ethanol	14	3.80E-02	-
Neuron migration	14	3.80E-02	-
Phospholipid metabolic process	9	3.80E-02	-
Positive regulation of fibroblast proliferation	9	3.80E-02	-
Collagen catabolic process	10	3.80E-02	-
Negative regulation of cell migration	13	3.90E-02	-
Negative regulation of interleukin-2 production	4	3.90E-02	-
Positive regulation of macrophage chemotaxis	4	3.90E-02	-
Cardiac muscle contraction	8	4.00E-02	-
Cardiac conduction	8	4.00E-02	-
Visual learning	8	4.00E-02	-
Glycosphingolipid metabolic process	8	4.00E-02	-
Positive regulation of protein secretion	7	4.10E-02	-
Learning or memory	7	4.10E-02	-
Response to glucocorticoid	10	4.20E-02	-
Regulation of blood pressure	10	4.20E-02	-
Muscle contraction	14	4.30E-02	-
Positive regulation of branching involved in ureteric bud morphogenesis	5	4.30E-02	-
Regulation of dendrite morphogenesis	5	4.30E-02	-
Positive regulation of endothelial cell migration	8	4.40E-02	-
Positive regulation of delayed rectifier potassium channel activity	3	4.50E-02	-
Peripheral nervous system axon regeneration	3	4.50E-02	-
Desmosome organisation	3	4.50E-02	-
Maintenance of organ identity	3	4.50E-02	-
Calcium ion transport	11	4.50E-02	-
Lipid transport	11	4.50E-02	-
Adherens junction organisation	7	4.60E-02	-
Patterning of blood vessels	6	4.70E-02	-
Excitatory postsynaptic potential	6	4.70E-02	-
Positive regulation of cell division	8	4.90E-02	-
Cell proliferation in forebrain	4	5.00E-02	-
Positive regulation of chemotaxis	4	5.00E-02	-
Positive regulation of cAMP-mediated signalling	4	5.00E-02	-
G-protein coupled receptor internalisation	4	5.00E-02	-
Fusion of sperm to egg plasma membrane	4	5.00E-02	-
Proteolysis	47	5.00E-02	-

Supplementary Table 5.4 List of GO pathways for SOD1 iAstrocytes at baseline

GO Pathway	Gene Count	p-value	Benjamini
Cell adhesion	56	1.00E-11	3.10E-08
Extracellular matrix organisation	33	1.10E-10	1.60E-07
Homophilic cell adhesion via plasma membrane adhesion molecules	28	1.10E-09	1.10E-06
Axon guidance	23	1.70E-06	1.20E-03
Collagen catabolic process	13	1.80E-05	1.10E-02
Skeletal system development	19	2.90E-05	1.50E-02
Heterophilic cell-cell adhesion via plasma membrane cell adhesion molecules	11	5.00E-05	2.10E-02
Positive regulation of synapse assembly	12	6.80E-05	2.50E-02
Sensory perception of sound	17	2.30E-04	-
Embryonic skeletal system morphogenesis	9	2.40E-04	-
Chemical synaptic transmission	24	3.60E-04	-
DNA-binding transcription factor activity	10	3.80E-04	-
Neurogenesis	9	4.00E-04	-
Signal transduction	76	4.10E-04	-
Type I interferon signalling pathway	11	4.30E-04	-
Osteoblast differentiation	14	6.00E-04	-
Positive regulation of heart rate	6	6.30E-04	-
Negative regulation of neuron apoptotic process	16	6.60E-04	-
Regulation of calcium ion-dependent exocytosis	8	6.80E-04	-
Cell fate commitment	9	7.70E-04	-
Positive regulation of MAPK cascade	12	7.70E-04	-
Thyroid hormone metabolic process	4	7.80E-04	-
Response to virus	14	1.00E-03	-
Somitogenesis	8	1.30E-03	-
Calcium ion-regulated exocytosis of neurotransmitter	8	1.30E-03	-
Collagen fibril organisation	8	1.30E-03	-
Negative regulation of Notch signalling pathway	7	1.40E-03	-
Regulation of neuron differentiation	6	1.40E-03	-
Negative regulation of viral genome replication	8	1.60E-03	-
Positive regulation of synaptic transmission	5	1.90E-03	-
Regulation of small GTPase mediated signal transduction	15	2.20E-03	-
Anatomical structure morphogenesis	12	2.20E-03	-
Odontogenesis of dentin-containing tooth	9	2.50E-03	-
Cardiac conduction	8	3.20E-03	-
Cardiac muscle contraction	8	3.20E-03	-
Cellular response to retinoic acid	10	3.30E-03	-
Positive regulation of transcription from RNA polymerase II promoter	62	3.40E-03	-
Locomotory behaviour	11	3.60E-03	-
Protein glycosylation	13	3.90E-03	-
Retina morphogenesis in camera-type eye	4	3.90E-03	-
Ventricular cardiac muscle tissue morphogenesis	6	4.00E-03	-
Kidney development	11	4.20E-03	-
Angiogenesis	20	4.30E-03	-
Regulation of exocytosis	6	4.80E-03	-
Positive regulation of mesenchymal cell proliferation	6	4.80E-03	-

Positive regulation of neuron projection development	11	5.40E-03	-
Mast cell differentiation	3	5.60E-03	-
Lung development	10	5.80E-03	-
Potassium ion transmembrane transport	13	6.70E-03	-
Pattern specification process	6	6.70E-03	-
Pharyngeal system development	5	6.80E-03	-
Positive regulation of cell migration	17	6.90E-03	-
Ventricular septum morphogenesis	6	7.80E-03	-
Glycosaminoglycan metabolic process	6	7.80E-03	-
Peripheral nervous system neuron development	4	7.90E-03	-
Anterior/posterior pattern specification	10	8.10E-03	-
Regulation of MAPK cascade	7	8.30E-03	-
Neural tube development	6	9.00E-03	-
Branching involved in ureteric bud morphogenesis	7	9.40E-03	-
Potassium ion transport	10	9.40E-03	-
Sialylation	5	1.00E-02	-
Regulation of heart contraction	6	1.00E-02	-
Positive regulation of tyrosine phosphorylation of Stat1 protein	4	1.10E-02	-
Positive regulation of ureteric bud formation	3	1.10E-02	-
Positive regulation of smooth muscle contraction	5	1.20E-02	-
Lens development in camera-type eye	6	1.40E-02	-
Cellular response to organic cyclic compound	8	1.40E-02	-
Vesicle fusion	8	1.40E-02	-
Cochlea morphogenesis	5	1.40E-02	-
Forebrain development	7	1.40E-02	-
Outflow tract morphogenesis	7	1.40E-02	-
O-glycan processing	8	1.50E-02	-
Muscle organ development	10	1.60E-02	-
Synapse assembly	8	1.70E-02	-
Mast cell degranulation	4	1.70E-02	-
Cardiac epithelial to mesenchymal transition	4	1.70E-02	-
Digestive tract development	6	1.70E-02	-
Wnt signalling pathway	16	1.70E-02	-
Otic vesicle development	3	1.70E-02	-
Semi-circular canal morphogenesis	3	1.70E-02	-
Cell maturation	6	1.90E-02	-
Regulation of cell shape	13	2.00E-02	-
Positive regulation of neuron differentiation	9	2.00E-02	-
Cellular response to interleukin-6	4	2.10E-02	-
Multicellular organism development	34	2.10E-02	-
Negative regulation of extrinsic apoptotic signalling pathway in absence of ligand	6	2.20E-02	-
Oligosaccharide metabolic process	5	2.20E-02	-
Somatic stem cell population maintenance	8	2.30E-02	-
Cell chemotaxis	8	2.30E-02	-
Cellular response to calcium ion	7	2.30E-02	-
Endochondral ossification	5	2.50E-02	-
Positive regulation of dopamine secretion	3	2.50E-02	-
Metanephros development	5	2.90E-02	-
Notch signalling pathway	11	2.90E-02	-
Positive regulation of calcium ion import	4	3.00E-02	-

Positive regulation of endothelial cell proliferation	8	3.10E-02	-
Calcium-dependent cell-cell adhesion via plasma membrane cell adhesion molecules	5	3.20E-02	-
Growth	5	3.20E-02	-
Synaptic transmission, glutamatergic	5	3.20E-02	-
Mesoderm formation	5	3.20E-02	-
Cell surface receptor signalling pathway	20	3.20E-02	-
Atrial cardiac muscle tissue morphogenesis	3	3.50E-02	-
Commitment of neuronal cell to specific neuron type in forebrain	3	3.50E-02	-
Regulation of somitogenesis	3	3.50E-02	-
Protein domain specific binding	3	3.50E-02	-
Dorsal spinal cord development	3	3.50E-02	-
Negative regulation of neuron differentiation	7	3.50E-02	-
Glycosaminoglycan biosynthetic process	6	3.50E-02	-
Calcium ion transmembrane transport	11	3.60E-02	-
Dentate gyrus development	4	3.60E-02	-
Negative regulation of smooth muscle cell proliferation	5	3.60E-02	-
Peptidyl-tyrosine phosphorylation	13	3.60E-02	-
Cellular response to fibroblast growth factor stimulus	5	4.00E-02	-
Response to vitamin A	4	4.20E-02	-
Ganglioside biosynthetic process	4	4.20E-02	-
Post-anal tail morphogenesis	4	4.20E-02	-
Cellular iron ion homeostasis	6	4.20E-02	-
Small GTPase mediated signal transduction	18	4.20E-02	-
Cell-matrix adhesion	9	4.30E-02	-
Transcription from RNA polymerase II promoter	32	4.40E-02	-
Cerebellar granule cell differentiation	3	4.50E-02	-
Secretion	3	4.50E-02	-
Negative regulation of collateral sprouting	3	4.50E-02	-
Cardiovascular system development	3	4.50E-02	-
Animal organ development	3	4.50E-02	-
Surfactant homeostasis	3	4.50E-02	-
Blood circulation	6	4.60E-02	-
Neural crest cell migration	6	4.60E-02	-
Regulation of neuron projection development	4	4.80E-02	-
Regulation of dendrite morphogenesis	4	4.80E-02	-
Retinal ganglion cell axon guidance	4	4.80E-02	-
Organ morphogenesis	9	4.80E-02	-
BMP signalling pathway	8	4.80E-02	-
Nervous system development	20	4.80E-02	-
Regulation of immune response	14	4.90E-02	-
Neuron development	6	4.90E-02	-
Positive regulation of interferon-gamma production	6	4.90E-02	-
Heart morphogenesis	5	4.90E-02	-
Positive regulation of vasoconstriction	5	4.90E-02	-

Supplementary Table 5.5 List of GO pathways for sALS iAstrocytes at baseline

GO Pathway	Gene Count	p-value	Benjamini
Cell adhesion	64	2.90E-13	9.10E-10
Extracellular matrix organisation	39	5.00E-13	7.70E-10
Angiogenesis	31	8.30E-07	8.50E-04
Homophilic cell adhesion via plasma membrane adhesion molecules	25	1.20E-06	9.00E-04
Skeletal system development	23	1.30E-06	7.70E-04
Collagen catabolic process	15	2.70E-06	1.40E-03
Inflammatory response	42	3.10E-06	1.40E-03
Cell fate commitment	12	1.30E-05	4.90E-03
Collagen fibril organisation	11	1.60E-05	5.50E-03
Leukocyte migration	19	3.70E-05	1.10E-02
Endothelial cell migration	9	6.50E-05	1.80E-02
Keratinisation	15	7.90E-05	2.00E-02
Axon guidance	21	1.40E-04	3.30E-02
Neuropeptide signalling pathway	16	1.50E-04	3.20E-02
Positive regulation of angiogenesis	17	2.00E-04	4.00E-02
Peptidyl-tyrosine phosphorylation	14	2.10E-04	4.00E-02
Regulation of calcium ion-dependent exocytosis	9	2.70E-04	4.80E-02
Calcium ion-regulated exocytosis of neurotransmitter	9	6.00E-04	-
Positive regulation of endothelial cell proliferation	12	6.00E-04	-
Locomotory behaviour	13	9.60E-04	-
Axon development	5	1.00E-03	-
Bone mineralisation	8	1.30E-03	-
Cell-matrix adhesion	13	1.80E-03	-
Platelet degranulation	14	1.90E-03	-
Chemical synaptic transmission	24	2.30E-03	-
Central nervous system development	15	2.80E-03	-
Sensory perception of sound	16	2.80E-03	-
Cell surface receptor signalling pathway	26	2.90E-03	-
Negative regulation of endopeptidase activity	15	3.00E-03	-
Negative regulation of calcium ion transport	5	3.10E-03	-
Synapse assembly	10	3.20E-03	-
Positive regulation of reactive oxygen species metabolic process	7	3.30E-03	-
Protein domain specific binding	4	3.80E-03	-
Neuronal action potential propagation	4	3.80E-03	-
Heterotypic cell-cell adhesion	6	4.10E-03	-
Retina layer formation	6	4.10E-03	-
Positive regulation of neutrophil chemotaxis	6	4.10E-03	-
Cell-cell signalling	24	4.60E-03	-
Signal transduction	79	5.00E-03	-
Nervous system development	26	5.30E-03	-
Response to hypoxia	18	5.90E-03	-
Associative learning	6	6.00E-03	-
Activation of protein kinase activity	8	6.70E-03	-
Calcium ion transmembrane transport	14	6.70E-03	-
Learning	9	7.30E-03	-
Tooth eruption	3	7.30E-03	-

G-protein coupled receptor signalling pathway, coupled to cyclic nucleotide second messenger	8	7.60E-03	-
Positive regulation of endothelial cell migration	8	7.60E-03	-
Zymogen activation	4	8.40E-03	-
Regulation of exocytosis	6	8.60E-03	-
Positive regulation of mesenchymal cell proliferation	6	8.60E-03	-
Endochondral ossification	6	8.60E-03	-
Blood vessel morphogenesis	5	8.90E-03	-
Vesicle fusion	9	8.90E-03	-
Single fertilisation	9	8.90E-03	-
Keratinisation	8	9.60E-03	-
Regulation of ion transmembrane transport	13	9.80E-03	-
O-glycan processing	9	9.90E-03	-
Endodermal cell differentiation	6	1.00E-02	-
Bone morphogenesis	6	1.00E-02	-
Sodium ion transmembrane transport	10	1.10E-02	-
Ephrin receptor signalling pathway	11	1.10E-02	-
Toll-like receptor 4 signalling pathway	5	1.10E-02	-
Blood coagulation, intrinsic pathway	5	1.10E-02	-
Heterophilic cell-cell adhesion via plasma membrane cell adhesion molecules	8	1.20E-02	-
Peptide cross-linking	8	1.20E-02	-
Memory	9	1.20E-02	-
Palate development	10	1.40E-02	-
Glycosaminoglycan metabolic process	6	1.40E-02	-
Generation of ovulation cycle rhythm	3	1.40E-02	-
Osteoblast differentiation	12	1.50E-02	-
Behavioural response to pain	4	1.50E-02	-
Negative thymic T cell selection	4	1.50E-02	-
Cell chemotaxis	9	1.60E-02	-
Response to glucocorticoid	9	1.60E-02	-
Branching involved in ureteric bud morphogenesis	7	1.80E-02	-
Activation of MAPK activity	12	1.80E-02	-
Synaptic transmission, glutamatergic	5	1.90E-02	-
Positive regulation of chemotaxis	4	2.00E-02	-
Activation of transmembrane receptor protein tyrosine kinase activity	4	2.00E-02	-
Negative regulation of pathway-restricted SMAD protein phosphorylation	4	2.00E-02	-
Positive regulation of macrophage activation	4	2.00E-02	-
Response to pH	4	2.00E-02	-
Hemidesmosome assembly	4	2.00E-02	-
Mesoderm development	6	2.10E-02	-
Peptidyl-tyrosine phosphorylation	15	2.20E-02	-
Regulation of synaptic transmission, cholinergic	3	2.30E-02	-
Desmosome organisation	3	2.30E-02	-
Blood circulation	7	2.40E-02	-
Positive regulation of protein kinase B signalling	10	2.50E-02	-
Axonogenesis	11	2.50E-02	-
Skin development	6	2.60E-02	-
Regulation of gene expression	11	2.80E-02	-

Digestive tract development	6	2.90E-02	-
Positive regulation of cell proliferation	34	2.90E-02	-
Protein heterotrimerisation	4	3.00E-02	-
Positive regulation of ERK1 and ERK2 cascade	16	3.00E-02	-
Social behaviour	7	3.20E-02	-
Positive regulation of dopamine secretion	3	3.30E-02	-
Regulation of norepinephrine secretion	3	3.30E-02	-
Negative regulation of leukocyte apoptotic process	3	3.30E-02	-
Negative regulation of neuron apoptotic process	13	3.40E-02	-
Positive regulation of phosphorylation	5	3.40E-02	-
Sprouting angiogenesis	5	3.40E-02	-
Positive regulation of synapse assembly	8	3.50E-02	-
Adherens junction organisation	6	3.60E-02	-
Response to nicotine	6	3.60E-02	-
Synaptic transmission, cholinergic	6	3.60E-02	-
Keratinocyte differentiation	9	3.60E-02	-
Matrix metalloproteinase activity	9	3.60E-02	-
Lung development	9	3.60E-02	-
Lipid transport	9	3.60E-02	-
Cell adhesion mediated by integrin	4	3.70E-02	-
Adenylate cyclase-activating G-protein coupled receptor signalling pathway	7	3.80E-02	-
Positive regulation of canonical Wnt signalling pathway	12	3.90E-02	-
Hair follicle development	6	4.00E-02	-
Organ morphogenesis	10	4.10E-02	-
Neurotransmitter secretion	7	4.10E-02	-
Chemotaxis	12	4.30E-02	-
Establishment of endothelial barrier	4	4.30E-02	-
Positive regulation of calcium ion import	4	4.30E-02	-
Neuron cell-cell adhesion	4	4.30E-02	-
Embryonic skeletal system morphogenesis	6	4.40E-02	-
Positive regulation of cell migration	16	4.40E-02	-
Negative regulation of smooth muscle cell differentiation	3	4.50E-02	-
Positive regulation of macrophage cytokine production	3	4.50E-02	-
Positive regulation of apoptotic cell clearance	3	4.50E-02	-
Positive regulation of inhibitory postsynaptic potential	3	4.50E-02	-
Adult locomotory behaviour	7	4.50E-02	-
DNA-binding transcription factor activity	7	4.50E-02	-
Phospholipase C-activating G-protein coupled receptor signalling pathway	8	4.70E-02	-
ERK signalling	9	4.70E-02	-
Growth	5	5.00E-02	-
Embryonic hindlimb morphogenesis	5	5.00E-02	-
Negative regulation of interleukin-6 production	5	5.00E-02	-
Wnt signalling pathway	16	5.00E-02	-
Sodium ion transport	9	5.00E-02	-
Positive regulation of MAPK cascade	9	5.00E-02	-

Supplementary Table 5.6 List of GO pathways for CTR iAstrocytes after S[+]-apomorphine treatment

GO Pathway	Gene Count	p-value	Benjamini
Adult locomotory behaviour	5	2.60E-03	-
Cellular response to organic cyclic compound	5	4.10E-03	-
O-glycan processing	5	4.40E-03	-
Peptidyl-tyrosine phosphorylation	7	7.20E-03	-
Calcium ion transmembrane transport	6	1.00E-02	-
Positive regulation of chondrocyte differentiation	3	1.80E-02	-
Response to drug	9	2.00E-02	-
Regulation of cardiac conduction	4	2.40E-02	-
MAPK cascade	8	2.70E-02	-
Response to ethanol	5	2.90E-02	-
Phosphatidylinositol-mediated signalling	5	3.00E-02	-
Cytidine to uridine editing	2	3.30E-02	-
Peyer's patch morphogenesis	2	3.30E-02	-
Ageing	6	3.70E-02	-
Membrane depolarisation during action potential	3	3.80E-02	-
Protein localisation to juxtaparanode region of axon	2	4.40E-02	-
Morphogenesis of an epithelial fold	2	4.40E-02	-
Hepatocyte proliferation	2	4.40E-02	-
Chemotaxis	5	4.70E-02	-
Positive regulation of GTPase activity	12	5.00E-02	-

Supplementary Table 5.7 List of GO pathways for C9ORF72 iAstrocytes after S[+]-apomorphine treatment

GO Pathway	Gene Count	p-value	Benjamini
Cell adhesion	12	3.40E-05	2.10E-02
Steroid metabolic process	4	1.60E-03	-
Hormone biosynthetic process	3	1.80E-03	-
Hydrogen peroxide catabolic process	3	5.10E-03	-
Homophilic cell adhesion via plasma membrane adhesion molecules	5	1.00E-02	-
Cerebral cortex GABAergic interneuron migration	2	3.20E-02	-
Angiogenesis	5	3.20E-02	-
Chemical synaptic transmission	5	4.00E-02	-
SMAD protein signal transduction	3	4.40E-02	-
Progesterone metabolic process	2	4.70E-02	-
Hydrogen peroxide biosynthetic process	2	4.70E-02	-
Omega-hydroxylase P450 pathway	2	4.70E-02	-

Supplementary Table 5.8 List of GO pathways for SOD1 iAstrocytes after S[+]-apomorphine treatment

GO Pathway	Gene Count	p-value	Benjamini
Inflammatory response	14	5.40E-05	5.50E-02
Signal transduction	26	6.80E-05	3.50E-02
Cellular response to organic cyclic compound	6	2.20E-04	-
Synaptic transmission, cholinergic	5	3.70E-04	-
Cellular response to retinoic acid	6	4.80E-04	-
Positive regulation of angiogenesis	7	7.10E-04	-
Xenobiotic metabolic process	6	7.90E-04	-
Positive regulation of mitotic nuclear division	4	1.70E-03	-
Immune response	12	1.90E-03	-
Positive regulation of epidermal growth factor-activated receptor activity	3	3.00E-03	-
Collagen fibril organisation	4	5.60E-03	-
Cell proliferation	10	7.30E-03	-
Positive regulation of macrophage derived foam cell differentiation	3	9.40E-03	-
Chloride transmembrane transport	5	1.10E-02	-
Positive regulation of cell proliferation	11	1.20E-02	-
Epoxygenase P450 pathway	3	1.20E-02	-
Long-chain fatty acid metabolic process	3	1.60E-02	-
Muscle contraction	5	1.80E-02	-
Angiogenesis	7	1.80E-02	-
Ovarian cumulus expansion	2	1.80E-02	-
Arachidonic acid secretion	3	2.10E-02	-
Positive regulation of cytokine production	3	2.10E-02	-
Response to wounding	4	2.10E-02	-
Biomineral tissue development	3	2.20E-02	-
Arachidonic acid metabolic process	3	2.20E-02	-
Neuromuscular synaptic transmission	3	2.40E-02	-
Positive regulation of vascular endothelial growth factor production	3	2.60E-02	-
Drug metabolic process	3	2.60E-02	-
Fever generation	2	2.80E-02	-
Cell adhesion	10	2.80E-02	-
Chemokine-mediated signalling pathway	4	2.80E-02	-
Cell-cell signalling	7	3.10E-02	-
Calcium ion transport	4	3.40E-02	-
Cytokine-mediated signalling pathway	5	3.40E-02	-
MAPK cascade	7	3.60E-02	-
Negative regulation of branching involved in ureteric bud morphogenesis	2	3.70E-02	-
Positive regulation of cell adhesion molecule production	2	3.70E-02	-
Regulation of heart rate	3	3.80E-02	-
Extrinsic apoptotic signalling pathway in absence of ligand	3	4.00E-02	-
Sodium ion transport	4	4.00E-02	-
Phosphatidic acid biosynthetic process	3	4.20E-02	-
Transport	8	4.40E-02	-
Ion transmembrane transport	6	4.60E-02	-
Oxidation-reduction process	11	5.00E-02	-

Supplementary Table 5.9 List of GO pathways for sALS iAstrocytes after S[+]-apomorphine treatment

GO Pathway	Gene Count	p-value	Benjamini
Collagen fibril organisation	5	6.20E-04	-
Epithelial cell differentiation	6	6.90E-04	-
Growth factor activity	4	7.30E-04	-
Vitamin A metabolic process	3	2.00E-03	-
Positive regulation of mitotic nuclear division	4	2.20E-03	-
Positive regulation of MAP kinase activity	5	2.90E-03	-
Retinol metabolic process	4	3.30E-03	-
Mesoderm development	4	4.00E-03	-
Synaptic transmission, cholinergic	4	6.10E-03	-
Retinal metabolic process	3	6.20E-03	-
Neural crest cell development	3	7.30E-03	-
Retinoic acid metabolic process	3	8.50E-03	-
Signal transduction	21	1.30E-02	-
Extracellular matrix organisation	7	1.50E-02	-
Cell migration involved in mesendoderm migration	2	2.00E-02	-
Response to stimulus	4	2.50E-02	-
Response to oxidative stress	5	2.50E-02	-
Angiogenesis	7	2.50E-02	-
Biomineral tissue development	3	2.60E-02	-
Ventricular cardiac muscle tissue morphogenesis	3	2.60E-02	-
Immune response	10	2.70E-02	-
Positive regulation of protein tyrosine kinase activity	3	2.80E-02	-
Pituitary gland development	3	3.20E-02	-
Patterning of blood vessels	3	3.20E-02	-
Cellular oxidant detoxification	4	3.40E-02	-
Oxidation-reduction process	12	3.70E-02	-
Heart development	6	3.80E-02	-
Inflammatory response	9	3.80E-02	-
Drug export	2	4.00E-02	-
Morphogenesis of an epithelial fold	2	4.00E-02	-
9-cis-retinoic acid biosynthetic process	2	4.00E-02	-
Cell adhesion	10	4.30E-02	-
Xenobiotic metabolic process	4	4.40E-02	-

Supplementary Table 5.10 List of GO pathways for CTR iAstrocytes after andrographolide treatment

GO Pathway	Gene Count	p-value	Benjamini
Antigen processing and presentation of peptide or polysaccharide antigen via MHC class II	4	1.70E-04	-
Aldo-keto reductase (NADP) activity	3	2.50E-04	-
Oxidation-reduction process	13	4.60E-04	-
Cellular response to prostaglandin D stimulus	3	6.20E-04	-
Retinoid metabolic process	5	6.60E-04	-
Metabolism of chemotherapy drugs	3	1.10E-03	-
Progesterone metabolic process	3	1.50E-03	-
Xenobiotic metabolic process	5	1.70E-03	-
Vesicle trafficking in neurons	4	4.70E-03	-
Positive regulation of transcription, DNA-templated	9	1.90E-02	-
Antigen processing and presentation of exogenous peptide antigen via MHC class II	4	2.20E-02	-
Ubiquitination through p62/KEAP1/NRF2 signalling	2	2.60E-02	-
Protein tetramerisation	3	2.80E-02	-
Peptide antigen assembly with MHC class II protein complex	2	3.20E-02	-
Positive regulation of cell proliferation	8	3.20E-02	-
Cell fate commitment	3	3.60E-02	-
Extracellular matrix organisation	5	3.90E-02	-
Response to organic cyclic compound	3	4.00E-02	-
Calcium ion transmembrane transport	4	4.20E-02	-
Antigen processing and presentation	3	5.00E-02	-
Odontogenesis of dentin-containing tooth	3	5.00E-02	-

Supplementary Table 5.11 List of GO pathways for C9ORF72 iAstrocytes after andrographolide treatment

GO Pathway	Gene Count	p-value	Benjamini
Response to metal ions	4	2.10E-04	-
Epithelial cell differentiation	5	1.50E-03	-
Sodium ion transport	5	2.50E-03	-
Cellular response to zinc ion	3	7.70E-03	-
Negative regulation of growth	3	7.70E-03	-
O-glycan processing	4	8.70E-03	-
Blood brain barrier & immune cell transmigration	3	1.50E-02	-
ERK signalling	5	1.60E-02	-
Xenobiotic metabolic process	4	1.80E-02	-
Inflammatory response	8	1.80E-02	-
Oxidation-reduction process	10	2.40E-02	-
Chemical synaptic transmission	6	2.70E-02	-
Aldo-keto reductase (NADP) activity	2	2.80E-02	-
Immune response	8	2.90E-02	-
Response to reactive oxygen species	3	3.10E-02	-
Positive regulation of interleukin-5 production	2	4.10E-02	-
Response to oxidative stress	4	4.20E-02	-
Cell adhesion	8	4.30E-02	-
Heme catabolic process	2	4.80E-02	-

Supplementary Table 5.12 List of GO pathways for SOD1 iAstrocytes after andrographolide treatment

GO Pathway	Gene Count	p-value	Benjamini
Metabolism of chemotherapy drugs	4	3.00E-05	2.40E-02
Response to nutrient	6	3.60E-04	-
Aldo-keto reductase (NADP) activity	3	4.00E-04	-
Oxidation-reduction process	14	1.20E-03	-
Digestion	5	1.80E-03	-
Progesterone metabolic process	3	2.30E-03	-
Xenobiotic metabolic process	5	3.90E-03	-
Retinal metabolic process	3	4.20E-03	-
Steroid metabolic process	4	5.30E-03	-
Extracellular matrix organisation	7	5.60E-03	-
Cellular response to ethanol	3	5.70E-03	-
Cytolysis	3	1.30E-02	-
Retinoid metabolic process	4	1.40E-02	-
Interleukin-5-mediated signalling pathway	2	1.60E-02	-
Farnesol catabolic process	2	1.60E-02	-
Positive regulation of interleukin-8 production	3	1.90E-02	-
Blood brain barrier & immune cell transmigration	3	2.10E-02	-
Ion transport	5	2.10E-02	-
Vitamin E metabolic process	2	2.40E-02	-
Response to toxic substance	4	3.30E-02	-
Synaptic transmission, cholinergic	3	3.70E-02	-
Innate immune response	5	4.60E-02	-
Positive regulation of oxidoreductase activity	2	4.80E-02	-
Flavone metabolic process	2	4.80E-02	-
Cellular response to prostaglandin D stimulus	2	4.80E-02	-

Supplementary Table 5.13 List of GO pathways for sALS iAstrocytes after andrographolide treatment

GO Pathway	Gene Count	p-value	Benjamini
Oxidation-reduction process	22	4.40E-06	5.80E-03
Metabolism of chemotherapy drugs	4	7.90E-05	-
Xenobiotic metabolic process	7	2.70E-04	-
Retinoid metabolic process	6	6.60E-04	-
Aldo-keto reductase (NADP) activity	3	7.70E-04	-
Positive regulation of cell proliferation	15	9.60E-04	-
Positive regulation of leukocyte chemotaxis	4	1.10E-03	-
Steroid metabolic process	5	1.40E-03	-
Cellular response to prostaglandin D stimulus	3	1.90E-03	-
Glomerular visceral epithelial cell differentiation	3	2.60E-03	-
Positive regulation of mitotic nuclear division	4	3.20E-03	-
Patterning of blood vessels	4	3.90E-03	-
Progesterone metabolic process	3	4.40E-03	-
Positive regulation of MAP kinase activity	5	4.60E-03	-
Regulation of complement activation	4	4.80E-03	-
Brain & heart development	8	5.20E-03	-
Response to glucocorticoid	5	6.50E-03	-
Cell chemotaxis	5	6.50E-03	-
Regulation of blood pressure	5	6.50E-03	-
Response to ethanol	6	7.10E-03	-
Positive regulation of renal sodium excretion	3	8.00E-03	-
Retinal metabolic process	3	8.00E-03	-
Epithelial cell differentiation	5	8.40E-03	-
Positive regulation of urine volume	3	9.30E-03	-
Neural crest cell development	3	9.30E-03	-
Positive regulation of angiogenesis	6	1.00E-02	-
Vesicle-mediated transport	9	1.10E-02	-
Retinoic acid metabolic process	3	1.10E-02	-
Inflammatory response	11	1.20E-02	-
Regulation of I-kappaB kinase/NF-kappaB signalling	3	1.20E-02	-
Leukocyte migration	6	1.30E-02	-
Positive regulation of endothelial cell migration	4	1.60E-02	-
Cell adhesion	12	1.70E-02	-
Response to organic cyclic compound	4	1.80E-02	-
Sensory perception of pain	4	2.20E-02	-
Farnesol catabolic process	2	2.30E-02	-
Glomerular parietal epithelial cell differentiation	2	2.30E-02	-
Odontogenesis of dentin-containing tooth	4	2.50E-02	-
Regulation of cardiac conduction	4	2.60E-02	-
Cell-cell signalling	8	2.70E-02	-
Learning	4	2.70E-02	-
MAPK cascade	8	3.10E-02	-
Peptidyl-tyrosine phosphorylation	6	3.10E-02	-
Ventricular cardiac muscle tissue morphogenesis	3	3.30E-02	-
Glomerular endothelium development	2	3.40E-02	-
Negative regulation of glial cell differentiation	2	3.40E-02	-
Positive regulation of nephron tubule epithelial cell differentiation	2	3.40E-02	-

Negative regulation of angiogenesis	4	3.40E-02	-
Activation of MAPK activity	5	3.40E-02	-
Response to wounding	4	3.50E-02	-
Response to oxidative stress	5	3.80E-02	-
Response to lipopolysaccharide	6	4.00E-02	-
Positive regulation of cytosolic calcium ion concentration involved in phospholipase C-activating G-protein coupled signalling pathway	3	4.00E-02	-
Vein smooth muscle contraction	2	4.50E-02	-
Drug export	2	4.50E-02	-
Paracrine signalling	2	4.50E-02	-
Positive regulation of odontogenesis	2	4.50E-02	-
Ubiquitination through p62/KEAP1/NRF2 signalling	2	4.50E-02	-
Sclerotome development	2	4.50E-02	-
Retinoic acid catabolic process	2	4.50E-02	-
Positive regulation of glomerular filtration	2	4.50E-02	-
Negative regulation of cellular protein metabolic process	2	4.50E-02	-
Retinol metabolic process	3	4.60E-02	-
Chemokine-mediated signalling pathway	4	4.80E-02	-

Supplementary Table 5.14 List of GO pathways for CTR iAstrocytes after riluzole treatment

GO Pathway	Gene Count	p-value	Benjamini
Calcium ion transmembrane transport	5	1.20E-03	-
Chemical synaptic transmission	6	2.40E-03	-
Ionotropic glutamate receptor signalling pathway	3	3.90E-03	-
Response to amphetamine	3	6.40E-03	-
Visual learning	3	1.30E-02	-
Morphogenesis of an epithelial fold	2	1.50E-02	-
Retinoic acid biosynthetic process	2	1.90E-02	-
Skeletal muscle thin filament assembly	2	1.90E-02	-
Regulation of sodium/potassium-coupled chloride cotransporters	2	2.30E-02	-
Vitamin A metabolic process	2	2.70E-02	-
Serotonin metabolic process	2	3.10E-02	-
Liver development	3	3.30E-02	-
Midgut development	2	3.40E-02	-
Lung development	3	3.50E-02	-
Spinal cord association neuron differentiation	2	4.90E-02	-

Supplementary Table 5.15 List of GO pathways for SOD1 iAstrocytes after riluzole treatment

GO Pathway	Gene Count	p-value	Benjamini
Synaptic transmission, cholinergic	4	1.30E-03	-
Zinc II ion transmembrane transport	3	4.90E-03	-
Homophilic cell adhesion via plasma membrane adhesion molecules	5	1.40E-02	-
Transport	7	1.60E-02	-
Cell adhesion	8	1.80E-02	-
Response to zinc ion	3	1.90E-02	-
Response to nicotine	3	2.00E-02	-
Release of sequestered calcium ion into cytosol	3	2.40E-02	-
Positive regulation of insulin secretion	3	2.40E-02	-
Response to purine-containing compound	2	2.90E-02	-
Cation transmembrane transport	3	3.20E-02	-
Transport of glucose, metal ions and amine compounds	5	3.50E-02	-

Supplementary Table 5.16 List of GO pathways for sALS iAstrocytes after riluzole treatment

GO Pathway	Gene Count	p-value	Benjamini
Immune response	11	7.20E-04	-
Glomerular visceral epithelial cell differentiation	3	9.90E-04	-
Cell adhesion	11	1.40E-03	-
Immune cell chemotaxis	6	1.60E-03	-
Response to pathogen	3	1.70E-03	-
Adherens junction organisation	4	2.20E-03	-
Inflammatory response	9	5.00E-03	-
Cell chemotaxis	4	1.10E-02	-
Extracellular matrix organisation	6	1.20E-02	-
Ventricular cardiac muscle tissue morphogenesis	3	1.30E-02	-
Chemokine-mediated signalling pathway	4	1.30E-02	-
Glomerular parietal epithelial cell differentiation	2	1.40E-02	-
Ossification	4	1.80E-02	-
Angiogenesis	6	2.00E-02	-
Positive regulation of nephron tubule epithelial cell differentiation	2	2.10E-02	-
Mesoderm development	3	2.10E-02	-
Homophilic cell adhesion via plasma membrane adhesion molecules	5	2.50E-02	-
Globus pallidus development	2	2.80E-02	-
Response to lipopolysaccharide	5	2.80E-02	-
Cell-cell signalling	6	3.30E-02	-
Desmosome organisation	2	3.40E-02	-
Bundle of His cell-Purkinje myocyte adhesion involved in cell communication	2	4.10E-02	-
Apoptotic process	9	4.50E-02	-
Peptide cross-linking	3	4.70E-02	-

Supplementary Table 6.1 List of transcripts for S[+]-apomorphine responders at baseline

Gene Name	p-adj	log2FC
Coiled-coil domain containing 3 (CCDC3)	1.32E-04	+5.968514399
Latent transforming growth factor beta binding protein 1 (LTBP1)	1.32E-04	+2.812221501
Collagen type IV alpha 1 chain (COL4A1)	2.70E-08	+6.902376077
Four and a half LIM domains 1 (FHL1)	0.001239989	+3.625659572
Internexin neuronal intermediate filament protein alpha (INA)	0.001239989	4.869168925
Versican (VCAN)	0.002591819	+6.137791828
ADAM metallopeptidase with thrombospondin type 1 motif 5 (ADAMTS5)	0.002621102	+7.757440947
Islet cell autoantigen 1 (ICA1)	0.002763029	-3.182989003
Junctophilin 1 (JPH1)	0.004427206	+4.823946636
Olfactomedin 2 (OLFM2)	0.004994229	+2.78418055
Adrenoceptor alpha 2A (ADRA2A)	0.005152966	+5.645351809
Anoctamin 3 (ANO3)	0.005152966	+6.730525659
Forkhead box P2 (FOXP2)	0.005152966	+4.641935085
Dynamin 1 (DNM1)	0.005731808	+4.689751948
Phospholipase A and acyltransferase 5 (PLAAT5)	0.005997904	+6.004604594
Mitochondrial ribosomal protein S9 (MRPS9)	0.007926962	-1.790471204
Nuclear receptor interacting protein 3 (NRIP3)	0.008085849	+3.541391126
Contactin 1 (CNTN1)	0.008138741	+7.03596454
G protein subunit alpha o1 (GNAO1)	0.009927691	+8.125838768
LDOC1 regulator of NFkB signaling (LDOC1)	0.009927691	+6.66311485
Meiosis specific with OB-fold (MEIOB)	0.009927691	+3.95186184
Nectin cell adhesion molecule 3 (NECTIN3)	0.011578209	+1.80096269
Glutamine amidotransferase like class 1 domain containing 3A (GATD3A)	0.011865584	+3.957125386
Glutamine amidotransferase like class 1 domain containing 3B (GATD3B)	0.011865584	+3.957125386
Ring finger protein 152 (RNF152)	0.013743651	+5.675585869
Solute carrier family 1 member 3 (SLC1A3)	0.015715115	+10.07376736
Collagen type V alpha 3 chain (COL5A3)	0.016575879	+8.299829125
OCIA domain containing 2 (OCIAD2)	0.016575879	+5.059196635
Glucosaminyl (N-acetyl) transferase 1 (GCNT1)	0.016877234	+6.649753919
LY6/PLAUR domain containing 6 (LYPD6)	0.017197276	+4.051552445
EPH receptor A3 (EPHA3)	0.018808847	+7.463762783
Double C2 domain beta (DOC2B)	0.019822483	+4.760357746
Interaction protein for cytohesin exchange factors 1 (IPCEF1)	0.020551437	+4.984578782
MFF divergent transcript (MFF-DT)	0.020551437	+2.10089669
Dickkopf WNT signaling pathway inhibitor 2 (DKK2)	0.02365336	+3.582472635
Insulin like growth factor binding protein 5 (IGFBP5)	0.023841488	+3.305056927
ADAMTS like 2 (ADAMTSL2)	0.033670262	+6.78677596
Cyclase associated actin cytoskeleton regulatory protein 2 (CAP2)	0.038128159	+3.414751831
Desmoplakin (DSP)	0.038128159	+4.087588368
Wnt family member 2 (WNT2)	0.038128159	+4.447073745
Rho associated coiled-coil containing protein kinase 1 pseudogene 1 (ROCK1P1)	0.04726124	-4.663338277
Dachsous cadherin-related 1 (DCHS1)	0.04861494	+3.254552127
EPH receptor B2 (EPHB2)	0.04861494	+5.473548173
Glutamate metabotropic receptor 4 (GRM4)	0.04861494	+3.705822056

Supplementary Table 6.2 List of transcripts for andrographolide responders at baseline

Gene Name	p-adj	log2FC
CD177 molecule (CD177)	1.84E-05	+23.69772545
SRY-box transcription factor 2 (SOX2)	1.84E-05	+11.39116047
Carboxypeptidase vitellogenic like (CPVL)	1.84E-05	+4.864436497
Myosin binding protein C, slow type (MYBPC1)	1.84E-05	-5.539309351
Small proline rich protein 2E (SPRR2E)	1.84E-05	-9.803831155
Internexin neuronal intermediate filament protein alpha (INA)	1.88E-05	+5.373074674
Cadherin 2 (CDH2)	5.12E-05	+8.599840562
Hypocretin neuropeptide precursor (HCRT)	5.43E-05	+22.09890679
Long intergenic non-protein coding RNA 2251 (LINC02251)	5.43E-05	+20.5716279
NFAT activating protein with ITAM motif 1 (NFAM1)	5.43E-05	+4.096962239
Serine protease 3 (PRSS3)	5.43E-05	-8.438352172
LDOC1 regulator of NFKB signaling (LDOC1)	7.05E-05	+7.479115082
Interaction protein for cytohesin exchange factors 1 (IPCEF1)	7.05E-05	+6.351298926
Coiled-coil domain containing 3 (CCDC3)	1.75E-04	+6.008352854
DNAJC9 antisense RNA 1 (DNAJC9-AS1)	5.87E-04	-6.168853242
Four and a half LIM domains 1 (FHL1)	6.49E-04	+4.207846013
Germ cell associated 1 (GSG1)	7.47E-04	-6.421622852
Integrin subunit beta 4 (ITGB4)	8.52E-04	-5.222829143
Glutamate ionotropic receptor NMDA type subunit 2B (GRIN2B)	8.52E-04	-8.522048538
EBF transcription factor 3 (EBF3)	0.00125898	+7.619713746
Glucosaminyl (N-acetyl) transferase 1 (GCNT1)	0.00125898	+7.088458457
Transmembrane protein with EGF like and two follistatin like domains 2 (TMEFF2)	0.00125898	+7.01912874
Phospholipase A and acyltransferase 5 (PLAAT5)	0.00125898	+6.572604163
Tumor protein D52 (TPD52)	0.00125898	+4.493641951
Tripartite motif containing 71 (TRIM71)	0.001618954	+7.118025007
Solute carrier family 1 member 3 (SLC1A3)	0.001746821	+10.67075694
Collagen type IV alpha 1 chain (COL4A1)	0.00230913	+7.384603108
RNA binding protein, mRNA processing factor (RBPMS)	0.002309601	+7.425872059
C-C motif chemokine ligand 2 (CCL2)	0.002397619	+7.347434422
OCIA domain containing 2 (OCIAD2)	0.002423607	+5.087699327
C-X-C motif chemokine ligand 12 (CXCL12)	0.002456406	+8.524367718
G protein subunit alpha o1 (GNAO1)	0.002762391	+8.745648121
Sortilin 1 (SORT1)	0.002762391	+2.500618023
ITGB2 antisense RNA 1 (ITGB2-AS1)	0.002848661	-5.098531716
CD200 molecule (CD200)	0.003530308	+9.260850264
Glypican 3 (GPC3)	0.003559166	+10.12852264
5-hydroxytryptamine receptor 7 (HTR7)	0.003559166	+7.376318973
Fibrous sheath interacting protein 1 (FSIP1)	0.003559166	-5.227079259
Macrophage stimulating 1 receptor (MST1R)	0.003879826	-4.665599645
Aldehyde dehydrogenase 1 family member A2 (ALDH1A2)	0.004084036	+11.6522931
ADAM metalloproteinase with thrombospondin type 1 motif 5 (ADAMTS5)	0.004084036	+7.457464103
TLR4 interactor with leucine rich repeats (TRIL)	0.004084036	+5.931960294
Signal regulatory protein alpha (SIRPA)	0.004084036	-5.708294018

Espin like (ESPNL)	0.005109846	+7.144337915
Meiosis specific with OB-fold (MEIOB)	0.005663099	+4.916653297
Solute carrier family 13 member 1 (SLC13A1)	0.006062345	-5.974647504
Solute carrier family 7 member 2 (SLC7A2)	0.00611777	+7.18166355
Cyclin D2 (CCND2)	0.006485898	+5.573101436
Dachsous cadherin-related 1 (DCHS1)	0.006717023	+4.173613942
Growth differentiation factor 3 (GDF3)	0.007299946	+7.085983436
Ring finger protein 152 (RNF152)	0.008362285	+5.758744712
Desmoplakin (DSP)	0.008362285	+4.030568349
Carboxypeptidase X, M14 family member 2 (CPXM2)	0.009264463	+6.533796715
Dihydropyrimidinase like 4 (DPYSL4)	0.009264463	+4.0953912
Glutamyl-peptide cyclotransferase (QPCT)	0.009319304	+5.655015165
NmrA like redox sensor 2, pseudogene (NMRAL2P)	0.009319304	+4.872187243
EPH receptor B2 (EPHB2)	0.009485992	+7.624253524
Inhibitor of DNA binding 4, HLH protein (ID4)	0.009720736	+6.138550503
Double C2 domain beta (DOC2B)	0.009720736	+5.260916198
Hexokinase domain containing 1 (HKDC1)	0.009890565	-4.486929237
Matrilin 3 (MATN3)	0.010043062	+3.723691129
Kallikrein B1 (KLKB1)	0.01066841	+8.380632686
Carboxylesterase 1 (CES1)	0.01066841	+7.399193886
Adrenoceptor alpha 2A (ADRA2A)	0.01066841	+6.26059011
Interleukin 4 induced 1 (IL4I1)	0.01066841	+5.441056922
Secernin 1 (SCRN1)	0.01066841	+4.818005063
Retinoid isomerohydrolase RPE65 (RPE65)	0.011212684	+8.556956276
Junctophilin 1 (JPH1)	0.011888628	+5.08660357
LY6/PLAUR domain containing 6 (LYPD6)	0.012637627	+4.860917455
Cyclase associated actin cytoskeleton regulatory protein 2 (CAP2)	0.013369197	+5.387742624
Lactoperoxidase (LPO)	0.013369197	-4.772187604
Wnt family member 7A (WNT7A)	0.013809578	-6.387932903
Corin, serine peptidase (CORIN)	0.013838633	+3.547653391
Kinesin family member 1A (KIF1A)	0.013896582	+9.756336054
WAS/WASL interacting protein family member 3 (WIPF3)	0.01392304	+6.196239819
Glutamate metabotropic receptor 3 (GRM3)	0.013925811	+9.846500839
Thymocyte selection associated high mobility group box (TOX)	0.013925811	+7.99908536
Rho guanine nucleotide exchange factor 15 (ARHGEF15)	0.013925811	+7.516480533
MER proto-oncogene, tyrosine kinase (MERTK)	0.013925811	+4.341384898
Solute carrier family 40 member 1 (SLC40A1)	0.014084343	+7.00767611
Forkhead box P2 (FOXP2)	0.014084343	+4.306890786
Mucolipin 2 (MCOLN2)	0.014851714	+3.968632845
Versican (VCAN)	0.01515761	+7.451285517
Ring finger protein 150 (RNF150)	0.01515761	+5.741857161
Prune homolog 2 with BCH domain (PRUNE2)	0.015470226	+7.682484444
Syntaxin 11 (STX11)	0.015470226	+7.391838307
Developmental pluripotency associated 4 (DPPA4)	0.015470226	+6.880014845
Potassium voltage-gated channel modifier subfamily G member 3 (KCNQ3)	0.015470226	+4.250139564
Potassium calcium-activated channel subfamily N member 4 (KCNN4)	0.015470226	-5.570461474
Laminin subunit alpha 1 (LAMA1)	0.016072075	+5.509110447
Neurofilament heavy (NEFH)	0.017099089	+3.344196341
ATP binding cassette subfamily A member 12 (ABCA12)	0.017255608	-5.097165816
Thrombospondin 2 (THBS2)	0.017878418	+4.552615585

Long intergenic non-protein coding RNA 678 (LINC00678)	0.018122858	+7.920583991
Phospholipase B domain containing 1 (PLBD1)	0.018122858	+4.093221809
Pellino E3 ubiquitin protein ligase family member 2 (PELI2)	0.018234678	+2.942811782
Cytochrome P450 family 26 subfamily A member 1 (CYP26A1)	0.018406774	+7.267502932
Zinc finger protein 556 (ZNF556)	0.018406774	+5.293207292
Contactin 1 (CNTN1)	0.018427397	+7.031894468
Brain derived neurotrophic factor (BDNF)	0.018674402	+4.84687531
Ameloblastin (AMBN)	0.019043065	+10.00369565
KRAB box domain containing 1 (KRBOX1)	0.019183759	+9.789475203
Stimulated by retinoic acid 6 (STRA6)	0.019183759	+6.556031687
Wnt family member 2 (WNT2)	0.019183759	+5.033014902
Integral membrane protein 2A (ITM2A)	0.019183759	+4.723138339
Chimerin 2 (CHN2)	0.019183759	+3.92587876
Neurotensin receptor 1 (NTSR1)	0.019183759	-6.248658287
ADAMTS like 2 (ADAMTSL2)	0.019628971	+7.780553422
Amyloid beta precursor protein binding family B member 1 interacting protein (APBB1IP)	0.019639631	-7.017912333
Dorsal inhibitory axon guidance protein (DRAXIN)	0.020025012	+2.557992208
Calmegin (CLGN)	0.020048025	+6.391195835
Zinc finger DHHC-type containing 23 (ZDHHC23)	0.0200672	+3.937549502
Activin A receptor type 1C (ACVR1C)	0.020076821	+6.896134143
Interleukin 19 (IL19)	0.020287607	-5.326530109
FXYD domain containing ion transport regulator 3 (FXVD3)	0.020620199	-5.209047328
Uncharacterized LOC100505501 (LOC100505501)	0.020894998	+7.034818379
GNG12, DIRAS3 and WLS antisense RNA 1 (GNG12-AS1)	0.020894998	+2.186262211
Carbonic anhydrase 2 (CA2)	0.021321458	+5.502972825
Fatty acid 2-hydroxylase (FA2H)	0.021435722	+6.020058088
Latent transforming growth factor beta binding protein 1 (LTBP1)	0.023009768	+2.560178651
Matrix metalloproteinase 28 (MMP28)	0.023009768	-5.530467698
T-box transcription factor 1 (TBX1)	0.023161174	+8.968672143
Anoctamin 3 (ANO3)	0.023460756	+6.340273001
Potassium calcium-activated channel subfamily M alpha 1 (KCNMA1)	0.023650785	-3.553247509
Sorbin and SH3 domain containing 2 (SORBS2)	0.024347765	-3.030962817
Secretin (SCT)	0.025753503	+8.117641592
Cholinergic receptor nicotinic alpha 9 subunit (CHRNA9)	0.026385919	+8.379813006
Complement factor I (CFI)	0.026841095	+4.913524163
Refilin B (RFLNB)	0.026957731	+4.574027135
Synaptotagmin 6 (SYT6)	0.028468155	+7.442006972
Zinc finger protein 365 (ZNF365)	0.028866145	+3.632508505
Forkhead box D2 (FOXD2)	0.029037775	-3.100795405
STEAP2 metalloproteinase (STEAP2)	0.02909787	+4.968792323
H2.0 like homeobox (HLX)	0.029286056	+7.711933216
Nuclear receptor subfamily 2 group E member 1 (NR2E1)	0.029286056	-5.732073114
Signal peptide, CUB domain and EGF like domain containing 2 (SCUBE2)	0.029727446	+4.034754536
Protein phosphatase 1 regulatory subunit 12A (PP1R12A)	0.029727446	-2.564706175
Brain abundant membrane attached signal protein 1 (BASP1)	0.029840515	+8.338916956
Microfibril associated protein 4 (MFAP4)	0.030568839	+6.129343647
Sprouty RTK signaling antagonist 3 (SPRY3)	0.031957506	+1.741359161
Zinc finger protein 90 (ZNF90)	0.031999308	+6.227784009
Retinoic acid early transcript 1E (RAET1E)	0.03238124	-4.569245245
Long intergenic non-protein coding RNA 2582 (LINC02582)	0.032497415	+6.560307251

Tetraspanin 5 (TSPAN5)	0.032497415	+3.678671812
Nuclear factor, erythroid 2 like 3 (NFE2L3)	0.034276457	+3.299588932
Calcium voltage-gated channel auxiliary subunit gamma 4 (CACNG4)	0.035691747	+6.241977019
UDP-GlcNAc:betaGal beta-1,3-N-acetylglucosaminyltransferase 3 (B3GNT3)	0.035844867	-4.635132453
Tachykinin receptor 1 (TACR1)	0.035860605	+6.607741735
Protocadherin 18 (PCDH18)	0.036130505	+2.331750695
Solute carrier family 16 member 10 (SLC16A10)	0.036400367	+5.351611378
Transmembrane protein 200A (TMEM200A)	0.036601994	+7.479801369
Frizzled class receptor 9 (FZD9)	0.036777514	+3.314199656
Calbindin 1 (CALB1)	0.037586176	+5.697774222
Embryonic stem cell related (ESRG)	0.037586176	+5.522144854
Polypeptide N-acetylgalactosaminyltransferase 16 (GALNT16)	0.037586176	+3.764810117
Gap junction protein beta 2 (GJB2)	0.037931241	-5.778579457
Chromogranin B (CHGB)	0.038400874	+5.916577794
Renalase, FAD dependent amine oxidase (RNLS)	0.038804413	+2.341724653
Forkhead box C2 (FOXC2)	0.039282289	+8.808793575
EMI domain containing 1 (EMID1)	0.040524389	+3.322712913
Growth arrest specific 1 (GAS1)	0.040985974	+2.995577618
Prostaglandin E receptor 2 (PTGER2)	0.042861169	+7.417178482
Family with sequence similarity 160 member A1 (FAM160A1)	0.042861169	+7.28007243
Transmembrane protein 255A (TMEM255A)	0.042861169	+5.955840607
RAB3B, member RAS oncogene family (RAB3B)	0.042861169	+4.085222416
Hydroxysteroid 17-beta dehydrogenase 2 (HSD17B2)	0.044046263	-3.602154477
Paired like homeodomain 1 (PITX1)	0.04479021	+3.933883908
Transmembrane protein 40 (TMEM40)	0.045519184	-3.520496782
Adenylate kinase 5 (AK5)	0.045597799	+4.153847587
Von Willebrand factor A domain containing 1 (VWA1)	0.045597799	+2.997790727
Chromosome 2 open reading frame 66 (C2orf66)	0.048456655	+6.192068096
RAS like family 12 (RASL12)	0.048456655	+5.559620286
Adhesion G protein-coupled receptor G6 (ADGRG6)	0.048456655	+4.894174692
Fasciculation and elongation protein zeta 1 (FEZ1)	0.048456655	+3.921821658
STT3A antisense RNA 1 (STT3A-AS1)	0.048456655	+3.921821658
Gap junction protein gamma 3 (GJC3)	0.048456655	-2.73125512
Interferon regulatory factor 6 (IRF6)	0.048456655	-3.820299195
Intercellular adhesion molecule 1 (ICAM1)	0.048484002	+4.587348123
Sodium voltage-gated channel alpha subunit 9 (SCN9A)	0.048681242	+3.401813162
Serine protease 30, pseudogene (PRSS30P)	0.049350963	+7.819538738
Goosecoid homeobox (GSC)	0.049350963	+7.102618128
Dynamin 1 (DNM1)	0.049350963	+4.380718935
Glutamate metabotropic receptor 4 (GRM4)	0.049350963	+4.127677713
PIK3CD antisense RNA 2 (PIK3CD-AS1)	0.049350963	+4.107202991
Dickkopf WNT signaling pathway inhibitor 2 (DKK2)	0.049350963	+3.359599947
SRY-box transcription factor 15 (SOX15)	0.049350963	-3.039179

Supplementary Table 6.3 List of transcripts for riluzole responders at baseline

Gene Name	p-adj	log2FC
Myosin binding protein C, slow type (MYBPC1)	8.75E-11	-6.197276306
Carboxypeptidase vitellogenic like (CPVL)	7.08E-05	+4.657685023
Coiled-coil domain containing 3 (CCDC3)	1.54E-04	+6.541867636
Four and a half LIM domains 1 (FHL1)	1.54E-04	+3.645152433
Gap junction protein gamma 1 (GJC1)	1.54E-04	-3.305787665
TLR4 interactor with leucine rich repeats (TRIL)	0.001136471	+6.475675559
Apolipoprotein L4 (APOL4)	0.002574136	+2.910621365
KRAB box domain containing 1 (KRBOX1)	0.002814655	+10.47124394
ADAM metallopeptidase with thrombospondin type 1 motif 5 (ADAMTS5)	0.002914446	+8.701666328
C-C motif chemokine ligand 2 (CCL2)	0.004179732	+6.839351152
Adrenoceptor alpha 2A (ADRA2A)	0.004277329	+6.3874973
SFT2 domain containing 3 (SFT2D3)	0.004487797	+10.36994819
CD200 molecule (CD200)	0.006407641	+8.71303089
Glutaminy-peptide cyclotransferase (QPCT)	0.006916153	+5.087518683
PAX8 antisense RNA 1 (PAX8-AS1)	0.006916153	-4.552510636
Coagulation factor VIII associated 2 (F8A2)	0.007493098	+9.487077344
Major histocompatibility complex, class II, DR alpha (HLA-DRA)	0.008079026	+9.38598501
Amphiregulin (AREG)	0.008666302	-9.477991014
Small proline rich protein 2E (SPRR2E)	0.009157764	-8.973458112
Iroquois homeobox 1 (IRX1)	0.017974946	-5.531647015
Contactin 1 (CNTN1)	0.018830004	+7.299183979
Serine protease 30, pseudogene (PRSS30P)	0.021051256	+8.226443081
Dynamin 1 (DNM1)	0.023990851	+5.304723501
Ras interacting protein 1 (RASIP1)	0.024429744	+7.166083638
NFAT activating protein with ITAM motif 1 (NFAM1)	0.024429744	+4.407210903
Claudin 10 (CLDN10)	0.024429744	-4.885149921
TNF alpha induced protein 6 (TNFAIP6)	0.029297762	+3.415148058
Collagen type I alpha 1 chain (COL1A1)	0.029297762	+2.310305576
STEAP family member 1B (STEAP1B)	0.033048746	+3.475586331
Uncharacterized LOC401312 (LOC401312)	0.033048746	+3.475586331
Paired box 8 (PAX8)	0.037222303	-3.922783344
Solute carrier family 40 member 1 (SLC40A1)	0.041567054	+6.623117218
Intercellular adhesion molecule 1 (ICAM1)	0.041567054	+3.419195705
Internexin neuronal intermediate filament protein alpha (INA)	0.04952992	+4.974606317
Olfactomedin 2 (OLFM2)	0.04952992	+3.154189243
Collagen type XVII alpha 1 chain (COL17A1)	0.04952992	-5.431186952
Serine protease 3 (PRSS3)	0.04952992	-8.230314743

Supplementary Table 6.4 List of transcripts for S[+]-apomorphine responders after treatment

Gene Name	p-adj	log2FC
MROH7-TTC4 readthrough (MROH7-TTC4)	6.57E-23	-11.38128914
Junctophilin 1 (JPH1)	5.94E-11	+4.276318278
DNAJC9 antisense RNA 1 (DNAJC9-AS1)	1.64E-07	-8.199912521
Adrenoceptor alpha 2A (ADRA2A)	2.89E-05	+7.426120223
SFT2 domain containing 3 (SFT2D3)	1.07E-04	+23.11804561
ADAM metallopeptidase with thrombospondin type 1 motif 5 (ADAMTS5)	1.47E-04	+9.204241492
Long intergenic non-protein coding RNA 1679 (LINC01679)	1.47E-04	+2.944214766
Phospholipase B domain containing 1 (PLBD1)	2.23E-04	+3.971488928
Crumbs cell polarity complex component 2 (CRB2)	2.23E-04	-4.893229397
RDH10 antisense RNA 1 (RDH10-AS1)	3.92E-04	+4.667336329
Latent transforming growth factor beta binding protein 1 (LTBP1)	4.25E-04	+3.415163978
LDOC1 regulator of NFkB signaling (LDOC1)	4.85E-04	+4.796165625
Dynamin 1 (DNM1)	4.85E-04	+3.572133266
Coiled-coil domain containing 3 (CCDC3)	5.63E-04	+6.051031322
Double C2 domain beta (DOC2B)	6.02E-04	+5.453542354
Dachsous cadherin-related 1 (DCHS1)	8.47E-04	+4.277059286
Collagen type IV alpha 1 chain (COL4A1)	0.001156215	+7.180282765
Phosphoinositide-3-kinase regulatory subunit 5 (PIK3R5)	0.001246272	+5.320719748
C-C motif chemokine ligand 2 (CCL2)	0.001372413	+7.428486267
Glutamyl-peptide cyclotransferase (QPCT)	0.001451564	+6.339049443
NmrA like redox sensor 2, pseudogene (NMRAL2P)	0.001922725	+5.933742161
Desmoplakin (DSP)	0.002194708	+4.709879493
Collagen type V alpha 3 chain (COL5A3)	0.002751126	+9.326740914
TLR4 interactor with leucine rich repeats (TRIL)	0.002789913	+5.823682542
Survival associated mitochondrial melanoma specific oncogenic non-coding RNA (SAMMSON)	0.002846526	-4.625995309
Cytochrome P450 family 1 subfamily A member 1 (CYP1A1)	0.002954449	+5.802049984
Nuclear factor, erythroid 2 like 3 (NFE2L3)	0.004792913	+2.187075745
Solute carrier family 1 member 3 (SLC1A3)	0.005120672	+9.791593878
ADAM metallopeptidase with thrombospondin type 1 motif 2 (ADAMTS2)	0.005320126	+5.216328118
Interaction protein for cytohesin exchange factors 1 (IPCEF1)	0.005320126	+4.704671463
Secreted and transmembrane 1 (SECTM1)	0.005320126	+3.904561871
Delta 4-desaturase, sphingolipid 2 (DEGS2)	0.005320126	-7.626497404
Solute carrier family 13 member 1 (SLC13A1)	0.00622844	-6.886920138
Nuclear receptor interacting protein 3 (NRIP3)	0.006781872	+2.890443646
Syntaxin 11 (STX11)	0.008309106	+7.170240215
Solute carrier family 40 member 1 (SLC40A1)	0.009459346	+6.849362197
Potassium voltage-gated channel modifier subfamily V member 1 (KCNV1)	0.009785573	+2.792706935
Collagen type I alpha 1 chain (COL1A1)	0.010519386	+2.647279169
Mesenteric estrogen dependent adipogenesis (MEDAG)	0.011053867	+6.406813559
Insulin like growth factor binding protein 5 (IGFBP5)	0.011359097	+4.332778769
Olfactomedin 2 (OLFM2)	0.011359097	+2.999113492
ADAMTS like 2 (ADAMTSL2)	0.011592694	+7.722446869
Vitrin (VIT)	0.011592694	+5.438384317

RAB38, member RAS oncogene family (RAB38)	0.011592694	+4.772301733
Forkhead box P2 (FOXP2)	0.011592694	+3.601062118
KH RNA binding domain containing, signal transduction associated 3 (KHDRBS3)	0.011592694	-6.640868249
Ameloblastin (AMBN)	0.011965301	+8.03689201
Tetratricopeptide repeat domain 12 (TTC12)	0.012282047	-6.107596583
Phospholipase A and acyltransferase 5 (PLAAT5)	0.014494758	+6.371598823
Transmembrane protein 119 (TMEM119)	0.015330643	+3.297006311
Glucosaminyl (N-acetyl) transferase 1 (GCNT1)	0.015732894	+5.193682073
Tudor domain containing 9 (TDRD9)	0.017759012	+6.019462594
Intercellular adhesion molecule 1 (ICAM1)	0.018443237	+4.406622555
ArfGAP with GTPase domain, ankyrin repeat and PH domain 11 (AGAP11)	0.019568118	+5.113643965
Wnt family member 2 (WNT2)	0.022953617	+4.431686027
Contactin 1 (CNTN1)	0.024648739	+6.505213819
Uncharacterized LOC25845 (PP7080)	0.02564762	-2.082370978
Transmembrane protein 26 (TMEM26)	0.02691717	+2.580199906
Versican (VCAN)	0.02803273	+5.219031205
Taxilin gamma pseudogene, Y-linked (TXLNGY)	0.02803273	-7.329620929
CD200 molecule (CD200)	0.029070992	+7.962869137
Glutamine amidotransferase like class 1 domain containing 3A (GATD3A)	0.029070992	+3.813851875
Glutamine amidotransferase like class 1 domain containing 3B (GATD3B)	0.029070992	+3.813851875
OCIA domain containing 2 (OCIAD2)	0.029937807	+4.903702192
Interleukin 4 induced 1 (IL4I1)	0.035215436	+4.620940691
Four and a half LIM domains 1 (FHL1)	0.035215436	+3.490191732
Internexin neuronal intermediate filament protein alpha (INA)	0.039685863	+4.529023972
Ubiquitin D (UBD)	0.043565794	+7.406251402
EPH receptor B2 (EPHB2)	0.043565794	+5.84102321
Adhesion G protein-coupled receptor G6 (ADGRG6)	0.043565794	+3.336702961
Fibroblast activation protein alpha (FAP)	0.043565794	+2.94819189
Hornerin (HRNR)	0.043565794	+2.934656335
Growth differentiation factor 7 (GDF7)	0.043565794	-4.088124854

Supplementary Table 6.5 List of transcripts for andrographolide responders after treatment

Gene Name	p-adj	log2FC
Myosin binding protein C, slow type (MYBPC1)	5.53E-18	-6.655767008
Carboxypeptidase vitellogenic like (CPVL)	2.18E-15	+5.41195762
NmrA like redox sensor 2, pseudogene (NMRAL2P)	1.10E-12	+9.338023397
Carboxylesterase 1 (CES1)	1.24E-08	+9.949499094
SFT2 domain containing 3 (SFT2D3)	9.48E-06	+24.26062349
STEAP family member 1B (STEAP1B)	9.48E-06	+3.902565477
Uncharacterized LOC401312 (LOC401312)	9.48E-06	+3.902565477
LDOC1 regulator of NFKB signaling (LDOC1)	7.89E-05	+7.212799095
Serine protease 3 (PRSS3)	1.93E-04	-8.687723916
SRY-box transcription factor 2 (SOX2)	2.39E-04	+11.34861719
Small proline rich protein 2E (SPRR2E)	2.39E-04	-10.54639686
TLR4 interactor with leucine rich repeats (TRIL)	3.53E-04	+6.721979438
Phospholipase B domain containing 1 (PLBD1)	3.53E-04	+4.435892702
DNAJC9 antisense RNA 1 (DNAJC9-AS1)	0.001217	-7.239502163
Chimerin 2 (CHN2)	0.001404101	+4.412172806
Coiled-coil domain containing 3 (CCDC3)	0.001604701	+5.922259092
Internexin neuronal intermediate filament protein alpha (INA)	0.002498685	+5.370361973
Germ cell associated 1 (GSG1)	0.003825078	-6.333685653
Espin like (ESPNL)	0.004156523	+7.527424029
Cadherin 2 (CDH2)	0.007161919	+7.989598045
ITGB2 antisense RNA 1 (ITGB2-AS1)	0.007161919	-4.744713845
C-C motif chemokine ligand 2 (CCL2)	0.007480533	+7.17833053
C-X-C motif chemokine ligand 12 (CXCL12)	0.007564936	+9.180405459
Coagulation factor II thrombin receptor like 2 (F2RL2)	0.007564936	+4.326170036
RAB6D, member RAS oncogene family (RAB6D)	0.007908464	-9.81185794
Putative uncharacterized protein DKFZp434K191 (LOC102725072)	0.007947663	-5.863001518
Anoctamin 3 (ANO3)	0.008174977	+6.30663354
Small proline rich protein 2D (SPRR2D)	0.008816154	-6.069047748
KRAB box domain containing 1 (KRBOX1)	0.010496548	+10.35012664
Chimerin 2 (CHN2)	0.010496548	+7.006016547
Collagen type IV alpha 1 chain (COL4A1)	0.01065406	+7.717072921
Survival associated mitochondrial melanoma specific oncogenic non-coding RNA (SAMMSON)	0.01065406	-4.190623586
Solute carrier family 7 member 2 (SLC7A2)	0.011162432	+7.210451895
Glucosaminyl (N-acetyl) transferase 1 (GCNT1)	0.011162432	+6.296216738
LYPLAL1 divergent transcript (LYPLAL1-DT)	0.011162432	+5.799376043
Armadillo repeat containing 12 (ARMC12)	0.011162432	+2.798279563
Sorting nexin 32 (SNX32)	0.011162432	+2.795905253
Adenylate kinase 5 (AK5)	0.012506721	+3.95523671
Tumour protein D52 (TPD52)	0.016527947	+4.435176412
Four and a half LIM domains 1 (FHL1)	0.016738343	+4.316473962
Glutamate metabotropic receptor 3 (GRM3)	0.017283931	+9.527077284
Inhibitor of DNA binding 4, HLH protein (ID4)	0.017283931	+6.158721241
Laminin subunit alpha 1 (LAMA1)	0.017283931	+4.788822446
Sortilin 1 (SORT1)	0.017283931	+2.206703854
EBF transcription factor 3 (EBF3)	0.018717902	+6.969438908
EPH receptor A3 (EPHA3)	0.018717902	+5.589942007

OCIA domain containing 2 (OCIAD2)	0.018717902	+5.261202234
Integrin subunit beta 4 (ITGB4)	0.018717902	-4.90299909
Syntaxin 11 (STX11)	0.020401465	+7.924135529
BTB domain containing 11 (BTBD11)	0.021775961	+9.692294422
Solute carrier family 40 member 1 (SLC40A1)	0.021775961	+7.527814082
Macrophage stimulating 1 receptor (MST1R)	0.022454252	-4.273900888
G protein subunit alpha o1 (GNAO1)	0.022570255	+8.630524467
Junctophilin 1 (JPH1)	0.022937401	+4.438521338
Dachsous cadherin-related 1 (DCHS1)	0.022937401	+4.292601762
Serine protease 30, pseudogene (PRSS30P)	0.024218271	+8.015799729
Leucine rich repeat neuronal 2 (LRRN2)	0.024218271	+5.588540925
Adrenoceptor alpha 2A (ADRA2A)	0.025010364	+6.829047891
Contactin 1 (CNTN1)	0.025441132	+7.002407466
FXFD domain containing ion transport regulator 3 (FXFD3)	0.025711975	-5.078208119
Matrilin 3 (MATN3)	0.026343651	+3.663104736
ADAMTS like 2 (ADAMTSL2)	0.026652392	+7.088125686
Neurexin 1 (NRXN1)	0.026652392	+5.889619939
von Willebrand factor A domain containing 1 (VWA1)	0.026652392	+3.157176192
Prostaglandin E receptor 2 (PTGER2)	0.027610957	+7.998892499
long intergenic non-protein coding RNA 678 (LINC00678)	0.027610957	+7.945647584
Wnt family member 2 (WNT2)	0.028319611	+5.0677205
Vitrin (VIT)	0.029016647	+7.126890559
CD200 molecule (CD200)	0.029025197	+8.817830386
Tripartite motif containing 71 (TRIM71)	0.029025197	+6.496305894
Lactoperoxidase (LPO)	0.030257864	-4.830643826
Goosecoid homeobox (GSC)	0.03271073	+7.562294798
Tudor domain containing 9 (TDRD9)	0.03271073	+5.806443641
MER proto-oncogene, tyrosine kinase (MERTK)	0.03271073	+4.352732614
5-hydroxytryptamine receptor 7 (HTR7)	0.034368709	+6.657587311
Double C2 domain beta (DOC2B)	0.036151577	+5.435922058
Activin A receptor type 1C (ACVR1C)	0.037309712	+6.831595266
Dihydropyrimidinase like 4 (DPYSL4)	0.037503251	+4.129583807
SSTR5 antisense RNA 1 (SSTR5-AS1)	0.037503251	-6.824150197
Phospholipase A and acyltransferase 5 (PLAAT5)	0.038369645	+6.728959938
Interleukin 4 induced 1 (IL4I1)	0.038857481	+4.994956164
Interaction protein for cytohesin exchange factors 1 (IPCEF1)	0.038873144	+6.33908254
Leucine rich repeat containing 74B (LRRC74B)	0.038873144	-2.641269345
Pellino E3 ubiquitin protein ligase family member 2 (PELI2)	0.039244491	+2.795234908
Neuropeptide Y receptor Y1 (NPY1R)	0.042271074	+4.555307089
Neuronal cell adhesion molecule (NRCAM)	0.042374762	+5.034850362
Calcium voltage-gated channel auxiliary subunit gamma 4 (CACNG4)	0.042804152	+6.166086738
Neurofilament heavy (NEFH)	0.042804152	+3.778575565
Sortilin related VPS10 domain containing receptor 3 (SORCS3)	0.043374265	-6.341735895
Neuronal pentraxin 2 (NPTX2)	0.044681278	+8.571252548
Solute carrier family 13 member 1 (SLC13A1)	0.044788439	-5.201625259
Carboxypeptidase X, M14 family member 2 (CPXM2)	0.045611997	+6.497485699
Calpain 6 (CAPN6)	0.046747353	+4.638366878
Amyloid beta precursor protein binding family B member 1 interacting protein (APBB1IP)	0.046809976	-6.666659047
Forkhead box P2 (FOXP2)	0.046997492	+2.945723665
Myosin VI (MYO6)	0.047187182	-2.934074171

Dynamin 1 (DNM1)	0.047402788	+4.650283167
Thrombospondin 2 (THBS2)	0.047523185	+4.420340548
Nuclear receptor subfamily 0 group B member 1 (NR0B1)	0.049366662	+8.862866057
Potassium voltage-gated channel modifier subfamily G member 3 (KCNG3)	0.049537685	+4.088234048
Transient receptor potential cation channel subfamily C member 6 (TRPC6)	0.049537685	+3.766907546
Protocadherin 18 (PCDH18)	0.049537685	+2.51931946
Gap junction protein gamma 3 (GJC3)	0.049537685	-3.328735561
Cholinergic receptor nicotinic alpha 9 subunit (CHRNA9)	0.049836569	+8.196343727
Prune homolog 2 with BCH domain (PRUNE2)	0.049836569	+7.309802365
Transmembrane protein with EGF like and two follistatin like domains 2 (TMEFF2)	0.049836569	+6.396418727
Meiosis specific with OB-fold (MEIOB)	0.049836569	+5.318416254

Supplementary Table 6.6 List of transcripts for riluzole responders after treatment

Gene Name	p-adj	log2FC
MROH7-TTC4 readthrough (NMD candidate MROH7-TTC4)	5.43E-12	-11.04851491
Myosin binding protein C, slow type (MYBPC1)	1.51E-07	-6.323725454
SFT2 domain containing 3 (SFT2D3)	1.21E-05	+11.24606608
Chromosome 17 open reading frame 102 (C17ORF102)	2.56E-05	+10.73414111
Carboxypeptidase vitellogenic like (CPVL)	1.78E-04	+4.85541514
DNAJC9 antisense RNA 1 (DNAJC9-AS1)	1.87E-04	-8.801317356
TLR4 interactor with leucine rich repeats (TRIL)	2.49E-04	+6.782011446
PAX8 antisense RNA 1 (PAX8-AS1)	4.02E-04	-5.325106917
Coiled-coil domain containing 3 (CCDC3)	4.26E-04	+6.884642001
ADAM metallopeptidase with thrombospondin type 1 motif 5 (ADAMTS5)	5.81E-04	+8.833388361
Glutathione S-transferase mu 1 (GSTM1)	5.81E-04	-24.30508922
KRAB box domain containing 1 (KRBOX1)	6.44E-04	+11.08032379
SRY-box transcription factor 2 (SOX2)	8.85E-04	+9.246835155
Adrenoceptor alpha 2A (ADRA2A)	9.77E-04	+6.763777351
Coagulation factor VIII associated 2 (F8A2)	0.001323072	+23.18943243
Major histocompatibility complex, class II, DR alpha (HLA-DRA)	0.001434484	+9.628079854
RAB6D, member RAS oncogene family (RAB6D)	0.001465996	-23.00037097
G protein subunit alpha o1 (GNAO1)	0.001477552	+9.011109889
Junctophilin 1 (JPH1)	0.001763939	+4.204946062
C-X-C motif chemokine receptor 1 (CXCR1)	0.002018324	-22.51885004
Four and a half LIM domains 1 (FHL1)	0.002535113	+3.664921282
Amphiregulin (AREG)	0.002535113	-9.734385923
C-C motif chemokine ligand 2 (CCL2)	0.002668901	+7.16083677
Serine protease 30, pseudogene (PRSS30P)	0.003100568	+8.837350722
Dynein axonemal assembly factor 1 (DNAAF1)	0.003100568	-4.856247627
Small proline rich protein 2E (SPRR2E)	0.003398201	-8.866020757
Stratifin (SFN)	0.00407685	-7.944018396
Ubiquitin D (UBD)	0.004657473	+8.451217741
CD200 molecule (CD200)	0.004657473	+8.436403106
Ring finger protein 152 (RNF152)	0.006466836	+6.624953264
Tetratricopeptide repeat domain 12 (TTC12)	0.009633449	-6.366218046
Glutamyl-peptide cyclotransferase (QPCT)	0.010616676	+5.153864521
Serine protease 3 (PRSS3)	0.011473812	-8.633081812
Iroquois homeobox 1 (IRX1)	0.012024688	-5.812189735
Glutamate metabotropic receptor 3 (GRM3)	0.01316508	+9.615290986
Leucine rich repeat neuronal 2 (LRRN2)	0.013816405	+6.131825081
LDOC1 regulator of NFKB signaling (LDOC1)	0.013816405	+5.391171568
Ras interacting protein 1 (RASIP1)	0.014138704	+6.948133174
Fibrous sheath interacting protein 1 (FSIP1)	0.014958776	-6.779024818
Glutamate ionotropic receptor NMDA type subunit 2B (GRIN2B)	0.014958776	-9.559709202
Protocadherin gamma subfamily B, 7 (PCDHGB7)	0.014966689	+5.512541664
C-X-C motif chemokine ligand 12 (CXCL12)	0.017160601	+7.402073902
Dynamin 1 (DNM1)	0.017823715	+3.853824424
Solute carrier family 40 member 1 (SLC40A1)	0.01830228	+7.032043652
Germ cell associated 1 (GSG1)	0.01830228	-6.934963005
Myeloma overexpressed (MYEOV)	0.018928413	-4.16171165

Odd-skipped related transcription factor 2 (OSR2)	0.018928413	-6.269631913
Neuronal pentraxin 2 (NPTX2)	0.02031555	+7.550179614
Protein tyrosine phosphatase receptor type Z1 (PTPRZ1)	0.02031555	-4.422823946
EBF transcription factor 3 (EBF3)	0.023822419	+7.190804467
Sialophorin (SPN)	0.025599902	-6.103698694
Thiosulfate sulfurtransferase like domain containing 1 (TSTD1)	0.027056929	+8.500324043
Contactin 1 (CNTN1)	0.027056929	+6.981266671
CD52 molecule (CD52)	0.027056929	-6.754518873
Delta 4-desaturase, sphingolipid 2 (DEGS2)	0.027056929	-7.980451555
Testis expressed 29 (TEX29)	0.031444596	-9.121256677
Transmembrane protein with EGF like and two follistatin like domains 2 (TMEFF2)	0.031689447	+5.727259587
Phospholipase B domain containing 1 (PLBD1)	0.031689447	+3.903449167
Apolipoprotein L4 (APOL4)	0.031689447	+2.853298383
Dachsous cadherin-related 1 (DCHS1)	0.032728698	+4.105705711
Anoctamin 3 (ANO3)	0.033434891	+6.547260002
STEAP family member 1B (STEAP1B)	0.033434891	+3.752060585
Uncharacterized LOC401312 (LOC401312)	0.033434891	+3.752060585
TNF alpha induced protein 6 (TNFAIP6)	0.034625779	+3.440783696
Internexin neuronal intermediate filament protein alpha (INA)	0.037258324	+5.317862131
Sclerostin domain containing 1 (SOSTDC1)	0.040581837	+7.629041029
Solute carrier family 7 member 14 (SLC7A14)	0.040581837	+6.251695668
Interaction protein for cytohesin exchange factors 1 (IPCEF1)	0.040581837	+4.863426297
LY6/PLAUR domain containing 6 (LYPD6)	0.041554689	+4.79344532
Tumour protein D52 (TPD52)	0.041554689	4.132311902
Small proline rich protein 2D (SPRR2D)	0.041554689	-4.931351797
KH RNA binding domain containing, signal transduction associated 3 (KHDRBS3)	0.041554689	-6.634561555
Long intergenic non-protein coding RNA 1550 (LINC01550)	0.042433096	+3.663243328
Paired box 8 (PAX8)	0.042433096	-5.313428327
Collagen type IV alpha 1 chain (COL4A1)	0.043203602	+5.929697776
Interleukin 4 induced 1 (IL4I1)	0.043353513	+5.002696422
Desmoglein 2 (DSG2)	0.043443442	-7.630544855
Tumour protein p53 inducible protein 11 (TP53I11)	0.044712004	+5.899842095
Gamma-aminobutyric acid type A receptor alpha3 subunit (GABRA3)	0.0450821	-8.287075695
OTU deubiquitinase 7A (OTUD7A)	0.047167107	+3.619965148
Hepatocyte nuclear factor 4 alpha (HNF4A)	0.047167107	-6.079489532
Interleukin 19 (IL19)	0.047167107	-6.455316248
ADAM metallopeptidase with thrombospondin type 1 motif 2 (ADAMTS2)	0.048622136	+4.692773528
Matrilin 3 (MATN3)	0.048785123	+4.009601003